INFORMATION TO USERS

This manuscript has been reproduced from the microfilm master. UMI films the text directly from the original or copy submitted. Thus, some thesis and dissertation copies are in typewriter face, while others may be from any type of computer printer.

The quality of this reproduction is dependent upon the quality of the copy submitted. Broken or indistinct print, colored or poor quality illustrations and photographs, print bleedthrough, substandard margins, and improper alignment can adversely affect reproduction.

In the unlikely event that the author did not send UMI a complete manuscript and there are missing pages, these will be noted. Also, if unauthorized copyright material had to be removed, a note will indicate the deletion.

Oversize materials (e.g., maps, drawings, charts) are reproduced by sectioning the original, beginning at the upper left-hand corner and continuing from left to right in equal sections with small overlaps. Each original is also photographed in one exposure and is included in reduced form at the back of the book.

Photographs included in the original manuscript have been reproduced xerographically in this copy. Higher quality 6" x 9" black and white photographic prints are available for any photographs or illustrations appearing in this copy for an additional charge. Contact UMI directly to order.

UMI

A Bell & Howell Information Company
300 North Zeeb Road, Ann Arbor MI 48106-1346 USA
313/761-4700 800/521-0600

MAGMATIC ACCRETION OF THE UPPER OCEANIC CRUST

by

Devamonie Dayanithie Naidoo

A dissertation submitted in partial fulfillment of the requirements for the degree of

Doctor of Philosophy

University of Washington

1998

Approved by _____
Chairperson of Supervisory Committee

Program Authorized
to Offer Degree School of Oceanography

Date January 23, 1998

Doctoral Dissertation

In presenting this dissertation in partial fulfillment of the requirements for the Doctoral degree at the University of Washington, I agree that the Library shall make its copies freely available for inspection. I further agree that extensive copying of this dissertation is allowable only for scholarly purposes, consistent with "fair use" as prescribed in the U.S. Copyright Law. Requests for copying or reproduction of this dissertation may be referred to University Microfilms, 1490 Eisenhower Place, P.O. Box 975, Ann Arbor, MI 48106, to whom the author has granted "the right to reproduce and sell (a) copies of the manuscript in microform and/or (b) printed copies of the manuscript made from microform."

Signature _____

Date 18 December 1997

University of Washington

Abstract

MAGMATIC ACCRETION OF THE UPPER OCEANIC CRUST

by Devamonie Dayanithie Naidoo

Chairperson of the Supervisory Committee:
Professor John R. Delaney
School of Oceanography

The focus of this work is the temporal and spatial evolution of upper oceanic crust accreted at the southern Juan de Fuca Ridge (JdFR), an intermediate rate spreading center. The area of concentrated study is along the steep escarpment forming the south-facing wall of the ridge-perpendicular West Blanco Depression (WBD) and exposes crust formed between 1.2 and 1.7 Ma. Data sets utilized include GLORIA, SeaMarc II and high resolution (110 kHz) side scan sonar imagery, multibeam bathymetric maps, and an extensive suite of rock samples, photographs and video coverage obtained with the French submersible *Nautile* along the scarp face. Detailed sections of lava flow morphologies are constructed from 14 dives, and analysis includes interpretation of petrographic and geochemical data within the context of that reconstruction.

In the model proposed, episodes of crustal building are linked to variations in mantle melting conditions and magma resupply with shallow mixing episodes. The upper crustal section accreted in 2-3 major on-axis extrusive stages involving normal (N-type)

mid-ocean ridge basalts (MORBs). Flow types associated with each stage imply an overall decline in effusion rate following a vigorous initial output. This magmatic accretionary process was interrupted at irregular intervals by subsidence and block faulting that resulted in a collage of crustal blocks recognizable as texturally distinct domains within the Deep-Tow sonar imagery.

Superimposed, time-dependent mantle diapiric flow beneath the north-westward migrating JdFR can explain a seamount chain located on the Juan de Fuca plate and the consistent, seamount spacing. Geochemistry of rocks exposed on the scarp is accounted for by batch-melting of a depleted spinel peridotite source (N-type) followed by fractional melting of an amphibolite-veined mantle residue (M-type). With ridge migration, a seamount forms near-axis while N- and M-type MORB sills are injected into the lower section of the upper crust after which massive M-type diabases are intruded at the base. Most recently, off-axis volcanism associated with Parks Plateau emplaced enriched MORBs into the upper crust.

TABLE OF CONTENTS

LIST OF FIGURES

LIST OF PLATES

LIST OF TABLES

POCKET MATERIAL

PREFACE

They that go down to the sea in ships, that do business in great waters;

These see the works of the Lord, and his wonders in the deep.

The Book of Psalms 107:23-24

I dive down into the depth of the ocean of forms,

hoping to gain the perfect pearl of the formless.

from: Gitanjali (Song Offerings)

by: Rabindranath Tagore (1917)

ACKNOWLEDGMENTS

I would like to express my heartfelt gratitude to all those who contributed in many, different ways to this endeavour.

I am greatly appreciative of the support by **R. Sternberg**. I would also like to acknowledge **J. Delaney**, with thanks, for his original conception of the Blanco project and for giving me the opportunity to undertake my first dive on the Endeavour hydrothermal vent field in the early 90's, which will remain vivid in my memory.

I have benefitted tremendously from the expertise of members on my dissertation committee who served at various times and all read some chapters: **J. Deming, R. Holcomb, D. Kelley, J. Karson, S. McCallum, D. McManus, B. Nelson** and **J.-C. Sempéré** - I am grateful for their comments which have improved the quality of this work.

I am deeply indebted to **T. Juteau** who welcomed me warmly to both the Blanconaute mission and the Université de Brest Occidentale (UBO) for subsequent work there and at IFREMER. His leadership of the Blanconaute team (**D. Bideau, O. Dauteuil, G. Man'ach, P. Nehlig, H. Ondreas, M. Tivey and K. Whipple**) made for an unforgettable cruise. I also appreciated the hospitality and assistance of UBO faculty, students and technicians during the summer of 1992 and the efforts of **J. Cotten** in particular, in extracting numbers.

My work has relied on several data sets, some of which were supplied by other researchers. I am grateful to **R. Embley** (NOAA) who generated Sea Beam maps to set specifications for the Blanconaute cruise, to **M. Holmes** (USGS) who shared the original layouts of SeaMARC II imagery, to **P. Johnson** (UW) who provided the optical disks of the GLORIA and SeaMARC II imagery, and to **O. Dauteuil** (CNRS) who made available early results of his Sea Beam processing. **D. Butterfield** (NOAA) also generously contributed USGS geochemical standards.

For my oceanographic field experience, I would like to thank the following Chief Scientists who invited my participation in their programs: **J. Delaney**, **P. Johnson**, **T. Juteau**, **J. Karson**, **J. Karsten**, **F. Spiess**, **M. Tivey**, and **D. Yoerger**. In addition, I also profited from my teaching assignments with **M. Holmes** and **R. Sternberg** who supervised the undergraduate cruises and research projects.

My research experience was broadened considerably by opportunities to attend the Ridge Theoretical Institutes at Tucson and Lake Tahoe, the Inter-RIDGE meetings at Durham and Paris and the AGU meetings in San Francisco. This was made possible by financial support from the **US-RIDGE** committee and **NSF** grants. I would like to thank all of those **colleagues** who spared me time for discussions, responded to my questions and who shared openly of their ideas.

As a by-product of my work, I evolved into a technopeasant through the efforts of **S. Willis** (University of Washington Geological Remote Sensing Group) who introduced me to the fundamentals of image processing, **F. Sajona** (UBO) who demonstrated graphics software, and **S. Veirs** (UW) who up-dated me in Web-craft. **V. Robigou** kindly shared her computer and the Blancotrough photomicrographs, **L. Sylwester** has given help and more during drafting forays, and **T. Watkins** along with the administrative staff has taken care of paperwork. For the rest, I've called upon my **fellow graduate students** who include those with whom I had a chance to work on projects in the Association for Graduate Women in Oceanography.

The completion of this dissertation is really the product of a much longer history than the years in Oceanography. In this regard, I am indebted to my **teachers** at St. Anthony's State Aided Indian High School and Durban Indian Girls Secondary School, in particular to **Sister Meryl** at the former who gave of herself. I am grateful to the late **P.J. Betton** and the late **A.J. Erlank** who engendered my interests in igneous petrology and geochemistry respectively while at the University of Cape Town. I would also like to thank **S. Bloomer** who while at Duke University introduced me to ophiolites - which determined my path here. At the UW, I have been a beneficiary of **A. Ginorio's** inspiring and generous mentorship for which I am sincerely appreciative. She provided a much needed framework on the relation of women and science and the opportunity to work

jointly on her Mentoring Project. In addition, the interaction with the project committee on my College Bound Survey (**J. Antony, M. Brown, M. Elekonich, J. Fournier, A. Ginorio, T. Marshall and H. Remick**) has been an intellectually rewarding experience.

The geological and volcanological spirit was nurtured in me by field trips to Oregon and Hawaii with R. Holcomb, and through field jaunts all over France, northern Spain, the south-western U.S.A. and the Cascades from Garibaldi to Lassen during which I benefited from the companionship of **P. Nehlig**.

The time here would neither have passed by as quickly and nor would the travails of work have faded as rapidly, were it not for the wonderful **office-mates and house-mates**, and circles of **friends** in Seattle (**E. Boss, G. Daum, L. Karp, L. Landrum, C. Lee and M. McCarthy among others**) and scattered over the U.S.A. (**A. Shah,** ...) and the globe (**B. Greiser-Johns,** ...). In particular, I thank my sisters of colour - **V. Date, R. Kalapurakal, M. LaMarre, L. Shutt and B. Subramaniam** - who remind me that the rainbow is enuf ...

Finally, I am grateful to **D. Naidoo** for passing on her raw intellect, creative talents and intense passion; to **V.G. Naidoo** who taught me to live with compassion through his lifelong service in the community, who shared with me his commitment to truth and justice, and from whom I learned to follow my convictions with courage; to **K. Pahliney** for her support especially in assuming all responsibilities at home; and to **G. Pahliney** and **A. Pahliney** who will perpetuate the memory.

And to them all, I give thanks - for their understanding of my absence from their lives.

This study has been supported by NSF grants OCE 86-14644, OCE 89-19244 and OCE 93-17611 to **J. Delaney**. In the last years, I was sustained by research assistantships from the **Northwest Center for Research on Women** (NWCROW), the **Equal Opportunity Office** (EOP), and the **School of Oceanography**.

15 August 1997

DEDICATION

For my parents

INTRODUCTION

The upper oceanic crust, which covers over 70% of the earth's surface, appears deceptively simple (BVSP, 1981) but there are some very fundamental gaps in our understanding of its formation and evolution. It is known that the interplay (Karson and Winters, 1992; Haymon, 1997) of volcanic, structural and hydrothermal activity (Macdonald, 1982; 1983) accretes the oceanic basement, that spatial and temporal variations in these processes are reflected in the crustal architecture (e.g. Perfit et al., 1994; Cannat et al., 1995) and that the magma budget is key to lithospheric attributes (e.g. the thickness of the oceanic basement and whether it will be laterally continuous or non-uniform - Chen, 1992). However, the mechanisms and conditions of vertical mass transfer is not as well understood and for this reason, only magmatic accretion is examined in this study.

The role of magmatism in shaping the internal structure as well as other physical and chemical characteristics of the upper crust has been gauged from monitoring (Embley et al., 1995), observing (Fornari and Embley, 1995), and/or sampling (Reynolds et al., 1992; Rubin et al., 1994) the ridge axis and submarine scarps (Hekinian et al., 1993), as well as by hard-rock drilling (Pezard et al., 1992) and off-axis dredging (Perfit et al., 1994; Batiza et al., 1996). My dissertation presents such research from three perspectives - tectonics, flow morphology and lava composition - ranging from the regional to the outcrop scale. These indicators are examined along the north scarp of the West Blanco Depression where the crustal exposure was created at the intermediate spreading rate, southern Juan de Fuca Ridge (JdFR) over the last 2 Ma. The centrally located site under study was formed over 1.2 Ma to 1.7 Ma (based on a 29 mm/yr half spreading rate). The introduction identifies the main questions addressed along with a brief description of

salient findings on these problems from previous studies, and finally gives an overview of the work undertaken here.

Is there distinctly "normal" and "anomalous", upper oceanic crust?

Fracture zone scarps afford a natural means of gaining direct access to the oceanic basement as opposed to ophiolites of unknown tectonic setting (Nicolas, 1989), anomalously exposed rifts (Robinson et al., 1982), ambiguously interpretable geophysical measurements (Detrick et al., 1994) or expensive and unreliable, seafloor drilling. Hence, from this unique viewpoint, the structure of the crustal section may be documented and a complete suite of well-located rocks can be obtained with depth. In addition, a continuous record of accretion is revealed.

Despite these obvious advantages and early successes (ARCYANA, 1975), it has been suggested that crust accreted near transform zones is "anomalous" with respect to the "normal" products further away.

This argument was partly based on the hypothesis that serpentinite diapirism (Francis, 1981), vertical tectonics (Bonatti et al., 1983) or deformation (Goud and Karson, 1985) associated with this strike-slip domain would severely alter and disrupt the crust on the fracture zone walls. However, it was found that these effects tend to be limited to the lower crust (Francheteau et al., 1990) or restricted to the transform fault valley (Fox and Gallo, 1984; 1986); and where present, they also occur in samples from the adjoining ridge (Karson and Dick, 1984).

It was also proposed that the crust thinned approaching transform zones to account for the full exposure of slow (Auzende et al., 1989), intermediate (Francheteau et al., 1992; Karson et al., 1992) and fast (Herbert et al., 1983) spreading rate crust in spite of Francheteau et al.'s (1976) prediction of a substantially reduced vertical extent.

However, the results of seismic experiments indicate neither a consistent nor systematic pattern of decreasing crustal thickness (e.g. Cormier et al., 1995 vs. Barth, 1994).

Likewise, a "cold-edge" effect was postulated (Bender et al., 1984) in some cases but in others, there was no difference between the basalts recovered from the fracture zone and adjacent ridge (Le Roex et al., 1983). Nonetheless, other 2°-4° order axial discontinuities do correlate with the absence of an interpreted magma lens (Detrick et al., 1987) and distinct differences in chemical signature (Sinton et al., 1991).

The inference of tectonic and magmatic cells with boundaries that do not necessarily correspond but which are topographically expressed along-axis (Batiza, 1996) adequately explains fracture zones as the distal ends of these segments (Johnson and Dick, 1992). Furthermore, such complex structures should result in various styles of crustal accretion which challenges the simple dichotomy of "normal" versus "anomalous" oceanic crust.

The history of accretion will be further complicated by the ephemeral nature of ridge crest segmentation (Gente et al., 1995) and even transform faults can become unstable under the influence of rift propagation (Kleinrock and Hey, 1989c). Given the frequency of the latter events at intermediate spreading rate ridges (Hey et al., 1989; Sempéré et al., 1996) and their long-term effects, it implies that the crust formed under even these conditions ought to be considered typical for this setting.

Consequently, an important aim of this work is to determine the contextual framework of crustal building and to define the range and time-scale of variability in constructional processes.

What can be inferred about the internal crustal structure formed at intermediate spreading rate ridges?

In general, the upper oceanic crust is a stratiform assemblage constituted by a 0.0 - 1.5 km thickness of basaltic lavas overlying a transition to a 0.6 - 1.3 km thick, sheeted complex of diabase dikes (BVSP, 1981). This internal structure will vary depending on the width of the accretion zone, distribution of the intrusions, width of horizontal strain zone, total lava production rate, size and shape of the lava-dike units, spreading velocity, faulting, and extent and nature of isostatic compensation (Cann, 1974; Palmason, 1980).

Intermediate spreading rate ridges have narrow, ridge-parallel zones of accretion causing centered emplacement and an orderly split of the volcanic edifice (Cann, 1974; Moore et al., 1974) that should form distinct lava and dike units (Atwater, 1979). This view is supported both at Hess Deep (Francheteau et al., 1990), which has 100-200 m of pillow lavas, 50-500 m of extrusives, intrusives and massive layers, and a 1200 m thick dike complex; as well as at Hole 504B (Leg 140 Shipboard Scientific Party, 1992), where there are 571.5 m of mainly pillows and thin flows, 209 m of pillow flows, thin flow, massive basalts and dikes, and at least a 945.5 m thickness of dikes and massive layers. Hence, despite the similar overall structure, the internal thicknesses vary considerably - this includes the total estimate for the upper crust of about 1.4 km at Hess Deep (Francheteau et al., 1990), 1.75 km at Hole 504B, and seismically measured thicknesses of 2-3 km from three segments of the JdFR (Davis et al., 1976; Morton et al., 1987; Rohr et al., 1988; Cudrak and Clowes, 1993; White and Clowes, 1994; Christeson et al., 1993).

The internal crustal structure is also affected by structural processes permitting magmatic accumulation as summarized by Karson et al. (1992). In these intermediate rate settings, accommodation has been by listric faulting (Verosub and Moores, 1981) presumably along the boundary fault (Ballard et al., 1979). However, the apparent trace 100-200 m below the Layer 2A-2B contact dips toward the axis at Hole 504B (Shipboard

Scientific Party, 1988) while it is interpreted to dip outward at Hess Deep (Karson et al., 1992). In addition, chaotic collapse (Haymon et al., 1993) at Hess Deep has created randomly oriented (43°-68°) dikes in discrete blocks (Hurst et al., 1994) while other vertical ones are either left so or post-date this event (Francheteau et al., 1992). Although there is no evidence of normal faulting (Atwater, 1979) with back-tilting of blocks (Macdonald, 1982) or subsidence accompanying rotation (Moore et al., 1974; Rosencrantz, 1982) here, the sample size of two is inadequate to omit these as possible mechanisms operating elsewhere.

Therefore, a major objective of this work is to provide data on the lithological structure, the thickness of lithological units, the orientation of dikes and lava flows, and to describe any other form related to internal assembly in order to infer the structure of the upper oceanic crust.

How is the upper oceanic crust built at intermediate spreading rate ridges?

The process of volcanic construction can be traced from the morphology of lava flows which changes in response to flow dynamics (e.g. eruption rate - Ballard et al., 1979; Griffiths and Fink, 1992), intrinsic lava properties (e.g. viscosity and temperature - Bonatti and Harrison, 1988) and emplacement conditions (e.g. slope, along-axis flow - Gregg and Fink, 1995; Wang and Cochran, 1995). The former kinematic and physical factors are influenced directly by lower crustal effects (e.g. permanence/ephemerality of magma lens, residence time in magma chamber, replenishment frequency, extent of mixing, etc.) and indirectly by their connection to the mantle (e.g. mantle temperature, 2- or 3-dimensional mantle upwelling, melt supply and delivery rate, number and timing of

magma reservoirs established along-axis, etc.). It is less clear if the timing of accretion is linked to discrete events across the mantle-crust interface.

Observations from ophiolites (Schmincke and Bednarz, 1990), the axial valley seafloor (Barth et al., 1994) and drill cores reveal pillow flows, massive basalts ± thin sheets and breccias in the upper part while massive basalts and dikes occur in a mixed zone. This general stratigraphy of flow forms varies by spreading regime. At slow rates, thin sheet flows become almost absent (Bonatti and Harrison, 1988) while breccia horizons are marked (Melson et al., 1979; Donnelly et al., 1980) suggesting prolonged periods of tectonic activity. At intermediate rates, the relative proportion of pillow flows decreases but still remains dominant over thin sheets (Adamson, 1985) with depth although massive basalts can become equally prominent (Salisbury, 1983).

In general, there is consensus from these studies that the crust is emplaced in eruptive cycles (Ballard et al., 1979; Hyndman and Salisbury, 1984; Pezard et al., 1992). The cycle starts with brief but voluminous eruptions of hot, low viscosity magma from elongate fissures producing sheet flows over a few hours to days. The cycle continues with steadier but slower eruptions of cooler and higher viscosity magmas around vents producing pillow flows over months and years. This volcanic cycle, probably lasting more than a decade (Ballard et al., 1979), may be interrupted by tectonic and hydrothermal events as follows: rapid crustal extension - massive sheet flow eruption - amagmatic extension and sheet flow collapse - hydrothermal activity - eruption of pillow lava or thin irregular sheet flows (Schmincke and Bednarz, 1990). Hence, the cycle ends with breccia and talus deposits at the top of the crustal sequence. In total, 3 sequences are identified over the 780 m of Hole 504B in intermediate spreading crust (Pezard et al., 1992), 7 over the 571 m of Hole 395A in slow spreading crust (Hyndman and Salisbury,

1984), and 6-10 such edifices each of 50-400 m thickness over 1200 m of extrusives in the Troodos ophiolite (Schmincke and Bednarz, 1990).

Alternatively for fast spreading rate centers, bimodal lava emplacement is proposed on the basis of a 100-160 m thick Layer 2A increasing by 200-600 m within 1-4 kilometers of the axis (Christeson et al., 1992; Harding et al., 1993; Vera and Diebold, 1994). In this model, the lower part of the extrusives is from flows within the axial summit caldera (ASC) but the upper part is dominated by flows extending outside of the ASC by off-axis eruptives and/or by off-axis intrusion (Hooft et al., 1996). Hence in this case, some to all of the massive basalts in the crustal section would represent sills.

In order to assess which (if either) of these models operates at intermediate spreading rate ridges, an important goal of this work will be to document the stratigraphy of flow forms on the scarp, to relate them to types already recognized by their flow surfaces, and thus to infer the style(s) of basaltic eruption and/or intrusion from the sequence of flow morphologies produced.

How does magmatic petrogenesis relate to upper crustal accretion?

The history of magmatic accretion can be interpreted from the petrographic and chemical diversity of basalts in the crustal section which derives from differences in mantle composition, melting processes and shallow-level effects over time. This strategy is particularly appropriate at medium (and slow) spreading ridges which more commonly contain enriched basalts and display significant intrasegment variation in melting conditions (Batiza, 1996). In addition, crustal processes which depend on the physical attributes of the magma chamber, the residence time in the magma lens, replenishment

frequency and degree of mixing (Sinton and Detrick, 1992), are responsible for an even smaller length scale of ridge segmentation. Nonetheless, the steady- or non-steady state nature of these magma reservoirs is mainly a function of mantle temperature at any spreading rate (Batiza et al., 1996).

A trend of increasing degree of differentiation over time is apparent from the 30 m deep Hole 425 of Galapagos crust. Here, three distinct chemical units of moderately evolved basalts could have been produced by up to 28% fractional crystallization of largely plagioclase and lesser olivine (Fodor et al., 1980) or by successively mixing ferrobasalts with more primitive basalts (Mattey and Muir, 1980).

A similar pattern along-axis has been interpreted as a cycle of magmatic evolution at Cleft Segment of the JdFR (Smith et al., 1994) and as the result of lateral dike transport at Explorer Ridge (Michael et al., 1989). The former (Smith et al., 1994) is initiated by low volume, mafic pillow lavas via diking (as in the overlap area with the Vance Segment), followed by voluminous eruptions of moderately evolved, lobate and sheet flows (as at N. Cleft) and then lastly by waning magmatic activity with the most fractionated, lobate flows (as at S. Cleft). The latter (Michael et al., 1989) distributes E-MORB melt from the center of the segment as at Endeavour Ridge (Karsten et al., 1990) to the end of the segment with T-MORBs possible in between. Note that both these models of magmatic accretion differ from accounts for E-MORB at fast spreading centers as the products of subsidiary reservoirs giving rise to volcanism and shallow intrusives off-axis (Perfit et al., 1994).

By comparison, the 45 m of ferrobasalts at Site 424 on Galapagos crust are geochemically uniform N-MORBs. They could result either from ~50% crystallization of clinopyroxene and plagioclase (Fodor et al., 1980) or a periodic influx of primitive

magma mixing with evolved ferrobasalt in open-system fractionation (Mattey and Muir, 1980).

This is similar to the compositional uniformity in the upper 561.5 m of Hole 504B which suggests steady-state conditions in the magma chamber (Emmermann, 1985). However, the intermediate spreading crust here differs in several other aspects. It is composed of highly depleted (Group D) lavas from multistage melting of an N-MORB source (Autio et al., 1989). The basalts are of primary composition indicating only a small degree of crystal fractionation prior to intrusion or eruption which implies either a short residence time or a chamber steadily replenished by one mantle source (Natland et al., 1983).

By contrast, Sites 482-485 south of the Tamayo Fracture Zone are all composed of N-MORB indicating a similar source (Saunders, 1983) but there are 12 chemical sub-types in the <150 m drilled with each representing a fractionation trend. The compositions of these single eruptive units is explained as the result of the magma being either crystallized or contaminated by a feldspathic peridotite at depth and then experiencing two episodes of polybaric fractionation at consecutively shallower levels (Barker et al., 1983). However, there is no chemical pattern with depth which removes any possibility of a large, long-lived chamber (Cambon et al., 1983).

Likewise, the apparent simplicity at Hole 504B belies a more complex accretionary scenario. There are seven chemical sub-types of Group D randomly interlayered in the section (Autio and Rhodes, 1983) which may reflect either sequential influxes of magma into a chamber or separate flows from different magma chambers. There are also two other rare groups (M' and T) interdigitated through the core with none being comagmatic (Kempton et al., 1985). It is suggested that such concentration variations could develop from the same parental magma but in different magma chambers

(O'Hara, 1977) or alternately, could reflect heterogeneity in the mantle source that is preserved by separate conduit-chamber systems (Emmermann, 1985).

Hence, there are three models of magmatic accretion at intermediate spreading rate ridges based on an absence of geochemical variability with time, a differentiation trend, or the lack of any pattern. Nor is there consensus among these on the origin of multiple MORB types. In order to evaluate the conditions which promote one form of magmatic petrogenesis over another, this study will systematically sample the scarp vertically and laterally and relate these findings to the previous questions.

Overview of dissertation

The project is delimited to an examination of magmatic processes responsible for creating the upper oceanic crust at intermediate spreading rates. The investigation is based on a scarp perpendicular to a well-described ridge and utilizes data-sets that were collected from mapping this cliff-face at large-, medium- and small scales. The goals of this dissertation are to (1) establish the tectonic and magmatic context of accretion on-axis; (2) document the upper crustal section in detail using multiple techniques; (3) derive models of magmatic accretion based on these perspectives; and (4) formulate an integrated model that synthesizes these views and incorporates the effects of spreading.

Chapter I introduces the site for this study along the north scarp of the Blanco Fracture Zone that adjoins the southern Juan de Fuca Ridge. The chapter describes the local and regional setting for context and reviews the findings for the area in the literature that bear on accretion.

Chapter II considers the prevailing tectonic and magmatic framework for the region according to which rift propagation terminated on the south flank of Parks Plateau at 1.5 Ma. These findings are re-evaluated because they imply that the study site, accreted between 1.2 Ma and 1.7 Ma, could have been affected by these anomalous conditions.

Chapter III examines geochemical evidence of propagation and explores the role of seamounts in the vicinity towards defining a new accretionary context. Evidence for recognizable examples is presented and their characteristics in combination with information on plate motion is used to demonstrate the effects of mantle processes on crustal architecture.

Chapter IV compiles a medium-scale geologic map of the site that reveals major sub-divisions (termed zones) and assesses the extent of crustal exposure and transform-related deformation. Past concerns on the appropriateness of submarine scarps for studying accretion are also addressed.

Chapter V traces the evolution in the physical conditions of the magmatic systems that successively constructed the crustal section. This is carried out by classifying and recording the lava flow morphology in detail, and tying the flow forms to reported experimental results.

Chapter VI examines how the crust might be assembled. Features (termed domains and sectors) possibly associated with this process are documented and analyzed as to whether they originate from time-varying volcanism or structural activity.

Chapter VII investigates the influence of the crystallization history on magmatic evolution from a petrographic standpoint. The chapter uses phenocryst assemblages and mineral textures to infer sequences of crystallization and the role of other shallow-level magmatic processes, as well as to further check the nature of zones, domains and sectors.

Chapter VIII determines the petrogenesis of the sample suite responsible for generating compositional groups. A modeling-based interpretation of major, trace and

rare earth element data identifies the magmatic processes that have affected chemical evolution.

Chapter IX establishes how magmatism varied in space and time by presenting the distribution of the compositional groups in the study site, and geochemical profiles reflecting magmatic evolution with depth. These results are integrated with the previous concepts of zones, domains and sectors and physical models of crustal building to produce a synthesized view of magmatic accretion.

CHAPTER I: THE STUDY AREA

1.1 Introduction

Study of the depth dimension in the oceanic basement is vital to understand magmatic accretion despite the difficulties of access. The use of submarine scarps is advantageous because they have no proven inherent problems, permit direct observations, and allow assessment of the time dimension as on fracture zone walls. The West Blanco Depression (WBD) offers such a "window" into the upper crust accreted at an intermediate spreading rate. In this chapter, the regional and local setting of the WBD is summarized with emphasis on those aspects bearing on the crustal section in the field site. The southern Juan de Fuca Ridge (JdFR) is also described because it constrains the physical and chemical conditions of magmatic accretion based on the 0 Ma state of the spreading center, as well as the spatial and temporal behavior of volcanic activity in the along-axis dimension. Lastly, the fracture zone setting of the study site is reviewed.

1.2 The West Blanco Depression

1.2.1 Regional Setting

The WBD (Figure 1-1) is located at the westernmost end of the Blanco Fracture Zone (BFZ). Its simple, orthogonal configuration with the 20°-striking, southern Juan de Fuca Ridge (JdFR) to the west and the 24°-striking, northern Gorda Ridge to the east (Embley et al., 1987 cf. Atwater and Macdonald, 1977) belies its 110°-113° trending, 20-75 km wide, and 360 km long, dextral transform fault domain (McManus, 1965). Embley

and Wilson (1992) outline the development of this ridge-perpendicular series of ~100 km long, sinistrally offset strike-slip faults in response to propagation (Figure 1-2).

To the north of the WBD at ~2110 m depth is the Juan de Fuca plate with abyssal hills typical of a normal spreading environment after 1.8 Ma (Figure 2-4). Other tectonic and magmatic features related to propagation or post-effects are discussed in Chapters II and III respectively.

To the south of the WBD, Parks Plateau (PP) is 12 km wide and 70 km long with an average depth of <2800 m, similar to the Juan de Fuca plate, but a shallower minimum depth of 1615 m (Dauteuil, 1995). The central part is dotted with volcanic cones and fresh lavas composed of enriched MORB and minor normal MORB and is interpreted to be a seamount (Blanconaute Shipboard Party, 1991). Its linear south edge marks the trace of the old BFZ and deepens by about 1000 m onto the Tufts Abyssal Plain but is interpreted not to be tectonically active (Juteau et al., 1995).

1.2.2 Local Setting

The 55 km long and at least 4834 m deep WBD (Embley and Wilson, 1992) extends from near the southern tip of the JdFR to a sill at 2900 m depth which separates it from the East Blanco Depression (EBD). Both walls of the trough are parallel (oriented at N115°E and N113°E respectively - Dauteuil, 1995) but in the central part, the north scarp (46°) slopes roughly twice as steeply as the south (21°) which is interrupted mid-slope by a flat-lying bench at 3300-3600 m depth (Figure 1-3).

This asymmetric profile (Nehlig et al., 1992), along with the anomalous depth, non-rectangular or non-rhombohedral shape, lack of cross-cutting lineations (Embley et al., 1987) or evidence of a small spreading center (deCharon, 1988; Embley and Wilson, 1992) is cited against an origin as a pull-apart basin (cf. Dauteuil, 1995). The trough is

interpreted to have formed at a maximum age of ~0.6 Ma, based on the truncation of abyssal hill lineations by the north WBD scarp, and a minimum age of 0.35-0.40 Ma, given the time necessary for EBD spreading (Embley and Wilson, 1992).

Rocks recovered from both walls of the WBD (Melson, 1969; Delaney et al., 1987) include glass basalts, pillow fragments porphyritic basalts with plagioclase and/or olivine phenocrysts, dolerite, hyaloclastites, quartz-veined greenstones, and breccias. Gabbros have only been dredged on the south side at the pseudofault tip (Fleutelot, 1995).

1.2.3 Geophysical Background

Magnetization profiles show an asymmetry in spreading over the Matuyama interval (0.78 - 1.79 Ma) with half-rates for the Pacific and Juan de Fuca plates of respectively 25 mm/yr and 29 mm/yr and symmetric accretion in the Brunhes of 26 mm/yr (Tivey, 1994). The magnetic anomalies are negative on the north side of the WBD giving a 1.5 Ma to 2.5 Ma age and positive in the central part of the WBD and adjoining portion of the south wall which is interpreted to be less than a million years old (Melson, 1969). There is also a strong positive anomaly at the ridge-basin intersection (Tivey, 1994) which is attributed to recent basaltic extrusion and intrusion (Melson, 1969).

Gravity data for the Blanco transform fault exhibit a negative free-air anomaly over the WBD (Dehlinger et al., 1970) from which compensation by crustal thinning is inferred (Melson, 1969). Gravity measurements of the 1 Ma crust on the north WBD scarp indicate that there is an 800 m thick upper section that is of low density and high porosity interpreted as Layer 2A and an underlying 500 m thick, altered transition zone (Johnson et al., 1996).

In terms of seismicity, earthquakes define the active transform boundary (Tobin and Sykes, 1968) with those occurring on the several, shorter master faults to the west of the Cascadia Depression being lower in magnitude (Spence, 1989; Dziak et al., 1991). They are predominantly right-lateral, strike slip faults (Chandra, 1974) with minor normal faulting possibly related to the extensional basins (Bolt et al., 1968). Ibach (1981) also contends that there is a compressive component of stress normal to the fracture zone in the central part as a result of clockwise rotation and northward differential motion of the plates.

1.3 The Cleft segment

1.3.1 Axial Morphology

The Cleft Segment (Figure 1-4) extends between the Vance Segment, from which it is offset 3 km right-laterally (the overlapping rift zone or ORZ), and the intersection with the Blanco FZ, where the ridge curves around the western cusp of the WBD before dying out. The axis reaches a minimum depth of 2150 m that, like the rest of the JdFR, stands about 300-500 m shallower than other segments of the EPR (see Figure 4 of Kappel and Ryan, 1986). Such axial highs are noted for efficient along-axis melt redistribution (Wang and Cochran, 1995). This segment is formed by an elongate high of 60 km length, 20 km width and 200-300 m height. The ridge crest is cut by a central graben about 1-3 km wide and 80-100 m deep (Embley et al., 1991) that represents the zone of crustal accretion (Goldstein et al., 1992). Hence, the neovolcanic zone is neither narrow nor localized although this inner valley is itself bisected by a semi-continuous, linear notch that is 30-50 m wide and 10-30 m deep (U.S. Geol. Surv. Juan de Fuca Study Grp., 1986). Kappel and Ryan (1986) propose that after a crestal ridge grows, magmatic

draw-down causes the axial high to collapse and form an elongate summit depression (ESD). The subsequent period is volcanically quiescent and the ridge is split further by fissuring and normal faulting as the tectonic zone widens and it is rafted off to the sides. The re-establishment of a magma chamber initiates the growth of another axial high.

1.3.2 Flow Morphology

Along the Cleft Segment (Figure 1-4), the notch is covered with collapse pit structures (e.g. bridges, pillars, rubble, remnant flow surfaces) and is interpreted as a drainback feature (Lichtman et al., 1983). The recent lavas decrease in age from south to north (Embley and Chadwick, 1994):

i) *the southern area* (44°32'N-44°44'N) has a lava plain to the south and a more fractured area to the north. The floor in both areas is covered dominantly by lobate flows with lesser sheet and pillow flows (Normark et al., 1982) which are estimated to have erupted in the last few hundred years (Normark et al., 1983). The faults and fissures in the northern area are confined to either side of the lava plain (Kappel and Normark, 1987). The axial valley walls, which include a low terrace 30 m above the floor, are formed by steeply dipping normal faults. These expose the pillow flows of an older central terrane which must be at least 16,000 years old (Lichtman and Eissen, 1983).

ii) *the middle area* (44°44'N-44°49'N) has centrally situated constructional mounds to the south, and many faults and fissures to the north (Kappel and Normark, 1987).

iii) *the northern area* (44°49'N-44°57'N) had a lava plain cut by numerous faults and fissures in 1980 (see Table 1 of Kappel and Normark, 1987). Young, lobate and lineated sheet flows with lava spires were observed at the margins in 1982 (Embley et al., 1991; Embley and Chadwick, 1994). A series of up to 35 m high, pillow mounds formed

in the ORZ between 1982 and 1987 (Chadwick et al., 1991; Chadwick and Embley, 1994).

1.3.3 Geochemistry

The lavas along the Cleft segment tend to be glassy to aphyric sheet flows and sparsely phyric (10%) pillows. They are low in potassium, and variably enriched in iron (< 14% - Vogt and Byerly, 1976) and titanium (> 1.5 wt. %) by comparison to other spreading centers (Kay et al., 1970). These basalts have experienced 35-40%, low pressure fractional crystallization. They become progressively less evolved to the north and are derived from separate magma chambers that are each in a different stage of evolution (Smith et al., 1994). The lavas contain glassy gabbroic xenoliths that crystallized from evolved liquids (Dixon et al., 1986). Mixing of this residual differentiate with a more primitive replenishment melt, that brought up the xenoliths, has produced ferrobasalts. The FeTi enrichment shows a maxima just north of the JdFR-Blanco intersection (Delaney et al., 1981) which is similar to propagating rifts (Sinton et al., 1983; Christie and Sinton, 1981) or ridge-transform intersections (Langmuir and Bender, 1984). Nevertheless, a constant helium isotope ratio at the Cleft Segment (Lupton et al., 1993) indicates that it is not propagating presently.

1.3.4 Geophysics

The southern JdFR, in comparison to the northern part, has a thinner crustal section. On the Cleft Segment, Layer 2 is about 2.4 km thick (cf. 2.7 km at the West Valley Segment - Davis et al., 1976) with the thinnest part in the axial valley close to the northern sheet flows and the largest variability (300 m changes laterally over several

kilometers) at the ORZ (Tivey, 1994). Layer 2A varies from 200 m to 550 m thick (McDonald et al., 1994) and is 350 m thick on average (cf. 1050-1450 m thick at the Endeavour Segment - White and Clowes, 1990 and 1994). The fissured area in the middle part of the segment can be explained by up to 17% porosity variations in the uppermost 400 m of the crust while the pillow mounds at the ORZ appear to be underlain by low-density material (Stevenson et al., 1994). There are weak multichannel seismic reflections at 2.3 km and 2.5 km depth respectively beneath the southern lava plain and at the juncture between the northern sheet flows and pillow mounds, which are interpreted as a flat-topped, 1-2 km wide magma chamber although the authors were unable to demonstrate a polarity consistent with a low velocity zone (Morton et al., 1987).

1.4 This Study

1.4.1 Nature of fracture zone crust

Fracture zone walls are a natural place to study crustal accretion because tectonic activity maintains their relief and exposes the oceanic basement. However, they have been deemed anomalous because of associated crustal thinning (White and Williams, 1986) and the "cold edge" effect (Langmuir and Bender, 1984). Johnson and Dick (1992) address these concerns and point out that the concept of "normal crust" is moot because of the variability arising from 1° to 4° tectonic (Macdonald et al., 1988) and magmatic (Sinton et al., 1991) discontinuities. Transform zone scarps have also been avoided due to the potential for normal faulting to disrupt the section and reduce the thickness available for observation (Francheteau et al., 1976) and because slumping in some areas obscures the crustal section (OTTER, 1984). These problems have not hindered this study.

1.4.2 The study site

The study site on the north WBD scarp (Figure 1-5) is outlined on the slope image map of Dauteuil (1995). It is situated between 34 km and 47 km off-axis and, according to spreading rate and magnetic age represents 1.15 Ma to 1.65 Ma crust created during the reversed polarity Matuyama epoch (Tivey, 1996). The wall here is 2.7 km high and steep (Figure 1-3) with slopes >30° continuous in the upper two-thirds (Figure 1-5). Nonetheless, only upper crustal rocks have been dredged here (Melson, 1969; Delaney et al., 1987). Areas of optimal outcrop exposure are evident with slopes >40° (Figure 1-5) and mass wasting on the cliff is clearly delineated (Figure 1-3). The extent of tectonic and chemical transform-related effects was unknown prior to this study although it was assumed to be minimized if the transform fault had only jumped northward in the last 500,000 years (Palmer et al., 1987; Embley and Wilson, 1992). In other respects, the spreading regime appears "normal" (Elvers et al., 1973; Riddihough, 1984) although the influence of propagation apparently only ended at 1.5 Ma (Embley and Wilson, 1992).

1.5 Summary

Chapter I has briefly documented the information on the region pertaining to magmatic accretion that was available at the time of this study.

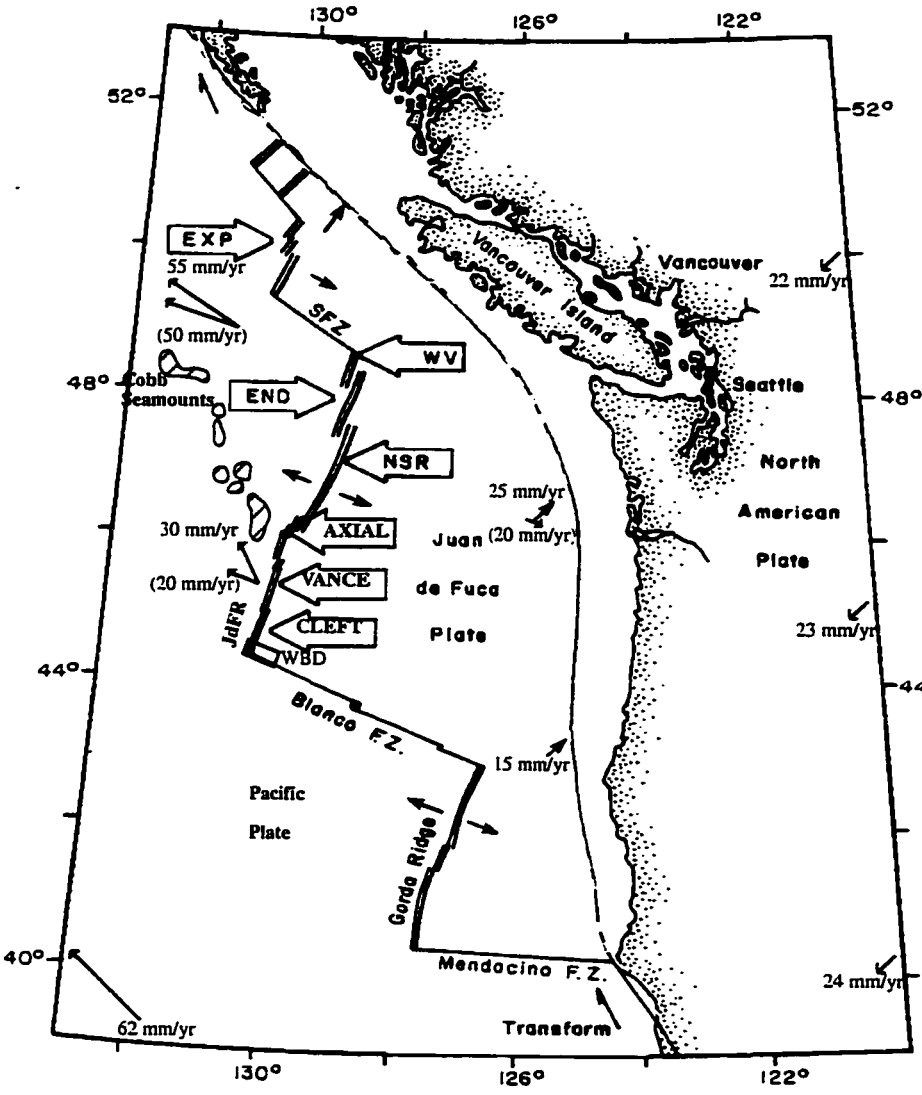

Figure 1-1: Regional map of the northeast Pacific showing the plate boundaries (modified from Johnson and Holmes, 1989).
Double lines = ridge segments;
Single lines = transform faults;
Dashed line = subduction zone
SFZ = Sovanco Fracture Zone;
EXP = Explorer Ridge;
WV = West Valley Segment;
END = Endeavour Segment;
NSR = Northern Symmetrical Ridge
Striped area = Seamounts;
Box = study area
Labelled arrows indicate absolute and ridge normal (in brackets) motions (Davis and Karsten, 1986; Spence, 1989).

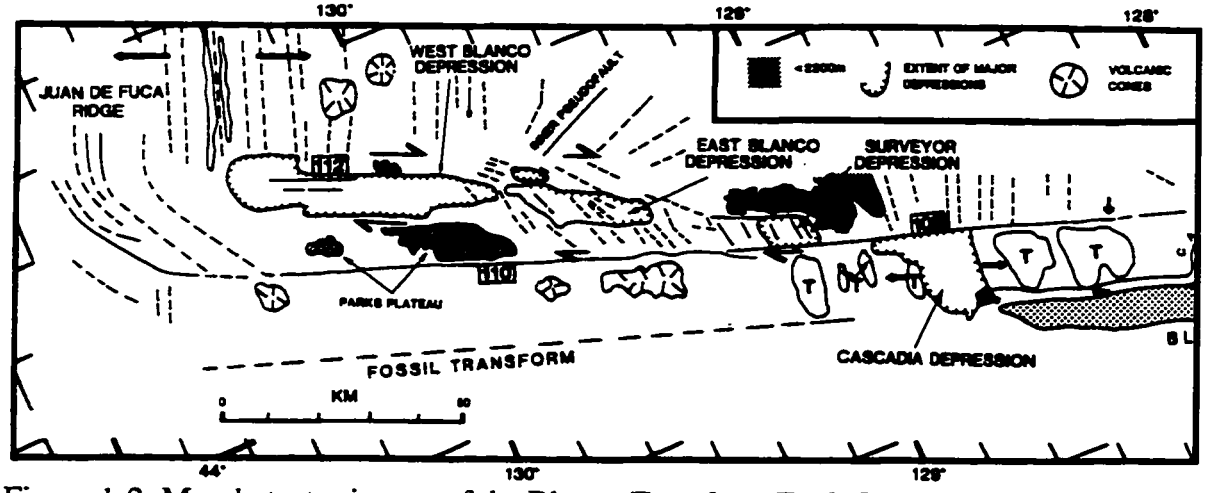

Figure 1-2: Morphotectonic map of the Blanco Transform Fault Zone (from Embley and Wilson, 1992)

Figure 1-3 a: SeaMARC II imagery along a 10 km wide swath of the WBD (Holmes et al., 1984). The north scarp clearly has the strongest backscatter signal due to its steepness along almost the entire length.

Figure 1-3 b: Interpretive map with key features labelled. The symbols each correspond to zones with a distinctive acoustic texture -

Diamonds = highly reflective with a high contrast; represents flat surface of the seafloor basement on both the Juan de Fuca Plate and Parks Plateau

Circles = highly reflective with a high contrast; represents flat surface of the seafloor basement that is distinguished by its mid-slope locality

Dark brick = low reflectivity; represents medium to steeply sloping scarp of outcrop

Light brick = medium reflectivity with internal structure; represents shallow to medium sloping scarp of outcrop

Heavy dots = homogeneous, high-medium reflectivity; represents gentle to shallow slopes that is possibly covered with uniform sized talus blocks

Light dots = high reflectivity with medium contrast; represents changes from flat to gentle slopes that are probably covered with sediment mostly

Interior dashed box outlines the site of this study.

44°27'
130°10'

Figure 1-3a

44°19'
129°51'

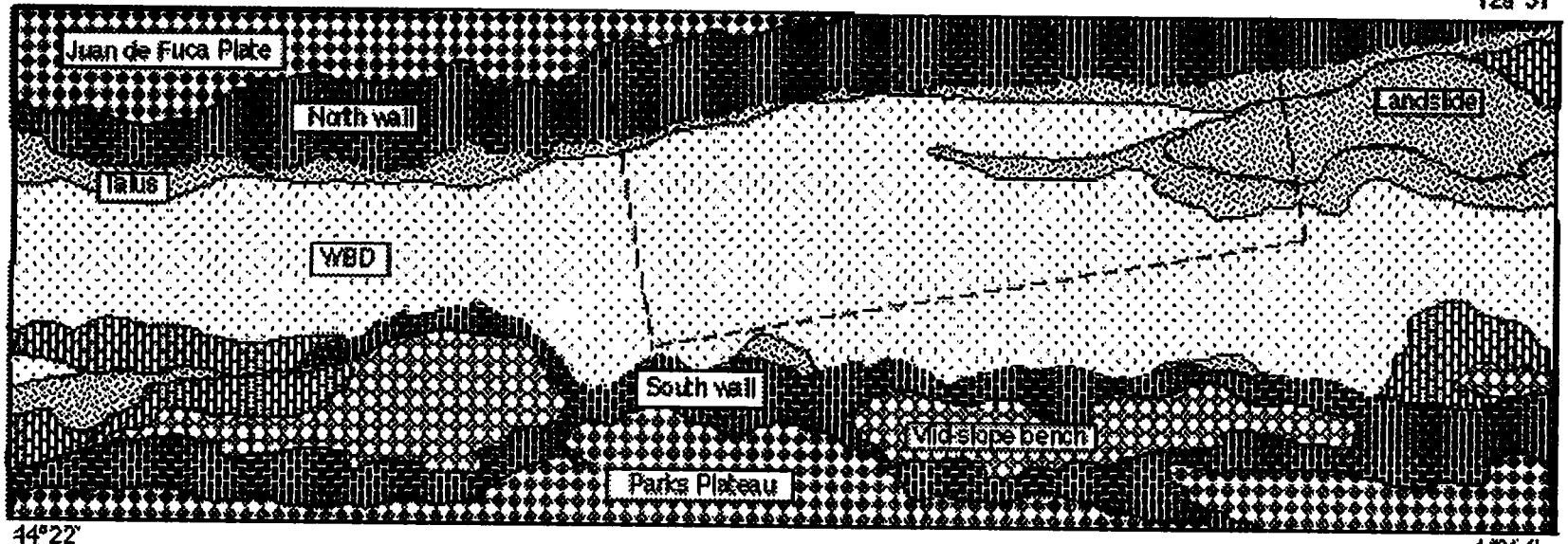

44°22'
130°13'

Figure 1-3b

44°14'
129°54'

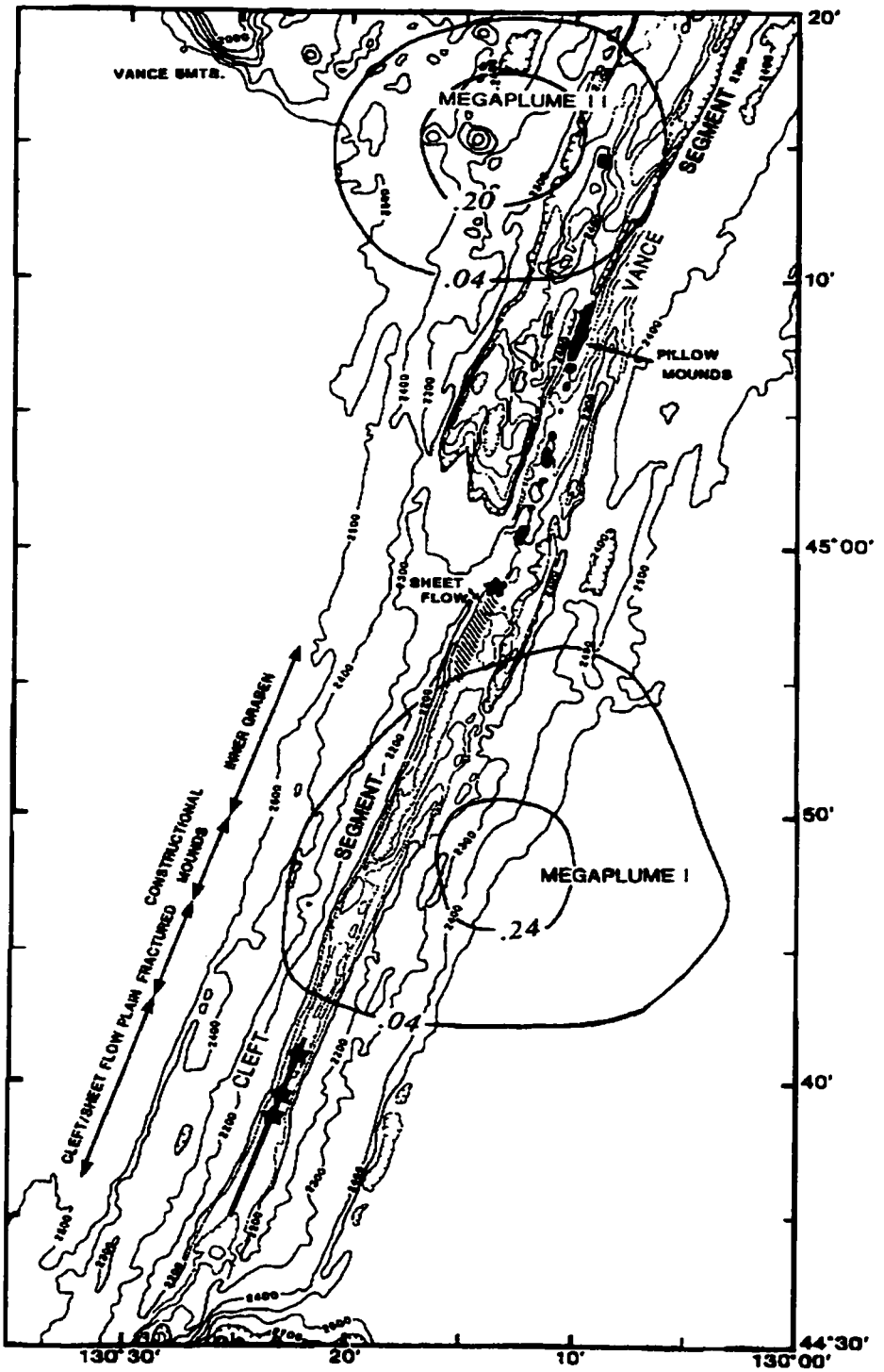

Figure 1-4: (after Embley et al., 1991)
Sea Beam map of the Cleft Segment showing the southern area with high temperature vents, the middle area coincident with Megaplume I in 1986, and the northern area with a young sheet flow and a high temperature vent.
The zone overlapping the Vance Segment is the site of the recent pillow mounds.
The southern Vance Segment was overhung by Megaplume II in 1987.

Figure 1-5: Slope image of the WBD (after Dauteuil, 1995). The colours indicate the following slope intervals:

Black = 0°-10°
Blue = 10°-20°
Green = 20°-30°
Yellow = 30°-40°
Red = 40°-50°
White = >50°

The Tufts Abyssal Plain in the south is evidently quite flat with slopes almost consistently <10°.

The south flank of Parks Plateau has an overall gentle slope of 10°-20° with discontinuous local zones sloping between 20°-30°.

Parks Plateau (PP) and the Juan de Fuca (JdF) Plate are both relatively flat. However, features with gently (10°-20°) sloping sides also occur on PP. The JdF plate is interrupted by abyssal hills which are highlighted by their ridge-parallel, gentle to shallow (10°-30°) slopes.

The north and south slopes of the WBD are both distinguished by medium slopes of >30° although the differences between the two areas, that are discussed in the text, are also readily apparent.

The large rectangle indicates the area of the SeaMARC II imagery shown in Figure 1-3. Despite the difference in resolution, the general correspondence between the two data sets is evident.

The small rectangle on the north slope indicates the study site. The area includes two, steeply (>40°) sloping zones.

The WBD orientation can be traced by the flat-lying axis.


44°24'
130°12'
130°00'
129°48'

CHAPTER II: THE TECTONIC SETTING

2.1 Introduction

Rift propagation plays a significant role in the reorganization of spreading centers. The main variation by spreading rate (Hey et al., 1992; Hey et al., 1995) is the distance of the offset between propagating and failing rifts, the frequency of these events, and the rate of propagation. For intermediate spreading rate ridges such as the Juan de Fuca Ridge (Wilson, 1988) and the Southeast Indian Ridge east of the Australian-Antarctic Discordance (Sempéré et al., 1996), propagation tends to be of small offset and common occurrence (Hey and Wilson, 1982). In addition, the propagation rate irrespective of the cause is 30-120 mm/yr (Wilson and Hey, 1995) as at the Cocos-Nazca spreading center where propagation is related to a hotspot (Searle, 1989). The elements and geometry of propagation for large (Engeln et al., 1988; Naar and Hey, 1986) and small offsets (Hey et al., 1989; Kleinrock and Hey, 1989a; 1989b; 1989c) are also now well-defined (Hey et al., 1980; 1988).

This propagation theory forms the basis of the prevailing tectonic model (Embley and Wilson, 1992) for the region of the Juan de Fuca Ridge (JdFR) - West Blanco Depression (WBD). The model indicates that the last southward propagator terminated at the Blanco Fracture Zone (BFZ) south of Parks Plateau (PP) at about 1.4-1.5 Ma (Hey and Wilson, 1982; Wilson et al., 1984). This suggests that the walls of the WBD could be used to document a complete history of the evolution in the system after passage of the rift tip as well as the post-propagation transition to a normally spreading ridge.

There is one problem, however - the model assumes, based on the theory, that the propagator reached the old BFZ but there is no obvious evidence of the inner pseudofault past the Juan de Fuca plate and on PP. If so, propagation could have ceased by about 2 Ma which has very different implications for the accretion of these two settings as well as for the field site in this dissertation. Given this importance, Chapter II re-examines existing bathymetric, magnetic and sonar data for the region. These observations are used to recreate the tectonic evolution over the last 5 Ma in more detail, and to study the case of multiple rift propagation for small offset systems and its consequences.

2.2 Data

The detailed tectonic history of the last southward propagator (#3) after 5 Ma is reconstructed from Sea Beam (Embley and Wilson, 1992) and magnetic anomaly (Wilson et al., 1984) maps, as well as GLORIA (EEZ Scan 84 Scientific Staff, 1986) and SeaMARC II (Holmes et al., 1984) imagery. Since these data-sets were collected prior to the availability of GPS, their coordinates have a mismatch of about 0°3' at a maximum based on a reasonable geological fit. An approximate timing for the events during this tectonic evolution is obtained as a function of distance from the ridge axis. This method assumes a full spreading rate for the JdFR of 58 mm/yr (Vine, 1966) that is constant as is indicated by magnetics (Elvers et al., 1973). Rates of propagation are calculated from the relation $Q = 2 \tan^{-1}$ (spreading half-rate/propagation rate) where Q is the angle subtended by the outer (OP) and inner (IP) pseudofaults (Hey et al., 1989).

2.3 Results and interpretation

2.3.1 3.4 Ma - 5 Ma

The magnetic anomaly map (Figure 2-1) shows the inferred location and orientation for the inner pseudofault (IP) of propagator #3 on the Juan de Fuca plate. On GLORIA imagery for the ~2 Ma to ~4 Ma period (Figure 2-2), the trace of the approximately 44° trending IP is marked by two groups of basement topography on otherwise heavily sedimented seafloor. It is thus constituted by a broad zone similar to the 13 km wide inner pseudofault zone (IPZ) in the Galapagos system (Kleinrock and Hey, 1989a). Given the constant orientation of the ridge for the last 3.4 Ma (Wilson et al., 1984), it can be assumed that the axis had its present-day trend of ~21°. Consequently, the pseudofault half-angle is 23° from which a propagation rate of 68 mm/yr is calculated that is similar to the 70 mm/yr estimate of Wilson and Hey (1984).

2.3.2 2.3 Ma - 3.4 Ma

Wilson et al. (1984) indicate that at 3.4 Ma the propagation rate decreased to 56 mm/yr but this point is omitted from Wilson's (1988) tectonic history. Nonetheless, the GLORIA imagery (Figure 2-2) clearly shows that the angle of the IPZ must have changed at this time because otherwise it would cross-cut the seafloor terrain with a disturbed fabric on the Juan de Fuca plate and intersect the East Blanco Depression (Figure 2-3). Instead, the ENE-striking (71°-84°) lineaments in the Surveyor Rift crust adjacent to the IP are interpreted to reflect a period of overlap between the propagating and failing rift zones.

A linear fault scarp of 100 m relief (Figures 2-1 and 2-3) further highlights the new trend at 67°. According to the previous reasoning, this gives an IP half-angle of 46° from which a propagation rate of 28 mm/yr is calculated. Embley and Wilson (1992) utilize the same scarp in locating the IP trajectory but they instead measure it to be 58°-60° in orientation giving a propagation rate of 36-38 mm/yr. Despite the difference in

these determinations, they both reflect a slowing in propagation at a rate considerably less than the 56-59 mm/yr estimate from magnetic anomalies (Wilson and Hey, 1984).

2.3.3 2 Ma - 2.3 Ma

The Sea Beam overlay on GLORIA imagery (Figure 2-3) indicates that an extrapolation of the 67°-trending IP intersects the saddle between the WBD and EBD at about ~2.3 Ma, the south wall of the WBD around ~2.2 Ma, and the north flank of PP at roughly ~2 Ma. It is proposed that propagation ceased here (Naidoo et al., 1994) which concurs closely with Wilson's (1988) estimate of 1.9 Ma for the timing. Consequently, PP was never penetrated and the propagating JdFR never captured the Surveyor Ridge in this model although the rift did become inactive at some point in its history to form the Surveyor Depression.

2.3.4 0.65 Ma - 2 Ma

After 2.0 Ma, crustal accretion at the JdFR should essentially have been "normal" although possibly influenced by post-propagation effects that are suggested to last several million years (Sinton et al., 1983) or at least 1.5 m.y. here (Smith et al., 1994).

Alternately, if propagator #3 subsequently halted along the south scarp of PP as suggested by Embley and Wilson (1992), its point of termination on the BFZ would occur at ~1.7 Ma (for a 67° trend), or at ~1.5 Ma (for a 58-60° trend). Irrespectively, this implies that the eastern part of PP should be constituted by crust which formed at the Surveyor Ridge while the western part of PP ought to have been accreted at the JdFR. Note that in this case the IP trace on PP would not be continuous with that on the Juan de Fuca plate because of the transfer of PP back to the Pacific plate after the BFZ relocated.

2.3.5 0.2 Ma - 0.65 Ma

It is assumed that the establishment of the transform fault zone after 2 Ma eventually lead to the opening of the WBD after 0.65 Ma. This upper bound is inferred from Sea MARC II imagery (Figure 2-4) which displays a fine abyssal hill fabric on the Juan de Fuca plate that apparently formed at least up to this time but was truncated sometime afterward presumably by strike-slip activity along the north WBD wall. Embley and Wilson (1992) suggest that the WBD formed at around 0.35-0.4 Ma. The creation of the EBD is less constrained. Nonetheless, such basins within the transform zone are also present in other propagator systems - an example is the series of grabens found in the Galapagos 95.5°W system (Kleinrock and Hey, 1989b).

Structural features within these depressions on the GLORIA and SeaMARC II imagery (Figures 2-5 and 2-6) can be related to the development of strike-slip activity after 0.65 Ma. A set of ~N113°E trending structures on the north flank of PP have the same orientation as the approximately N112°E trending north scarp of the WBD (Figure 2-5). They most likely represent the history of the transform zone as it moved successively northward. There is another series of ~N130°E trending lineaments on the north flank of PP (Figure 2-5) similar to an *en echelon* pattern of N135°E faults recognized by Dauteuil (1995) cross-cutting the trough floor which he interpreted as a dextral wrench component of a pull-apart basin. Such SE-trending lineations are also prominent in the EBD (Figure 2-6) and probably reflect the transfer of shear motion from the transform fault in the WBD to the old BFZ south of the EBD.

2.3.6 0 Ma - 0.2 Ma

The constructional terrain of the present JdFR curves around the WBD on the Sea Beam map (Figure 2-3). This is confirmed by a strong positive magnetic anomaly at the junction of the ridge axis and the trough that is interpreted to result from recent basaltic extrusion or magma intrusion (Melson, 1969). At the intersection with PP, there are two,

~N104°E trending lineaments that extend across the WBD (Figure 2-5). They were identified by Dauteuil (1995) as a N100°E trending band from a bathymetric slope image. He interprets these structures to be the most recent jump in the active strike-slip zone that now connects the southernmost tip of the JdFR to the northern wall of the EBD with a minor branch along the western part of the north WBD scarp.

2.4 Discussion

Rift propagation systems of small offset, have a high frequency of propagation events - 22 are counted over 39 Ma at the JdFR (Wilson, 1988). They are also distinguished by multiple propagators being active at the same time - examples at the JdFR include propagators #13 to #19 at 30 Ma, and propagators #1, #2, #3, #9 and #10 at 9 Ma (Wilson, 1988). The combination of these factors increases the likelihood of the OP and IP pseudofault structures of a previous propagator (that is now the failing rift) to intersect the presently active one. Here, I demonstrate the result of such a convergence and the impact on the tectonic evolution of the JdFR - WBD region. These interference effects further complicate the development of the shear zone (Karson, 1986) and undoubtedly also influence the associated formation of deep basins.

2.4.1 Why did the rate of propagation slow at ~3.4 Ma?

Propagating rifts in small-offset systems commonly display an evolutionary pattern in which the pseudofault angle increases discretely over time. This has occurred in the history of 11 out of the 22 JdFR propagators and for up to four occasions as in the 13 million year history of propagator #17 (Wilson, 1988). This is explained in two ways: (i) a decrease in propagation rate as the propagator migrates from capturing one doomed rift

to the next failing rift (Wilson, 1988); or (ii) a shift in the rotation pole caused by a change in plate motion direction that may in turn result in ridge re-orientation which can decrease the pseudofault half-angle (Wilson et al., 1984).

Wilson et al. (1984) and Wilson and Hey (1984) invoked the former in accounting for a change in the pattern of magnetic anomalies for propagator #3 at about 3.4 Ma. However, the problem with this explanation is that no other failing rift besides the Surveyor Ridge can be identified. Although this finding was subsequently omitted by Wilson (1988), the result is confirmed here independently from interpretation of GLORIA imagery. Furthermore, this work shows that the decline in rate from 68 mm/yr to 28-38 mm/yr (Embley and Wilson, 1992) was drastic (cf. from 70 mm/yr to 56-59 mm/yr - Wilson and Hey, 1984).

An understanding of what occurred can be gained from magnetic anomaly charts (Hey and Wilson, 1982) which show that the OP's of propagators #2 and #3, from the Surveyor Rift and JdFR respectively, merge (Figure 2-1). This feature is not incorporated in Embley and Wilson's (1992) model of the tectonic evolution because they view the OP tip of propagator #2 at 2.5 Ma to be aligned with propagator #3 which they place further to the north.

To determine if and when such interference would have taken place requires information on the spreading rate of the Surveyor Rift and the OP angle of propagator #2. The spreading rate is calculated using the Surveyor propagation rate of 60 km/Ma (Wilson, 1988) and its total pseudofault angle of 63° (Wilson et al., 1984), from which a value of 37 mm/yr is obtained. The OP trend of 327° is that interpreted by Hey and Wilson (1982) from magnetic anomalies (Figure 2-1).

Figure 2-7 displays a graphical reconstruction for 3.4 Ma. Given that the Surveyor Ridge ceased propagating at 4.85 Ma (Wilson, 1988), it can be calculated that the OP tip of propagator #2 would lie 54 km to the west of the present depression marking its location. The latitudinal location of the propagator #3 tip at 3.4 Ma is determined by horizontally extrapolating the position of the dogleg in the propagator #3 IP. As can be seen, the propagator tip intersects almost exactly with the #2 OP given the level of precision involved!

The reason for the dramatic drop in propagation rate at this time is two-fold. Firstly, it becomes constrained by the geometry of the failing rift and its pseudofault. In this case, the Surveyor spreading rate and OP angle permits a maximum propagation rate of 57 mm/yr. The second constraint depends on the age difference in the crust across the pseudofault. Here, the tectonic tip of propagator #3 would have been attempting to penetrate crust created by the Cascadia Ridge which is much older and colder than the Surveyor Ridge section.

2.4.2 What is the evidence for propagation having terminated by ~2 Ma?

Based on the above reconstruction, the perpendicular distance between the extrapolated JdFR and Surveyor Ridges is approximately 116 km. Given the calculated spreading rate for the Surveyor Ridge of 37 mm/yr, it would mean that the #2 OP tip would be aligned with the JdFR at 1.8 Ma. Hence, the rift propagator could plausibly have reached the BFZ at 1.7 Ma or later in which case the western part of PP ought to be composed entirely of crust created at the JdFR. However, there is little evidence to support this claim.

Instead, it is proposed here that propagation terminated at the north flank of PP on the following grounds: (i) the GLORIA imagery (Figure 2-5) of PP displays no obvious expression of crosscutting structures which would mark the trace of the #3 IP although it is possible that such a feature might be completely masked by recent volcanism (Blanconaute Shipboard Party, 1991); (ii) the GLORIA (Figures 2-3 and 2-5) and SeaMARC II (Figure 2-4) imagery for the surface of the western PP and north flank shows none of the fine abyssal fabric that is apparent on the Juan de Fuca plate and which evidently distinguishes crustal formation at the JdFR; (iii) a review of the magnetic anomaly lines (Figure 2-8b) indicates that the anomalies identified as 1, 1A and 2 on PP (Embley and Wilson, 1992) do not have the same distinctive characteristics as those on the Juan de Fuca plate; (iv) Parks Plateau is negatively magnetized along its entire length (Tivey, 1994) rather than just in the western and central parts which suggests that it is not necessarily of Matuyama age but may instead reflect the magnetic signature of >5 Ma old crust.

The implication is that if the propagation rate falls below the 30-120 mm/yr range which is typical for intermediate spreading rate ridges, as it does here with a calculated value of 28 mm/yr, then propagation will likely cease as a result. Such incomplete capture of the failing rift is not unknown at the JdFR. Embley and Wilson (1992) likewise contend that the Cascadia Depression represents the remnants of a segment that was not entirely eliminated by the propagating rift.

2.4.3 How does this model compare to the previous tectonic framework?

The tectonic model presented in this study is summarized schematically in Figure 2-9. This sequence of tectonic events in the JdFR-WBD region clearly builds on the

framework set forth by Embley and Wilson (1992). Their version of the evolution in the JdFR-WBD region over the last 5 Ma is relatively straightforward until 1.5 Ma when the propagator terminates at the BFZ south of PP. By contrast, it is suggested here that propagator #3 decreased in rate at 3.4 Ma and then ceased at ~2 Ma north of PP (Figure 2-9). For the period after 1.5 Ma, the Embley and Wilson (1992) version requires a major northward jump in the transform zone, significant ridge retreat that would leave behind a fossil ridge and WBD formation between 0.2 and 0.4 Ma. Neither the sequence or the cause of this behavior is explained and nor is any evidence cited in the Sea Beam bathymetry for such a ridge (see Figure 2-8a). By comparison, it is simply proposed here that the establishment of strike-slip activity from 2 Ma on lead to the opening of the WBD sometime after 0.65 Ma (Figure 2-9).

The most important difference between the Embley and Wilson (1992) framework and the model here is in their implications for accretion of the region.

One can infer from the Embley and Wilson (1992) reconstruction that PP is constituted by a western part accreted at the JdFR and an eastern part built at the Surveyor Ridge. I suggest that the basement of PP is of the same composition throughout (Naidoo et al., 1994) with the exception that the central area has also experienced off-axis volcanism (Blanconaute Shipboard Party, 1991).

With respect to the north WBD scarp, the Embley and Wilson (1992) version predicts a major break at 1.5 Ma. Accordingly, the crustal exposure to the east would represent the evolution after passage of the rift tip but nonetheless under conditions of propagation. Juteau et al. (1995) interpret their findings of a peak in crustal-level processes as consistent with these magmatic consequences (Christie and Sinton, 1981). However, Chapter IV argues that what they view as the high in a long wavelength signal is only one of five, shorter wavelength phases of magmatic development.

By comparison, this work proposes that if post-propagation effects last for 1.5 to several million years (Sinton et al., 1983; Smith et al., 1994), then the north WBD wall should reflect the transition from propagator influenced accretion until 2 Ma to normal crustal building (as opposed to only between 1.5 Ma and 0 Ma - Embley and Wilson, 1992). This alternative is supported by findings of gradually increased amounts of partial melting (Karsten and Delaney, 1991) or progressive shallowing in the depth of partial melting (Chapter IX) toward the axis.

2.5 Conclusions

The tectonic model outlined here makes two key points:

1. The general theory of rift propagation in intermediate spreading rate systems has been expanded by demonstrating that increases in pseudofault angle are due to decreases in propagation rate caused by the intersection of the propagating rift with either pseudofault of the failing rift.

2. The revised tectonic evolution of the JdFR - WBD region shows that the JdFR propagator #3 terminated on the north flank of PP at ~2.0 Ma and consequently, did not impact it. The north WBD scarp is only influenced by post-propagation effects to the extent that it records such a transition to a mature spreading center.

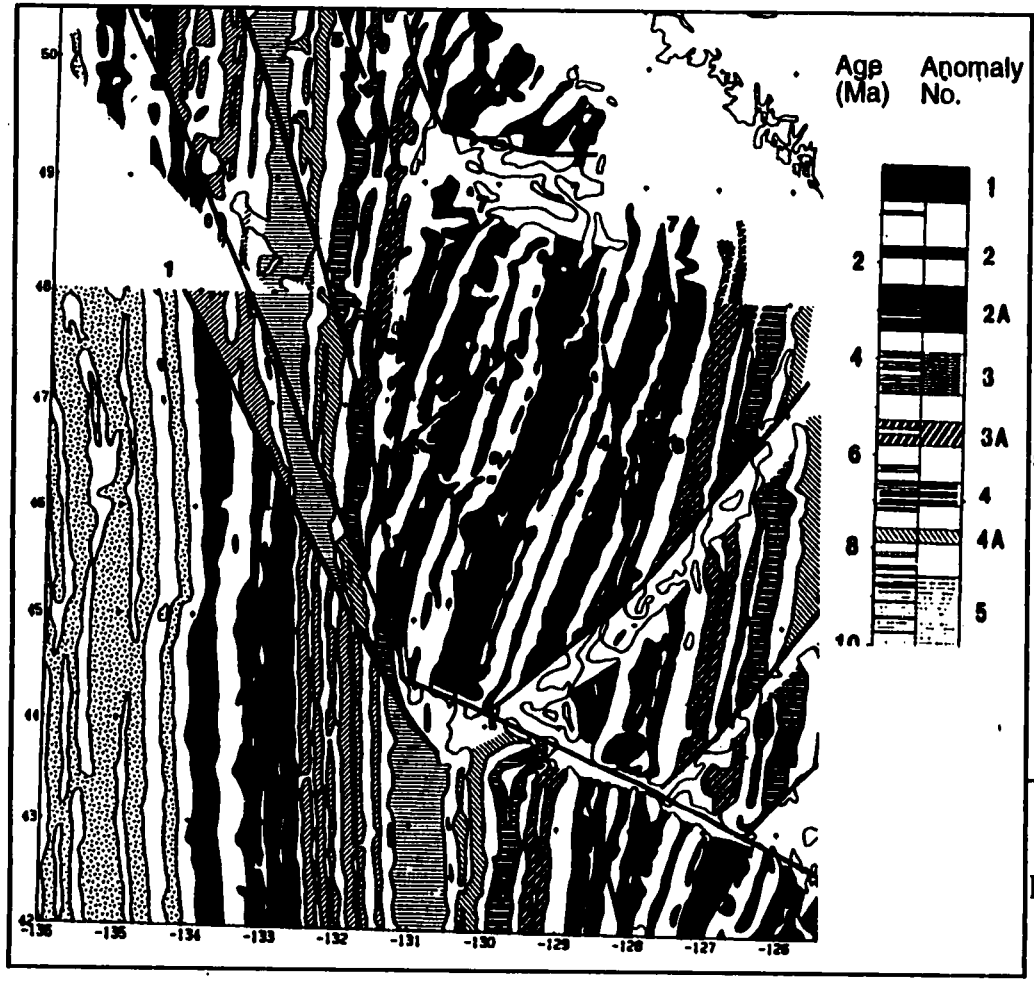

Figure 2-1a: (from Wilson et al., 1984)
Magnetic anomalies around the Juan de Fuca Ridge on both the Pacific and Juan de Fuca Plates. Dark areas = positive magnetisation; Light areas = negative magnetisation; Heavy lines = propagator pseudofaults; Double lines = fracture zones; Box = WBD area.

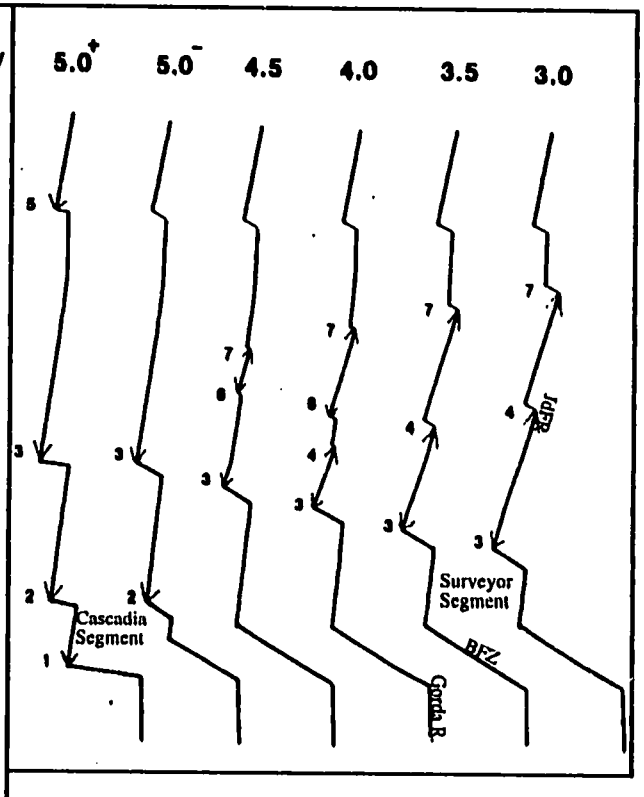

Figure 2-1b: (from Wilson et al., 1984)
Schematic history of the Juan de Fuca Ridge between 5 Ma and 3 Ma during which six propagators, numbered according to their pseudofault traces in Fig. 2-1a, were active and the BFZ developed. Note that the Cascadia Segment is eliminated here by propagator 2 (cf. Embley and Wilson, 1992).

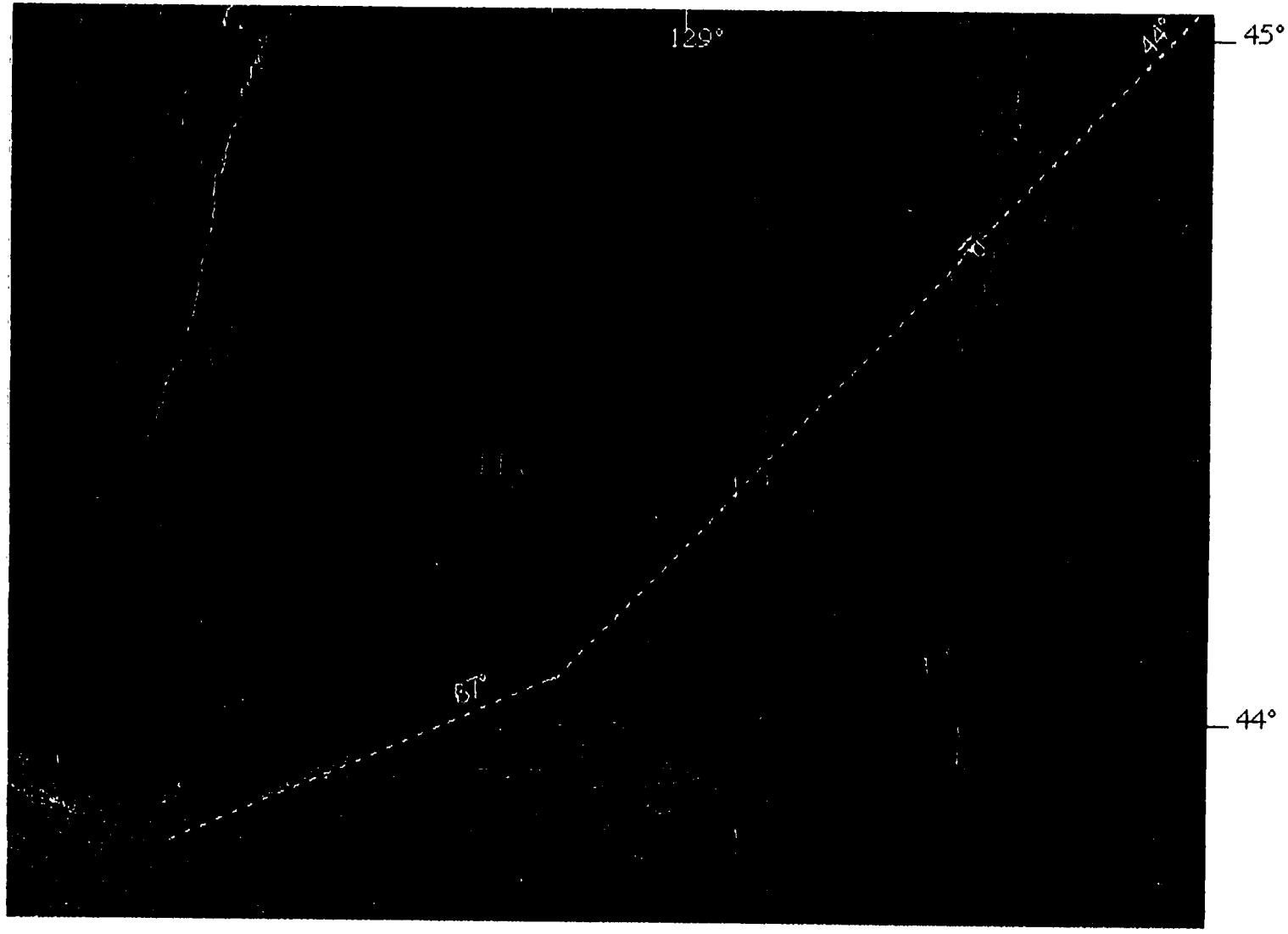

Figure 2-2: Location of the inner pseudofault (IP) on the Juan de Fuca plateau in a GLORIA mosaic (EEZ Scan 84 Scientific Staff, 1986) with normal polarity. The IP here trends at 44° from ~4 Ma to ~3.4 Ma and then changes to a 67° trend. The trace of the IP is highlighted by a linear scarp feature before it intersects the saddle between the two depressions at ~2.3 Ma.

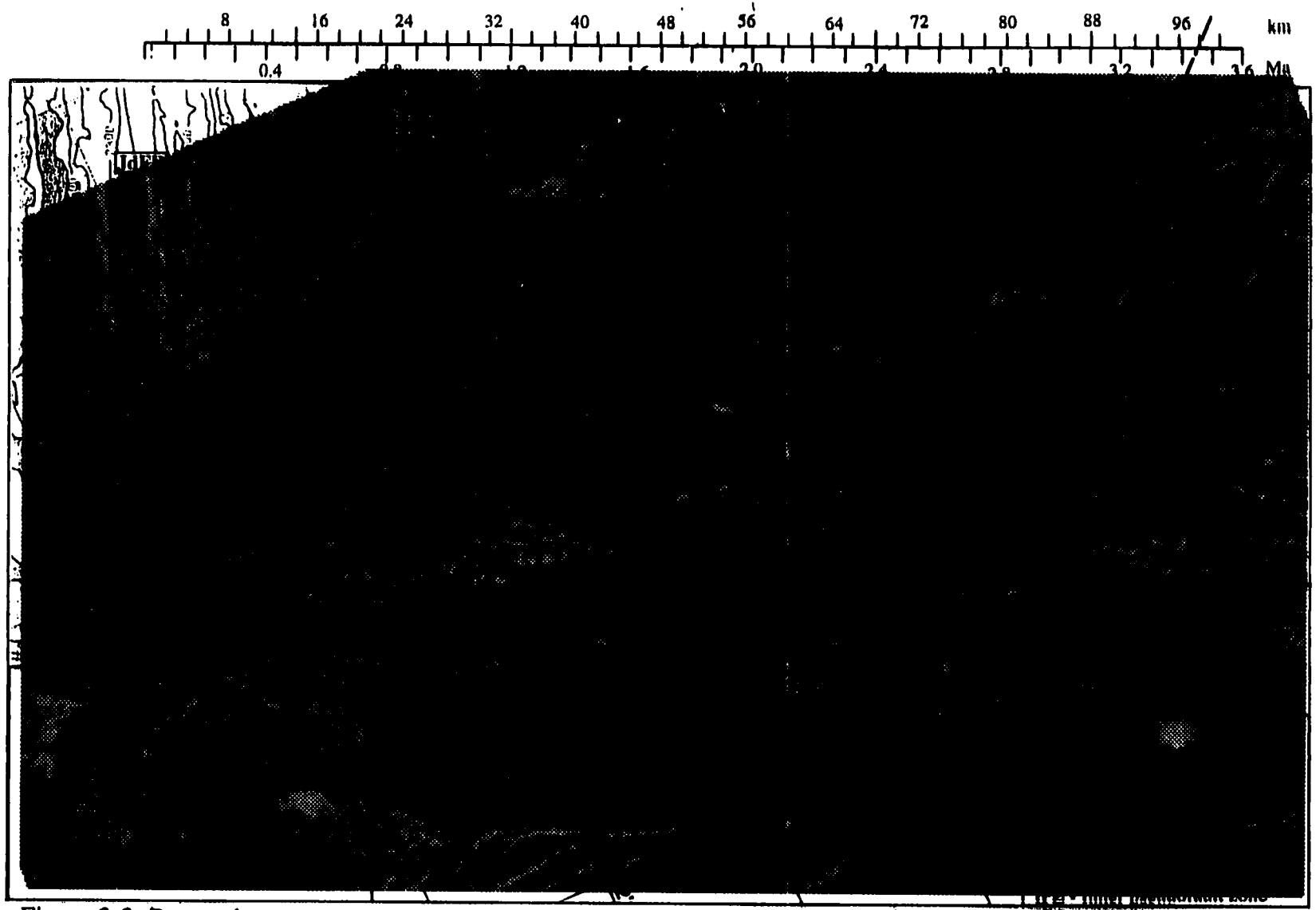

Figure 2-3: Pre- and post-propagator structural features evident from the underlying GLORIA imagery (EEZ Staff, 1986) are superimposed on a Sea Beam map (after Embley and Wilson, 1992) of the region.

Figure 2-4 a: SeaMARC II imagery of an area on the north WBD wall (Holmes et al., 1995). The location of the area is given by latitude-longitude co-ordinates in Fig. 2-4 b. The track line is oriented at 65°and the swath is 5 km wide on each side. The image shows abyssal hill structures on the Juan de Fuca Plateau which are cross-cut by the north scarp. The extension of these structures in the subsurface appears to be reflected in the topography of the face.

Figure 2-4 b: Interpretive map based on the image texture. The Juan de Fuca plate has distinct abyssal hill structures that appear to be perpendicular to the axis of the trough. The abyssal hills extend to the seafloor edge where they are truncated by the north WBD wall. The north scarp itself has a serrated rim that subtends a face of fairly rugged topography. The break at the base of the steep cliff exposure is sharp and leads, in the eastern part into the basin but in the western part to a lower sloping ramp. The floor of the WBD is covered with at least three kinds of mass wasting deposits. In addition, the trace of extensive lineaments which probably indicate the path of strike-slip motion, is evident on both sides of the depression. In the southernmost part is Parks Plateau which clearly lacks the fabric of the Juan de Fuca plate.

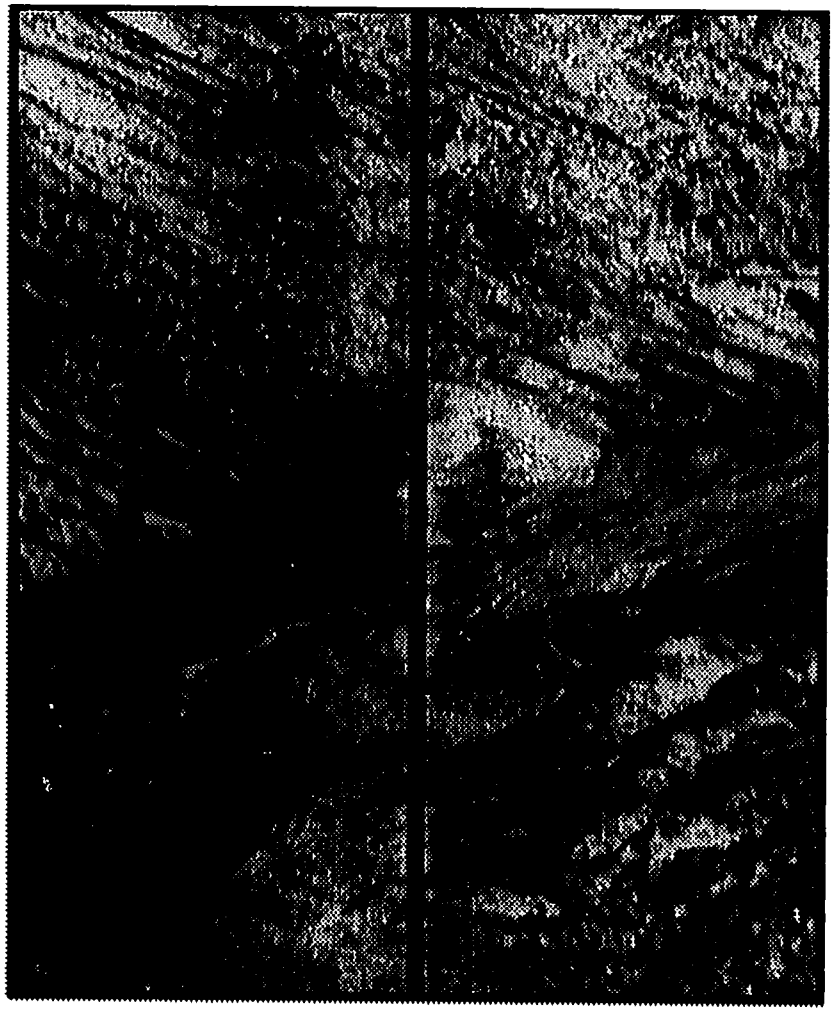

Figure 2-4a

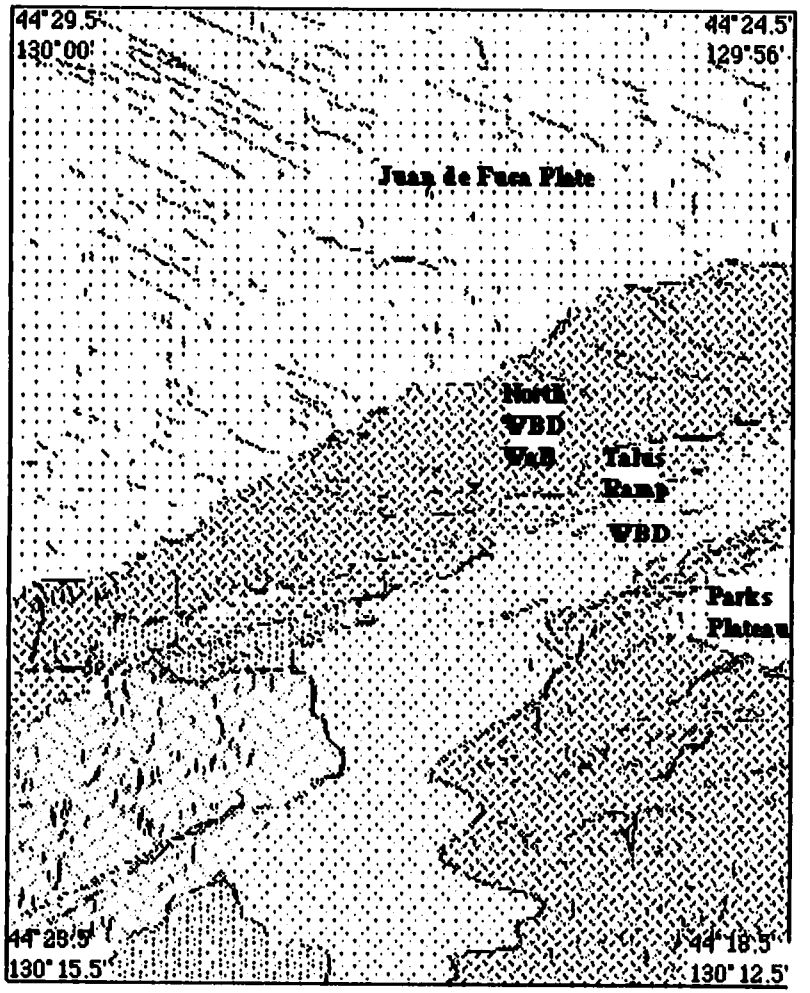

Figure 2-4b

Figure 2-5: Post-propagator features and their trends identified in GLORIA imagery (BBZ Staff, 1986) of the area around the WBD. The abyssal hill fabric provides evidence of the magmatic system while the structural lineaments indicate the evolution of strike-slip movement in establishing a transform zone.

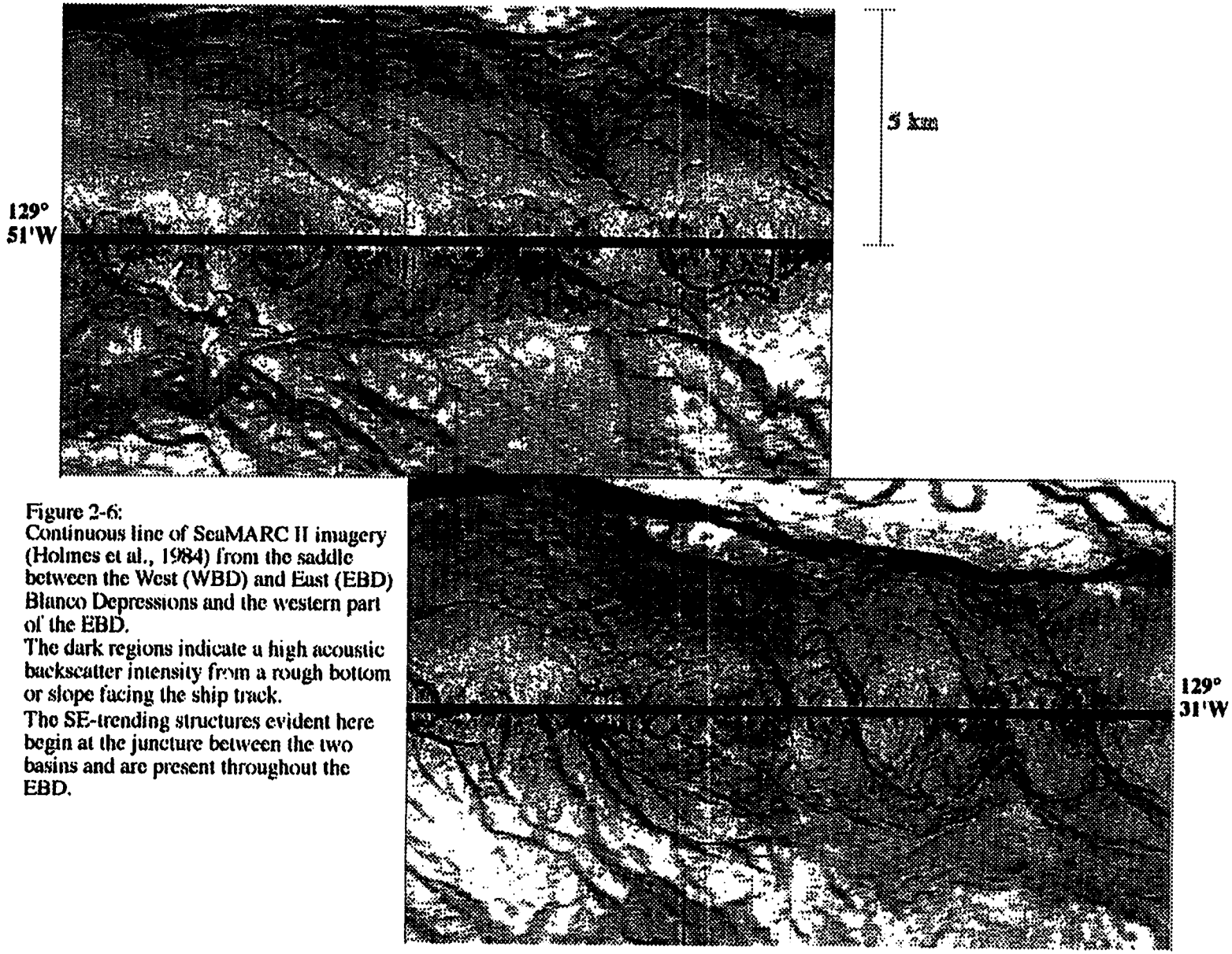

Figure 2-6:
Continuous line of SeaMARC II imagery (Holmes et al., 1984) from the saddle between the West (WBD) and East (EBD) Blanco Depressions and the western part of the EBD.
The dark regions indicate a high acoustic backscatter intensity from a rough bottom or slope facing the ship track.
The SE-trending structures evident here begin at the juncture between the two basins and are present throughout the EBD.

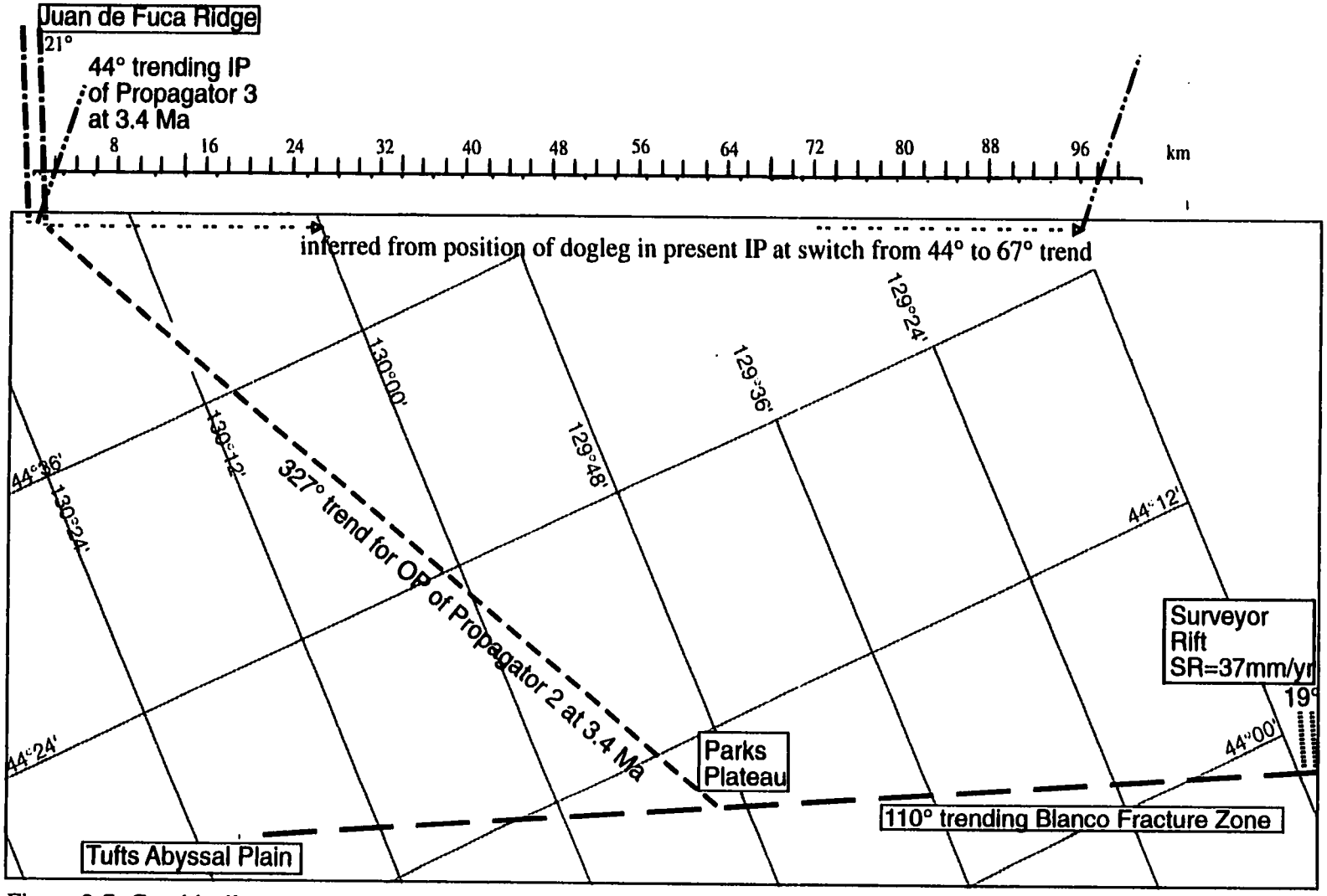

Figure 2-7: Graphically reconstructed positions of Propagator 3 and the outer pseudofault (OP) of Propagator 2 at 3.4 Ma when the IP angle increased show that the JdFR propagator tip intersected the OP. The OP location 54 km from the Surveyor axis is calculated from having spread for 1.5 m.y. at 37 mm/yr. The latitudinal position of the JdFR propagator tip is extrapolated from the dogleg in its present-day IP.

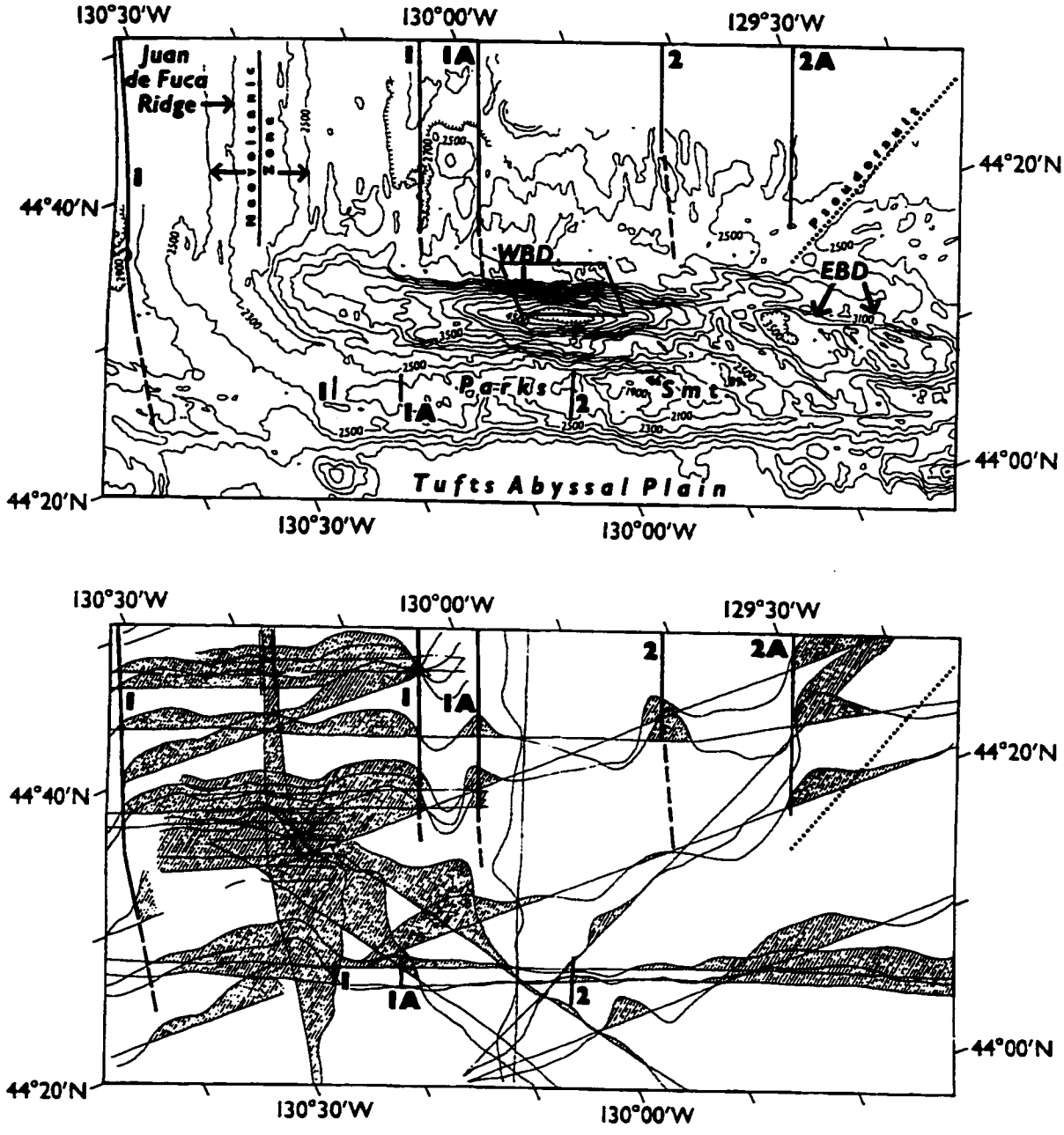

Figure 2-8: (after Embley and Wilson, 1992)

(a): Sea Beam map of the Blanco Transform Fault Zone at its intersection with the southern Juan de Fuca Ridge. This western segment includes the West (WBD) and East (EBD) Blanco Depressions. Superimposed on the bathymetry are magnetic anomalies 1 (~0-0.75 Ma), 1A (~1 Ma), 2 (~1.6-1.9 Ma) and 2A (~2.5-3.5 Ma). The boxed area indicates the site for intensive study here.

(b): Magnetic anomalies for the area above. Anomalies 1, 1A, 2 and 2A have been identified on the Juan de Fuca and Parks Plateau. The picks south of the WBD are discussed in the text.

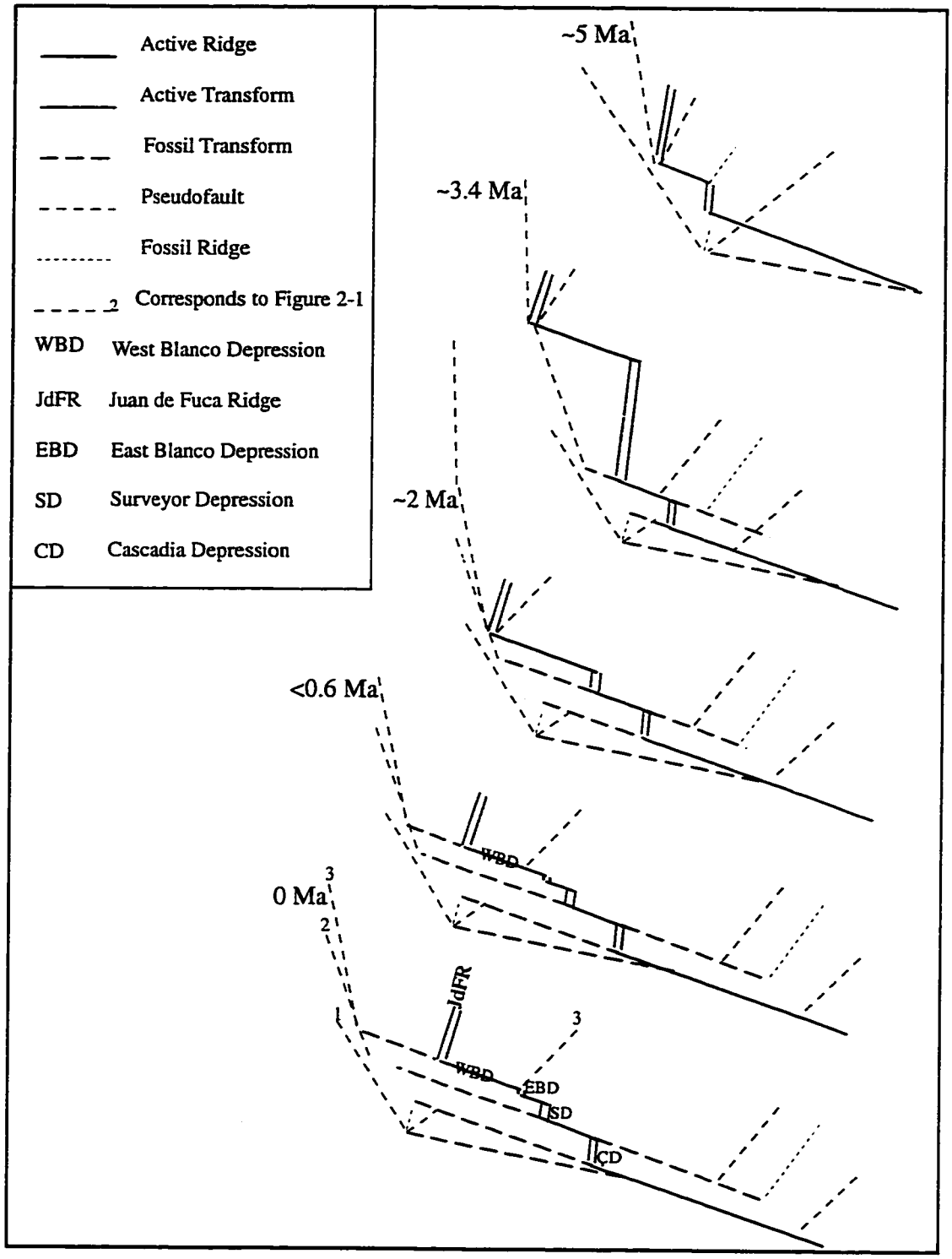

Figure 2-9: Revised tectonic evolution of the JdFR - WBD region for the past 5 Ma, after Embley and Wilson (1992). Modifications include a slowing of the propagator at 3.4 Ma due to it intersecting a previous inner pseudofault, propagator termination at 2 Ma north of Parks Plateau, and long-term establishment of strike-slip activity here leading to formation of the WBD after 0.6 Ma.

CHAPTER III: THE MAGMATIC SETTING

3.1 Introduction

Knowing where and when the last southward propagator along the Juan de Fuca Ridge (JdFR) terminated, is critical to unravelling the magmatic history in the region around the West Blanco Depression (WBD). This chapter uses available geochemical data to trace the inner pseudofault and so determine its half-angle. The work shows that the saddle area of the WBD - EBD (~2.3 Ma) and the north flank of Parks Plateau (~2.0 Ma) exhibit the predicted geochemical consequences of a propagation regime (Christie and Sinton, 1981). If Parks Plateau were penetrated, the rift tip would have reached the south flank at ~1.7 Ma but irrespectively, it implies that the study site was accreted under post-propagation conditions (cf. Embley and Wilson, 1992). Chapter III also utilizes Sea Beam and GLORIA maps to identify an asymmetric chain of five seamounts on the Juan de Fuca plate. It is proposed that their physical characteristics result from non-steady state mantle flow at the JdFR which migrates with respect to the absolute reference frame. Under these circumstances, a three-stage model of accretion on- and near-axis is outlined for a magmatic pulse which combines the insights of Johnson and Dick (1992) on time dependent mantle diapiric flow .

3.2 Data

This chapter utilizes the Sea Beam (Embley and Wilson, 1992) and GLORIA (EEZ Scan 84 Scientific Staff, 1986) datasets discussed in Chapter II. In addition, geochemical data is obtained for 6 dredges (Melson, 1969) from the literature and for 3 *Nautile* dives (Juteau et al., 1995) between the JdFR axis and the East Blanco Depression

(EBD). The dredge and dive locations, with the exception of one dredge north of the EBD, are plotted in Figure 3-1 from the on- and off-bottom points logged (Melson et al., 1977). The samples represent the Cleft Segment of the JdFR (dredge #10), the Surveyor Ridge (dredge #N), the north and south flanks and top of Parks Plateau (BN-14, BN-15 and BN-16), the pseudofault in the saddle area between the depressions (#11), the rift tip intersecting the north flank of Parks Plateau (dredge #1), and the north WBD scarp (dredges #5 and #6 on the lower and upper slopes). Note that (i) dredge #1 does not lie along the bathymetric profile drawn in Figure 5 of Melson (1969); and (ii) dredge #6 is on the upper slope of the north WBD scarp as shown in Figure 5 of Melson (1969) and not on the Juan de Fuca plate according to the given coordinates because the depth of 3084 m recorded by a precision depth recorder is considered more accurate than the 15 minute spaced, Loran A fixes (Melson, pers. comm.).

The major element compositions of the dredges were analyzed using an electron microprobe by Melson et al. (1977). Their method along with the precision limits of the data (SiO_2=0.70, Al_2O_3=0.30, FeO*=0.34, MgO=0.22, CaO=0.30, Na_2O=0.08, K_2O=0.04, TiO_2=0.12 and P_2O_5=0.04) is reported by Melson et al. (1976). The bulk compositions of the Blanconaute dive rocks listed by Juteau et al. (1995) were obtained through inductively coupled plasma emission spectroscopy. The analytical procedure and precision limits are given in Appendix F. The dive samples from the eastern part of the study site produce similar results as for dredges #5 and #6 (see Chapter VIII); hence, there are no systematic differences between the two datasets used here. There are four outliers - one each from the JdFR (#10), the study site (#6), Parks Plateau (BN-14), and the rift tip (#1) - which tend to plot outside the outlines of these end-member groups in Figures 3-2 to 3-4.

3.3 Results and interpretation

3.3.1 Geochemistry

The samples in this study vary from relatively unevolved to highly evolved with MgO from 4.7 to 8.8 wt. % (Figure 3-3), and Mg#'s ([Mg]/[Mg+Fe]*100) from 41 to 61 (Figure 3-4a). This spans almost the entire range of Pacific Ocean basalts which vary in MgO from 4.8 to 8.8 wt. % (Melson et al., 1976), and in Mg# between 36 and 67 (Wilkinson, 1982). The geochemical variation in this region is displayed by sample locale using major element variation diagrams of K_2O vs. SiO_2 (Figure 3-2), as well as Al_2O_3, CaO, FeO*, TiO_2, K_2O, and SiO_2 vs. MgO (Figures 3-3). The effects of crustal level processes and the phase assemblages involved are also shown in a plot of CaO/Al_2O_3 vs. Mg# (Figure 3-4a). Olivine fractionation cannot change the CaO/Al_2O_3 ratio but the fractionation of plagioclase or CaO-rich clinopyroxene would cause it to increase or decrease respectively. The relative importance of shallow fractionation in comparison to partial melting variations is conveyed in a plot of TiO_2 vs. K_2O (Figure 3-4b). TiO_2 is more compatible during mantle melting because of clinopyroxene involved in the spinel or garnet stability fields while K_2O is more compatible due to plagioclase crystallization at low pressures (Hanson, 1989). The ranges in composition and evolutionary trends for the various localities are summarized below.

The low-K, subalkaline lavas of the JdFR and the study site have similar K_2O and SiO_2 contents (Figure 3-2), medium-high CaO/Al_2O_3 ratios (>0.74), and are moderately to highly evolved (Mg#: 40.6-54.2) (Figures 3-3 and 3-4a). Samples of the JdFR and part of the study site produce correlations with MgO (Figure 3-3) that are indicative of clinopyroxene dominated fractionation (Figure 3-4a) which is consistent with the

presence of FeTi basalts (FeO* >12.5 wt. % and TiO_2 >2.25 wt. %) in the study site. On the TiO_2 vs. K_2O plot (Figure 3-4b), regression lines for the JdFR and study site both intersect the TiO_2 axis, albeit with different slopes. However, there is one distinction between these locales. For other parts of the lower slope in the study site, the trends are positive for Al_2O_3, FeO* and SiO_2, and negative for TiO_2 and CaO (Figure 3-3) which suggests plagioclase dominated fractionation (Figure 3-4a). Hence, there is evidently a two-part process to crustal building in the study site which is consistent with the geological findings (see Chapters IV and V).

The sub-alkaline lavas of central Parks Plateau are characterized by enriched K_2O to varying extents (Figure 3-2) and medium CaO/Al_2O_3 ratios (0.73-0.81) (Figure 3-4a). They are slightly to moderately evolved (Mg#: 51.7-58.6) except for a few on the south flank which are more highly evolved (MgO: 4.7-6.6 wt. %) (Figures 3-3 and 3-4a). Parks Plateau is unusual because neither the group or sub-groups show obvious correlations of major elements with MgO on variation diagrams (Figure 3-3). However, its negative trend for CaO/Al_2O_3 versus Mg# (Figure 3-4a) reflects clinopyroxene controlled fractionation (see Section 8.4.2). This group is scattered on the TiO_2 vs. K_2O plot (Figure 3-4b) but a regression line would intersect the TiO_2 axis almost horizontally indicating the dominance of mantle processes on its evolution, which is consistent with the findings in Chapter VIII.

The low-K, subalkaline lavas of the rift tip and the Surveyor Ridge are both moderately evolved (Mg#: 50-56) with low CaO/Al_2O_3 ratios (0.62-0.71) (Figure 3-4a). The Surveyor Ridge lies within the JdFR-study site grouping for K_2O and SiO_2 (Figure 3-2) while the rift tip partially overlaps but also has samples lower in SiO_2 (Figure 3-2).

This indicates that the rift tip area is composed predominantly but not entirely by Surveyor Ridge crust. However, neither overlaps with the JdFR-study site in Al_2O_3 or CaO content (Figure 3-3) which suggests that they can be distinguished from the crust on the north WBD scarp. The rift tip further differs from the JdFR-study site in FeO and TiO_2 content (Figure 3-3) implying that the second crustal component here could not represent normal spreading crust.

The rift tip trends for the various major elements versus MgO (Figure 3-3) indicate the influence of clinopyroxene controlled fractionation. This however differs from the effects for the JdFR-study site or Parks Plateau in that the positive correlation for CaO/Al_2O_3 versus Mg# (Figure 3-4a) occurs at a lower CaO/Al_2O_3 ratio. By contrast, the Surveyor Ridge occurs as a small cluster on all these plots indicating little chemical evolution except to a minor degree in SiO_2 (Figure 3-3). On the TiO_2 vs. K_2O plot (Figure 3-4b), a regression line for the rift tip intersects the TiO_2 axis indicating that the dominant influence has been partial melting variations while the Surveyor Ridge forms a tight but overlapping cluster.

The low-K, subalkaline lavas from the saddle area close to the pseudofault are distinguished by K_2O and SiO_2 contents that lie outside the group created at the JdFR (Figure 3-2). They share the same low CaO/Al_2O_3 ratios as the Surveyor Ridge but by comparison are only slightly evolved in composition (Mg#: 56.5-58.3) (Figures 3-3 and 3-4a). They are further highlighted on variation diagrams with MgO or Mg# (Figures 3-3 and 3-4a) by a negative trend in Al_2O_3, CaO and CaO/Al_2O_3, and a positive trend in FeO*, TiO_2, K_2O and SiO_2 indicating plagioclase controlled fractionation. This suggests that the physical-chemical conditions which promoted the process here might have recurred in accreting the crustal exposure on the lower slope in the study site.

3.3.2 The seamounts

Sea Beam bathymetric coverage (Embley and Wilson, 1992) of the Juan de Fuca plate does not continue as far eastward as the GLORIA image (EEZ Scan 84 Scientific Staff, 1986). Nonetheless, both show a chain of seamounts which appear ~38 km in the rear of the tectonic tip (Figures 2-2 and 2-3) as it intersects the north flank of Parks Plateau and extend linearly to the present-day tip of the JdFR axis (Figures 3-1 and 3-5). The best-preserved of these volcanic forms occur closer towards the ridge which implies a younging in this direction. However, the tallest one is north of the western part of the study site after which they progressively decrease in height towards the spreading center until the last fades at the juncture of the JdFR with the WBD at about 0.3 Ma (Figure 3-1).

Altogether, 5 of these rounded structures are identified along an 82° trending line (Figure 3-5). By separating this series of cones equi-distantly along their bathymetric lows with ridge-parallel boundaries, the north WBD scarp can be divided into 6 magmatic provinces. Each is 9-12 km in width and took an average of 0.36±0.04 million years to construct. They are denoted: JdFR - from 0-8 km or 0-0.3 Ma, E. JdFR from 8-20 km or 0.3-0.7 Ma, N. WBD - from 20-31 km or 0.7-1.1 Ma, W. study site from 31-40 km or 1.1-1.4 Ma, E. study site from 40-50 km or 1.4-1.75 Ma, and rift propagator - from 50-60 km or 1.75-2.1 Ma from the axis.

3.4 Discussion

The results indicate that the JdFR-Blanco region is complex and that the geochemical evolution at various localities is distinct. Three possible scenarios or some combination thereof could account for the variability: off-axis volcanism, rift

propagation, or on- and near-axis accretion. The evidence for or against these possibilities is considered here.

3.4.1 Consequences of rift propagation

These initial results demonstrate that the JdFR and Surveyor Ridge can be distinguished geochemically if it is assumed that the samples recovered from each are typical of their spreading history. This opens the possibility for tracing the boundary between crust that formed at either spreading center and hence, determining the path of propagator #3 and the crustal evolution after its passage. Its point of termination cannot be deduced directly in this study, however, because the dives only recovered samples from the area of off-axis volcanism that obscures the underlying crust.

The saddle area close to the pseudofault would have formed about 11 km north of the rift tip (Figure 3-1). Its lack of overlap in geochemical characteristics with the Surveyor Ridge clearly indicates a change to the propagator regime. Furthermore, its slightly evolved nature in comparison to the rest of the sample collection supports the presence of a 3-20 km zone behind the tectonic tip where conditions would be optimal for unfractionated lavas (Christie and Sinton, 1981). In addition, its distinct characteristics as compared to the JdFR crust confirms that even after spreading has occurred for around 0.35 million years as here (Figure 3-1), magmatic accretion under conditions of rift propagation still differs considerably from normal spreading ridges (Sinton et al., 1983).

By comparison, the rift tip vicinity on the north flank of Parks Plateau shows considerable overlap with the Surveyor Ridge which implies that this crust is present here. The other low SiO_2 end-member incorporated in this suite could be related to

propagation effects. Both these observations are consistent with a 3 km long zone behind the tectonic tip in which there are only intrusions into the existing basement (Christie and Sinton, 1981), or alternately with underplating ahead of the rift propagator (Calvert et al., 1990; Hasselgren et al., 1992).

Other evidence for propagator #3 having reached the north flank of Parks Plateau at this location can be found in the subsequent crustal evolution along this scarp. Although the central Parks Plateau was resurfaced by off-axis volcanism as interpreted above, there is another dredge (#2) between these localities (Melson, 1969). It represents the spreading regime <0.25 million years after passage of the propagator tip (Figure 3-1); this data is overlaid on Figure 3-4a. The suite mostly overlaps the Surveyor Ridge field as at the rift tip area which suggests little disruption of the original basement. It also includes some samples which overlap with the Parks Plateau field indicating that the off-axis volcanism spread out to this point. In addition, there are a few samples that are even less evolved than those in the saddle area. This could be because of the 0.1 million year difference in period of spreading or alternately be due to the different magmatic conditions if propagation has indeed ceased here.

The study site in ~1.7 Ma crust reflects the state of the magmatic system after about 18 km or 0.6 million years of spreading (Chapter II). The consistent geochemical overlap of the upper slope samples with the JdFR field indicates the presence of such normal spreading crust here. This is slightly less than the <0.7 million years predicted by Christie and Sinton (1981) as the transition period needed for a ridge to evolve from zero to full spreading rate. If rift propagation only ceased between 1.4 Ma (Sinton et al., 1983) and 1.7 Ma (Chapter II), then the study site would lie roughly 19 km north of the tectonic tip. Nonetheless, the high degrees of fractionation here are more consistent with the maximum extents predicted for a 20-100 km zone behind the tip (Christie and Sinton,

1981). Also, normal mid-ocean ridge basalt (N-MORB) clearly forms the crust here instead of only appearing 100 km beyond the tip as predicted (Christie and Sinton, 1981). While these discrepancies do not confirm that the rift propagator terminated at ~2 Ma, it does suggest a more rapid transition and supports the possibility that the magmatic system between 2 Ma and 1.4-1.7 Ma did not continue to evolve under conditions of propagation.

3.4.2 The seamounts - near-axis volcanism

One explanation for this seamount chain in a relative reference frame is that it could represent a melting anomaly progressively migrating southward along the axis between 2.1 Ma and 0.3 Ma. However, there is no mechanism for why or how the process should occur. If it were associated with propagation, there is no reason why it too would not have halted by 1.4 Ma or earlier. Neither is there an explanation for why or how these forms were consistently preserved intact to the east in the last 1 million years when spreading has been symmetric (Tivey, 1994).

An alternative account considers the orientation and age trend of this volcanic trail in an absolute reference frame (Figure 1-1). On the west side of the JdFR, the absolute motion of the Pacific plate to the NW (N315°E) at 55 mm/yr is large compared to the spreading rate of the JdFR to the WNW (N296°E) at 30 mm/yr (Davis and Karsten, 1986). Consequently, seamounts tend to be aligned in the direction of the absolute Pacific plate motion vector (e.g. Endeavour seamounts).

On the east side of the JdFR, the absolute motion of the Juan de Fuca plate is to the NE (N43°E) at 25 mm/yr and spreading is to the ESE (N110°E) at a half-rate of 30 mm/yr (Davis and Karsten, 1986). It can be calculated or shown graphically (Figure 3-5)

that the combined motions produce a vector with a total rate of 46.2 mm/yr along an 80° trend. This closely approximates the 82° trend of these volcanic constructions.

The absolute ridge motion (Davis and Karsten, 1986) as a result is 30 mm/yr to the NNW (N338°E) which converts to 20 mm/yr in a ridge normal direction (N296°). Hence given the half-rate of spreading, any seamount on the Juan de Fuca plate for example will be moved eastward in relation to the mantle. This implies that the age of these cones will increase away from the axis which is consistent with the interpreted observations.

The seamounts on the trailing plate behind the NW-migrating JdFR are spaced roughly at a constant distance of 11 km apart on average. It suggests a regular episodicity in the time-varying mantle flow (assuming that all else remains constant within the system) which could originate in either a non- or steady state situation (Johnson and Dick, 1992).

In a steady-state case, long-term pulses of enhanced upwelling cannot arise from only a single thermal anomaly since it could not be embedded far in advance of the ridge without causing magmatism on the leading plate (cf. Davis and Karsten, 1986; Schouten et al., 1987). However for a newly created spreading center, it is possible that the asymmetric ascent velocities in the melt regime resulting from the difference in absolute plate velocities may not yet be as broad as for a mature ridge. Consequently, the excess melts for the last 2 Ma could have been produced from melting successive anomalies under influence of the approaching ridge which then passes over them leading to continued magmatism near-axis. However, it would be highly unusual for such anomalies to form one linear trail through the mantle which suggests that even this modified model does not apply here.

In a preferred non-steady state case, melts would solely be derived from continual initiation of diapiric flow (Whitehead et al. 1984; Johnson and Dick, 1992) which invokes buoyancy-driven mantle flow. According to Spiegelman (1996), buoyant upwelling is favoured by relatively lower spreading rate or viscosity (i.e. high temperature) that possibly applies to intermediate rate spreading centers. This process is time dependant because of the faster ascent rate of melt from residual mantle (McKenzie, 1985).

Consequently, with incorporation of the insights from these previous studies, it is suggested that volcanic activity from one such magmatic pulse would occur in three stages (Figure 3-6).

In the first stage (Figure 3-6a), the ridge is situated above the high melting rate region and as a result receives high degree melts that are erupted on axis over a mantle that is depleted to a lesser extent (Johnson and Dick, 1992). Even in this active mode, the flow of melt is less focussed beneath the spreading center and is instead delivered over a distance of about ten times the half-width of the accretion zone (Spiegelman, 1996). For the JdFR with a 1-3 km wide central graben (Embley et al., 1991; Goldstein et al., 1992), that means within 5-15 km of the ridge axis. However, this range will potentially be affected by the asymmetry in the mantle stream lines from distortion beneath the leading (Pacific) and trailing (Juan de Fuca) lithospheric plates (Schouten et al., 1987). Nonetheless, it coincidentally matches the 9-12 km average width of the magmatic provinces that is defined by the spacing of the 5 volcanic cones in the chain (Section 3.3.2). Melts initially arriving near-axis would have been derived from the low melting rate region and as a result, the melt supply will be low (Spiegelman, 1996). Furthermore, since this mode causes solid convergence in the melting zone, the incompatible element concentrations are diluted on-axis while enriched melts are produced farther away (Spiegelman, 1996). Such volcanic activity within 1-4 km of the axis has been interpreted

for fast spreading ridges (Vera and Diebold, 1994), and Pacific seamounts near-axis typically range from enriched to depleted basalts (Batiza and Vanko, 1984). However, it should be noted that no similar evidence has been reported for intermediate spreading ridges. Hence, it is inconclusive as to whether these seamounts actually originate during this stage.

In the second stage (Figure 3-6b), the ridge migrates westward past the core of the diapir which continues melting. Consequently, it can be predicted that the melt supply will increase substantially on the trailing plate and there should be a shift from enriched (E-) or transitional (T-) to N-type MORBs in building the seamount. The seamounts are constrained to be near-axis by the last in the E. JdFR province (Figure 3-1) lying within 12-17 km of the ridge suggesting that volcanism occurs on crust which is 0.3-0.6 million years older than the active spreading center.

In the third stage (Figure 3-6c), the JdFR migrating at 20 mm/yr has completely passed over the diapir. The final melts from this solid residue are very depleted. They are emplaced into the thickening lithosphere between the Stage 2 seamount and the axis due to the slightly higher spreading rate of the JdFR (30 mm/yr). This material will also flow west of the JdFR where it will constitute a third source contributing to the heterogeneity of the mantle. Additional melting of such a component in advance of the approaching JdFR could account for the highly depleted compositions of Vance seamount (Smith et al., 1994).

3.4.3 Off-axis volcanism on Parks Plateau

The lavas covering the north and south flanks and top of Parks Plateau have varying extents of enrichment spatially with the least enriched on top. Neither the composition nor the lack of a progressive chemical trend can be explained in terms of

either the post-propagation evolution i.e. an east to west change (Christie and Sinton, 1981), or a propagation attempt across Parks Plateau after ~2 Ma i.e. a north to south change.

Instead, there is strong evidence that the central Parks Plateau has experienced recent volcanism. This was suggested by Gaetani et al. (1995) based solely on the compositional variability in Melson's (1969) dredge #2 between the rift tip and here (Figure 3-1). The hypothesis is supported by magnetic data which shows a positive magnetic anomaly crossing the central part of Parks Plateau (Tivey, 1994). This indicates that the crust here is of Brunhes or Jaramillo age and would be less than a million years old. The age estimate is further constrained by the absence of these enriched lavas from the study site on the north WBD wall. This implies that they must have erupted after the opening of the WBD around 0.35-0.4 Ma (Embley and Wilson, 1992). Such a young age is also inferred by direct observations of numerous volcanic cones covering the plateau (Dauteuil, 1995), the relative freshness of the flows, and the abundant fauna (Blanconaute Shipboard Party, 1991).

This off-axis volcanic activity has two possible origins, both of which have been suggested for other seamounts associated with the JdFR. One option is that it reflects a thermal anomaly in the mantle with differences in composition attributed to melting processes. Such an example would be Axial seamount (Rhodes et al., 1990 cf. Goldstein et al., 1992). Another alternative is that the spectrum of enriched MORB represents the product of mixing depleted mantle with variable amounts of an enriched component. Such an example would be the Cobb-Eikelberg seamount chain (Goldstein et al., 1992; Smith et al., 1994). These possibilities are examined further in Chapter VIII.

3.4.4 Implications for magmatic accretion

The multi-stage model outlined for magmatic activity resulting from diapirism under conditions of buoyant mantle flow beneath a migrating ridge bears specific implications for crustal accretion. Note that along-strike, several such blobs are rising (Figure 3-7). When the Propagator 3 province was accreted, the shallowest of these diapirs were evidently tapped at the center of the segment where the seamount formed near-axis (Figures 3-1 or 3-5). For the successive four provinces, the magma supply was progressively focussed closer to the Blanco Transform Fault. By contrast, findings near offsets elsewhere indicate that these blobs are tapped at deep levels before they achieve a large size (Niu and Batiza, 1994). However, in this case the scenario is consistent with the gradual northwestward migration of the ridge over a high in the magma delivery system. This implies that the melt source either readjusts at a longer time-scale than ~2 Ma to along-axis shifts of the ridge or that this core is thermally distinct and remains fixed in the mantle until it is consumed. Nonetheless, the main point here is that the same process occurs along the spreading segment although melts are more focussed in the vicinity of the ridge where seamounts eventually form near-axis.

The crustal section produced during Stage 1, is likely to be most akin to a typical layered structure. The seamounts in Stage 2 are topographically similar to calderas complexes as at Hawaii or Iceland (Dziak et al., 1995). They should thus have a central conduit for the magma supply with magma injected down rift initially rising below such circular calderas that develop into collapse structures over time. This should result in upper and lower volcanic layers with lateral dike injection possible up to a 30 km long distance (Embley et al., 1991; Embley and Chadwick, 1994) complicating the crustal structure. In Stage 3, the eruptives and sills would disrupt the crustal section. Note that in

all three stages, the crustal and asthenospheric evolution is decoupled and that the crust affected in Stages 2 and 3 will include the output from different magmatic pulses.

The lower and upper slopes in the WBD site are dominated respectively by plagioclase and clinopyroxene fractionation which could reflect a volcanostratigraphic sequence with the less evolved magmas underlying the more evolved lavas. However, the lower slope itself is moderately to highly evolved which suggests that plagioclase dominated fractionation may result from a more complex magmatic process, a conclusion that is supported by petrographic evidence (Chapter VII).

Juteau et al. (1995) have found a differentiation maxima (Figure 3-8) at the boundary between the "West Study Site" and "East Study Site" provinces. They interpret it as the peak of a continual increase in fractionation after passage of the propagator (Figure 3-7). On this basis, they support the Christie and Sinton (1981) model despite the obviously uneven sampling that was biased towards such a discovery in the study site because of the concentration of dives there. This conclusion is negated by evidence of another peak in degree of differentiation at the boundary between the "East Juan de Fuca Ridge" and "North West Blanco Depression" provinces which is confirmed by results from dredge data of Karsten and Delaney (1991). It suggests that these highs may be characteristic of the lull between magmatically robust phases of crustal construction.

3.5 Conclusions

1. The refined trace of the pseudofault is at 67° (cf. ~58-60°). Consequently, the rift tip would theoretically have reached the Blanco Fracture Zone at 1.7 Ma (cf. 1.4-1.5 Ma). Even in this case, the 1.1-1.7 Ma study site would have been accreted post-propagation.

2. The propagation regime dominates the WBD - EBD saddle and the north flank of eastern Parks Plateau until ~2 Ma. No geochemical data are available to assess whether propagator #3 penetrated further southward.

3. A model in which propagation terminated at 2 Ma is supported by: (i) the start of a seamount chain implying establishment of a spreading-related magmatic system; and (ii) the geochemically "normal" characteristics of the study site that is closely akin to the JdFR, thus providing for a prior 300 000 year transition period.

4. Volcanism on Parks Plateau is of recent age (<0.4 Ma) and hence, is unrelated to the earlier propagation history. This off-axis event was limited to the central part of Parks Plateau.

5. Between 0 Ma and 2 Ma, a three-stage process of accretion on- and near-axis is applicable for the JdFR as a result of non-steady state diapiric mantle flow and a NW-migrating ridge.

6. The mantle dominates over crustal level processes at most localities except for the study site on the north WBD scarp where they have both affected crustal formation.

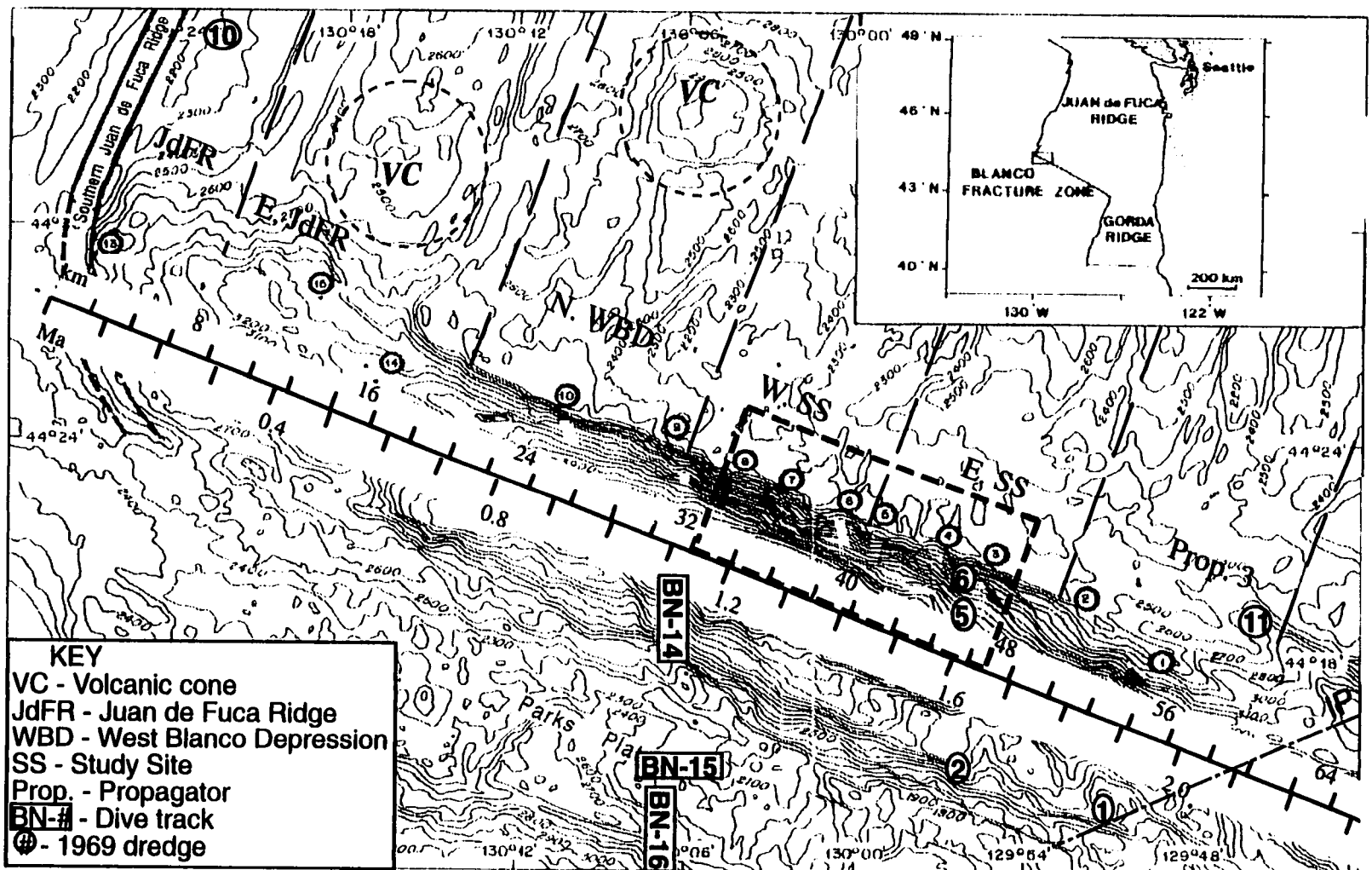

Figure 3-1: The location of dredges and dives along the western segment of the Blanco FZ is overlain on a Sea Beam map of the area (after Embley and Wilson, 1992). The dredge data is from Melson (1969) and the dive data is from Juteau et al. (1995). The small, numbered circles in the background show the position of Delaney et al.'s (1987) dredges, referred to in Chapter X. Also marked is the location of the propagator 3 inner pseudofault (IP) and the boundaries between a series of volcanic cones on the Juan de Fuca plateau.

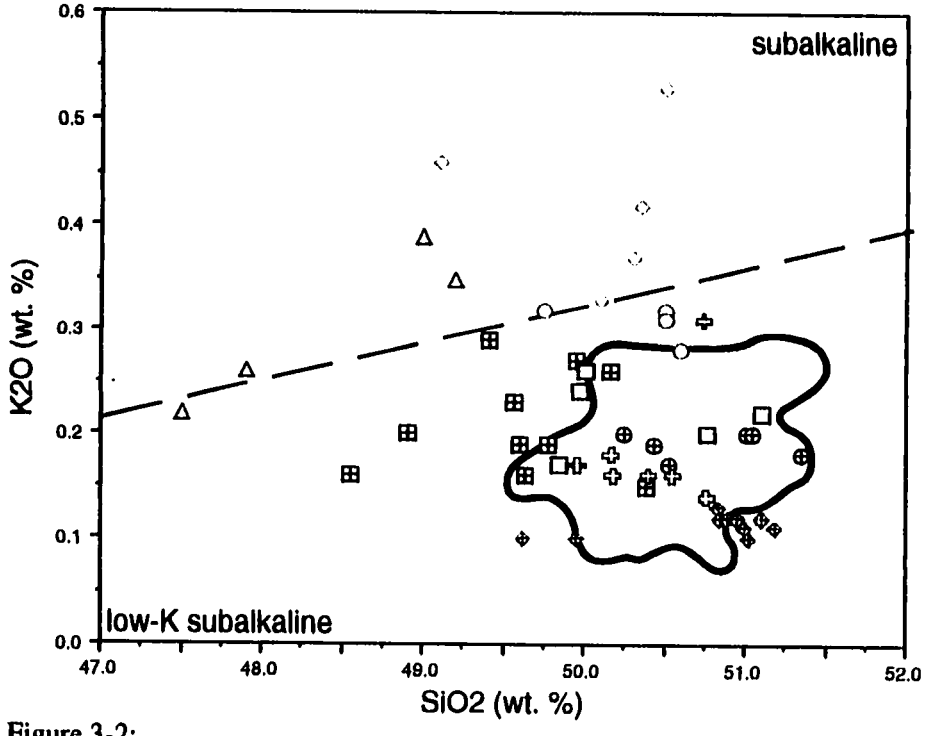

Symbol	Location	Suite Outline
✣	Upper site (#6)	———
□	Lower site (#5)	———
◆	P-fault at saddle (#11)	—·—·—
⊕	Surveyor Ridge (#N)	—— ·
⊞	R-tip at NE PP (#1)	.....
	S. PP (BN-16)	- - - -
○	Top of PP (BN-15)	— — —·
△	N. PP (BN-14)	.....
	JdFR (#10)	———
Middlemost (1975)	——	——

Figure 3-3 a-f (i) and a-f (ii): (overleaf) Major element variation diagrams for Al2O3, CaO, FeO*, TiO2, K2O, SiO2 vs. MgO for basalts from different localities in the JdFR-Blanco region. The samples are denoted by symbols (except for the JdFR where there a large number of data points) and the localities (except for Parks Plateau) are outlined to show the chemical trend.

Figure 3-2:
Variation of K2O (wt. %) vs. SiO2 (wt. %) highlights the alkali-enriched basalts constituting central Parks Plateau (PP) although the top (BN-15) is less enriched than the north (BN-14) and south (BN-16) flanks. By comparison, the rest of the suite is composed of low-K, subalkaline basalts. The Juan de Fuca Ridge (JdFR - #10), the upper (#6) and lower (#5) slopes of the study site, and the Surveyor Ridge (#N) samples all group together. The pseudofault in the saddle area (#11) and the rift tip on the north flank of eastern Parks Plateau (#1) both lie outside the previous cluster.

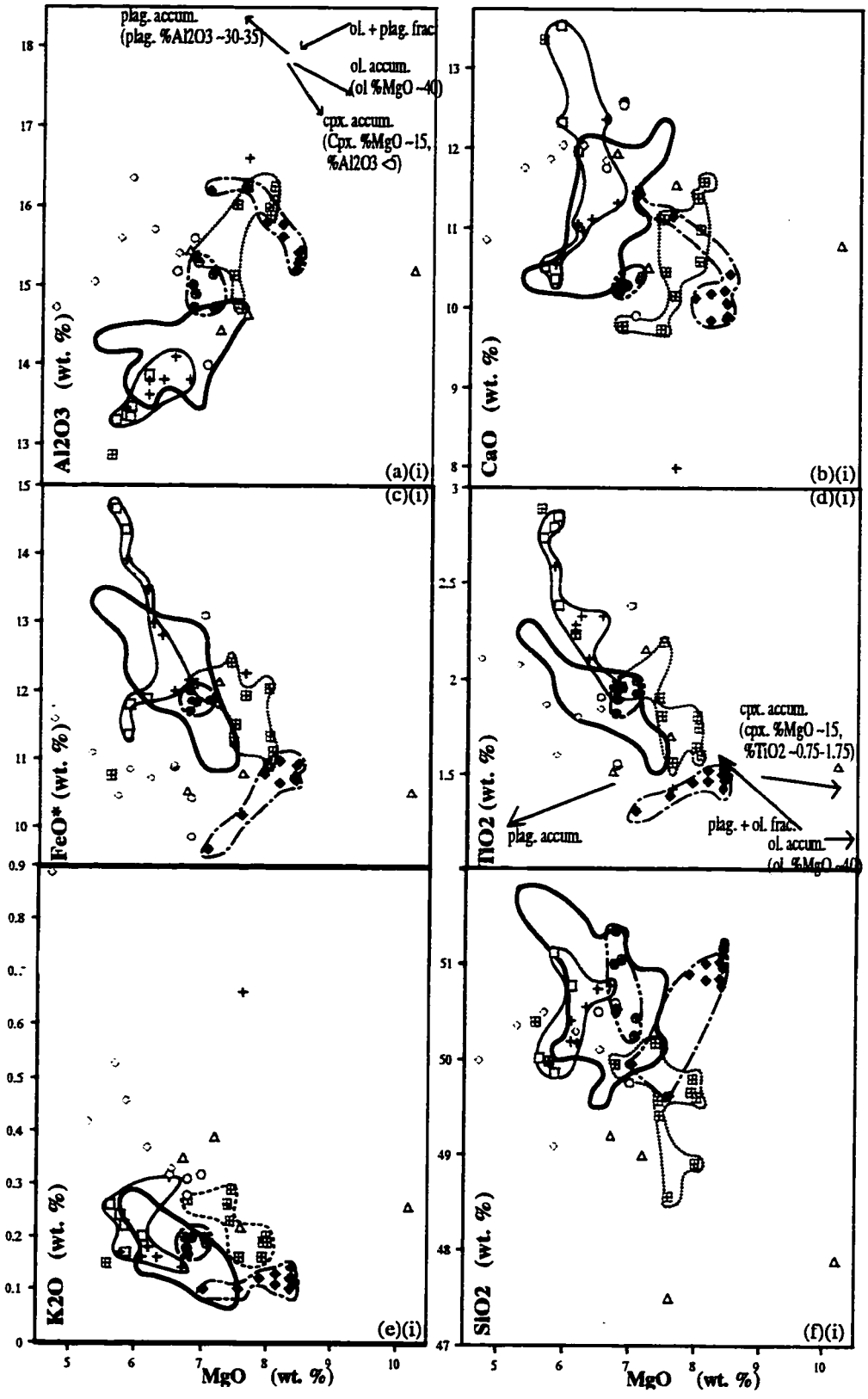
plag. accum.
(plag. %Al2O3 ~30-35)
ol. + plag. frac.
ol. accum.
(ol %MgO ~40)
cpx. accum.
(Cpx. %MgO ~15,
%Al2O3 <)
Al2O3 (wt. %)
(a)(i)
CaO (wt. %)
(b)(i)
FeO* (wt. %)
(c)(i)
TiO2 (wt. %)
(d)(i)
cpx. accum.
(cpx. %MgO ~15,
%TiO2 ~0.75-1.75)
plag. accum.
plag. + ol. frac.
ol. accum.
K2O (wt. %)
(e)(i)
SiO2 (wt. %)
(f)(i)
MgO (wt. %)
MgO (wt. %)

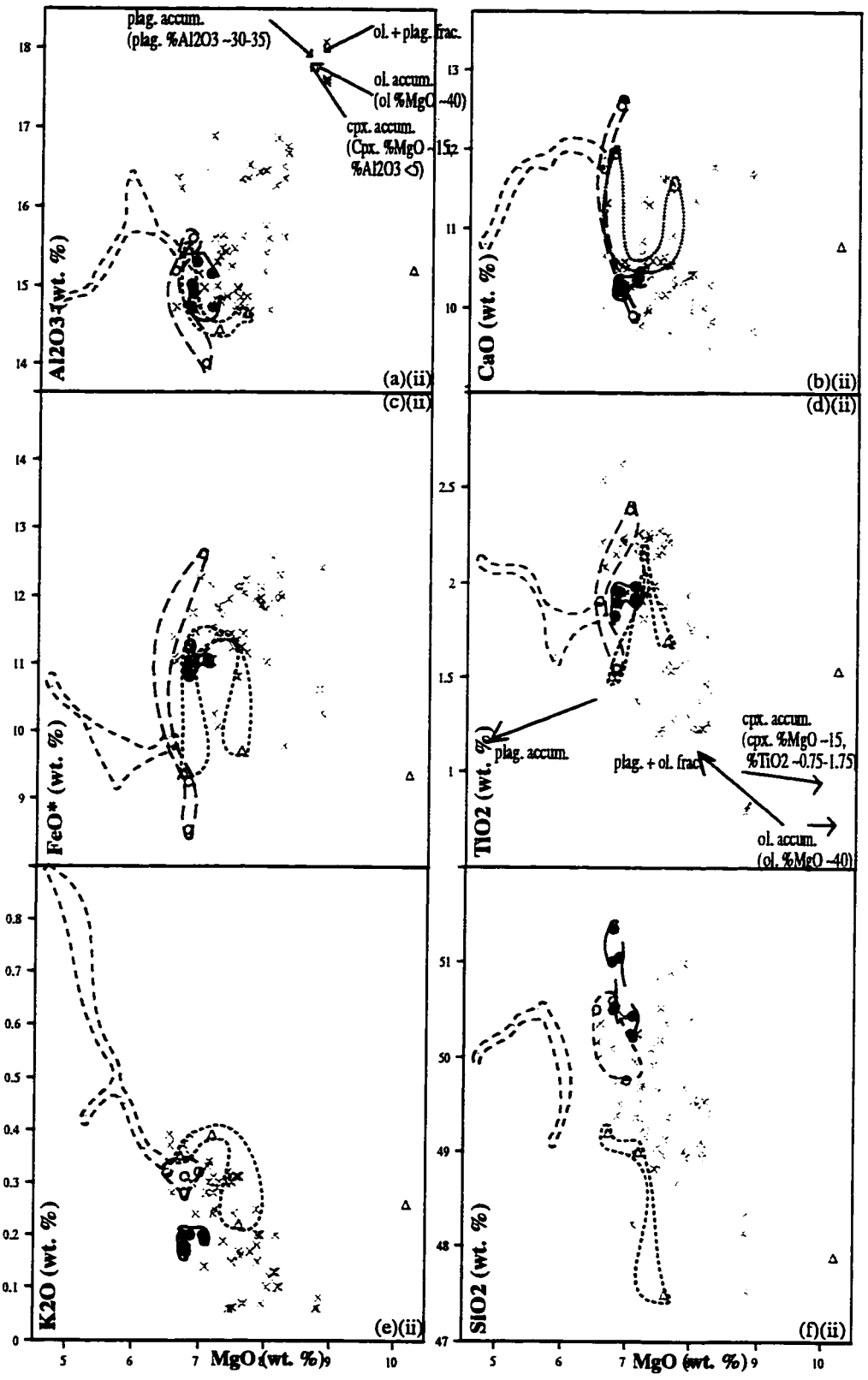
plag. accum.
(plag. %Al2O3 ~30-35)
ol. + plag. frac.
ol. accum.
(ol %MgO ~40)
cpx. accum.
(Cpx. %MgO ~15,
%Al2O3 <5)
Al2O3 (wt. %)
(a)(ii)
CaO (wt. %)
(b)(ii)
(c)(ii)
FeO* (wt. %)
(d)(ii)
TiO2 (wt. %)
plag. accum.
plag. + ol. frac.
cpx. accum.
(cpx. %MgO ~15,
%TiO2 ~0.75-1.75)
ol. accum.
(ol. %MgO ~40)
K2O (wt. %)
(e)(ii)
SiO2 (wt. %)
(f)(ii)
MgO (wt. %)
MgO (wt. %)

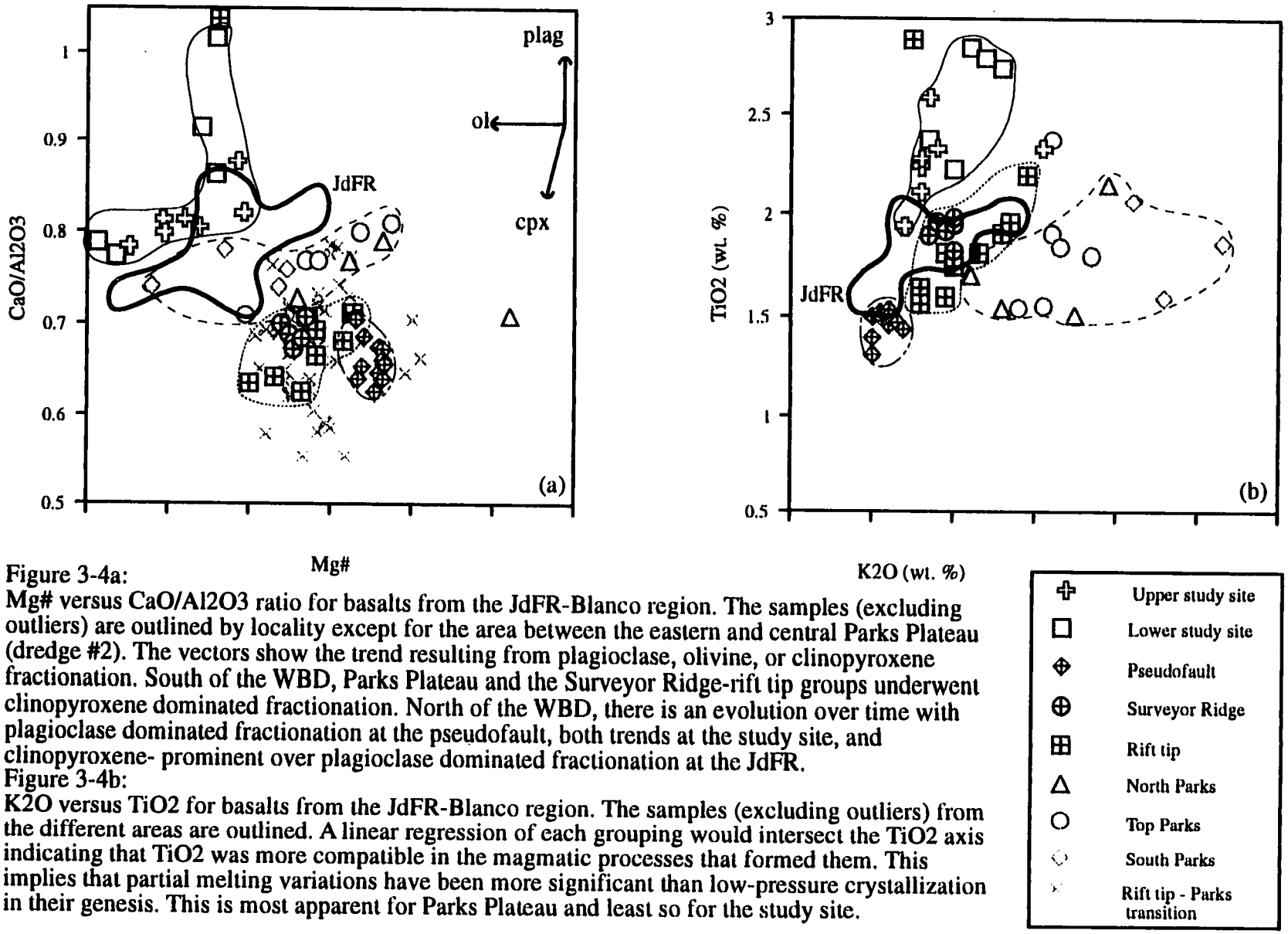

Figure 3-4a:
Mg# versus CaO/Al2O3 ratio for basalts from the JdFR-Blanco region. The samples (excluding outliers) are outlined by locality except for the area between the eastern and central Parks Plateau (dredge #2). The vectors show the trend resulting from plagioclase, olivine, or clinopyroxene fractionation. South of the WBD, Parks Plateau and the Surveyor Ridge-rift tip groups underwent clinopyroxene dominated fractionation. North of the WBD, there is an evolution over time with plagioclase dominated fractionation at the pseudofault, both trends at the study site, and clinopyroxene- prominent over plagioclase dominated fractionation at the JdFR.
Figure 3-4b:
K2O versus TiO2 for basalts from the JdFR-Blanco region. The samples (excluding outliers) from the different areas are outlined. A linear regression of each grouping would intersect the TiO2 axis indicating that TiO2 was more compatible in the magmatic processes that formed them. This implies that partial melting variations have been more significant than low-pressure crystallization in their genesis. This is most apparent for Parks Plateau and least so for the study site.

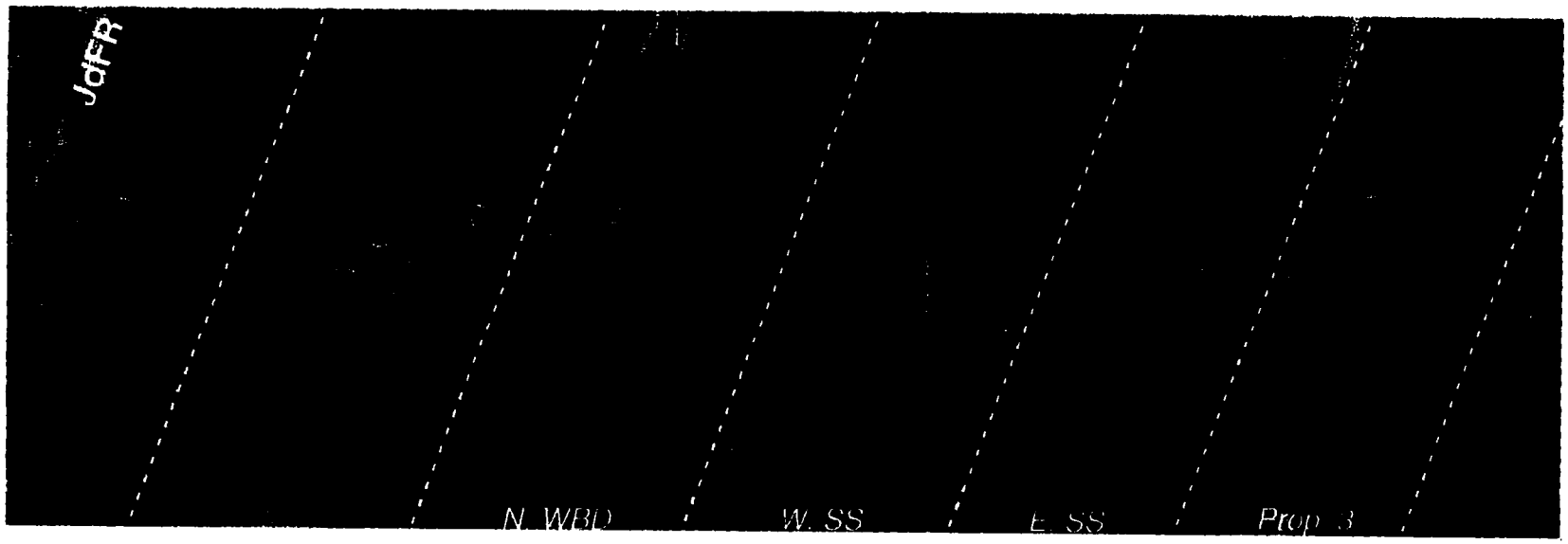

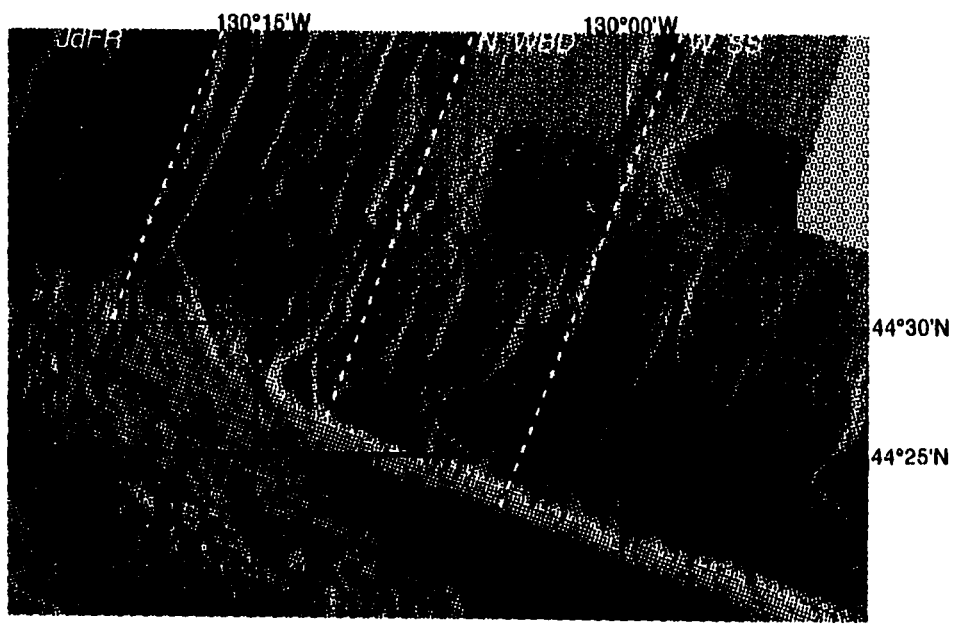

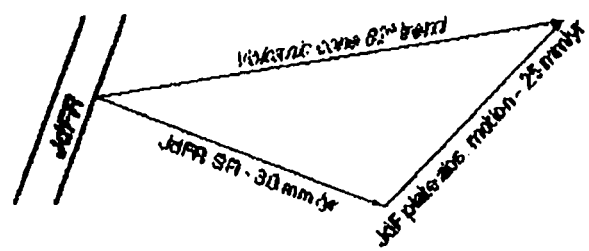

Figure 3-5:
GLORIA image (top) and a Sea Beam map (left) respectively display five and three volcanic cones that interrupt the abyssal hill fabric and divide the Juan de Fuca plateau into ridge-parallel magmatic provinces. The five seamounts lie along an 82° trend as a result of the velocity vectors (drawn above) from the JdFR spreading and the absolute motion of the Juan de Fuca plate.

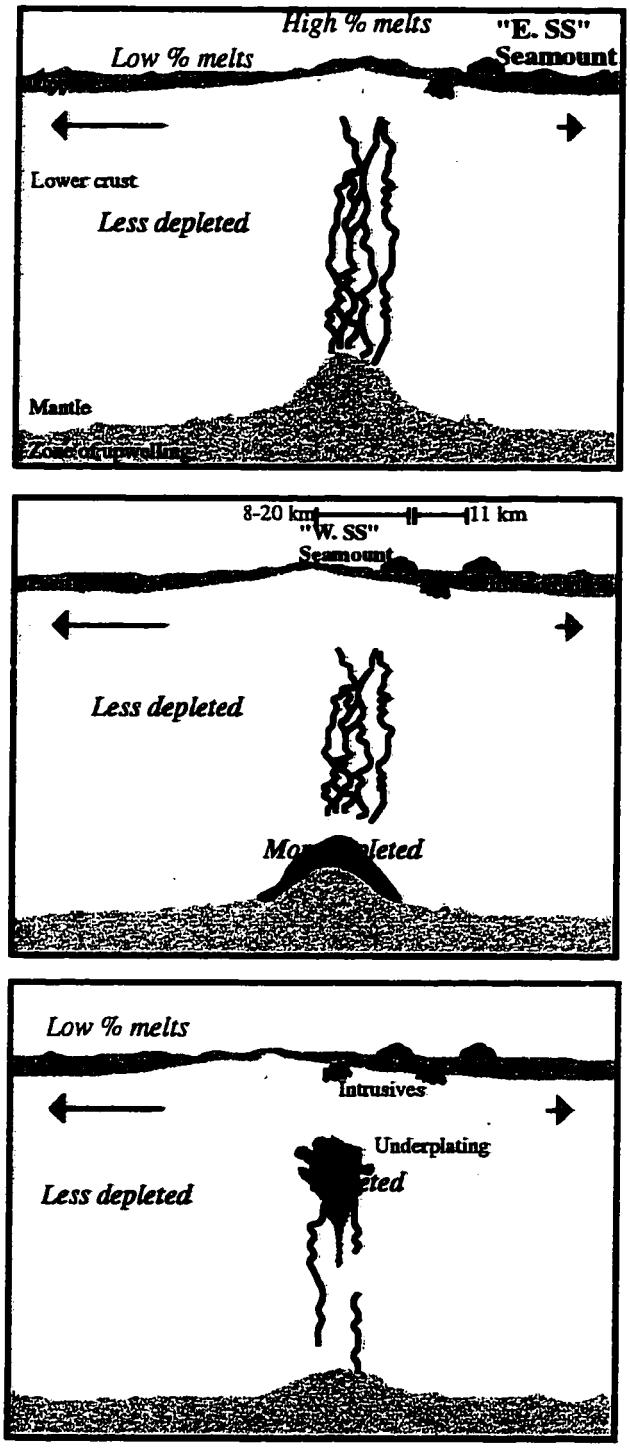

Start of magmatic pulse: ~1.1 Ma

Figure 3-6a:
A third magmatic pulse begins from a diapiric upwelling rooted in the asthenosphere (Whitehead et al., 1984) in advance of the migrating ridge. Basalt compositions in the "North WBD" province reflect a higher degree of melting than the less depleted mantle section below it (Johnson and Dick, 1992) because of the faster ascent rate of melts (McKenzie, 1985).

At ~0.9 Ma

Figure 3-6b:
As the JdFR migrates westward, the melts are focussed beneath the trailing Juan de Fuca plate producing the "West Study Site" seamount near-axis on 1.1-1.4 Ma crust. At this stage, the ridge and the seamount can still share the same mantle source and crust and crust continues to be accreted on axis in what will become the "North WBD" province.

End of magmatic pulse: ~0.7 Ma

Figure 3-6c:
As the ridge migrates further westward (20 mm/yr), the higher spreading rate (30 mm/yr) moves the seamount eastward. The slower ascending residual mantle now intersects the thickening lithosphere of the Juan de Fuca plate. This results in intrusions into the upper crust and underplating at the base of the lower crust that are emplaced between the ridge and the seamount provinces.

Figure 3-6: Model of diapiric mantle flow for a migrating ridge in an absolute reference frame. The process is repeated with the renewed initiation of a diapir from the same point. This episodicity, in a system where the rates of ridge migration, plate motion and spreading remain the same, account for the roughly constant, 11 km spacing of the seamounts on the Juan de Fuca plate (Figure 3-5).

Mantle upwells as many small blobs (Niu and Batiza, 1994) with the shallowest in the center of the ridge segment. The north-westward migration of the JdFR offsets the magma supply from the axis. This causes the "Propagator 3" seamount to be built near-axis east of the JdFR.

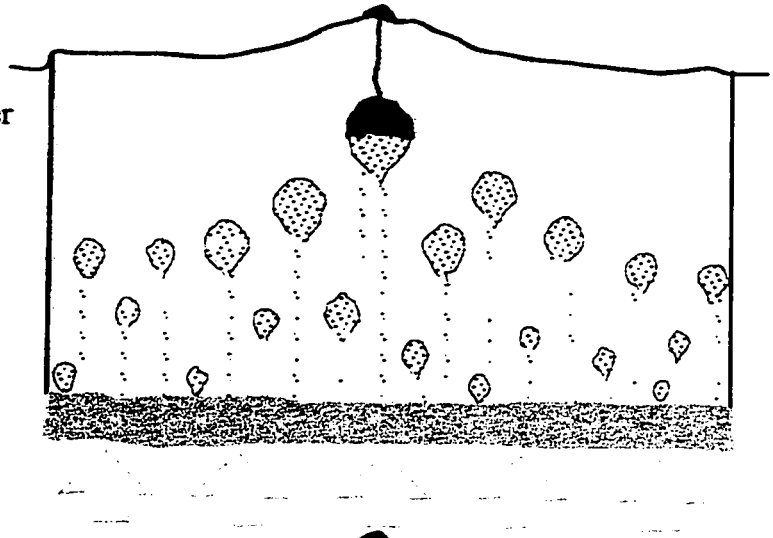

The core of this diapiric upwelling is rooted in the asthenosphere so that the southern end of the Cleft Segment gradually encroaches upon it over time as the JdFR migrates north-westward.

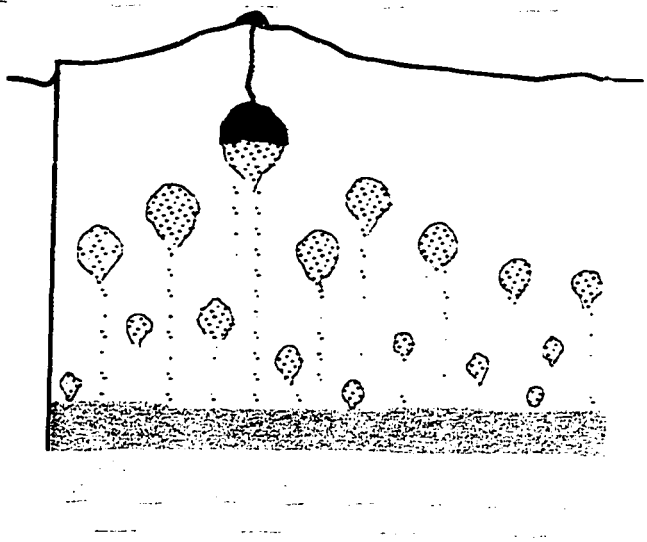

Over time, each seamount appears closer to the southern end of the Cleft Segment such that the last "E. JdFR" seamount was built near the ridge-transform intersection. The present bathymetric profile of the Southern JdFR is consistent with this view.

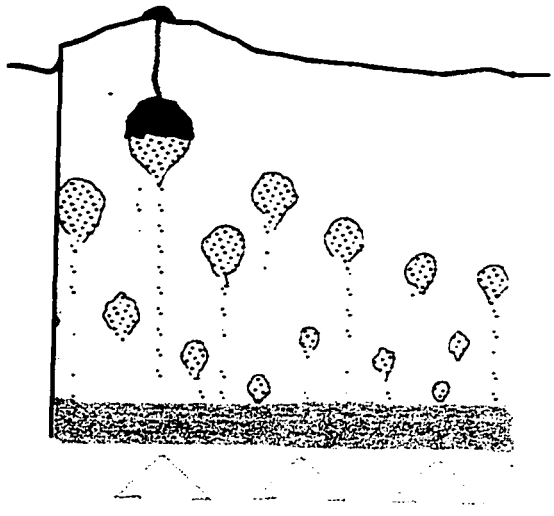

Figure 3-7: Schematic model of the evolution in the along-strike profile of the Southern JdFR (Cleft Segment) between ~2 Ma and 0 Ma.

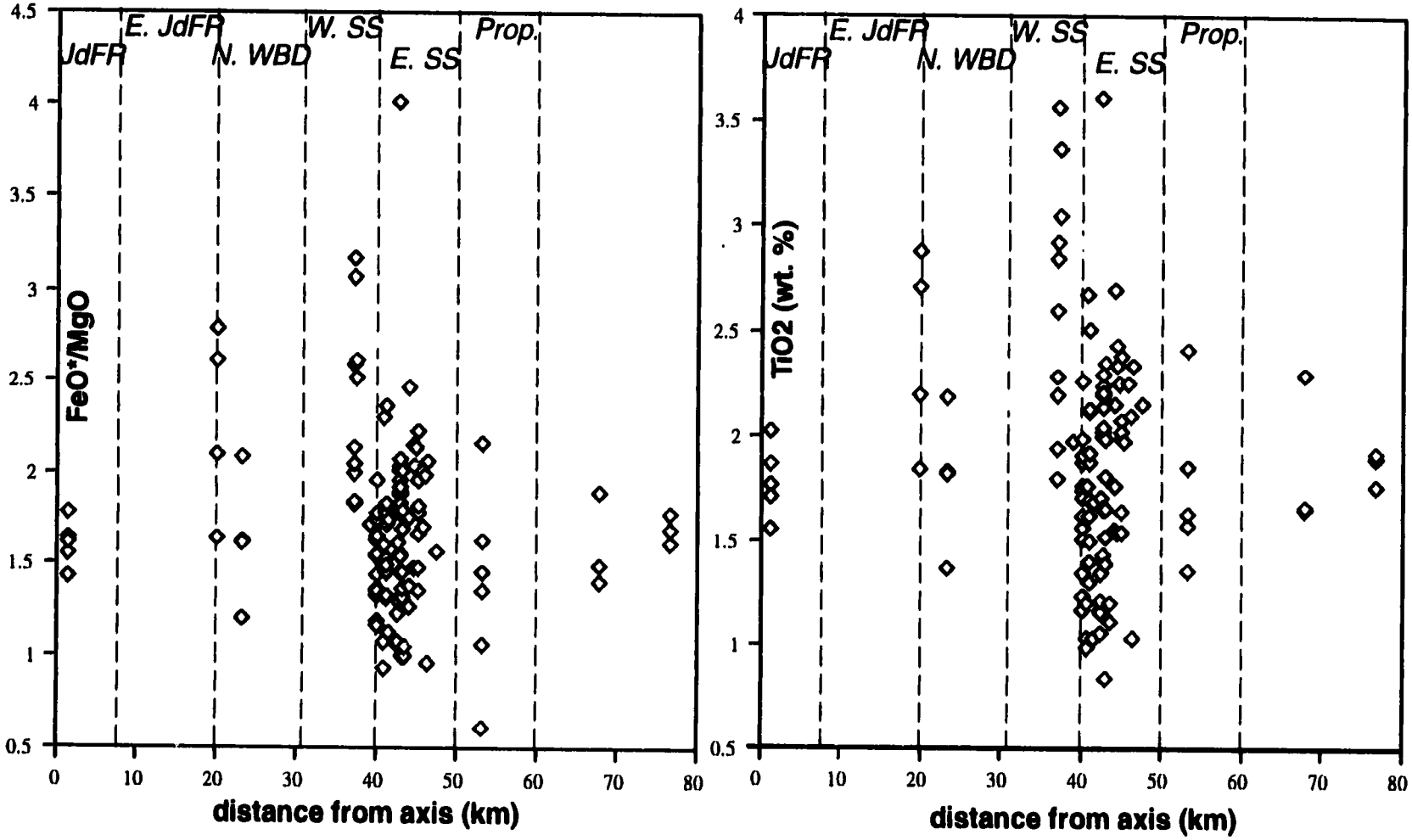

Figure 3-8: Distribution of FeO*/MgO and TiO2 (wt. %) versus the distance from the Juan de Fuca Ridge (JdFR) axis, along the north West Blanco Depression (WBD) scarp. The data shown is from the dive (Juteau et al., 1995) samples discussed in Chapters VIII and IX. Note the differentiation maxima at the boundaries of the East JdFR and North WBD provinces, and the West (W. SS) and East (E. SS) study sites.

CHAPTER IV: GEOLOGY - PART 1

4.1 Introduction

The internal structure of the upper crust is partly the product of volcanic activity and is thus useful for reconstructing magmatic accretion. As the oceanic basement is probed more extensively by geophysical techniques, hard-rock drilling, and scarp mapping, these studies reveal a complicated and diverse architecture. A simple model of sequentially building up the extrusive pile through laterally continuous lava flows from feeder dikes cannot fully explain such a crustal structure. Nor can differences in structural processes between spreading rate regimes adequately account for the variation. Instead, even among the few examples of intermediate spreading rate crust, there is considerable variability some of which stems from magmatic processes, as previously noted in the Introduction.

In order to better understand crustal construction in a medium spreading rate setting, the north wall along the West Blanco Depression (WBD) was examined. Advantages of this area include the 2.6 km of vertical relief, the potentially unobscured outcrop along a steep face, a previous recovery of upper crustal rocks (Melson, 1969), the minimized transform-related effects due to the recentness of exposure (Palmer et al., 1987), the option to correlate surface and subsurface features, and the available constraints on accretionary processes imposed by the southern Juan de Fuca Ridge (JdFR) where the section formed (see Chapter I).

Given the absence of much previous data on this study site, a comprehensive investigation was undertaken in which the north WBD scarp was mapped at successively

finer scales to provide geologic context. This involved the collection of Sea Beam bathymetry and magnetic data (Tivey, 1994) at the largest scale, Deep Tow side-scan sonar images (Delaney et al., 1987) at a medium scale, photographs and dredge samples (Karsten and Delaney, 1988; 1991) at a small scale, and direct observations, rock sampling and magnetic profiling (Tivey, 1996) from *Nautile* (Juteau et al., 1995) at an outcrop scale. The benefits of this design include the ability to check an interpretation by correlation with another analysis, to provide direct ground-truth for acoustic features, and to extrapolate from the highest levels of resolution to the entire area.

The purpose of Chapter IV is to improve our knowledge of the crustal architecture created at intermediate spreading rate ridges. This objective is accomplished here by documenting the method of mapping the WBD site, presenting the various data, and integrating these data sets. On this basis, an overall zonation to the scarp (Delaney et al., 1987) is described in detail and the zonal boundaries are refined. Evidence is also given for the lithologic attributes and tectonic features from which this morphological development results. An ~1500 m thick upper and ~450 m thick lower zone forming the crustal exposure are interpreted respectively as an extrusive basaltic sequence overlying a diabasic sill complex. Lastly, the significance of this internal structure for magmatic accretion is discussed.

4.2 Methods and Data

The geologic setting of the JdFR-WBD area is summarized in Chapter I. The 1.2 Ma to 1.7 Ma (based on a 29 mm/yr half spreading rate) site studied is located centrally along the north WBD scarp, as outlined on the regional Sea Beam map (Figure 3-1 after Embley and Wilson, 1992). The data sets utilized here were collected during several

cruises to the WBD site and have been co-registered to produce a geologically reasonable fit, as noted in Appendix A. In displaying the data sets, a 1024*1024 meter square reference grid (labelled numerically from west to east and alphabetically from south to north) is superimposed to permit inter-comparison.

4.2.1 Topographic variation

Sea Beam bathymetry of the study site (Figure 4-1b) highlights the 2.7 km of relief and steep topography on the cliff face. A slope image map (Figure 4-1b) derived by Dauteuil (1995) shows the distribution of irregular parts with a >40° slope that almost certainly expose outcrop. Supplementary bathymetric profiles were obtained along the four lines drawn in Figure 4-2 (1.3A, 1.7, 1.6 and 1.1B from west to east) using a 2° beam width, 125 kHz sounder on Deep Tow that gives a theoretical resolution of 2-5 m horizontally and ~20 cm vertically. They demonstrate that the Deep Tow vehicle can be flown at a constant height of 100 m off bottom during the imaging survey and also capture subtle slope features. The latter are confirmed in continuous, 4 kHz echo-sounder records produced at the same time which provide penetration into the sediment to determine its thickness and any internal structure to depths of about 50 m.

4.2.2 Sonar imaging

For sonar imaging the WBD scarp, two 3/4° beam width, 110 kHz transducers which correspond to <1 m theoretical resolution were mounted on both sides of Deep Tow in order to survey in two directions. An opposite pair was configured at 15°-20° up and the other at 20°-25° down from the horizontal so that only one transducer on either side is switched on at a time and can be reversed during turning. Altogether six scarp-parallel track lines, as indicated in Figure 4-2, were run at 1-2 knots and roughly 1 km apart in order to obtain complete overlapping coverage of the <1.5 km wide swaths.

At Scripps Institute of Oceanography (SIO), the digitized data were processed to correct radiometric and geometric distortions, allotted a meter square per pixel, and stored in data blocks of 1024*1024 meter square. Using the WISP image processing system (Shippert et al., 1990), each block has been adaptive-filtered (Eliason and McEwan, 1990) with a 3*3 kernel to remove speckle noise. The swath views were separated and mosaicked into uniquely up- or down-looking blocks, that were further enhanced by histogram equalization and averaged to 512*512 pixel images. The results of this procedure are shown by some examples in Plates 4-1 and 4-2.

The manually separated up- and down-looking sonar images of the study site are displayed respectively in Figures 4-3 a and b. Their contrast in acoustic backscatter is largely a function of the sonar angle of incidence which significantly reduces the intensity in the down-looking image (Figure 4-3b) particularly for slopes >65° or overhanging as on the upper part of the cliff face. The difference in acoustic backscatter within these images is mainly due to target impedance with the reflectivity, for example, being lower for sediment than for the basement. Variation in acoustic backscatter within a target results from its morphology as for instance shown by the rugged nature of the exposed outcrop. These three factors are responsible for characteristic textural patterns as may be observed for the crustal exposure on the plateau versus that on the scarp. This forms the basis of the preliminary interpretation of these mosaics by Delaney et al. (1987) presented in Figure 4-4.

4.2.3 Visual data and rock samples

Photographs taken from Deep Tow at 10-12 m off the bottom provide a 3-5 m field of view. The track locations along with a graphical summary recording observations of outcrops occasionally with ledges, isolated or fields of blocks, and sediment are displayed in Figure 4-2. The placement of fourteen *Nautile* traverses, which was guided

by the sonar imagery (Figure 4-3), are also drawn on Figure 4-2. Structural measurements of dikes and faults from these video tapes have an estimated accuracy of ±15° for the strike and dip.

Rock samples were obtained by dredging over a <2 km distance. The eight tracks (BT-3 to BT-8 up-slope, as well as BT-11 and BT-12 along-slope) are indicated in Figure 4-2 and their characteristics in Table A-1. Rock types recovered are shown in Plate A-1 and include volcanic breccia, hyaloclastite, glassy basalt, crystalline basalt, diabase, veined basalt, veined diabase, and fine-grained sediment. In addition, 146 rocks collected from *Nautile* represent 16 breccias, 75 basalts, 17 altered basalts, 32 diabases, 3 altered diabases, and 3 sediment samples. The depth of retrieval and petrographic properties of each sample is shown in Appendices B-1 to B-13.

4.3 Results

The western and eastern parts of the site only have >40° slopes in the uppermost portion of the face (Figure 4-1b) where some outcrop remains (Figure 4-3). The rest is largely obscured by the products of mass wasting processes which include two large landslides in the east (Plate 4-1a) as described by Whipple and Naidoo (1991) and Juteau et al. (1995).

4.3.1. Geomorphic provinces

The central part of the north WBD site can be sub-divided into five, east-west oriented zones as outlined in Figure 4-4. These zones essentially overlap those delineated by Delaney et al. (1987) except for the boundary between the upper and lower outcrop zones (e.g. grid square e-6). The zones are described below from north to south with more detail given in Chapter VI. This pattern of zonation is inherited from a particular balance

between lithologic, tectonic, and geomorphic processes that is associated with the crustal section exposed on a steep scarp in a transform fault regime.

4.3.1(a) Plateau zone:

The Juan de Fuca plate lying north of the Blanco wall, grades over 13 km from 2200 m in the west to 2400 m in the east of the study site (Figure 4-1a). This seafloor plateau therefore reaches depths of the 0 Ma Cleft axis which is itself unusually shallow in comparison to other intermediate spreading-rate segments of the EPR (cf. ~2700 m between 16°-18°N; Sempéré and Macdonald, 1987). The plateau (Figure 4-1b) is generally flat-lying (0-10°) and covered by indurated sediment (Figures B-1&4). Close to the scarp, the smooth sediment (line 3.1 in grid square i-3) has roughly east-west oriented ripples which imply that fine material is swept toward the WBD trough. Also on the plateau are ridge-parallel abyssal hills averaging 10-20° in slope (Figure 1-5) but which locally may be as steep as 40° (Figures 2-4, 3-5b). Near the edge of the plateau, these structures tend to be approximately 100 m wide and spaced 750 m apart on average (Figures 4-3 a and b; 6-12). Outcrops of lava flow fields (Plate 4-1b) are composed of very fine- to medium-grained pillow basalts (Figures B-1,6&13) that range from sparsely to highly phyric with plag-cpx-ol (plagioclase-clinopyroxene-olivine) or plag-cpx. The scarp-plateau intersection at 2200 m (Figure 4-1a) is sharp (Figure 4-1b) with the steep (<50°) cliff top rolling over a narrow (<300 m wide), 10-20° lip onto a gentle, <10° sloping plain. This has lead to the interpretation of the linear escarpment as the surface expression of a master fault with subsidiary splays (Juteau et al., 1995).

4.3.1(b) Upper outcrop zone:

The upper outcrop zone is distinguished on the up-looking mosaic (e.g. grid squares g-6 or e-9 - Figure 4-3a) by its high reflectivity and a comparatively uniform

image texture (Plate 4-1c). It also stands out in relief on the down-looking mosaic (Figure 4-3b) since the scarp is steep (Figure 4-1a) with semi-continuous areas of 40-50° slope (Figure 4-1b) that in reality are about 60-70° (Figures B-1,4,6,10&13).

The upper zone is constituted by mostly lava flows that include pillows and various sheet flow types as well as local feeder dikes (Figures B-1,4,6,10&13). The dikes tend to be dispersed in orientation in the upper part but are mainly oriented N119/77N i.e. almost ridge perpendicular, in the basal transition (Table 4-1a).

The base of the upper outcrop zone, which is marked by scree (Plate 4-1d), occurs between 3625 m (Figure B-6) and 3870 m (Figure B-13) depth amongst six profiles. Hence, the apparent thickness of the zone ranges systematically from 1325 m (Figure B-6) in the central part to 1760 m (Figure B-13) in the west of the study site and averages 1504±157 m. These are maximum estimates given the impact of faulting on the section and the unknown dip of the flows despite their horizontal trace on the face.

The upper zone is dominated by volcanic breccia, glassy basalt, veined basalt and hyaloclastite (Table A-1) amongst the rock types dredged in the site. The basalts show considerable variation from glassy to coarse-grained and aphyric to highly phyric based on the dive samples examined. The phenocryst assemblages include plag-cpx-ol, plag-cpx or plag commonly and also plagioclase-clinopyroxene-oxide in ferrobasalts (Figures B-1,4,6,10&13). In addition, there is some diabase that can be fine-grained and aphyric to sparsely plag phyric, or coarse-grained and aphyric. The transition to the lower zone has no ferrobasalts but also includes sparsely to moderately phyric plag-ol basalts and medium-grained, aphyric diabase.

4.3.1(c) Lower outcrop zone:

The lower outcrop zone is distinguishable from the upper zone by its lower relief on the down-looking sonar mosaic (Figure 4-3b). It has a 40-50° slope on average (Figure

4-1b) although the faces are actually about 60° steep (Figures B-2,3,5,6,11,12&13). On the up-looking sonar mosaic (Figure 4-3a), this zone has a characteristic banded pattern (Plate 4-1e or grid square e-6 in Figure 4-3) that is distinct from a mottled/checkered texture at the cliff base (Plate 4-1f or grid square d-7 in Figure 4-3).

This zone is constituted mainly by a massive, jointed lithology and a thick sheet flow type (Figures B-2,3,5,6,11,12&13). The former, which could possibly represent sills, gives rise to benches in the face that are separated by tens of meters (Figures 4-2 or B-6), as displayed in a 4 kHz profile (Figure 4-6c). Local dikes that are present have two sets of orientations - N18/40E i.e. ridge-parallel, and N66/90 (Table 4-1). The cliff face in this zone is also visibly altered by metric size whitish scars and veins (Plate 5-1k&l). The veins are prominent at the contact with the upper zone where their trace runs either sub-horizontally or in cross-cutting nets.

The base of the lower zone corresponds to the deepest outcrop exposure on the WBD scarp (Plate 4-1f) that is observed between 4150 m (Figure B-7 and B-12) and 4310 m (Figure B-5) amongst six profiles. The apparent thickness of the outcrop thus averages 474±128 m and ranges from 330 m (Figure B-13) to 660 m (Figure B-5) but these estimates must be considered a minimum if the zone continues with depth.

The rocks dredged in this zone are predominantly crystalline basalt and veined diabase (Table A-1). They both range from fine- to coarse-grained (Figures B-2,3,5,6,11,12&13). The basalts are aphyric, sparsely plag phyric, or highly plag-cpx phyric. The subequigranular diabases are sparsely plag or plag-cpx phyric to mostly aphyric in thin section.

4.3.1(d) Debris zone:

The debris zone represents a 10°-30° sloping apron along the cliff base as highlighted on the slope image map (Figure 4-1b). The zone is formed by mass wasting material as is apparent from the sonar imagery (Figure 4-3 and Plate 4-2a).

The contact between the cliff and the debris zone is marked by a sharp break in slope (Figures B-2,3,5,6&13) that is accentuated on the down-looking sonar mosaic (Figure 4-3b) by a highly reflective band. Photographs here (e.g. grid square 6-d on Figure 4-2) reveal a continuous mass of blocks in an approximately 30 m wide rim (Figure B-2,3&13) along the cliff base. The blocks are tabular in shape, and decimeter to meter sized with a rare decameter sized one. Other blocks are commonly white in color and have a striated exterior indicating the effects of tectonism. The blocks recovered are veined and/or altered, and include basalt breccias as well as texturally distinct coarse-grained basalt and fine-grained diabase (Figures B-2,3&12). Altogether, these characteristics are suggestive of an origin in the lower outcrop zone.

Within the 20°-30° sloping body of the debris zone, there are subtle changes in topography as evident from variations in backscatter intensity and texture on the sonar images (Figure 4-3). A semi-spherical shape (Plate 4-3b - grid square e-4) that is about 610-680 m in width and strewn with a complete range in size (up to 15 m) of talus blocks (Figures 4-2 and B-3) is interpreted to be a slump form. There are also well-defined talus cones (e.g. grid square d-6 - Plates 4-2a and 4-3a) that emanate from points at the cliff base and extend to the 10-20° sloping edge of the debris zone (grid square d-5 in Figure 4-3a). In general, the coarse constituent blocks (Plate 4-3a) are bare at the head of these grain-flows indicating recent deposition from the active, oversteepened face; they acquire a fine-grained sediment drape downslope (Figure B-3).

The debris zone is thus not only a receptor for debris from the cliff but is itself an active mass wasting slope. This would explain why the SIO transponder left here (grid

square c-6 in Figure 4-2) in 1987 could indeed have shifted by 1991 as assessed by Method I in Appendix A.

4.3.1(e) Sediment trough zone:

Within the study site, the trough deepens from about 4500 m in the west to 4800 m in the central part and shallows to about 4200 m toward the east (Figure 4-1a). This zone is almost flat-lying with a slope of 0-10° (Figure 4-1b). It is identifiable on the up-looking mosaic (Figure 4-3a) by a uniformly smooth texture (Plate 4-2e) that corresponds to pelagic sediment pockmarked only by the imprints of fauna (Figure 4-2). The unusual abundance of fauna here and on the scarp (Blanconaute 1991, unpubl. rept.) would account for the biogenic material recovered in cores from the trough (Selk, 1978). It also implies that there must be a sufficient food source which could be derived either from the manganese-enriched sediment (Selk, 1978) or a current. A 0.1-0.2 knot current was measured in the Blanco trough in an east to west and a west to east direction on the south and north faces respectively at a depth of 2200-2500 m (pers. comm. of *Nautile* pilots).

4.3.2. Tectonic effects

4.3.2(a) Upper outcrop zone:

The effects of structural processes are evident throughout but fault-related features become more common and closely spaced toward the basal part of the upper zone (Figure 4-5a). Fault scarps with three main orientations are apparent.

Dip-slip faults are inferred from approximately east-west striking (N80° - Juteau et al., 1995) fault planes, scarp-parallel fissures, as well as some vertical and oblique striations (Figures B-1,4,10,12,13). In addition, large, inverse V-shapes on the sonar mosaics (Figures 4-5 a and b) were observed to be crestal forms that occur more

frequently at a smaller scale on the face (Figures B1-13). These features, also imaged in a 4 kHz profile (Figure 4-6b), are likely to be the result of faulting (Figure 4-5b). Magnitudes of throw estimated from repetitions in flow morphology (e.g. the pillow outcrop overlying blocky outcrop which occurs above and below the fault at 2405 m in Figure B-6) tend to be less than 50 m. However, there is one example of a fault block that may have down-dropped as much as 750 m based on a 40 m thick section of pillow outcrop now at 3500 m (Figure B-4).

A second type are roughly north-south striking (N15° - Juteau et al., 1995), high-angle fault planes, that are mainly westward-dipping (e.g. grid square g-6 and h-3), as interpreted from the sonar mosaics (Figure 4-5a). Their traces are only apparent to 0.5 km below the surface where they become obscured by the scree slope (Plate 4-2b). In one instance, a fault (grid square g-6) may extend through a talus chute (grid square f-6 and Figure B-4) to the base of the exposed section where a cove of outcrop has been carved out (Plate 4-2c - grid square e-5).

The third type shows horizontal striations (Plate 4-1f) caused by lateral shear (Figures B-13 and B-10). The striations are present to shallow depths varying from 2750 m (Figure B-13) in the west to 3100 m (Figure B-10) in the east of the study site. They were observed on a NW-trending face (grid squares f-5 and g-5 - Figure B-13) in the central part of the site and a 345° striking plane (grid square d-9 - Figure B-10) at the head of the smaller landslide (Figure 4-3b). However the latter scarp, which extends to 1.15 km below the plateau surface (Plate 4-2d), also has oblique and vertical striations (Figure 4-5a) indicating a more complex history of faulting. Furthermore, it is intersected by a 35° trending, steep scarp (Figure 4-3b) and there is another such set with the same trends (Figure 4-5a) on the western margin of this double-headed landslide (grid-square e-9). Based on the low 50° angle between these faults and the shear on the NW-NNW planes, they could represent conjugate sets.

4.3.2(b) Lower outcrop zone:

Faulting in the lower outcrop zone (Figures B-2,3,5,6,11,12&13) appears to have been down-dip, parallel to the scarp (N120°). Normal fault planes are more evident to the west while crestal forms corresponding to the inverse V-forms on the up-looking sonar mosaic (Figure 4-5b) are more apparent to the east (Figure 4-5a).

4.3.2 (c) Debris zone:

A set of lineaments in the debris zone (Plate 4-3d) occurs in the west of the north WBD site. They extend continuously for about 3 km and change in trend from 112° to 134°, and finally to 116° (grid squares f-1, f-2 and e-3 - Figures 4-3 and 4-5a). One strand is demarcated in a 4 kHz (Figure 4-6a) and a 125 kHz profile by a distinct indentation at about 4370 m that has created a break in slope. Another set occurs in the east of the study site along the boundary with the sediment trough zone (Plate 4-2). They vary in trend between 116° to 122° (grid square a-9 and a-10 - Figure 4-3) and could possibly be a continuation of those to the west. These have 1-5 m high, mostly south- and some north-facing scarps of basaltic breccia/rubble (Figure B-9) indicating an associated component of normal faulting (Figure 4-5a). Their steep faces also suggest that the scarp is young and that tectonic activity was relatively recent.

Within the larger landslide, there are two other sets of lineaments (Figure 4-5a) - one oriented at ~136°-166° (Plates 4-2f and 4-3c) and another which are sinuous and have an average trend of 112° (grid square c-10). These indicate that active faulting occurred subsequent to this landslide failure. The last mentioned set terminates abruptly at the boundary with the smaller landslide (Plate 4-1a) that consequently must be younger than both the lineaments and the larger landslide. Hence, movement on these lineaments is inferred to have ceased between the two mass failure events.

4.4 Discussion

4.4.1. Tectonic effects on the crustal section

The structural data show two major orientations of features.

One group has NNW to NNE trends which correspond with ENE to ESE extension that would be compatible with the dynamics of the JdFR environment.

The one set of ridge-parallel, east-dipping (N18/40E) dikes in the lower outcrop zone could have been intruded on- or near-axis. The group includes N15°W fault planes in the upper outcrop zone in the western part of the WBD site that could be related to structural processes during on-axis accretion. Likewise, Juteau et al. (1995) find that joint orientations are concentrated between N150°-170°.

Also included in this group are conjugate sets of N345° and N35° trending fault planes in the upper outcrop zone in the eastern part of the WBD site. One or both sets could originally have formed on-axis and then been re-activated along the transform fault. Alternately, they could simply occur in response to shifts in orientation of strike slip activity in this complex regime as indicated by the one set of N166° trending lineaments on the easternmost landslide. The former hypothesis is preferred because these trends do not correspond to the orientations of the major structural lineaments in the basin mapped from GLORIA images (Figure 2-5). This implies a possible change in accretionary style across the site. It also suggests a predisposed connection between these intersecting faults and the location of major landslides.

The second group has E-W to ESE trends which correspond with N-S to NNE extension that would be compatible with the mechanics of the Blanco transform fault regime.

The N112°-120° trending lineaments lack any clear dextral criteria but their presence in the debris zone is consistent with expected strike-slip tectonism. The evidence that the lineaments are of relatively recent age implies that the associated shear has not continuously deformed the cliff face.

The group includes normal faults with magnitudes of throw generally less than 50 m in both the upper and lower outcrop zones. Although they certainly reduce the extent of the crustal section to be expected from the 2.7 km of scarp relief or 2.1 km of crustal exposure, they are nonetheless not as numerous nor so extensive (Figure 4-5a) as predicted by Francheteau et al. (1976). This implies that representative areas of the crust remain permitting reconstruction of the geological section.

Also included in this group are N120° striking dikes in the upper zone and N66/90 trending dikes in the lower zone. The latter are consistent with the N60°-80°S orientations preliminarily measured by Juteau et al. (1995). These could have been emplaced or rotated perpendicular to the trend of the rift valley, similar to obliquely oriented faults at other ridge-transform intersections (OTTER, 1984). The dike trends would therefore be compatible with accretion of the crust close to the inner intersection of the JdFR with the Blanco Fracture Zone.

These structural observations demonstrate that the location, effects and relative ages of tectonic activity can be well-documented. The lineaments in the debris zone (Figure 4-5a) are interpreted to result from strike-slip activity since they conform to the finding that such movement tends to be confined to the transform valley (Fox and Gallo, 1984). In this case, there is also evidence of localized horizontal shear on the cliff face

which further indicates that deformation is not pervasive on the scarp. In addition, the two groups differentiate between the features produced on-axis versus those relating to the transform zone, although there may be some overlap with re-activation of structures. Consequently, the crustal section at the WBD site can be reliably used to study accretion.

4.4.2 The nature and thickness of the WBD section

The 2.1 km thick exposure of the crustal section along the north WBD scarp shows two distinct zones (Figure 4-7): (1) an ~1500 m thick upper volcanic zone of lava flows and local dikes that is composed of basalt and minor diabase and in which the petrographic diversity decreases up-section; and (2) an ~475 m thick lower volcanic zone of lava flows, possibly sills and local dikes, that is composed of basalt and diabase which are limited in their petrographic characteristics. Juteau et al. (1995) define a separate 465 m thick transition zone at the base of the upper unit (between 3160 m and 3625 m) due to its tectonized and veined nature, a change in the alteration mineralogy, and increased mass wasting deposits. This division is omitted here because of the lack of any lithological grounds or petrographic evidence. The apparent thicknesses of these units are likely to be greater than the actual thickness but the extent to which they have been tectonically thickened is assessed in Chapter V. Juteau et al. (1995) suggest a maximum thickness of 900 m for the upper unit, a 150-400 m thickness for the transition and a minimum thickness of 700 m for the lower unit. Altogether, this still represents a 1.75-2 km thick section.

The nature of this sequence is similar to that at other intermediate spreading rate sites. Hole 504B (Leg 140 Shipboard Scientific Party, 1992) and Hess Deep (Karson et al., 1992) have pillow lavas ± thin flows overlying a mixed transition of extrusives and

intrusives and at both (Adamson, 1985; Francheteau et al., 1990), massive layers form a distinct component of the transition zone. Likewise in the Oman ophiolite, there is a sill complex between the dikes and the Geotimes volcanic unit (Pflumio, 1991). If intrusion tends to occur along this interface, then the complete extrusive section may be exposed at the WBD site.

In terms of thickness, Hole 504B has an upper zone that is 571.5 m thick and a transition zone that is 209 m thick giving a total thickness of 780.5 m (Adamson, 1985). At Hess Deep, the upper zone of pillow lavas is 100-200 m thick and the mixed zone of extrusives, intrusives and possibly sills is 50-500 m thick (200 m on average) giving a total thickness of 150-700 m (Francheteau et al., 1992). Thus, the upper zone section is more than twice as thick at the WBD as compared to other intermediate-rate spreading sites.

The thickness of the WBD upper zone however is validated in other studies. It compares quite favorably to the Geotimes Unit in the Oman ophiolite which is 1-1.6 km thick (Pflumio, 1991). The Oman ophiolite is a valid analog if it was accreted at a spreading rate of 4-10 cm/yr as proposed by Kempner and Gettrust (1982). The WBD upper zone thickness is also close to a combined estimate for Layers 2A and 2B of 0.85-1.25 km (Cudrak and Clowes, 1993) or 1.45 km (White and Clowes, 1990) that was obtained in seismic refraction studies of the Endeavour segment on the JdFR.

Thickness estimates for Layer 2A on the JdFR differ. At the Cleft Segment, Layer 2A is 200-500 m thick (McDonald et al., 1994) while on the Endeavour segment it is 400±200 m thick based on a seismic refraction survey (White and Clowes, 1990; Cudrak and Clowes, 1993). However, this low velocity layer may stem from lithologic differences (Herron, 1982) or the porosity contrast (Carlson and Herrick, 1990) between an uppermost pillow unit and the underlying sheet flow forms. By comparison, a seismic

reflection line on the Endeavour segment shows a 600-1000 m deep reflector that does not vary with age (Rohr et al., 1988) and is similar to the thickness found for the WBD site.

If it is assumed that the upper and lower zones are underlain by a sheeted dike complex, it implies that the upper crust at the WBD site must be 2 km or greater in thickness. Support for this prediction is gained from seismic refraction (Cudrak and Clowes, 1993) and tomography (White and Clowes, 1994) studies on the Endeavour segment of the JdFR, which both give a Layer 2 thickness of ~2 km. A seismic reflection study (Rohr et al., 1988) on the same JdFR segment gives a 2-3 km thickness for Layer 2. Another indicator of upper crustal thickness is given by the axial magma chamber (AMC) depth which is at depths of ~3 km on the Northern Symmetrical Segment of the JdFR (Christeson et al., 1993) and at ~3-3.5 km on the Valu Fa Ridge (Collier and Sinha, 1990). Hence, the Layer 2 thickness of at least some intermediate-rate spreading ridges may lie at the upper end of the 1.2-2.4 km range obtained on the fast-spreading EPR (Detrick et al., 1987).

4.5 Conclusions

1. The north scarp of the WBD comprises 5 geomorphic zones from north to south: lava fields and sediment on the Juan de Fuca plateau, upper and lower outcrop zones on the cliff face, a debris slope, and sediment in the trough.

2. The upper volcanic zone is constituted by basaltic flows and has an apparent maximum thickness of 1504±157 m. The lower volcanic zone is constituted by flows and possibly sills and is composed of mixed basalts and diabases; it has an apparent thickness of 474±128 m.

3. The orientations of structural features on the scarp cluster in two groups. The E-W to ESE trends are compatible with formation in the JdFR setting. The NNW to NNE trends are compatible with formation in the Blanco transform fault regime.

Table 4-1a: Dike orientations along the north WBD scarp as estimated from video. The error is unknown but assumed to be at least 20°. The estimates compare well to a few measurements taken from the submersible (eg. 85/60N vs. 97/50N - P. Nehlig; or 10/45W vs. 00/45W - D. Naidoo)† and from the video after the dive (eg. 50/60S, 60-70/90, 40/75E vs. 33/60S, 65/80S, and 62/70S, - O. Dauteuil)¶.

	BN-13	BN-24	BN-04	BN-23	BN-02	BN-06	BN-05	BN-10	BN-01
Upper zone: ~2110 m - ~3500 m		110/90 105/45S	100/75N 130/45S 170/45E			150/45W		160/60E 20/60W 160/40E 155/90 15/60E	10/45E 160/60E 135/45N 20/30W 145/45W 115/60N 90/45N 100/45N
Upper zone:	120/75N 120/75N	120/90 85/60N †		75/30S 40/45S 10/45W † 20/60W	150/60E 145/50N	125/90	105/30N 120/80N 120/60N		
Lower zone: ~3625 m - ~4310 m		90/30N		50/60S ¶ 70/90 ¶ 40/75S ¶ 60/90 ¶ 30/30E	15/45E 35/60W 0/90 30/30E 15/45W 15/30E 85/75N 30/30E	135/45S			

Table 4-1b: The dikes in the WBD study site show a broad dispersion in orientation but there are density peaks when plotted by outcrop zone.

	# obs.	Density maximum	Other density peaks
Volcanic and diabasic zones	48	N12/40E	N132/45S, N120/76N, N157/56N
Upper zone - blocky and pillow	19	- scatter	N144/45S, N163/49E, N90/43N
Upper zone - thick sheet	14	N119/77N	
Lower zone - thick sheet	15	N18/40E, N66/90	

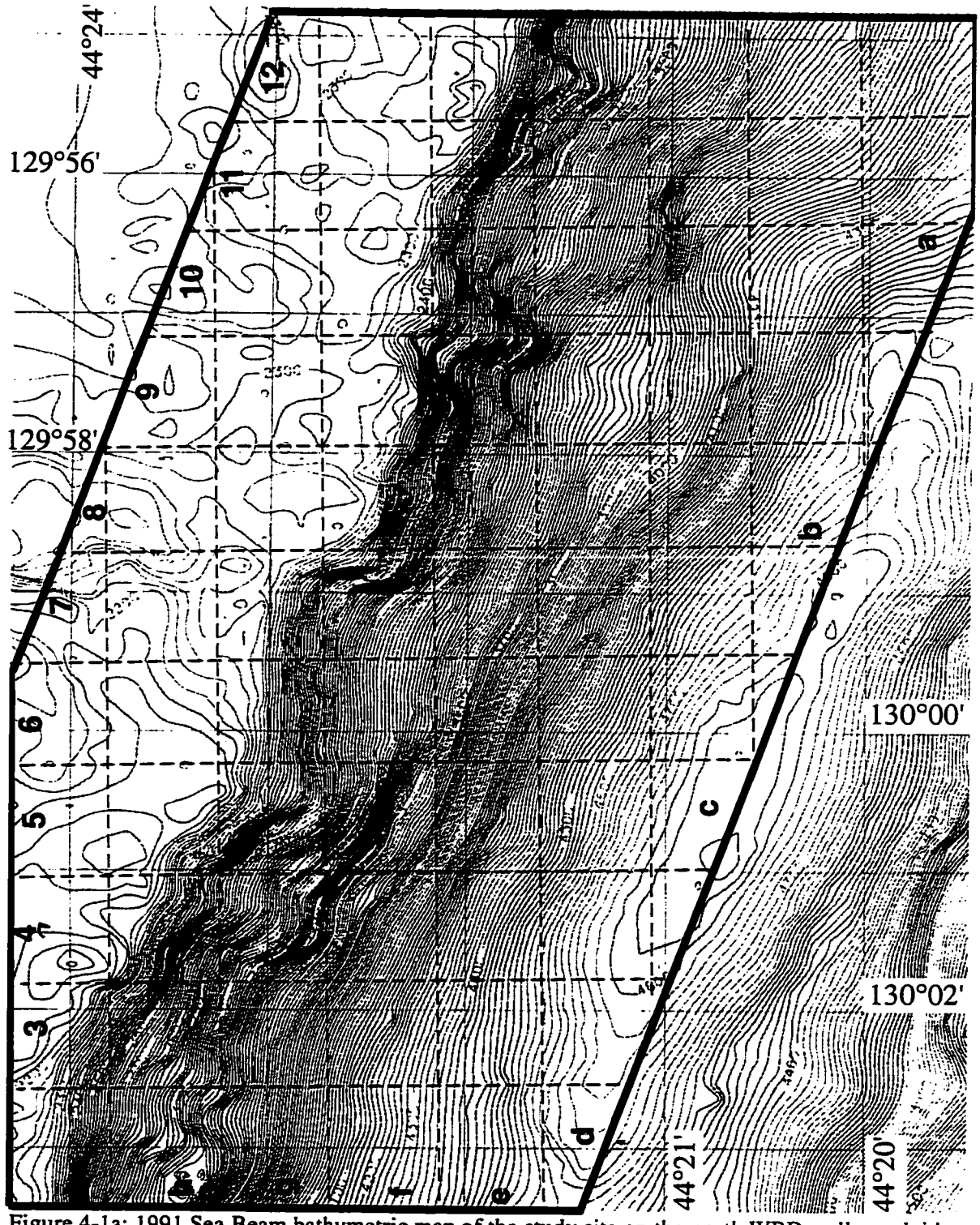

Figure 4-1a: 1991 Sea Beam bathymetric map of the study site on the north WBD wall overlaid with a labelled reference grid. The Blanco trough has a depth of 4850 m while the Juan de Fuca plateau changes from 2110 m in the west to 2290 m in the east.

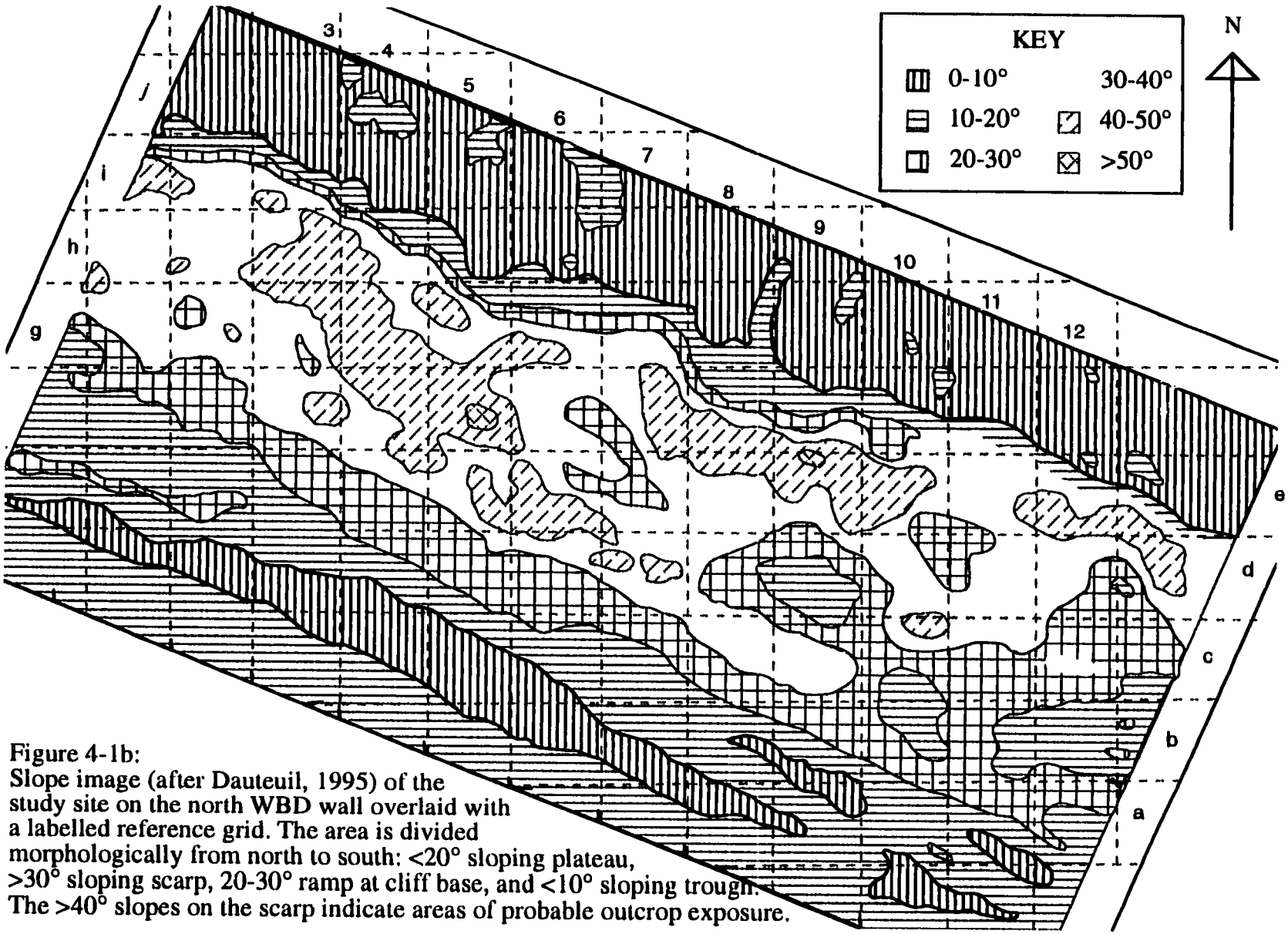

Figure 4-1b:
Slope image (after Dauteuil, 1995) of the study site on the north WBD wall overlaid with a labelled reference grid. The area is divided morphologically from north to south: <20° sloping plateau, >30° sloping scarp, 20-30° ramp at cliff base, and <10° sloping trough. The >40° slopes on the scarp indicate areas of probable outcrop exposure.

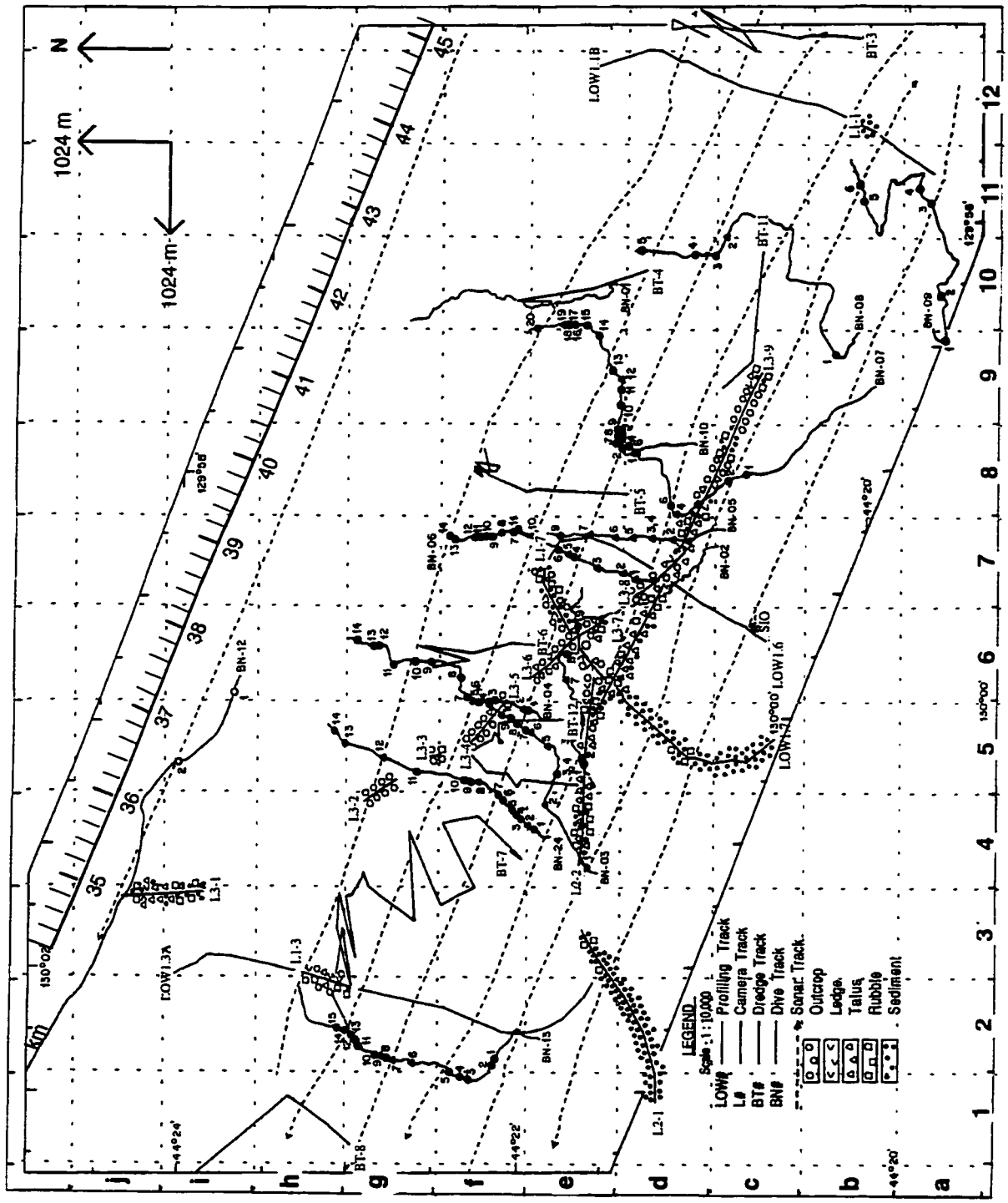

Figure 4-2: Compilation of the track lines for topographic profiling, sonar imaging, camera towing, dredging and diving within the WBD study area. The zig-zag nature of the dredge paths approximates the location of that haul. The dive tracks and remaining lines are geographically situated by the latitude and longitude co-ordinates shown on the interior and exterior border-frames respectively. The positions can be related to the imagery that appears in Figure 4-3 by means of the alphabetised and lettered grid. The location of an SIO transponder deployed in 1987 is marked by an asterisk in c-6.

Figure 4-3: Mosaicked imagery from digitised sonar data of the study site on the WBD north wall.
Each grid square is 1024 m x 1024 m. The grid is lettered (a-j) from south to north and numbered (1-12) from west to east. The a-b line boundary corresponds to 44°20'N while the 5-6 line boundary corresponds to 130°00'N. Both the up- and down-looking mosaics display an uppermost swath of typical Deep Tow side-looking sonar imagery for the flat-lying seafloor north of the Blanco wall. The white line depicting the cliff edge on the mosaics was not directly imaged in this survey but has been traced from the Sea Beam map (Figure 4-1a). .
The polarity of Deep Tow imagery is the same as that for GLORIA, with the light pixels representing strong reflections from rough bottom (eg. outcrop on steep face in a) or slopes facing the ship track (eg. shallow, mass wasting slopes on face in b) while the dark pixels indicate low backscatter energy from a smooth bottom (eg. sediment on seafloor plateau in a and b) or acoustic shadows (eg. mass wasting form in grid square e-4).
a. Up-looking mosaic (with the exception of the lowermost swath which shows a mixed view to the north and a down-looking view to the south).
b. Down-looking mosaic, which lacks data for the two lowermost lines.

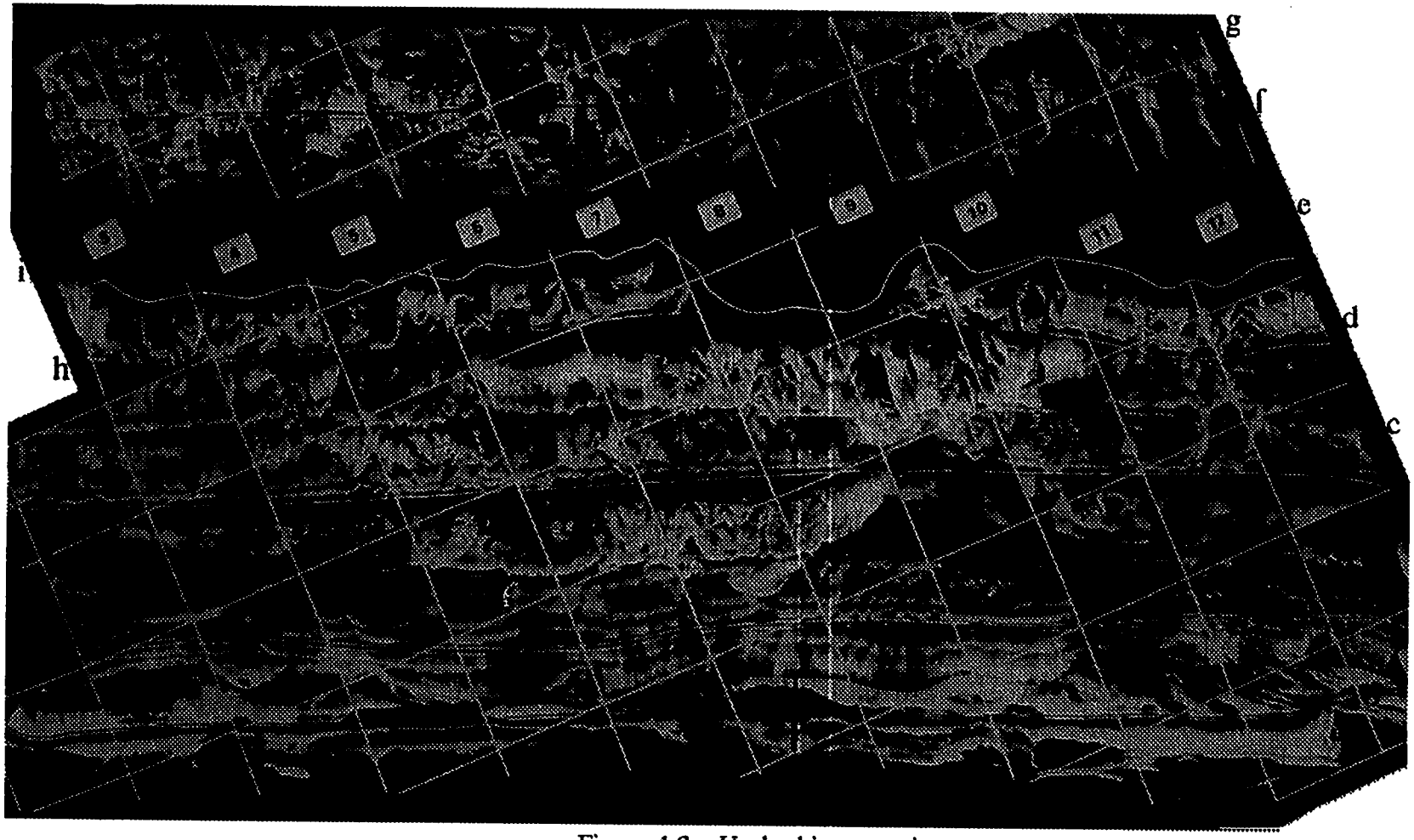

Figure 4-3a: Up-looking mosaic

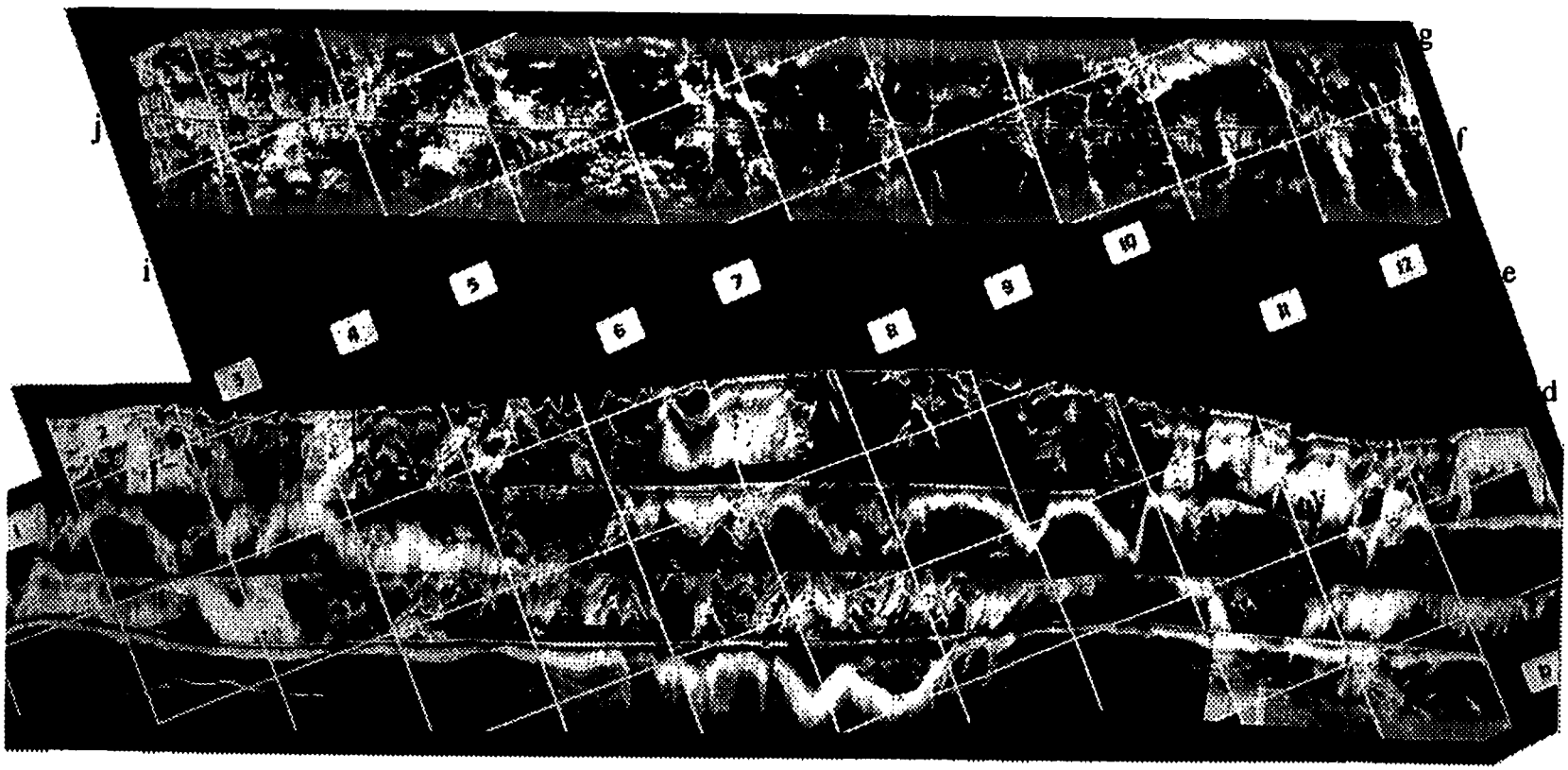

Figure 4-3b: Down-looking mosaic

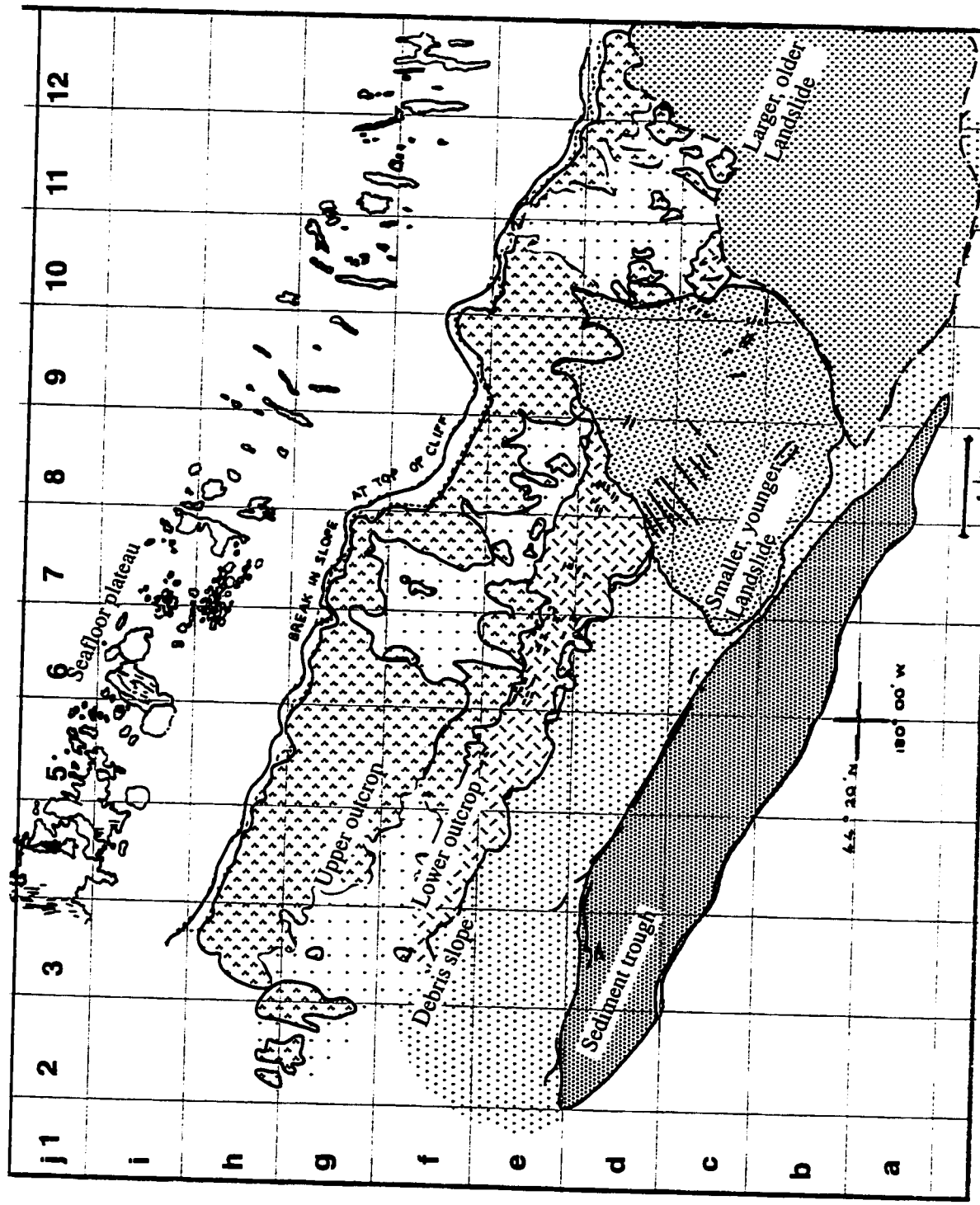

Figure 4-4: The five main zones discussed here along the northern wall of the West Blanco Depression are essentially the same as those recognised by Delaney et al. (1987). The interpretations differ in defining the contact between the upper and lower zones which here now lies at a greater depth between 3625-3800 m. In addition, a large older landslide is identified in the eastern part of the study site.

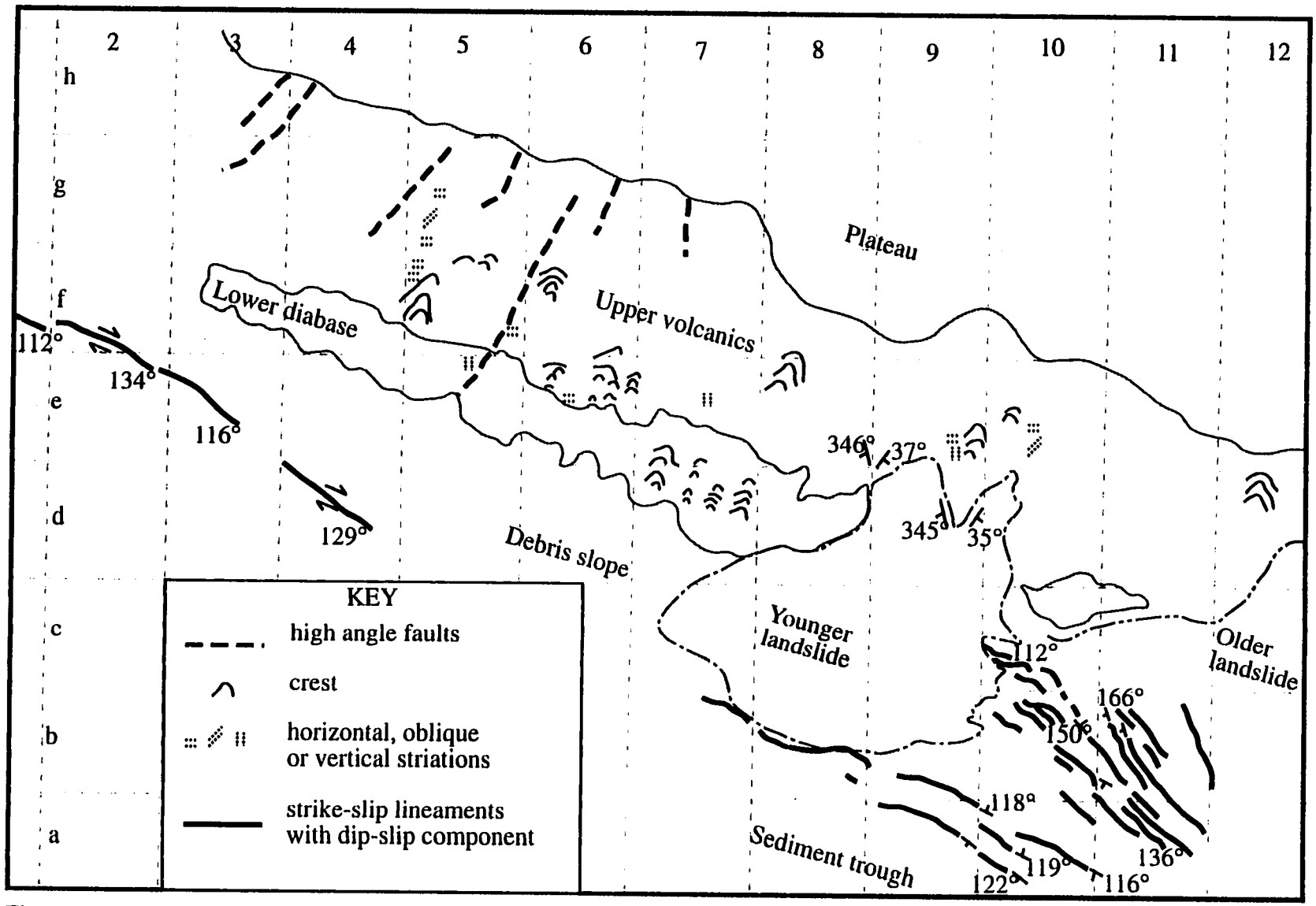

Figure 4-5a: Large-scale structural features within the main geomorphological zones on the north WBD scarp.

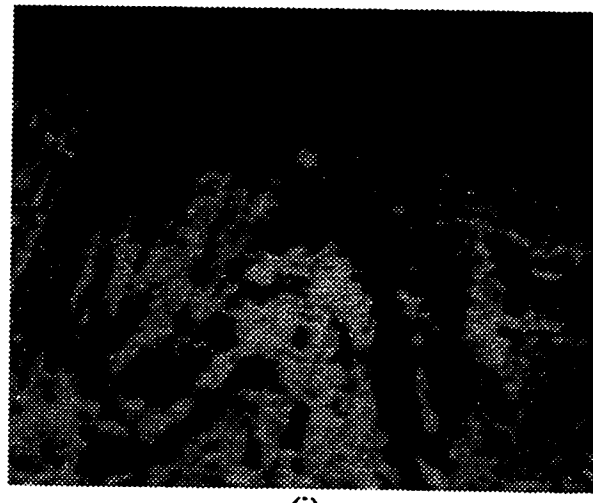

(i)

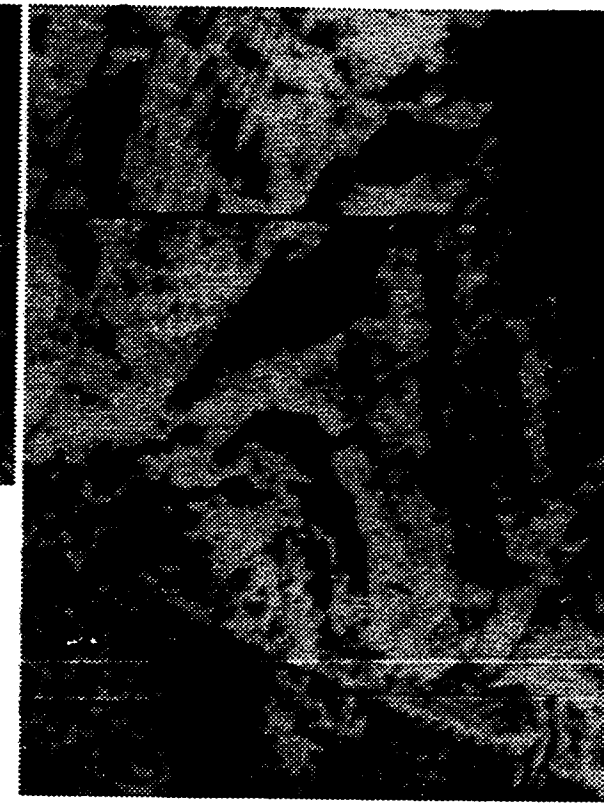

(ii)

Figure 4-5b:
V-shaped shadows observed on the up-looking sonar mosaic, for example in -
(i) grid-square e-7
(ii) grid square e-8

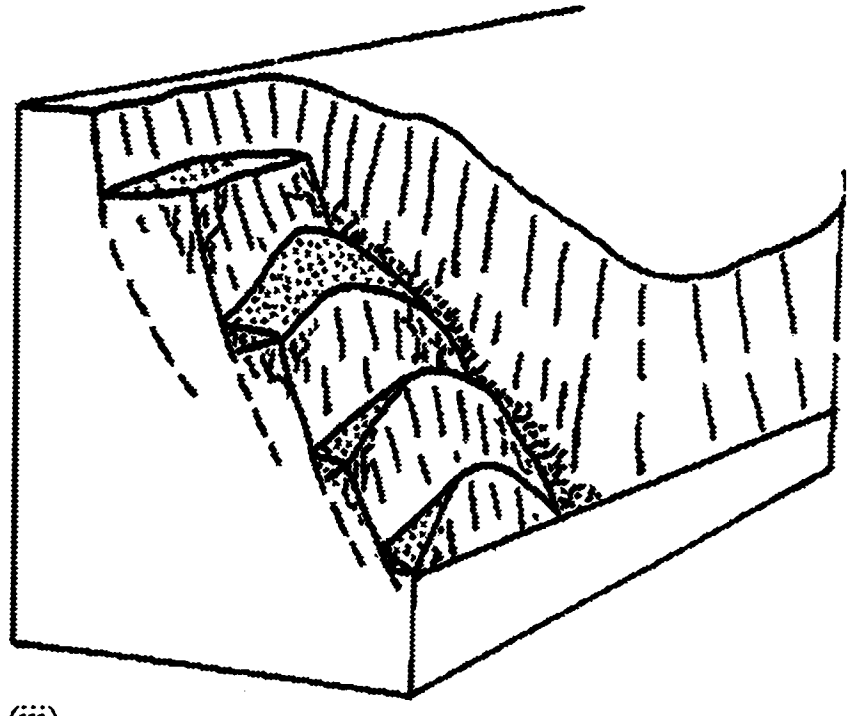

Figure 4-5b: (iii)
The acoustic features appear to represent successive crests on the WBD scarp based on observations recorded by D. Bideau in dive BN-01 and by others in subsequent dives.

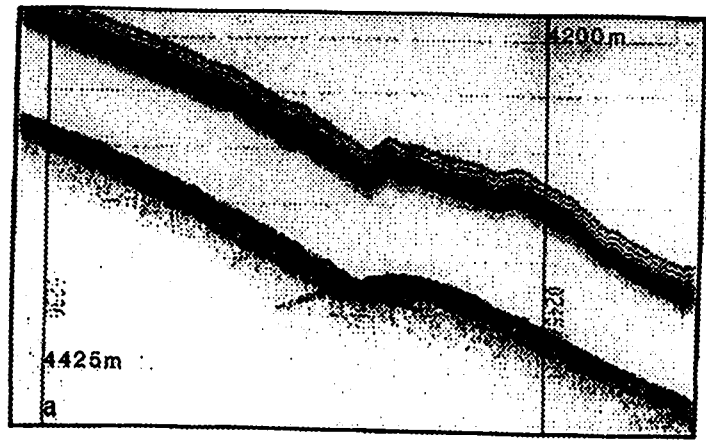

a. Line 1.3 shows a break in the debris slope at 4370 m that is associated with a lineament on the sonar mosaics (grid square f-2) which is interpreted as a strike-slip fault.

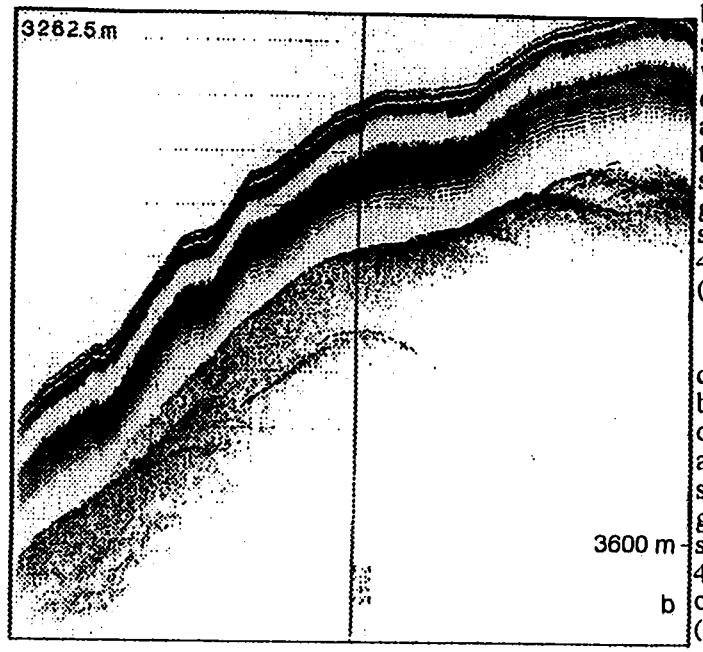

b. Line 1.6 displays structures associated with a crest in the upper outcrop zone of the face at 4310 m. The top of the crest is covered by sediment as evident in grid square e-7 on the sonar mosaics (Figue 4-3) and in dive BN-05 (Figure B-5).

c. Line 1.6 shows a bench in the lower outcrop zone of the face at 3920 m. Such structures in this area of grid-square d-7 on the sonar mosaics (Figure 4-3) were commonly observed in dive BN-05 (Figure B-5).

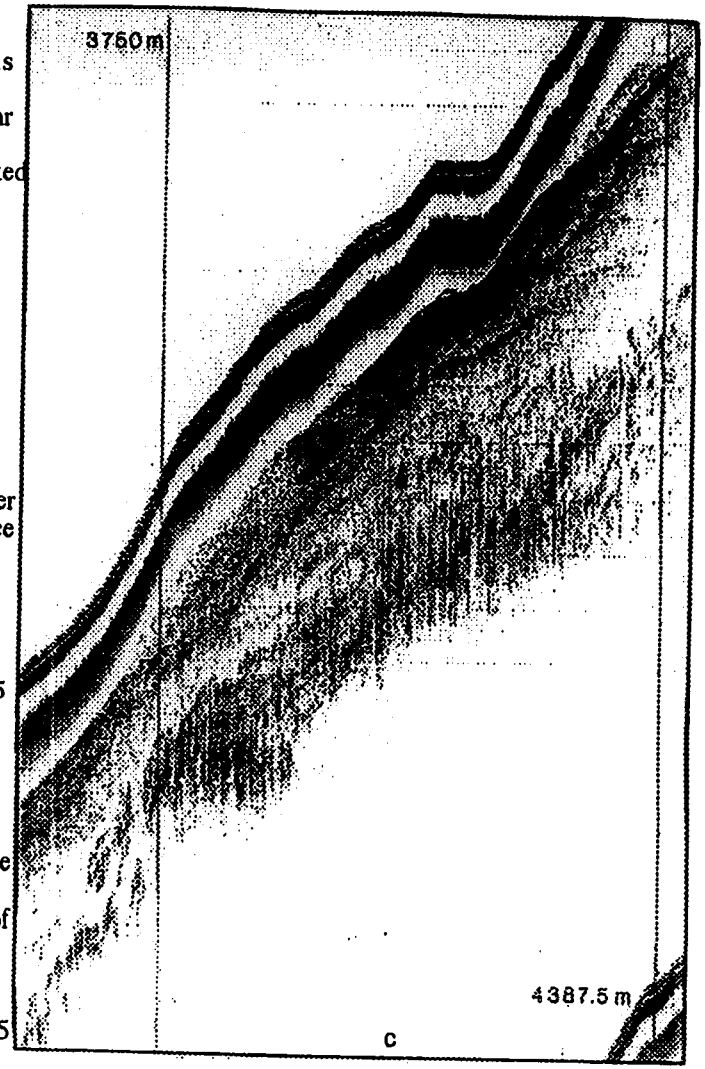

Figure 4-6: 4 kHz sounder profiles for boxed areas along lowerings 1.3 and 1.6 (Figure 4-2). In each figure, the horizontal lines have a 37.5 m spacing while the vertical lines give the time along the track.

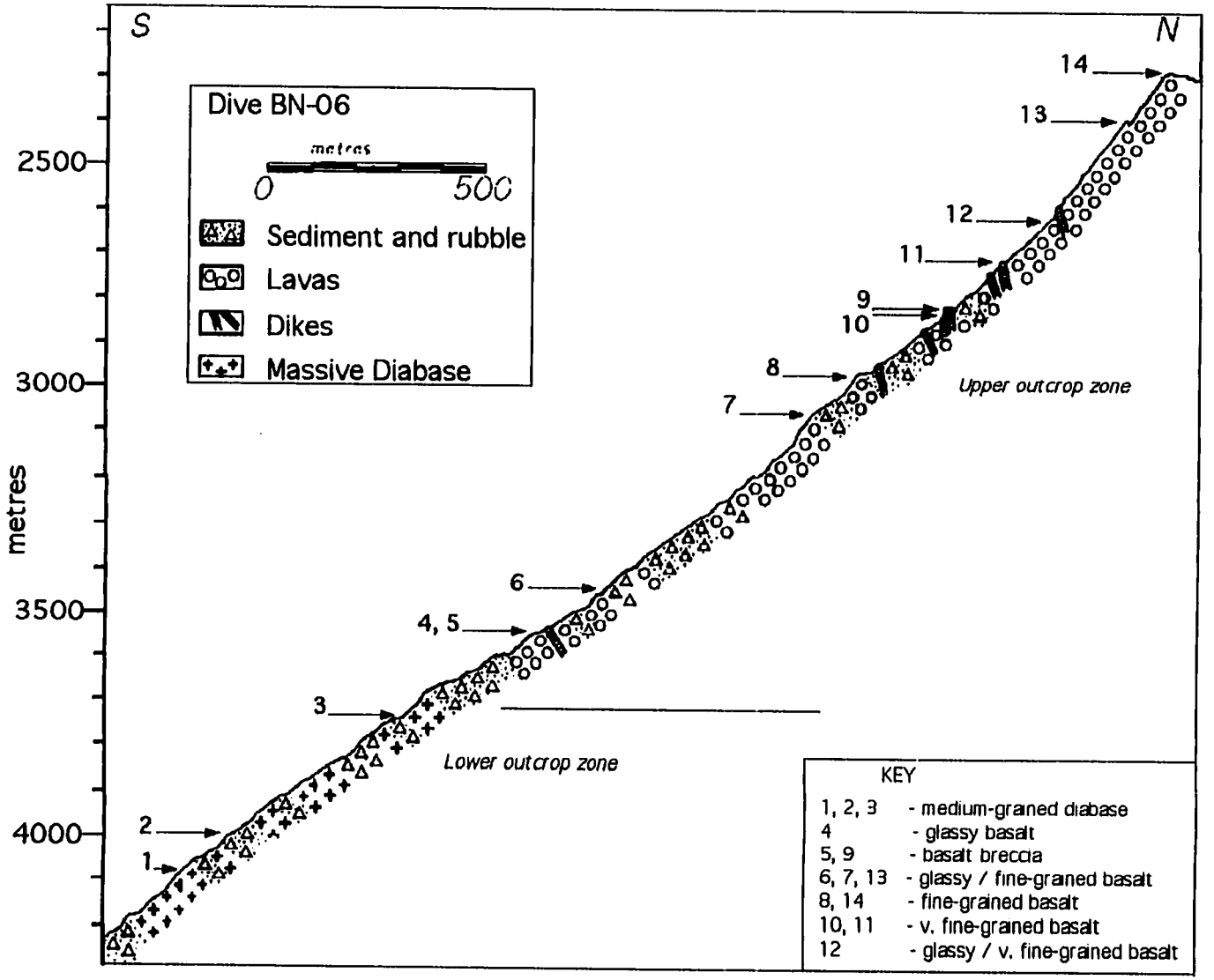

Figure 4-7: ~1.07 Ma north-south profile of the north WBD scarp showing the upper zone with basaltic flows and the lower zone with massive diabase.

Plate 4-1: Morphologic features of the outcropping zones in the north WBD site from the up-looking sonar imagery (Figure 4-3a). The blocks have been processed as described in the Methods section and labelled by grid-square as in Figure 4-3. They are generally 1024 m * 1024 meter squares except for Plate 4-1a which is 2048 m * 2048 meter squares.

(a) Grid squares c-9, c-10, d-9 and d-10 show the eastern part of a recent, rotational landslide. A series of sinuous fault scarps (grid square c-10) on an older landslide terminate against the younger one indicating the relative age relations. These mass wasting features are not discussed in detail in this study.

(b) Grid square h-7 shows lava fields (high reflectivity) on the generally sedimented (low reflectivity) Juan de Fuca plateau near the scarp edge. The different morphological forms displayed reflect changes in accretionary style over time.

(c) Grid square g-5 shows that the uppermost outcrop zone on the 60°-70° sloping scarp is distinguished by a high reflectivity and uniform texture.

(d) Grid square f-5 shows the transition between the upper and lower outcrop zones. The base of the upper outcrop zone which slopes at 50°-60° becomes increasingly scree-covered as indicated by the smooth-textured appearance that obscurs the contact.

(e) Grid square e-6 shows that the lower outcrop zone on the 40°-50° sloping scarp has a distinctive texture of horizontal, light and dark bands. These are interpreted to result from volcanic layers and the shadows cast by their bench-like topography on the cliff face.

(f) Grid square d-7 shows the contact between the lowermost outcrop exposure and the debris zone by their contrast in reflectivity and texture of the acoustic backscatter. The outcrop has a unique cross-hatched texture that indicates a change in rock type within the lower zone.

(a)

(b)

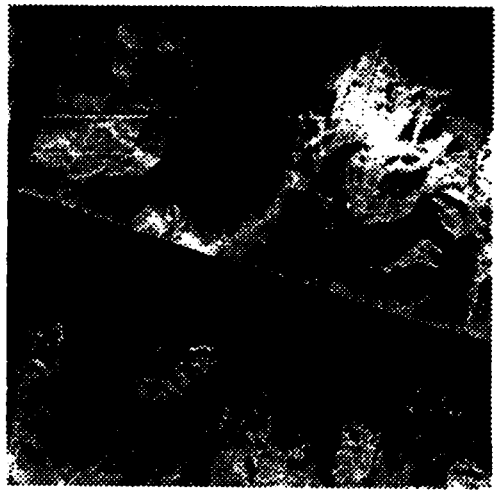

(c)

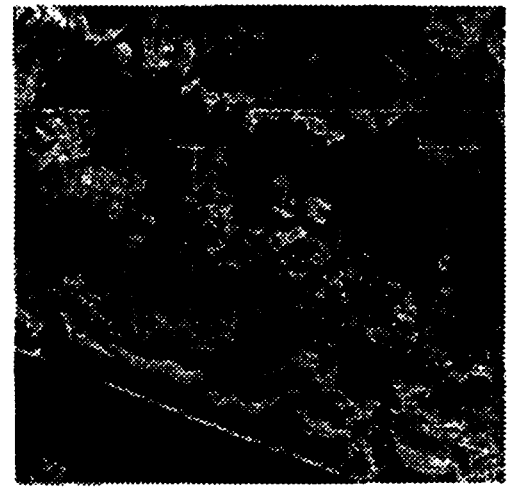

(d)

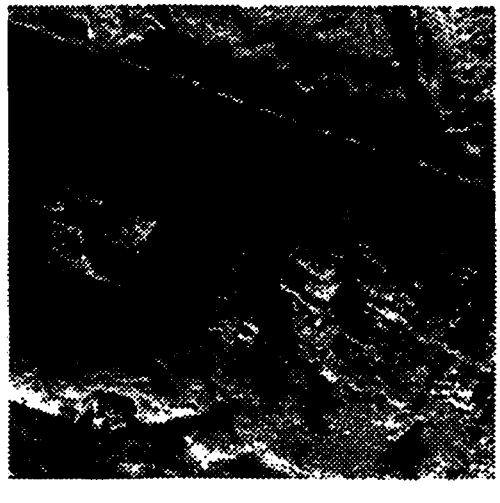

(e)

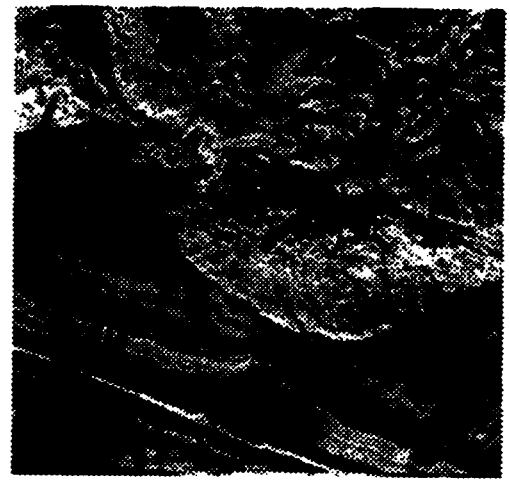

(f)

Plate 4-1

Plate 4-2: Examples of the mass wasting zones and structural features in the study site from the up-looking sonar imagery (Figure 4-3a). The blocks have been processed as described in the Methods section and labelled by grid-square as in Figure 4-3. They are generally 1024 m * 1024 meter squares except for Plates 4-2e and 4-2f which are 2048 m * 2048 meter squares.

(a) Grid square d-6 shows the 10°-30° sloping debris zone along the cliff base. Emanating from this sharp break in slope are at least two rills of coarser boulders that range from roughly 2 m to 25 m in size and which are actively distributed toward the sediment trough. On the more sedimented area inbetween, a teardrop form is indicated by lower backscatter intensity and is suggestive of a grain flow deposit.

(b) Grid square f-7 shows the traces of possibly two, high angle, westward dipping normal faults in the upper outcrop zone that, with one exception (Plate 4-2c), are apparent to ~0.5 km depth as interpreted from the sonar imagery.

(c) Grid square e-5 shows the one exception to Plate 4-2b in which the fault possibly extends into the lower outcrop zone where it terminates creating an overhanging cove structure at the cliff base.

(d) Grid square e-9 shows the head wall of the western part of the younger, double-headed landslide (Figure 4-4). The cliff here is formed by intersecting fault planes trending at N346° and N37° (Figure 4-5a) which cast immense shadows on the face that continues up behind it. Striations were observed (Figure B-10) on a similar fault pair at the other head of this landslide.

(e) Grid squares a-9, a-10, b-9 and b-10 show a set of N116°-122° trending lineaments (Figure 4-5a) at the edge of the poorly but homogeneously reflective, sediment trough zone. The lineaments were observed to be 1-5 m high, mostly south-facing scarps of basaltic breccia (Figure B-9) and interpreted to result from strike-slip faulting with an associated component of normal faulting.

(f) Grid squares a-11, a-12, b-11 and b-12 show a series of N136°-166° trending lineaments (Figure 4-5a) on the larger and older of the two landslides. An enlargement of grid square b-11 is displayed in Plate 4-3c. These are also interpreted to be related to strike-slip faulting in the transform fault regime.

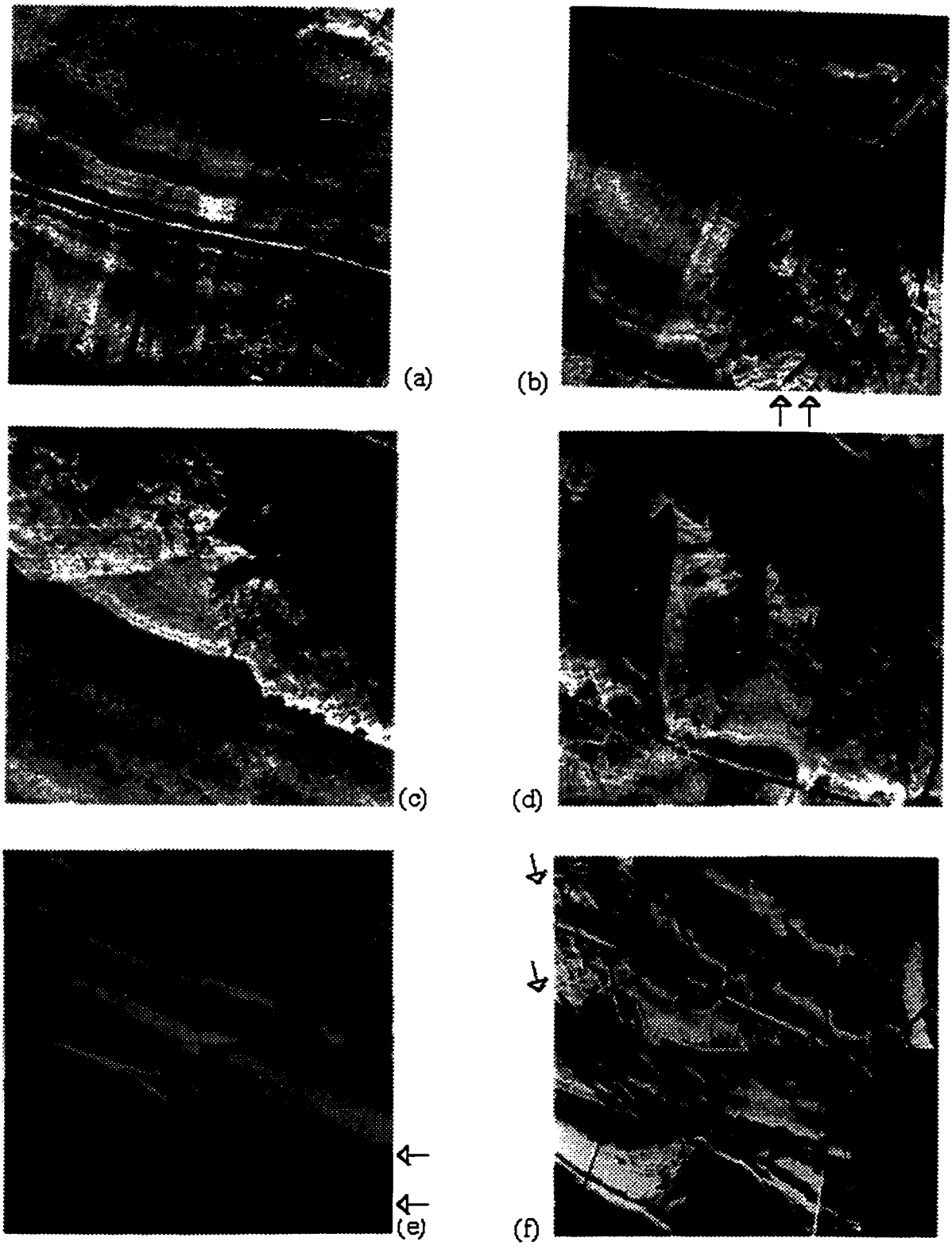

Plate 4-2

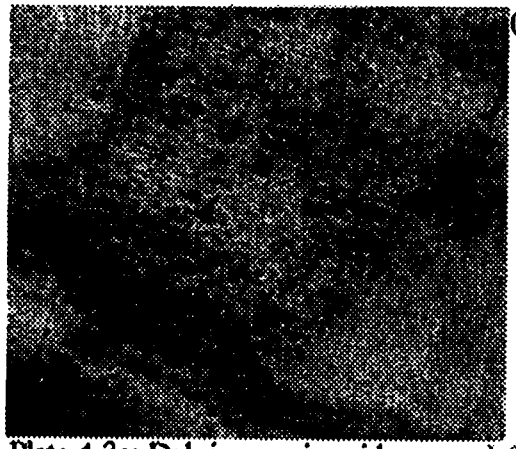

(a)

Plate 4-3a: Debris zone in grid square d-6

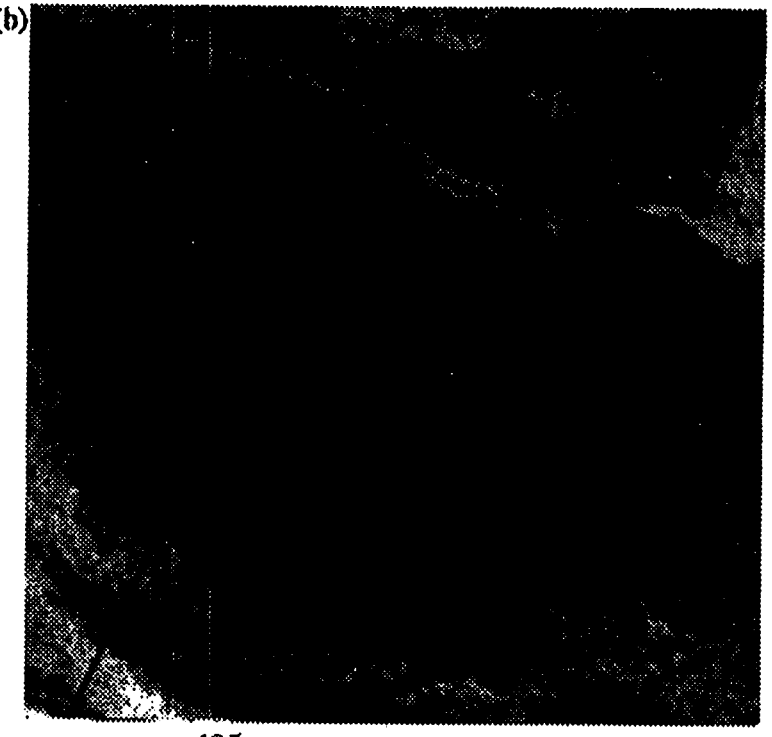

(b)

N

~ 405 m

Plate 4-3b: Slump in grid square e-4

(c)

Plate 4-3c: Fault scarps in grid square b-11

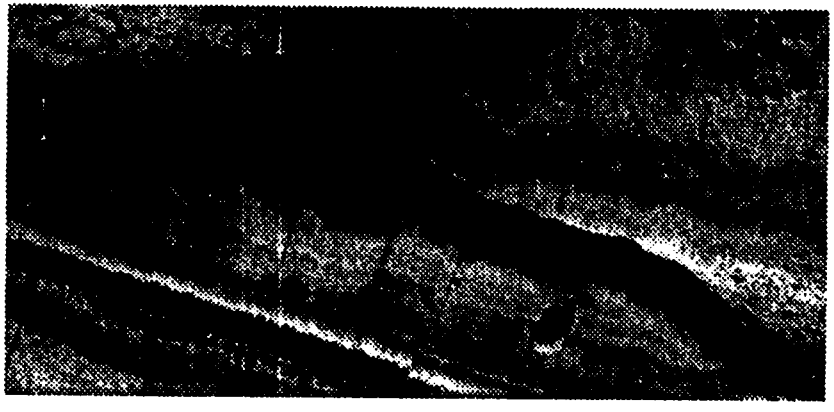

(d)

Plate 4-3d: Strike-slip lineament in grid square f-2

CHAPTER V: GEOLOGY - PART 2

5.1 Introduction

Given the logistical and technical difficulties of monitoring ridge-crest activity in real-time (Fox et al., 1995), lava morphology is a useful alternative to infer eruption conditions and emplacement parameters and ultimately, to understand how volcanic processes evolve in accreting the oceanic crust.

The nature and thickness of these lithologic units, as observed on the seafloor, from drill-core and in ophiolites, typically varies within a three-layer sequence in the upper crust. There is (from top to bottom): a ~0.0-1.5 km thickness of pillow basalts, sheet flow basalts, massive basalts, and basalt breccias; a transition of massive basalt with minor dikes; and a ~0.6-1.3 km thickness of a mafic sheeted dike complex with minor basalt. The sheet flow basalts can be classified further into lobate, lineated, ropy and jumbled types (Bonatti and Harrison, 1988). Other forms defined from the seafloor include "jumbled flows", "loose blocks" and "broken basalt" (Barth et al., 1994).

Based on land observations (Holcomb, 1980), laboratory experiments (Griffiths and Fink, 1992) and numerical modeling (Gregg et al., 1996) of lava flows, these morphologic differences are attributed (Ballard et al., 1979; Bonatti and Harrison, 1988) to physical factors (e.g. eruption temperature, effusion rate, viscosity, and crystallinity) and emplacement conditions (e.g. terrain slope, spreading rate) but are unrelated to the chemistry (Batiza et al., 1989).

Consequently, Ballard et al. (1979) proposed that the upper crust ought to be built by decade-long episodes of intermittent volcanism in which early sheet flow complexes become overlain by slightly older pillowed volcanics. They also suggested that the

volumetric proportions of these two types should be similar at all ridges irrespective of spreading rate with apparent differences ascribed to volcanic topography. By comparison, the uppermost 500-600 m from intermediate- (and slow-) spreading ridges (Donnelly et al., 1980) tend to be composed of mostly pillows with minor massive units and breccias although thin flows (Adamson, 1985) and lobate sheet flows (Francheteau, 1990; 1992) are observed separately at other localities.

Hyndman and Salisbury (1984) inferred that there were 7 eruptive cycles in a 571 m thick section of slow-spreading Mid-Atlantic Ridge [MAR] crust in which each began with massive flows and progressed to pillows with breccia and talus at the top. However, their cycles of decreasing resistivity do not always concur with this lithologic sequence, nor are massive flows consistently present at each base, while breccia units may also be found within one of these magmatic cycles.

Pezard et al. (1992) inferred that 2-3 volcanic phases separated by tectonic intervals formed the uppermost ~0.8 km of basement from the intermediate-spreading East Pacific Rise [EPR]. It comprises an upper 575 m of pillow basalts and thin flows alternating with massive units and a 200 m thick transition which also includes dike margins (Adamson, 1985). However, the massive units (27 and 2D) which they indicate as hydrologic markers are not of significantly greater thickness or resistivity than others.

Hence, the type, proportion and stratigraphy of lava morphologies vary considerably and there is no well-constrained model of upper crustal building. In this chapter, the method of logging ODP/DSDP core is applied to the WBD site (Chapter I) with the aim of reconstructing lithostratigraphic profiles from visual observations of a submarine scarp and correlating these lithologic units with previously described flow forms. The data is used to examine the volcanic history of this study site and is the basis

for extracting two possible accretion models. This detailed record is also important in assessing the variability between different areas of intermediate spreading rate.

5.2 Method

The locations of fourteen *Nautile* traverses in the N. WBD study site are shown on Figure 4-2. The placement and path of these tracks before and during the dive were guided by the sonar imagery (Figure 4-3). The track lines shown (Figure 4-2) were obtained by editing (eliminating points based on velocity jumps as well as comparison to the in-hull Doppler navigation) the acoustic navigation (the ship's fixes on the submersible) collected in Universal Transverse Mercator (UTM) coordinates.

In order to describe the lava morphology in a scarp perspective, a nomenclature of 11 identifying terms was introduced. The classification also includes 4 other categories for tectonically affected flow forms, distinctive features of the outcrop, structurally related characteristics of the outcrop, and mass wasting forms as summarized in Appendix B. Each label has an attached symbol in the legend (Appendix B) for graphical representation.

This standardized scheme was used to interpret the 35 mm camera and video data taken from the submersible and allocate the material into lithologic units. The 3725 color photographs, archived at IFREMER, were individually annotated producing a discontinuous section. Observations from the 14 color video tapes were logged at a 2-3 m scale, tabulated and compiled separately into a continuous section. The two sections for each dive were then compared and any differences were resolved by re-examining the notes and data. At a later time, all the sections were re-checked against the video data for

consistency. These verified stratigraphic profiles are presented in Figures B-1 to B-13 with adjacent structural information on outcrop features estimated from the video tapes.

A detailed profile of the scarp along each dive traverse was obtained from the depth and altimeter records in the edited acoustic navigation. Slope changes were calculated from these profiles and are shown in the penultimate column of Figures B-1 to B-13. The smaller scale changes in slope were estimated from the video data and are indicated immediately alongside these lithologic sections (Figures B-1 to B-13).

In total, 146 rocks were collected comprising 16 breccias, 75 basalts, 17 metabasalts, 32 diabases, 3 metadiabases, and 3 sediment samples. For each rock, its depth of retrieval and petrographic properties is shown next to the lithologic unit sampled in Figures B-1 to B-13.

5.3 Results - Definition of lithological types

The rocks on the north WBD scarp can be allocated to one of 8 to 10 different types based on their morphological characteristics, as defined below.

A *pillow lithology* includes inflated mounds on the plateau (Plate 5-1b) but on the scarp the forms are bulbous and cross-sectional outlines range from round to ellipsoidal. This lithology generally occurs in discrete layers but there are also some partial pillows within the blocky unit (see below). The pillows average about 1-2 m in diameter but can be up to ~5 m long (Figure B-1). A pillow interval tends to be 19±9 m thick on average but can be up to 65 m thick (Figure B-1) or even 80 m thick where there are crestal features (Chapter IV) in the cliff face (Figure B-4). The pillow outcrop is present within the uppermost 50 m (Figures B-24) to 700 m (Figure B-1) but is most commonly found in

the upper 400 m (Figure B-6). The only exception is in the transition zone between depths of 3035 m (Figure B-4) and 3860 m (Figure B-13) where they either occur over <3, brief (<5 m thick) intervals (Figures B-12&13) or as a single isolated block (Figure B-4) that appears to be out of place. This unit is composed of glassy to medium-grained, moderate to highly phyric basalts with plag-cpx-ol and plag-cpx phenocryst assemblages (Figures B-1,2,4&6).

A *broken basalt lithology* (Plate 5-1c) represents ~10-20 cm size blocks with angular broken surfaces that are *in situ* although they appear to be poorly cemented together. These intervals, which can be up to ~50 m thick (Figure B-13), are generally present within the uppermost 500 m (Figure B-1). Below 500 m, this unit is found in down-dropped fault blocks (Figure B-6) associated with crests or benches (Chapter IV). The one sample recovered (BN-6-6) is a glassy, highly phyric, plag-cpx-ol basalt (Figure B-6).

A *blocky lithology* is cohesive and composed of either large, ~30 cm blocks (Plate 5-1d) or small, ~15 cm blocks (Plate 5-1e) throughout. The two types have a similar maximum interval thickness of 40 m (fine - Figure B-3) to 50 m (coarse - Figure B-10) although the coarse type can be up to 170 m thick where there are crests or benches in the face and small talus accumulations on the ledges (Figure 4-2 - grid square h-2/3). Both types occur mostly in the upper 700 m (Figure B-1,4,6&13) with the exception of one tectonized profile (Figure B-13). The more common, coarse blocky outcrop tends to be present between 1150 m and 1500 m while the fine blocky type is found between 1100 m and 1200 m (Figures B-5&3). The coarse blocky outcrop is composed of mainly fine-grained, sparse to moderately phyric basalts and medium-grained, aphyric to highly

phyric basalts with plag, plag-cpx and plag-cpx-ol phenocrysts (Figures B-1,3,4,5,6&10). Glass rinds, glassy basalt and basalt breccia were also sampled from this lithology.

A *thin-sheeted lithology* is formed by roughly ~10 cm thick sheets and are thinner than those observed on-axis (Plate 5-1a). This lithology occurs below depths of 3350 m (Figure B-5) over 5-35 m (Figure B-2) or 5-20 m (Figures B-5,12&13) intervals in the Upper and Lower Outcrop Zones (Chapter IV) respectively. This unit is composed of glassy to fine-grained, sparsely-phyric, plag-cpx basalt (Figures B-3,6&13).

A fractured equivalent of this lithology is termed a diced unit. It has the same grain size but the glassy basalts are moderately plag-cpx phyric (Figure B-2) or highly plag-cpx-ol phyric (Figure B-6) while the fine-grained basalts are highly plag-cpx phyric (Figure B-12). There is also basalt breccia in parts of this outcrop (Figure B-10), evidently from the fracturing.

A *thick-layered lithology* (Plate 5-1g) is formed by >0.5 m thick, massive layers composed of basalts and diabases. This lithology occurs below 2655 m over 10-70 m (Figure B-4) or 5-35 m (Figure B-6) intervals in the Upper and Lower Outcrop Zones respectively although the maximum thickness is up to 55 m where there are faults or benches. The basalts are medium- to coarse-grained with plag or plag-cpx phenocrysts but in the upper zone, they vary from aphyric to highly phyric while in the lower zone, they are sparsely phyric. Likewise, the diabases are fine- to coarse-grained and aphyric but in the lower zone, they can also be sparsely plag phyric. Massive slabs out-of-place on sedimented slopes are possibly derived from tectonized areas of this unit (Plate 5-1f).

A *jointed-massive lithology* is internally homogeneous and massive with faint grooves on the surface possibly from sub-horizontal joint planes (Plate 5-1h). Individual

layers can be up to 20 m thick and give rise to natural benches on the scarp (Figure 5-1). These units occur over intervals that may be up to 55 m thick (Figure B-5) in areas with crestal forms indicating some faulting. This lithology is restricted to the Lower Outcrop Zone. It is composed of medium- to coarse-grained aphyric diabase.

Rare *dikes* are found 80 m (Figure B-1) - 380 m (Figure B-6) below the seafloor (Figure 4-7) and continue to be present locally throughout (Plate 5-1i). The dikes are associated with three lithologies.

Where present with the pillow and blocky outcrops (Plate 5-1d), the dikes are 1-2 m wide (Figure 6-10) and occur either singly in which case they tend to be deformed or numbering up to 5 in a sub-parallel series. In these units, the dike orientations are scattered (Table 4-1). These dikes are composed of medium- to coarse-grained basalt that is sparsely plag-cpx phyric or moderately plag-cpx-ol phyric (Figures B-1,12&13). Basalt breccia is also recovered, presumably from the dike margin as a result of forceful intrusion as has been described in Hole 504B (Anderson et al., 1982).

Where found with the thick-layered lithology (Figure 5-4a), they are scarp-parallel in trend with an ESE-strike and N-dip in the upper zone (Table 4-1). In the lower zone, they have two main trends (Figures B-2,6&12) - one is ridge-parallel with a NNE-strike and E-dip while the other vertical set is ENE-striking (Table 4-1). These dikes are composed of fine- to medium-grained, sparsely plag phyric basalt and diabase as well as aphyric diabase.

Spire structures (Plate 5-1j) protrude vertically upward in the face as tapering, round columns. They are 2-3 m in diameter at the base and narrow to about 1 m at the top although one spire was measured to be 6 m wide (Figure B-6). The structures are 1-5 m high but two have been measured with heights of 11 m (Figure B-4) and 20 m (Figure B-

4). The sides sometimes show fine, centimetric, horizontal banding while the flat top surface is often highlighted by a yellow-orange alteration (Figure B-4). There is commonly only 1 but in a few places there are up to 3 spires (Figure B-1,3,6&13). In the Upper Outcrop Zone, they are rooted in the fine (e.g. 2520 m in Figure B-13) or coarse (e.g. 2390 m in Figure B-4; 2600 m in Figure B-6) blocky lithology and overlain by the pillow or broken basalt lithology. In the Lower Outcrop Zone, some are also associated with the thickly-layered massive lithology (e.g. 3135 m in Figure B-4; 4075 m in Figure B-12). These structures are composed of mainly fine-grained, sparsely to moderately phyric basalt with plag-cpx or plag-cpx-ol phenocrysts, and rare glassy basalt breccia.

Two other types recovered from the Upper Outcrop Zone by dredging (Delaney et al., 1987) include a *volcaniclastic breccia lithology* from the western part (BT-8) and a *hyaloclastite lithology* from the central part (BT-5&6) of the study site.

5.4 Interpretation - Correlation with other lithological units

In order to understand the implications of these morphological types and their stratigraphy for magmatic accretion, they have to be correlated with other lava forms that have been described from laboratory simulations, ophiolites, the seafloor, and drill cores of intermediate spreading rate oceanic crust.

5.4.1 The pillow lithology

The pillow lithology on the WBD scarp is equivalent to the pillow basalt type described in ODP/DSDP cores, the axial seafloor (Barth et al., 1994) and in ophiolites

(e.g. Troodos - Schmincke and Bednarz, 1990). However, there are variations in other parameters.

At the WBD site, pillow flows occur within the uppermost ~415 m forming a cap to the section (Figures B-1,4,10&13). This is similar to Hess Deep where mostly pillows are found in the uppermost 300 m (Francheteau et al., 1990; 1992). However in Hole 504B, pillow units are present over the upper 780 m suggesting a much longer period of low effusion rate flows.

One profile (Figure B-6) is similar to Site 482 where no pillows are present respectively within 55 m and 87 m of the basement top (Lewis et al., 1983a). This implies that the pillow lithology does not always form in the final stage of crustal building at intermediate spreading ridges.

In the WBD section, there are 9 pillow intervals within the uppermost 415 m and 11 in the upper 780 m which contrasts with Hole 504B where they recur at least 20 and 40 times over the same intervals. This indicates that the WBD magmatic system by comparison did not as frequently attain the 1 m^3s^{-1} effusion rate (Griffiths and Fink, 1992) that is thought to be required for pillow formation.

In the study site, the pillow diameters are 1-2 m on average which is larger than those measured in Hole 504B (0.3-0.8 m - Adamson, 1985) or in Cyprus (0.5 m - Kidd, 1977). Consequently, despite the 65 m maximum thickness of pillow intervals which is greater than the 30 m (Lewis et al., 1983b) and 50 m (Unit 63 - Adamson, 1985) respectively at Site 483B and Hole 504B, this does not necessarily imply that more flows were extruded. The larger pillow size could be a reflection of a lower eruption temperature, higher crystallinity and/or lower angle of slope on which the WBD lavas were extruded (Walker, 1992a). Of these possible causes, there is certainly evidence that the WBD lavas with an average 10-25% phenocryst content (Chapter VII) are more phyric than the Hole 504B lavas with an average 2-10% (Kempton et al., 1985).

At the WBD, whole pillows comprise 17-20% of the upper zone (or 26-29% if broken basalts are considered disrupted equivalents) which is similar to the value given for the EPR at 21°N albeit from surface observations (Ballard et al., 1981). By contrast, it can be calculated that pillow basalts represent 53% of the combined upper and transition zones in Hole 504B and a similar estimate is obtained for the Galapagos Rift at 86°W (Ballard et al., 1981). Therefore in this regard, the WBD section is unlike the intermediate spreading rate examples and is more like fast spreading crust.

5.4.2 The broken basalt lithology

The broken basalt lithology is similar to two other lava forms described on the seafloor - a rubbly sheet flow (Ballard et al., 1979), or a disrupted pillow flow (Ballard and Moore, 1977) that results from breakage along the radial cracks into *in situ* blocks due to faulting (Moos and Marion, 1994). Support for the latter case could be drawn from outcrops on the scarp where the broken basalts are associated with pillows (e.g. 2440-2490 m in Figure B-4 or 2950-3010 m in Figure B-1) and for the former case where they are not (e.g. Figure B-10).

5.4.3 The blocky lithology

The blocky lithology most closely resembles jumbled sheet flows. In some places, the layering almost grades into the thinly-layered lithology (e.g. Figure B-10, 2570-2710 m in Figure B-4) which is consistent with jumbled sheet flows being an end-member of a morphological spectrum (Gregg and Fink, 1995). These flows result from a critical transition between the inversely related rate of shear strain and viscosity (Peterson and Tilling, 1980). Their formation is favored by high shear rates on the solidifying crust

generated by extrusion rates >3000 m^3s^{-1} and by a decreased cooling rate and increased slope or flow rate relative to the rest of the above continuum (Griffiths and Fink, 1992).

This blocky lithology has been described from the Galapagos Ridge (Ballard et al., 1979) and Axial Volcano (Embley et al., 1990) but not in Hole 504B. Along the northern Cleft Segment, such jumbled flows constitute 40 m high ridges and cap massive, columnar jointed units that are much like the structural zones of sheet flows sketched by Schmincke and Bednarz (1990) from the Troodos ophiolite. Such blocky flows interbedded with basaltic pillow flows are also reported in the Oman ophiolite (Alabaster et al., 1982).

5.4.4 The thin-sheeted lithology

The thin-sheeted lithology is interpreted to be a sheet flow form (e.g. lineated, ropy). These flows are indicative of effusion rates between 1-3000 m^3s^{-1} (Griffiths and Fink, 1992). The presence of glassy basalt in this unit (Figure B-6) is consistent with sheet flow margins (Natland and Rosendahl, 1980). Such flows have been described extensively on the seafloor (see references in Barth et al., 1994) but differ from those labeled "thin flows" in Hole 504B.

5.4.5 The thick-layered lithology

The thick-layered, massive lithology in the WBD section is morphologically equivalent to the massive basalt at Sites 424-425, 482-485 and forming "thin horizons" in Hole 504B, although there are some minor differences. These layers are 0.5 m, 2 m and 2.5 m thick respectively at Sites 424-425, Hole 504B and at Sites 482-485 which is at the

same scale as the >0.5 m thickness of the WBD flows. The WBD site and Sites 482-485 are also alike in that this unit occurs over intervals up to 70 m and 29 m thick respectively. By comparison, these intervals are shorter at Sites 424-425 and in Hole 504B where they are <5.9 m and <11 m thick respectively.

The thick, massive units are present below 600 m from the basement top at the WBD site and 520 m in Hole 504B which contrasts with Sites 424-425 where they dominate the uppermost 45 m. Hence, they are not interbedded with the pillow flows as in Hole 504B, at Sites 482-485, in the Geotimes Unit (V1) of the Oman ophiolite (Alabaster et al., 1982; Pflumio, 1991), in the Troodos ophiolite (Vine and Smith, 1990), and the northernmost exposures of the Bay of Islands complex (BOIC) (Rosencrantz, 1983). The implication is that accreting the WBD crust did not involve abrupt changes in flow rate from >>3000 m^3s^{-1} to <1 m^3s^{-1} (Griffiths and Fink, 1992).

There are three possible origins for the thick-layered, massive lithology which cannot be further constrained with the given observations.

These massive units could be thick sheet flows erupted at the spreading center, as have been reported from the EPR at 21°N (Juteau et al., 1980). This is supported by some units being spatially associated with the lava pillars (see Section 5.4.7). The coarser grain sizes of this lithology could reflect crystallization in the middle of these flows.

Alternatively, they could be sills injected above a shallow melt lens as it grows (Gudmundsson, 1988) or intruded sheets such as pervade the central volcanoes in Iceland where swarms are up to 15 km in diameter (Saemundsson, 1986). Walker (1992b) suggests that such coherent complexes are promoted where there is a magma supply locus which cannot be accommodated except vertically because the volcano is buttressed by other edifices or the spreading rate is inadequate. The sill or sheet hypothesis for the WBD site is supported by one sample of a fine-grained basalt breccia (Figure B-5) which

could represent the intrusive margin of these bodies. The spire structures associated with this unit would thus be dike remnants.

A third possibility is that the unit includes both basaltic flows extruded on-axis and diabasic sills intruded on- and/or near-axis. In this case, the ridge-parallel and transform-parallel orientations of the spatially related dikes could merely be an indicator of the site's proximity to the strike-slip zone (Chapter II) and do not serve to distinguish between these accretion environments.

5.4.6 The jointed-massive lithology

The jointed, massive lithology with a diabasic texture that characterizes the Lower Outcrop Zone in the study site has two possible origins - as extrusives or intrusives.

It could be equivalent to the massive unit in Hole 504B that forms up to 25 m thick horizons (Adamson, 1985) but this lava form is interlayered throughout the EPR basement. It is also similar to massive basaltic flows which are on average 10 m thick in Iceland (Bodvarsson and Walker, 1964) and 10-40 m thick in Cyprus (Kidd, 1977). There are massive and jointed flows in the Oman ophiolite too (Alabaster et al., 1982) that are 20 m (in V3) and 40 m (in V2) thick but they are andesitic in composition.

Dolerite bodies described within the oceanic crust tend to be much larger in size. Those exposed in the eroded central volcanoes of Iceland are up to 10 km^2 in area (Saemundsson, 1986). Another on the east valley wall of the MAR south of the Kane Fracture Zone (MARK)(Karson, pers. comm.) is 1 km high and 8-10 km long parallel to the axis although it similarly underlies a mixed zone of dikes and pillows that is overlain by minor sheet flows and pillows.

In the BOIC, 10% of the diabase is comprised by 100-400 m wide and 1-2 km long bodies (Rosencrantz, 1983). However, these medium-grained outcrops lie between

the sheeted dikes and the gabbroic rocks and are interpreted to result from the thickening of the magma chamber roof zone on-axis.

A more analogous example is in the northern Oman ophiolite (Pflumio, 1991) where a sill complex occurs at the interface between dikes and an earlier volcanic sequence (V1 or Geotimes Unit). The sills which are fed by differentiated plutons that cross-cut the gabbroic series are chemically related to a second volcanic sequence (V2 or Lasail Unit) interpreted to arise during an off-axis event (Alabaster et al., 1982). Given the added similarity in thickness to the WBD section, this last hypothesis is the most preferred.

5.4.7 The dikes

The section of the Upper Outcrop Zone (80-380 m below the seafloor) in which dikes are mixed with volcanics should be designated a transition, as elsewhere. Its ~1 km thickness is much greater than either in one profile of Hess Deep (250 m - Francheteau et al., 1992) or Hole 504B (209 m - Adamson, 1985). This is significant given the absence of a sheeted dike complex in the 2 km of crustal exposure on the WBD scarp compared to its presence at these other sites.

The sheeted dikes at Hess Deep have a ridge-parallel orientation (Francheteau et al., 1992) and there is no evidence of another perpendicular set as occurs at the WBD site. This suggests that the study site was accreted near a strike-slip zone or in at least two, distinct tectonic regimes. Furthermore in Hole 504B, the sheeted dikes are composed entirely of medium-coarse grained diabase which cannot be ascribed to wider centers than in the WBD section since they also have a 1-2 m width. This implies that the study site experienced a faster cooling history during some period(s) of accretion than is typical on-axis. The three dip directions of the dikes at the WBD site could be related to fault blocks

rotating on-axis due to crustal subsidence or later as the trough opened, similar to the effects at Hess Deep (Karson et al., 1992; Hurst et al., 1994).

5.4.8 The spires

Juteau et al. (1995) suggest that the spire structures in the WBD site are the relicts of dikes. An alternative hypothesis is that these are basaltic pillars similar to those described at fast (e.g. EPR at 21°N and 13°N - CYAMEX Scientific Team, 1981; Gente et al., 1986), medium (e.g. Galapagos Rift - Ballard et al., 1979) and slow spreading centers (e.g. MAR at 37°N - Fouquet et al., 1995), on axial volcanoes (Embley et al., 1990) and in ophiolites (e.g. Troodos - Schmincke et al., 1983). Similar to those in the WBD site, they are 0.5-2 m in diameter and 10-15 m high on the EPR (Francheteau et al., 1979), and 6 m wide and 4 m high in the Troodos ophiolite. Likewise, they occur below pillow units or are rooted in either jumbled sheet flows (Embley et al., 1990) or "subhorizontal lava bodies" (Schmincke et al., 1983). The spires form as conduits for water escaping from beneath a lava pool which causes the characteristic alteration while the fine exterior rings result as the lava pool drains. This would account for why the structures are consistently composed of fine-grained basalts and cannot be dikes which vary here from fine- to coarse-grained basalts and diabases. These spire structures are thus also indicative of high effusion rates.

5.4.9 The lithostratigraphy

The lithostratigraphic profiles (Figures B1 to B13) show a 4-5 tier division to the basement in the WBD study site based on the appearance of lava forms down-section.

This is illustrated by a simplified profile for one dive (BN-06 - Figure 5-1) that omits the lithologic units occurring over brief intervals (Figure B-6).

The Upper Outcrop Zone is comprised of 3-4 sections. An uppermost, 180±140 m thick section lying between ~2250-2400 m depth is constituted by extensive intervals of the pillow, broken basalt and blocky lithologies. There are also 2-3 intermediate sections with dikes which would represent a ~1-1.3 km thick transition according to the Hole 504B definition (Adamson, 1985).

An Upper-Intermediate, 490±160 m thick section lying between ~2400-2900 m depth consists of the previous lithologies as well as local dikes, spire structures and minor horizons of the thin- and thick-sheeted lithologies. A Middle-Intermediate, 840±410 m thick section between ~2900-3700 m depth is recognized by the dominance of the thick-layered lithology amongst the previous types. In some places, it is reduced in extent by an underlying Lower-Intermediate, 470±175 m thick section between 3350-3800 m depth with jumbled and thin sheet flows. This section is roughly concordant with the transition between 3160-3625 m depth that was defined by Juteau et al. (1995) based on the prominence of alteration patches (Plate 5-1k) and vein networks (Plate 5-1l).

The Lower Outcrop Zone consists of a 370±100 m thick section identified between ~3850-4250 m depth by the absence of the pillow, broken basalt and blocky lithologies and the presence instead of the jointed-massive lithology in addition to the thick-layered and thin-sheeted lithologies and local dikes.

5.5 Discussion

The division of the WBD basement into uppermost, intermediate and lowermost zones conforms with the typical structure of upper oceanic crust. The lithological types of the former two zones which represent the Upper Outcrop Zone clearly contribute to the

textural distinction from the Lower Outcrop Zone as interpreted from the high and low resolution acoustic data in Chapter IV. Here, the implications of these lithostratigraphic profiles for magmatic accretion and its evolution in time and space is discussed.

5.5.1 Magmatic accretion models for the WBD section

In summary, 6 of the 8 morphologic types can be correlated with known lava forms. The pillow lithology corresponds to pillow lavas, the thin-sheeted lithology is equivalent to thin sheet flows, and the blocky lithology represents jumbled flows. These flows are diagnostic of flow rate (Gregg and Fink, 1995) and in this order, they reflect an increase from <1 to >3000 m^3s^{-1} (Griffiths and Fink, 1992). Also, dikes are as denoted and spires are relict basaltic pillars. The preferred interpretation of the jointed-massive lithology is that these units are diabase intrusions. The equivalents of the other 2 morphologic types are more ambiguous. The broken basalt lithology could be derived from either pillows or sheet flows but in either case, they are clearly extrusive. However, the thick-layered lithology may be either thick sheet flows or sills. Consequently, there are at least two possible models of magmatic accretion in the study site (Figure 5-2).

The reconstructions here assume that a sequence of lithologic units in which the effusion rate progressively declines reflects a short-term episode of crustal building. These models therefore follow the approach of Ballard et al. (1981), Stakes et al. (1984) and Bonatti and Harrison (1988). Using this criterion of flow rate, the stratigraphic profiles in Figures B1 to B13 can be re-examined. An example of such an analysis is given for Dive BN-06 (Figure B-6).

One model (A) interprets the thick-layered lithology exclusively as thick sheet flows. In this case, repetitions of flow sequences can be grouped into stages of crustal

construction. As a result, a five-fold division of the basement exposure can be discerned as shown in Figure 5-1 and schematically in Figure 5-2. The other model (B) treats all the thick-layered lithologic units as basaltic and diabasic sills. Such substantial thickening of the section is supported by more than half of major basaltic volcanoes which actually contain intrusive complexes rather than dikes (Walker, 1992b). In this case, it implies a possible additional phase of crustal accretion.

5.5.2 Reconstructing magmatic accretion

Accretion can be reconstructed from the lithostratigraphic profiles such as displayed in Figure 5-1 as follows:

Stage Ia involves repetitions of the flow sequence - thick sheet flows -> thin sheet flows in Model A whereas mainly thin sheet flows are extruded in Model B. This stage is evident over ~370 m and corresponds to the Lower Outcrop Zone (Chapter IV).

In the central-eastern sector of the study site, Stage Ib in both Models A and B consists of - jumbled sheet flows -> thin sheet flows in one profile (BN-05 - Figure B5) and the broken basalt lithology dominating the other (BN-06 - Figure B6). This stage is present over 350-600 m and represents the bottom part of the Lower-Intermediate Zone (Section 5.4.9). In this sector, the progression from thick sheet flows in Stage 1a to jumbled sheet flows in Stage 1b represents an overall decrease in flow rate. Hence, this is inferred to be the first major phase of crustal building.

In the eastern sector of the WBD site (BN-10), there are sequences of - thick sheet flows -> jumbled sheet flows while the central-western sector (BN- 02,03&24) has in addition - thick sheet flows -> thin sheet flows. These flow sequences are found over an ~840 m thickness and are the same as those in the Middle-Intermediate Zone. Hence, in these two sectors of the site, this stage is labelled IIa instead and marks an earlier start to

a second phase of crustal construction. The commencement of such sequences with thick sheet flows explains why this lithology becomes hidden from view at the surface although they form a significant component of drill-cores (Hall and Robinson, 1979).

Stages IIb and IIc comprise the sequence: jumbled sheet flows -> pillow flows in both Models A and B with alternations over an ~430 m thickness. Stage IIb is distinguished from Stage IIa by conditions that permitted diking to these levels and spires to form within the Upper-Intermediate Zone as opposed to the Uppermost Zone.

A schematic comparison of Models A and B is shown in Figure 5-2. The first four stages in both models occur within the neovolcanic zone.

In Model A, there is an *overall* decrease in flow rate up-section between Stages Ia and Ib from thick to jumbled sheet flows and again between Stages IIa and IIc from thick sheet flows to jumbled sheet flows and to pillow flows. Such a positive correlation between high extrusion rate and deepening level of exposure was also found in sequences drilled through a volcano flank in East Iceland (Saemundsson, 1986). Hence, the evidence in Model A suggests that there have been two major volcanic phases in accreting the WBD basement.

In Model B by comparison, there is a gradual change in effusion rate from jumbled and thin sheet flows in the Lowermost Zone and Lower-Intermediate Zone to jumbled sheet flows and pillow lavas in the Upper-Intermediate Zone and Uppermost Zone. Hence, according to Model B, accretion occurs on-axis as one progressive process although it could be interrupted by injection of thick sills into the Lowermost, Middle-Intermediate and Lower-Intermediate Zones.

In both models, there is another phase of diabase intrusion into the Lowermost Zone, possibly at the contact with underlying sheeted dikes. The relative timing of these intrusive events both with respect to each other and the extrusive stages is unknown.

However, it is constrained by the reversed polarity of the basement throughout the study site (Tivey, 1996) which implies that accretion was completed prior to 1 Ma. Hence, both these lithologic units had to have been emplaced on-axis or at most near-axis.

5.5.3 Comparison of magmatic accretion models

The WBD site differs significantly from Hole 504B in the nature and sequence of the extrusives which implies that the physical conditions of eruption at both were markedly different.

Hole 504B is limited to only 4 lithological types as compared to the 8 on the WBD scarp. Also in Hole 504B, flow sequences of declining effusion rate include (Griffiths and Fink, 1992): thin flows -> pillows; layered-massive units -> pillows; layered-massive units -> thin flows -> pillows; and layered-massive units -> thin flows. Of these, only the last also occurs in the WBD section, if the layered-massive unit is considered to be thick sheet flows.

The thick sheet flows and pillow flows are of equal abundance in Hole 504B (Adamson, 1985). This could just be an artifact of the shorter length of core recovered (~1 km) as compared to the WBD section (~2 km) or could indicate a relatively lengthier period of pillow extrusion for the Hole 504B crust. By comparison, pillow lavas form a significantly lesser proportion of the WBD section similar to the fast-spreading EPR exposure on the axial graben wall near 13°N (Gente et al., 1986) where sheet flows are more conspicuous. The two flow types are also interbedded throughout the upper and transition zones of Hole 504B which contrasts with their distinct separation at the WBD site.

Pezard et al. (1992) view Hole 504B as being constructed by successive flows up-section which is similar to Model A, except for the Stage II intrusives. They further

suggest that the crust was formed by 2-3 volcanic pulses which is akin to the 2 extrusive phases and 1-2 intrusive stages inferred for the WBD site. Here, the thick sheet flows in Stages Ia and IIa are interpreted as flooding the elongate summit depression (ESD) in the beginning of a magmatically robust phase. By contrast, Pezard et al. (1992) select just two layered-massive units but these are not unique in their high resistivity. Also, the implication of their model is that there is an intermediate time-scale ($<<10^4$ years) episodicity to accretion although Natland et al. (1983) deduced on geochemical grounds that there was a steady-state magma chamber throughout. Hence, the accretion model for Hole 504B is problematic despite some apparent points of consensus with the WBD site.

Recent models for accretion at the fast-spreading EPR (Harding et al., 1993; Kent et al., 1994; Vera and Diebold, 1994) are similar to Model B in that they invoke lava emplacement through lateral tube conduits (Christeson et al., 1992) to explain a two- to three-fold increase in Layer 2A thickness within 1-4 km of the axis. In the case of the JdFR, such crustal construction could also continue on the east side near-axis on account of the ridge migrating westward beyond the focused plane of buoyant upwelling. This speculatively could lead to injection of the thickly-layered massive unit as sills. In this situation, the jointed-massive lithology would be the diabasic intrusions resulting from the diapiric residue. Hence, both Models A and B are consistent with the tectonic-magmatic scenario for accretion proposed in Chapters II and III.

5.6 Conclusions

1. At least 6 lava morphologies are recognized and correlated with pillow lavas, thin sheet flows, jumbled sheet flows, lava pillars, dikes and massive intrusions. Another

2 are more ambiguous - a broken basalt lithology that is clearly extrusive and a thickly-layered lithology which could be either thick sheet flows or sills of basalt and diabase.

2. The upper crust in the central part of the WBD site can be sub-divided into 4 sections on the basis of flow form (from top to bottom): an ~180 m thick zone of jumbled sheet flows and pillow lavas; an ~490 m zone of jumbled sheet flows, pillow lavas, local dikes and basalt pillars; an ~840 m zone of all the lithologic types besides the diabase intrusives; and an ~370 m zone with only the diabasic intrusives, the thin sheet flows, the thickly-layered lithology and dikes. The former three sections correspond to the Upper Outcrop Zone and the last to the Lower Outcrop Zone defined in Chapter IV.

3. Two models of magmatic accretion are posed depending on whether the thickly-layered lithology represents sheet flows/sills. In the extrusive case, two major phases of volcanism are recognized by an overall declining effusion rate in each based on the succession of flow forms. In the intrusive case, the sills could be injected on- or near-axis. In both cases, diabases are intruded at the lava-dike interface in a final stage near-axis, consistent with the geodynamic scenario in Chapter III.

Figure 5-1: Basement lithostratigraphy along dive-track BN-06 in the WBD study site simplified from Figure B-6.The locations of tectonic features noted alongside. Four zones are identified based on the presence of different sets of lava morphologies. The Upper and Lower Outcrop Zone divisions recognized in Chapter IV are shown for comparison. The domain boundaries to the left of the profile are discussed in Chapter VI.

The key below gives the morphologic types mapped and their interpreted lithologic designations. The reconstruction assumes a declining rate of effusion for the sequence: thick sheet flows - jumbled sheet flows - thin sheet flows - pillow flows (Griffiths and Fink, 1992). The repetition of such a flow sequence(s) defines a stage of magmatic accretion.

Model A is reconstructed here with all the thick-layered lithologic units as thick sheet flows. Six stages are defined. There is an overall decline in flow rate from Stages Ia to Ib and from Stages IIa through to IIc that are interpreted as two major phases of crustal construction. Stage III represents synchronous or near-axis intrusion into the Lowermost Zone.

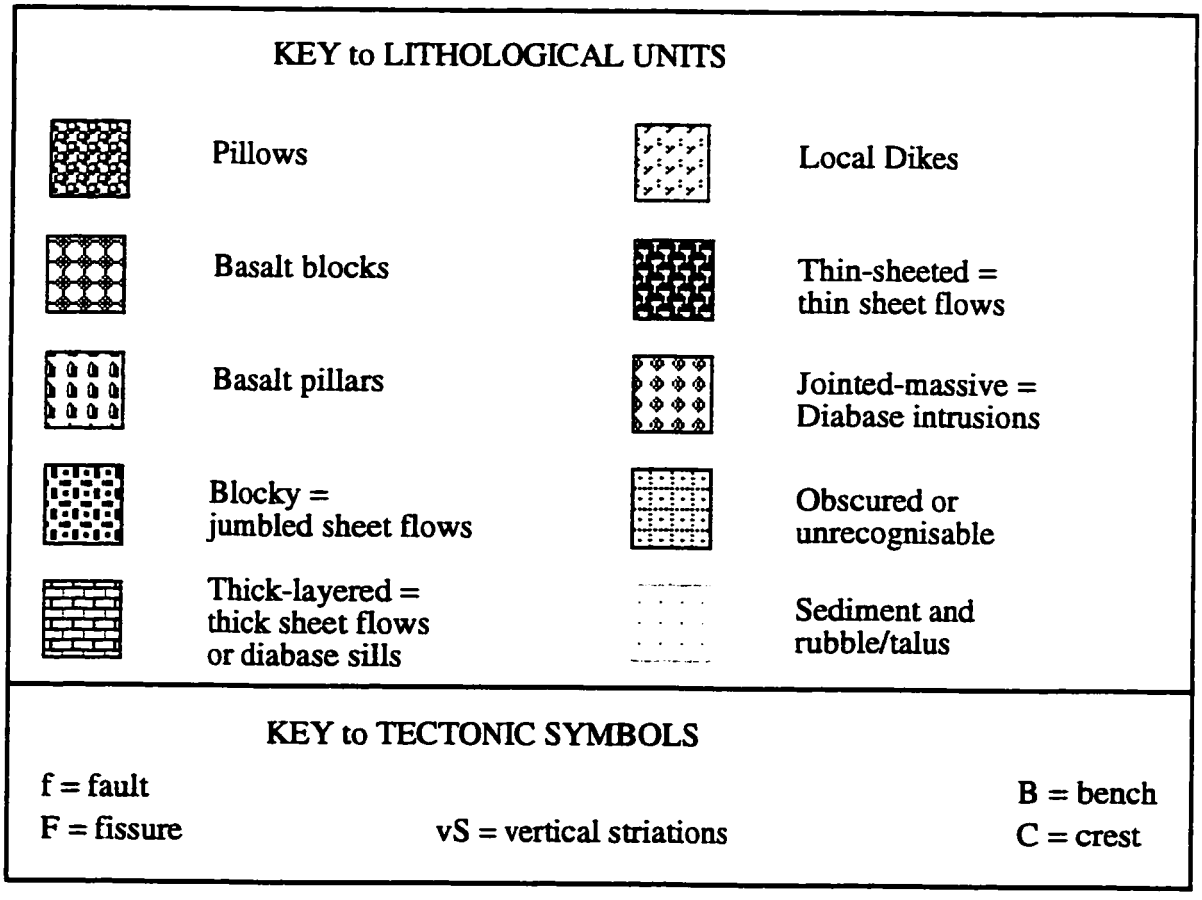

Dom
-ain
BN-06
CH.5
CH.4
E5
E7
E8
E9
-N
E9
-S
2400
2600
2800
3000
3200
Stage IIc
(i) jumbled sheet flows -> pillow flows
Stage IIb
(i) jumbled sheet flows -> pillow flows
(ii) dikes, spires
Stage IIa
(i) thick sheet flows -> thin sheet flows
(ii) thick sheet flows -> jumbled sheet flows
(iii) dikes, spires
UPPERMOST ZONE
UPPER INTERMEDIATE ZONE
MIDDLE INTERMEDIATE ZONE
UPPER OUTCROP ZONE
E
10
F3
F5
G4
G5
3400
3600
3800
4000
4200
Stage Ia
(i) thick sheet flows -> thin sheet flows
(ii) dikes
Stage III
(iii) diabase intrusives
Stage Ib
(ii) jumbled sheet flows -> thin sheet flows (e.g. BN-05)
Stage IIa
(iii) thick sheet flows -> thin sheet flows (e.g. BN-02 & BN-05)
(iv) thick sheet flows -> jumbled sheet flows (e.g. BN-03, BN-10 & BN-24)
LOWERMOST ZONE
LOWER INTERMEDIATE ZONE
LOWER OUTCROP ZONE

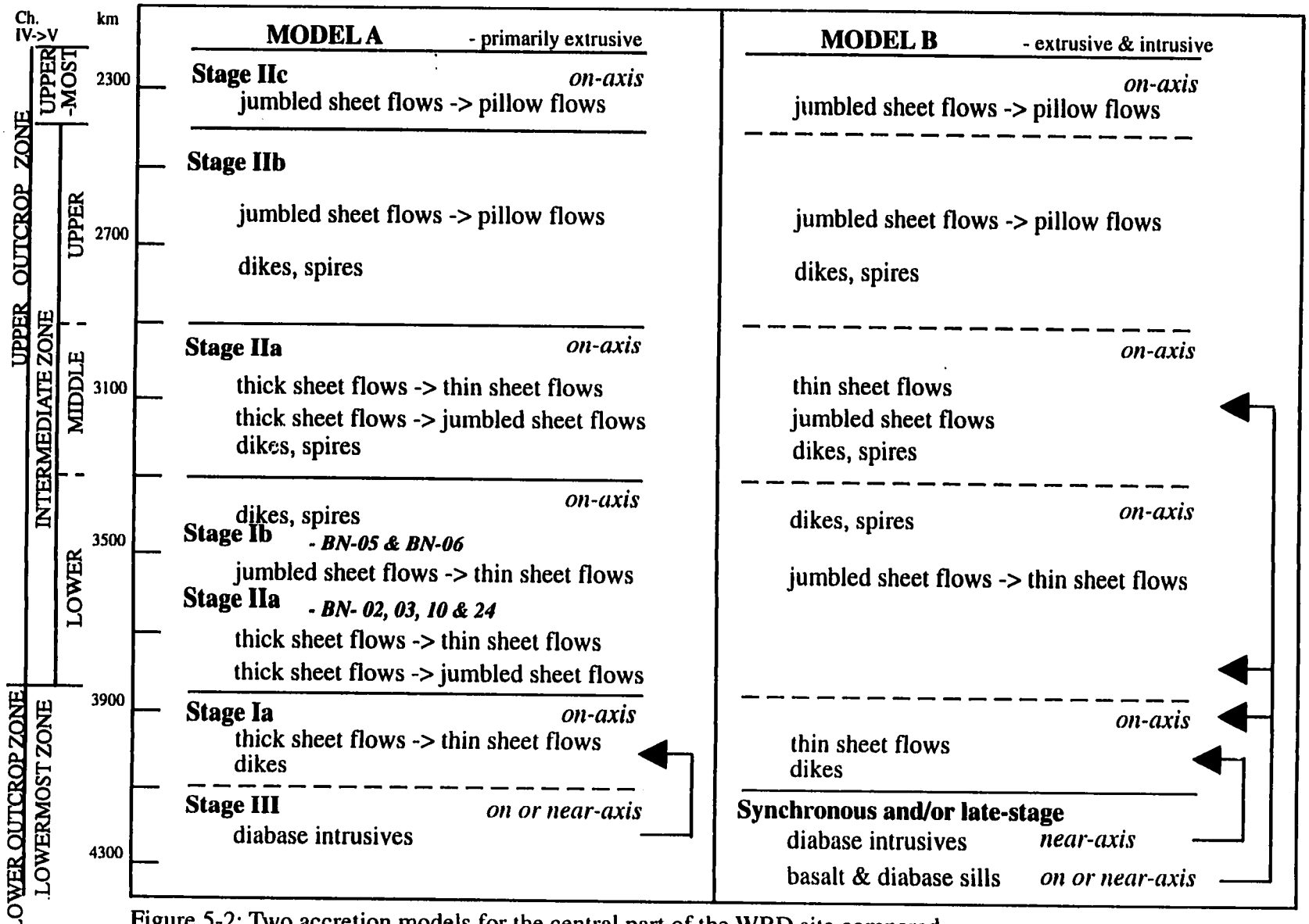

Figure 5-2: Two accretion models for the central part of the WBD site compared.

Plate 5-1: Examples of lava flow morphologies

5-1a: A lobate flow overlies a sheet flow near-axis at 2167 m depth (BN-17) but both lithologies are absent from the N. WBD site. Although the lobate flow could appear similar to the bulbous pillows on the scarp, the latter are always gradational within a pillow lithologic unit in the study site. Likewise, the sheet flow is thicker than the "thin-sheeted lithology" and not as massive as the "thick-layed lithology".

5-1b: In the western part of the N. WBD site (BN-12), lavas exposed on the sedimented plateau (2190 m depth) closely adjacent to the scarp include inflated mounds. They have also been described from the summit of Axial Volcano (Embley et al., 1990) and represent highly fluid flows.

5-1c: Also in the western part of the N. WBD site (BN-12) are fragments of a flow partially covered by sediment on the plateau. The rubble is similar to that produced by pillow lavas as described on other areas of the seafloor (Ballard and Moore, 1977). It is speculated that these block-sized pieces could represent the "broken basalt lithology" identified on the scarp.

5-1d: The "blocky lithology" with cohesive, coarse-sized (~30 cm) blocks on the scarp (BN-03 at 3712 m depth). The orange alteration arises from the "spire structures" with which it can be associated. It is interpreted as a jumbled sheet flow.

5-1e: The "blocky lithology" with cohesive, fine-sized (~15 cm) blocks on the scarp (BN-04 at 2532 m depth). It is also interpreted as a jumbled sheet flow but with smaller blocks.

5-1f: The "thick-layered lithology" is identified by its massive nature and distinct layers that tend to be >0.5 m thick as can still be seen in the background (BN-01 at 3036 m depth). The smoothed, striated appearance is indicative of a tectonized face that is a fault plane. Fissures, such as here, could contribute to the shearing off of slabs such as are observed out-of-place on the scarp.

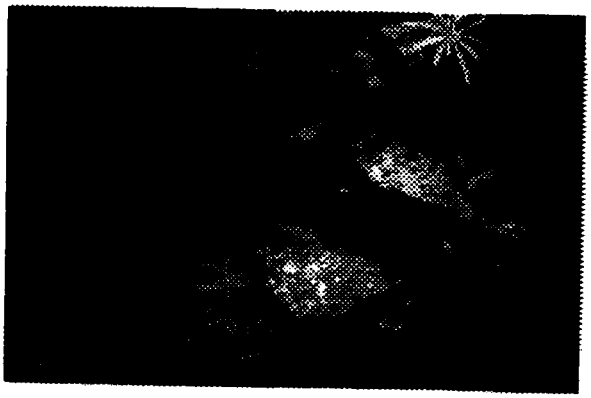

Plate 5-1a

Plate 5-1b

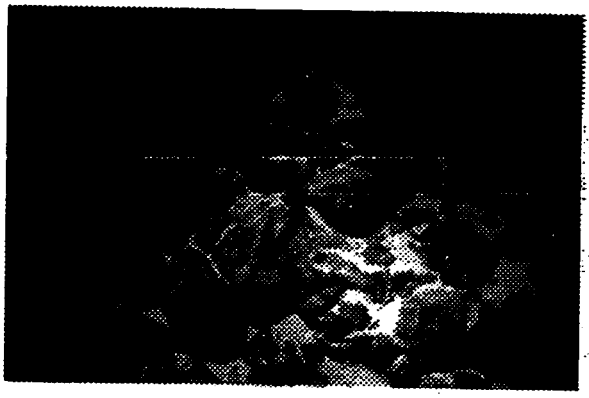

Plate 5-1c

Plate 5-1d

Plate 5-1e

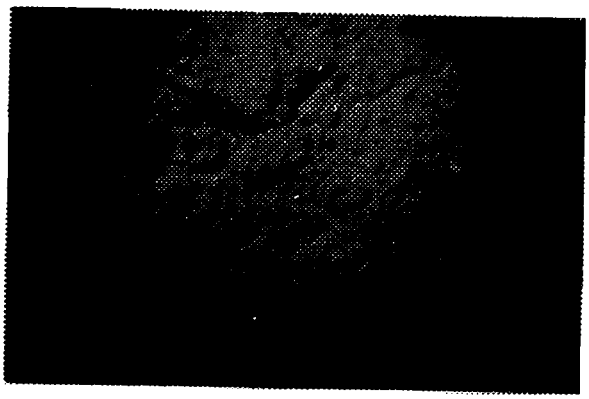

Plate 5-1f

Plate 5-1: Examples of lava morphologies

Plate 5-2: Examples of lava flow morphologies and alteration features

5-2a: A more typical example of "thick-layered" lithologic units with two intervening "thin-sheeted" flows (BN-03 at 3932 m depth). The latter is interpreted as a thin sheet flow. The former appears here to be a thick sheet flow but in other places, their contacts are more ambigous and they could be sills.

5-2b: The "jointed-massive lithology is recognised by its massive nature even though these outcrops are generally obscured by sediment (BN-05 at 3250 m depth). The complete layer is not captured in this frame and they can be up to 20 m thick. They are interpreted as diabase intrusives which create a distinct Lower Outcrop Zone.

5-2c: An unusual local exposure with a series of 5-6, parallel dykes that are <1 m wide and with N270/45N orientations (BN-01 at 2927 m depth).

5-2d: A spire structure, representing a tapering rock column in the cliff face (BN-02), is interpreted as a fossil lava pillar.

5-2e: The original features of the lava morphologies can become obscured by superimposed tectonic (Plate 5-1f) or alteration effects. Here (BN-23 at 4084 m depth), the rock is brecciated and completely altered forming a white scar on the cliff face. These processes add to the mass wasting of the steep scarp. See Appendix B - legend (b).

5-2f: Other characteristics described for each lithologic unit include veins. Here (BN-05 at 3865 m depth), a dense net of white veins mark the vicinity of the contact between an underlying "thick-layered" lithologic unit and overlying N120/70N oriented dykes. See Appendix B - legend (a).

Plate 5-2a

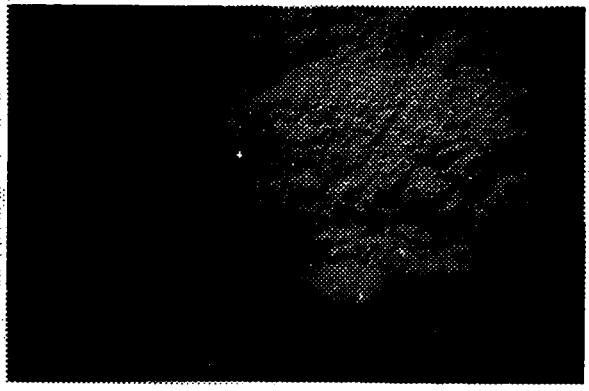

Plate 5-2b

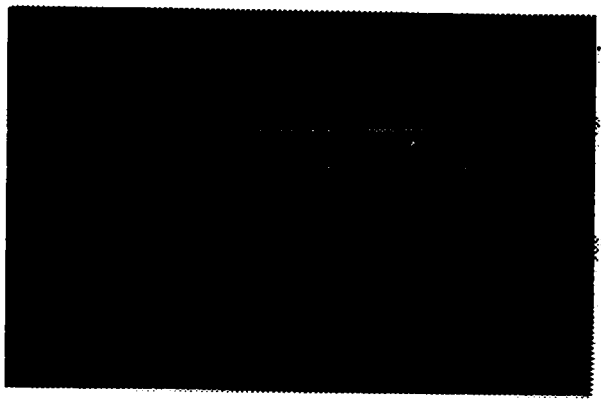

Plate 5-2c

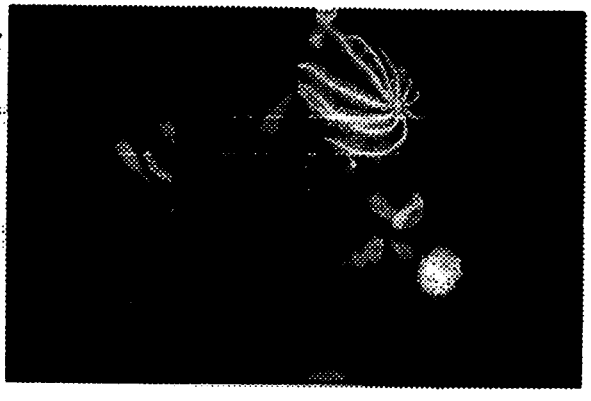

Plate 5-2d

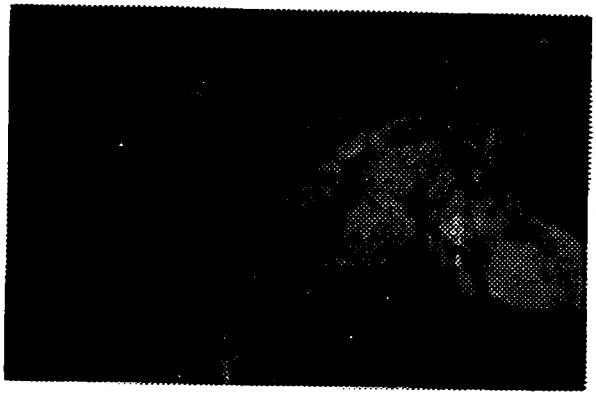

Plate 5-2e

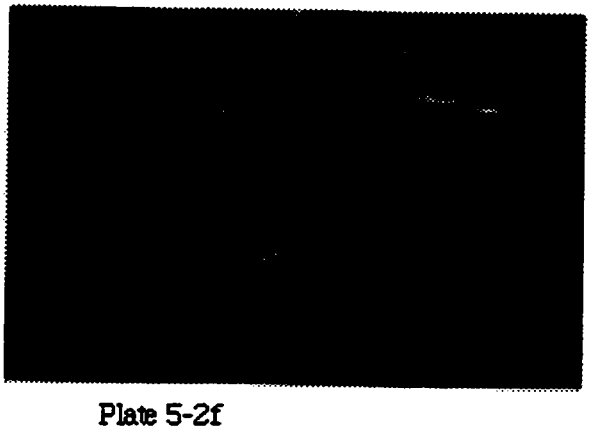

Plate 5-2f

Plate 5-2: Examples of lava morphologies (continued) and alteration features

CHAPTER VI: GEOLOGY - PART 3

6.1 Introduction

The axial high at the medium spreading, Southern Juan de Fuca Ridge (S. JdFR) is similar to the broad elevated topography at fast spreading ridges (Scheirer and Macdonald, 1993) that is thought to be associated with a high magma supply rate and steady-state conditions. Consequently, a relatively stratiform volcanic sequence, as observed in ophiolite complexes (Alabaster et al, 1982), would be predicted in which a relatively continuous, thick layered sequence of extrusives should overlie sheeted dikes. Recent results for the East Pacific Rise (EPR), however, indicate that even magma chambers can be non-steady state at a 0.2-0.5 m.y. time-scale (Batiza et al (1996) and that the upper crust is structurally complex due to possible tectonic rotation (Hurst et al., 1994) resulting from intermittent axial collapse (Haymon et al., 1993).

This study investigates the internal structure of the upper crust along the north scarp of the West Blanco depression (WBD) that was accreted at the southern end of the Cleft Segment. The relatively unobscured exposure in an ~2 km thick section and over a span of ~0.5 m.a. has permitted extensive examination both indirectly from Deep Tow sonar imaging (Delaney et al., 1987) and directly from *Nautile* dives (Juteau et al., 1995). Chapter IV presented a broad overview of the site geology and highlighted the upper and lower outcrop zonation. This chapter describes the WBD scarp and the adjoining Juan de Fuca plateau in some detail and documents more subtle patterns of crustal organization and variation. These include a collage of discrete "domains" and lateral changes by "sector". Here, hypotheses on their potential roles in crustal assembly or indications of crustal evolution are evaluated.

6.2 Sectors on the Juan de Fuca plateau and the WBD scarp

6.2.1 Results

Abyssal hills are considered here to reflect divisions between specific periods during accretion since they are formed through some regular combination of tectonic and/or volcanic processes near the ridge axis (Goff, 1991 and references therein). On the Juan de Fuca plate, GLORIA imagery (EEZ Scan 84 Scientific Staff, 1986) shows that the abyssal hill structures become increasingly subdued in relief approaching the WBD scarp (Figure 4-9a). In general, the abyssal hill fabric fades approximately 4.7 km to the north where the plateau shallows (Figure 3-7). Nonetheless, it is assumed that all the major abyssal hill slopes of 30°-40° can be extrapolated linearly to the cliff edge on bathymetric maps (Figures 6-1 a-b) given that the interest is in the relative variation between these areas rather than in defining their limits.

On the plateau close to the scarp edge, the outcrop differs in extent, form and structural characteristics as evident from the Deep Tow sonar imagery (Figure 4-3a). Based on such morphologic differences, the outcrop can also be divided into discrete provinces that are interpreted here as recording changes in magmatism and faulting. This interpretation is supported by direct observations of variations in lava morphology and structural features (Figure 6-2).

On the scarp, these provinces correspond to five areas of upper outcrop zone exposure separated by scree, as highlighted on the down-looking sonar mosaic (Figure 4-3b). Those in the western and eastern parts of the site also clearly differ in relief.

These two forms of lateral subdivision can be compared by tracing the abyssal hills and boundaries of the outcrop provinces in the study site on a slope image map (Dauteuil, 1995 - Figure 1-5). Figure 6-3 shows that they coincide closely with the exception of the West/Central-West divide where the limited sonar imagery does not permit a more precise outline. These five, north-south oriented sectors have been labelled West (W), Central-West (CW), Central (C), Central-East (CE), and East (E). The sectors have widths of 3.9 km, 1.8 km, 3.3 km, 3.3 km and 3.6 km respectively as measured on the Sea Beam map (Figure 6-1a). In the subsequent sections as well as Figures 6-2 and 6-5, the main features of each sector are highlighted from the available data.

a. The West (W) sector

The West (W) sector extends from ~31.2 km to ~35.1 km off-axis and encompasses 1.1 Ma to 1.2 Ma crust. The western boundary is marked in SeaMARC II imagery (Figure 2-4) by the appearance of a penetrative abyssal hill fabric that is continuous to the plateau edge. The plateau shallows in depth from 2300 m in the west to a <2200 m peak in the east (Figure 6-1a) which constitutes the youngest part of the broad high within the study site that is characterized by the presence of sheet flows (Figure 6-2).

The scarp in Sector W undulates as indicated by dark lineaments in SeaMARC II imagery (Figure 2-4), and prominent spurs or protruding points apparent on the Sea Beam (Figure 6-1b) and slope image (Figure 6-3) maps. Only the upper basaltic zone is imaged on the down-looking sonar mosaic (Figure 4-3b). It has a very high acoustic backscatter intensity that is indicative of the least steeply sloping cliff face (~30-40°) on average (Figure 6-3). The top part of this outcrop zone is dominated by volcaniclastic breccias (BT-8) with lesser crystalline basalts (Table A-1).

b. The Central-West (CW) sector

The Central-West (CW) sector, extending from ~35.1 km to ~36.9 km off-axis, represents 1.2 Ma to 1.3 Ma crust. The sector is comprised of the middle <2200 m peak on the plateau high (Figure 6-1a) with a minor peak to the east. The plateau is covered by expansive outcrop even in the valley that lies immediately east of the W/CW boundary (Figure 6-4). Jumbled sheet flows (Figure 6-2) dominate the two peaks and take the form of discrete domes with bulbous pillows interspersed in the valley between them.

The scarp here is generally linear on a WNW- (~126°) trending face (Figure 6-1b). Some outcrop remains in the upper outcrop zone with a tone and texture similar to that of the C sector (Figure 4-3). The boundary between the CW and C sectors is intensely tectonized as indicated by the veined, sheared and fractured basalts recovered (BT-7 - Table A-1). This has contributed to the development of sediment and talus that largely obscures the outcrop (Figure B-11). The exposure remaining is formed by the massive, thick sheets/sills (e.g. domains U1-U3 in Figure B-11) and scarp-parallel dikes in the lower part of the zone (Table 4-1b). The rocks are mainly glassy- to medium-grained basalts that are aphyric to highly phyric with plagioclase-clinopyroxene (plag-cpx), plagioclase (plag) or plagioclase-clinopyroxene-olivine (plag-cpx-ol) phenocrysts (Figure 7-8). There are also some basalt breccias. The cliff below is covered with rubble (domains V1-V5 in Figure B-11) composed of breccias and glassy- to fine-grained basalts that are aphyric to moderately phyric with the same phenocryst assemblages as in the upper outcrop zone.

c. The Central (C) sector

The Central (C) sector, which extends from ~36.9 km to ~40.3 km off-axis, encompasses 1.3 Ma to 1.4 Ma crust. The sector is constituted by the oldest of the <2200 m peaks within the plateau high (Figure 6-1a). The plateau adjacent to the scarp is characterized by broad expanses of outcrop with intervening sediment (Figure 6-5). Mounds range in diameter from 10 m to 80 m (Figure 4-3 - grid squares h-6 and h-7) while other exposures can extend up to 340 m (Figure 4-3 - grid square i-5).

On the scarp, two promontories - a major central one and a minor one to the west - stand out in relief (Figure 6-1b) and appear to be of tectonic origin. The former has a NW-trending face which slopes on average at 40-50° (Figure 6-3) and has horizontal and oblique striations that indicate strike-slip and dip-slip faulting (Figure 4-5a). Its E-W-trending face slopes on average at 30-40° (Figure 6-3). The upper and lower outcrop zones are present on both faces although scree obscures the contact between the zones on the NW-face (Figure 4-3 - grid square f-4) and most of the upper zone on the E-W-face (grid square f-6).

d. The Central-East (CE) sector

The Central-East (CE) sector extends from ~40.3 km to ~43.6 km off-axis and represents 1.4 Ma to 1.5 Ma crust. It is constituted by two, <2300 m highs that are separated by a broad valley (Figure 6-1a) as the plateau depth increases eastward. The plateau here is largely sediment-covered with emergent traces of an elongate outcrop form (Figure 6-5 - grid squares h-8&9 and g-8&9). Such exposure is confirmed by the presence of a blocky lithomorphology with some pillows near the scarp edge (Figure B-6).

The scarp is formed by three promontories (Figure 6-1b) with the western two jutting out in a rectangular shape and the eastern one being quite narrow (Figure 6-1a).

The exposure is characterized by a uniformly low backscatter intensity on the down-looking sonar mosaic (Figure 4-3b) that is indicative of the steepest slopes (>50°) amongst the sectors (Figure 6-3). The upper zone is present throughout the sector, although just partially on the eastern protruding point, whereas the lower outcrop zone is retained only in the western protrusion (Figure 4-3a). The latter has mostly been removed in an unusual double-headed mass failure event by a coherent, ~2300-2600 m wide and 3050 m long landslide (Whipple and Naidoo, 1991) that is detailed further in Section 6.3.1. The basaltic rock types retrieved in this sector are characteristic of what was once clearly the upper outcrop zone (BT-3&11 - Table A-1; Figures B-7&8).

e. The East (E) sector

The East (E) sector, extending from ~43.6 km to ~47.2 km off-axis, encompasses 1.5 Ma to 1.6 Ma crust. The plateau near the scarp edge, is constituted by a <2300 m high (Figure 6-1a) that is characterized on the sonar imagery by a series of four elongate outcrop forms (Figure 6-6) with minor outcrop traces amidst the intervening sediment (Figure 4-3 - grid squares h-10,11&12 and g-11&12). The outcrop exposures are up to about 100 m in width and 750 m in length, and are consistently northerly trending (at 9°, 2°, 356° and 359°). Their distance of separation decreases progressively from west to east (1060 m, 750 m and 445 m).

On the scarp (Figure 4-3b - grid squares d-11&12), there is another double-headed landslide, similar to that in Sector CE. One main promontory (Figure 6-1b) slopes at >40-50° (Figure 6-3) and exposes outcrop of the upper outcrop zone (Figure 6-7). The rest of the cliff is covered by sediment and rubble (domain Q3 - Figure B-8) except for brief outcrop exposure of the blocky lithomorphology (domain Q6 - Figure B-8). The rocks sampled are medium- to coarse-grained basalts that are aphyric to moderately, plag-cpx-

ol phyric (Figure 7-8). In addition, glassy basalt dominates dredges of this zone (BT-3 and BT-4 - Table A-1). The lower outcrop zone remains in a small, 40-50° sloping area between the two landslides that is composed partly of medium-grained diabase (domain Q7 - Figure B-8). The remainder of the sector has a <30° slope in the typical, triangular shape of a landslide (Figure 6-3).

The landslide is approximately 6500 m wide and 3300 m long, which is thrice the width of that in the CE sector (Figure 1-5). The 20-30° sloping minor scarp (Figure 4-3 - grid square d-12) at the head suggests that some outcrop is still present. The sunken 10-20° slopes of the landslide (Figure 6-3), that are in shadow on the sonar imagery (Figure 4-3 - grid squares b-12 and b/c-10), outline the rest of the depletion area. Photographs (line 1-1B in Figure 4-2) and observations (Figures B-8 and B-9) show that these areas are occupied by sediment with rare rubble. The one sample retrieved here (Figure B-9) is a phyric, crystalline basalt with a slickenside exterior and a pervasively fractured interior. The 20-30° sloping depositional area of the slide (Figure 6-3) has a comparatively smooth textural pattern on the sonar imagery (Figure 4-3) that is indicative of a sediment mantle. The only outcrop present is on structural lineaments (Figure 4-3 - grid square a-11 and b-11) which expose thin sheet flows and thick sheet flows/sills composed of medium-grained, moderately plag-ol phyric basalt (Figures B-8 and B-9). These lithologic types are present in the lower part of the basaltic zone within the other sectors.

6.2.2 Interpretation

In summary, sectors in the study site have been delineated on the basis of variations in abyssal hill structure, plateau outcrop morphology and expression on the scarp and further defined by differences in lithology, structural and compositional

characteristics of the exposed outcrop. The review here emphasizes the changes in the magmatic and tectonic construction of these sectors which are interpreted as reflecting the distinct differences in their accretion over this 0.5 m.y. period.

Overall, the sectors can be divided into two groups based on the plateau outcrop (Figure 6-7): Sectors W, CW and C from 1.1 Ma to 1.4 Ma comprise the broad high that is covered with expansive outcrop; and Sectors CE and E from 1.4 Ma to 1.6 Ma which constitute more typical depths that are predominantly sediment covered with periodic outcrops. This grouping corresponds to the 1.1-1.4 Ma and 1.4-1.8 Ma sub-divisions each comprised of one volcanic cone in a series identified on the adjoining Juan de Fuca plateau in Chapter IV.

The younger group of sectors are distinguishable from each other on the plateau by the prominence of thin sheet flows and massive flows in sector W, jumbled sheet flows in Sector CW, and lobate flows and mounds in Sector C (Figure 6-2). On the scarp, Sectors W and CW are evidently intensely tectonized. Sector W is characterized by the largest proportion of basalt breccia in any dredge haul (Table A-1) while Sector CW has the largest proportion of veined basalts dredged (Table A-1) and poor exposure (Figure B-13). Sectors W and CW are also both cut by at least 11-13 faults of <17 m throw. In Sector W, the ~N-trending faults are equally W- and E-dipping in number on the plateau whereas in Sector CW, the ~NNE-trending faults are E-dipping on the plateau (Figures 6-2 and 4-5a) but only west-dipping faults are expressed in the upper outcrop zone (Figure 4-5a). Sector C is distinguished by the highest proportion of hyaloclastite material that progressively increased in abundance from Sector E (Table A-1) but was not dredged again. This sector has only three major scarps penetrating the surface and upper outcrop zone with total fault throws of 70 m on the two that are E-facing and 110 m on the W-facing one (Figure 4-5a).

The older group of sectors are distinguished on the plateau by their comparatively greater extent of sediment cover to outcrop exposure (Figure 6-7). The outcrop is only barely emergent from beneath the sediment in Sector CE whereas elongate forms are visible in Sector E. These ~N-trending structures decrease in frequency and become less prominent prior to the formation of Sector CE. It is unknown whether this effect is tectonic and/or magmatic related. The upper outcrop zone of Sector E is highlighted by the highest proportion of glassy basalts that were otherwise dredged only in Sector CE (Table A-1).

The lower outcrop zone extends from Sector C to Sector E according to the diabase sampled (Figure 7-2) forming a sill/intrusive complex (Chapter V) that is about 8.5 km long and with an exposed thickness of <1 km (Figure 6-7). Its presence in only three of the five sectors suggests that the diabasic complex was injected *en masse* rather than being intruded as a consistent feature of accretion at the axis. Limits on the timing of formation are inferred from the metadiabase and metabasalt that are present respectively on the west (domain G8 - Figure 6-7) and east (domain Q7 - Figure 6-7) flanks of the landslide in Sector CE and which appear to have been altered by this mass movement (Figures B-10 and B-8). This implies that the diabasic complex had to have been produced prior to the landslide event but post-dated crustal growth of the upper outcrop zone in the C sector.

6.3 Domains on the WBD scarp

6.3.1 Results

Domains within the WBD study site (Figure 6-7) refer to discrete areas of visually similar backscatter intensity and image texture on the sonar mosaics (Figure 4-3). An overlay of the dive track lines (Figure 6-8a) and the Sea Beam bathymetric map (Figure 6-8b) on the interpreted sonar domains indicates that the boundaries between the domains generally correspond to concavities in the face that form corridors for the course of a dive (grid square e-10 in Figure 6-8a: BN-01 between P1 and Q2 or BN-10 between P1 and K7, or K10 and K7) as well as natural conduits for debris (Figure 6-7 - between D2 and D4 in grid square e-5 or between G4 and G6 in grid square d-7).

These overlays are further used to determine the depth interval over which a domain was traversed during a dive. In this way, the lithological profiles in Figures B1-13 have been subdivided according to domain. The profiles indicate that many of the domain boundaries occur at either major changes in degree of outcrop exposure (e.g. between D4 and B6 in Figure B-3) or in lava morphology (e.g. between D1-N and B6 in Figure B-3), or correspond to breaks in slope as for example occurs in six cases on Figure B-13 where 11 domains are represented. Slope here is determined from the detailed bathymetric profiles of *Nautile* up the cliff and displayed for comparison in the penultimate column of Figures B1-13.

This method of identifying domains in Figure 6-7 can be illustrated using the landslide in Sector CE as a simple example. Mapping from the sonar imagery (Figure 4-3) demonstrates that the landslide is comprised of two domains of depletion (L1/Q4 and L4), on either side of the main scarps, and three domains of accumulation (L5, 6 and 7). Observations indicate that the 20-30° sloping minor scarp (Figure 6-3) at the head is formed by altered and brecciated massive outcrop that grades to talus and to sediment with rubble (Figures B-1 and B-10). Domain L4 (Figure 6-7) is that area in shadow on the sonar imagery (Figure 4-3a) and represents the sunken 10-20° slope that is becoming

infilled with sediment (Figure B-10). Domain L5 (Figure 6-7) corresponds to the initial, 20-30° sloping area (Figure 6-3) overlying the rupture surface which is rotated slightly towards the cliff (Figure 4-3a). It shows outcrop exposures between which are distributary rills (grid squares d-8 and c-9) that are filled with rubble in photographs (Figure 4-2 - line 3-9). Glassy and crystalline basalts were recovered (BT-3 - Table A-1) from here together with a small amount of veined basalt and hyaloclastite. Domain L6 (Figure 6-7) occupies the 30-40° sloping (Figure 6-3), depositional part of the main body which exposes brecciated outcrop with basal talus (Figure B-7). The rocks in this relict upper zone outcrop are glassy and crystalline basalts that are altered, veined and cracked (BT-11 in Table A-1 and Figure B-7) which implies a displacement of at least about 2400 m. Domain L7 (Figure 6-7), from which glassy basalt (Figure B-8) was sampled, denotes the foot of the landslide which is covered by talus on the 30° sloping area and sediment with rubble on the 20° slope towards the toe (Figures 6-3 and B-7).

Other domains outlined within the upper and lower outcrop zones are shown in Figure 6-7. They are irregular in shape, generally less than a kilometer in size, and overall suggest a collage of crustal blocks. Examples of the differences within the cliff exposure that are captured by the sonar imagery are given in Figures 6-9 and 6-10 and could originate from lithological and/or structural variations.

In documenting the complete nature of these domains, Appendix C lists the sequence of lava morphologies for every domain from the base upward. The accuracy of the observations have been checked where at least two dives crossed a domain over the same depth interval as in domains B1, D1, E9-S, E10, F3, G4, G8, L2, L3, Z2 and Z3. In these cases, there is general consistency in the sets of dive descriptions. The only exception is domain E9-S, the base of which is marked by a slope break in Figure B-5. In both dives (BN-05 and BN-06), the domain is comprised predominantly of the thickl

sheet flows/sills. However in Figure B-6, the exposure is extensively tectonized which indicates the extent of variation over 300 m. In addition, brief intervals of jumbled and thin sheet flows that are present in Figure B-5, are not evident in Figure B-6. Their absence might be due to the effects of tectonism. Alternately, it could reflect the error inherent in this subjective identification especially for such horizons that are less than 5 m thick.

6.3.2 Interpretation

The domains in the upper and lower outcrop zones are not exclusively basaltic and diabasic respectively (Figure 7-2). In the upper outcrop zone, diabase occurs locally in the upper part (domains X1 or K7) and more commonly toward the basal part (domains Y2, X4, D1, F3 and L2) where it is retrieved from dikes (domains K7 and Y2) and thick sheet flows/sills (domain K7) (Figures B1 to B13). In the lower outcrop zone, basalt occurs at both the western (domains Z2, D3 and D5) and eastern (domain Q7) ends (Figure 7-2) where it is sampled from thick sheet flows/sills (domains Z2 and D3) and thin sheet flows (domain Q7) (Figures B-1 to B-13). Hence, the creation of domains is apparently not linked to the accretion of these outcrop zones.

The individual domains are rarely constituted by a single lava morphology. The few examples are domains K4 which is composed of jumbled sheet flows, and domains Q2 and V1 which are composed of thick sheet flows/sills (Figures B1 to B13). However, even these examples could be the result of only partial observation (K4 and Q2) or obscured exposure (V1). Therefore, neither does the formation of domains necessarily follow a period with the same style of eruptions.

Overall, there is a lack of lateral continuity in the lithologic units between adjacent domains. One of the few similarities is the thin sheet flows which dominate both the western part of F3 and the upper part of E4 (Figures B-2 and B-12). This would imply that domains do not always encompass the full extent of lava flows. However, in domains Z2 and D4 (Figures B-3 and B-13), the jointed-massive unit is overlain by sheet flows/sills but the latter is composed of a medium-grained, sparsely plagioclase phyric basalt in Z2 and a fine-grained, aphyric diabase in D4 (Figure 7-2). Consequently, despite the morphologic similarity, these are still likely to have been separate flows. Thus, domains seem to be largely distinct entities that re-inforce volcanic constructions. However, this conclusion is limited by the number of domains available for comparison which is restricted by the closeness of the spaced profiles.

An alternative scenario can be proposed using the distinctive basaltic pillars. In domain E7, they could be correlated with others 50 m below in domain E8 or 150 m below in domain E9-N (Figures 6-7 and B-6). In this case, the production of domains would be structurally-related and require large rates of subsidence or slip on faults.

6.4 Discussion

The basement section exposed along the north WBD scarp shows evidence of two modes of organization defined here as domains and sectors. The ~1 km wide domains appear to derive from the assembly/disassembly process during the accretion of discrete, ~3 km wide sectors. The consistency of this pattern suggests that it reflects the normal process by which the upper oceanic crust is accreted at the S. JdFR.

6.4.1 The sectors

The five sectors along the WBD scarp range in width from 1.8 km to 3.9 km and are on average 3.2±0.8 km wide which is equivalent to a ~0.11 Ma spacing based on a 2.9 mm/yr half spreading rate.

By comparison, the axial graben of the Cleft Segment is presently between 1-3 km wide (Embley et al., 1991). In this scenario, the ~1.5 km thickness of volcanics should have been extruded in about 17,000-52,000 years. This is 2-3 times the minimum duration estimated for Hole 504B in which the 780 m thick volcanics are calculated to have been built up in 15,000 - 20,000 years (Pezard et al., 1992).

Furthermore, if symmetrical spreading is assumed (Hey and Wilson, 1982), a sector that resulted purely from volcanic construction ought to be between 0.5-1.5 km wide on the north WBD scarp. By contrast, the sectors formed between 1.2 Ma and 1.7 Ma ago are between 2-6 times this width. If tectonism were to account for the remaining 0.6-0.9 Ma time span, its effects would dominate the WBD section which is not the case. Hence, these sectors must have a different origin.

At fast and intermediate spreading ridges (Carbotte and Macdonald, 1994; Goff et al., 1995; Macdonald et al., 1996), abyssal hill structures vary in average distance respectively from 2.0 km (or 0.04 Ma) to 4.2 km (or 0.15 Ma). The 0.11 Ma sectors at the WBD are of similar wavelength and are therefore more likely related to abyssal hill formation that is superimposed on accretionary processes.

6.4.2 The domains

The crustal collage at the WBD site is similar in size to blocks that have also been inferred at Hess Deep (Hurst et al., 1994). These could have formed in two possible ways: as volcanic constructions that are reinforced as fault-bounded blocks or as solely tectonic blocks that would disrupt lava flows.

According to the latter hypothesis, the WBD domains would result from periodic collapse whenever the axis deflates creating blocks that subside chaotically and are rotated in an unorganized manner as the upper crust founders (Hurst et al., 1994). Even if this cycle did not follow every eruption (Walker, 1988 cf. Haymon et al., 1993), a highly disrupted crust would be predicted with much smaller blocks than the actual size of the domains. However, such wide-scale deformation is absent on the WBD scarp and the domains appear to be preserved as largely intact structures. Furthermore, if rotation is mainly about a subhorizontal ridge-parallel axis as at Hess Deep (Hurst et al., 1994), then there ought to be parts of lithologic sequences that are similar in adjacent domains since flow units change at the tens of metres scale. There are a few examples (e.g. Z2 and D4) in the WBD section but this is not the general case which implies that only some of the boundaries are wholly tectonic related. Hence, a mixed magmatic-tectonic origin is favored.

In either case, subsidence or collapse is proposed to be a key component of the process since it is necessitated by having to build up a ~1.5 km thick section while the axial graben of the Cleft Segment is only 80-100 m deep (Embley et al., 1991).

In one "piston" model, pertaining to inflated axes as described from the fast-spreading EPR (Scheirer and Macdonald, 1993), a cycle begins with dike intrusion leading to volcanic eruption (Haymon et al., 1993). Subsequent magma drainage causes withdrawal of support for the elevated topography (Macdonald and Fox, 1988) and the consequent decrease in pressure leads to collapse at the summit resulting in a caldera (ASC) (Haymon et al., 1991). The cycle is completed with the ASC widening by amagmatic cracking and mass wasting (Haymon et al., 1993).

In alternative "loading" models, caldera subsidence is related to shallow magma intrusion.

Collapse will occur around a shallow, sill-like magma chamber on fractures which are generated as the magma pressure increases during chamber growth (Gudmundsson, 1988). These conditions are fulfilled at fast and intermediate rate spreading centers where magma lenses have been detected (Sinton and Detrick, 1992). At fast spreading rates, the melt lens is tens-hundreds of meters high, <4-6 km wide, and lies at 1.2-2.4 km depth below the seafloor (Detrick et al., 1987) while at intermediate rates, the lens is 1-2.5 km wide and at 3 km depth (Rohr et al., 1988; Collier and Sinha, 1990). Thus, the radius/depth ratio at fast and intermediate rate settings is as high as 2.5 and 0.4 respectively. The former case satisfies the criteria for a ratio >2.5 at which the tensile stress will be greatest at the chamber margins (Gudmundsson, 1988). However, if magma lenses are steady-state features of fast spreading ridges, then the width of the axial graben (e.g. 50-300 m at 9°N-10°N and 250-600 m at 13°N EPR) will always be smaller than the chamber dimension indicating that this mechanism may not apply here. If chambers are quasi-steady-state features however, then their excess pressure on intrusion and expansion into the lower crust would seem to be more likely to generate fractures and faults leading to the development of a graben. For intermediate spreading rate ridges, repeated intrusions could increase the volcano mass causing down-sagging of the infrastructure which would be expressed at the surface in caldera formation (Walker, 1988).

6.5 Conclusions

Chapter VI provides evidence of two other concepts in accretion. Domains with a distinct acoustic textural pattern are visually outlined from the sonar imagery. Based on

the lithologic characteristics of these kilometer-sized, irregular blocks, they are interpreted as volcanic constructions that are reinforced by faulting during punctuated subsidence of the axial valley during accretion. At a larger scale laterally, 5 sectors (labelled W, CW, C, CE and E from west to east) are identified based on the coincidence of changes in abyssal hill fabric, flow morphology imaged at the plateau edge, and acoustic intensity of discrete outcrop exposures in the sonar images. Their spacing indicates that they are likely to have originated during abyssal hill formation rather than being strictly a product of on-axis accretion. The presence of the lower outcrop zone overlaps with a major break at the C/CE boundary which corresponds to the divide between two seamount provinces (Chapter IV).

Figure 6-1a: Sea Beam bathymetric contour map (after Embley and Wilson, 1992) of the central part of the north WBD scarp showing the study area and dredge locations.

On the plateau, parallel lines along the steep slopes of abyssal hills are extended to the scarp edge.

These define five sectors within the study site: West (W), Central-West (CW), Central (C), Central-East (CE) and East (E).

Figure 6-1b: Sea Beam shaded relief map of the same area as in (a). The colour bar gives the depth variation.

The figure to the left shows the original map. It highlights the steep fault scarps that form the abyssal hills and along which the sector boundaries have been traced.

In the figure to the right, the previous map has been annotated with the sector boundaries and labels as in (a).

(a)

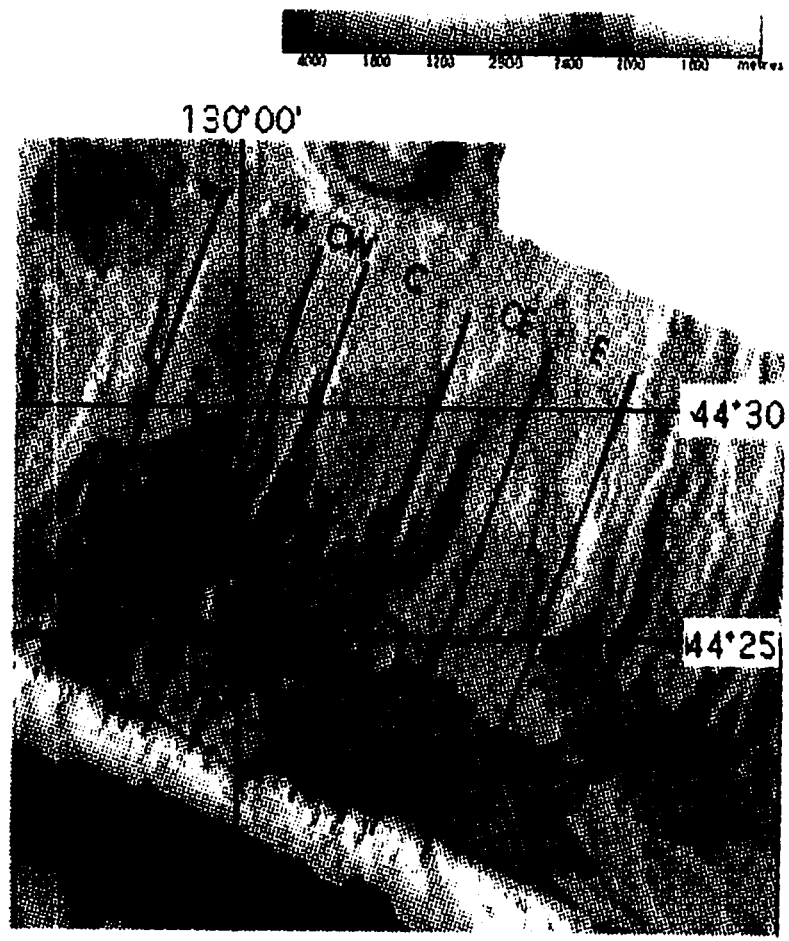

(b)

Figure 6-2: Cross-sectional profile of dive BN-12 across the Juan de Fuca plateau showing the observations of lava flow morphology and structure made from the video and photoraphs of the *Nautile* traverse. The West (W), Central-West (CW) and Central (C) sectors correspond to peaks within the broad plateau high which in general, are covered respectively by sheet flows, jumbled sheet flows, and lobate flows and mounds. A more detailed description is given in the table below.

	Sector W	**Sector CW**	**Sector C**
Lava flow morphology	The easternmost part of the peak shows continuous outcrop exposure on the sonar imagery (Figure 4-3 - grid square j-3). Sheet flows are the dominant flow form found on fault scarps, as mounds, or as individual flows on sediment (Figure 6-2). Massive flows occur in a few (~3) localities and are unique to this sector since they were not observed in the CW and C sectors. The blocky lithologic unit is also present with tube flows and common bulbous pillows.	The top of the smaller peak (Figure 6-2) is covered by approximately 11 lava fields of the blocky lithology that have 180°-210° trending contacts with the intervening sediment. Each summit of the larger peak is covered by the blocky lithology and either bulbous pillows or tube flows on sediment. In total, there are at least 21 of these blocky fields which have roughly N-S oriented contacts with the intervening sediment and about the same number of the 2 other flow fields combined. The southern extent of the outcrop on the plateau (Figure 4-3 - grid square i-3/4) has talus and rubble (Figure 4-2). Based on the contact between the talus and sediment, the blocks appear to be the in-place weathering products along a flow margin rather than randomly distributed tectonic rubble.	From E to W: thin, sheet flow mounds in the middle of the sector -> lobate flows -> lobate flow mounds (Figure 6-2). The 2090 m summit of the peak is capped by fields of the blocky lithology (Figure 6-2). Close to the scarp edge, only small bulbous pillows with rubble occur on the sediment (Appendix B or Map 1 - BN-6).
Faulting	The outcrop is characterized by closely-spaced (~25 m), sinuous faults (Figure 6-8) trending roughly north-south (between N160°-210°). At least thirteen faults are observed across the peak (Figure 6-2) with half of those dipping eastward. Fault throws, measured from the heights of scarps crossed with *Nautile* on the plateau, range between 11-13 m on the east-facing slope, and from 2-7 m further eastward.	The only tectonic features associated with the smaller peak are 2, east-facing faults forming the eastern flank. The faults, which have throws of 14 m and 3 m respectively on the lower and upper scarps, both expose the pillow lithomorphology. The larger peak (Figure 6-2) is cut by about 11, 21°-25° trending east-facing faults with measured fault throws of 1 m to 17 m.	It is the only exposure within the sector to show lineaments spaced on the order of 55 m apart (Figure 4-3 - grid square i-5). These stem from the eastern flank where two east-facing scarps, which both expose the blocky lithology at the base and tube flows approaching the top, are each comprised of three faults (Figure 6-2). The lower (N160-220/60E) and upper (N195-225/45E) scarps have total throws of about 30 m and 40 m respectively. The only west-facing faults are a 10 m high scarp (N195/45W) on the eastern flank between the two main scarps, and an 80-110 m high scarp forming the western flank.

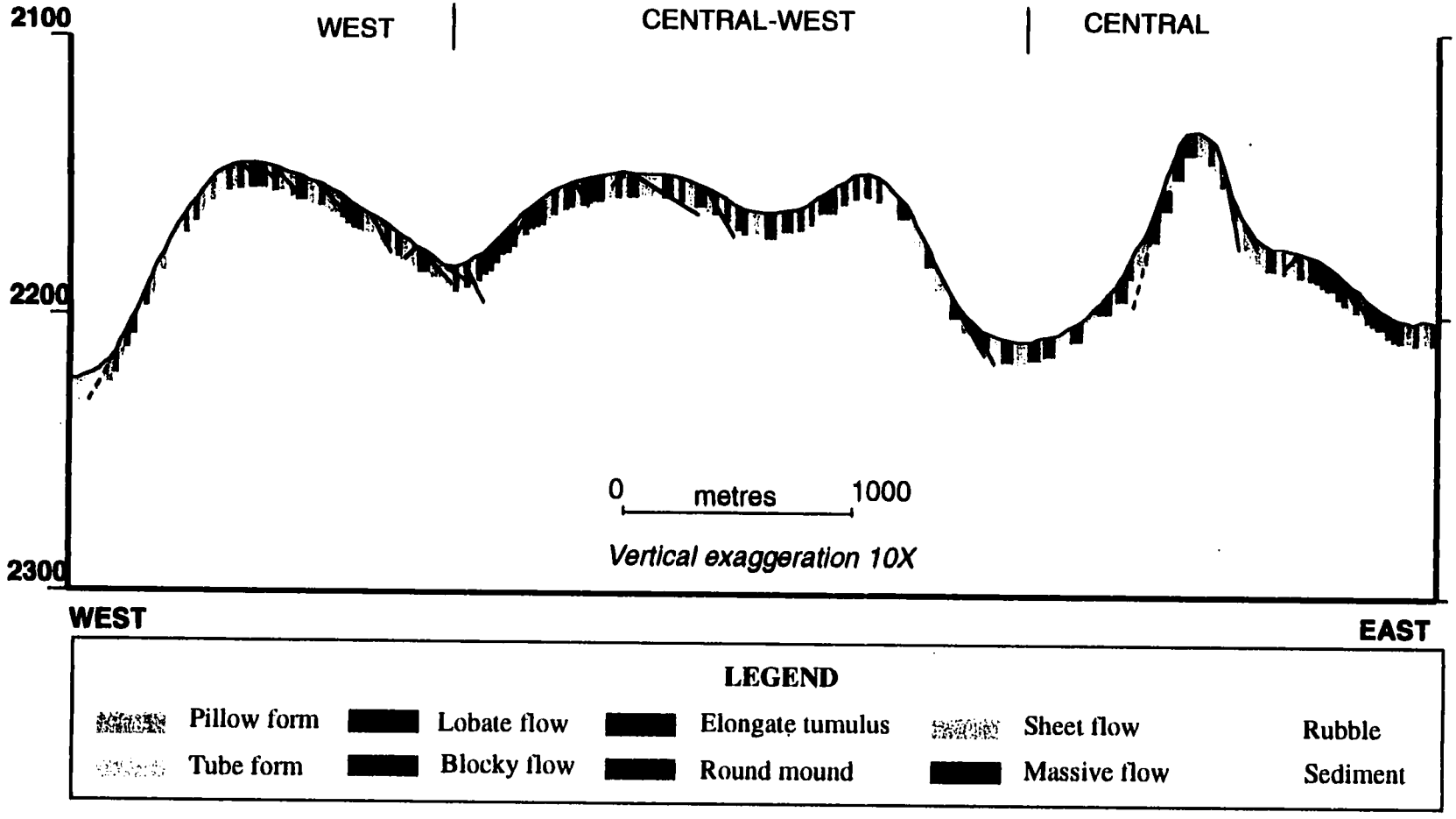
2100
2200
2300
WEST
CENTRAL-WEST
CENTRAL
0 metres 1000
Vertical exaggeration 10X
WEST
EAST
LEGEND
Pillow form
Lobate flow
Elongate tumulus
Sheet flow
Rubble
Tube form
Blocky flow
Round mound
Massive flow
Sediment

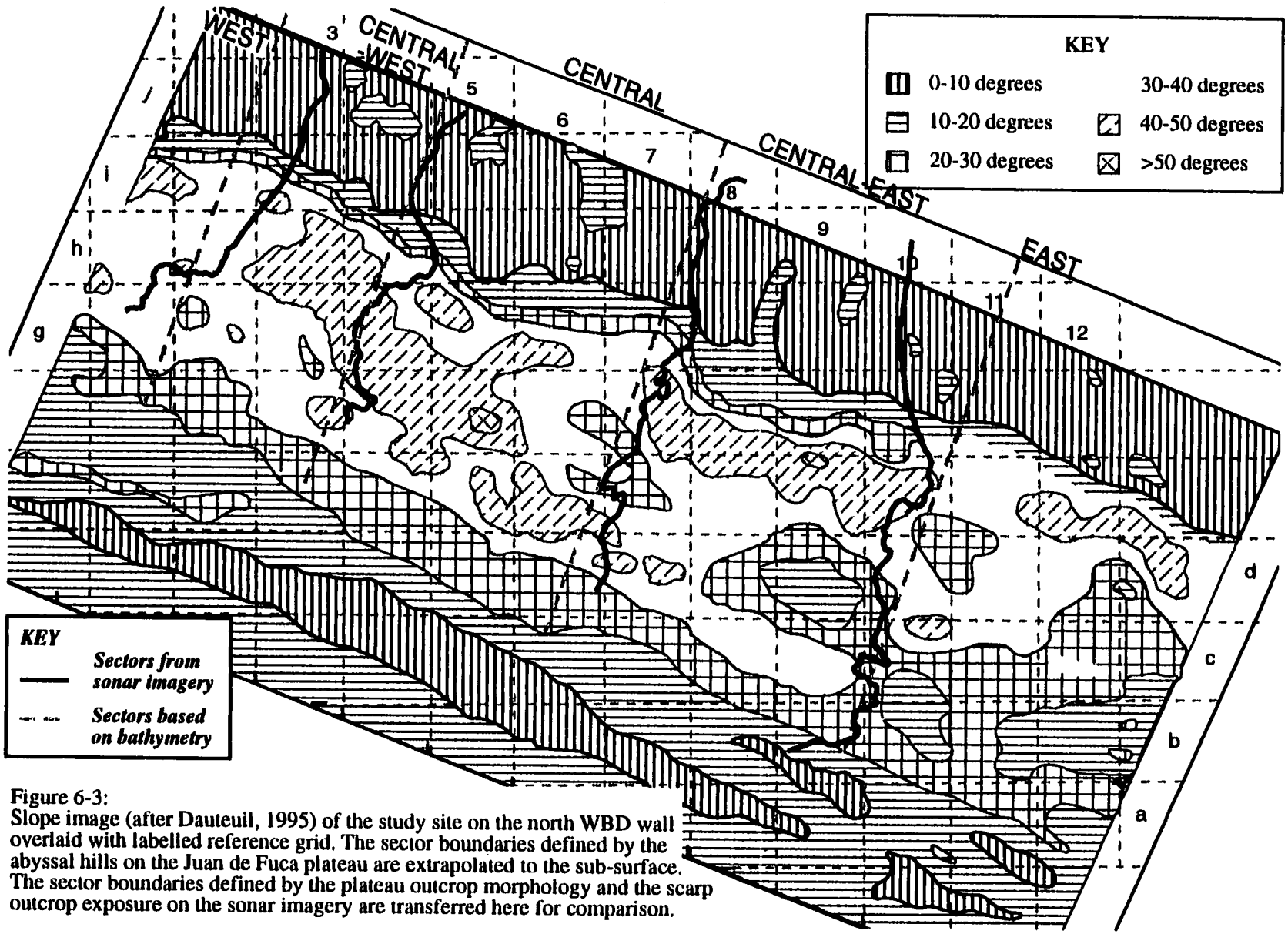

Figure 6-3:
Slope image (after Dauteuil, 1995) of the study site on the north WBD wall overlaid with labelled reference grid. The sector boundaries defined by the abyssal hills on the Juan de Fuca plateau are extrapolated to the sub-surface. The sector boundaries defined by the plateau outcrop morphology and the scarp outcrop exposure on the sonar imagery are transferred here for comparison.

Figure 6-4 : Normal Deep Tow sonar imagery of the Juan de Fuca plateau showing the difference between the outcrop exposed in the West (W) and Central-West (CW) sectors.

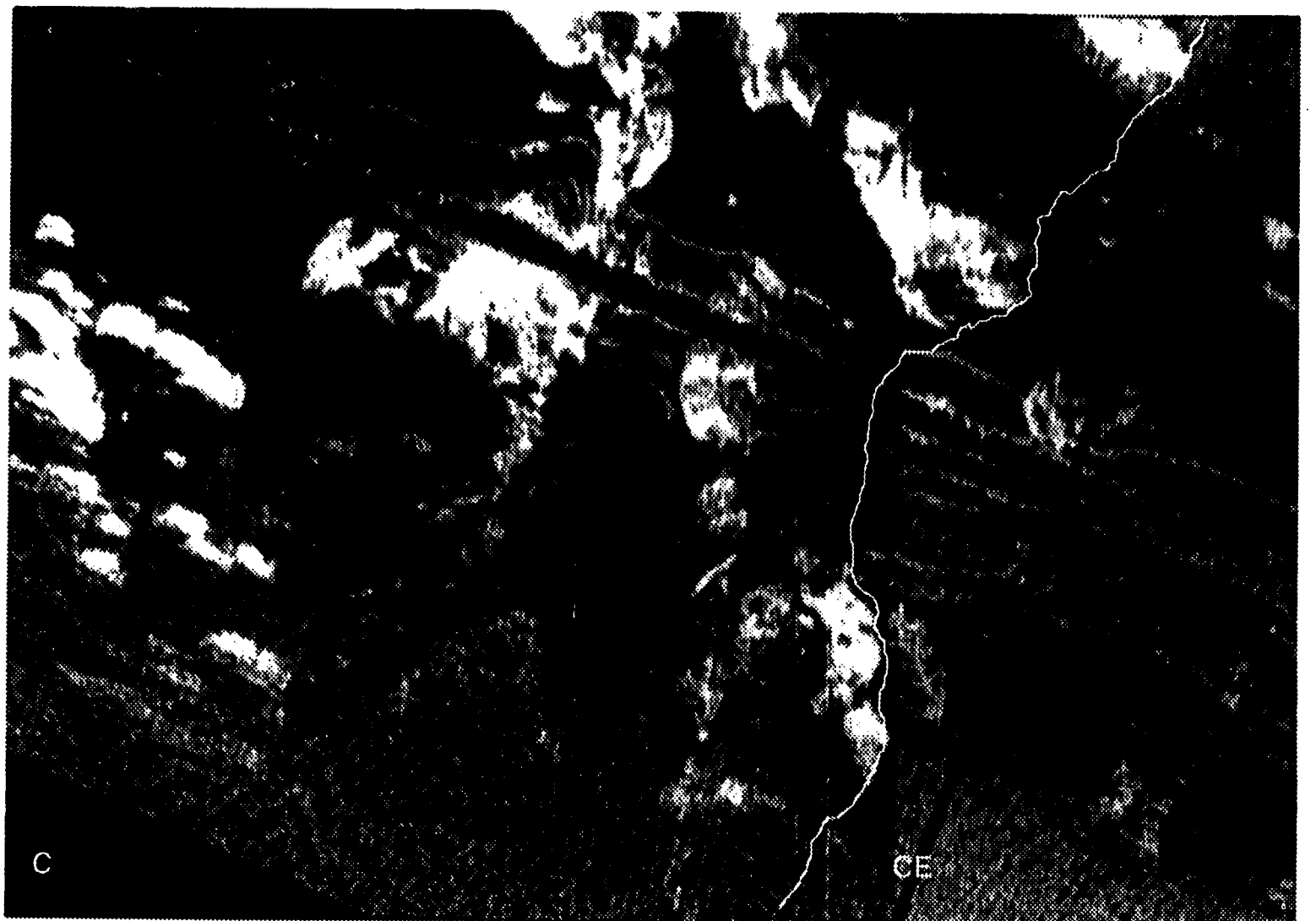

Figure 6-5 : Normal Deep Tow sonar imagery of the Juan de Fuca plateau showing the difference between the outcrop form and the extent of exposure in the Central (C) sector in comparison to the heavily sedimented Central-East (CE) sector.

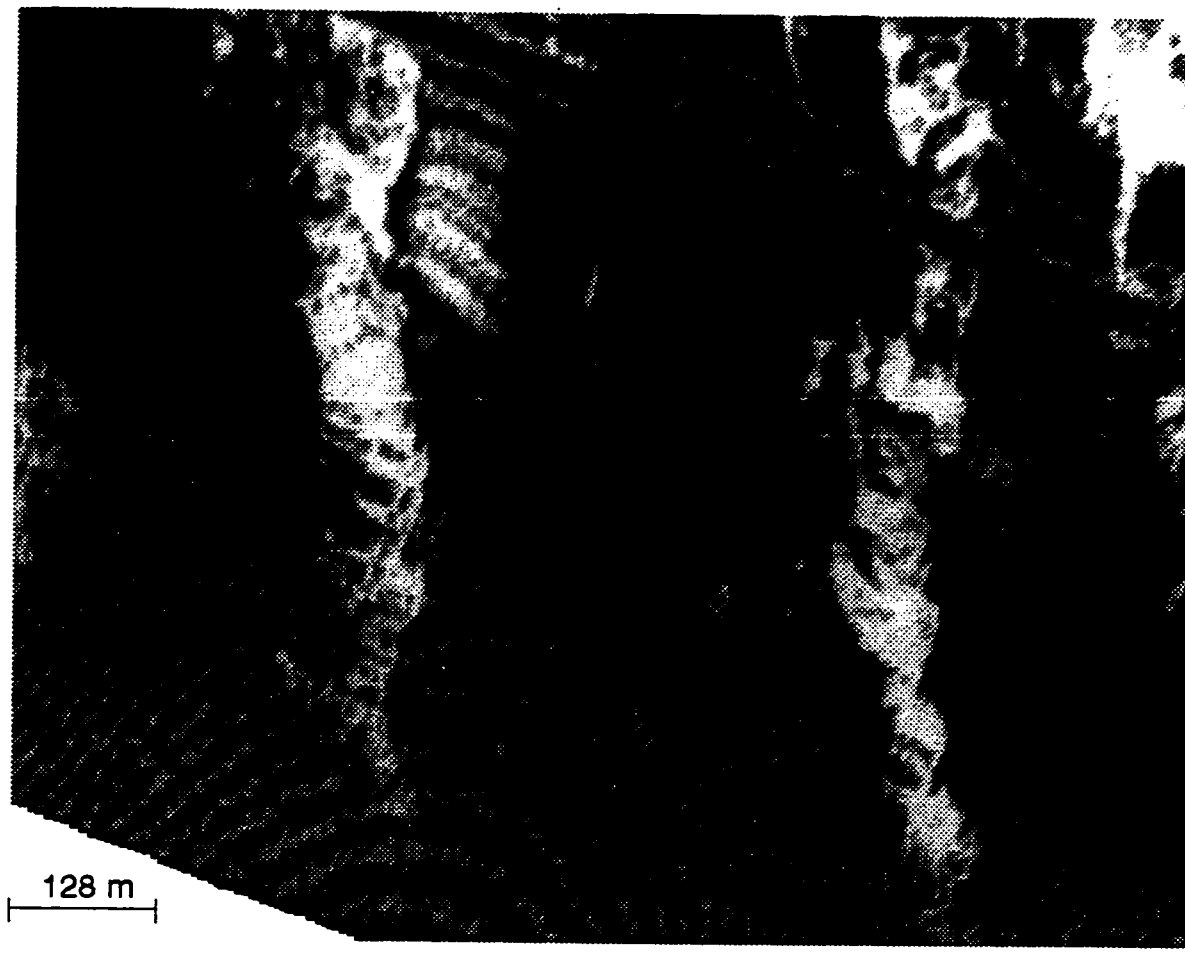

Figure 6-6 : Grid square f-12 of the Deep Tow sonar imagery showing the East (E) sector. The sector is characterised by a series of elongate, N-trending outcrop exposures on the sedimented plateau.

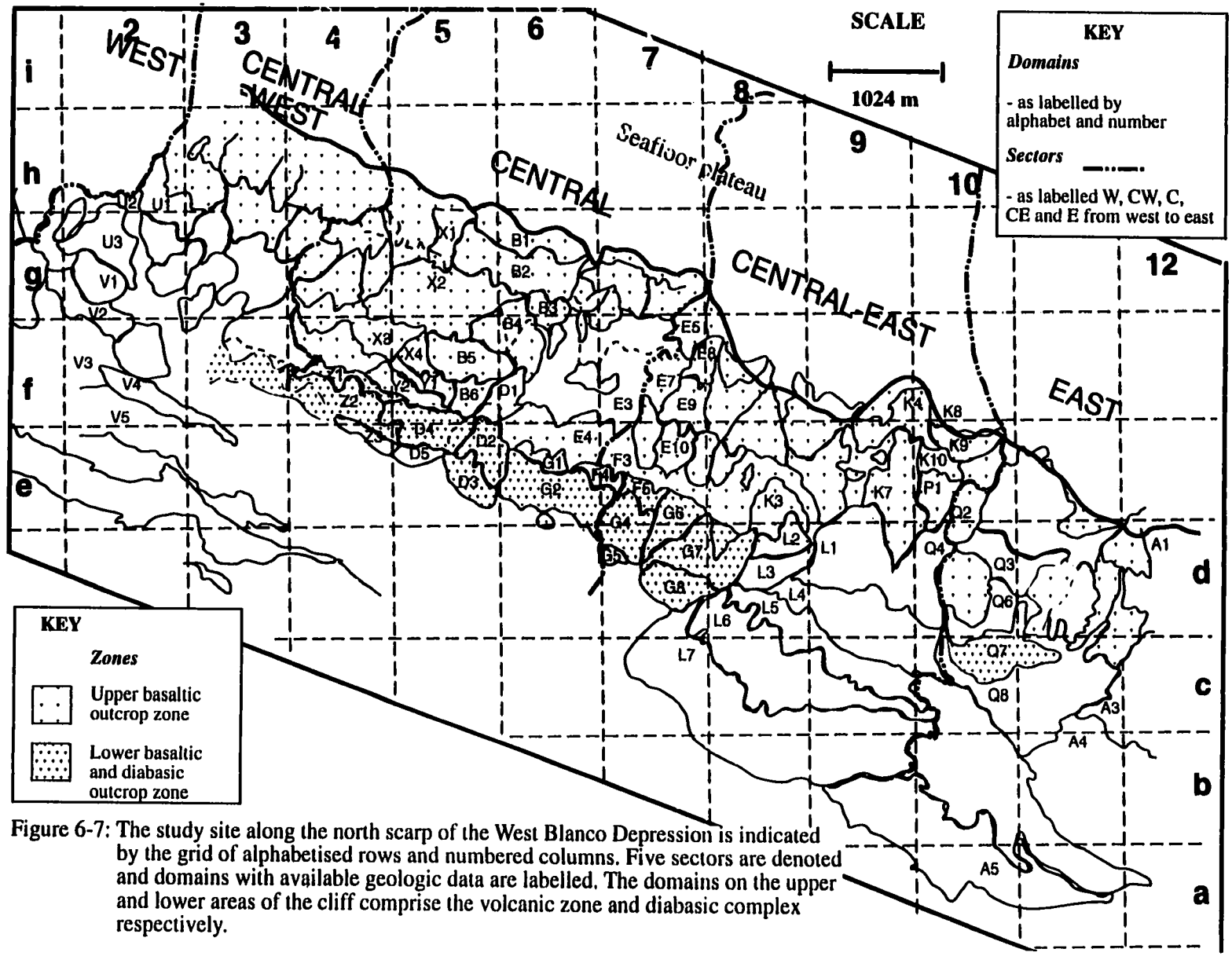

Figure 6-7: The study site along the north scarp of the West Blanco Depression is indicated by the grid of alphabetised rows and numbered columns. Five sectors are denoted and domains with available geologic data are labelled. The domains on the upper and lower areas of the cliff comprise the volcanic zone and diabasic complex respectively.

Figure 6-8a: The *Nautile* traverses overlaid onto a map of the domains and sectors on the north WBD scarp. At the start of a track, the dive number (BN-#) is given and along each, the location, number, and rock type of the samples retrieved are indicated. This concentration of dives and density of sampling within the 7km*11km study site provides direct geological observations of the domains crossed. These domains are labelled in Figure 6-8b.

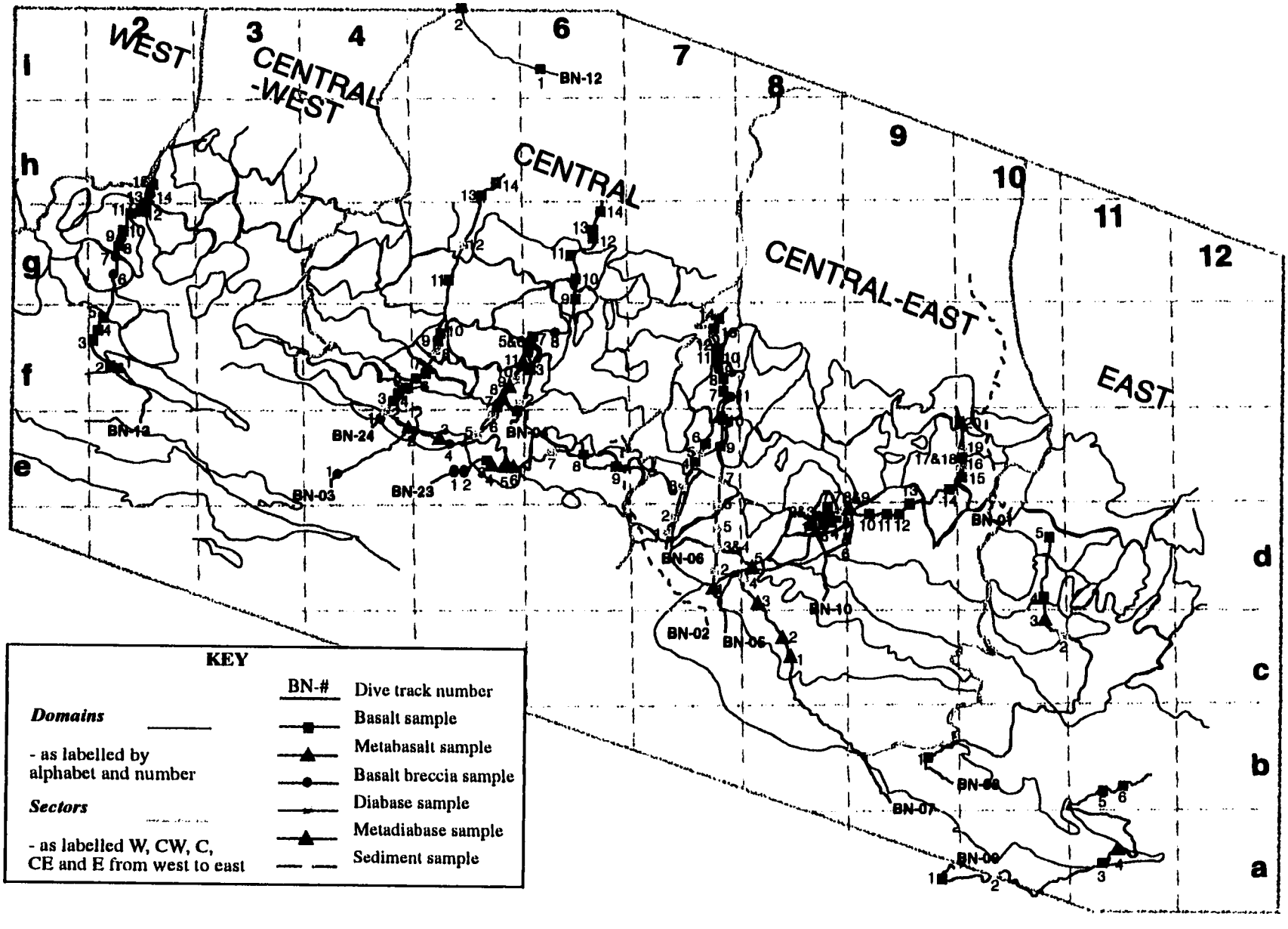
WEST
CENTRAL-WEST
CENTRAL
CENTRAL-EAST
EAST
BN-12
BN-24
BN-04
BN-03
BN-23
BN-06
BN-10
BN-02
BN-01
BN-07
BN-08
KEY
Domains
- as labelled by alphabet and number
Sectors
- as labelled W, CW, C, CE and E from west to east
BN-# Dive track number
Basalt sample
Metabasalt sample
Basalt breccia sample
Diabase sample
Metadiabase sample
Sediment sample

Figure 6-8b: A map of the domains and sectors overlaid on the Sea Beam bathymetry of the north WBD scarp. The domains labelled are those with geologic data made available from submersible dives (Figure 6-8a). The bathymetry permits one to determine the depth at which the boundary of a domain was crossed during a dive. This depth is transferred to the lithomorphological profiles documented from each dive (Appendix B). These profiles are used to interpret the sonar pattern of every domain (Appendix C). Consequently, the nature of the differences between domains can be characterized, as discussed in the text.

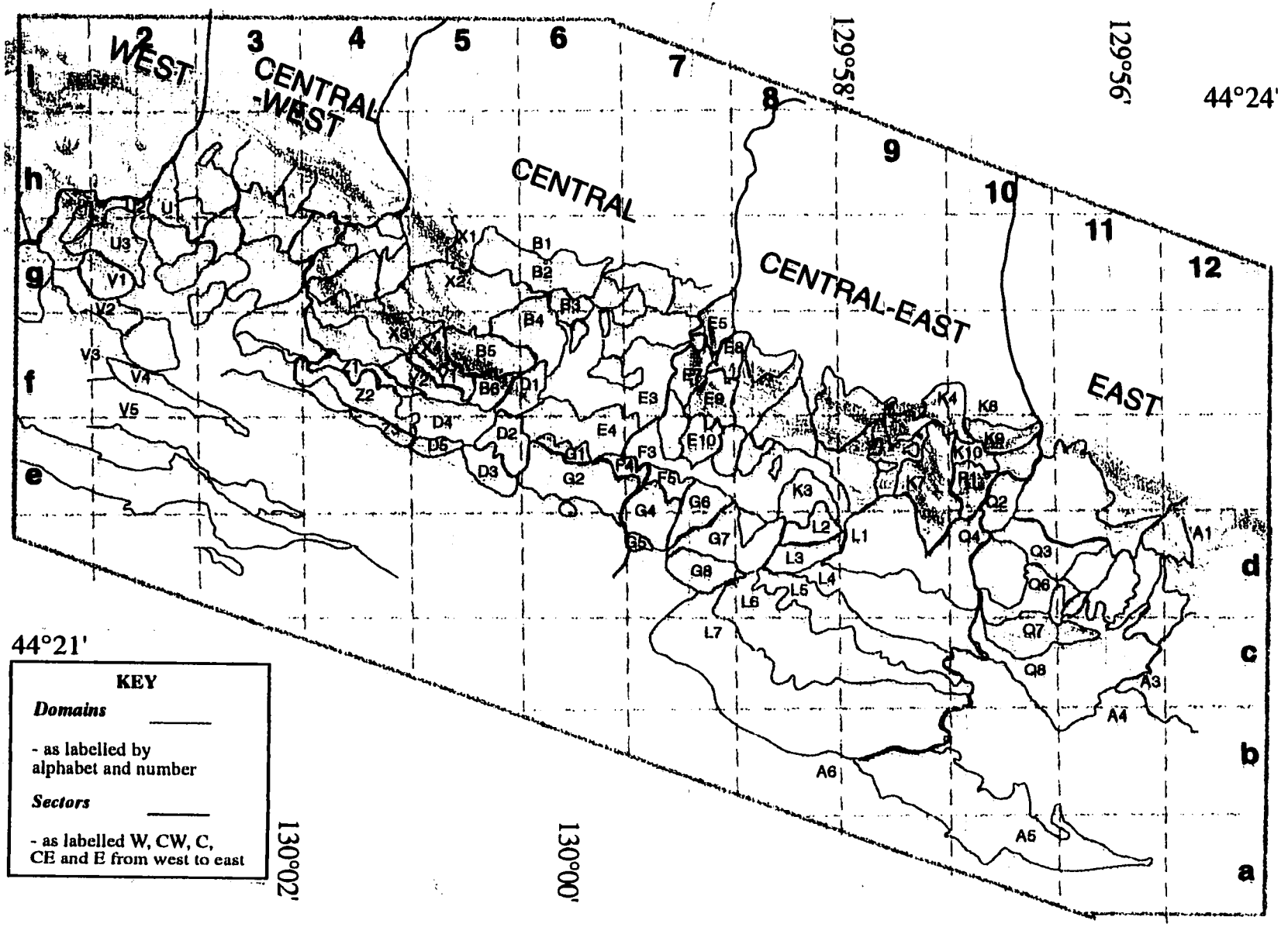
WEST
CENTRAL-WEST
CENTRAL
CENTRAL-EAST
EAST
129°58'
129°56'
44°24'
44°21'
130°02'
130°00'
KEY
Domains
- as labelled by alphabet and number
Sectors
- as labelled W, CW, C, CE and E from west to east

Figure 6-9:
Filtered and processed up-looking sonar imagery of areas within the study site on the WBD scarp. The high resolution backscatter imagery displays distinctive variations in texture and tone. These visual differences, in concert with those on the down-looking sonar imagery, form the basis of domains that are outlined on the overlays. Where direct geological observations are available, the domains are labelled. The overlays also have a scale bar for the underlying figure.

Figure 6-9: This mosaic is of grid squares f-7 (upper left), f-8 (upper right), e-8 (lower right) and e-7 (lower left). It shows mainly the highly reflective volcanic zone of the upper crust as exposed on the north wall. The seafloor plateau in the extreme right-hand upper corner is poorly reflective and has a homogeneous textural pattern. The diabasic complex with a strongly banded pattern visible in the extreme left-hand lower corner (domains F5, G4, G6 and G7) is less reflective because of it's comparatively lower slope. These three areas therefore contrast strongly in textural pattern.

Figure 6-9: (overlay)
The domains within the volcanic zone are defined by their varying backscatter characteristics. For example: Domain E9 is distinguished by a finely banded pattern. This pattern is not evident in the triangular domain further eastward in which crestal forms are emphasised instead. Domains may also be characterised in terms of the extent of outcrop. The relatively smooth pattern of domain F3 indicates mainly scree. In domain E10 and those laterally eastward, outcrop is emergent from beneath the sediment cover. These domains nonetheless differ in outcrop expression as can be seen between domain E10 and that in the extreme right-hand lower corner.

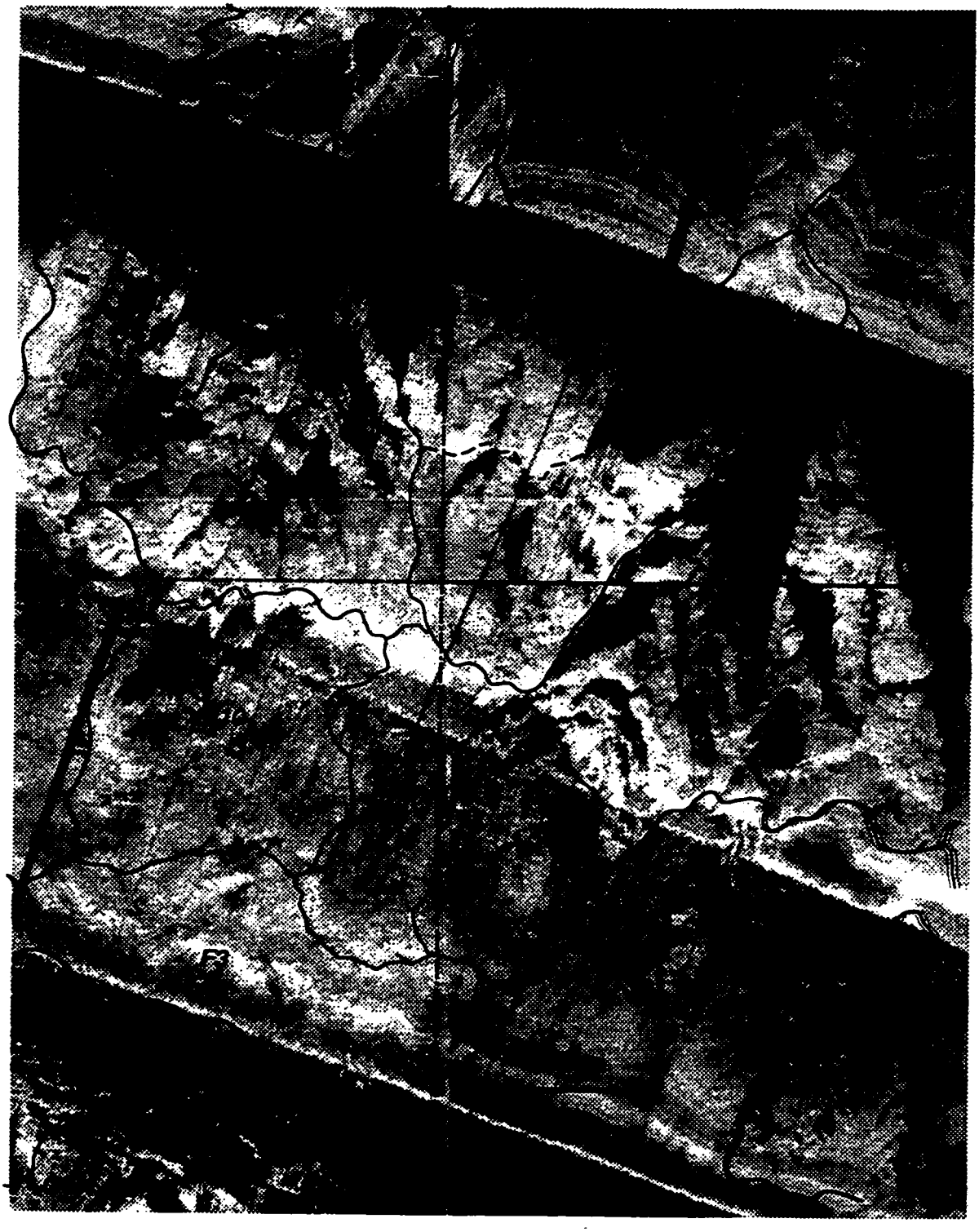

Figure 6-10:
Filtered and processed up-looking sonar imagery of areas within the study site on the WBD scarp. The high resolution backscatter imagery displays distinctive variations in texture and tone. These visual differences, in concert with those on the down-looking sonar imagery, form the basis of domains that are outlined on the overlays. Where direct geological observations are available, the domains are labelled. The overlays also have a scale bar for the underlying figure.

Figure 6-10: This mosaic of grid squares e-6 (upper left), e-7 (upper right), and d-7 (lower right) shows mainly the diabasic complex of the upper crust as exposed on the north wall. The volcanic zone is visible in the uppermost part and the talus slope is present in the lowermost part of the figure. The high resolution of the Deep Tow imagery is evident from the individual boulders (light faces and dark shadows cast behind) that can be seen amidst the talus apron fringing the cliff base.

Figure 6-10: (overlay)
Within the diabasic complex, domains may be defined by their varying acoustic characterictics. A strongly banded pattern is typical of domain G2. In domains F4 and F5, the pattern is less reflective probably because of a decrease in slope. In domain G6, the bands are still present but there are also intermediate-size crestal features. Domain G4 is dominated by a series of large crestal forms. In domain G7, the crests are relatively small. Domains G5 and G8 are similar in their mottled pattern.

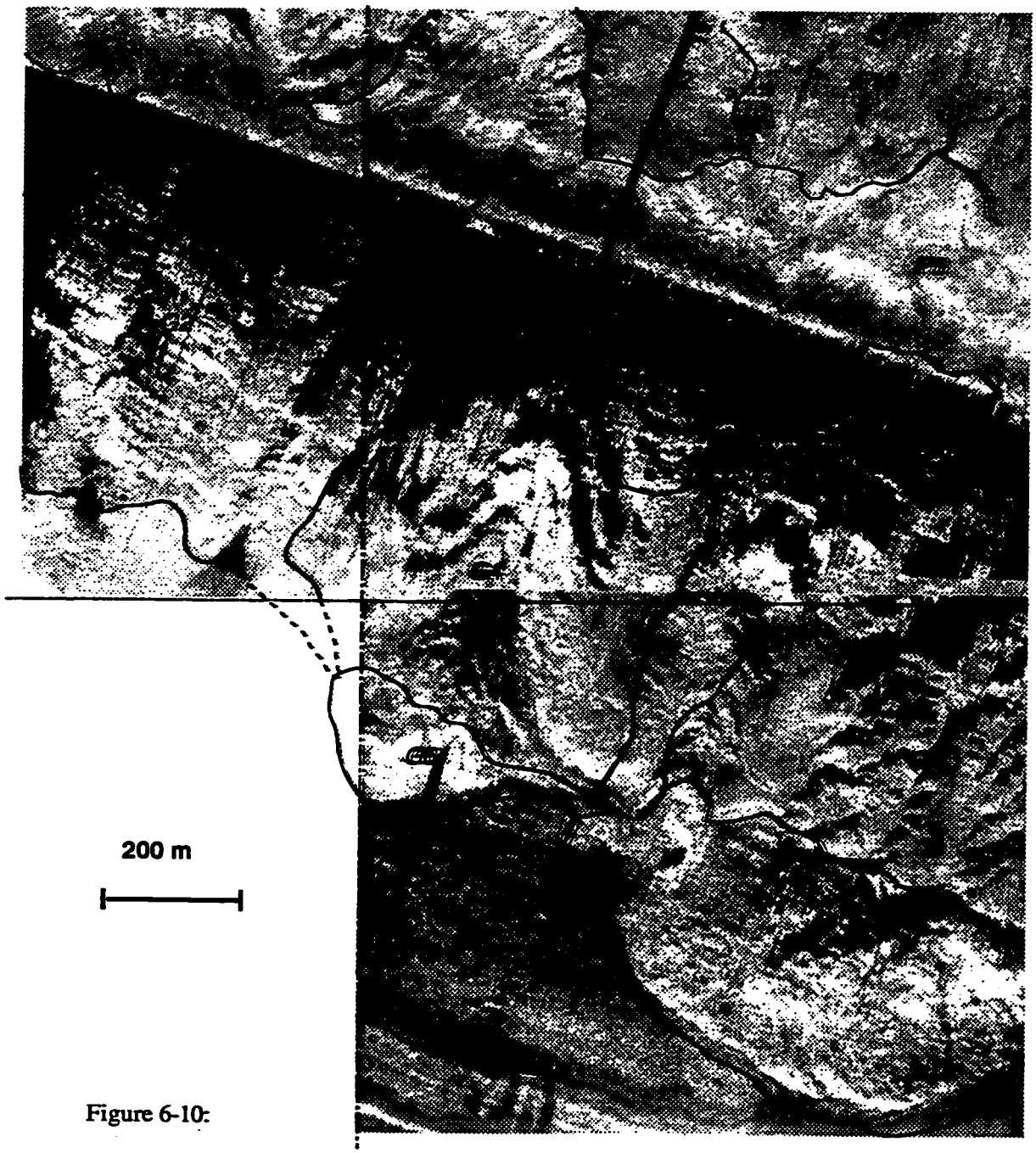

Figure 6-10:

CHAPTER VII: MINERALOGY OF THE BASALTS: INFERENCES ON CRYSTALLIZATION

7.1 Introduction

Spreading ridge rocks contain disequilibrium assemblages of minerals that preclude systematic relations between phenocryst compositions, phase proportions, and liquid compositions (Natland, 1991 vs. Bryan, 1983). Nonetheless, the mineralogy is useful in identifying distinctive types and hence, in tracing changes in magmatic evolution. Here, the basalts and diabases retrieved by submersible from the study site provide an opportunity to examine the petrographic variation in the 2 km thick section of upper oceanic crust exposed on the north scarp of the West Blanco Depression (WBD). In this chapter, the phase assemblages, crystallinity, grain size, crystal morphologies, and mineral relationships of the samples are described. The igneous rock textures are used to interpret crystallization sequences and infer the nature of magmatic processes associated with basement construction. These petrographic attributes, as well as other features such as vesicles or veins, permit further definition of the upper and lower outcrop zones, sectors and domains outlined in Chapters V and VI. This spatial distribution forms the basis for expanding on the models of crustal construction being proposed. The significance of these findings for magmatic accretion is discussed by comparison to other settings, in particular to Hole 504B.

7.2 Data

The density of rock sampling within the context of the domains traversed by the *Nautile* submersible at the 7 km by 13 km WBD site is illustrated in Figure 6-4a. Figure

7-1 displays the depth location of each sample by dive and in relation to the labelled domains and sectors. The number of rocks recovered varies between 5 and 20 per dive and average about 11. Most of the sampling is concentrated in the Central (C) and Central-East (CE) sectors with 60 (42%) and 58 (40%) rock samples, respectively, while the Central-West (CW) and East (E) sectors have only 15 (10%) and 11 (8%) samples each. In general, there are between 0 and 9 rocks per domain with an average of 3. Of the 144 rocks described in hand specimen (unpubl. Blanconaute rept., 1991), 100 were selected according to the criteria in Appendix E-1 for thin section examination. A summary of the petrographic characteristics for each dive is presented in Appendix E-2 while the complete descriptions are given in Appendix E-3.

7.3 Results

7.3.1 Rock Types

Three rock types - basalts, diabases, and basalt breccias - are present on the north WBD scarp (Appendix E). The terms "basalt" and "diabase" are distinguished here texturally (see MacKenzie et al., 1982 for examples), as opposed to the general definition by mineral assemblage. Basalt refers to a glassy to fine-grained (<1 mm) mafic rock commonly while diabase refers to a medium-grained (1-5 mm) basic rock typically with an equigranular groundmass displaying an ophitic to subophitic intergrowth of plagioclase and clinopyroxene. The relative abundances of these rock types across the WBD site in Figure 7-3a shows that the upper oceanic crust here is constituted by 65% basalt, 24% diabase and 11% breccia.

7.3.2 Classification of Rocks

The basalts and diabases are described according to 3 main petrographic attributes in Appendix E.

Among the terms for grain size - very fine, fine, medium and coarse - denote crystal diameters, respectively, of <0.25 mm, 0.25-1.5 mm, 1.5-3 mm, and 3-5 mm (cf. MacKenzie et al., 1982 where coarse means >5 mm). The grain size variation at the WBD site is shown in Figure 7-5a. It includes, in order of decreasing percentage, fine- (34%), medium- (28%), very fine- (19%), glassy (13%) and coarse- (5%) grained rocks.

Rock samples with 0% phenocrysts are referred to as "aphyric", with 0-10% as "sparsely phyric", with 10-25% as "moderately phyric", and with >25% as "highly phyric". Their relative abundances at the study site are illustrated in Figure 7-7a. The porphyritic rocks comprise 67% of the samples. The basalts are mostly sparsely to moderately phyric while the diabases are mainly aphyric.

The rock types are also labelled with the phenocryst phase/assemblage present. The prefixes are "A" for aphyric or "P/-C/-O" for respectively plagioclase, clinopyroxene and olivine, in order of relative proportion. On this basis, 9 petrographic types are identified and their relative proportions at the site displayed in Figure 7-9a. There are 5 basalt and 3 diabase types: aphyric, P- and PC- basalts and diabases as well as PO/OP and PCO basalts. They are labelled from Type I to Type VIII in decreasing order of abundance while Type IX represents basalt breccias which are not discussed further. The PC basalts, aphyric diabases and PCO basalts are the dominant types while basalt breccias, P diabases and PC diabases are the least common.

7.3.3 Petrographic Types

The characteristics of the 8 petrographic types are described below. Table 7-1 gives their relative proportions in the WBD suite and a summary. The phenocryst morphology of the 6 porphyritic types is described for comparison in Table 7-3.

(a) PC or Type I basalt

Type I are very fine- to medium-grained basalts that are sparsely to highly phyric with plagioclase and clinopyroxene as glomerocrysts in a fifth of the samples, phenocrysts in a tenth, and as both in two-thirds of this group. In some samples (15%), plagioclase gives rise to seriate (BN- 5-9, 24-14) and trachytic (BN- 10-18, 24-5) textures. Plagioclase and clinopyroxene occur as phenocrysts (BN- 3-7, 3-11, 6-4, 8-1, 10-11), glomerocrysts (BN- 5-9, 6-13, 10-18) or both (BN- 4-7, 6-10, 7-4, 10-15, 12-1, 12-2, 13-3, 13-4, 13-5, 13-8, 13-15, 23-8, 23-9, 24-5, 24-6, 24-9, 24-13, 24-14). Their characteristics (Table 7-3) include the presence of plagioclase megacrysts (BN- 12-1, 13-3, 24-5, 24-13). Scarce evidence of olivine is retained only in the crystal outlines that are now completely filled with clays (BN- 3-11, 10-11, 13-3). One unusual Type I sample (BN-4-7) is marked by coarse grained clots of plagioclase-clinopyroxene-olivine-magnetite that are largely unaltered.

A fifth of the Type I group are glassy basalts. In the rest, the groundmass is composed of 10-60% plagioclase, 2-30% clinopyroxene, and 5-10% opaques. Plagioclase ranges from crystallites to 2 mm, subhedral laths and 0.2-0.5 mm equant grains, some of which are intrafasciculate (BN- 3-7, 5-9). The clinopyroxene grains range from microlites to 0.8 mm, are anhedral in form, a few are Carlsbad twinned (BN- 10-19) and some are titanaugites (BN- 6-3, 24-13) based on their purplish-gray pleochroism. The black opaques, interpreted as Fe-Ti oxides, are absent from samples with a glassy groundmass (BN- 2-11, 6-13, 7-4, 8-1, 13-11 and 13-15) but are otherwise ubiquitous. They range

largely between 0.01 mm and 0.3 mm and are anhedral due to their interstitial growth, indicating that this is the last phase to crystallize.

The PC basalts include 1-10%, round vesicles that are 0.2-0.8 mm in diameter. They vary from empty to rimmed or filled with chlorite, opaques, brown alteration minerals (saponite/celadonite) or groundmass material. Half of the samples show 1-2% veins that are 0.02-3 mm wide and composed of brown alteration, chlorite and lesser albite and opaques. The presence of amphibole in one sample (BN-13-4) could stem from alteration of augite. A quarter of the samples display 1-8% cracks, that are 0.25-2 mm wide and either unfilled or rimmed by brown alteration minerals.

(b) PCO or Type III basalt

The Type III group (BN- 1-2, 1-3, 1-4, 4-9, 4-11, 4-12, 4-13, 4-14, 6-6, 6-7, 6-11, 6-12, 8-5, 10-20, and 13-05) are fine- to coarse-grained basalts that are sparsely to highly phyric with plagioclase, clinopyroxene and olivine (as euhedral to anhedral grains or 0.1-1 mm iddingsite replacements) as both phenocrysts and glomerocrysts (Table 7-3), and have a marked seriate texture.

The groundmass is formed by 5-60% plagioclase, 1-35% clinopyroxene, and 5-15% opaques. Plagioclase grains range from microlites to 2 mm subhedral laths in a seriate texture. Clinopyroxene grains range from 0.1-0.75 mm and include both anhedral and euhedral forms. A few are of diopside-hedenbergite composition based on their intense green color and slight pleochroism (BN- 4-11, 6-11). Opaque minerals are 0.1-0.8 mm in size and are largely anhedral. They tend to be in small concentrations (BN- 1-2, 1-4, 4-10, 4-11, 4-14) associated with chlorite.

The PCO basalts include 1-10%, irregular to round vesicles from 0.4-1.8 mm in diameter. They range from empty to rimmed or filled with chlorite, opaques, glass or

other brown alteration minerals. Only two-fifths of the samples have 1-2% veins that are 0.05-0.1 mm wide and lined to filled with the same material as the vesicles.

(c) Aphyric or Type IV basalt

The Type IV group (BN- 2-12, 10-10, 13-1, 13-2, 13-12, 24-4, and 24-10) are very fine- to medium-grained, aphyric basalts. The groundmass is composed by 35-50% plagioclase, 15-40% clinopyroxene, and 5-20% opaques. Plagioclase occurs mostly as 0.2-1 mm sub- to anhedral laths and less commonly as tabular grains or 0.1-0.5 mm crystallites. It also forms 1-2 mm megacrysts (BN- 13-2, 24-4). Clinopyroxene, a few of which show simple twinning (BN- 8-4, 24-10), ranges from microlites to 0.5 mm anhedral grains except in a fifth of the samples where they are completely altered to chlorite. Opaques are 0.05-0.2 mm in size, anhedral and scattered throughout. Alteration consists mainly of 5-25% chlorite in three-fifths of the samples. This group has only 1-2%, round vesicles which are 0.4-0.8 mm in diameter, and are either unfilled, rimmed with brown alteration phases, or filled with chlorite or quartz. The group is also marked by a 1-7% abundance of veins in half the samples. The veins are only 0.05-0.1 mm wide and filled mostly with chlorite, and additional minor brown alteration phases, albite, quartz, opaques or carbonate.

(d) P or Type V basalt

The Type V group (BN- 2-10, 4-5, 6-8, 10-13, 13-13, 24-3 and 24-11) are fine- to medium-grained, sparsely plagioclase phyric basalts (Table 7-3). The groundmass is formed by 35-50% plagioclase, 15-30% clinopyroxene, 5-15% opaques. Plagioclase ranges from microlites to 1.5 mm, and occurs as subhedral laths and anhedral tabular forms. Clinopyroxene grains are 0.2-0.5 mm in size and anhedral. The opaque crystals are of 0.1-0.4 mm size and are anhedral. The P basalts include 1-5%, round vesicles which

are 0.4-3 mm in diameter and vary from rimmed to filled with mainly chlorite, brown alteration, and/or opaques, as well as minor chloritized groundmass, epidote, carbonate or quartz. Half of the samples have 1-2% veins that are 0.05-0.2 mm wide and rimmed to filled with iddingsite/saponite/celadonite, opaques and/or chlorite. Half also have 1-15% cracks that are 0.2-0.7 mm wide and vary from empty to filled with a red-brown alteration mineral and oxide.

(e) PO and OP or Type VI a and b basalt

The Type VI basalts comprise two sub-groups.

Type VI-a are fine- to medium-grained, sparsely phyric basalts (BN- 2-9, 4-1, 8-4, 10-1) in which phenocrysts of plagioclase dominate over olivine or grains completely altered to iddingsite (Table 7-3). The groundmass is hypohyaline (BN-8-4) to crystalline with 40-45% plagioclase, 30-35% clinopyroxene and 2-5% opaques. Plagioclase forms up to 1.5 mm, subhedral laths; rare features include a seriate texture (BN-2-9) or equant grains that are intrafasciculate or oscillatory zoned (BN-4-1). Clinopyroxene is less than 0.5 mm in size, and sub- to anhedral; minor features include simple twinning (BN-8-4) or titanaugite composition (BN-10-1) based on the purple pleochroism. Black, anhedral, <0.2 mm size opaques are interpreted as Fe-Ti oxides. The rocks are altered by the presence of <10% chlorite patches. Half the samples (BN- 2-9, 4-1) have 2-10% of 0.1-1.5 mm veins composed of quartz, carbonate and albite. Three-quarters of the samples (except BN-2-9) have 1-3% vesicles which are 0.4-2 mm in diameter and vary from empty to rimmed or filled with chlorite.

Type VI-b are glassy to medium-grained, sparsely to moderately phyric basalts (BN- 4-10, 5-10, 9-1, 9-3, 10-6) in which phenocrysts of olivine predominate over plagioclase (Table 7-3). The groundmass is composed of 38-45% plagioclase, 10-40% clinopyroxene and 5-8% opaques. Plagioclase occurs as <1.6 mm subhedral to anhedral

laths, clinopyroxene as <1.2 mm anhedral grains, while the opaques are 0.1-1 mm in size and vary from irregular to elongate. Chlorite forms 0.05-2 mm patches. Most (4 of 5) have 1-5% vesicles that are 0.3-1 mm in diameter, round to irregular, and varying from unfilled to to rimmed or filled with carbonate ± quartz, or chlorite ± quartz.

Plagioclase and olivine also occur as phenocrysts in 18% (5 of 28) of the PC and 14% (2 of 14) of the PCO basalts where clinopyroxene is only included in the glomerocrysts.

(f) Aphyric or Type II diabase

The Type II group are fine- to coarse-grained, aphyric diabases. The groundmass is composed of 40-55% plagioclase, 25-40% clinopyroxene, and 3-5% opaques (exceptions: 7-10% in BN- 10-19 and 3-5). Plagioclase occurs as 0.5-4.5 mm, subhedral laths and tabular grains. Many plagioclase show Carlsbad (BN-5-4) and albite twins (BN-2-1, 2-8, 3-10, 6-1, 24-2) as well as pericline twinning (BN- 2-8, 24-2). Some display oscillatory zoning (BN- 2-1, 2-3, 2-8, 3-6, 5-4, 24-12). Several are altered (BN- 2-1, 3-5, 5-4, 6-2, 24-2). Plagioclase also forms a 2.2 mm megacryst with a growth rim indicating reaction with the groundmass (BN-10-19). Anhedral clinopyroxene are 0.2-3 mm in size, with the exception of a 7 mm megacryst (BN-3-6). Some are twinned (BN- 2-1, 2-8, 10-7) and a few show oscillatory (BN-3-5) or sector (BN-3-6) zoning. Several are clearly titanaugites in composition (BN- 2-1, 5-5, 6-3, 23-7). Anhedral opaques are 0.2-1 mm in size and occur interstitially. Most of the samples (65%) are cut to a minor extent by 1-5% veins that are <<1 mm wide and filled with chlorite, quartz, carbonate, or albite. Three-quarters of the aphyric diabases are altered between 5% and 20% by chlorite in up to 3 mm large patches. Among the other quarter, most are marked by 2-14% of brown alteration material (BN- 10-19, 3-10, 10-7). The rest (BN- 2-3, 3-6) are characterized by 1-2% of vesicles that are 0.8-1.2 mm in diameter, subrounded and filled with chlorite.

One sample includes both alteration and vesicles (BN-6-2) while another is unaltered (BN-24-8).

(g) P or Type VII diabase

The Type VII group (BN- 2-7, 7-7, 23-3, 24-7) are fine- to coarse-grained, sparsely plagioclase phyric diabases (Table 7-3). The groundmass is formed by 30-40% plagioclase, 25-30% clinopyroxene, and 5-10% opaques. The plagioclases occur as 1.4-3 mm laths that are generally altered (exception: BN-24-7). The clinopyroxenes are 0.8-1.8 mm and anhedral. In one case (BN-7-7), they are clearly of titanaugite composition. The opaques are anhedral, 0.2-0.8 mm minerals that have grown interstitially. Three of the four samples are highly altered since they are cut by 10% veins and altered by 10% chlorite. The veins are 0.05-0.6 mm wide, filled with chlorite, quartz and minor carbonate, and in one case they are sub-parallel (BN-23-3). The three samples also contain 20% of 1.2-1.4 mm wide, chlorite patches. The fourth (BN-24-7) has 0.4 mm size patches of brown alteration that are 10% in abundance. It is also unusual because it includes 9% vesicles that are round, 1.6 mm in diameter, and vary from empty to rimmed to partly filled with green-brown alteration material.

(h) PC or Type VIII diabase (2% of total, 8% of diabases)

The Type VIII group (BN- 2-4, 5-2) are fine- to medium-grained, sparsely phyric diabases with plagioclase and clinopyroxene phenocrysts (Table 7-3). The groundmass is formed by 40% plagioclase, 30-35% clinopyroxene, and 5% opaques. The plagioclase occurs as 0.5-1.4 mm laths and tabular grains while the clinopyroxene is 0.2 mm and subhedral. The 5% of anhedral opaques are 0.4-0.5 mm crystals that have grown interstitially. This group is altered by 10% chlorite in 0.8-2.8 mm patches as well as 8%

veins that are 0.05-0.2 mm wide and filled by albite, chlorite, brown material and carbonate.

7.4 Interpretation

7.4.1 Implications of the petrography

(i) Crystallization Sequences

Two main sequences of crystallization can be inferred from petrographic relationships in the WBD suite:

(a) In the OP basalts, there is evidence for olivine accumulation in the form of a few, distinctly larger phenocrysts (Table 7-3). Even with their exclusion, olivine is still more abundant which suggests that it preceded plagioclase in the crystallization history. Therefore, the OP type must originate in the olivine stability field from the sequence O->OP.

(b) The P basalts and diabases are an exception to the majority of phyric types here which are multiply saturated. Assuming an absence of convection, they could be explained by plagioclase separating at a slower rate than either olivine or clinopyroxene from the basaltic liquid. It can further be presumed that effective separation of the two magma batches requires a relatively long period of time since the density contrast is small. However, this conflicts with their average Mg# of 59±5 (Appendix G) which indicates that they are only slightly to moderately evolved. The other alternative is that crystallization commenced in the plagioclase stability field to produce the P-type.

(c) In the PO basalts, the dominance of plagioclase over olivine and their subophitic relation in one case suggests that plagioclase has preceded olivine in crystallizing. Therefore, the PO type could be derived by the sequence P->PO.

(d) The timing for appearance of clinopyroxene can be inferred from some PCO basalts in which plagioclase and lesser olivine occur as phenocrysts but clinopyroxene only forms in the glomerocrysts suggesting that it crystallized later in the sequence P->PO->POC.

(e) In the PC diabases, the subophitic to ophitic intergrowth of plagioclase enclosed by clinopyroxene indicates that plagioclase is the earlier phase. Therefore, the PC-types would be derived from either the sequence P->PO->POC->PC or O->OP->OPC->PC. The close spatial association of the PC- with the P-type diabase supports the former sequence.

(f) Opaques occur in the interstices between plagioclase and clinopyroxene and must have been the final minerals to crystallize. Thus, in both sequences, Fe-Ti oxides are the last to join the crystal assemblage.

(ii) Shallow-level magmatic processes

The petrographic observations provide evidence that crystal fractionation played a major role in the evolution of the magmas parental to these rocks. This interpretation is based on the wide spectrum of assemblages (5 among the basalts and 3 among the diabases) and amounts of phenocrysts (Figure 7-10), the notable abundance of clinopyroxene and oxides in the PCO basalts, and the absence of Cr-spinel, which ceases to crystallize at an early stage. Cr-spinel grains have been found only in picritic basalts from the extreme eastern area of the scarp (Juteau et al., 1995).

The extensive differentiation indicated by the crystallization sequences (Figure 7-6) requires one or more relatively long-lived, sub-axial magma lenses. Furthermore, the highly porphyritic nature in 67% of the samples (Figure 7-7) suggests that replenishment events (if at all) had to have been comparatively infrequent since any suspended crystals would be partially to completely melted by the incoming, hot liquid. It may also be inferred from the reaction rims of plagioclase and clinopyroxene in the PC and PO basalts that the phenocrysts continued to react with the melt in Sectors C and CW. This implies that thermal or compositional disequilibrium evolved within the storage system (Table 7-3).

The plagioclase megacrysts occur in aphyric diabase and PCO basalt in the eastern part of Sector CE (BN-1&10) and in PC basalt and aphyric basalt in Sectors C (BN-12&24) and CW. They could result from accumulation in an ascending magma (Flower, 1991) but this would require that all their petrogenetic groups (the N, M and T magmatic types - Appendix G) were subjected to high pressure effects. Hence, they are interpreted rather as evidence of the dynamic conditions during shallow-level crystallization. They could stem from scavenging of the wallrock (Wilkinson, 1982), from physical processes such as gravity sorting (Bryan, 1983), or from mixing of primitive and evolved magmas (Dungan et al., 1978). The evidence for magma mixing is the most compelling and includes the association of megacrysts with aphyric lavas and the interpreted melt-phenocryst reaction from zoning patterns and growth rims (Table 7-3).

The plagioclase-clinopyroxene-olivine-opaque mineral aggregates in Sector CW do not differ from their host except in that olivine is only a relict phenocryst phase in the PCO basalt. Hence, there is little to support an origin from solid rock-melt interaction in magmatic conduits (Leg 140 Shipboard Scientific Party, 1992). Instead, they are more compatible with an interpretation of crystal clots as forming early during an undercooling

event after the input of hot melt into a storage system at the end of a relatively amagmatic cycle (Dick and Johnson, 1995).

7.4.2 Relation of petrographic characteristics to lithologic units

The petrographic types in Table 7-4, ranked in the order - PC basalt, PCO basalt, P diabase, PO basalt, A basalt, P basalt, PC diabase, and A diabase - show a general increase in average grain size and a decrease in average crystallinity. The lithologic units in Table 7-5, ranked as - thin sheet flows, whole and broken pillows, blocky flows and spires, dikes, thick sheet flows/sills, and diabase intrusives - likewise show an overall increase in grain size and a decrease in crystallinity. Consequently, the petrographic attributes of each lava morphology is limited in range and can be summarized as follows:

The jointed, massive unit is unique in its restricted grain size range from medium to coarse, and in being composed only of aphyric diabase.

The dikes and thickly-layered, massive unit both range from very fine- to coarse-grained, from aphyric to highly phyric, and are represented by 6-7 petrographic types of both basalts and diabases. The medium- and coarse-grained members most likely represent the central portions of flows/sills and dikes, and the very-fine and fine-grained members the chilled margins. The thickly-layered, massive unit includes two basalts with plagioclase displaying a swallowtail habit (BN-13-11) and sheaf-like growth (BN-24-3) in a glassy and fine-grained groundmass respectively (Appendix E-3). Such features are typical of rapid crystallization and favor an origin, for at least some of these units, as sills rather than thick sheet flows. The juxtaposition of the BN-13-11 sample with a brecciated altered part (Appendix E-3) further supports this interpretation.

The pillow and blocky basalt flows are similar in their variation from glassy to medium-grained and yet being mainly fine-grained. They are also both composed of mostly PC and PCO basalts and they are the only two types to include plagioclase megacrysts. They differ in three significant ways, however. Only the pillow lavas include quench plagioclase in sheaf-like aggregates. The pillow flows tend to be highly phyric while the blocky flows are generally sparsely phyric. The pillows also include lesser PO basalt while the blocky flows include minor A and P basalts.

The spires are typically very fine-grained, moderately phyric and composed of PC basalt. They share affinities with blocky flows since they include P basalt, with pillow flows because of their quench plagioclase (BN-6-11), and with both flow forms in their glassy nature.

The thin sheet flows and diced units are similar in their glassy and fine grain size and in consisting of mainly PC basalt. They differ in the more extensive grain size and crystallinity range of the diced unit and in their minor phenocryst assemblages. This supports the view that the diced unit is mostly but not entirely a jointed equivalent of the thin sheet flows.

Thus, there is an overall correlation between lithologic units and petrographic attributes. Consequently, the texture of a rock sample is considered to be representative of and hence assigned conservatively to the rest of that lithologic unit in that domain. This output, from the basic data in Figures 6-6 a-d extrapolated using the detailed lithologic map in Figure 5-7, generates the corresponding Figures 7-2, 7-4, 7-6 and 7-8. This procedure is important because sampling was not at regular intervals but rather when a new lithologic unit was encountered. These figures therefore show plausible extents (and proportions) of the petrographic characteristics along each profile. The advantage of this

presentation lies in the greater continuity within the section which highlights both the variation and approximate boundaries of these changes.

7.4.3 Petrographic differences between the upper and lower outcrop zones

The differences in rock type, grain size, crystallinity and type of phenocrysts respectively displayed in Figures 7-2, 7-4, 7-6 and 7-8 support the division of the crustal section into upper and lower zones in Sectors E, CE and C while the upper zone is continuous through Sector CW (see Chapter V).

The textures also permit a consistent delineation of the contact between these zones except in 2 of the 9 dive profiles which lie toward the eastern (BN-10) and western (BN-24) margins of the lower zone and where tectonic effects mask the original position. However, there is considerable variation in the boundary location between the profiles such that the break occurs at about 3600 m in Sector E, 3500-3625 m (Exception: to 3725 m in BN-10) in Sector CE, and 3400-3800 m (Exception: 3250-4200 m in BN-24) in Sector C which implies that it is irregular. Nevertheless, the contact itself is relatively sharp, as indicated in the BN-2 and BN-6 profiles, where the sample separation on either side of these zones is <125 m. The abrupt nature of this divide emphasizes the distinctness of these zones and supports a hypothesis that the lower zone is intrusive into the upper crust.

The petrographic aspects further provide a detailed description of the upper basaltic and lower diabasic zones as summarized in Table 7-6. In addition, Figure 7-6 shows that the lower zone is constituted by a core of medium- and coarse-grained diabases surrounded by very fine- and fine-grained diabase on the basal and western

margins. This zonation actually occurs at different levels with a more shallowly emplaced core in Sector C (~3700 m) than in CE (~4000 m). Thus, the diabase comprises at least two intrusive bodies. It should also be noted that there are no diabase equivalents in terms of phenocryst assemblage for the PO- or PCO-basalts and even the PC-diabase does not occur in the upper zone. Therefore, feeder dikes for these three types have not been identified in the WBD section. Furthermore, the aphyric and P-diabases in the lower zone are not necessarily related chemically to the same types in the upper zone.

7.4.4 Petrographic variation between sectors

The variation by sector across the study site is evident in the textural characteristics as displayed in Figures 7-3, 7-5, 7-7 and 7-9.

The three rock types are not distributed uniformly (Figure 7-3b-e). Sectors C and CE have the same relative proportions with basalt being the largest and breccia the smallest. By contrast, diabase does not occur in Sector CW and given that little is found on the western margin of Sector C (BN-24 in Figure 7-2), it confirms that the lower zone does not extend westwards. The comparatively small amount in Sector E indicates the eastern extent of the diabase body or alternately, its removal by the landslide. Likewise, breccia either do not occur in Sector E, implying a substantial temporal variation in accretion, or may be obscured by the pelagic sediment. Their comparative abundance in Sector CW is presumably due to the greater vertical extent of the upper zone.

The grain size distribution shows minor lateral variation (Figures 7-5b-e) implying a consistency in the crustal cooling regime over time. Among the basalts, glassy to medium-grained varieties are present in Sectors CW, C and CE (with a sole coarse-

grained sample in Sector C) while only the glassy and fine-grained classes are found in Sector E. Sectors CW, C, CE and E also differ slightly in that they are dominated respectively by basalts that are fine-grained, very fine- and fine-grained, medium-grained, and glassy plus fine-grained. However, according to the lithologic distribution (Figure 7-5), even Sector CE is formed mainly by fine-grained basalt. Since grain size is correlated with lithology (Table 7-5), the relative strength of the upper outcrop zone in these sectors should be roughly the same. Nonetheless, the location of the medium-grained basalts at the top of BN-01 rather than at the base of and hence supporting the upper zone as in the other profiles could explain the failure here (Whipple and Naidoo, 1991) and account for the localization of landslides along the scarp (see Chapter V). Likewise among the diabases, the grain size range and their relative proportions in Sectors C and CE are similar. Note that a very fine-grained diabase is present in both sectors although the metadiabase sample in Sector CE was not included in the petrographic study.

The phenocryst abundance of the two diabase varieties shows no lateral variation but the four basalt classes display a distinct shift across the site (Figures 7-7b-e). Sectors C and CE are similar in their diversity and in the dominance of aphyric diabases and sparsely phyric basalts. However, in terms of actual lithologic distribution (Figure 7-6), moderately phyric basalts are more prominent in Sector CE. By comparison, Sector CW includes the complete basalt range but Sector E only has aphyric and moderately phyric basalts. Sectors CW and E differ further in being respectively dominated by aphyric and moderately phyric basalts. This indicates that the Sector CE to C divide represents a major change in magma chamber dynamics from the production of mostly moderately to aphyric basalts.

The phenocryst assemblage also indicates another shift across the site (Figures 7-9b-e). Sectors C and CE both include all 9 petrographic types and are dominated by PC basalts and aphyric diabases with PCO basalts being common in Sector CE. By contrast, Sectors CW and E each have a different set of only three basalt types among which PC and PO basalts are respectively prominent. Since the petrographic assemblage is related to the degree of crystallization, it implies that the Sector E to CE divide represents a change within the magmatic system from producing PO to PC basalts and thus becoming more highly evolved geochemically over time.

7.4.5 Petrographic aspects of domains

The domains and their boundaries defined in the WBD site are indicated in Figure 7-1. In total, 72 domains were traversed of which 11 were not sampled at all. Samples were collected at the boundaries between domains in at least 35 cases which implies that the scientific observer on these dives was recognizing where distinct changes occurred in the lithologic units. This gives independent confirmation of the concept because the domains had not been identified prior to the *Blanconaute* program. Of the 61 domains sampled, at least one rock was retrieved in 20 of them and more than one was recovered in 41 domains. These multiple samples are useful in assessing the petrographic variation within domains.

In terms of rock type (Figure 7-2), the domains are comparatively homogeneous with only 11 producing both basalt and diabase samples which emphasizes the upper/lower zone division.

For grain size (Figure 7-4), data is available for 34 multiply sampled domains of which 11 have one size, 19 have 2 sizes, and 4 have 3 sizes in either basalts or diabases.

This implies that there are substantial variations in the cooling regime within the upper crust during accretion of more than half of the domains.

According to phenocryst content (Figure 7-6) among the 33 domains that are available, there are 17 with 1 class of crystallinity, 13 with 2 classes, and 3 with 3 classes of phenocryst abundance in either basalts or diabases. However, Figure 7-10 shows that the diabase domains (e.g. D4, G4, G7) actually have a constant phenocryst abundance. This is consistent with the idea that the diabases are emplaced rapidly as intrusive bodies. It also suggests considerable evolution in the state of the magma reservoir during the construction of most basalt domains in the upper zone. Furthermore, with increased shallowing in a domain, 35% show an increase, 22% show a decrease, and 30% show both increases and decreases in phenocryst abundance. Indeed between domains that are stratigraphically associated, there are only a few examples of consistently increasing (e.g. Sector C - B3->B2->B1->Plateau) or decreasing (Sector CE - E7->E5->Plateau) phenocryst abundance and these tend to cap the crustal section. This implies that each domain of the upper zone does not necessarily reflect the products of a single magma batch evolving in a closed system except towards the final stages of accreting the sector when replenishment evidently wanes.

In considering petrographic assemblage (but excluding basalt breccia in Figure 7-8) among the same 33 domains as previous, there are 17 of 1 type, 13 with 2 types, and 5 with 3 types. This indicates that significant fractionation occurs within the magmatic system during the building of at least half of the domains. In relation to depth, it is clear that none of the profiles represents a continuous crystallization sequence of a single magmatic system in constructing the complete section. With increased shallowing in a domain, some follow a sequence of crystallization (e.g. B5, E4, K7) while others are

reversed in order (e.g. B3, U2, U3). This suggests that domains could form from the output of either single or multiple magmatic systems, resulting from different sources or replenishment of the same reservoir.

Another parameter for evaluating the nature of domains is the estimated vesicle abundance of samples that is plotted by depth in Figure 7-11. Most domains have a constant volume percentage of vesicles (e.g. G2, G4) or only vary within 1% (e.g. B3, D4, D1, E4, E10, E9, G7, K7, L1, Plateau) or 2% (e.g. B1, P1, U2, V3, X4) but there is some variation of up to 9% (e.g. B5, B6, K8, L2, X1, Y2, Z2). In these latter cases, there is no consistent up-section pattern to the varying abundance (e.g. B1, B5, B6, K8 and P1 decreases; X1 and Y2 increases; L2, U2, V3, X4 and Z2 are non-systematic). Between domains, there are only two examples of a consistent trend both involving increases in vesicle abundance that occur at the top of two profiles in Sectors C (X1->Plateau) and CE (P1->K7->K10->K4->K8). Overall, four of the profiles in Sectors C and CE show an increase in vesicle abundance with shallowing depth above 3650 m. The high percentages point to water being entrained into the magma over the time-frame of accreting a sector.

7.5 Discussion

7.5.1 The plagioclase conundrum

The sequence produced by differentiation from the olivine field is typical of most mid-ocean ridge basalts (Wilson, 1989). By comparison, petrographic evidence for crystallization from the plagioclase field has only been reported for Hole 504B but is supported by melting experiments on the basalts (Autio and Rhodes, 1983) and crystallization models for the diabase (Leg 140 Shipboard Scientific Party, 1992). The

Leg 140 Shipboard Scientific Party (1992) proposes that the plagioclase series is favored by a combination of low total alkalis and high Al_2O_3 and CaO. This should form anorthite-rich plagioclase which requires a host liquid with a minimum CaO/Na_2O <10 (Fisk, 1984) that is not found at the WBD (Appendix G). Instead, Elthon (1991) suggests that the order is a consequence of these crystals being suspended in a magma during mixing. If this excess is not all resorbed by the primitive liquid, then the composition of the porphyritic mixtures can lie within the plagioclase field (Figures 7-12a-b from Elthon, 1984). The converse of this cycle is that OC and CO basalts or diabases ought to be generated but neither were recovered at the WBD site (cf. Legs 111 and 140).

7.5.2 Implications for the WBD site

The rocks recovered from the WBD site record distinct lateral and vertical petrographic variation. An upper basaltic zone of extrusives overlies a lower diabasic zone that is intrusive while four sectors along the scarp reflect the major textural changes. Synthesizing these observations and interpretations reveals a complex magmatic evolution.

Crystallization originated in the olivine phase field and derived OP basalts at the base of Sector E (BN-9-1&3) and midway through Sectors C (BN-4-10) and CE (BN-5-10). Yet in general, crystallization commenced primarily in the plagioclase phase field and generated P-type lavas followed by PO basalts. The location of P-basalts and P-diabases (Figure 7-8) indicates that the requisite conditions of fractionation, replenishment and incomplete mixing (Elthon, 1984; 1991) occurred in constructing both the upper and lower zones. A similar event must have also taken place in Sector E to produce PO basalts (BN-8-4) stratigraphically overlying OP basalts (BN-9-1&3). The presence of megacrysts at two levels in Sectors C (BN-12-1, BN-24-4&5) and CE (BN-1-

2&4, BN-10-2&19) demonstrates that this process C and CE recurred at least in the building of these sectors.

In other respects, magma dynamics in Sector E differed from the rest of the site. The system did not fractionate considerably producing at a maximum moderately phyric (Figure 7-7) and PCO (Figure 7-8) basalts which suggest a higher frequency of recharge. The shorter length of this interval accounts for the absence of megacrysts which require a stagnant reservoir for slow growth. In addition or as a consequence, basalt breccia were not a common component in accretion (Figure 7-3).

Sectors CE to CW trace the progressive decline in replenishment rate. The melt storage system fractionated substantially during these long intervals to form highly phyric and PC basalts (Figures 7-7 and 7-8), as well as megacrysts. In Sectors CE and C, the return to OP basalts in the middle of two upper zone profiles, implies that the new magma batch either did not intersect the previous one and established another chamber, or that these lenses are not very robust and hence, ephemeral. By Sector C, the melt resupply rate was so low that crystal clots (BN-4-7) formed from undercooling due to the fresh input (Dick and Johnson, 1995). In Sectors C (BN- 2-9, 3-7, 23-9, 24-6) and CW (BN-13-5), disequilibrium developed locally causing overgrowth rims on phenocrysts reacting further with the melt. This evolving state of the magma reservoir in Sectors CE through CW, is accompanied by a corresponding shift from mainly moderately to mostly sparsely and then dominantly aphyric basalts as is common with advancing differentiation (Natland et al., 1983).

The history of the lower zone in Sectors CE and C fits into this scenario in two possible ways: either diabase intrusion was synchronous with construction of the upper zone on-axis in each sector, or the diabase was emplaced off-axis simultaneously in both

sectors. The former option is preferred because the diabases crystallized from the plagioclase field which also prevailed during the build-up of the upper zone. Hence, the switch into the plagioclase field could be explained as part of the repetitive fractionation-mixing cycles outlined above. It would also account for the absence of intermediate diabasic products in the P->PC sequence as forming the overlying PO and POC basalts. This alternative is further supported by the two diabase lobes documented previously with each roughly occupying a sector.

The domains in the upper zone show marked within-variation in grain size, phenocryst abundance, and petrographic assemblage. This indicates that the frequency of their formation is much lower than the changes in the underlying magmatic system. It also implies that domains are passive recorders of the petro-chemical dynamics i.e. occurring neither in response to and nor impacting the magma source. Thus, while domains may form by caldera collapse (Chapter VI) in association with some magmatic event, this mechanism primarily re-structures the upper crust.

7.5.3 Comparison with other mid-ocean ridge settings

The petrographic features of the WBD site have previously been noted in other areas of the ocean floor. The five basalt types have been described from several localities (Hekinian, 1982) and of the three diabase types, aphyric and PC microdiabases have been drilled off-axis from the East Pacific Rise [EPR] (Leg 34 - Thompson et al., 1976; Leg 140 Scientific Party, 1992). Highly porphyritic samples have also been recovered from the Mid-Atlantic Ridge [MAR] (30% - Leg 78 Scientific Party, 1984; 50% in Leg 37 - Byerly and Wright,.1978), the Galapagos (45% in Leg 70 - Emmermann et al., 1983), the intermediate-spreading EPR (35% - Leg 111 Scientific Party, 1989) and the fast-spreading EPR (40-60% in Leg 92 - Goldfarb, 1986). The megacrysts, which are

abundant in Atlantic MORB (Flower, 1991), and the rare crystal clots have been observed in Hole 504B (Leg 140 Scientific Party, 1992; Leg 148 Scientific Party, 1993) but not at other intermediate- to fast spreading areas.

The main distinction of the WBD lavas is in the petrographic diversity and its spatial extent within the study site. The area includes a total of eight petrographic types from two crystallization series. With the exception of Hole 504B, four petrographic types at most, which are from the plagioclase series, are recorded along the EPR. Examples include the basalts from Galapagos (aphyric, P, PC and PO types in Leg 70 - Laverne and Vivier, 1983), 21°N EPR (aphyric, POC, O, and P types - Juteau et al., 1980), 8-9°N EPR (PC, POC and PC types in Leg 54 - Hekinian and Morel, 1980), and 19°S EPR (PC, PO, P and aphyric types in Leg 92 - Goldfarb, 1986; Pearce et al., 1986). Along the MAR, a large basalt variety is present in the rift valley as at 45°N or at 36°50'N, where five basalt types (picrite, O, PO, P and aphyric) are observed across-axis, with the plagioclase and olivine series separated between the valley wall and floor (Hekinian, 1982). Therefore, the WBD site bears more similarities petrographically to slow rather than fast spreading centers.

The WBD site does share many petrographic similarities with Hole 504B however. Hole 504B (Leg 140 Scientific Party, 1992) also has a sharp, 50-100 m thick transition between the basalt and diabase zones (Becker et al., 1989) across which the petrographic types increase from 3 to 5 downsection, and an olivine series commences. The petrographic types are the same at both locales except for the P basalts and diabases at the WBD and an OC diabase in Hole 504B (Leg 111 Scientific Party, 1989). The two sites are also alike in that two-thirds of the samples are porphyritic with the same spread in phenocryst abundance over a broad range (0-35%) for the basalts and a narrow range

for the diabases (<10%). Other similarities include the fine- to medium-grained, POC basalts at the top of the section while the aphyric (Kempton et al., 1985) and OP (Leg 148 Scientific Party, 1993) basalts become more abundant with depth. At Site 896 near Hole 504B, PO basalts are found at shallower levels than OP basalts in the core mirroring the situation at the WBD (Leg 148 Scientific Party, 1993). Other common features include the megacrysts and crystal clots (Leg 140 Scientific Party, 1992) although they are only found in the upper basaltic zone at the WBD.

However, there are differences. In Hole 504B, the proportions of the aphyric, POC and PO basalts are 42%, 37% and 21% respectively (Leg 83 - Kempton, 1985) whereas at the WBD, they comprise only 11%, 21% and 12% of the basalts which are mainly of PC type (44%). In addition, only one-third of the sheeted dike complex is aphyric in Hole 504B as compared to the more than two-thirds of the intrusives in the WBD although this may be partly due to the different modes of diabase emplacement.

These comparisons suggest that there are a number of petrographic attributes and a consistent pattern of evolution that is unique to intermediate-rate spreading settings. However, in terms of textural characteristics, these settings share a closer affinity to slow rather than fast spreading ridges. Consequently, there is likely to be a spectrum in style of magmatic accretion by spreading rate regime.

7.6 Conclusions

A summary of the major points presented in this chapter include the following:

1. The WBD site exposes upper crustal rocks (basalts, diabases, and basalt breccias) with a variety of grain sizes (glassy to coarse-grained), a range in degree of crystallinity (aphyric to highly phyric) and diverse phase assemblages (9 types).

2. The volcanic suite has been derived from two extensive sequences of crystallization originating in both the olivine (O->OP->OPC->PC) and plagioclase (P->PO->POC->PC) stability fields suggesting that these lavas span the range from relatively primitive to highly evolved.

3. The igneous textures indicate a complex history of crystallization in a long-lived storage system that stagnated and developed disequilibrium melt pockets but which was interrupted by episodes of magma replenishment and mixing followed by continuing *in-situ* fractionation in the upper crust.

4. On petrographic grounds, the crustal section is divided at 3596±171 m depth into an upper zone of extrusive basaltic lavas and a lower intrusive zone of at least two diabasic bodies.

5. Four sectors are defined by changes in the magmatic system over time. The Sector E to CE divide marks a shift from low to high extents of crystallization (and by implication from less to more highly evolved magmas) and in style of accretion that involved producing breccia and intruding diabase to the west. The Sector CE to C divide reflects a shift in magma chamber dynamics from developing dominantly moderately phyric to aphyric lavas. The Sector C to CW divide represents a return to upper crustal construction without diabase intrusion.

6. The basaltic domains can not represent solely magmatic constructs because they do not correspond texturally either to internally consistent characteristics or to systematic trends. Instead, the cooling regime was variable and significant fractionation occurred over the course of their buildup. They could be the output of multiple or replenished magmatic systems with closed system behavior only becoming prevalent during accretion of the top of the sector.

7. The megacrysts, clots and phenocryst assemblages reflect a complex history of magma injection, occasional mixing and continuing fractionation at shallow levels during accretion of the WBD section.

8. The petrographic similarities between the WBD section and Hole 504B suggest that the magmatic processes interpreted here can be generalized to intermediate-rate spreading settings and that the style of accretion varies between the spreading rate regimes.

Table 7-1: Summary of petrographic types, defined by rock type (B=basalt, D=diabase) and phyric content, that were recovered by *Nautile* from the N. WBD study site. The petrographic types are characterised further by abundance, textural features, and normative composition from Table 7-2.

Petro Type	% of B/D	% of Total	Rock Type	Phyric Content	Crystal-linity	Granularity	Textural Features and Normative Characteristics
I	44	30	Basalt	plagioclase-clinopyroxene	sparsely- to highly phyric	glassy to medium-grained	Phenocrysts, glomerocrysts and megacrysts in crystal morphology Some clinopyroxene of titanaugite composition Rare megacryst clots Di-Hy-Q, Di-Ol-Hy and Di-Ne-Ol in the norm
III	21	14	Basalt	plagioclase-clinopyroxene-olivine	sparsely- to highly phyric	glassy to medium-grained	Phenocrysts, glomerocrysts and megacrysts in crystal morphology Few clinopyroxene of diopside composition Some marked Fe-rich olivine compositions Di-Hy-Q and Di-Ol-Hy in the norm
IV	11	7	Basalt	-	aphyric	very fine- to medium-grained	Di-Hy-Q, Di-Ol-Hy and Di-Ne-Ol in the norm Plagioclase xenocrysts
V	11	7	Basalt	plagioclase	sparsely phyric	fine- to medium-grained	Only phenocrysts in crystal morphology Di-Hy-Q and D-Ol-Hy in the norm
VI	14	9	Basalt	plagioclase-olivine	sparsely- to moderately phyric	glassy to medium-grained	Only phenocrysts in crystal morphology Few clinopyroxene of titanaugite composition in groundmass Di-Hy-Q and Di-Ol-Hy in the norm
II	77	21	Diabase	-	aphyric	very fine- to coarse-grained	Several clinopyroxene of titanaugite composition in groundmass Plagioclase xenocryst Only Di-Ol-Hy in the norm
VII	15	4	Diabase	plagioclase	sparsely phyric	fine-grained	Includes only phenocrysts in crystal morphology Scarce clinopyroxene of titanaugite composition in groundmass Only Di-Ol-Hy in the norm
VIII	8	2	Diabase	plagioclase-clinopyroxene	sparsely phyric	fine- to medium-grained	Only phenocrysts in crystal morphology Only Di-Ol-Hy in the norm
IX	-	-	Breccia	-	-	-	Di-Ol-Hy and Di-Ne-Ol in the norm

Table 7-2: Relation of normative composition (Di=diopside, Ol=olivine, Hy=hypersthene, Q=quartz, Ne=nepheline) to petrographic type (Appendix G).

	No type	I	III	IV	V	VI	II	VII	VIII	IX	Total	% of total
Di-Hy-Q		10	9	3	2	3					27	31
Di-Ol-Hy	3	10	4	4	5	5	18	3	1	4	57	66
Di-Ne-Ol	1	1				1					3	3

Table 7-3: Characteristics of the phenocryst phases in the seven, phyric petrographic groups among the WBD basalts and diabases (abbreviation: diab).

Petrographic Grp.	Phenocrysts	%	mm	Morphology	Features
Type I or PC basalt	plagioclase	1-20	0.1-3.6	Phenocrysts - sub- to euhedral laths and tabular grains	Albite twinning (BN-3-7); oscillatory (BN- 4-7, 24-14) and hour-glass (BN-10-15) zoning; overgrowth rim (BN- 3-7, 23-9, 24-6)
		2-25	0.6-2.2	Glomerocrysts - subeuhedral laths and tabular grains	Carlsbad twinning (BN-24-6); zoning (BN-24-6)
		<6	1-4.6	Megacrysts - euhedral laths and tabular grains	Rare - <10% of samples (BN- 13-3, 24-5)
	clinopyroxene	1-5	0.1-2	Phenocrysts - euhedral to anhedral	Some Carlsbad twinning (BN- 10-11, 24-5) and Ti-augite compositions (BN- 8-1, 10-11); overgrowth rim (BN-13-5)
		1-15	0.2-1.8	Glomerocrysts - euhedral to anhedral	Some Carlsbad twinning (BN-24-6) and Ti-augite compositions (BN-5-9)
Type III or PCO basalt	plagioclase	2-20	0.2-1.8	Phenocrysts - euhedral to anhedral laths and tabular grains	Carlsbad twinning (BN- 1-3,1-4,4-14,6-6,6-7) and oscillatory zoning (BN- 1-3,4-13,6-7,8-5)
		3-24	0.2-3	Glomerocrysts - <3 mm laths <1 mm tabular grains	Carlsbad twinning (BN- 4-12,4-14) and oscillatory zoning (BN- 1-3,4-9)
			2.8-6	Megacrysts	In 17% of rocks; more An-rich (BN-1-2) than glomerocrysts; twinning and zoning (BN-1-4)
	clinopyroxene	2-5	0.5-2.8	Phenocrysts - sub- to euhedral	Some Carlsbad twinning (BN-8-5)
		2-20	0.2-1.5	Glomerocrysts - anhedral to euhedral	Some Carlsbad twinning (BN- 4-9, 4-13)
	olivine	1-5	0.4-1.4	Phenocrysts - euhedral to anhedral	Marked pleochroism=>Fe-rich comp. (BN-6-11); oscillatory and sector zoning (BN-1-3)
		1-2	0.3-0.6	Glomerocrysts - sub- to anhedral	Marked pleochroism => Fe-rich comp. (BN-1-4)
Type V or P basalt	plagioclase	1-10, 1-2 av.	0.5-2.4	Sub- to euhedral tabular grains and laths	Carlsbad and albite twinning; oscillatory and discontinuous oscillatory zoning
Type VIa or PO basalt	plagioclase	4	1-3	Sub- to anhedral laths and tabular grains	Carlsbad (BN- 2-9, 4-1, 10-1) and albite (BN-4-1) twinning, oscillatory zoning (BN- 4-1, 10-6); overgrowth rim (BN-2-9)
	olivine	1	<3	Equant to anhedral	
Type VIb or OP basalt	olivine	2-20	0.1-1.2	An- to subhedral	4 of 5 samples with 1-2 of 1, 1.6, 2.4 and 3 mm
	plagioclase	1-10	1-1.8	Eu- to anhedral laths; some tabular	Oscillatory (BN- 5-10, 10-6) and sector (BN-5-10) zoning; few overgrowth rims (BN-4-10)
Type VII / P diab.	plagioclase	5-10	2-4	Tabular grains and laths	
Type VIII / PC diabase	plagioclase	3-4	1.6-4	Subhedral	Carlsbad twinning, altered
	clinopyroxene	3-7	2-2.6	Sub- to anhedral	

Table 7-4: Relation of petrographic type (in order of average maximum granularity) to grain size and phyric abundance from Appendix E-3.

Types	II - A diabase	VIII - PC diab	V - P basalt	IV - A basalt	VI - PO basalt	VII - P diabase	III - PCO bas	I - PC basalt	Total observations
Glassy					1		3	7	11
Very fine-grained	1			2			4	11	18
Fine-grained	3	1	6	4	4	4	4	8	34
Medium-grained	11	1	1	1	4		3	3	24
Coarse-grained	5								5
Aphyric	20			7					27
Sparsely phyric		2	7		7	4	2	10	32
Moderately phyric					2		4	13	19
Highly phyric							8	6	14
Total of type	20	2	7	7	9	4	14	29	92

Abbreviations: Gl = glassy, V.fg = very fine-grained, Mg = medium-grained, Cg = coarse-grained; Ap = aphyric, Sp = sparsely phyric, Mp = moderately phyric, Hp = Highly phyric; Types I-VIII as defined in Appendix E and in text; Bas = basalt, Diab = diabase, and Brx = breccia.

Table 7-5: Relation of lithologic units to grain size, petrographic type and rock type based on numbers of observations recorded in Appendix D.

	Gl	V.fg	Fg	Mg	Cg	Ap	Sp	Mp	Hp	I	II	III	IV	V	VI	VII	IX	Bas	Diab	Brx
Joint/massive				3	2	5					5								7	
Thick-layered		1	11	8	4	13	6	1	1	2	10		3	2	3	1	3	12	11	3
Dykes		1	4	2	1	1	4	1	1	2	1	1		1		2	1	5	4	1
Blocky flows	1	2	8	2		2	5	3	3	5		4		3				14		
Spires	1	3				1		2		2		1		1			1	4		1
Pillow flows	1	3	4	3			3	3	5	5		5			1			11		
Broken pillows	1								1			1						1		
Thin sheets	1	1					2			2							1	3		1
Diced units	2	1		1		1		1	1	2	1	1						3	1	

Table 7-6: Petrographic attributes of the upper and lower outcrop zones in the WBD study site.

	UPPER ZONE	LOWER ZONE
EXTENT	Present in all four sectors of the site	Present in Sectors C and CE (minor in E)
ROCK TYPE *Figure 7-2*	Composed of basalt with minor diabase, metabasalt and breccia horizons. These minor rock types with the addition of metadiabase (BN-24) increase in abundance from 3300 m to 3650 m depth and form an altered transition zone.	Consists of diabase. Metabasalt and basalt breccia become prevalent between 4050 m and 4300 m reflecting the alteration associated with the landslide (grid square d-8 in Figure 6-1c) in Sector CE and with a major fault (grid square e-5 in Figure 4-5a) that truncates the outcrop exposure in Sector C.
GRAIN SIZE *Figure 7-4*	Comprises dominantly fine-grained basalt with a few intervals of very fine-grained basalt. Sector CE includes minor horizons of basalt breccia and very fine-grained diabase while Sector C has rare occurrences of coarse-grained basalt and diabase. BN-01 is an exception and consists primarily of medium-grained basalt. A 350 m thick transition above the contact is formed by medium-grained basalts and an increased abundance of basalt breccia and very fine-grained diabase. West of BN-03, the upper zone below 3650 m is distinguished by a change from fine- to very fine-grained basalt up-section and includes minor horizons of very fine- and fine-grained diabase.	Composed of a core of medium-grained diabase and lesser coarse-grained diabase with fine-grained diabase concentrated along the base below 4050 m depth and the western margin in BN-03. This indicates some zoning by grain size in the diabase body.
PHENOCRYST ABUNDANCE *Figure 7-6*	Ranges from highly phyric to aphyric basalts. It includes a small proportion of aphyric diabases that occur mainly in BN-10. There is some distinction by sector with the aphyric basalts prominent at shallow levels in Sector C but not in CE. There is no evidence of a transition based on phenocryst abundance.	Aphyric diabase is prominent with lesser, sparsely phyric diabase especially at deeper levels in Sector CE.
PHENOCRYST CONTENT *Figure 7-8*	Constituted by PC, PCO and aphyric basalt as well as minor aphyric diabase above 2900 m. Between 2900 m and 3650 m, P basalt and basalt breccia also occur. A transition is apparent only by the additional presence of PO basalt from 3550 m to 3700 m depth. The upper zone below 3650 m is distinguished by the absence of PCO and PO/OP basalt as well as PC diabase west of BN-3 and by the presence of OP basalt east of BN-8.	Comprised mostly by aphyric diabases with lesser P diabases particularly at the deepest levels of outcrop exposure and minor PC diabase in BN-02.
OXIDES	Magnetite abundant (Nehlig, unpubl. data)	Titanomagnetite widespread; ±ilmenite-sphene (Nehlig, unpubl. data)

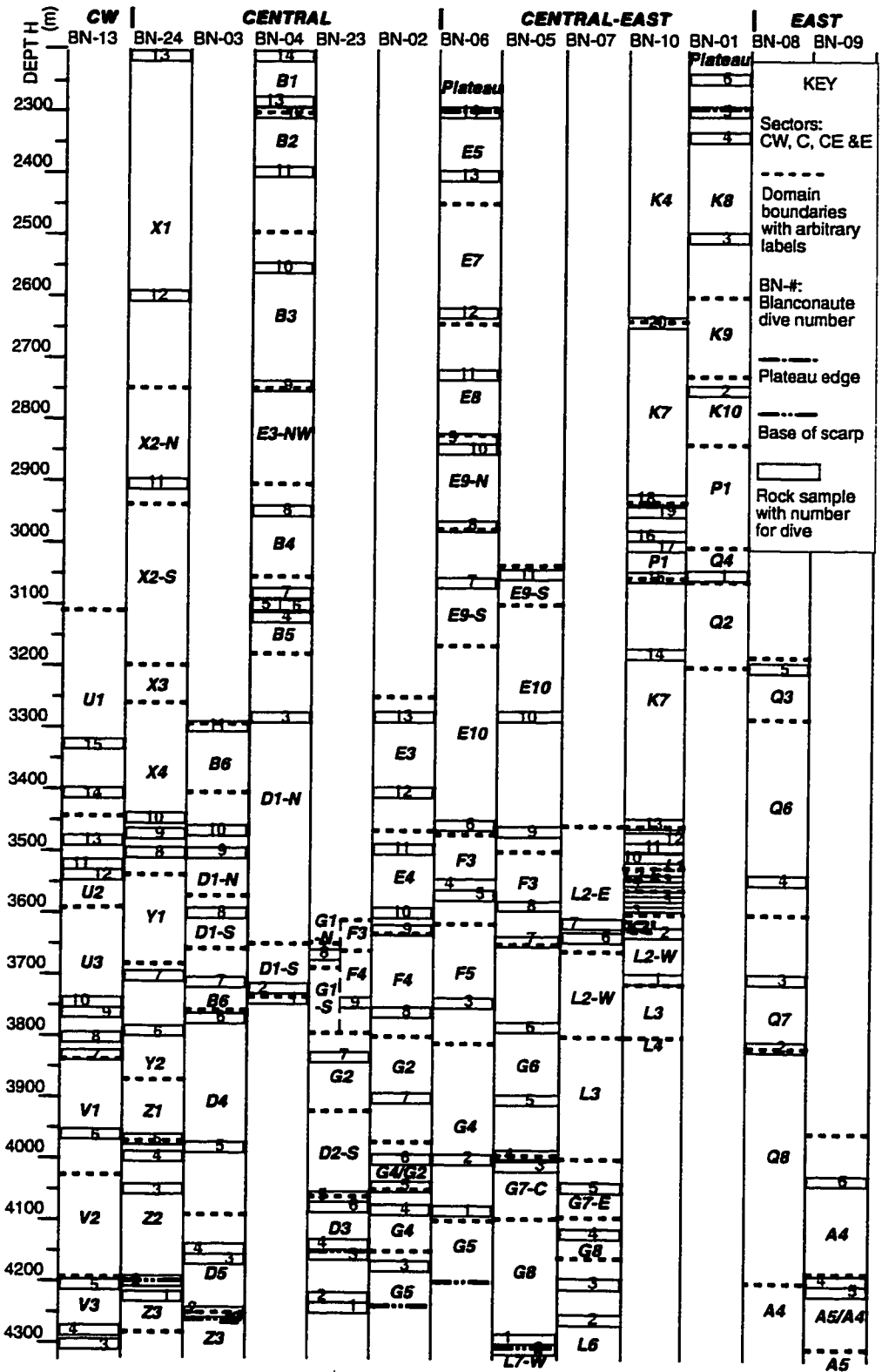

Figure 7-1: Location of samples along roughly vertical dive traverses (except for the horizontal BN-23) up the north WBD scarp. The profiles, arranged from west to east across the study site, show the rock in relation to depth, and to the domains and sectors.

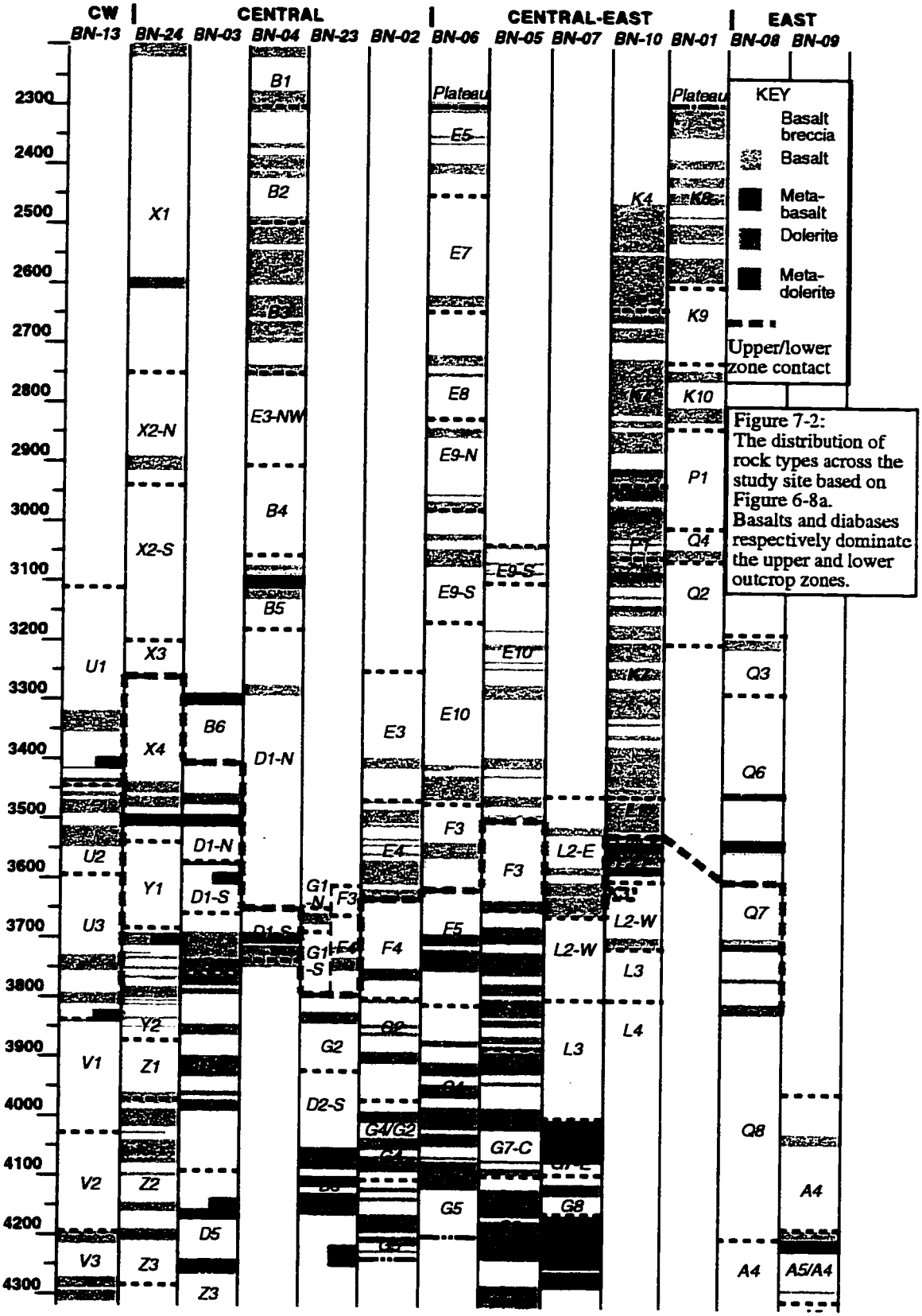

Figure 7-2:
The distribution of rock types across the study site based on Figure 6-8a.
Basalts and diabases respectively dominate the upper and lower outcrop zones.

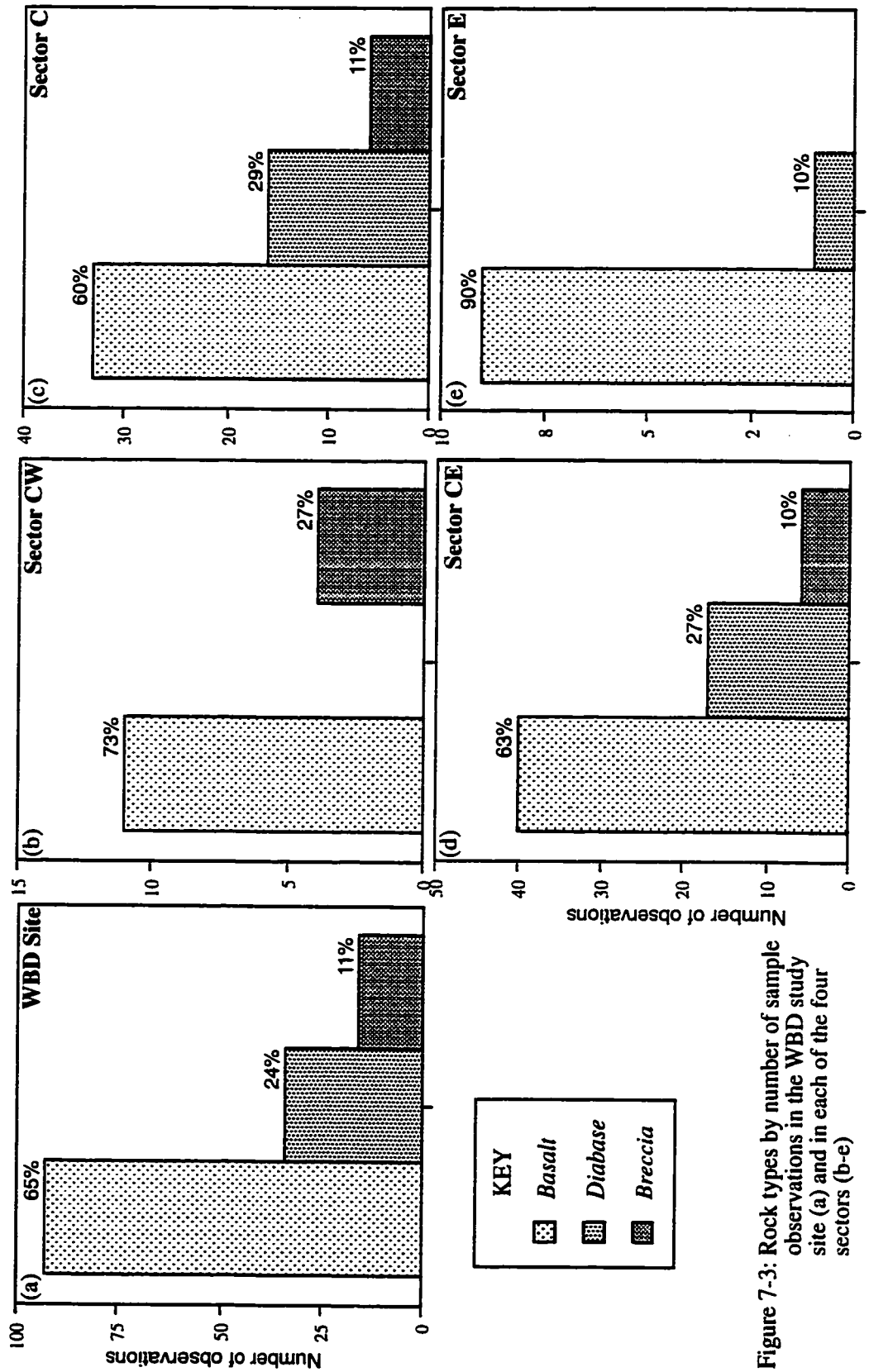

Figure 7-3: Rock types by number of sample observations in the WBD study site (a) and in each of the four sectors (b-e)

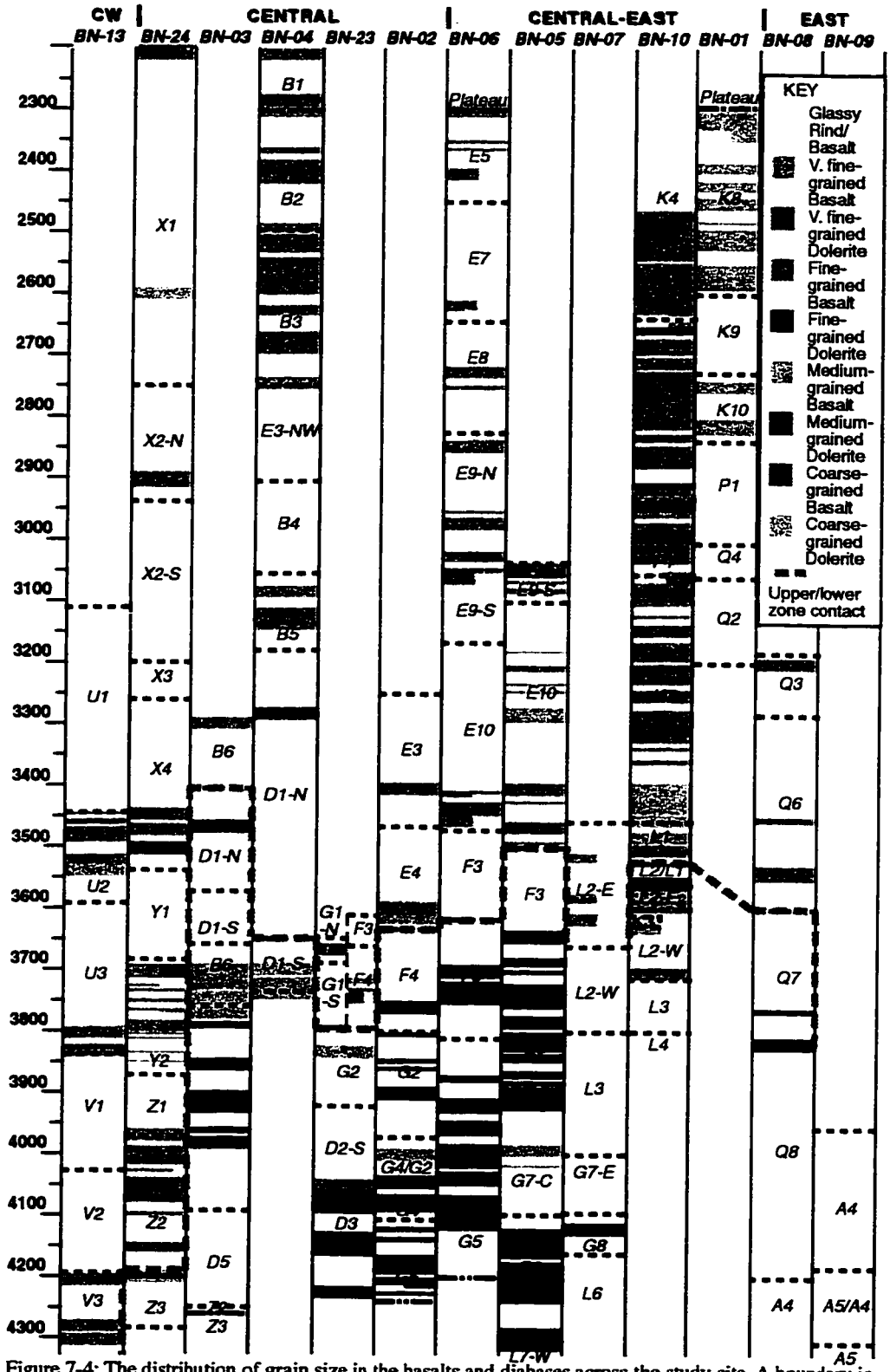

Figure 7-4: The distribution of grain size in the basalts and diabases across the study site. A boundary is delimited by the medium- to coarse-grained diabases in the lower zone and the glassy to very fine-grained basalts and diabases in the upper outcrop zone.

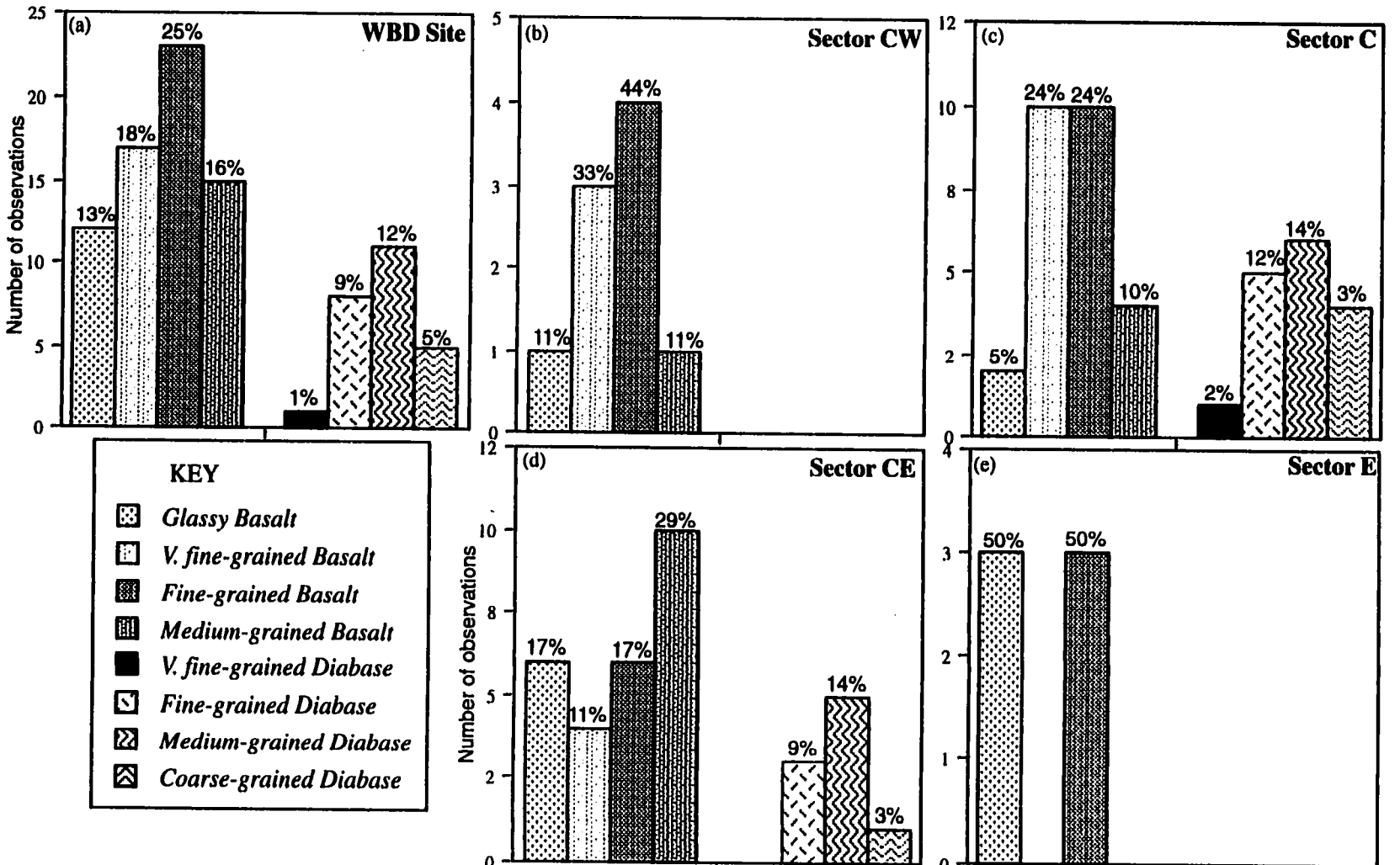

Figure 7-5: Grain size by number of sample observations and percentage in the WBD study site (a) and in each of the four sectors (b-e). Note that the one coarse-grained basalt sample (BN-4-3) in Figure 7-4 was labelled from hand specimen but not included in this petrographic study.

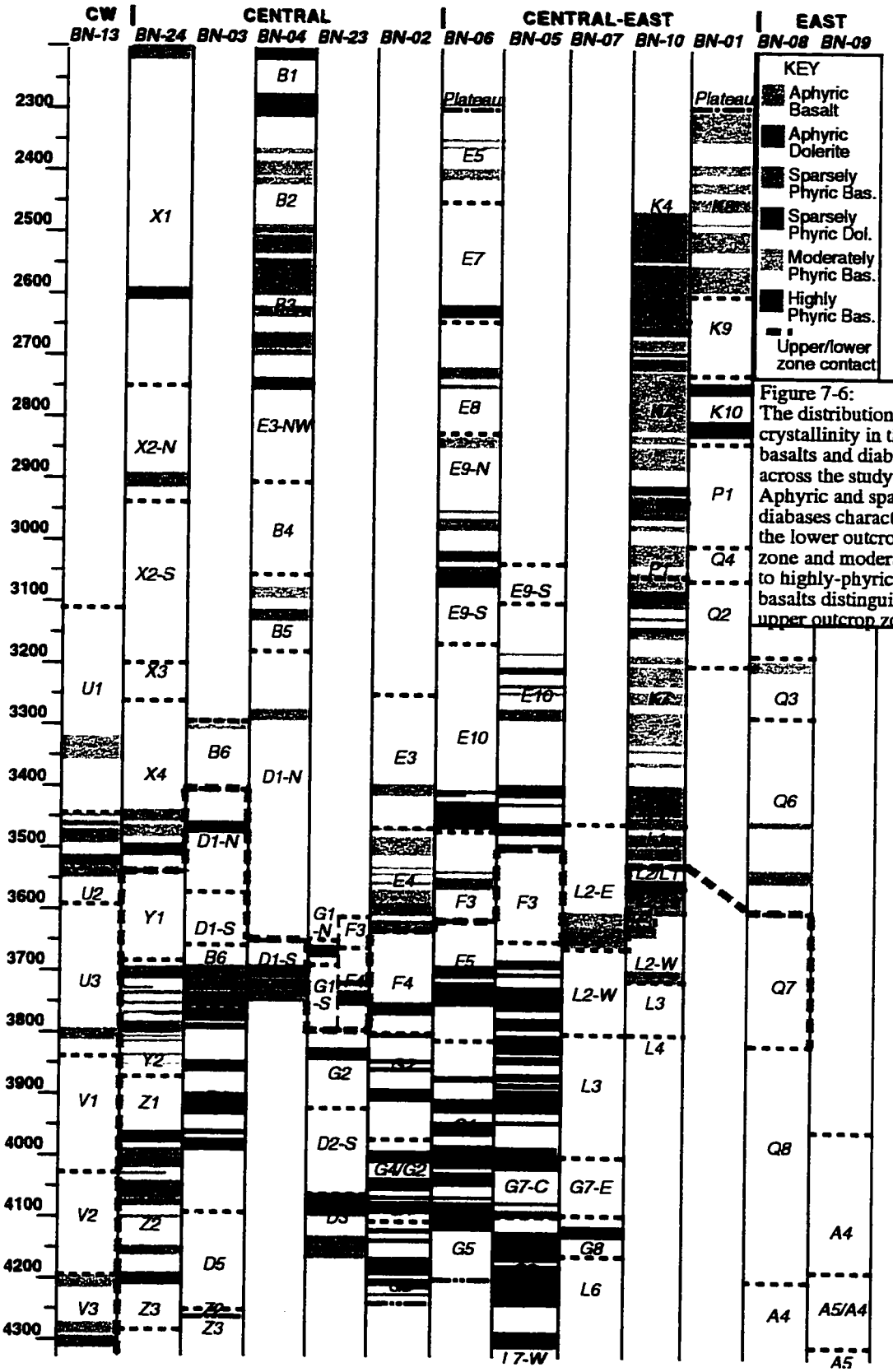

Figure 7-6:
The distribution of crystallinity in the basalts and diabases across the study site. Aphyric and sparsely diabases characterize the lower outcrop zone and moderately- to highly-phyric basalts distinguish the upper outcrop zone.

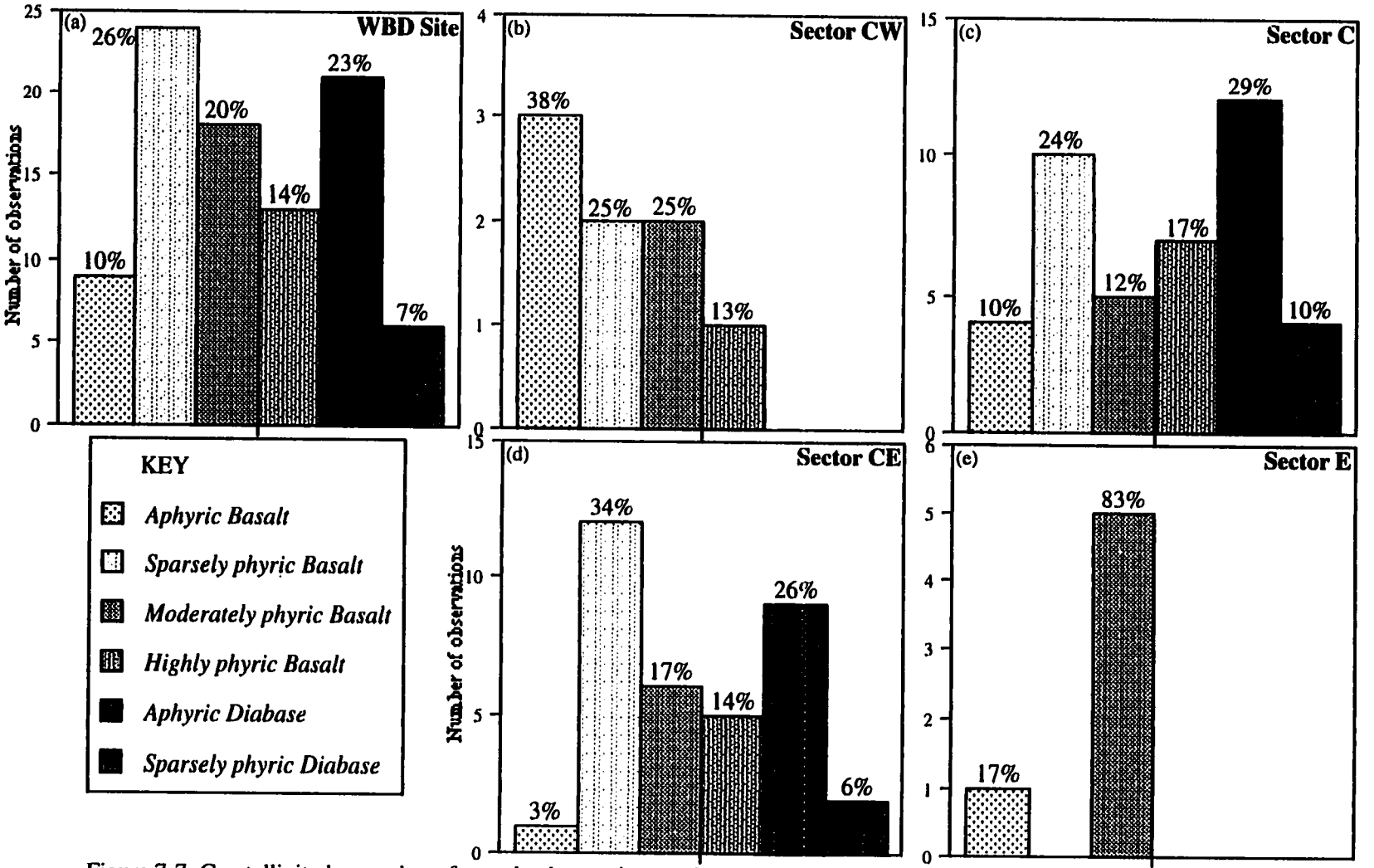

Figure 7-7: Crystallinity by number of sample observations and percentage in the WBD study site (a) and in the four sectors (b-e)

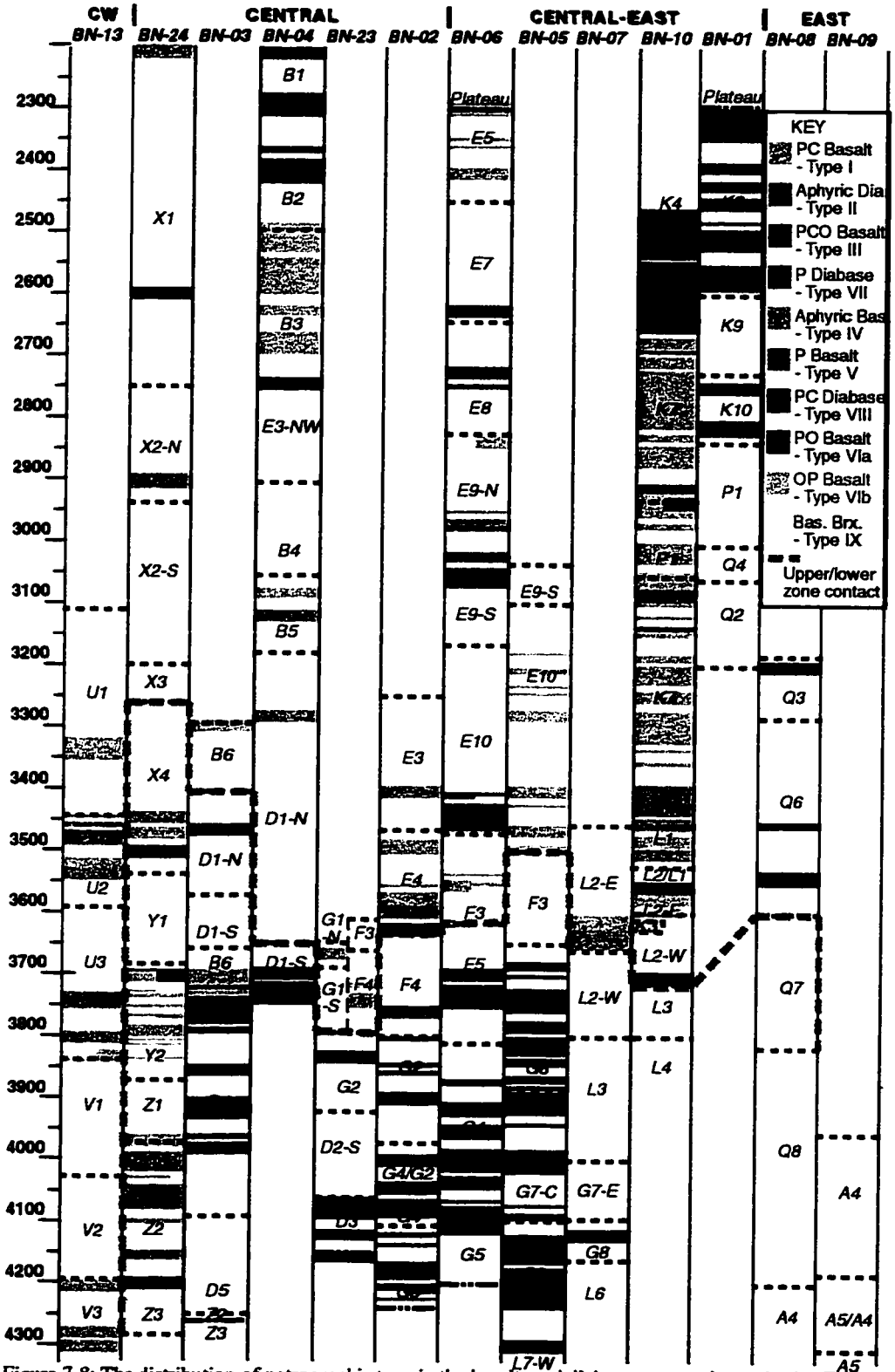

Figure 7-8: The distribution of petrographic type in the basalts and diabases across the study site. The OP and PCO basalts are present only in the upper zone while the P and PC diabases are found only in the lower zone.

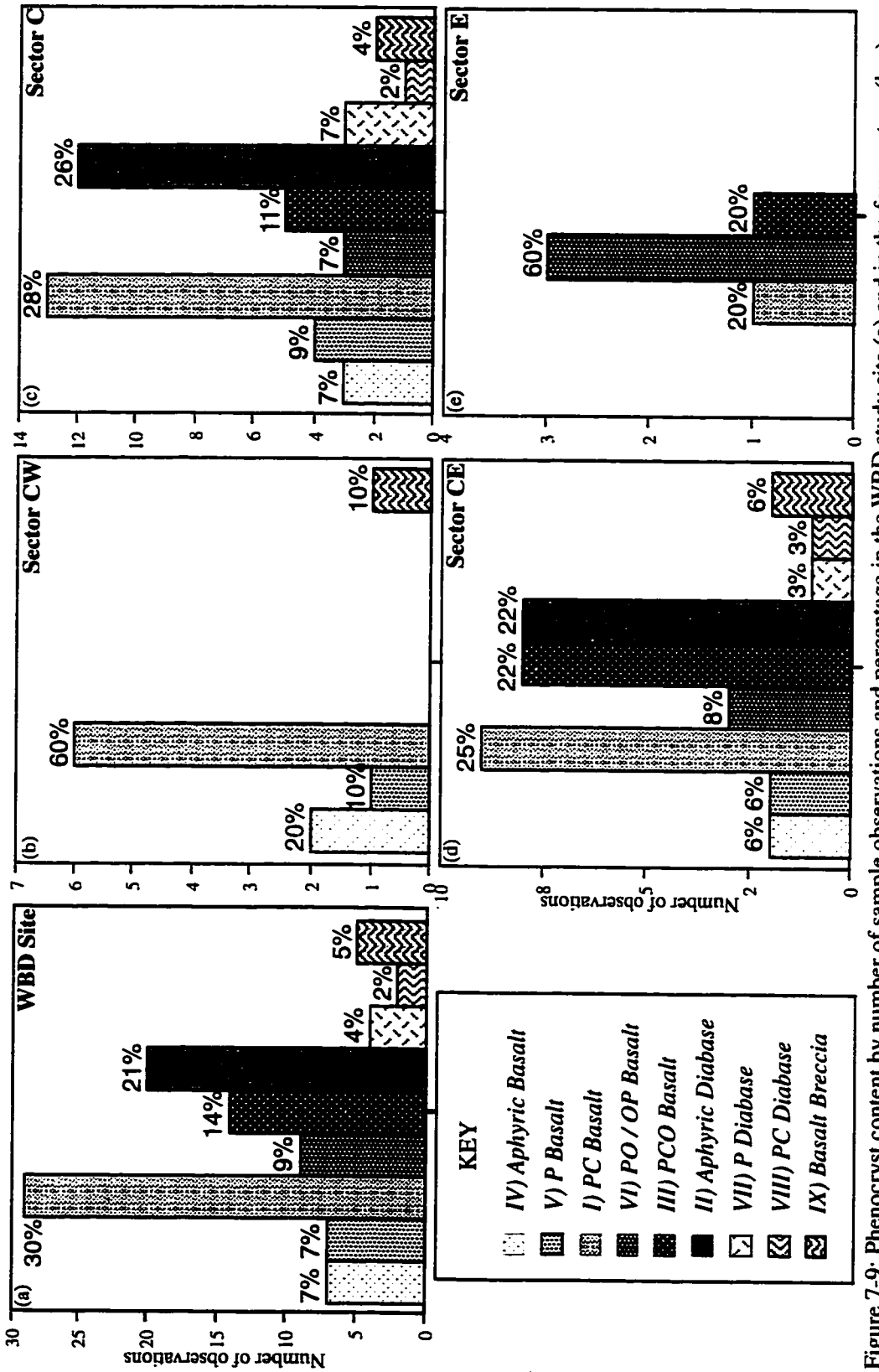

Figure 7-9: Phenocryst content by number of sample observations and percentage in the WBD study site (a) and in the four sectors (b-e)

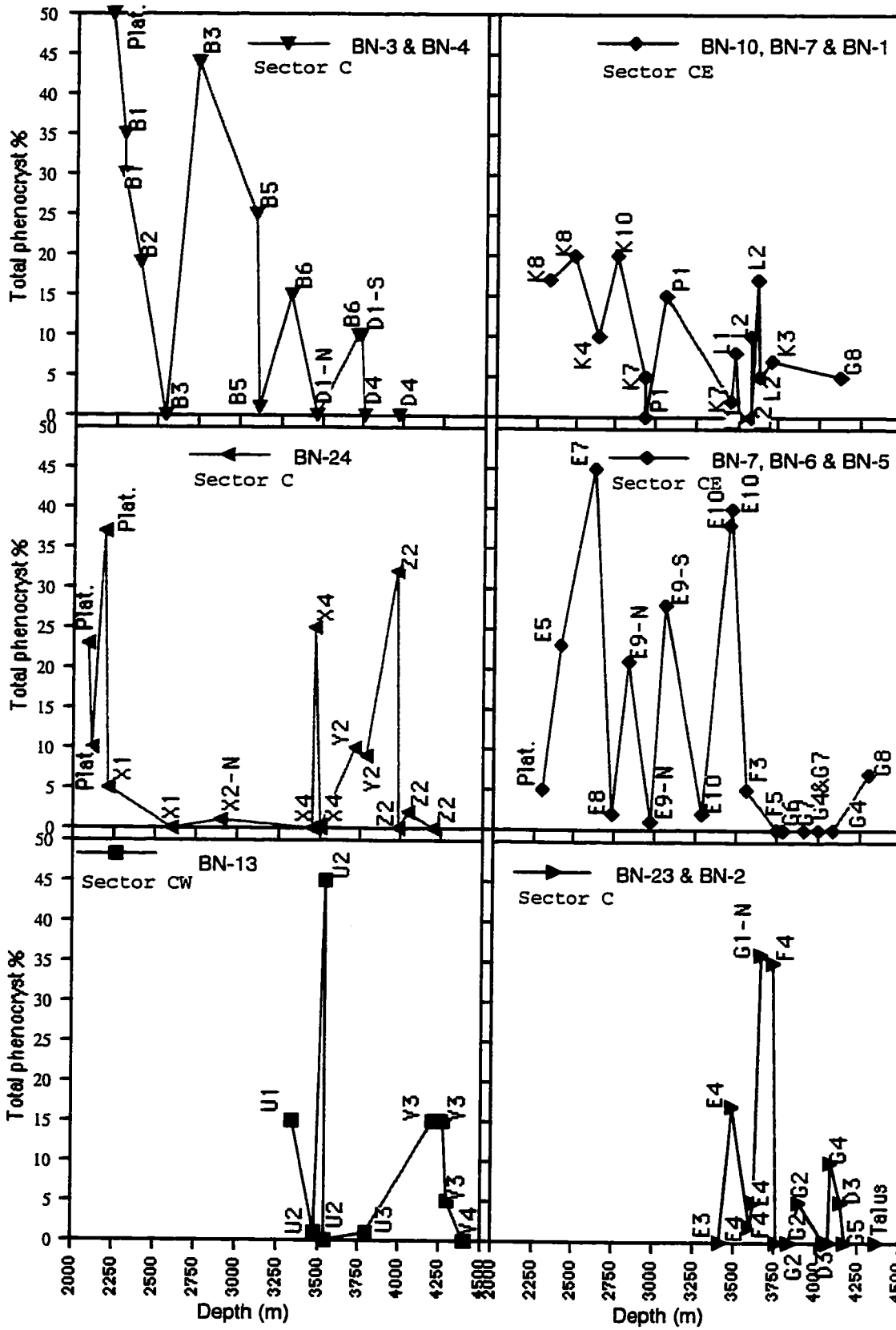

Figure 7-10: Total phenocryst abundance (estimated as percentage from thin section) by depth in the WBD section and labelled by domain

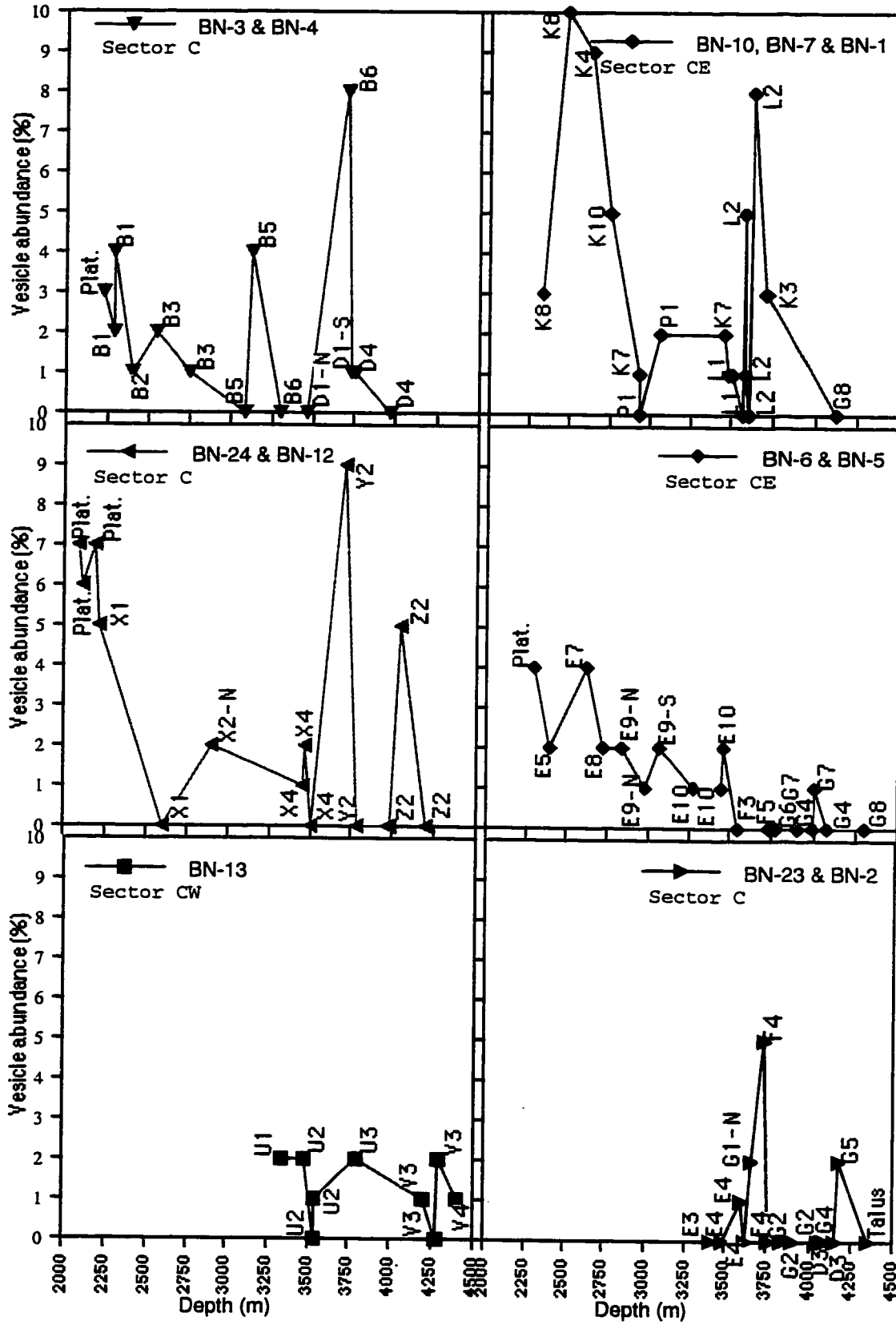

Figure 7-11: Vesicle abundance (estimated as percentage of thin section surface area) by depth in the WBD section and labelled by domain

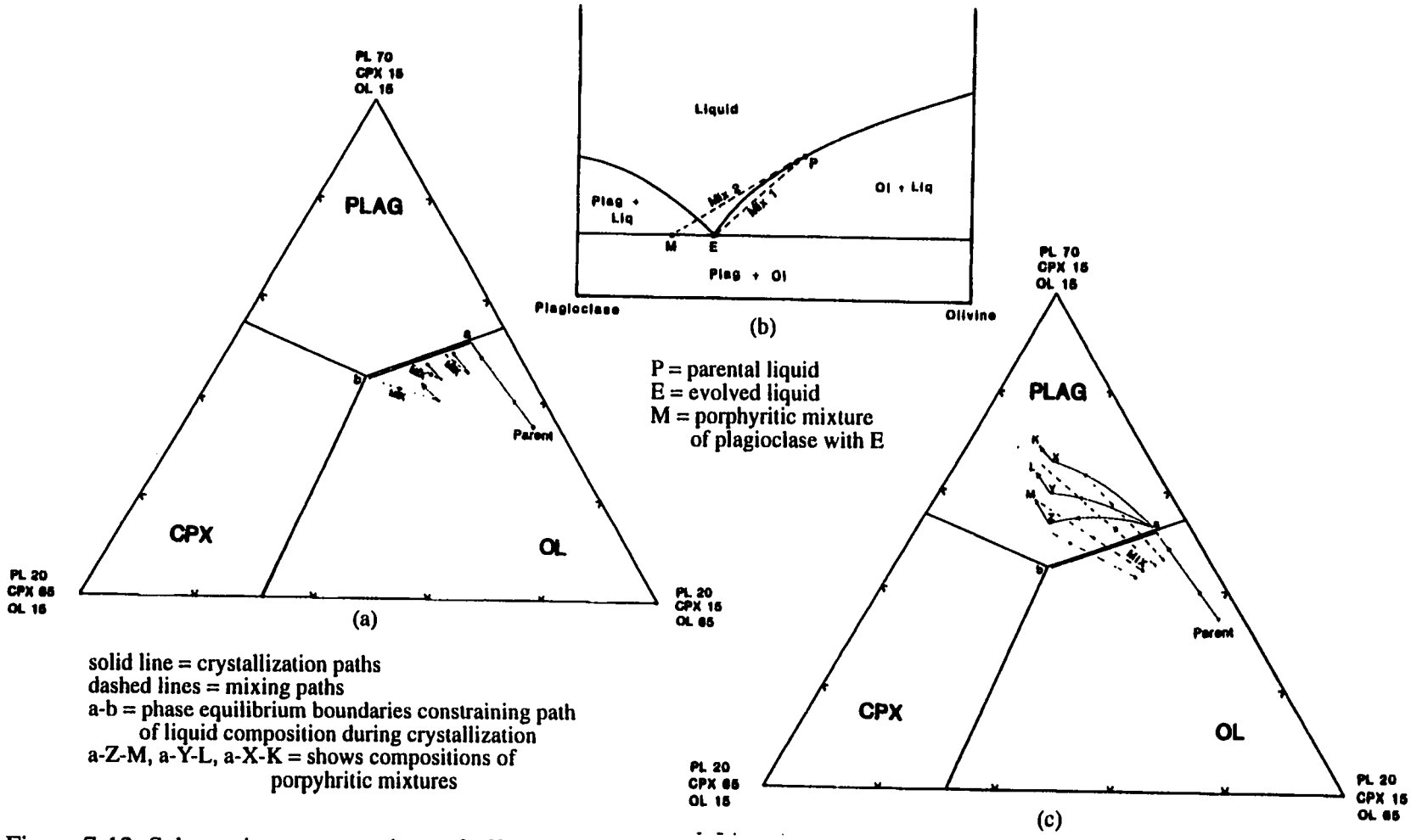

Figure 7-12: Schematic representations of effects of magma mixing (from Elthon, 1984)
(a) The effects of magma mixing when a parental liquid episodically replenishes a fractionating magma chamber
(b) Two thermal effects of magma mixing produced by varying percentage of suspended plagioclase
(c) If plagioclase crystallizing from liquid remains suspended, the input of a parental batch will result in mixing lines with hybrids lying within the plagioclase or olivine fields, or along the pseudo-divariant surface.

CHAPTER VIII: GEOCHEMISTRY OF THE LAVAS: EVIDENCE FOR HETEROGENEITY AND IMPLICATIONS FOR MAGMAGENESIS

8.1 Introduction

The along- and across-axis variability in mid-ocean ridge basalt [MORB] composition from the capping veneer of lava flows is better known than the geochemical variation in accreting a local section of the upper crustal basement. Despite this bias, the diversity in petrology (Hekinian, 1982; Natland, 1991) and geochemistry (BVSP, 1981; Sun and McDonough, 1989), resulting from the various processes involved in magmatic evolution (Wilkinson, 1982; Langmuir et al., 1992), is linked to differences in spreading rate (Niu and Batiza, 1993; Niu and Hekinian, 1997), the geometry of magma chambers (Sinton and Detrick, 1992), structural segmentation of the axis (Thompson et al., 1985; Langmuir et al., 1986), or mantle temperature (Klein and Langmuir, 1987; Langmuir et al., 1992).

Detailed studies of a more representative number of spreading centers indicate that such correlations are not entirely valid. Several such examples can be cited in terms of shallow crustal behaviors. Megacrysts, which are inferred to be the products of mixing (Stakes et al., 1984), are not only present at the slow-spreading Mid-Atlantic Ridge [MAR] (Flower, 1991) implying that this magmatic process is not spreading rate dependent. Likewise, it is now found that East Pacific Rise [EPR] magma chambers are not always robust and their long-term state can vary (Batiza et al., 1996). Similarly, petrological segments need not correspond to structural segmentation (Batiza, 1996). The same applies to mantle conditions where heterogeneities (Sleep, 1984; Hart, 1988), variations in melt extraction (Niu and Batiza, 1991) and migration (Spiegelman and

Kenyon, 1992), or the kind of mantle flow regime (Spiegelman, 1996) can all significantly affect MORB petrogenesis. Consequently, the geochemical characteristics of crustal construction cannot be pre-determined from simplistic dichotomies of fast versus slow spreading, middle or ends of segments, or hot versus cold thermal anomalies.

The history of magmatic accretion can be understood by systematic and small-scale sampling with depth. Continuous suites of such samples along a flowline could be obtained by drilling but thus far only Hole 504B has substantially penetrated Layer 2 with 0-36% recovery in the extrusive section (Shipboard Scientific Party, 1992). This chapter presents the major, trace and rare earth element chemistry for *Nautile* dive samples from a central, 7 km * 13 km area along the south-facing scarp of the Blanco Fracture Zone (Figure 4-2). The study is supplemented with geochemical data from north-south oriented submersible transects across the entire Parks Plateau (Juteau et al., 1995). Previous workers in this region reported major and trace element data (Melson et al., 1976; Karsten and Delaney, 1988; Gaetani et al., 1995) for rocks dredged along the north and south walls of the intervening West Blanco Depression [WBD]. Here, the goal is to characterize the crustal composition of the central, ~2 km thick exposure and to determine the nature of the magmatic processes operating. The results from the study site are then compared with other seafloor areas to assess the extent to which these findings can be generalized.

8.2 Methods

A rigorous approach in this study is limited by the density of sampling across the WBD site (Figures 6-4a and 7-1). The available samples were further reduced in number after examination of the rocks and from their thin section descriptions (Appendix E-3). Rocks were excluded if they were intensely altered or of insufficient amount for

geochemical analysis (Appendix F-1) leaving 95 suitable samples. The samples were prepared by the procedure outlined in Appendix F2-3 and the method for acquiring whole-rock data by ICP-ES, AES and AAS analysis is documented in Appendix F-4. The detection limits and error estimates of the data, based on analysis of duplicate samples as well as external standards, are listed in Table F-1. In general, analytical errors are between 1-3% for major elements, and approximately 5% for trace and rare earth elements (REE) except Er which has an error of 10%. The analyses are tabulated in Appendix G.

8.3 Results

8.3.1 The Effect of Alteration on Bulk-rock Chemistry

Although the samples for geochemical analysis were selected and prepared so as to exclude obvious signs of alteration (i.e. minor veins or cracks), all the rocks are altered to varying degrees.

The extent of alteration has been visually estimated in thin section (Appendix E-3) from the percentage of secondary minerals. These are dominated by chlorite in the groundmass which exceeds any other secondary phase or material that rims or fills vesicles and vugs. For reference, three of the most altered basalts (BN- 3-11, 10-2, 24-5) not included in the geochemical part of this study have 30-50% chlorite in thin section (Figure 8-1e). In general, the WBD rocks are no more altered than those studied from drill-holes (e.g. <60% in Hole 504B diabases - Bach et al., 1996).

The effects of alteration on bulk-rock chemistry can be gauged by the loss on ignition (LOI) since LOI values broadly correlate with low-temperature hydration of basalts (Alt et al., 1993). In general, the WBD rocks have high LOI values up to 3.5 wt.

% (Figures 8-1a-d) in comparison to <1.61 wt. % for Hole 504B diabases (Leg 148 Shipboard Scientific Party, 1993). There are six outliers (BN- 6-4, 13-1, 23-2, 24-1, 24-6 and 24-9) with LOI >5 wt. % which are omitted in considering the primary compositions (Table 8-1).

Secondary variations are recognizable in the abundances of K and Na which vary systematically with LOI (Figures 8-1a-b). The altered samples are characterized by K_2O >0.75 wt. % and Na_2O >4 wt. %, and accordingly, another 2 samples are excluded from subsequent analysis (BN- 7-5, 13-5). High LOI and K_2O commonly indicates replacement of olivine (as for Leg 92 - Pearce et al., 1986) which supports the petrographic inference (Chapter VII). The WBD rocks display a tendency towards an inverse relation between K_2O and the intensity of chlorite alteration (Figure 8-1e) as well as percentage of vesicles (Figure 8-1f) which reflects infilling by smectite. Similarly, correlations of alteration and enrichment in the large ion lithophile (LIL) elements Rb and Ba are observed (Figures 8-1c-d).

The mobility of other elements also emerges from plotting elements versus LOI. SiO_2 and Co systematically decrease with increasing LOI (Figures 8-2a-b), CaO shows more scatter but decreases in the same direction (Figure 8-2c), while MnO and Sr are not well-correlated with LOI (Figures 8-2d-e). The "mobile" elements identified for the WBD suite (K, Na, Rb, Ba, Si, Co, and Ca) further display a lack of coherency in variation diagrams versus MgO, as for example with CaO (Figure 8-4f). The rest of the elements, which includes the normally resistant, high field strength elements (HFSE) are minimally affected, as was noted for the Hole 504B diabases (Sparks, 1995). P_2O_5, TiO_2, Zr, Y, Nb and V slightly increases with LOI below 1 wt. % before declining with increasing LOI above 1 wt. %. This pattern is reversed for Al_2O_3, MgO (Figure 8-2f),

Mg # and Ni, and is more pronounced for some elements than others. The one exception is Cr which is unaffected by alteration.

8.3.2 Geochemistry of the WBD study site

The WBD lavas are comprised of four distinct groups, the N-, M-, T- and EG-types (Figure 8-3a). This classification is based on the extent of incompatible element depletion and enrichment relative to degree of differentiation. Selected major and trace element contents and useful ratios are plotted in Figures 8-4 to 8-7, while typical patterns of rare-earth element abundances normalized to primitive mantle (Sun and McDonough, 1989) are plotted in Figure 8-8. The averages, standard deviations and ranges in chemical composition of the groups are summarized in Table 8-1. Note that this scheme does not conform strictly to the criteria of Batiza and Vanko (1984) or Hekinian et al. (1989) who used cut-off values of (La/Sm)n and Zr/Nb, respectively, to define depleted, transitional, undepleted and alkalic groupings.

59% of the suite are normal or N-type MORBs (Figure 8-3a). Their average values (Table 8-1) of characteristic trace and rare earth element [REE] ratios (Zr/Nb: 29.3, Zr/Y: 2.8, Ti/Zr: 93 - Table 8-1) are close to those defined for this group from the seafloor (Zr/Nb: 31.8, Zr/Y: 2.6, Ti/Zr: 103 - Sun and McDonough, 1989). The group is on average moderately evolved (Mg #: 53 av. - Table 8-1) while ranging from relatively unevolved to highly evolved (Mg #: 40-67 - Figure 8-5). The samples are mainly (59%) olivine tholeiites with a smaller number (38%) of quartz tholeiites and two (4%) which are nepheline normative (BN- 13-11, 24-10)(Figure 8-3d). Texturally, the majority (77%) are basalts with a lesser amount (20%) of diabases (Figure 8-3b). About half of the group (56%) is FeTi rich with high TiO_2 (>2 wt. %), Fe_2O_3* (>12 wt. %) and V (380-600

ppm) but low Al_2O_3 (11.9-15.8 wt. %) concentrations. The FeTi lavas also occur mostly (90%) as basalts with some (10%) diabases.

A minor proportion of the suite (5%) is formed of transitional (Sun et al., 1979) or T-type MORBs (Figure 8-3a). Ratios involving only the highly and moderately incompatible elements (Figures 8-6a-f) show an overlap of the T- (e.g. Zr/Nb = 24-32) with the N-type MORB (Zr/Nb = 32). However, ratios of highly (e.g. Nb, La) or moderately (e.g. Nd, Zr) incompatible elements to slightly (e.g. Ti, Y, Yb) incompatible elements distinguish the T-type (eg. Figure 8-15). Accordingly, their geochemical characteristics (Nb: 3.6-12.1 ppm, Ti/Zr: 64-83, Zr/Y: 3.1-3.3, (La/Yb)n: 0.99-1.06) are consistent with intermediate enrichment between N-type (Nb: 2.33 ppm, Ti/Zr: 103, Zr/Y: 2.6, (La/Yb)n: 0.588) and E-type (Nb: 8.3 ppm, Ti/Zr: 82, Zr/Y: 3.3, (La/Yb)n: 1.908) MORB (Sun and McDonough, 1989). This group is moderately evolved on average (Mg #: 47 av. - Table 8-1) but varies from slightly to extremely evolved (Mg #: 34-62 - Figure 8-5) such that more than half (60%) are FeTi basalts. Unlike the N- and M-types, the samples include more quartz (60%) than olivine (40%) tholeiites (Figure 8-3d). Like the N-type, the T-type is composed by mainly (80%) basalts and lesser (20%) diabases (Figure 8-3b).

About a quarter of the suite (26%) form a group labelled M-type MORB (Figure 8-3a). They are highly depleted as compared to even N-MORB (Yb: 3.05, Y: 28 ppm, Zr: 74 ppm, La: 2.50 ppm, Nb: 2.33 ppm - Sun and McDonough, 1989) with low incompatible element abundances (Table 8-1) for their degree of evolution. This contrast to the N-type is also evident from their lower abundances for the same maximum Mg # (Table 8-1; Figures 8-6 and 8-7a-b). If M-type basalt simply originated by partial melting

of an extremely depleted mantle source, they ought to have lower Zr/Ti, Zr/Y, Nb/Nd, La/Nd, (La/Yb)n and higher Zr/Nb and Zr/La ratios than the N-type based on the relative incompatibilities of these elements. Of these ratios, the (La/Yb)n is commonly higher and >1 (Figures 8-7c-d) while the Zr/Nb and Zr/La ratios are lower (Figures 8-6b&d) which suggests that the strongly incompatible elements are comparatively less depleted than the moderately or slightly incompatible elements. Furthermore, they have unexpectedly low Zr/Nd values (Figure 8-6f) which implies that Zr may also be relatively over-depleted in this group. In addition, concentrations of the compatible elements (Cr and Ni) are considerably enhanced (Table 8-1) in some samples.

The M-type is only slightly evolved on average (Mg #: 61 av. - Table 8-1) and ranges from relatively unevolved to moderately evolved (Mg #: 47-69 - Figure 8-5). It includes some of the most primitive compositions (e.g. BN-9-1) - high Mg # (68.05), high MgO (10.10 wt. %), Ni (255 ppm) and Cr (366 ppm) abundances, and low TiO_2 content (1.03 wt. %) - for which there is no petrographic evidence to suggest that they might be cumulates (Appendix E). The samples are predominantly (85%) olivine tholeiites with minor (8%) quartz tholeiites and one (4%) which is nepheline normative (BN-3-2)(Figure 8-3d). Unlike the N- and T-MORBs, the M-type is composed more of diabases (60%) than basalts (36%) and of these, one diabase (4%) is FeTi rich (Figure 8-3b).

The fourth group is represented by a single sample of slightly evolved (Mg #: 60 - Table 8-1), olivine tholeiitic basalt (Figure 8-3d). It is similar in major, trace and rare earth element composition to those from the central Parks Plateau [PP], south of the Blanco trough (Figures 8-9a&c). Since this cluster is elongated toward enriched MORBs (Figure 8-9a) or primitive mantle (Figure 8-9c), it is labelled an enriched group or EG-type MORB. It is selectively enriched in only the highly incompatible elements (e.g. Rb,

Ba, Sr) (Figure 8-1) and LREE (Figure 8-6a&c) relative to the average N-type values. For example, this group has a Sr abundance up to 202 ppm that is the highest from the northeast Pacific. Its slightly incompatible element and HREE contents tend to be slightly less than the N-type (Table 8-1) which is consistent with its somewhat higher Mg # (57 vs. 53). Consequently, the group is distinguished by Zr/Nb, Zr/La and (La/Yb)n ratios (Figures 8-6a&c and 8-9a) approaching E- rather than N-type values (Sun and McDonough, 1989). It also has a mantle normalized REE pattern (Figure 8-8d) as well as Ti/Zr and Zr/Y ratios that are consistent with an E-MORB (see Figure 1 of Sun and McDonough, 1989). Among the two varieties of E-MORB recognized (Le Roex et al., 1989), these samples share the Zr/Nb, Zr/Y and Y/Nb characteristics of the DUPAL-type but the lower Ba/Nb ratio (5.1 cf. 5.1-9.0) of the Marion-type (Figure 8-9c).

8.4 Interpretation

The compositional variability found in the WBD site could be caused by magmatic processes at mantle and/or crustal levels, and/or by source heterogeneity. Here, these roles are qualitatively assessed while the processes of fractional crystallization and partial melting are quantitatively evaluated by trace element modeling, and the hypothesis of mixing is tested by calculating mixing hyperbolas. The distribution coefficients used in the models are highlighted in Table H-1 while the calculations are based on the mixing equations of Langmuir et al. (1978).

8.4.1 Crustal level processes

(i) Low-pressure, crystal fractionation

The N-, M- and T-groups all show a type of chemical variation that is consistent with shallow level magmatic differentiation. Among the major elements (Figures 8-4a-d), MgO correlates positively with Al_2O_3 and negatively with TiO_2, FeO* or P_2O_5. Such an iron enrichment trend generally results from low-pressure fractional crystallization. The scatter for Na_2O partially and CaO (and SiO_2 or K_2O) is due to alteration (Figures 8-4e-f). Among the trace elements, the compatible elements Cr (7.5-396 ppm) and Ni (15-255 ppm) vary from relatively high to very low contents with increasing degree of fractionation. Apart from early olivine removal, plagioclase-dominated crystallization would account for the increase in the CaO/Al_2O_3 ratio (Figure 8-5a) while the slight rather than rapid increase in Sc with decreasing Mg # (cf. the highly incompatible V) suggests that minor clinopyroxene is also present in the fractionating assemblage (Figures 8-5c-d). It must be followed by clinopyroxene-dominated crystallization to explain the decrease in Cr, Sc and the CaO/Al_2O_3 ratio at Mg # of 54 (Figures 8-5a,c&e), particularly for the T-types. The marked decline in Ni during the final stages of crystallization for the N- and T-type groups (Figure 8-5f) can be related to the appearance of opaques (see Chapter VII), and in particular to the magnetite series (possibly trevorite - $NiFeO_4$) which is the predominant oxide in the basalts (Table 7-6). The width of these trends for every group, as for Sc vs. Mg # (Figure 8-5c) or the positive correlation of Cr with Mg # (Figure 8-5e), implies that they originate from several parental magmas with different trace element contents.

Trace element crystallization models for the four groups are shown in Figures H-1 to H-5. They examine 6 combinations of immobile elements that are compatible in olivine (i.e. Ni, Cr), clinopyroxene (i.e. Cr, Ni, V, Y), plagioclase (i.e. La) and/or spinel (i.e. Ni, Cr, Nb, Zr). For the T- and EG-types, potential parental magmas that are more primitive than any sample of these groups in the site are also considered. Those from

outside the WBD site are similar in Mg # (66-69) to the parents identified for the N- and M-groups (Mg #: 67) which thereby permits inter-comparison. In every case, fractional rather than batch crystallization more closely approaches the trend of the data. The process has involved plagioclase, clinopyroxene and olivine as observed (Appendix E)(see Section 8.4.2-ii below on the EG-type) crystallizing in varying proportions (Table 8-2)(see (iii) below on the T-type). A summary of the modeling results is given in Table 8-2.

Among the N- and M-types in the study area are a few quite primitive samples (Mg #: 67-69) although they are not necessarily primary melts (Mg #: 66-75 - Hess, 1989). In both cases, fractional crystallization produces a good fit to the data except for La in the N-type (Figure H-1) and Nb in the M-type (Figure H-2). The N- and M-types have respectively experienced ~74% and ~68% of fractionation and are dominated by plagioclase and clinopyroxene in the crystallizing assemblage.

The EG-type (Figure H-3) is reasonably fit by ~21% fractional crystallization. Despite being the least influenced by fractionation, the assemblage is dominated by clinopyroxene over olivine; the significance is discussed in Section 8.4.2-ii below.

The T-type parent from the north scarp east of the site does not fit the data except for Cr (Figure H-5). It has an extremely high Ni content of 220 for a Mg # of 66 which suggests that it includes accumulated olivine. Consequently, the most primitive T-type sample from within the study site is also modeled (Figure H-4) and provides a reasonable fit to the data although less so for V, Nb and Y. Accordingly, the T-type has undergone ~66% fractional crystallization with the dominant phase being clinopyroxene. However, this is a minimum estimate because the parent only has a Mg # of 62. Using the N-type parent (Figure H-5) results in a poor fit to the data except for Ni and Y which indicates that it cannot be related to the T-type by fractionation.

For the N-type MORBs (Figure H-1), the crystallization models are successful in matching the concentrations of the compatible elements (e.g. Ni and Cr). However, the incompatible elements in most evolved lavas are excessively enriched (except for Nb and V) for either batch or fractional crystallization. This decoupling may be due to open system fractional crystallization (Bryan et al., 1979; Le Roex et al., 1981). In this process (O'Hara, 1977), the major element abundances are preserved while the incompatible element concentrations and ratios involving the least incompatible elements (e.g. Ti, Y, HREE) are increased. This would explain the increase in Zr/Y with increasing Zr (Figure 8-7a) or the linear trends between (La/Yb)n and Zr/Ti or Zr/Y (Figures 8-7c-d) for the N-type. Such open system behavior in a periodically refilled magma chamber should also result in mixing, as is deduced in 8.4.1(ii) below.

Note, however, that the resultant enrichment in this open system cannot account for the T-type although this group lies at the end of the N-type data arrays in Figure 8-7. Despite the limited number of samples, they exhibit a positive correlation between Ti/Zr versus Nb/Zr and La/Zr versus Y/Zr (Figures 8-15b&d) and a negative correlation between La/Ti versus Nb/Zr (Figure 8-15a), which is opposite to the N-type.

The degree of evolution ascertained from modeling is also consistent with and evidently controls the proportion of ferrobasalts formed in each group with 85% among the N-type but only 12% for the T-type and 3% in the M-type while there are none among all the EG-type. The presence of FeTi lavas implies that thermal conditions (Natland, 1980) conducive to their formation were likely attained here by low frequency of magma replenishment or eruption during crustal accretion. This would result in extensive fractionation with clinopyroxene as the last phase to crystallize (Grove and Bryan, 1983) as observed (Chapter VII). While some of the extremely FeTi-rich lavas are phyric with

clinopyroxene and plagioclase (e.g. BN- 13-3, 13-15), others are aphyric (e.g. BN- 2-12, 13-2, 13-12) as is more commonly the case. This apparent paradox is generally explained by magma mixing or assimilation (Fisk et al., 1980), isolation of these magma bodies from the principal magma chamber (Natland et al., 1983) or unusually effective phenocryst segregation (Allan et al., 1987). Bender et al. (1978) also suggest fractionation at depth as another possibility but it is excluded by lack of evidence here (Section 8.4.2-ii).

(ii) Low-pressure magma mixing

Evidence of low-pressure magma mixing is deduced from a plot of the compatible element Cr versus the incompatible element Zr in Figure 8-10. The data are presented by sector from east to west (except for Sector E) in the site so as to show hybrids and end-members that are spatially associated. Most of the samples lie between the fractional crystallization curves of the T- (Figure 8-10c) or EG- (Figure 8-10b) MORBs and M- (Figure 8-10a) MORBs, but there are at least five N-type samples (Figures 8-10a&c) which cannot be adequately explained as simple fractionation products. This does not necessarily imply an absence of mixing in the T-, M- and EG-types but rather that mixing was more prevalent for the N-type.

It is reasonable to assume that one of the potential end-members may be a primitive, incoming magma and that the other might be a relatively evolved magma if replenishment was infrequent. This accounts for the mixing lines drawn for Sectors CW, CE and E although it is feasible that intermediate compositions could also be mixing end-members. The absence of these hypothetical parents in all three sectors is not unusual given that preserving an end-member should be geologically rare while mixing is occurring.

Accordingly for Sector E (Figure 8-10c), the N-type hybrids lie on a mixing line for which T- and M-type end-members actually exist in Sector C (Figure 8-10b). Also, the hybrids are closer in composition to the primitive end-member which implies that the incoming batch was of larger volume than that in the magma chamber. In Sectors CW and CE (Figure 8-10a&c), the N-type products lie on the same mixing line. It is more steeply sloping as compared to Sector E which indicates that only one of the end-members involved an extreme composition. Consequently, it may be inferred that the recharge frequency was relatively higher in Sectors CW and CE than in Sector E. Also, these hybrids are closer in composition to the evolved end-member. If they erupted immediately after mixing, then it would imply that the resident batch was of larger volume than the incoming magma being delivered to the system.

(iii) Crystal accumulation

The modeling of the two T-type parents in crystal fractionation indicates that, in keeping with their Mg #'s (62 and 66), they underwent slightly differing extents of fractionation (56-75% vs. 62-86%). However, they have different assemblages and proportions of phases crystallizing (Table 8-2). The presence of spinel and the high proportion of olivine in the model assemblage of BN-22-12 is most likely due to crystal accumulation which has certainly affected another picritic sample with a Mg # of ~77 (BN-22-14 - Juteau et al., 1995).

Olivine accumulation is also evident in the N- and M-type basalts within the study site. In a plot of Ni versus Cr in Figure 8-5f, two of the samples (BN- 9-1, 9-3) lying farthest away from the main trend have excess Ni relative to their Mg #. This is in keeping with petrographic observations which classifies them both as olivine-pyroxene

basalts (Chapter VII) with some olivine phenocrysts (Table 7-3) interpreted to be either adcumulates or to have overgrowth rims (Chapter VII).

8.4.2 Mantle processes

(i) Partial melting

Assuming a uniform mantle composition, the role of depth and degree of partial melting in producing the differences between the four groups can be inferred, respectively, from the calculated $Fe_{8.0}$ and $Na_{8.0}$ values (Appendix G). The averages and ranges of these parameters for the N-, T-, M- and EG-types are given in Table 8-1 and summarized graphically in Table 8-3. Based on these $Fe_{8.0}$ and $Na_{8.0}$ values, Table 8-3 also defines the relative terms "very low", "low", "medium", "high" and "very high" which are used below in reference to the pressures and extents of partial melting. Other terms with respect to melting follow the usage in the literature (Brodholt and Batiza, 1989; Klein and Langmuir, 1989) - a global trend and a Pacific-type local trend between $Fe_{8.0}$ and $Na_{8.0}$ refers to their negative correlation while an Atlantic-type local trend refers to their positive correlation.

According to the average $Fe_{8.0}$ values, the N-, T- and M-types (Fe_8: 8.7-9.4) are distinguished by a medium depth of melting as compared to the EG-type with a shallow melt depth (Fe_8: 7.2).

In terms of range, the EG- (Figure 8-9b) and M- types both have the largest span from very low to very high pressures (Fe_8: 5.6-13.2) in melting. In the case of the EG-type, the unusually low $Fe_{8.0}$ values are all from the south flank of Parks Plateau (Figure 8-9b). They indicate that melting ceased at much shallower depths as compared to normal

spreading centers which could occur where there is a thinner lithosphere as is found at or approaching fracture zones (Fox and Gallo, 1984). In keeping with the tectonic-magmatic model in Chapters II and III, this could only reflect melting in close proximity to the former Blanco Fracture Zone during an off-axis magmatic event. This event must also post-date the opening of the WBD since the EG- (with the exception of one sample) and M-types on either wall are spatially separated by the Blanco trough.

By comparison, the N-type only ranges from low to very high pressures (Fe_8: 6.7-13) in melting. Such deep depths for the EG-, M- and N-types are more typical of Atlantic Ridges and associated hotspots (Klein and Langmuir, 1987). The T-type (Fe_8: 8.3-11) varies the least from medium to high pressures of melting. The three nepheline normative samples (Fe_8: 5.9-9.4) are produced at very shallow (for an M-diabase) to medium (for the N-basalts) depths of melting by very small degrees of melting ($Na_{8.0}$: 3.1-4.1) which is consistent with their genesis based on experimental results (Fujii and Bougault, 1983).

According to the average $Na_{8.0}$ values, the EG-, N- and T-type source regions (Na_8: 2.2-2.4) have all undergone high degrees of melting but the M-type (Na_8: 2.9) has only experienced moderate degrees of melting. Likewise, the maximum extents of melting for the EG-, N- and T-types are very high (Na_8: 1.6-1.7) while the M-type is less high (Na_8: 2.1). Although the $Na_{8.0}$ measure is less reliable here, it cannot be ascribed to alteration effects (Figure 8-1b) given the consistency of this difference between the M-type and the other three groups. While it may be the cause for some of the scatter in plots of $Fe_{8.0}$ and $Na_{8.0}$ (Figures 8-9b and 8-11a-c), those data points at high and low $Fe_{8.0}$ would still lie outside the global field and could not be affected that drastically in $Na_{8.0}$ so as to change the trend of the group.

In $Fe_{8.0}$ vs. $Na_{8.0}$ plots, the few T-type samples (Figure 8-11c) follow the global trend between depth at which the mantle column intersects the peridotite solidus and the extent of partial melting (Klein and Langmuir, 1987), as for Pacific-type local vectors (Klein and Langmuir, 1989). By comparison, the N-type samples (Figure 8-11b) are scattered due to alteration of Na_2O with 6 obvious outliers. Nonetheless, with the exception of another 6 samples which lie outside the global field, the remainder are distributed throughout the length of the field although the trend is not as well-defined as for the Cleft Segment (Figure 8-11d). These plots also illustrate that the N- and T-MORBs vary widely in the pressure range over which melting occurs (Figures 8-11b-c) as compared to even the north and south parts of the Cleft Segment together (Figure 8-11d). Such variation in the N- and T-types could result from potential temperature or veining of the mantle (Langmuir et al., 1992). These options are considered in Section 8.4.3-i.

By contrast, the M- (Figure 8-11a) and EG- (Figure 8-9b) types define a co-linear Atlantic-type local vector. Such a local trend is more typical of Mid-Atlantic Ridge segments (Klein and Langmuir, 1989) or East Pacific Rise seamounts (Niu and Batiza, 1993) where it has been ascribed to volatiles involved in melting (Langmuir et al., 1992), high pressure crystal fractionation (Grove et al., 1992), or melt-solid re-equilibration/interaction (Niu and Batiza, 1993; Gaetani et al., 1995). These possibilities are examined in 8.4.2(ii) below.

In beginning to assess the role of mantle processes in producing the four MORB types, simple partial melting models were derived (Figures 8-12). The accuracy of these models depends on the trace elements utilized. Johnson and Dick (1992) note that a plot of Zr/Y vs. Zr (Figure 8-12a) may not be suitable because the temperature dependance of

these partition coefficients affects the absolute concentration of these elements. This is the case here for the M- and T-type results which are not reproduced by other trace element models (Figures 8-12b or 8-13).

The model in Figure 8-12b demonstrates that non-modal batch melting of a depleted MORB source in the spinel stability field provides a reasonable fit to the parental compositions (Table 8-2) identified for these groups. The T- (3.5±1.9%), EG- (4.4±0.9%), N- (8.3±2.7%) and M- (11.3±7.2%) types reflect a progressive increase in extent of melting. However, this order contradicts some previous findings. The T- and EG-types seem to be reversed since the latter is more enriched and therefore should show the lower percentage of melting. The M-type also appears to be at the reverse end in order of these groups given its higher average $Na_{8.0}$. These conflicts suggest that degree of melting alone cannot account for the differences between the groups. This problem is discussed in Section 8.4.3 which further explores the nature of the mantle source.

(ii) High pressure, crystal fractionation

As noted, the EG- and M-types form Atlantic-type local vectors that cross-cut the global trend. To constrain the origin of these trends, the EG- and M-types are compared on $Fe_{8.0}$ vs. $Na_{8.0}$ plots (Figures 8-9b and 8-11a) to the polybaric melting curve and vectors of interaction determined by Gaetani et al. (1995) for dredge samples from the north flank of eastern Parks Plateau (Figure 3-1). The superimposed curve was generated for a primitive upper mantle with 0.5 wt. % melt initially extracted that is incrementally batch melted at a rate of 0.13% per GPa up to 1.3 GPa (Gaetani et al., 1995). The vectors result from crystallizing 5 wt. % olivine and assimilating 6.75 wt. % orthopyroxene from the surrounding depleted harzburgite (Gaetani et al., 1995). These liquids are then fractionated along the same liquid line of descent as the unreacted melts to 8 wt. % MgO

which is the maximum value of their samples. The EG-type (with one exception) has a maximum of 7.6 wt. % MgO (Appendix G) which would require greater extents of interaction. Although Gaetani et al. (1995) note that progressively less crystallization is required leading to a comparatively greater decrease in $Fe_{8.0}$ than in $Na_{8.0}$, a 0.4 wt. % MgO difference between these sample sets cannot justify the extent to which these vectors would have to be extrapolated (Figure 8-9b) in order to match the sample variations. The M-type (with one exception) has a maximum of 8.6 wt. % MgO (Figure 8-4) which should require lesser extents of interaction than shown by their vectors (Figure 8-11a). Hence, mantle-melt interaction during percolation through the cooler lithosphere is not a plausible option for either the EG- or M-types.

A similar mechanism suggested by Niu and Batiza (1993) requires that the re-equilibration process occur only in the melting regime of bouyant diapirs. This would leave a harzburgite residue due to the very high extents of melting. The EG-type has some very low $Na_{8.0}$ values on the south Parks flank (Figure 8-9b) but overall, the group has higher $Na_{8.0}$ (Table 8-3) and lower extents of melting (Figure 8-12) than even the N-type. Furthermore, it also has high incompatible element abundances (Figure 8-9a). These characteristics are therefore inconsistent with melt-solid re-equilibration for the EG-group. The evidence is conflicting for the M-type which has medium $Na_{8.0}$ values (Table 8-3) indicating only moderately low extents of melting but very depleted incompatible element abundances which suggests high extents of melting.

A third and preferred proposal calls for polybaric, high-pressure crystal fractionation (Grove et al., 1992).

The EG-type in the study site experienced only 9-38% fractional crystallization (Figure H-3) indicating that the sample is only slightly evolved. However, the calculated

assemblage is dominated by clinopyroxene (Table 8-2) which contradicts the petrographic observations of this sample as a sparsely (<1%) plagioclase phyric basalt (BN-24-11 - Appendix E). This finding could be reconciled if the clinopyroxene were resorbed as is expected during high-pressure crystallization (O'Donnell and Presnall, 1980).

Such modeling or petrographic evidence is absent for the M-type but its high Na_2O abundances (Figure 8-4e) is consistent with high-pressure fractionation. Given the uncertainty in interpretation for the M-group, other possibilities that must be considered include the involvement of volatiles in melt generation (Langmuir et al., 1992) and/or source differences.

8.4.3 Mantle heterogeneity

(i) Nature of the N- and T-type sources

The T- (and possibly N-) types follow roughly 60-70% the length of the global trend and display a Pacific-type local vector (Figures 8-11b-c). This would certainly require more than half of the 160°C variation in mantle potential temperature estimated for the global trend (Kinzler and Grove, 1992). However, even this is much greater than the 25-50°C range in mantle temperature gradient required to build a 2 km thickness of oceanic crust (Klein and Langmuir, 1987; McKenzie, 1984, Su et al., 1994). Nevertheless, excessive magmatism could be associated with the chain of seamounts north of the site (Chapter III). Such near-axis seamounts tend to have similar compositional variations as the adjacent ridge (Hekinian et al., 1989) suggesting that both are supplied by the same source. In the case of the EPR, they occupy broad fields from which the zone of upwelling is inferred to be 100 km wide (Niu and Batiza, 1991). By

comparison, the chains along the northern (Karsten et al., 1990) or southern (see Figure 8 of Smith et al., 1994) JdFR have been interpreted to originate from mantle heterogeneities but the multistage melting model in Chapter III links them to the melt extraction cycle at the ridge.

While a thermal anomaly is appropriate in explaining the N-type, it does not fully account for the compositional features of the T-type. The difference between the two groups in their Zr/Y or (La/Yb)n ratios (Figure 8-7) could be due to varying degrees of partial melting since their similar Zr/Nb, Zr/La and Zr/Nd ratios (Figure 8-6) indicate that they are derived from the same source. This interpretation of a smaller degree of melting (3.5%) for the T-type as the cause of its enriched characteristics is also supported by trace element modeling. According to the range in $Na_{8.0}$ (Table 8-1) however, it is the N-type which is modeled by some much lower degree melts than the T-type. The higher $Na_{8.0}$ values of the N-MORB (and M-type) cannot be due to alteration because there is no reason why the T-MORB (and EG-type) would not be likewise affected. The T-type also has a more restricted range in depth of melting than the N-type. These features are likely to stem from localized clinopyroxene veins modifying the spinel peridotite source at moderate to deep depths (Langmuir et al., 1992). The conflicting major and trace element results on the extent of melting imply that their abundances are decoupled as could possibly occur if the veins differ in composition or mineralogy from the surrounding mantle (Bryan and Dick, 1982; Allan et al., 1987; Langmuir et al., 1992).

(ii) Nature of the M-type source

By comparison to the other three groups, the M-type is offset from the common melting path in a trace element model (Figure 8-12c) to high Ti/Zr and/or (Nd/Yb)n

ratios. Differences in partial melting alone cannot produce the shift in both these ratios since it would increase one while decreasing the other.

An originally high Ti/Zr ratio (Figure 8-12c) could stem from large extents of melting. The resulting ultra-depleted characteristics are also shared by the Vance seamounts west of the southern JdFR (see Figure 8 of Smith et al., 1994), as can be compared for Zr/Y versus Zr (Figure 8-7a) where the data points lie outside the N-MORB field (Zr/Y > 2.25). Hence, such extensive melting appears to be a common feature at the JdFR.

This demands a simultaneous increase in (Nd/Yb)n (Figure 8-12c) which could occur by the addition of specifically LREE in relation to the HREE or other incompatible trace elements. Consequently, such mechanisms as open system behaviour in magma chambers (Elthon and Casey, 1985 vs. Natland, 1989), zone refining (Langmuir et al., 1977) or melt interaction with a fertile mantle (Natland, 1989) which would enhance both LREE and HREE are ruled out. Instead, the higher (Nd/Yb)n may reflect a difference in source composition but melt models of a garnet peridotite (plot not shown) or primitive spinel peridotite source (Figure 8-12c) do not result in a better fit. It is therefore inferred that the M-type must be derived from a modified source of depleted spinel lherzolite.

This process would involve multistage melting (Duncan and Green, 1987) of a depleted mantle source. Such repeated melting in a non-transport model is proposed to have occurred beneath the Costa Rica Rift giving rise to the Group D lavas in Hole 504B (see Figure 8 of Autio et al., 1989). Subsequently, an exotic melt component representing crystallized fractions of trapped melt which could have resulted from metasomatic processes (Hawkesworth et al., 1984), incompatible-enriched blobs (Allegre and Turcotte, 1986) or impregnating liquids of alkali basalt (Bonatti et al., 1986) is introduced into the mantle residue by veins. The enrichment is then followed by further melting. Although this sequence of events has not previously been described, a lherzolite at the

Troodos Massif in Cyprus could represent such a highly refractory, depleted residue (Moores and Vine, 1971) while amphibole/biotite veins have been observed in some lherzolite xenoliths (Harte, 1987). Refertilization of a strongly depleted harzburgite mantle with a basaltic liquid has also been suggested by Elthon (1992) as an alternative to fractional melting of peridotites (Johnson et al., 1990).

(iii) Nature of the EG-type source

Trace element modeling using moderately to slightly incompatible ratios suggests that the EG-type could be derived from the same mantle source as either the N- or T-type (Figures 8-12 and 8-13). However, the similar degree (4.4% vs. 3.5%) of average partial melting for the EG- and T-types based on both the modeling and $Na_{8.0}$ values (Table 8-1), cannot account for the differences between these two groups. On the other hand, the modeling indicates that the EG-type parent was generated by partial melting at about half (4.4% vs. 8.3%) the extent of the N-MORB which could be the cause of its relatively enriched nature. Yet, this is not in agreement with the $Na_{8.0}$ values (Table 8-1) which imply a high average degree of melting that is similar to the N-type. Furthermore, partial melting or differentiation of the N-MORB source should not alter the La/Nd or Nb/Nd ratios which differ significantly in the EG-type (Figure 8-14). This reveals that the EG-type cannot be the product of a clinopyroxene veined and/or depleted spinel peridotite.

The chemical characteristics of this group are compatible with the source of E-MORB. The origin of this fertile or refertilized mantle that supplies plumes or the ridge axis is obscure but is thought to stem from mantle heterogeneities (Batiza and Vanko, 1984) which could possibly result from melting subducted oceanic crust (Ringwood, 1982). The systematic variability of the EG-type on incompatible ratio-ratio plots

involving a slightly incompatible element (Figures 8-9 and 8-15a-c) cannot be due to partial melting because of the limited range inferred from the $Na_{8.0}$ values (Table 8-1) and the lack of a correlation between any indicator of enrichment and $Na_{8.0}$ (plots not shown). Nor can it be explained by mixing, as discussed below (Section 8.4.4-i). Instead, the diversity is probably an outcome of high pressure, crystal fractionation (Section 8.4.2-ii).

8.4.4 Melting/differentiation events versus mixing processes

Binary ratio plots (Langmuir et al., 1978) are used here to assess whether mixing between sources or magmas also contributed to the trace element variations of these four groups. Partial melting and differentiation affects the ratio of a slightly incompatible/incompatible element (Figure 8-15a&c) but not the ratio of both incompatible elements (Figure 8-14a&c). Consequently, mixing relations should be reflected in ratio-ratio plots involving exclusively incompatible elements. In this case, magma mixing (but not source mixing) will also show a trend on ratio-ratio plots involving a slightly incompatible element. In each example, the companion plot alongside (Figures 8-14b&d and 8-15b&d) checks for consistency because mixing ought to result in a linear trend.

(i) The N-type

The N-type forms a positive trend on the ratio-ratio plots with a slightly incompatible/incompatible ratio for La/Ti versus Nb/Zr or La/Zr versus Nb/Y (Figures 8-15a&c). This could result either from differentiation (Section 8.4.1-i) or partial melts

varying by minor degrees. Both these possibilities are consistent with their negative trend for Ti/Zr versus Nb/Zr or La/Zr versus Y/Zr on the companion plots (Figures 8-15b&d).

(ii) The T-type

Hekinian et al. (1989) have suggested that T-MORBs could be produced by the mixing of N- and E-MORB. On exclusively incompatible ratio-ratio plots (Figures 8-14a&c), the T-types are scattered relative to the N-types for La/Nd versus Nb/Zr (Figure 8-14a) and overlap for La/Zr versus Nb/Nd (Figure 8-14c). Thus, in neither case do they lie between the two groups on the mixing curve. This conclusion is supported by the absence of any E-MORB here as opposed to fast spreading ridges where N-, T- and E-MORB can erupt persistently for at least 800 ka (Reynolds et al., 1992; Batiza et al., 1996).

The T-type is further distinguished from the N-type on Figure 8-15, although a larger number of samples will be necessary to define this apparently separate and opposing trend. Given the limited range of partial melting for this group based on $Na_{8.0}$ values, such a trend could develop from incorporating differing proportions of the spinel lherzolite and clinopyroxene veins in magmas from this source. A few of the samples, which lie at the one end of the N-type trend representing low degree melts, would be constituted mainly by depleted spinel lherzolite. The samples with more La and Y but less Ti and Nb would presumably represent mostly vein material.

(iii) The M-type

Trace element modeling using two compositions (Z-38 and Z-206) of the Zabargad amphibole peridotite indicates that the M-type formed by 24-24.5% modal

fractional melting based on the LREE relative to the HREE (Figures 8-13b-c). However, the modeling does not reproduce the moderately or slightly incompatible REE parental concentrations of this group (plots not shown). This suggests that the M-type mantle source differs slightly from this example of primitive mantle material which is present at several ultramafic localities (Bonatti et al., 1986 and references therein).

It further supports a multistage geochemical evolution of this group (Section 8.4.3-ii). Despite the broad scatter of the M-type on ratio-ratio plots involving slightly incompatible elements (Figures 8-7c-d), the group overlaps only minimally with the N-type. This implies that its mantle source had to have undergone a previous phase of melting before the veining occurred to bear depleted Zr/Ti and Zr/Y but an enriched (La/Yb)n signature. The wide variation in these ratios is in accord with the large range in extent of partial melting as indicated by $Na_{8.0}$ values (Table 8-1).

Although the estimated degree of partial melting is high in relation to the other three groups at the WBD site, it is not unreasonable. Allan et al. (1987) suggest that similar extents (25%) of modal, albeit batch melting of an undepleted amphibole peridotite source formed the lavas in the seamounts flanking the EPR at 21°N. Likewise, Johnson et al. (1990) and Johnson and Dick (1992) find that up to 23-25% of non-modal, incremental/fractional melting of a depleted spinel lherzolite occurred at the South-West Indian Ridge, far from hot-spot influence.

The compositional variability of these magmas was evidently not derived by mixing since no such curve is observed on incompatible ratio-ratio plots involving a slightly incompatible element (Figure 8-15a&c). This demonstrates that the variety of extremely low to high degree melts were produced independently and have been retained by a lack of mixing between the various liquids enroute to the surface.

Increased bulk melting of the source ought to incorporate both depleted spinel and enriched amphibole lherzolite. This accounts for the apparent binary mixing of the M-type on plots of Zr/Y versus Zr (Figure 8-7a) or La/Zr versus Nb/Nd (Figure 8-14c). On this basis, it can be inferred that the heterogeneities must be smaller than the melt regions. Batiza and Vanko (1984) concluded that such domains had to be on the scale of a few meters to kilometers in order to generate the full compositional series at each of the tiny seamounts off-axis from the EPR (8-12°N).

(iv) The EG-type

The hypothesis of mixing in the generation of the EG-type is tested according to the arguments of Langmuir et al. (1978). As the enriched component, the EG-type sample with the highest (La/Yb)n ratio is used since it most closely approximates an E-MORB. For the depleted end-member, the N-type parental composition in Table 8-2 is used.

On the ratio-ratio plots of incompatible elements (Figures 8-14a&c), the calculated curve fits the trend of the EG- and N-type lavas signalling either source or magma mixing. However, their normalized plots in Figures 8-14b&d show that mixing could only have occurred with the high La and/or low Nb subset of the N-type that is intersected by the linear array for the EG-type.

The ratio-ratio plots with a slightly incompatible element (Figures 8-15a&c) again display a mixing curve between the two groups which suggests mixing of magmas. The magma mixing could have occurred after separation from the source either in the mantle or even in crustal level chambers. However, no evidence of low-pressure mixing is found for this group (Section 8.4.1-ii) which implies that mixing must have occurred in the mantle.

These normalized plots indicate that the mixing end-member was of high La rather than low Nb (Figures 8-15b&d) based on where the N-type array is intersected by the regression line of the EG-type. The N-type lavas of relatively high La (>5.35 ppm average) could reflect low degree partial melts or a minor compositional difference within the depleted spinel peridotite itself. The former is ruled out by their range in $Na_{8.0}$ between 1.6 wt. % and 3.1 wt. % indicating that they are medium to very high degree melts (Table 8-3). Instead, the enhanced La could result in at least two possible ways: (i) there might be some entrainment of the E-MORB source into the surrounding mantle causing simultaneous partial melting of this modified N-MORB source; or (ii) the enriched magma may leave residual melt trails through the N-MORB mantle which then begins partial melting and mixing with the subsequent E-MORB upflow.

8.5 Discussion

8.5.1 Alteration

The results demonstrate that the basement exposed along the Blanco Fracture Zone is not excessively metamorphosed and deformed by the complex strike-slip tectonic regime (Dauteuil, 1995). Furthermore, the secondary mineralogy, the elements mobilized and the extent of alteration along the north WBD scarp is similar to other DSDP holes (Thompson, 1991). Therefore, this study site is appropriate for investigating the petrogenesis of the upper oceanic crust despite its location along a transform fault zone.

8.5.2 Comparison to other oceanic sites

The primary geochemistry of the WBD site is unusual in its diversity even within any individual profile (e.g. BN-2&23) of the crustal section. The suite includes ferrobasalts that are typically found near transform faults (Sinton et al., 1983), along propagating rifts (Fornari et al., 1983), or on-axis oceanic islands (Thy, 1989). T-MORBs have been recovered elsewhere from spreading ridges, seamounts and aseismic ridges (Bryan et al., 1976). The M-types have not previously been described although they are similar in terms of their depletion to the dominant lavas (Group D) from Hole 504B (Autio and Rhodes, 1983). The EG-type is equivalent to E-type or P-MORBs that are commonly present in the vicinity of mantle plumes (Le Roex et al., 1983; 1992).

Areas of the mid-ocean ridge which exhibit compositional variability (without nearby hotspots) are the fast spreading (10.7-11.0 cm/yr) segments of the East Pacific Rise between 9°30'N (Batiza et al., 1996; Perfit et al., 1994) and 12°50'N (Reynolds et al., 1992; Hekinian et al., 1989). Intermediate-rate spreading areas tend to be restricted to normal or Type I MORBs. Off-axis in Holes 425 (north of GSC - Mattey and Muir, 1980) or 482-485 (EPR south of Tamayo FZ - Flower et al., 1983), the N-MORBs vary only from relatively primitive to moderately evolved (MgO: 6.4 - 9.1 wt. %). At any on-axis site, the compositional variation is more limited as at 21°N on the EPR (Juteau et al., 1980). However, the homogeneity does decrease near certain transform faults (e.g. Tamayo FZ - Langmuir and Bender, 1984).

8.5.3 Relation of petrogenesis to tectonic setting

The tectonic setting (Chapter II) could have contributed to the compositional diversity displayed at the WBD site and it is therefore necessary to assess its role.

One is the influence of post-propagation effects. Juteau et al. (1995) propose that although propagation halted on intersecting the older Blanco Fracture Zone to the south at 1.5 Ma (Wilson et al., 1984), a mantle temperature gradient persisted. Consequently, high levels of differentiation to 50 km behind the ridge-transform intersection (Sinton et al., 1983) combined with mixing between primitive and fractionated magmas (Christie and Sinton, 1981) continued in small chambers for another 0.4-0.5 m.y., that is until about 1.0-1.1 Ma. If normal spreading was achieved in 0.7 m.y. (Hey et al., 1980), then the full rate here would only have been reached by 0.8 Ma. However, this is inconsistent with the evidence for propagation terminating earlier at ~2 Ma (Chapter III) in which case a normal spreading environment would have been in place by 1.3 Ma. Furthermore, crustal level processes have certainly affected the lava chemistry in the WBD site but mantle processes and sources have also determined the composition of the four groups which is not considered in this simple model.

Another is the proximity to the Blanco Fracture Zone (Dauteuil, 1995) depending on when strike-slip activity jumped from the south to the north side of Parks Plateau (Chapter III). Comparative studies of lavas from fracture zones and ridge segments show that the former tend to be geochemically more evolved but that their source regions do not differ compositionally (Le Roex et al., 1983; Johnson and Dick, 1992). This effect could well account for the FeTi lavas among the N- and T-types.

A third factor is the impact of recent, off-axis volcanism. Only the EG-type in the study site is also recovered from Parks Plateau where they are comparatively prominent in the central part. These lavas are clearly derived from the same melting event despite their physical separation by the Blanco Trough. However, this process has not involved "mantle/melt interaction during transport through depleted lithospheric harzburgite" as

suggested by Gaetani et al. (1995). Instead, magma mixing in the mantle which is unique to this group (Table 8-4) is a more important mechanism for producing the within-variation.

A fourth factor is the nature and extent of heterogeneity that can be generated on- or near-axis. For the WBD suite, a brief summary of the effects of mantle sources as well as mantle and crustal-level processes experienced is given in Table 8-4. Ultimately, multistage mantle melting of a normally depleted source has given rise to the N-, T- and M-types. These groups differ due to the additional veining and differences in magmatic processes. As regards the EG-type, the enriched component if it was present in the vicinity of the spreading center did not melt during 1.2 - 1.7 Ma when the ridge axis had been spreading for about 0.3 - 0.8 m.y. while the magmatic system was still relatively youthful/immature. Alternately, this "blob" might have been absent or not available as a potential source prior to 0.35 - 0.4 Ma when these lavas erupted on Parks Plateau (Section 3.4.3). This source presently accounts for the spectrum at the 0 Ma Cleft segment between enriched (Cobb Seamount) and overly-depleted (Vance seamounts) components (Smith et al., 1994). Hence, the JdFR is now similar to the EPR where E-type or undepleted lavas are sampled on both the ridge and off-axial seamounts (Hekinian et al., 1989).

8.5.4 Reconstruction of the magmatic history

The magmatic history of the WBD site as reconstructed in Chapter III is further constrained here by integrating the petrogenetic characteristics of the four compositional groups within the tectonic context of the region. In this model (Section 3.4), there are

three stages of accretion relating to pulsed diapiric mantle flow (Figure 3-6) followed by a fourth stage associated with off-axis volcanism.

During the first stage beneath the mid-ocean ridge, diapirs were most likely initiated by non-modal batch melting of slightly depleted mantle commencing at very deep depths to generate the most prevalent N-type lavas (Tables 8-3&4). A compositional heterogeneity such as clinopyroxene veined mantle at medium-high depths in the path of the upwelling would feasibly have melted between moderate and very high degrees to produce the T-type flows (Tables 8-3&4).

During the second stage as the ridge moved westward past the ascending diapirs in an absolute framework, it can be expected that the core of the magma supply system continued melting to shallow depths which would have resulted in more focussed melts of N-type erupting east of the axis to build a seamount edifice.

Sometime prior to the third stage, the very depleted diapirs near the Blanco Transform Fault north of Parks Plateau (or at least, parts of them) must have been metasomatized by amphibolite veining which with modal fractional melting gave rise to the M-type (Table 8-4). The former effect would invalidate the Fe_8 calculation (Table 8-3) and consequently, the depths of melting cannot be inferred. The late timing of this process is demanded by the lack of any evidence for magma mixing (Table 8-4) either with the N- or T-type which would be predicted if this sequence of events had occurred earlier in Stages 1 and/or 2. Assuming that no such source previously existed, a lengthy interval is also required to melt the N-type diapir from very high to extremely low degrees and create significant depletion (Table 8-3).

Within the past 0.4 Ma, Parks Seamount has originated by off-axis volcanic activity (Section 3.4.3). These lavas were evidently derived by non-modal batch melting of enriched mantle followed by magma mixing with a depleted component after which high pressure fractionation further contributed to the compositional spectrum of the EG-

type. Melting (Figure 8-9b; Table 8-3) occurred at moderate depths with medium degrees of melting on the north flank of Parks Plateau (above a mid-level bench) and at very shallow depths with high degrees of melting on the south flank of Parks Plateau. This suggests that partial melting proceeded from north to south across the Plateau which is consistent with a model of northward plate boundary migration. The sole sample recovered in the study site would therefore represent the initial tapping of this source as it apparently became perturbed possibly by the strong thermal contrast across the Blanco trough. Such a connection between surface features (e.g. spreading rate) and deep-level processes (e.g. extent of mantle melting) has been posited by Niu and Hekinian (1997).

8.6 Conclusions

The ~2 km thick crustal section exposed in the central part along the north scarp of the West Blanco Depression (WBD) has been sampled extensively. Major, trace and rare earth element analyses of these lavas lead to the following conclusions:

1. Four compositional groups occur within the WBD study site:

(a) the majority are typically 'depleted' N-type MORB; (b) the second most volumetrically abundant is an M-type with ultra-depleted incompatible elements on which are superimposed LREE enhancement; (c) the second least abundant is a T-type with transitional characteristics; and (d) a minor proportion of an EG-type that is LREE enriched intermediately between N- and E-MORB.

2. Major element studies and trace element modelling indicate that the four groups range from moderately (21% for the EG-type) to highly (74% for the N-type) evolved due to varying extents of low pressure fractional crystallization. Fractionation has occurred by the removal of olivine, plagioclase and clinopyroxene in varying proportions to form ferrobasalts in the N-, M- and T-types.

3. Other crustal level processes, which include olivine accumulation for the N-, M- and T-types and low pressure magma mixing in the N-type, are further able to account for intra-group but not inter-group variations in composition.

4. Quantitative modelling shows that varying degrees of modal (8-20%) or non-modal (4-8%) batch melting can generate the N-, EG- and T-types but that the M-type requires a higher degree (~25%) of modal fractional melting.

5. Distinct incompatible element ratios suggest that although the four groups were all derived from an earlier depleted spinel peridotite, this mantle source is variously modified by clinopyroxene veins for the T-type, enriched domains for the EG-type, or by metasomatism with amphibolite veining of the solid residue from MORB extraction in the case of the M-type.

6. A history of multi-stage melting (with magma extraction creating source heterogeneity), mixing of sources/magmas, and mantle processes are proposed to explain the unusual diversity. In a preferred model, the ~NW-migrating JdFR (in an absolute reference frame) consistently initiates diapiric upwelling (Johnson and Dick, 1992) in advance of itself. This gives rise to buoyancy-driven mantle flow (Spiegelman, 1996) of which the N-, T- and M-types are the time-varying consequence. When the JdFR directly overlies this melt zone, the N- and T-type lavas are erupted on-axis. Continued melting now eastward of the overlying ridge causes the N-type lavas to build seamounts near-axis. With time, metasomatic fluids hydrate the highly depleted diapiric residues near the Blanco transform fault giving rise to the M-type melts that intrude or underplate the crust near-axis. Lastly, the EG-type is produced by a <0.4 Ma off-axis melting event centered on Parks Plateau as the fracture zone boundary is also translated northward.

Table 8-1: Averages (AVG.), standard deviations (S.D.) and ranges of variation (MIN. and MAX.) for the major oxides, trace elements, REE and selected ratios of the normal (N-), transitional (T-) and highly depleted but selectively enriched (M-) TYPEs from the WBD site; also, for the enriched (EG-TYPE) group from the WBD site and Parks Plateau.

	N-AVG.	N-type S.D.	N-MIN.	N-type MAX.	T-type AVG.	T-type S.D.	T-type MIN.	T-type MAX.	M-AVG.	M-S.D.	M-MIN.	M-MAX.	EG-AVG.	EG-S.D.	EG-MIN.	EG-MAX.
SiO_2	49.19	0.99	46.00	52.20	49.57	0.56	48.85	50.25	49.14	1.15	46.80	51.40	49.54	1.08	47.50	50.60
TiO_2	2.04	0.42	1.11	3.57	2.38	0.95	1.21	3.61	1.41	0.39	0.85	2.68	1.82	0.26	1.51	2.38
Al_2O_3	13.88	0.72	11.90	15.77	13.25	1.27	11.62	14.65	15.14	1.44	12.60	19.40	15.20	0.58	14.00	16.35
Fe_2O_3*	13.08	1.49	9.53	18.00	14.44	3.37	10.20	19.10	10.82	1.76	7.90	14.85	11.27	1.18	9.50	14.00
MnO	0.21	0.03	0.17	0.33	0.22	0.03	0.18	0.26	0.19	0.04	0.14	0.25	0.19	0.02	0.16	0.22
MgO	6.60	0.63	5.14	8.57	5.63	1.33	4.27	7.44	7.38	0.84	5.81	10.10	6.67	1.23	4.72	10.20
CaO	10.70	1.06	7.45	12.27	9.71	1.36	7.78	11.45	10.41	1.37	7.16	12.50	11.63	0.79	9.90	12.60
Na_2O	2.79	0.49	2.08	4.77	3.09	0.31	2.75	3.40	3.09	0.67	2.27	4.82	2.83	0.15	2.59	3.10
K_2O	0.21	0.12	0.06	0.74	0.36	0.16	0.11	0.55	0.20	0.17	0.04	0.62	0.38	0.17	0.21	0.89
P_2O_5	0.22	0.06	0.12	0.45	0.30	0.14	0.16	0.52	0.16	0.04	0.10	0.30	0.22	0.05	0.16	0.32
Sc	43.68	1.90	36.00	47.00	41.80	1.48	40.00	44.00	39.56	3.40	31.00	45.00	40.07	2.81	36.00	44.00
V	397.88	58.59	244.00	600.00	386.20	89.82	261.00	480.00	292.24	55.83	192.00	420.00	324.00	31.58	270.00	370.00
Cr	156.73	79.93	18.00	350.00	105.30	133.76	7.50	330.00	234.72	97.67	66.00	396.00	220.07	97.16	70.00	450.00
Co	45.48	2.30	41.00	53.00	44.20	2.95	41.00	47.00	42.68	4.74	32.00	56.00	47.27	5.23	40.00	58.00
Ni	63.38	20.13	21.00	135.00	38.00	22.57	15.00	72.00	84.20	41.55	45.00	255.00	96.00	71.75	41.00	330.00
Rb	2.61	1.56	0.70	7.30	4.50	2.88	1.20	9.00	2.19	1.70	0.40	6.60	4.99	3.76	2.20	17.20
Ba	17.27	10.61	6.00	78.00	25.20	10.83	12.00	38.00	21.12	18.17	4.00	73.00	38.60	18.77	18.00	96.00
Nb	4.61	1.38	2.05	8.75	7.17	3.46	3.55	12.10	3.29	1.25	1.20	7.15	7.13	2.56	4.30	13.00
La	5.35	1.46	2.35	10.60	8.35	3.26	5.00	13.35	4.03	1.35	2.30	8.15	6.71	1.82	4.70	10.80
Ce	16.93	4.46	9.00	31.00	25.50	10.65	14.50	42.00	12.65	3.97	6.50	24.50	17.33	4.42	12.50	27.00
Sr	111.05	13.57	79.00	156.00	120.00	9.90	109.00	131.00	113.48	27.67	47.00	168.00	164.47	15.90	138.00	202.00
Nd	16.33	3.98	8.00	30.00	23.00	10.68	14.00	40.00	11.73	4.04	6.50	25.50	14.30	2.99	11.00	21.00
Zr	133.09	36.19	60.00	270.00	193.80	86.19	114.00	332.00	70.52	23.48	40.00	145.00	132.40	28.85	100.00	200.00
Eu	1.66	0.33	0.90	2.80	2.08	0.80	1.25	3.30	1.21	0.32	0.85	2.05	1.55	0.23	1.25	2.05
Dy	7.82	1.72	4.40	14.50	9.96	4.12	5.80	16.20	5.32	1.50	2.90	9.50	6.35	1.06	5.00	8.80
Y	47.13	11.26	23.00	91.00	60.00	25.47	35.00	100.00	31.96	9.58	17.00	55.00	40.07	6.80	32.00	56.00
Er	5.01	1.06	2.50	8.60	6.30	2.83	3.50	10.70	3.30	0.91	1.70	6.00	3.97	0.74	3.00	5.80
Yb	4.58	1.05	2.20	8.58	5.80	2.47	3.38	9.68	2.95	0.80	1.55	5.13	3.62	0.63	2.80	5.05
Mg#	53.47	4.68	40.01	67.20	47.16	11.42	33.74	62.43	60.88	5.41	47.12	68.61	57.08	5.64	46.99	68.46
CaO/Na_2O	3.97	0.80	1.73	5.90	3.18	0.68	2.51	4.16	3.57	0.99	1.49	5.23	4.13	0.38	3.50	4.70
CaO/Al_2O_3	0.77	0.06	0.58	0.85	0.73	0.04	0.67	0.78	0.69	0.07	0.50	0.77	0.77	0.04	0.71	0.83
Al_2O_3/TiO_2	7.14	1.79	3.38	14.21	6.68	3.60	3.22	12.11	11.65	3.85	4.99	22.82	8.54	1.39	5.88	10.23
Si(8.0)	48.76	0.99	45.42	51.48	48.84	0.97	47.69	50.08	48.95	1.14	46.12	51.19	49.12	0.91	47.37	50.23
Na(8.0)	2.26	0.51	1.60	4.10	2.21	0.45	1.71	2.80	2.86	0.62	2.07	4.57	2.33	0.39	1.80	3.47
Fe(8.0)	9.44	1.03	6.70	12.95	9.06	1.13	8.25	10.98	8.71	1.65	5.64	13.21	7.92	1.95	5.46	13.29
Eu*-man	1.32	0.77	-0.40	4.00	2.52	1.82	0.53	5.36	0.62	0.96	-1.50	3.06				
Zr/Nb	29.29	3.45	20.00	38.64	27.90	3.45	24.28	32.11	22.83	6.54	11.88	37.86	19.43	3.03	13.04	25.12
Zr/Y	2.81	0.19	2.43	3.17	3.22	0.07	3.14	3.32	2.21	0.31	1.54	2.67	3.29	0.27	2.94	3.91
Ti/Zr	92.75	6.43	73.83	105.80	74.08	9.17	63.63	83.47	123.52	23.22	84.88	175.65	83.51	6.54	69.94	92.32
(La/Yb)n	0.83	0.08	0.66	0.98	1.04	0.03	0.99	1.06	0.98	0.14	0.77	1.24	1.35	0.33	0.69	2.01

Table 8-2: Observed and calculated trace element abundances in representative parent and daughter samples of the four MORB groups in the study site. For the sole EG-type sample in the site, a parent is located on the south WBD scarp (Juteau et al., 1995). For the T-type, three possible parents are modelled. One is the most primitive N-type parent for a maximum estimate. Another is the most primitive T-type sample from the site to provide a minimum estimate. A third utilises a picrite from the eastern part of the north WBD scarp since it has a Mg-number (Mg #) comparable to the parental samples of the other chemical groups. The most recently available distribution coefficients are used as listed in Appendix H. Values were calculated according to both an equilibrium and a perfect fractional crystallisation model but the latter produced a better fit to the data in every case, as shown in Figures H-1 to H-4, and these ranges are reported here. F = fraction of liquid remaining; Xstln = crystallisation; Plag = plagioclase; Cpx = clinopyroxene; Ol = olivine

Type	**N**			**M**			**EG**		
Parent	BN-7-4			BN-5-4			BN-14-7		
Mg #	67			67			69		
Daughter		BN-13-12			BN-3-5			BN-24-11	
Mg #		40			47			60	
		Observed	*Calculated*		*Observed*	*Calculated*		*Observed*	*Calculated*
Zr	63	270	154-354	40	145	59-241	108	125	118-171
La	2.35	10.6	5.1-10.7	2.3	8.15	3.2-10.3	4.7	6.6	5.1-7.4
Nb	2.05	8.75	5.0-11.5	1.2	7.15	1.8-7.2	4.3	6.85	4.7-6.8
Y	24	91	50-99	17	55	24-79	32	36	34-45
V	254	600	454-783	192	420	256-715	270	295	282-338
Ni	118	34	34-11	77	62	61-27	330	135	238-63
Cr	350	28	31-3	268	130	129-9	450	300	298-56
Average F			0.26±0.09			0.32±0.18			0.79±0.10
% Xstln.			60-83			33-84			9-38
Plag.			45			60			10
Cpx.			45			35			65
Ol.			10			5			25

Type	**T**	**(with N**	**as parent)**	**T**	**(with parent**	**in site)**	**T**	**(with parent**	**on scarp)**
Parent	BN-7-4			BN-2-3			BN-22-12		
Mg #	67			62			66		
Daughter		BN-2-12			BN-2-12			BN-2-12	
Mg #		34			34			34	
		Observed	*Calculated*		*Observed*	*Calculated*		*Observed*	*Calculated*
Zr	63	332	185-456	114	332	253-437	131	332	332-869
La	2.35	13.35	6.1-13.6	5	13.35	10.3-16.8	4.65	13.35	11.9-31.4
Nb	2.05	12.1	6.0-14.8	3.55	12.1	7.9-13.6	1.8	12.1	4.6-11.9
Y	24	100	56-113	35	100	65-101	31	100	66-146
V	254	410	471-792	261	410	412-563	215	410	377-672
Ni	118	15	32-11	72	15	18-7	220	15	2.5-0.0
Cr	350	7.5	7.7-0.3	330	7.5	19-3	213	7.5	8.3-0.3
Average F			0.19±0.07			0.34±0.06			0.30±0.09
% Xstln.			67-87			56-75			62-86
Plag.			40			35			
Cpx.			55			55			40
Ol.			5			10			50
Spinel									10

Table 8-3: Graphical summary of the depth and extent of melting based respectively on $Fe_{8.0}$ and $Na_{8.0}$ values calculated for the N-, T-, M- and EG-types. Abbreviations: "o" = average; "x" = minimum and maximum ends of range

D	E	P	T	H		D	E	G	R	E	E
	x	o	-	x	*N*	x	-	-	-	o	x
		o	x		*T*				x	o	x
x	-	o	-	x	*M*	x	-	-	o	x	
x	o	-	-	x	*EG*			x	-	o	x
4-6 V. LO	6-8 LO	8-11 MED	10-12 HI	12-14 V. HI	*Fe/Na (8.0)*	>4	3.5-4 V. LO	3-3.5 LO	2.5-3 MED	2-2.5 HI	1.5-2 V. HI

Table 8-4: Comparative summary of magmatic processes and source compositions determining the chemical differences between the four groups among the WBD suite. (* or melt-solid re-equilibration - Niu and Batiza, 1993).

Grp	*Low-P, frac.*	*Low-P mix*	*Crystal accum-ulation*	*Partial melting*	*Mode of melting*	*High-P, xstal. frac.*	*Nature of source*	*High-P. mixing*
N	~74%	Yes	Olivine	8.3-20.3%	Non-modal batch	No	Depleted sp. perid. + thermal anomaly	No
T	>66%	No	Olivine	3.5-7.8%	Non-modal batch	No	Clinopyroxene veins in depleted sp. perid.	None
M	~68%	No	Olivine	11.3-24.5%	Modal fractional	Possible*	Amphibolite veins in highly depleted sp. perid.	"Source"
EG	~21%	No	None	4.4-10.8%	Non-modal batch	Yes	High La end-member of depleted sp. perid. & enriched sp. perid. (E-)	"Magma"

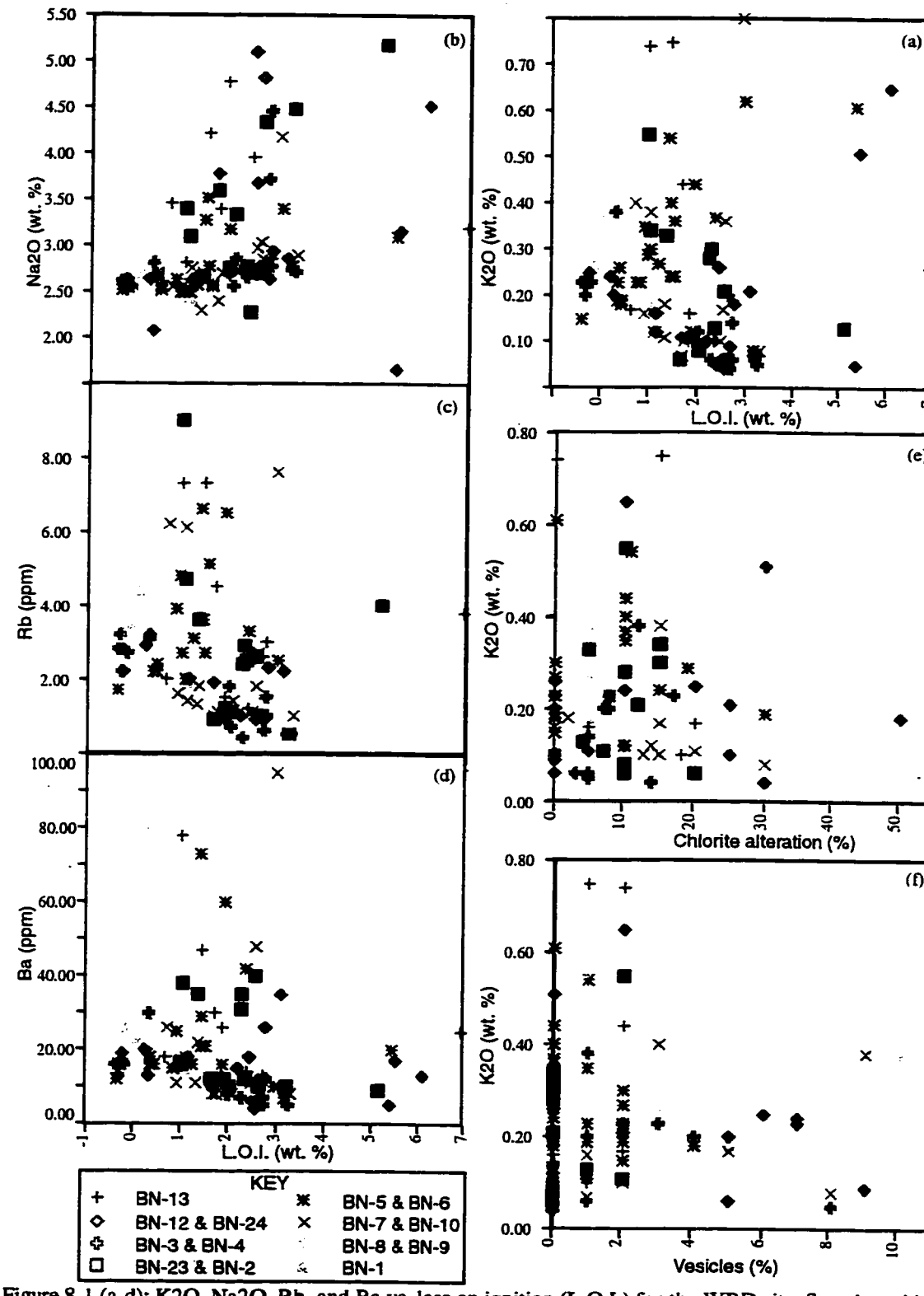

Figure 8-1 (a-d): K2O, Na2O, Rb, and Ba vs. loss on ignition (L.O.I.) for the WBD site. Samples with L.O.I. > 3.5 wt. % or K2O > 0.45 wt. % are classified as altered.
Figure 8-1 (e-f): Inverse relation of K2O (wt. %) with percentage of chlorite alteration (e) or vesicle abundance (f) reflects smectite involvement.

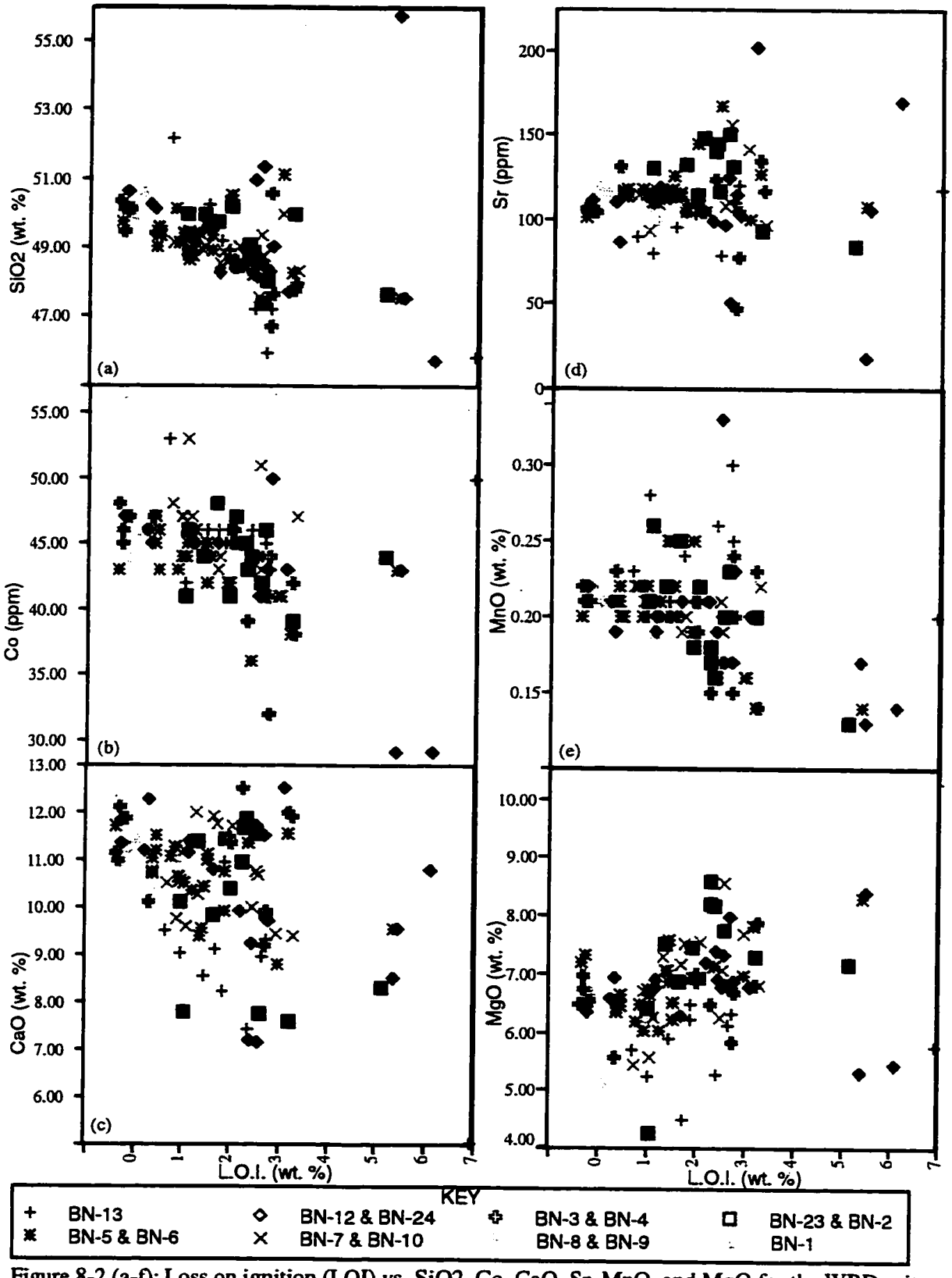

Figure 8-2 (a-f): Loss on ignition (LOI) vs. SiO2, Co, CaO, Sr, MnO, and MgO for the WBD suite.

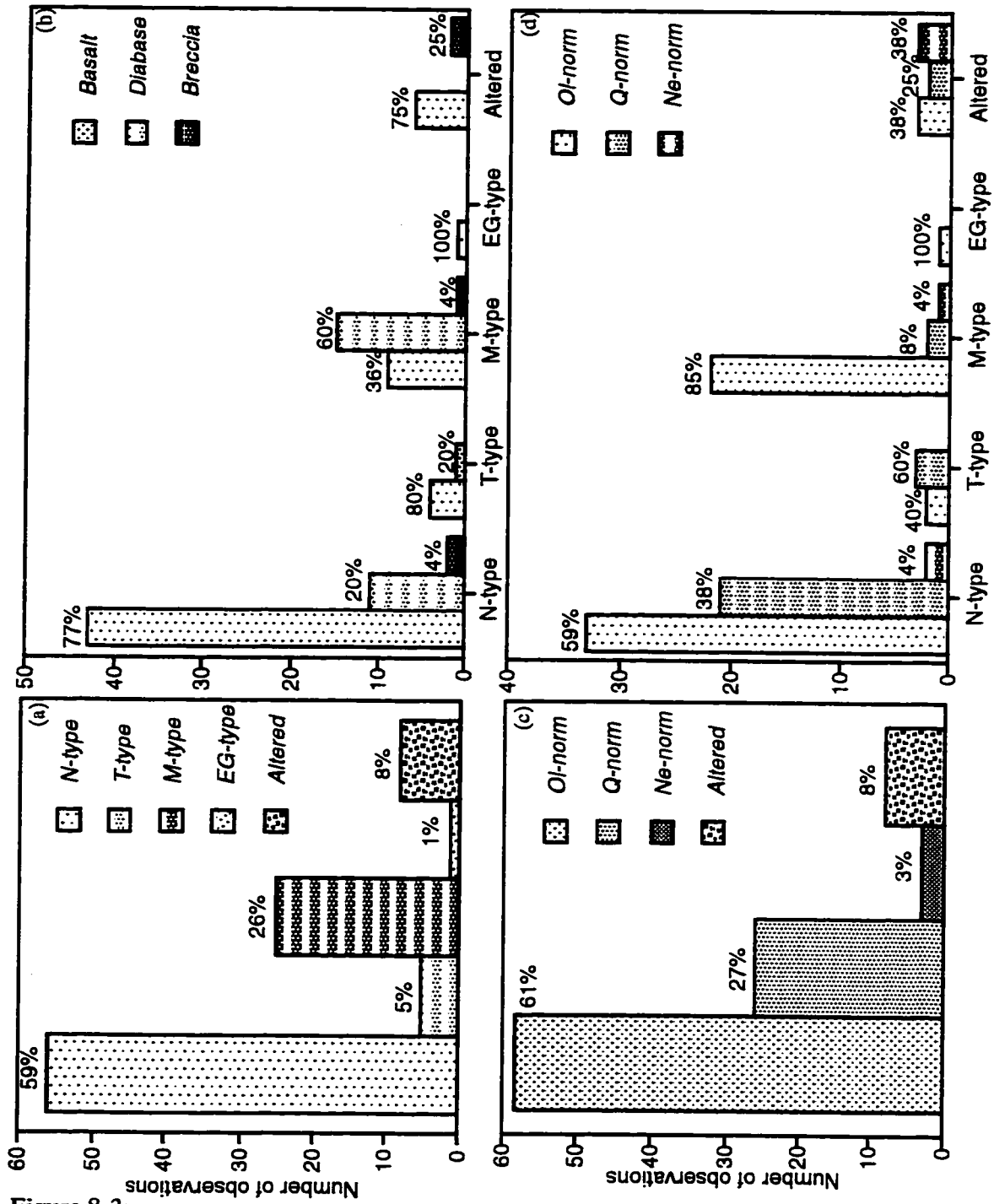

Figure 8-3:

(a) Percentages of petrogenetic types and altered samples in the study site.

(b) Proportions of basalts, diabases and breccias among the petrogenetic types and altered samples in the WBD suite

(c) Percentages of olivine (Ol), quartz (Q) and nepheline (Ne) - normative rocks and altered samples in the study site

(d) Proportions of the normative rock types among the petrogenetic types and altered samples in the WBD suite

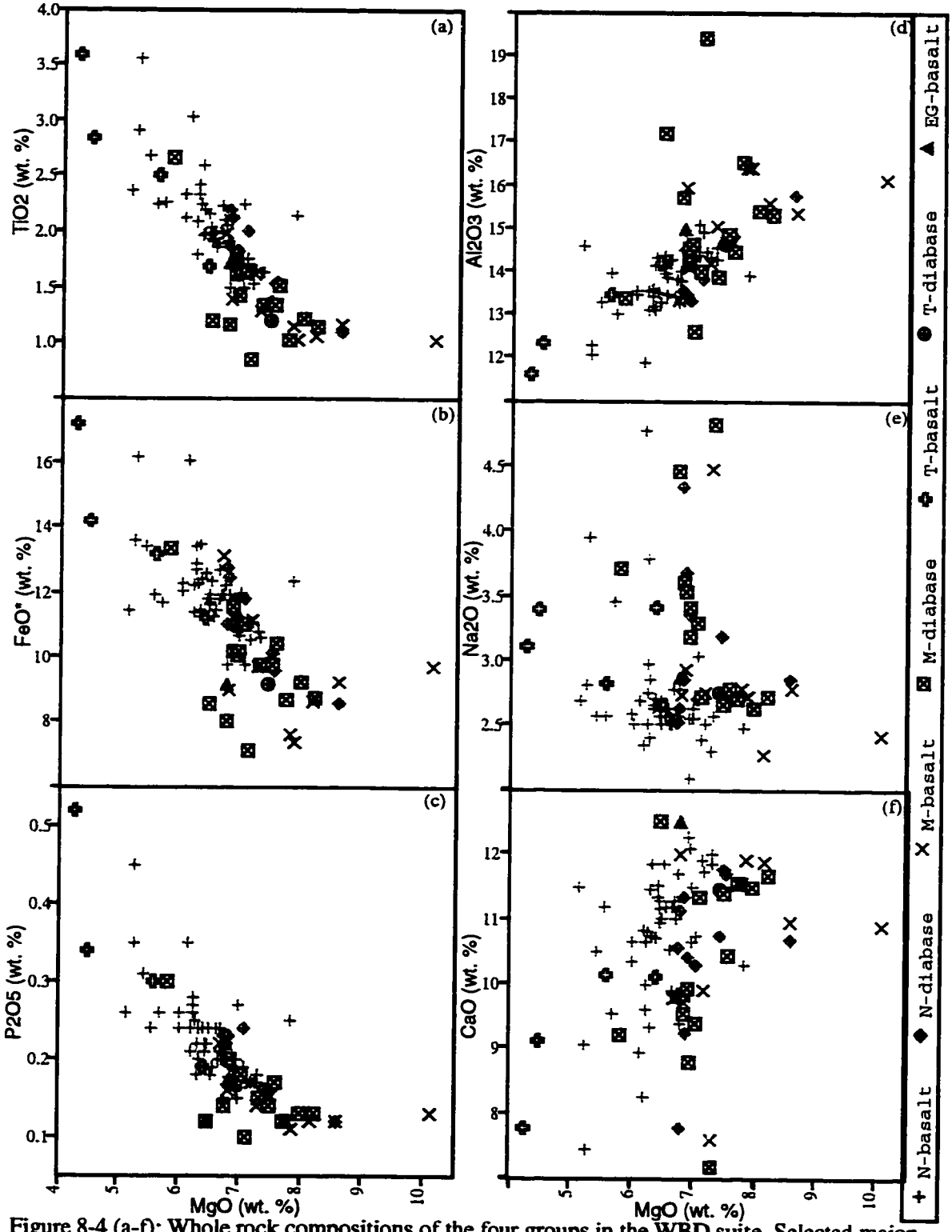

Figure 8-4 (a-f): Whole rock compositions of the four groups in the WBD suite. Selected major and minor elements display fractionation related trends with respect to MgO. CaO and Na2O show the effects of varying extents of alteration.

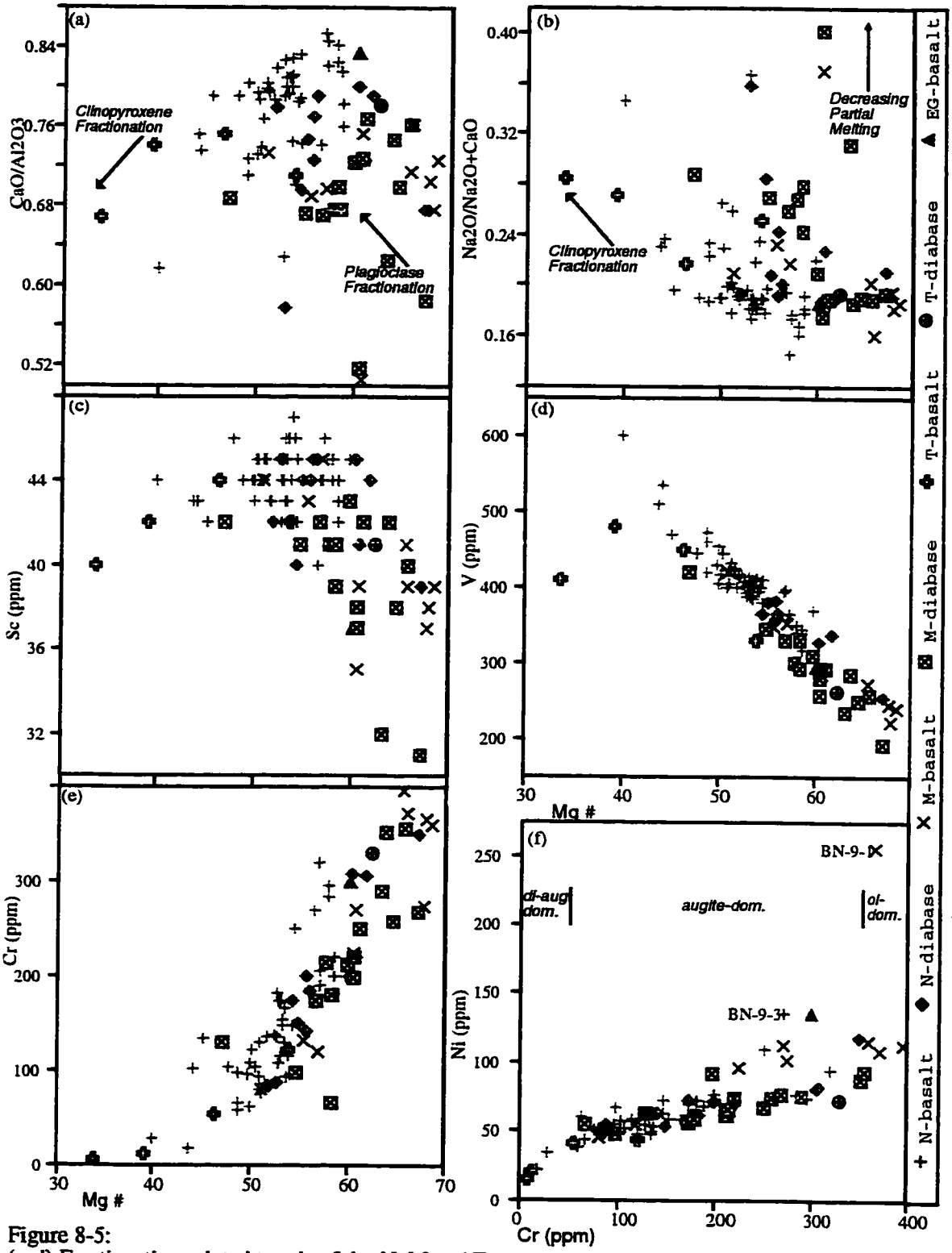

Figure 8-5:
(a-d) Fractionation related trends of the N, M and T compositional groups.
(e-f) The process involves successive olivine (ol-), augite (aug-) and diopsidic augite (di-aug) dominated crystallisation as discussed in the text.

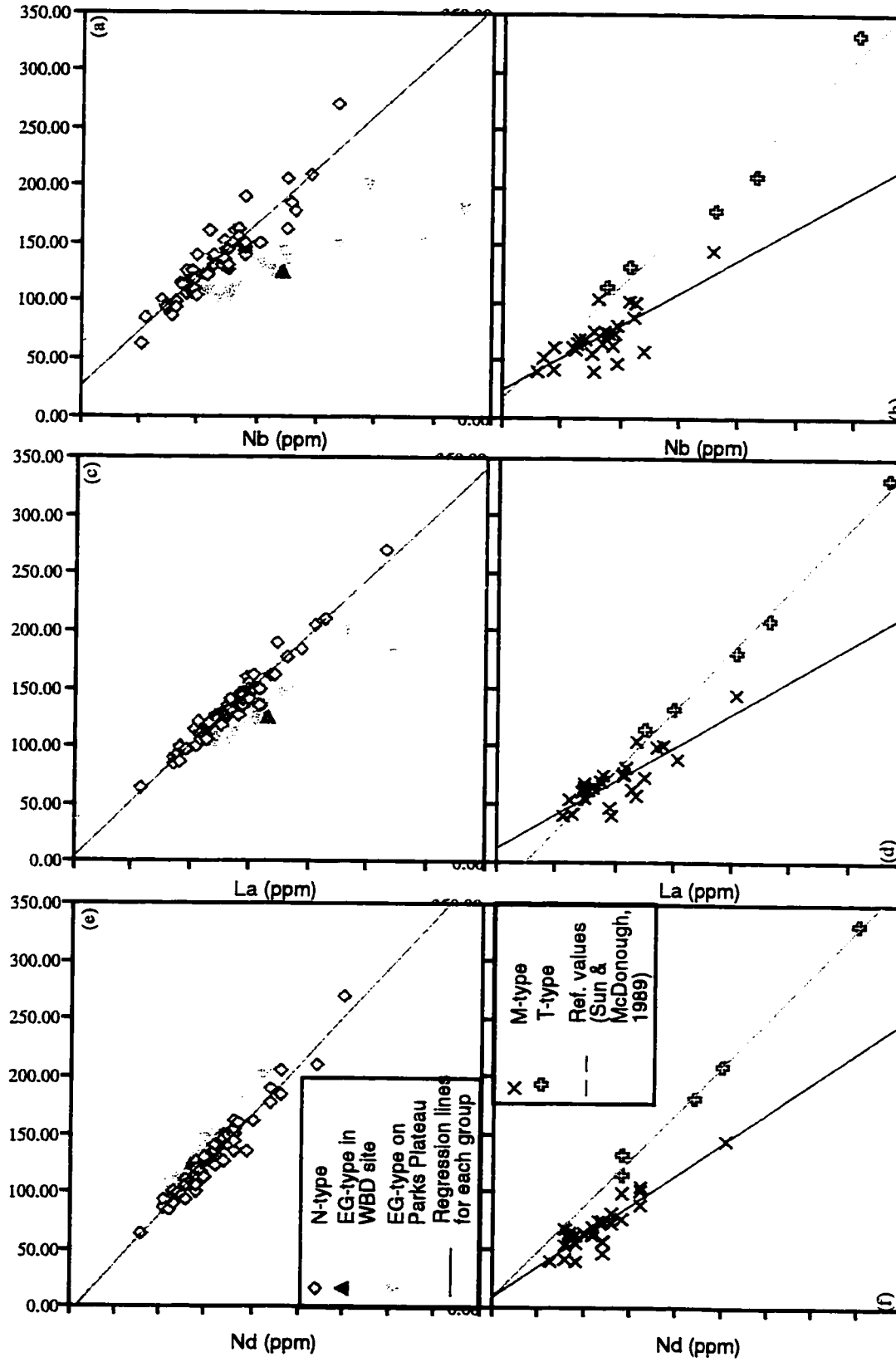

Figure 8-6: Incompatible element-element plots illustrate a similar linear trend between the N- (a, c and e) and T-MORBs (b, d and f) but the difference in ratio to the M- (b, d and f) and EG- (a, c and e) types. The lines represent the calculated best fit for each group.

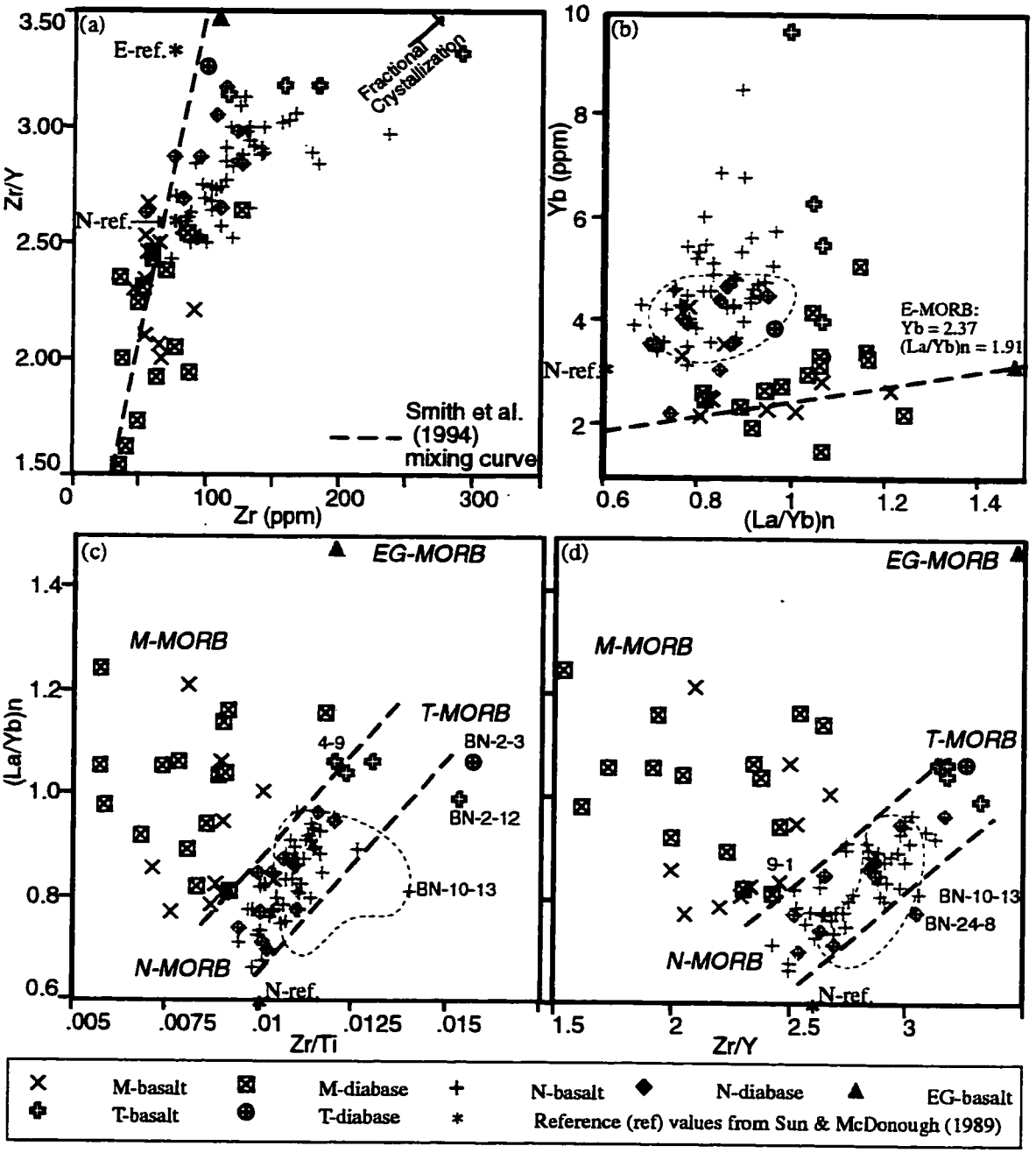

Figure 8-7:
(a-b) Zr vs. Zr/Y and (La/Yb)n vs. Yb displays fractional crystallization trend for N- & T-MORBs and apparent mixing trend for M-MORBs.
(c-d) Zr/Ti and Zr/Y vs. (La/Yb)n shows M- and EG-type MORBs which lie away from the array defined by N- and T-MORBs.
The irregular dashed field outlined in (a-d) represents the southern Juan de Fuca Ridge from dive BN-17 (Juteau et al., 1995). In each case, it overlaps only with the N-types and, together with the reference values indicated, further emphasizes the distinction between the four groups at the north WBD study site.

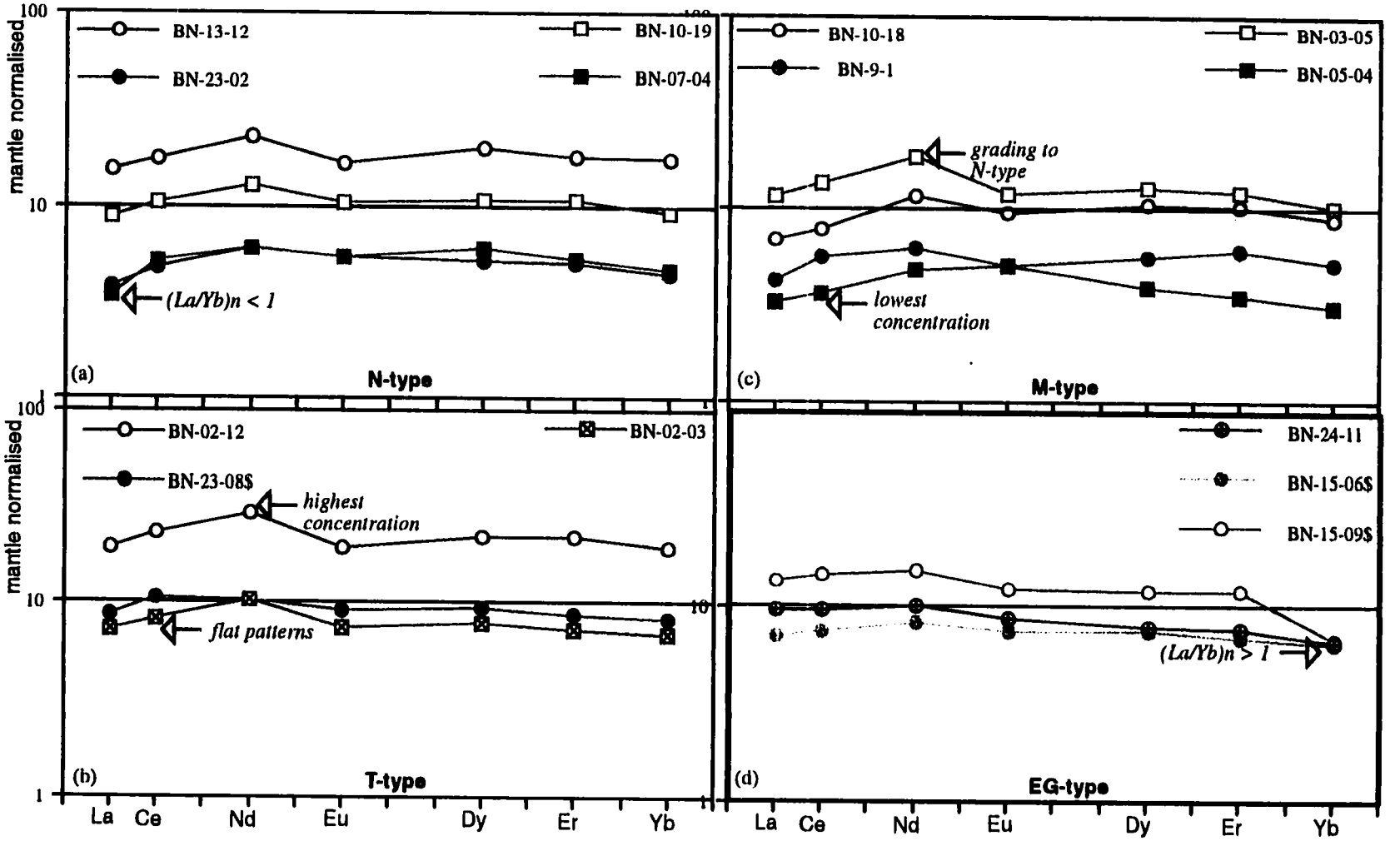

Figure 8-8: Mantle normalised REE plots comparing the 4 geochemical groups in the WBD site. The EG-type includes two samples that bracket the range for this group on Parks Plateau. Normalising values are from Sun and McDonough (1989). The samples selected in each group represent the span in basalt (blue circles) and diabase (red squares) concentrations with open and closed symbols for the highest and lowest values respectively. A symbol with an internal cross indicates that there is only a single basalt/diabase within the group.

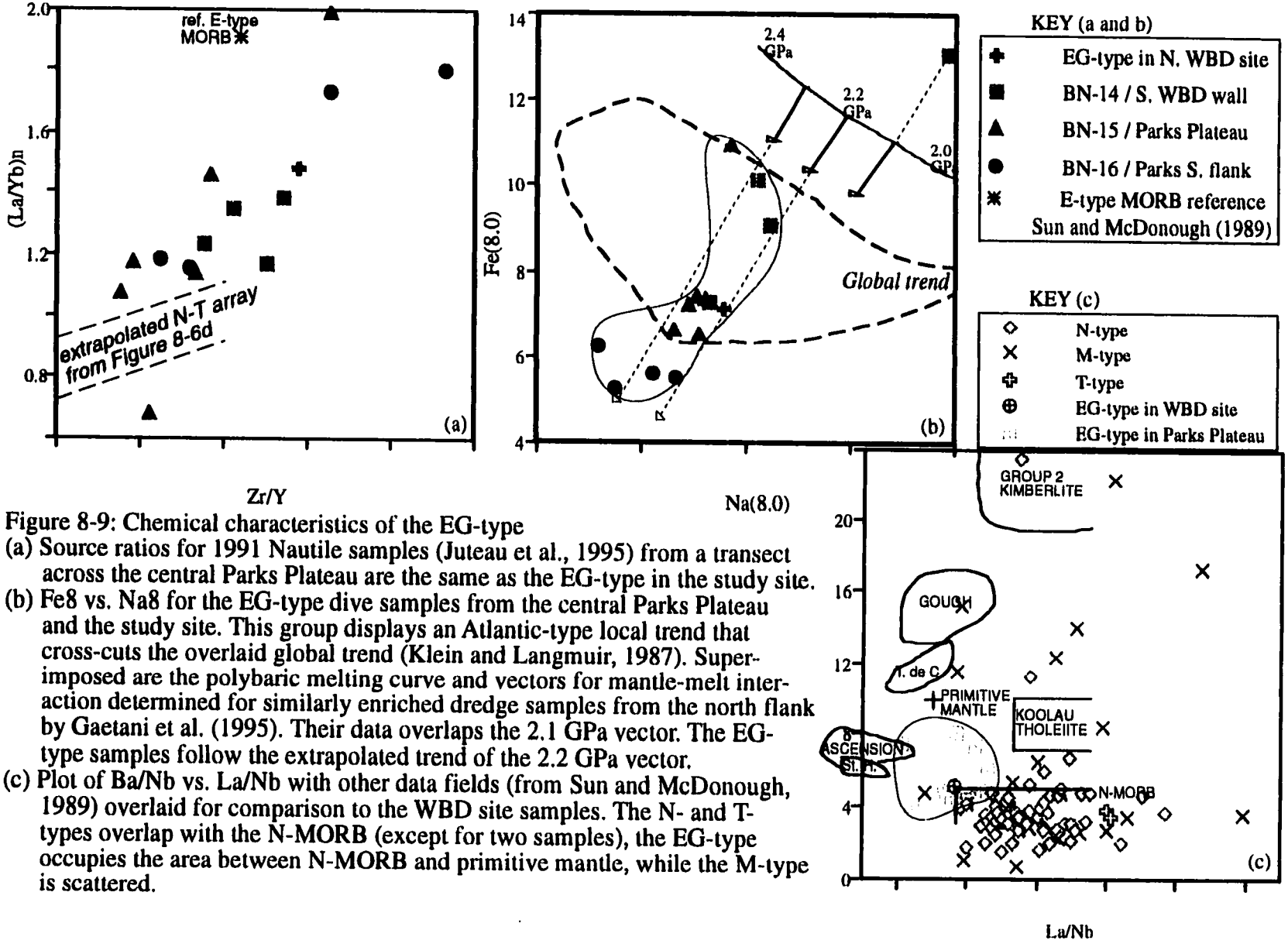

Figure 8-9: Chemical characteristics of the EG-type

(a) Source ratios for 1991 Nautile samples (Juteau et al., 1995) from a transect across the central Parks Plateau are the same as the EG-type in the study site.

(b) Fe8 vs. Na8 for the EG-type dive samples from the central Parks Plateau and the study site. This group displays an Atlantic-type local trend that cross-cuts the overlaid global trend (Klein and Langmuir, 1987). Superimposed are the polybaric melting curve and vectors for mantle-melt interaction determined for similarly enriched dredge samples from the north flank by Gaetani et al. (1995). Their data overlaps the 2.1 GPa vector. The EG-type samples follow the extrapolated trend of the 2.2 GPa vector.

(c) Plot of Ba/Nb vs. La/Nb with other data fields (from Sun and McDonough, 1989) overlaid for comparison to the WBD site samples. The N- and T-types overlap with the N-MORB (except for two samples), the EG-type occupies the area between N-MORB and primitive mantle, while the M-type is scattered.

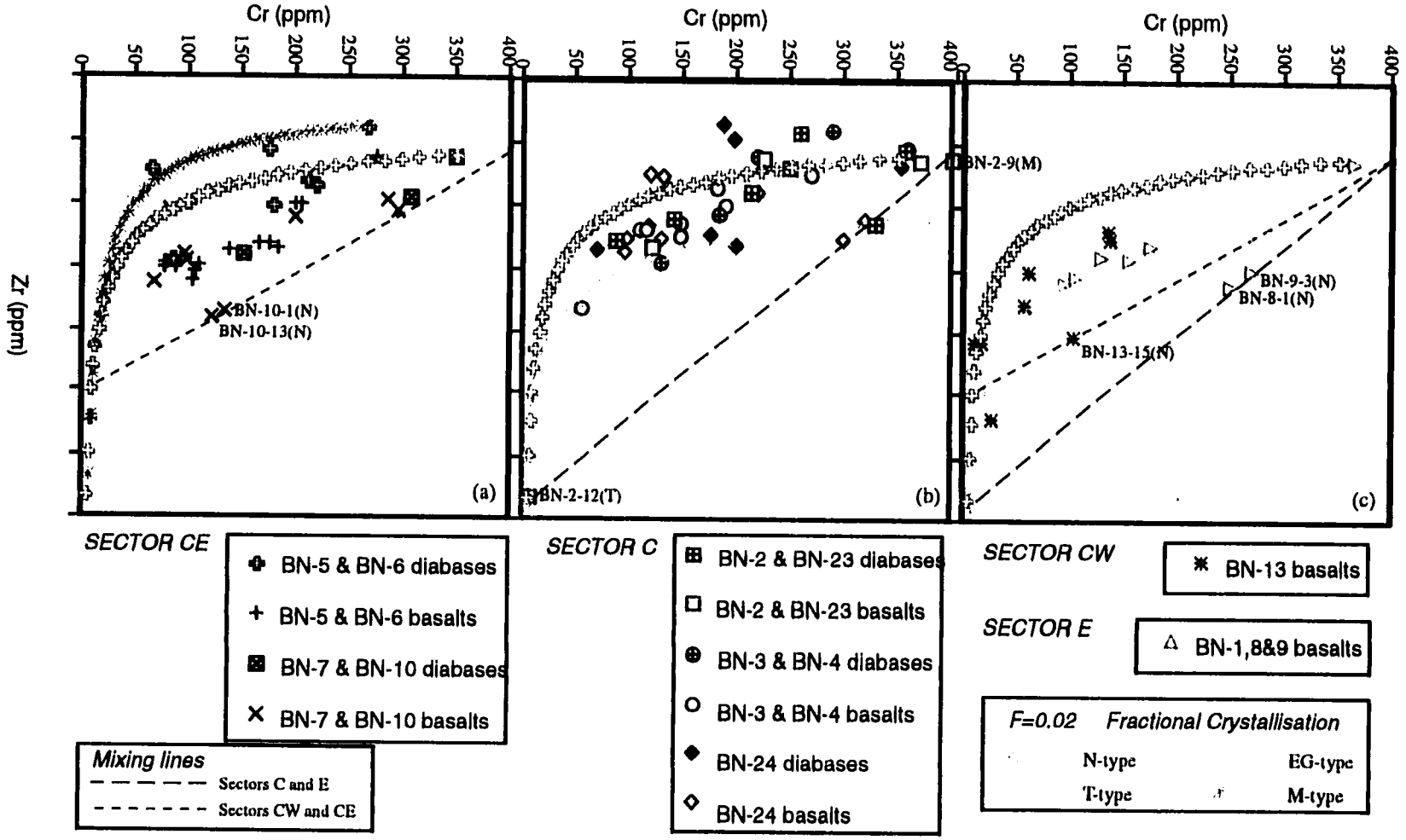

Figure 8-10: Variation of Cr vs. Zr in the sectors (a-c) of the WBD site. Superimposed are the fractional crystallisation curves for the four groups (Figures H-1 and H-4) with the N-type for reference in each plot. Most samples lie along these crystallisation trends. A few of the N-MORBs in each of the sectors lie along the dashed lines for mixing. The line for Sectors C and E is not the same as that for Sectors CW and CE reflecting mixing between different end-member compositions.

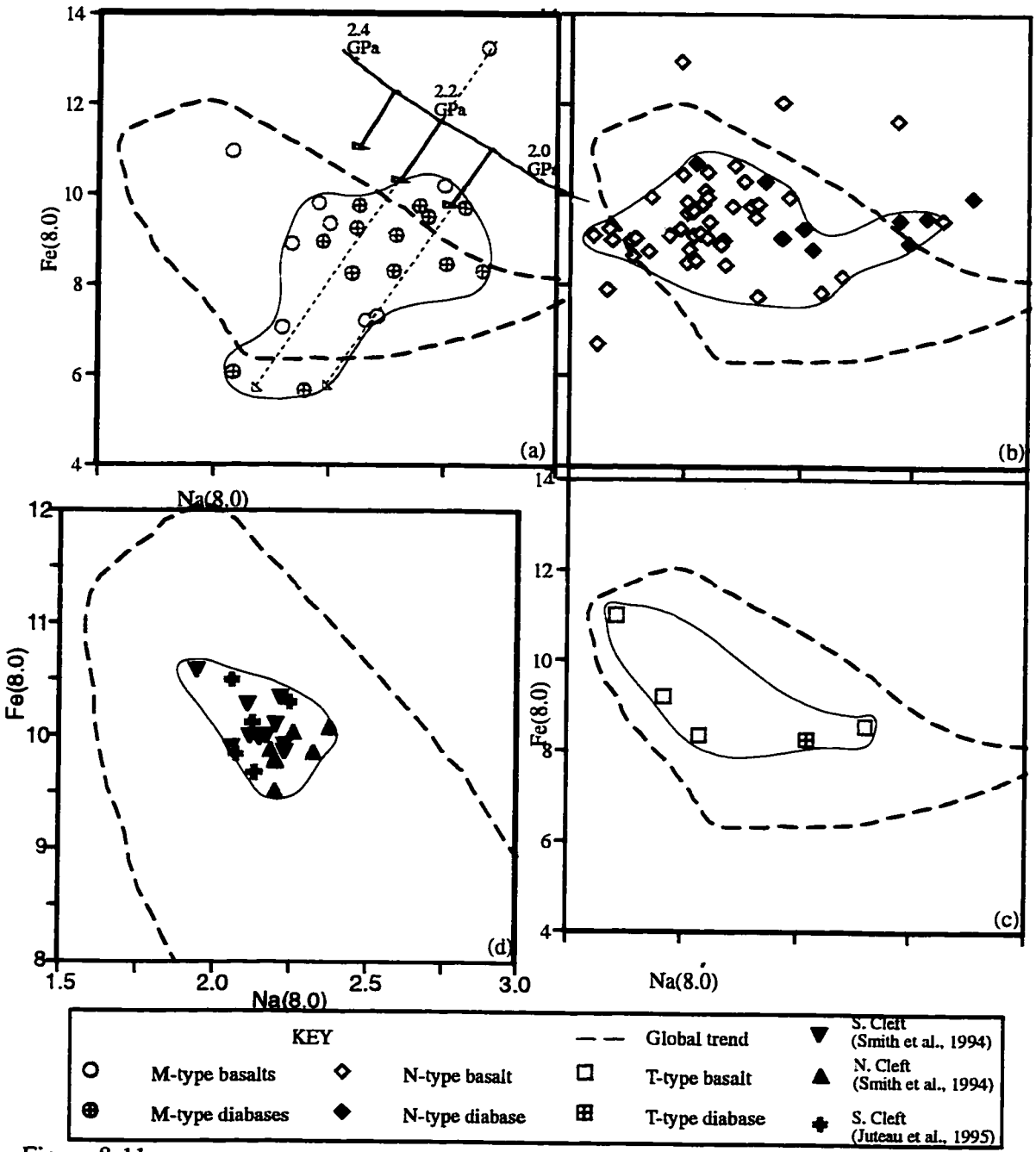

Figure 8-11:
Plots of Fe(8.0) vs. Na(8.0) comparing the values for the:
(a) M-type, (b) N-type, (c) T-type, and (d) Cleft segment to the regionally averaged MORB compositions (Klein and Langmuir, 1987). The polybaric melting curve and vectors of mantle-melt interaction (Gaetani et al., 1995) on (a) are the same as in Figure 8-9b. The N-type is scattered due to alteration of Na2O with 6 outliers. Almost all the rest of the samples (except for another 6) lie within the global field although the trend is not as obvious as for the N-MORBs at the Cleft Segment (d). The few T-MORB samples (c) follow the global trend (from Gaetani et al., 1995) and define a Pacific-type local vector while the M-MORBs (a) cross-cut the field and define an Atlantic-type local vector.

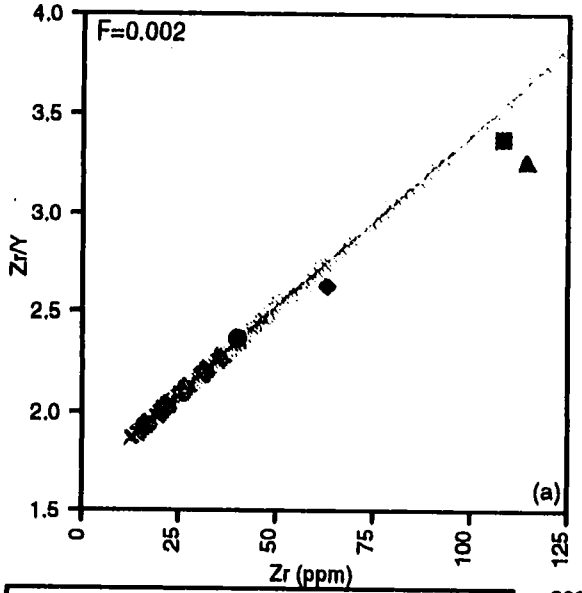

Figure 8-12: Melt generation model for the four geochemical groups in the WBD suite. The symbols represent the potential parental lavas for the N-, M-, T- and EG-types from Table 8-2. Also plotted is the source composition with the model curves produced by non-modal melting under isobaric conditions.

(a) Plot of Zr/Y vs. Zr with superimposed model curves for 0.2% increments to simulate nearly continuous decompressional melting. Batch melting results in a good fit for all but the T-type which overlaps the fractional melting curve. However, the temperature dependance of partition coefficients cannot be ignored here because it affects absolute element concentrations (Johnson and Dick, 1992).

(b) Plot of Ti/Zr vs. (Nd/Yb)n with superimposed model curves for 1% melting increments. The partition coefficients of these elements respond similarly to temperature change (Johnson and Dick, 1992). Batch melting is clearly a more appropriate model for all these groups. Note that melting of a garnet lherzolite source in the garnet stability field does not produce a fit to the data in such modelling (see parameters in Appendix H - plot not shown).

(c) Enlargement of (b) shows an increase in degree of melting from T- (3.5±1.9%) to EG- (4.4±0.9%) and to N- (8.3±2.7%) and M- (11.3±7.2%) types. Here, the M-type has the poorest fit to the non-modal batch melting curve. Also shown is the non-modal batch melt of a primitive source for comparison.

KEY

■ EG-type		non-modal batch melt of depleted source
◆ N-type		non-modal fractional melt of depleted source
● M-type		non-modal batch melt of primitive source
▲ T-type	F	weight fraction of melt formed

MODEL PARAMETERS

A. Sources - McKenzie and O'Nions (1991, 1995)

Depleted MORB source (in ppm):

Ti = 1020, Zr = 7.19, Nd = 0.815, Y = 3.18, Yb = 0.347

Primitive source (in ppm):

Ti = 1020, Zr = 8.51, Nd = 1.08, Yb = 0.372

B. See Appendix H for -

Initial phase proportions in spinel peridotite: Spiegelman (1996)

Proportions of phases entering the melt in the spinel stability field: Johnson et al (1990)

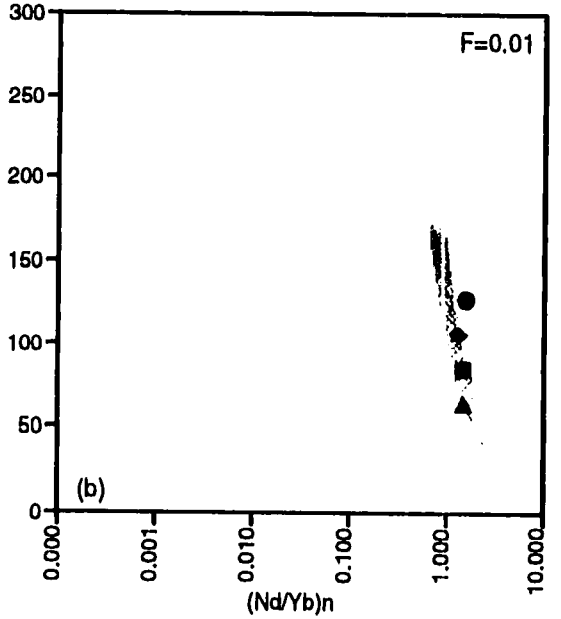

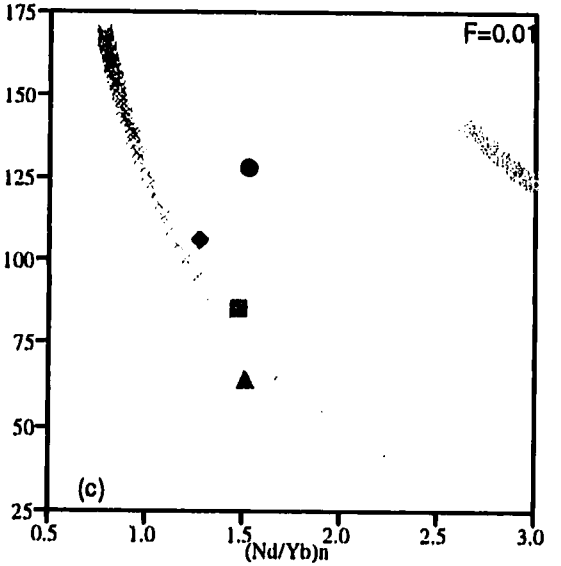

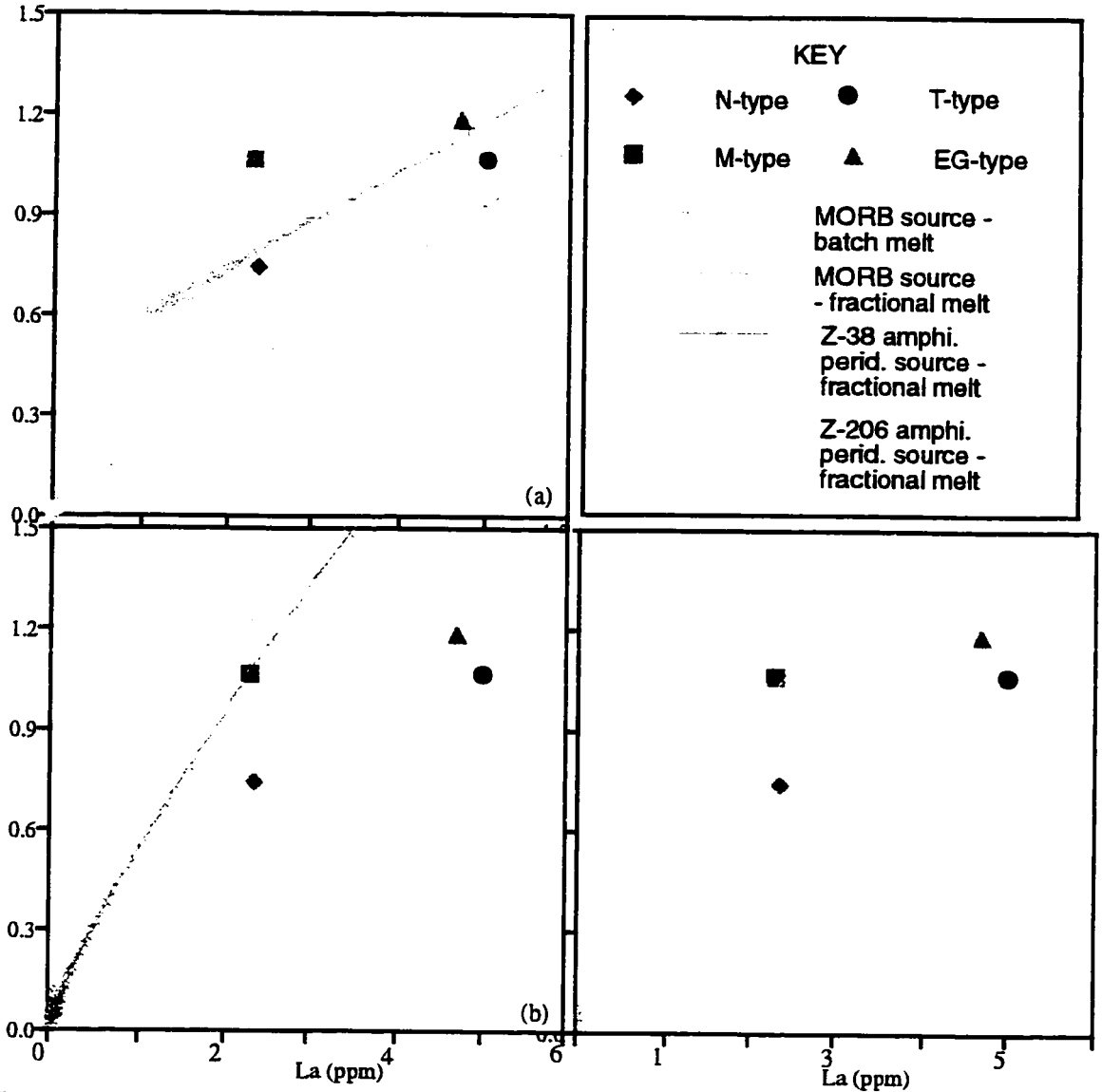

Figure 8-13: Melt generation model for the M-type in the WBD site and on Parks Plateau as compared to that for the other three groups in the study site. Modal models are utilised in the absence of available melt modes for an amphibole peridotite. Calculated (La/Yb)n is plotted versus calculated La (in ppm) to illustrate LREE-enriched characteristics.

(a) Plot showing modal models of batch and fractional melting the depleted MORB source in Figure 8-12. A modal batch model is able to produce the parental concentrations of the N- and EG-types by respectively 20.3±1.6% and 10.8±1.3% melting. A modal batch model can also generate the T-type by 7.8±1.6% melting but the fit is not as good possibly due to minor clinopyroxene veins in the source. Neither of these models is able to reproduce the M-type.

(b and c) Plots showing that a modal fractional melt model using source compositions of amphibole peridotite (b: Z-38; c: Z-206) from Zabargad Island (Bonatti et al., 1986) can reproduce the M-type by 24.5±0% (b) to 25±0.7% (c) melting.

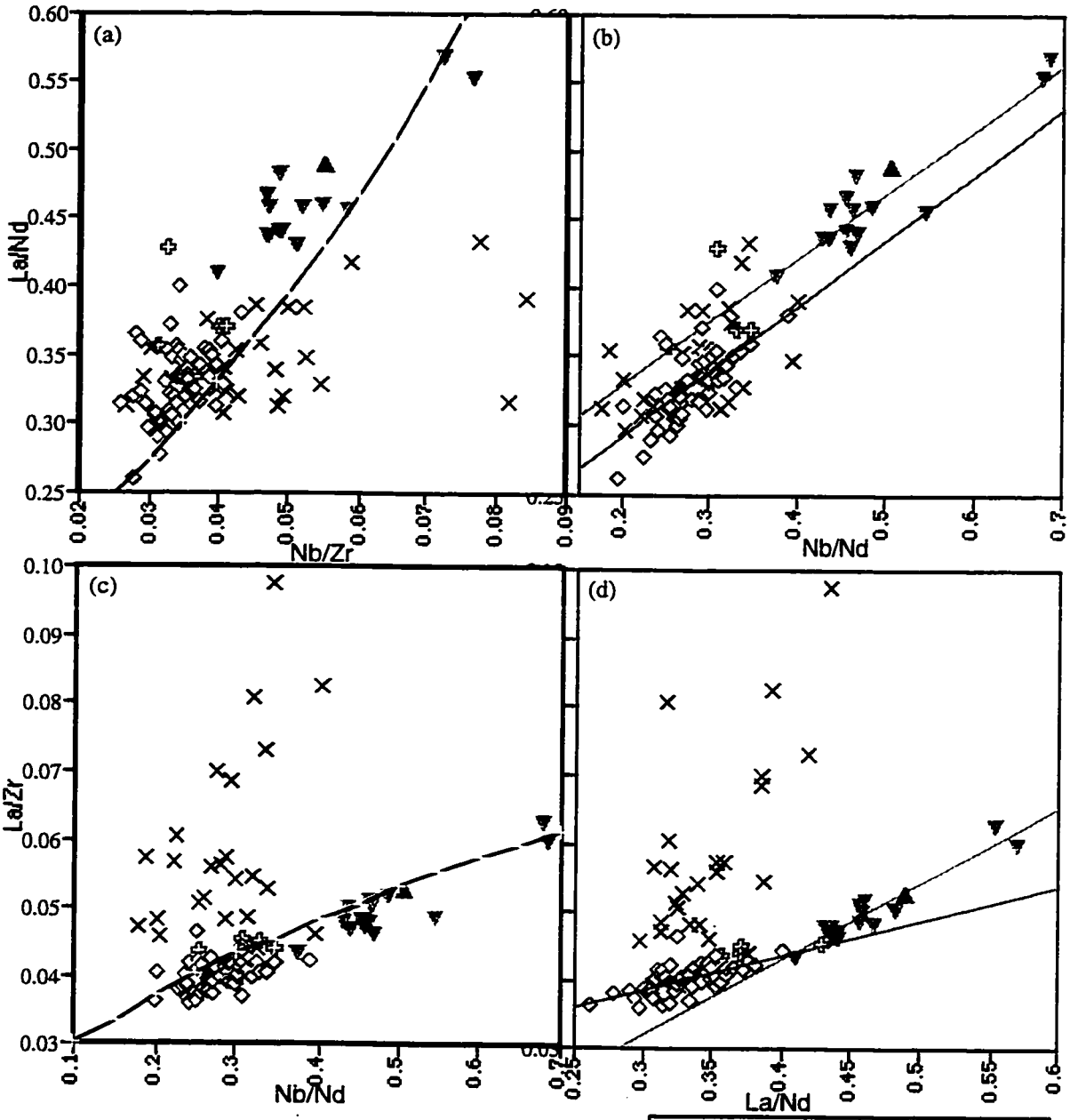

Figure 8-14: Test for mixing - I

(a and c) Incompatible ratio-ratio plots for the four lava types with a mixing curve between the N- (BN-4-11) and EG- (BN-16-3) types. Shows possibility for mixing between these two sources or magmas.

(b and d) Companion plots with separate linear regressions for the N- and EG-types. The two linear data arrays indicates that no mixing occurred between these sources or magmas but there is a possibility for mixing within each of these groups.

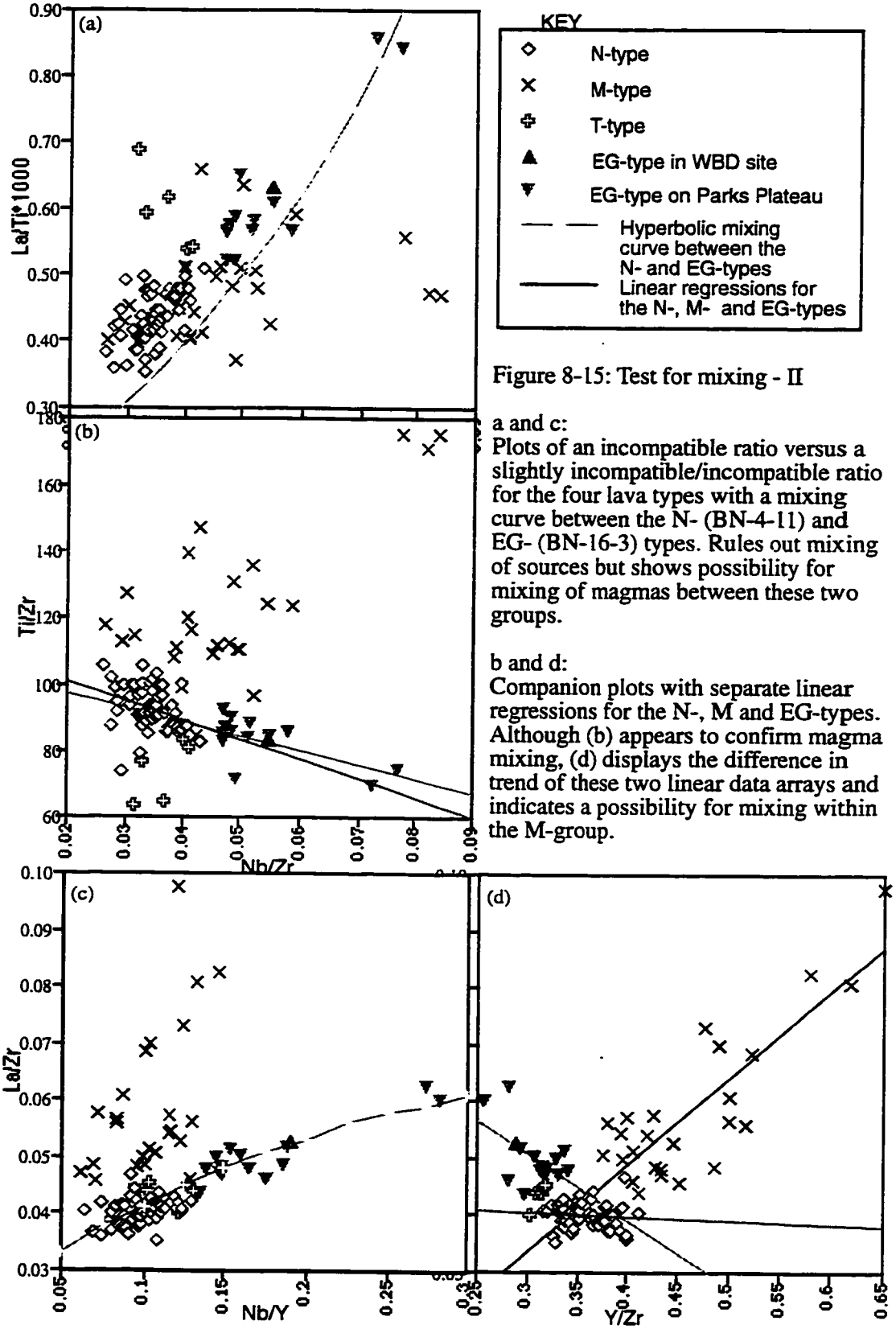

Figure 8-15: Test for mixing - II

a and c:
Plots of an incompatible ratio versus a slightly incompatible/incompatible ratio for the four lava types with a mixing curve between the N- (BN-4-11) and EG- (BN-16-3) types. Rules out mixing of sources but shows possibility for mixing of magmas between these two groups.

b and d:
Companion plots with separate linear regressions for the N-, M and EG-types. Although (b) appears to confirm magma mixing, (d) displays the difference in trend of these two linear data arrays and indicates a possibility for mixing within the M-group.

CHAPTER IX: TEMPORAL VARIABILITY IN THE LAVA GEOCHEMISTRY: IMPLICATIONS FOR MAGMATIC ACCRETION AND CRUSTAL EVOLUTION

9.1 Introduction

Fracture zone walls often expose the upper oceanic crust accreted at the ridge axis near the same lithospheric flow line over millions of years. These cliff faces reveal at least a semi-complete section through the extrusive pile (e.g. Auzende et al., 1989; Hébert et al., 1983) which allows for the chemical evolution in crustal building to be traced. In addition, these scarps present a continuous record of the geochemical histories generated repeatedly at the same point in relation to the ridge axis which permits assessment of changes in magmagenesis over time.

Systematic and closely spaced spot sampling along and up these walls offers an opportunity to evaluate the magnitude of chemical variability in the lavas erupted during crustal construction, and to resolve any variation in basalt composition at a finer scale than magnetic stripes. Such investigations have introduced new petrologic perspectives.

Results of the latter work emphasize the importance of mantle over crustal level processes. At a slow spreading-rate ridge, major temporal changes have been found in the depth and nature of mantle flow (Johnson and Dick, 1992). At a fast spreading-rate ridge, magma supply is the most significant determinant of thermal variation and consequently, of magma chamber development and the resultant average composition (Batiza et al., 1996).

In this study, basalts were collected using *Nautile* along several traverses (Figure 4-2) up the north scarp of the West Blanco Depression (WBD). Major, trace and rare-earth element analyses of these lavas (Appendix G) have shown that there are four

distinct compositional groups of normal (N), metasomatic (M), transitional (T) and enriched (EG) origin (Chapter VIII). The former three types are proposed to arise from multistage melting with diapiric mantle flow beneath the migrating Juan de Fuca Ridge (JdFR)(Chapter III) and the latter by an off-axis melting event focused beneath Parks Plateau (Chapter VIII).

In Chapter IX, these data are examined in terms of their spatial relations vertically and laterally in the study site. The latter represent their relative ages in the case where magmatic accretion is sequential up-section, crustal evolution is time progressive and the spreading history is simple. However, the geologic evidence suggests that the basement here is complicated by near- (and off-) axis intrusion forming Upper and Lower Outcrop Zones (Chapter IV), possible sill injection on- and/or near-axis (Chapter V), and repeated crustal subsidence creating domains (Chapter VI).

Hence, the purpose of this chapter is two-fold:- to assess whether these geologic "building blocks" have geochemical underpinnings; and to determine the relation (if any) between the compositional groups and their petrographic and lithologic units. The aim is to gauge whether the prior hypotheses on upper crustal formation are consistent with the geochemical data and to refine these models of magmatic accretion and crustal evolution.

9.2 Results and interpretation

9.2.1 Geochemical Characteristics of the Upper and Lower Outcrop Zones

The Upper (UOZ) and Lower (LOZ) Outcrop Zones in the Central (C), Central-East (CE) and East (E) sectors of the WBD site that were recognized on the basis of geologic data (Chapter IV) also have distinct geochemical characteristics. Such evidence includes the normative compositions (Figure 9-1), chemical groupings (Figure 9-2) and

major and trace element concentrations (Figures 9-4 to 9-6) that are displayed according to depth and from west to east by sector.

The UOZ is distinguished by the presence of Diopside-Hypersthene-Quartz (Di-Hy-Q) normative samples that are restricted to above ~3700 m except in Sector CW (Figure 9-1). This zone is composed predominantly by N-type lavas (Figure 9-2) with Zr/Nb ratios mostly between ~26-33 (Figure 9-3a). These basalts result in the UOZ having TiO_2 (Figure 9-4), P_2O_5, CaO, V, Y, Nb and Zr (Figure 9-5) concentrations that are distinctly higher than in the LOZ.

The LOZ is distinguished by the presence of Diopside-Nepheline-Olivine (Di-Ne-Ol) normative samples that are limited to below ~3450 m (Figure 9-1). In this zone, M-type lavas with Zr/Nb ratios mainly between ~16-30 (Figure 9-3a) predominate except in Sector CW (Figure 9-2). These basalts and diabases result in the LOZ having MgO and Na_2O concentrations and Mg # (Figure 9-6) higher than in the UOZ. In addition, their MnO content displays large variations in this zone.

The ~3450-3700 m interval of overlap between these zones in terms of composition corresponds to the Lower-Intermediate Zone (LIZ) (Figure 9-3f) defined on lithologic grounds (Chapter V). This transition is also highlighted by geochemical variations. Within the LIZ, the N-type lavas in two profiles show large chemical variability over short vertical distances (Figures 9-4, 9-5 and 9-6 a&f) as compared to the overlying part of the UOZ. Such wide compositional fluctuations are assumed to be primary because these samples are not more altered or different in any other aspect from the rest. Likewise, the M-type lavas mark the LOZ and LIZ contact by abrupt shifts as indicated by the sharp decline in TiO_2 (Figure 9-4 b-e) and increase in Al_2O_3 or Mg-# (Figure 9-6 b-e). This pattern is consistent in all four profiles despite the small number of

available samples on which it is based. It is interpreted as a second magmatic pulse that possibly stems from mixing the prior M-type melts differentiating in the chamber with a more primitive input. This results in the switch to less evolved compositions being emplaced in the LIZ.

9.2.2 Relation of chemical groups to petrography and lithology

While the petrographic (Chapters VII), lithologic (Chapter V) and chemical characteristics independently distinguish between the UOZ and the LOZ, an understanding of how these parameters are linked is useful to constrain the dynamics during accretion. Consequently, correlations for chemical group versus petrography and lithology are given in Tables 9-1 and 9-2.

The N-type is mostly plagioclase-clinopyroxene (P-C) phyric while the M-type is mainly aphyric (Table 9-1). This difference in phyric assemblage can be explained by the N-type being more evolved than the M-type (Figure 9-3). As a result, the distribution of P-C basalts in the UOZ and aphyric diabases in the LOZ (Figure 7-8) is actually tied to the emplacement of the two chemical groups.

The M-type forms thick sheet flows/sills, massive diabase intrusions and dikes primarily in the LOZ (Table 9-2). It is therefore mainly intrusive in nature and the thick sheets are more likely to be sills injected at the base of the crustal section. Given that these sills overlie the massive diabase (Figure 5-1), it appears that sill injection into the crust preceded the diabase emplacement at the base of the section.

The N-type dominantly forms jumbled sheet flows, thick sheet flows/sills and pillows (Table 9-2) which is consistent with the prominence of these lava morphologies

throughout the UOZ (Figure 5-2). The above resolution of the flow/sill ambiguity in favor of intrusion implies that there was also N-type magma injection into the basement.

Although the N-type is present in the LOZ, it is never associated with the M-type, massive diabase intrusives. Consequently, it is inferred that the N-type source was not available by this final stage of accretion which suggests a near-axis location. Hence, the timing of sill injection is potentially bracketed between N-type emplacement that is synchronous with on-axis crustal construction and M-type emplacement near-axis.

9.2.3 Geochemical variation with depth

The geochemical processes involved in forming the UOZ and LOZ are elucidated from other chemical variables (Figure 9-3) which show more continuous variation with depth.

Apart from the LIZ (Figure 9-3f), the N- and T-type lavas in the rest of the UOZ have a narrow range of $Na_{8.0}$ (Figure 9-3d) indicating that they were generated by a constant high degree of melting (Table 8-3).

The depth of melting for the N- and T-types as expressed by $Fe_{8.0}$ (Figure 9-3e) reflects moderate pressures overall in the UOZ. However, for the N-type over the Upper-Intermediate (UIZ) and Uppermost (UZ) Zones, there are slight decreases with decreasing depth which signal a gradual shallowing in melting as the crust was constructed during each of these stages. The Middle-Intermediate Zone (MIZ), by contrast, displays the reverse trend which suggests a deepening in melting with time. This change in melting behavior at ~2900 m depth is significant because the boundary coincides with a pronounced shift in lithology (Figure 5-2). Thus, it is inferred that eruptive dynamics may be indirectly linked to mantle processes.

A plot of Mg # versus depth (Figure 9-3c) shows the N-type changing from moderately to slightly evolved compositions up-section in the MIZ, UIZ and UZ. The implication is that lavas in the UOZ are erupted during periods of magma replenishment rather than fractionation. Consequently, there is the potential for low-pressure magma mixing of which there is both petrographic (Chapter VII) and chemical (Chapter VIII) evidence.

The CaO/Al_2O_3 ratio (Figure 9-3b) ratio increases upward through the LIZ, is variable in the MIZ, increases again through the UIZ and decreases through the UZ while the lavas concomitantly become less evolved over the latter three zones (Figure 9-3c). Given the typical fractionation curve for these variables (Figure 8-5a), the trend in the UIZ could result from highly evolved magma progressively mixing with more moderately evolved magma or alternately, from their sequential tapping in a zoned magma chamber. Similarly, the trend in the UZ could be produced by either progressively mixing moderately evolved magmas with more primitive/slightly evolved magmas, or by selectively erupting these magmas from a density stratified chamber. This temporal evolution is important because it implies that accretion of the crustal section commences after an extensive period of fractionation and is completed within a magmatically robust phase of the melt lens.

In the LZ and LIZ, the N-type lavas were generated by high to moderate degrees of melting as inferred from $Na_{8.0}$ (Figure 9-3d and Table 8-3). This implies, given the two competing models of magmatic accretion (Figure 5-2), that the degree of melting between the LOZ and UOZ either gradually increased over time in the extrusive case or decreased if there was subsequent sill injection. The same interpretation applies to the M-types which display the overall N-type trend within the LZ and LIZ. The T-types here are at the high end of melting implying no change in extent with depth.

The depth of melting for the N- and T-type lavas in these zones, as inferred from $Fe_{8.0}$ (Figure 9-3e and Table 8-3), remains at moderate pressures but with no obvious trend(s) in the N-type up-section as for the UOZ. By comparison, the M-type lavas were produced over a broader range to lower pressures.

In terms of Mg # (Figure 9-3c), the T-types in the LZ and LIZ are extremely evolved while the M-type tends to be more primitive. For the M-type, the Mg # decreases while the CaO/Al_2O_3 ratio (Figure 9-3b) increases with decreasing depth. This suggests that the M-types represent at least one fractionation series and that these diabases are successively emplaced at shallower levels over time. The N-type lavas are scattered in between these extremes and are therefore more variable in composition in the LOZ than in the UOZ. Of these, the likely intrusive diabases tend to be toward the less evolved side while the extrusive basalts are at the differentiated end. This supports the emerging view that the lavas initially erupted at the base of the upper crustal section largely represent the end-products of the prior magmatic phase mixing with the fresher input.

9.2.4 Geochemical variation within domains

The geochemical variation within domains in relation to the constituent lithologies can be examined for 15 of them (basalts in upper outcrop zone: B3, B5, E4, E10, K7, K8, P1, V3, X1; diabases in lower outcrop zone: D3, D4, G4, G7, Z3; basalt and diabase in upper outcrop zone: X4) with two samples each, and for 5 (basalts in UOZ: E9, L1, U2; basalts in LOZ: Z2; diabases in LOZ: G8) with three samples analyzed. These labelled areas are outlined in Figure 6-1c and their approximate boundaries along the dive traverses have been transferred to the columns in Figures 9-1 and 9-2. Examples of their mantle normalized abundance patterns, with elements in order of decreasing incompatibility from left to right (Sun and McDonough, 1989), are

displayed in Figures 9-7 and 9-8. Both the basalt and diabase domains exhibit four types of "spidergrams":

(i) The spidergrams of rock samples in a domain can be almost identical with the exception of a few highly incompatible elements which tend to be mobilized by alteration. Examples include the basalt domains (Figures 9-7a,c,d&f) E4, K8, and sections of E9 (Exception: BN-6-7), L1 (Exception: BN-10-11) and U2 (BN-13-12), as well as the diabase domain Z3 (Figure 9-8f). These lavas frequently have the same morphology within a domain irrespective of the vertical distance between them. In domain U2, the thick sheet flow/sill lithology was retrieved at a vertical separation of 52 m. In domain Z3, massive flows/intrusions were recovered 67 m apart vertically. In cases when they stem from different lithologies, one of the forms is often a dike or spire structure. Such pillow units can be linked to local dikes 25 m above in E4 and 156 m below in K8. Likewise, jumbled sheet flow units are compositionally similar to spires 134 m above in E9. In the absence of major faults, the lava thickness of ~130 m implies that the underlying magmatic system sometimes either evolves little or is buffered over time.

(ii) Other spidergrams from a domain have the same shape but are offset due to fractionation effects. Examples include the basalt domains (Figures 9-7b,d,e&f) B5, K7 and sections of L1 (BN-10-11) and U2 (BN-13-12) as well as the diabase domain (Figure 9-8e) D3. In these cases, the lithologies of these geochemically related lavas are the same, unless they involve dikes or spires, and the sample depths correspond to steadily increasing differentiation upward in the domain. In domain D3, the less fractionated sample lies 58 m below within the same unit of massive flows/intrusions. In domain U2, the most fractionated rock was recovered from the same thick sheet

flow/sill lithology sampled above and below it. In domain K7, a thick sheet flow/sill unit is less fractionated than a dike 55 m above. In domain B5, spire structures are a more fractionated equivalent of dikes 30 m below.

(iii) Some spidergrams within a domain have different shapes or even cross indicating that these lavas are geochemically unrelated although they are all of either the N- or M-type. Examples include the basalt domains (Figures 9-7c and 9-8b) X1 (not shown), sections of E9 (Exception: BN-06-07) and Z2 (Exception: BN-24-3), as well as the diabase domains (Figures 9-8a,d&f) D4, G4 and G7. In all these cases, different lithologies were sampled in a domain. In domains X1 and Z2, the dikes respectively overlie a tectonized and an obscured lithology with vertical separations ranging from 8 m to 381 m. In domains E9, G4 and G7, the vertical distance between lithologies varies from 54 m to 90 m and involves jumbled and thin sheet flows in E9, thick and massive sheet flows/sills in G4, and thin sheet flows, massive flows/intrusions and tectonized units in G7. These observations indicate rapid changes in both the chemical and physical conditions of the magmatic system. Hence, it is inferred that these domains are either the product of multiple magma chambers which are contemporaneous or that domains include a significant portion of intrusions.

(iv) Other domains have lavas of different chemical types. For example, the N- and T-types are present in the B3 and P1 basalt domains while the N- and M-types are found in the basalt domain V3, and sections of the diabase domains D3, G8 and Z2.

The geochemical nature of domains is thus highly variable and there appears to be no systematic relationship between their formation and events in the magmatic system. Some domains may not even differ considerably in either primary or secondary

chemical characteristics, such as between B5 and E10 (Figure 9-7b). However in other cases, the geochemical distinctions between domains are obvious as can be compared for K8 and E4 (Figure 9-7a). In addition, the effects of alteration on the elements Ba, K, Sr and Zr can serve as a useful attribute in identifying domains. For example, although domains K8 and E10 (Figures 9-7a&b) are both depleted in Ba and Sr, they differ in degree. Likewise, the basalt domains L1 and K7 (Figures 9-7e&f) and the diabase domains D3 and Z3 (Figures 9-8e&f) are depleted in Ba, K and Sr but their relative extents differ. These secondary features of domains indicates that they have separate metamorphic histories and that such evidence is retained. This would be possible if the domains were fault bounded blocks which is in accord with the model of repeated crustal subsidence presented in Chapter VI.

9.2.5 Geochemical variation between sectors

Geologic evidence of lateral variation across the WBD site (Tables 6-1 and 6-2) is confirmed by the geochemical data. The chemical groups in Figure 9-2 can be used to map out the core of an M-type diabase body in the LOZ of Sectors C and CE. The margin with Sector CW is outlined by M-type basalts and altered samples that are consistent with an intrusive origin. The eastern margin is not well-defined because of the removal of this part of the scarp by landslides (Chapter IV) but does not appear to extend beyond Sector E. The major divide between Sector CW and the rest of the site is also apparent in the ranges of major and trace element contents, REE abundances and element ratios.

Sector CW has higher Fe_2O_3, TiO_2 (Figure 9-9a), P_2O_5, V (Figure 9-10a), Zr, Y, Nb, La, Nd, Eu and Yb, but lower Mg # (39-53), MgO (4.48-6.48 %), Cr and Ni than the other sectors. It is therefore moderately to highly evolved with the highest incompatible

element contents. This sector displays a subtle to well-defined negative Eu anomaly (Figure 9-7d) indicating the strong influence of plagioclase fractionation. The low CaO/Al_2O_3 ratios (Figure 9-9c) correspond to Mg #s of 39-50 which indicates the influence of extensive clinopyroxene crystallization (Figure 8-5a). These effects are consistent with the high proportion of FeTi basalts in this sector (75%).

By comparison, Sectors C, CE and E have similar ranges in concentrations of major oxides and trace elements (Figure 9-9) but Sector E amongst these has the narrowest dispersion, with one sample excluded. In addition, Sector E is primarily moderately evolved while Sectors C and CE vary from relatively primitive to moderately evolved, with one exception in Sector C (Figure 9-9b).

The middle sectors differ in that the T-type, generated from heterogeneous mantle domains at the commencement of a magmatic pulse (Chapter VIII), is present only in Sector C. Sector C also has a wider range in CaO, Al_2O_3, Na_2O and Sr (Figure 9-9d) while Sector CE is more enriched in Rb and Ba. The range of the CaO/Al_2O_3 ratio (Figure 9-9c) in Sector C is broadest with some very low ratios. These cannot be ascribed to solely clinopyroxene fractionation because they only have intermediate Mg #s of 53-61. Instead, these values could arise by mixing of primitive and evolved magma batches (the latter being represented by the one unusual sample) which would drastically change the average Mg # while the CaO/Al_2O_3 ratio remained low. This suggests that mixing is also occurring in Sector C as it does in the rest of the study site (cf. Figure 8-10).

A plot of TiO_2 versus CaO/Na_2O (Figure 9-10) demonstrates the variability between and within Sectors C and CE. The N- and M-types separate into two clusters with more overlap between the diabases in Sector CE. For the N-type, liquid lines of descent (LLD) indicate that there is significant divergence in evolution between the

basalts and diabases in a sector than between the basalts or between the diabases in Sectors C and CE. Three of the LLDs for the N-type potentially intersect which suggest that they have a common origin but evolved along separate paths. The M-type clearly has multiple derivative paths even amongst the basalts or diabases within a sector. On this basis, it is deduced that the diabase was not emplaced as a single, homogeneous mass into the lower zone but rather as separate bodies.

Apart from the effects of shallow magmatic processes, the differences between Sectors CW, C/CE and E also stem from mantle variations. Sectors C and CE have broader ranges in Zr/Nb and (La/Yb)n (Figure 9-11b) relative to the other two sectors. This is a consequence of their containing all three chemical types, in comparison to Sectors CW and E with principally N-type. Sectors C and CE also include a few samples with lower $Fe_{8.0}$ than the other two sectors. This implies that these sectors contain melts generated at comparatively shallower depths. By comparison, Sectors E and CW have higher $Fe_{8.0}$ (Figure 9-29b) indicative of melting at greater depths than in the rest of the site. This simple pattern by sector, however, does not apply for the extent of melting since $Na_{8.0}$ (Figure 9-12a) is relatively uniform across the study site except for a few lower degree melts in Sectors C and CW.

9.2.6 Regional-tectonic context of WBD site geochemistry

The geochemical variation across the WBD site is highlighted within the regional context. The typical pattern of ranges in element concentrations is displayed by V (Figures 9-11a) while its inverse pertains for Mg #. These ranges are limited at the JdFR axis and in the vicinity of the inner pseudofault indicating a restricted number of sources and no excessive effects of mantle or crustal processes. The range generally increases

from both locations towards the study site where there is a broad compositional variability. In detail, there is a greater increase from the west and decrease from the east for V and other incompatible elements, which reaches a high in Sector CW and a low in Sector C (vice versa for Mg #). The change evidently marks an abrupt shift from a system characterized by mixing as a result of more frequent replenishment to one dominated by shallow fractionation due to less frequent magmatic input. Coincident with the westward decline in robustness of the magmatic system, is a gradually diminishing intensity of fractionation and an overall deepening of the Juan de Fuca plateau (Figure 3-5a).

The magmatic history reveals that the wide range in incompatible element ratios is not unique to the WBD site (Figure 9-11b). The pseudofault trace on the Juan de Fuca plateau is associated with equal proportions of N-type and a variety that is even more depleted than the M-type (BN-20) lavas (Figures 9-13a&b). At the eastern termination of the north WBD scarp (BN-22) that is interpreted in Chapter III as the edge of the inner pseudofault zone (IPZ), there are equal proportions of 3 chemical groups - N-type, M-type and a third variety that lies outside of all the defined fields (Figures 9-13a&b). Hence, there is clear evidence that source variability has always been a primary influence on accretion, at least at the southern end of the Cleft Segment.

The study site further demonstrates that the involvement of multiple sources is progressive over time. In Sector E, the N-type is predominant with only minor M-type lavas. Between Sector CE and C, there are four chemical groups. With the exception of minor T-type lavas in Sector CW, only N-type lavas (BN-18&19) are present westward. This implies that source variability beneath the southern JdFR only exerts its influence episodically which provides strong support for diapiric upwelling in the magmatic-tectonic model developed (Figures 3-6 and 3-7).

There were also variations in melting conditions over the long-term evolution. In Figures 9-12(a-b), $Na_{8.0}$ (1.5 to 2.5) and $Fe_{8.0}$ (7 to 11) display an overall increase with decreasing age. This indicates a relative (Table 8-3) change from very high extents of partial melting at shallow depths during rift propagation to high extents of partial melting at high depths near the 0 Ma JdFR.

Superimposed on these overall trends is the highly variable $Na_{8.0}$ and $Fe_{8.0}$ almost 0.7 million years after passage of the propagator (Figure 9-12a-b). Between 1.7 Ma and 1.2 Ma, there were short-term shifts to extremely deep levels (Fe_8: <14) of melting in Sector E and again in Sector CW, and the generation of some extremely low degree partial melts (Na_8: <5) in Sector C. West of the WBD study site, melting resumed at moderate depths (Fe_8: 8-10) and high/very high degree partial melts (Na_8: 1.5-2.5) were generated by 0.7 Ma (Figure 9-12).

9.3 Discussion

The chemical variability of the lavas in the N. WBD site is explained as the result of a magmatic pulse beneath the JdFR that is derived by multistage melting, magma extraction and mixing of normally depleted mantle (Chapter VIII) which gives rise initially to the T- and N-types followed later by the M-type. Subsequent melting of an enriched source underlying Parks Plateau produces the EG-type. The time-dependent nature of this process should result in a systematic and consistent pattern of crustal evolution at oceanic ridges (Johnson and Dick, 1992). Under the conditions of diapiric mantle flow inferred for the S. JdFR (Chapter III), the successive eruption/intrusion of the T-, N- and M-types on-axis could form an age progressive spatial association across-axis, in one possible end-member model. However, this picture is likely to be complicated by the westward migration of the JdFR (Chapter III). Thus, the question remains as to how

accretion of these lava types actually occurs spatially and temporally. Here, the results obtained are discussed in terms of the ideas on crustal building and magmatic evolution developed in previous chapters to further constrain these reconstructions.

9.3.1 Refining the magmatic history model

There is abundant evidence that magmatic accretion at oceanic spreading centers is episodic. At short time scales (10^3-10^6 years), rift valleys apparently alternate between the volcanically and tectonically dominated states observed along ridge segments (Gente et al., 1986; Kappel and Ryan, 1986; Karson et al., 1987) and low order axial discontinuities are unstable (Macdonald et al., 1988). In the long term (10^6-10^8 years), abyssal hills are interpreted to represent oscillations in ridge magmatism (Pockalny et al., 1988) that are due to pulses of high degree decompressional melting and mantle upwelling (Scott and Stevenson, 1989) which can prevail over an 11 m.y. period (Johnson and Dick, 1992). Along the north scarp of the Blanco Fracture Zone, there are two main scales of variation in lava composition.

The one trend extends over the past 2 m.y. It was also noted by Karsten and Delaney (1988) based on systematically increasing Mg # toward the ridge. Diagnostic chemical parameters indicate that overall there is a slight decline in the extent of melting and an increase in the depth of melting between when the propagator intersected the scarp, and at the present-day southern JdFR. It is suggested that these trends are a post-propagation effect as proposed by Juteau et al. (1995). The variation in incompatible element concentrations for the N-type also gradually widens to about 1.2 Ma before diminishing again toward the axis. This pattern is interpreted to reflect the progressive change from immature, replenishment-dominated magma chambers to a well-established,

fractionation-dominated magmatic system (Christie and Sinton, 1981). Other chemical ratios demonstrate that there is a broad diversity in composition within the IPZ, some of which are never replicated again along this lithospheric flow line. This situation is attributed to the small and ephemeral nature of the early chambers which result in a low residence time, while the later steady lenses buffer the composition (Christie and Sinton, 1981). The geochemical evolution here further demonstrates that there is a long lag time between the commencement of normal spreading at 2 Ma (Chapter II) and the thermal evolution of the new rift.

Superimposed is another pattern with a predicted wavelength of 9-12 km or 0.36 m.y. (Chapter III). This is based on the chemical correlation between the geologically defined sectors in the study site and the provinces defined by the seamount chain on the adjoining Juan de Fuca plateau (Figure 3-5). Using the distance from the axis (Figure 3-1), Sector CW corresponds to the middle of the "W. SS." province, the Sector C/CE boundary corresponds to the divide between the "W. SS." and "E. SS." provinces, and the Sector E corresponds to the center of the "E. SS." province.

These volcanic cones are later near-axis constructions of a magmatic pulse, but they appear to be built on basement accreted earlier on-axis from the same pulse (Figure 3-6). The T-type in Sector C, melted from heterogeneous mantle domains (Chapter VIII), marks the commencement of this pulse of magmatic activity. The areas of the crust that were subsequently generated at relatively greater depths become overlain by the seamount built near-axis, as in Sector CW (and previously in Sector E). In the end-stage, the M-type diabase is emplaced in between the basements created by this and the next pulse concurrently active on-axis due to the relative rates of migration versus spreading (Chapter III). This development is significant because it implies that the accretionary

components of each seamount province are connected to the same period of magmagenesis.

The emplacement of the M-type in between magmatic pulses is also found at the eastern edge of the Blanco scarp (Figure 9-13a) which corresponds to the boundary between the "E. SS." and "Prop. 3" provinces (Figure 3-1). Consequently, it is inferred that the sub-surface pattern of accretion in the study site is continuous along the scarp in parallel with the seamounts. The along- and across-axis offset between the formation of the volcanic cones and emplacement of the very depleted M-type diabases is accounted for by ridge migration as described in the tectonic model proposed for the region (Figures 3-6 and 3-7).

9.3.2 Refining the magmatic accretion models

The relation between the downhole variation in selected geochemical parameters, petrography and lithology has been considered in drill cores through the oceanic basement. These have the advantage of far more closely spaced sampling than can be retrieved *in situ* from the scarp and consequently, have the capability to detect finer-scale changes in the magmatic system than is possible in this study.

In the slow spreading crust of Hole 395A, matching sequences of change in the physical properties and lithology were found (Hyndman and Salisbury, 1983). In the intermediate spreading rate crust of Hole 504B, an approximate correspondence between the contacts of lithologic units (defined from flows, textures or petrography) and those of chemical units (group M or defined by degree of depletion in group D) was noted (Autio and Rhodes, 1983). At both sites, each unit was interpreted as an eruptive cycle although no systematic fractionation trends were evident within. In Hole 504B, the sharp breaks between chemically related groups were explained by influxes of magma into a

differentiating chamber or in either case, as separate flows from different magma chambers since there are three unrelated N-MORB series (Melson et al., 1979) in Hole 395A.

In the WBD site, the stratigraphic interlayering of the three distinct chemical types permits analysis of less subtle variation. The distribution of the N- and M-types is clearly consistent with the textural (Chapter IV) and lithologic (Chapter V) sub-division of the scarp exposure into an UOZ and a LOZ. The occurrence of the T-type in both zones, rather than just at the top of the basement, indicates that they cannot be off-axis lavas. In addition, they are interdigitated with the N-type throughout Sector C which further supports their closely related magmatic evolution during each magmatic pulse on-axis (Chapter VIII). The preservation of this small melt batch implies that the magma chambers during this 1.2 Ma - 1.7 Ma period of accretion were still discontinuous even if they had become more long lived by Sector CW, as suggested by the high extent of fractionation.

Mineral assemblages are also related to these liquid compositions (Natland, 1991; Bryan, 1983). The high correlation of plagioclase-clinopyroxene±olivine phyric lavas with the N-type and aphyric lavas with the M-type reflects the more moderate stage in evolution of the N-type as compared to the slightly evolved M-type. In addition, it accounts for the distribution of the petrographic types in the crustal section (Figure 7-8).

On the other hand, morphologic differences between lava flows are unrelated to the chemistry (Batiza et al., 1989) as can be seen for the N-type which produces a spectrum of forms. The apparent correlation in this case between N-types and basalt flows or M-types and diabase bodies is not a function of their different chemistry but rather of their extrusive versus intrusive emplacement. This point is important because it

is the basis for arguing that the thick sheets of M-type in the basement are sills. The interpretation is supported by the proposed magmatic evolution (Chapter VIII) in which the M-type is only extracted at an end-stage of melting after metasomatism has occurred. Accordingly, if these were flows, they should be extruded toward the top of the crustal section and not at the base whereas the M-type (with one exception) is absent from the UZ, UIZ and MIZ. The inference that the thick sheets of N-type must also be sills, given the same morphology, is supported by their large chemical variability in the LIZ and LZ as compared to the overlying extrusive section. Consequently, this favors the mixed extrusive-intrusive model (Figure 5-2) of crustal building that emerged from the lithologic data. However, there is no chemical constraints on whether sill injection commenced on- or near-axis.

This preferred construction model for the study site can be expanded by relating the chemical variation with depth to the lithologic sub-zones (Figure 5-2) as illustrated schematically in Figure 9-14.

Periods of little melting evidently promote extensive crystal fractionation of the magma in discontinuous chambers while the ridge is volcanically quiescent. The onset of a magmatic pulse is marked by generation of the T-type and production of the N-type by a relatively high degree of melting at moderate depths (Table 8-3). The resupply of the chambers results in mixing with the extreme differentiates and also eruptions of these highly evolved lavas in the form of the thin and jumbled sheet flows. This conforms to Eaby-Dixon et al.'s (1986) observation that even the ferrobasalts carry a mixing signature. Whilst these flows are erupted up until the MIZ, melting possibly deepens slightly over time. By the end of this first replenishment stage, the N- and T-type chambers should also include moderately evolved compositions.

The next stage is prompted by a slight shallowing in the melt depth with time which supplies a new magma batch and initiates mixing between the moderately and highly evolved compositions. As a result, moderately evolved compositions are extruded in the form of jumbled sheet flows and pillows in the UIZ. This process of replenishment recurs shortly but mixing now occurs between the remaining moderately and the slightly evolved compositions introduced. Eruptions of the same lava flows completes the UZ.

In a third stage, melting of the N-type source continued from the same medium depths but declined to moderate degrees giving rise to the sills in the LZ, LIZ and MIZ. Next, high degrees of melting the M-type source over a range of depths results in more sill injection. A decline to moderate degrees of melting produces the bodies of massive diabase intruded into the LZ. Their primitive compositions indicate only minor fractionation and a low residence time in the crust. This implies that there was little interaction with pre-existing chambers; their absence would be consistent with this magmatic activity occurring in a near-axis setting.

Finally, the lack of unique criteria for domains indicates that their formation is unrelated to magmatic processes and hence, more likely to originate from structural processes. It was suggested that repeated crustal subsidence could form such fault-bounded blocks (Chapter VI).

9.4 Conclusions

This chapter has examined the temporal variability of lava compositions laterally and vertically on the north WBD scarp and integrated this analysis with the previous findings from tectonic, geologic, lithologic, petrographic and geochemical data. The results demonstrate that there is a systematic, long-term pattern of magmatic accretion that can be explained by time dependent, diapiric mantle flow in the tectonic context of

the migrating JdFR. The construction of the upper oceanic crust over one of these magmatic pulses is documented within the study site and shows that there are at least 4-5 successive stages. Despite the high density of sampling, the resolution of the information does not permit an in-depth investigation of the relation between lithologic, petrologic and chemical units or of the role of shallow magmatic processes at this scale as has been done for drill cores. In that sense, the study here is preliminary; nonetheless, this synthesis illustrates the potential for addressing some of the basic questions about crustal accretion and evolution. Some of the conclusions drawn here include:

1. The upper oceanic crust in the central part of the study site is composed predominantly by N-type flows in the UOZ, and M- and N-type extrusives and intrusives in the LOZ, while the western part has no LOZ. Within the LIZ at the base of the UOZ, a mix of these compositional groups and high chemical variability denotes a transition zone.

2. Longer-term trends in geochemical variation can be related to the ending of propagation. An increasing range of variation between ~2-1 Ma is attributed to increased effects of magma replenishment and fractionation as the discontinuous and ephemeral magma chambers change to more long-lived ones. A decline in the range of variation between 1-0 Ma is ascribed to compositional buffering in a magmatic system that becomes well-established by 0 Ma.

3. Superimposed, shorter time-scale variations in chemistry across the WBD site (by sector) are interpreted as fluctuations in mantle melting over the past 2 m.y. While multi-stage melting accounts for the production of the T-, N- and M-types (Chapter VIII), their spatial arrangement is explained by the timing and location of their emplacement on- or near-axis as a function of time-dependent diapiric mantle flow in conjunction with the migrating JdFR.

4. Magmatic accretion has involved 2-3 major stages of N-type extrusion on-axis, and another 2 stages of N- and M-type intrusion, on- and near-axis. These episodes of crustal building are linked to changes in mantle melting conditions and magma resupply with mixing prior to eruption or intrusion. Periods of fractionation are volcanically quiescent on-axis.

Table 9-1: Petrographic characteristics of the chemical groups based on number of observations from combining the data in Appendices E and G.

	N-type	M-type	T-type	EG-type
Aphyric	11	12	2	
Olivine-plagioclase phyric	6	2		
Plagioclase phyric	6	4		1
Plagioclase-clinopyroxene-olivine phyric	12		1	
Plagioclase-clinopyroxene phyric	17	3	2	
Breccias	2	2		

Table 9-2: Lithologic characteristics of the chemical groups based on number of observations from combining the data in Appendices D and G.

	UPPER OUTCROP ZONE			LOWER OUTCROP ZONE		
	N-type	T-type	M-type	N-type	T-type	M-type
Pillow basalt lava	8	1				1
Disrupted lava flow (broken basalt)	1					
Basalt lava pillar	4					
Jumbled sheet flow (blocky basalt)	10		1			1
Basaltic and diabasic thick sheet flows/sill (thick-layered)	9	1		3		8
Local dike	2					4
Fractured thin sheet flow (diced)	1	1				1
Diabase intrusions (jointed-massive)				1	1	4

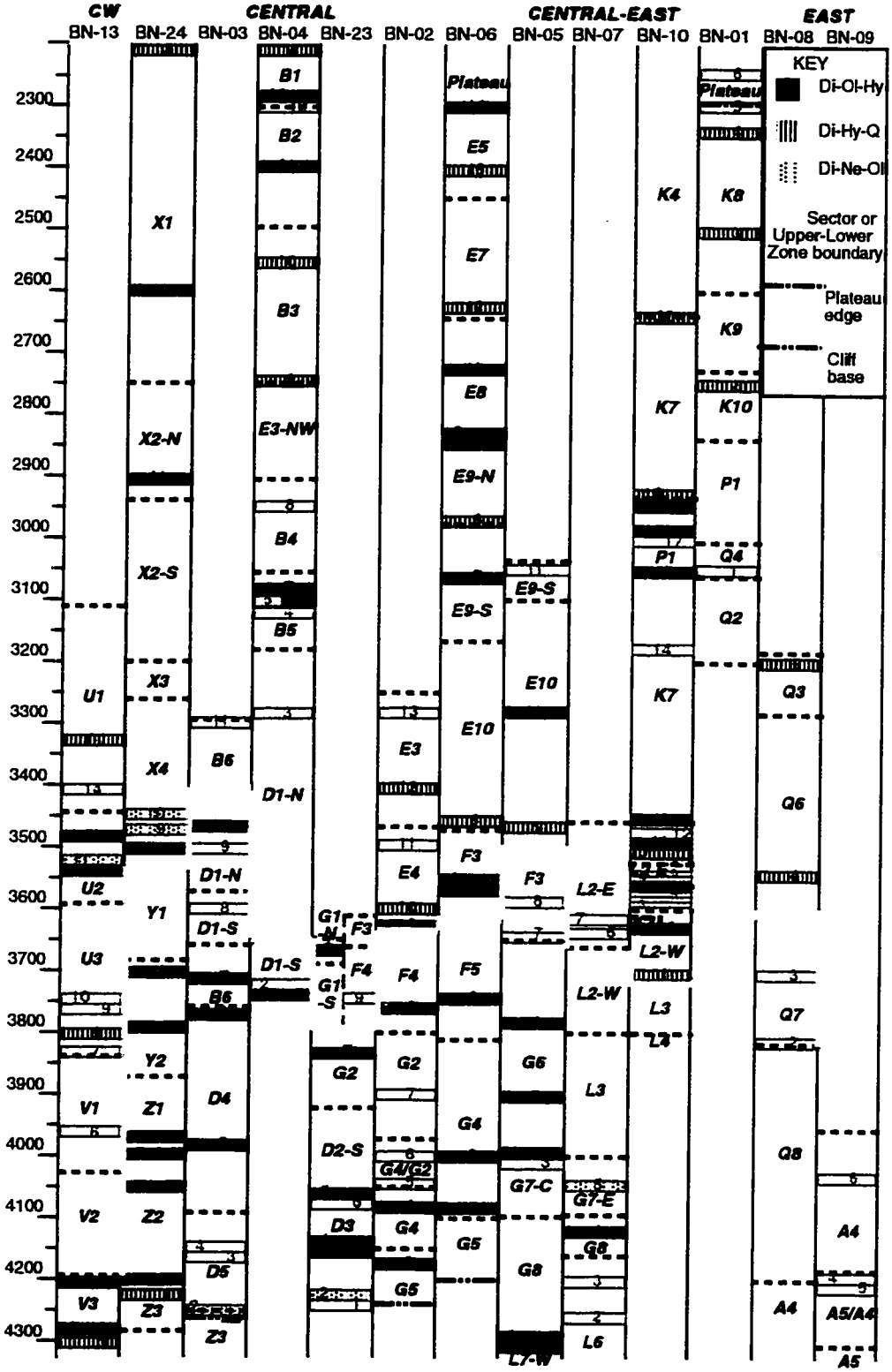

Figure 9-1: Location of the normative compositions in the WBD study site. The boundary between the upper and lower outcrop zones is from Chapter VII; for BN-10, the contact between ~3525-3700 m is placed here at ~3700 m. Note that all the quartz normative samples (Di-Hy-Q) are confined to the upper zone while the nepheline normative samples occur on the margins of the lower zone.

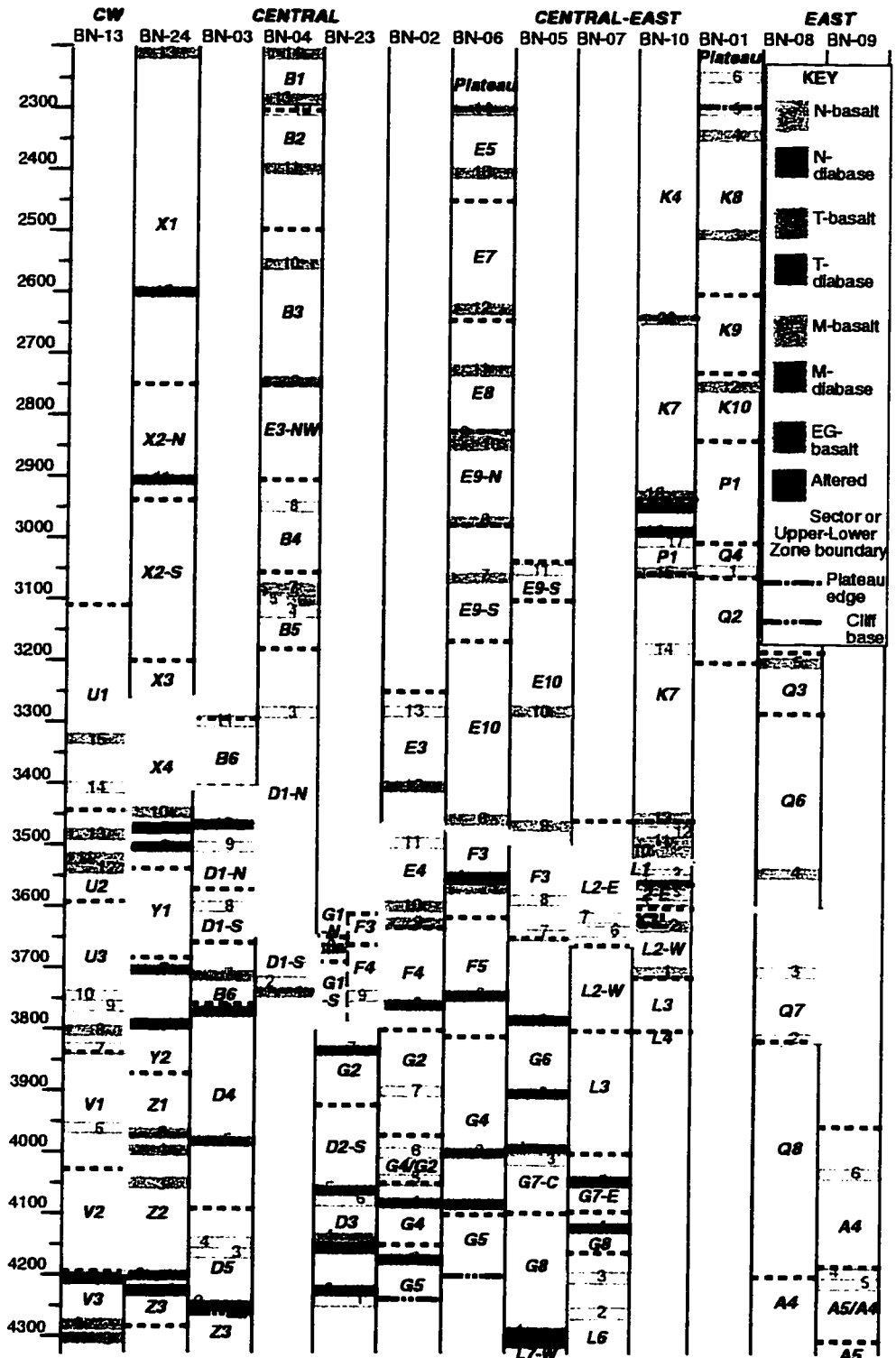

Figure 9-2: Location of the four chemical groups in the WBD study site. The boundary between the upper and lower outcrop zones is from Chapter VII. For BN-24, the contact between ~3250-4200 m is placed at ~3250 m to include the altered sample. For BN-2 and BN-6, the boundaries at respectively ~3650 m and 3625 m are moved to ~3475 m to include the M-type basalts and altered sample on the margin. In general, the N-types dominate the upper zone while the T- and M-types are concentrated in the lower zone. The one EG-type sample occurs in the upper outcrop zone.

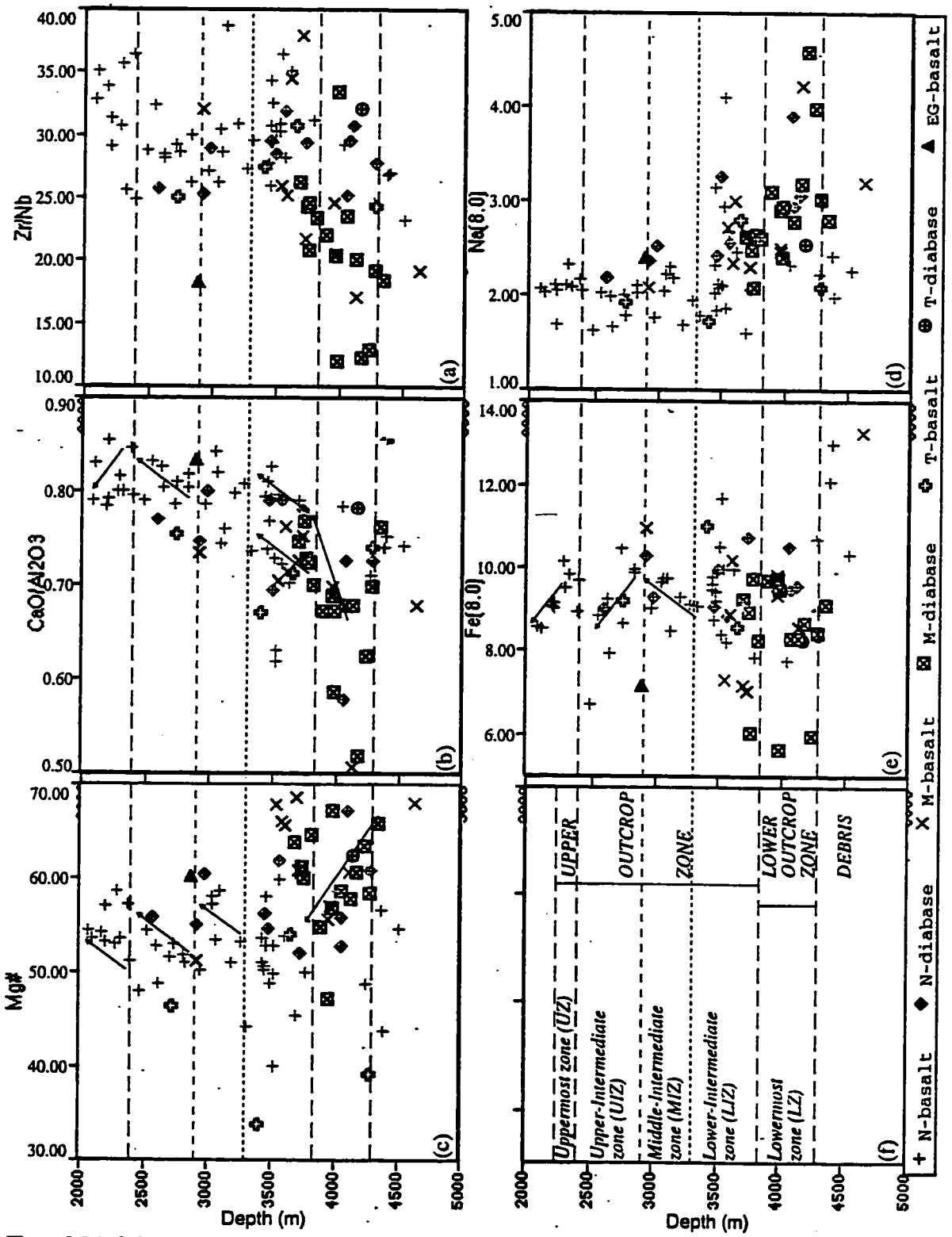

Figure 9-3 (a-f): Mg'-number (Mg #), CaO/Al2O3, Zr/Nb, Fe(8.0) and Na(8.0) of the four chemical groups (a-e) plotted against sample depth in the WBD site. The dashed lines denote lithologic zones (f) from Figure 5-2. The arrows indicate trends in the data.

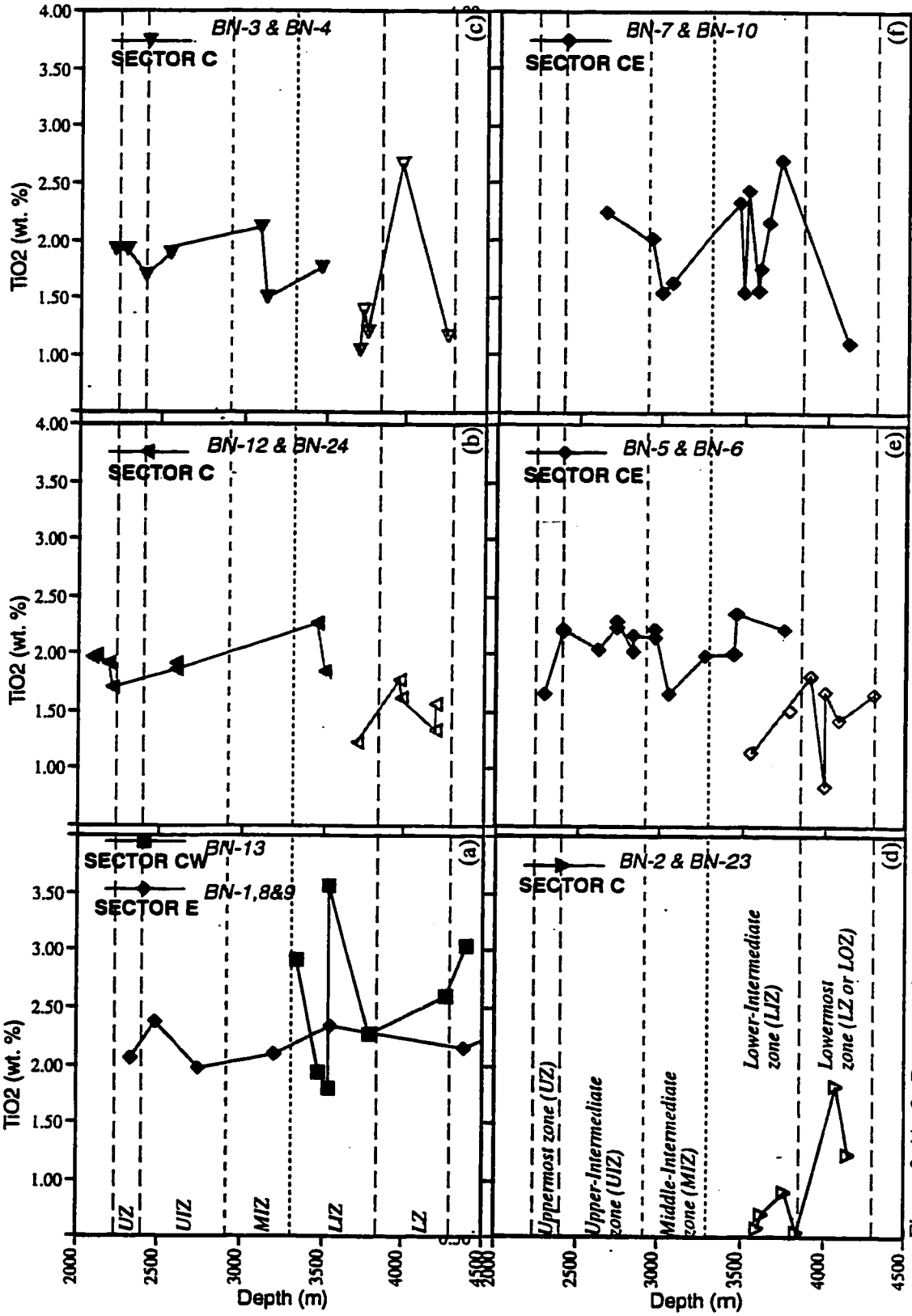

Figure 9-4(a-f): Downsection variation of TiO2 from west to east (except for Sector E) in the WBD site. The closed and open symbols respectively show the N- and M-type samples. Zone boundaries are from Figure 9-3f.

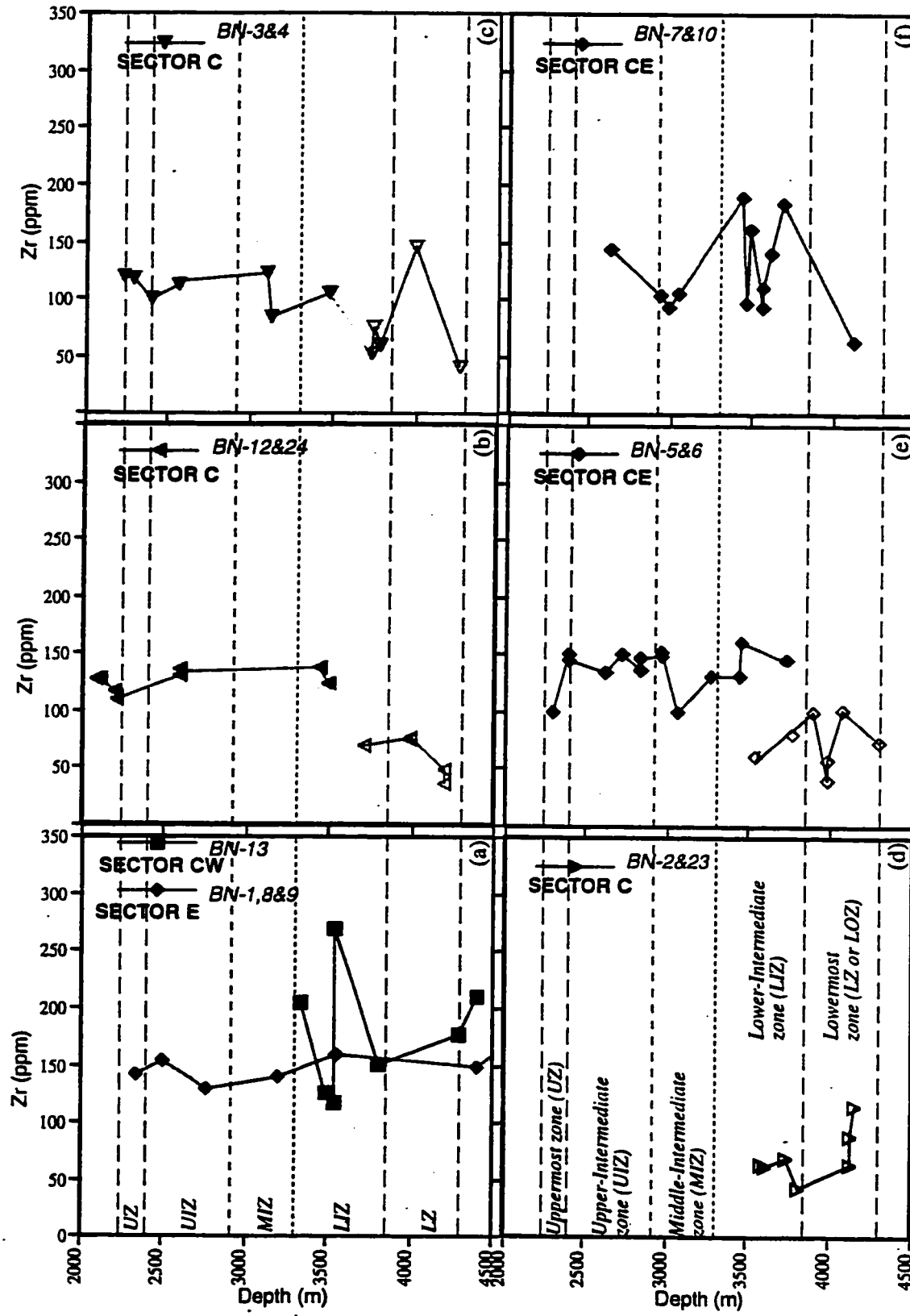

Figure 9-5(a-f): Downsection variation of Zr from west to east (except for Sector E) in the WBD site. The closed and open symbols respectively show the N- and M-type samples. Zone boundaries are from Figure 9-3f.

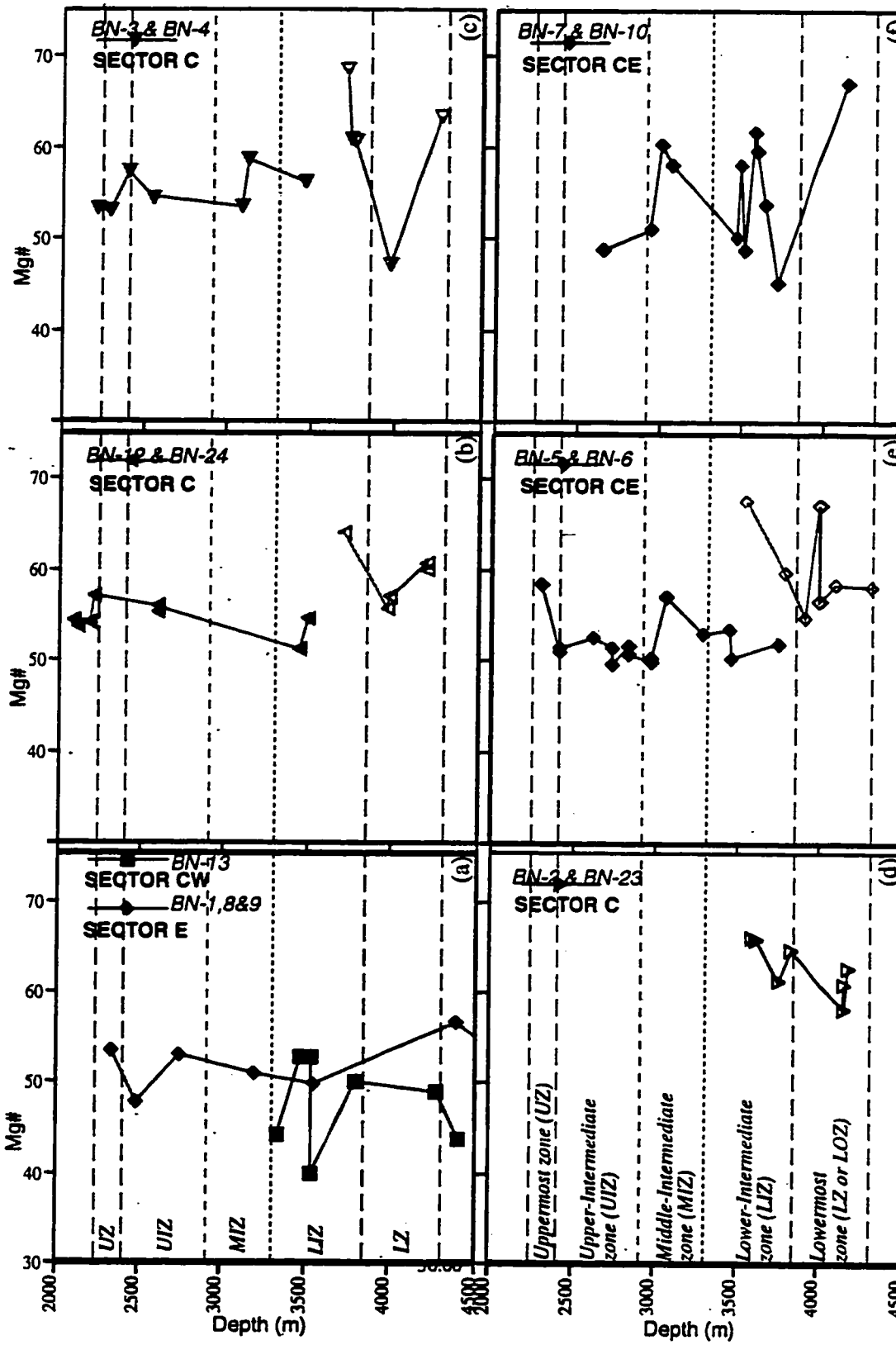

Figure 9-6(a-f): Downsection variation of Mg-number from west to east (except for Sector E) in the WBD site. The closed and open symbols respectively show the N- and M-type samples. Zone boundaries are from Figure 9-3f.

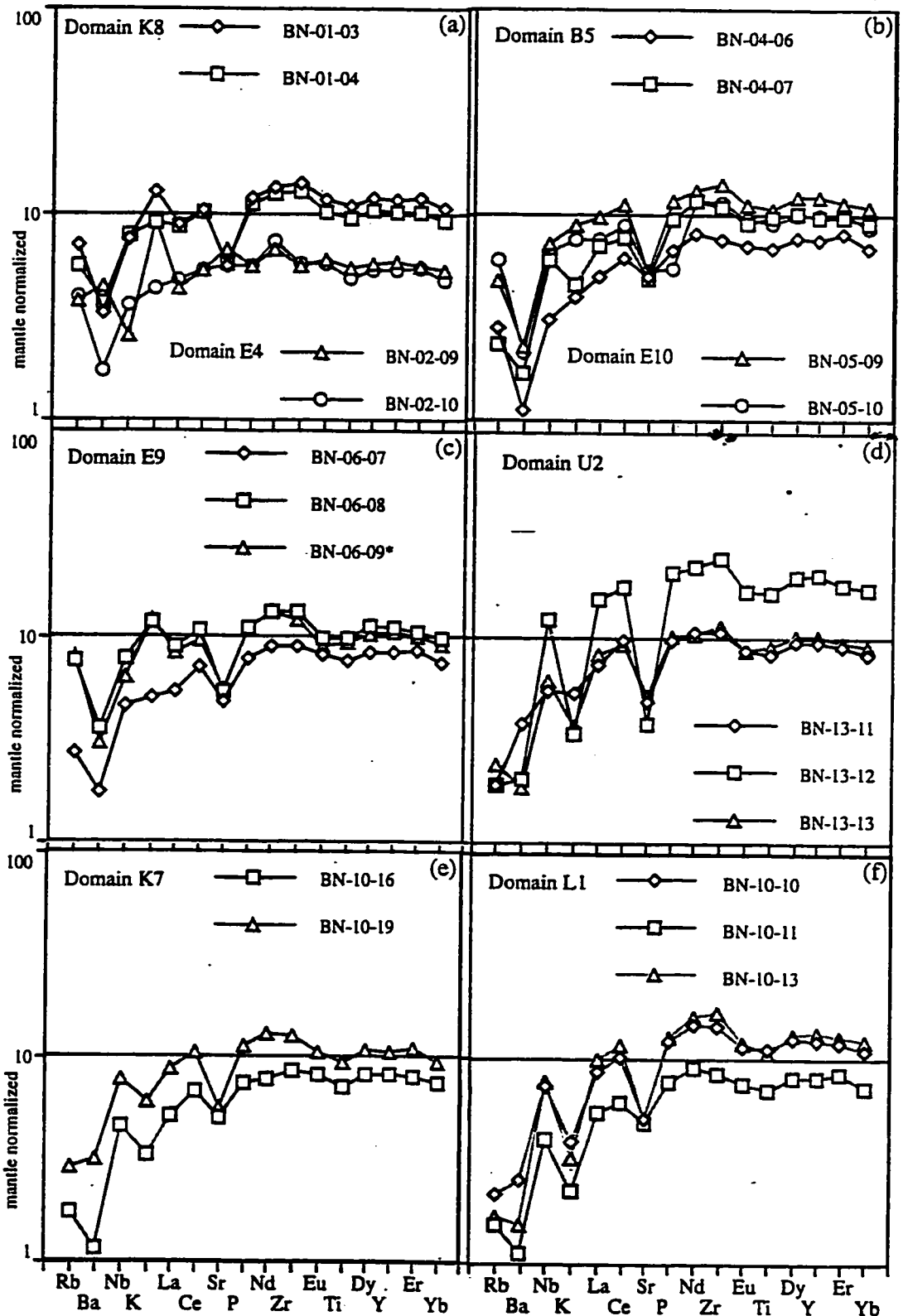

Figure 9-7 (a-f): Mantle normalized abundance patterns for N-type basalt domains in the upper outcrop zone of the WBD site.

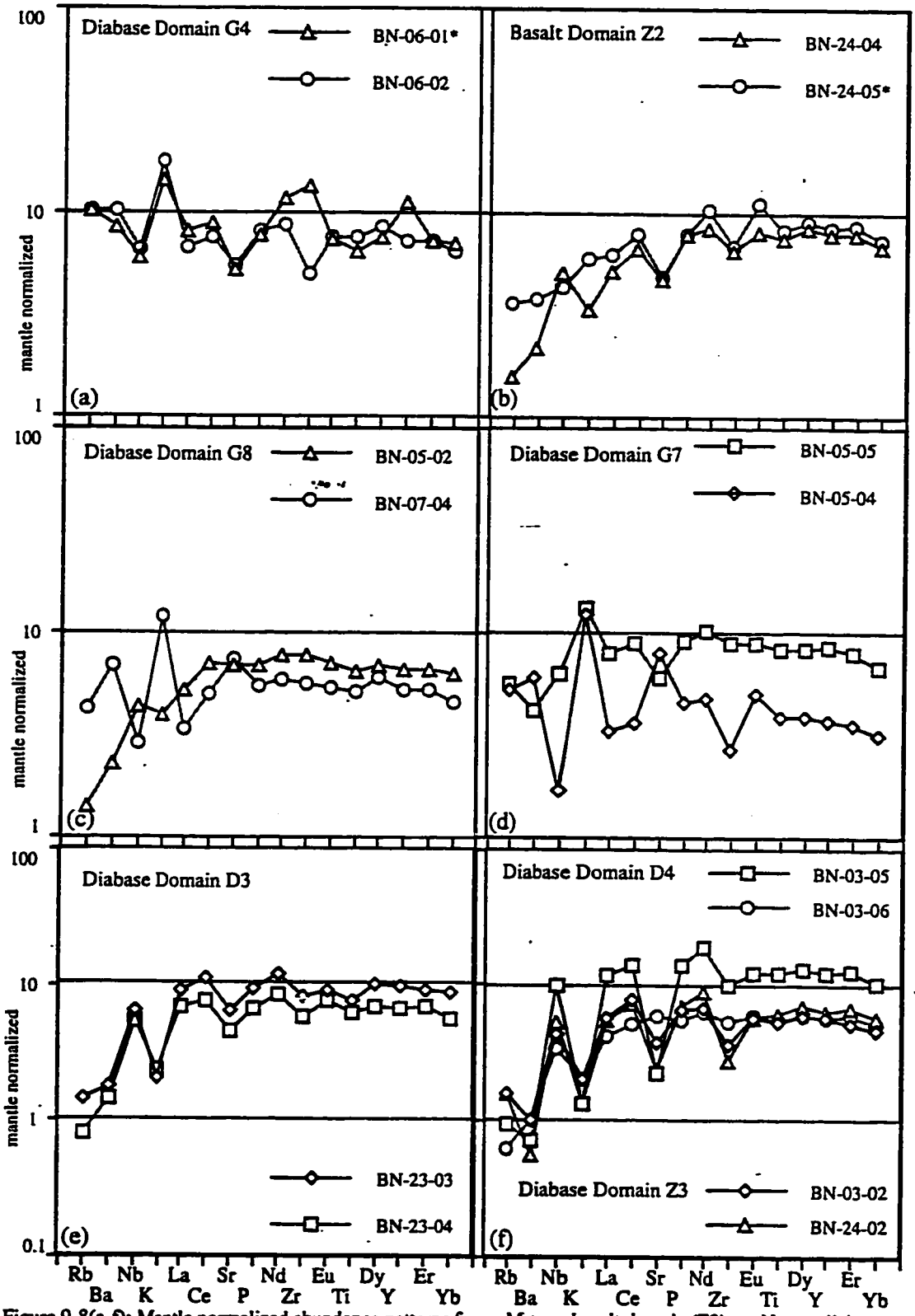

Figure 9-8(a-f): Mantle normalized abundance patterns for an M-type basalt domain (Z2), an N-type diabase domain (G8) and M-type diabase domains (G4, G7, D3, D4) in the lower outcrop zone of the WBD site.

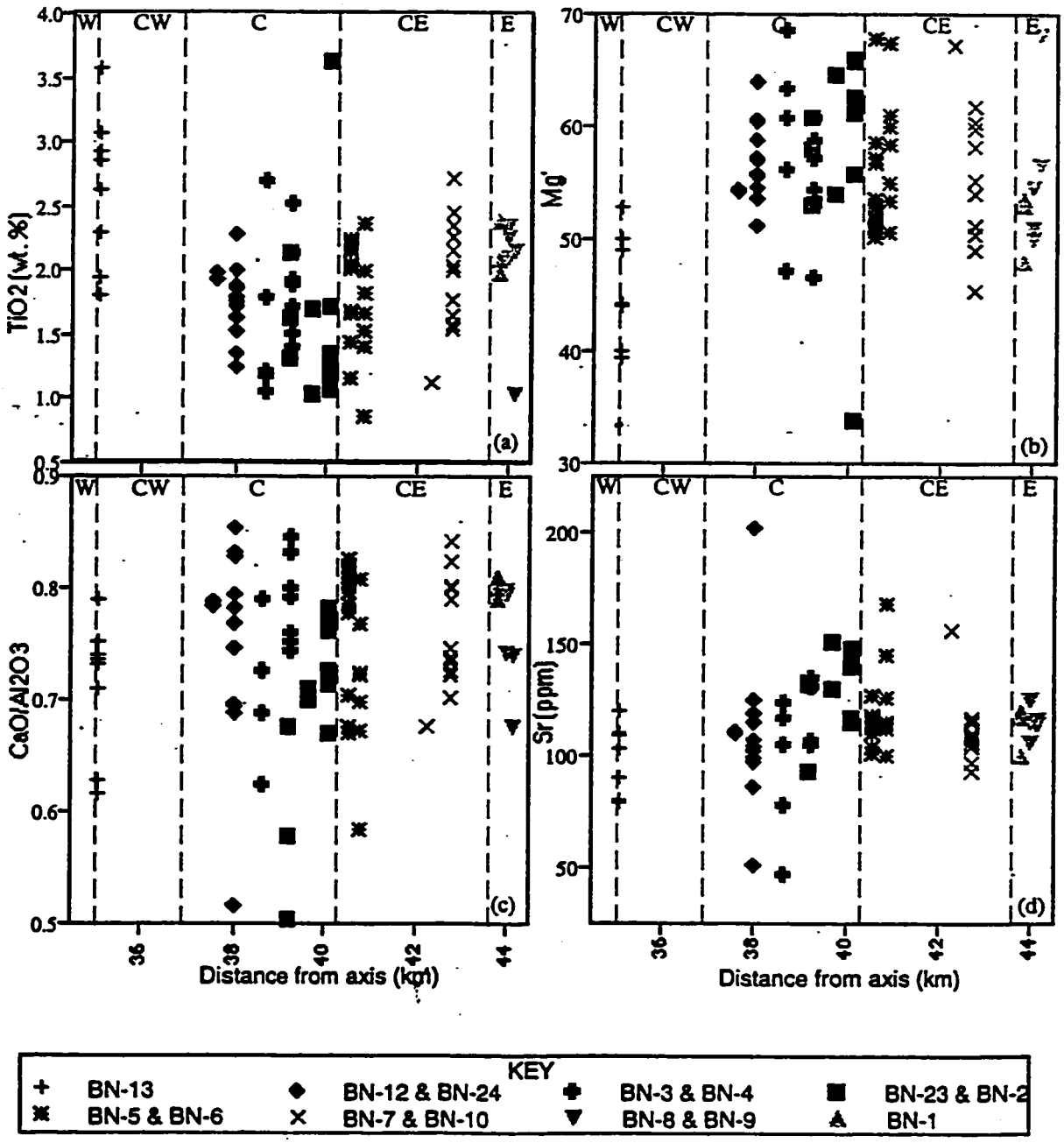

Figure 9-9(a-d): Primary (a-c) and secondary (d) variations across the sectors in the WBD study site. TiO2 reflects the main pattern and Mg'-number the inverse which distinguishes Sector CW from the rest. The other sectors are distinguishable by the alteration effects as on Sr.

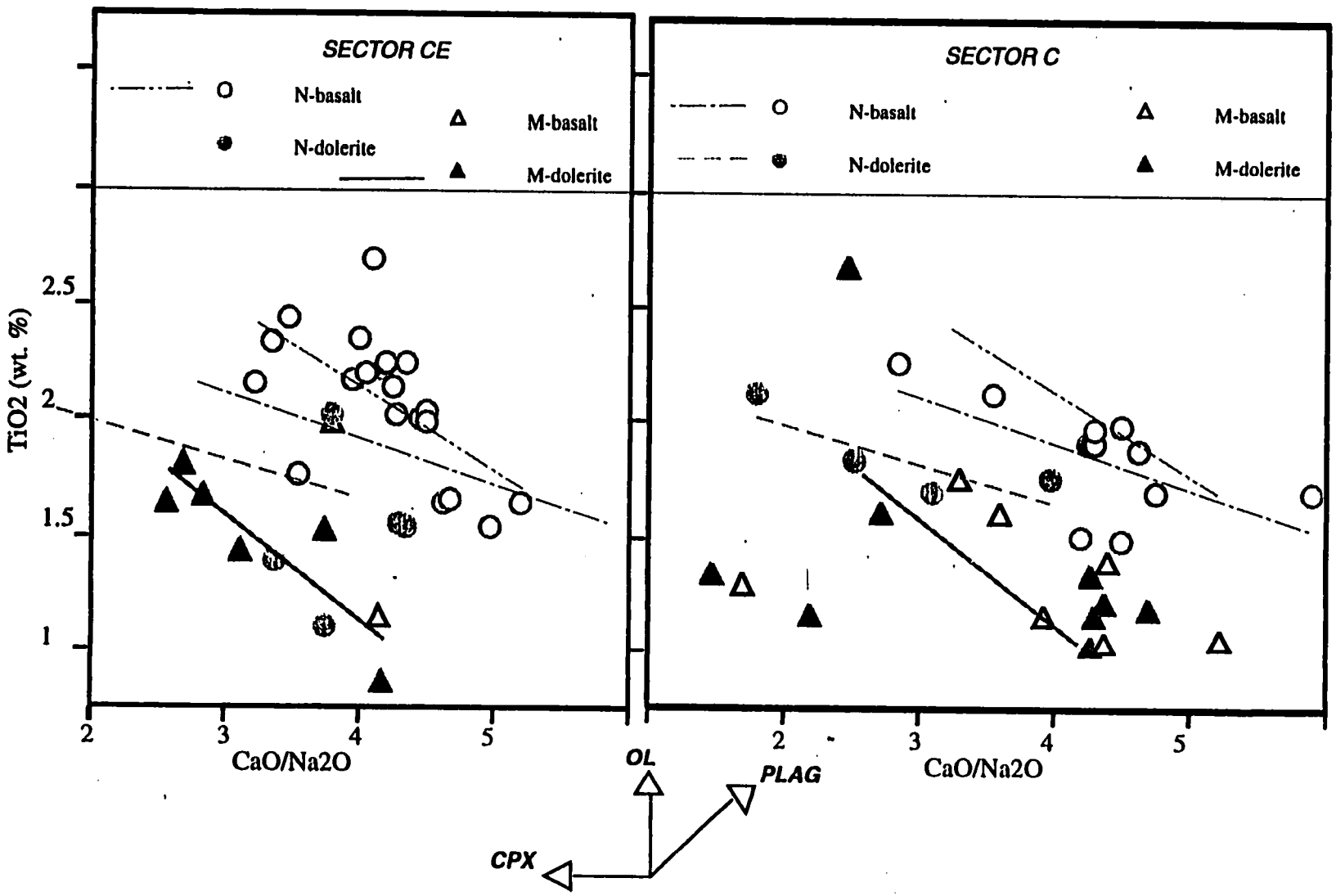

Figure 9-10: CaO/Na2O vs. TiO2. The WBD suite lies within the field for mid-ocean ridge basalts (see Autio et al., 1989). Vectors for the fractionation of olivine (OL), plagioclase (PLAG), and clinopyroxene (CPX) are shown for reference. The lines are linear best fits to the data and are shown on both plots for comparison.

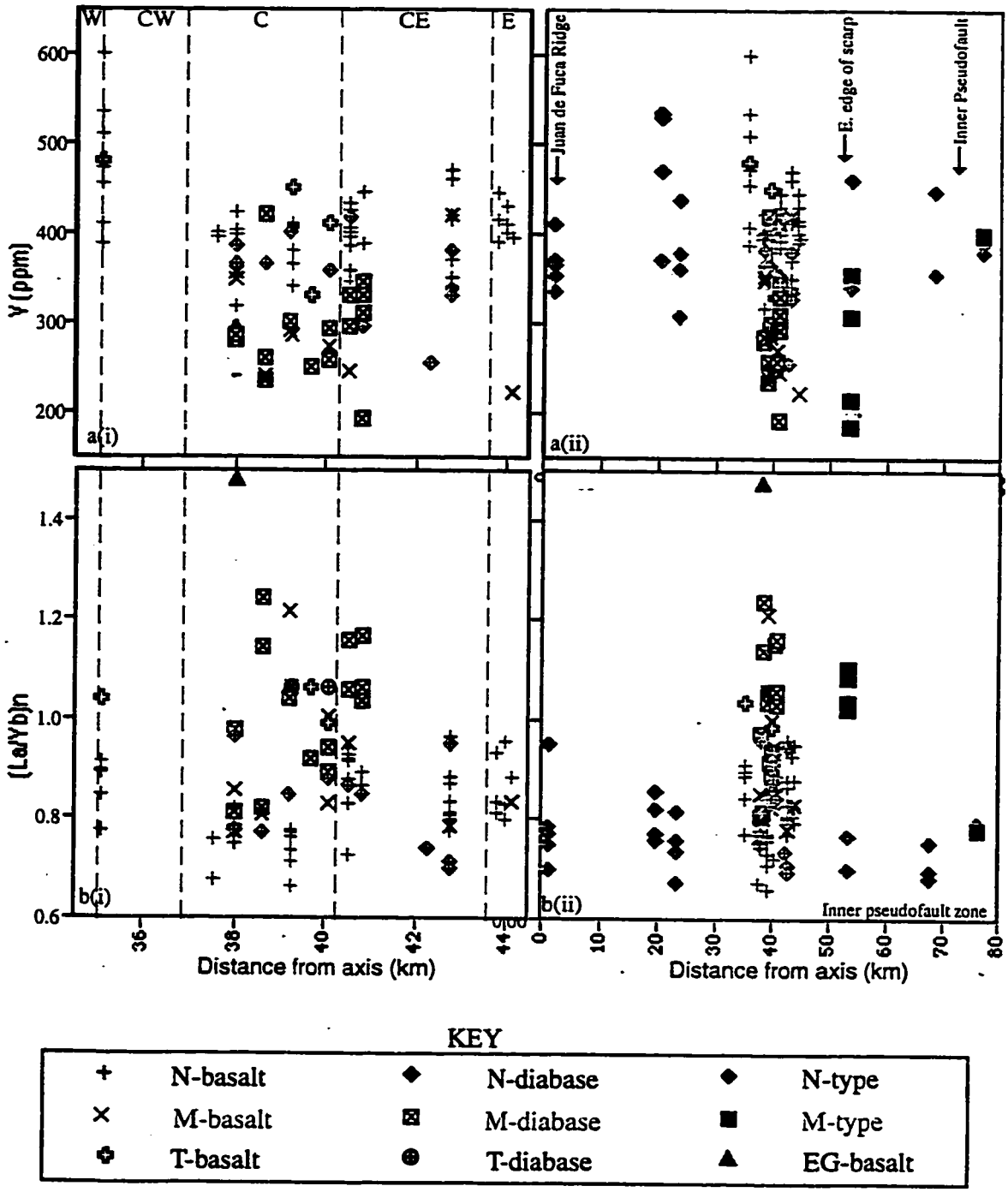

Figure 9-11 (a-b): Chemical variation with distance from the JdFR axis for the study site alone (i) and in the context of the entire north WBD scarp (ii - includes data from Juteau et al., 1995).

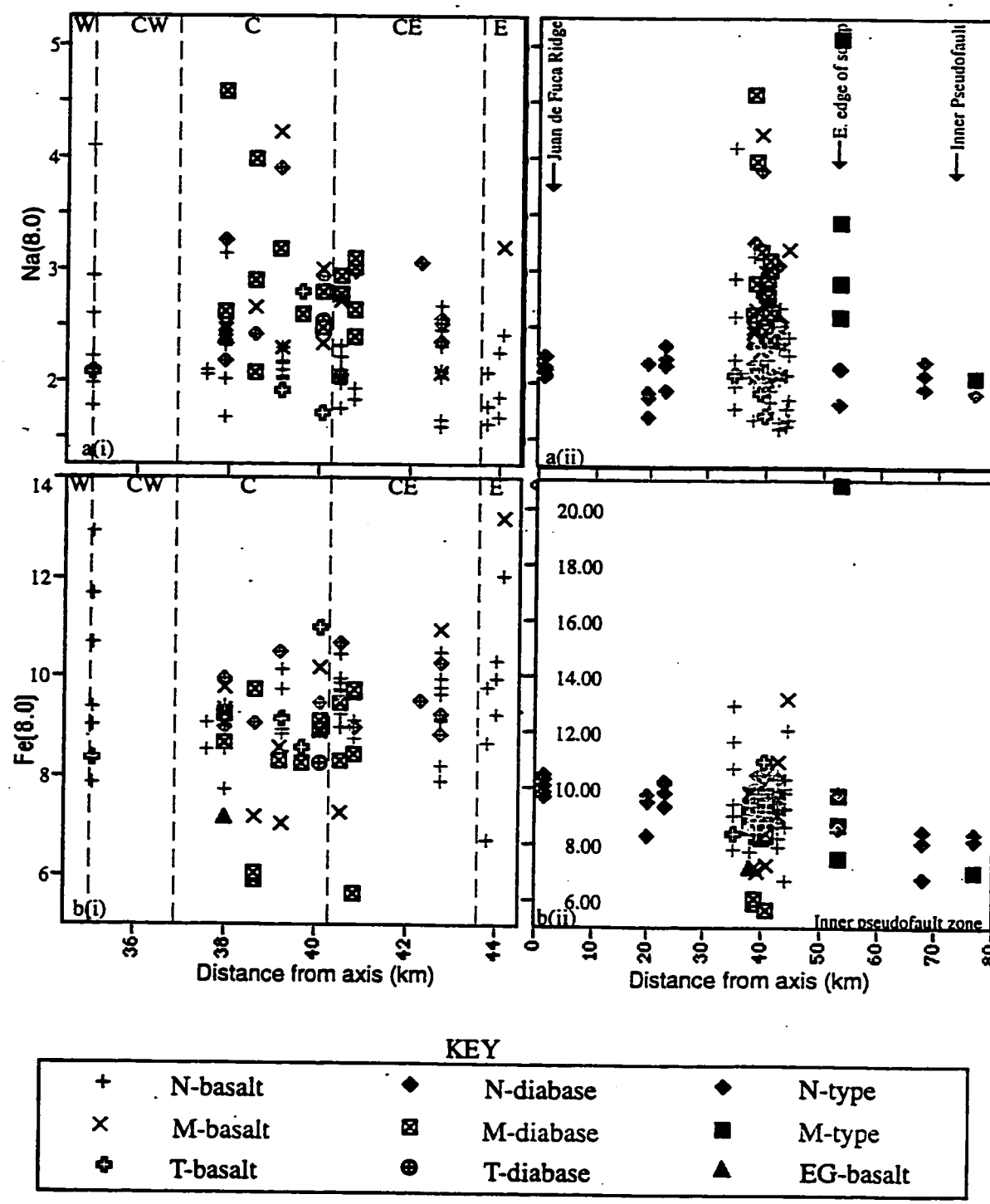

Figure 9-12 (a-b): Na(8.0) and Fe(8.0) versus distance from the JdFR axis for the study site alone (i) and in the context of the entire north WBD scarp (ii - includes data from Juteau et al., 1995).

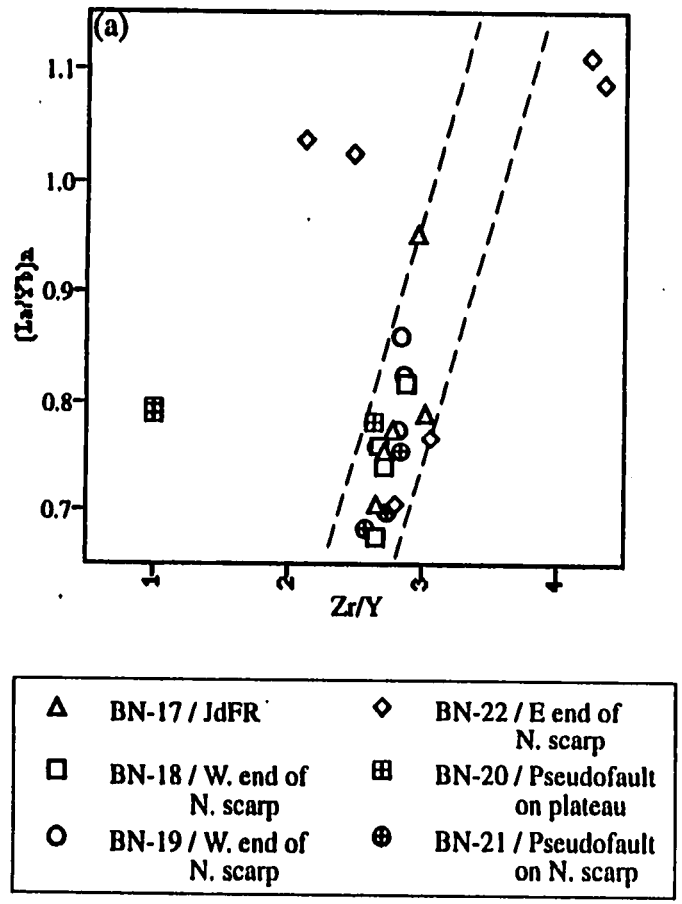

Figure 9-13a:
Zr/Y vs. (La/Yb)n for area along the N. WBD scarp from the JdFR to the last pseudofault but excluding the study site (1991 Nautile samples). The parallel lines indicate the N-T MORB array in the WBD site (Figure 9-13b)

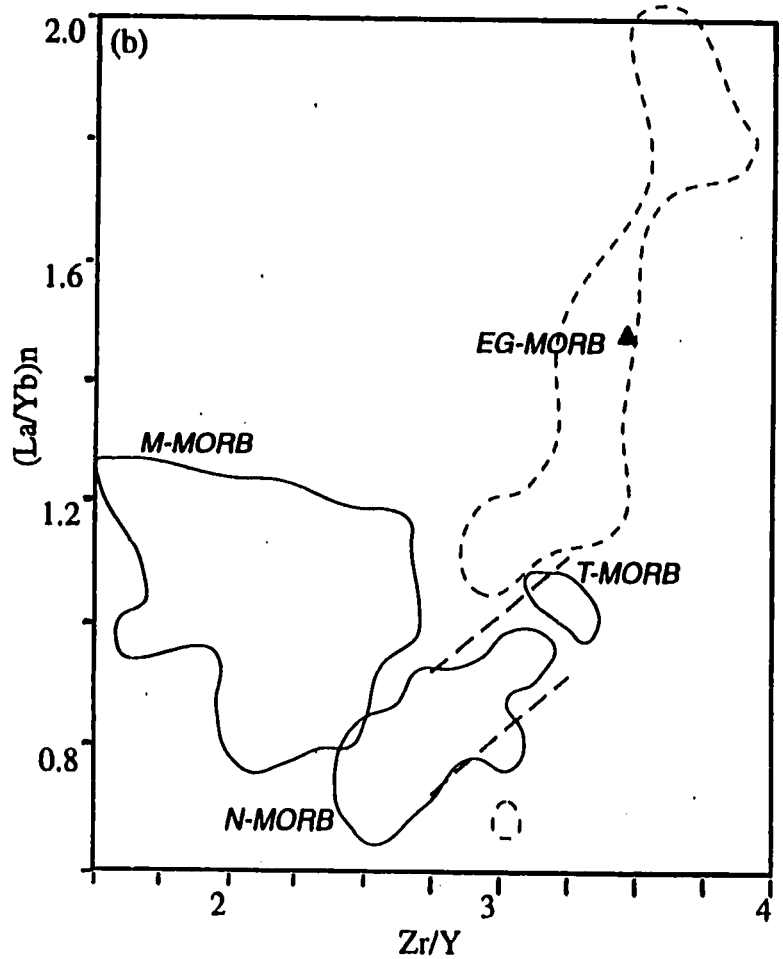

Figure 9-13b:
Fields for the source ratios of the N-, T- and M-MORB types in the WBD site. The one EG-type sample in the site lies within the field for Parks Plateau. Note in Figure 9-13a that two of the samples from the east end of the N. WBD scarp (BN-22) and two from the vicinity of the pseudofault trace do not lie in any of the defined fields.

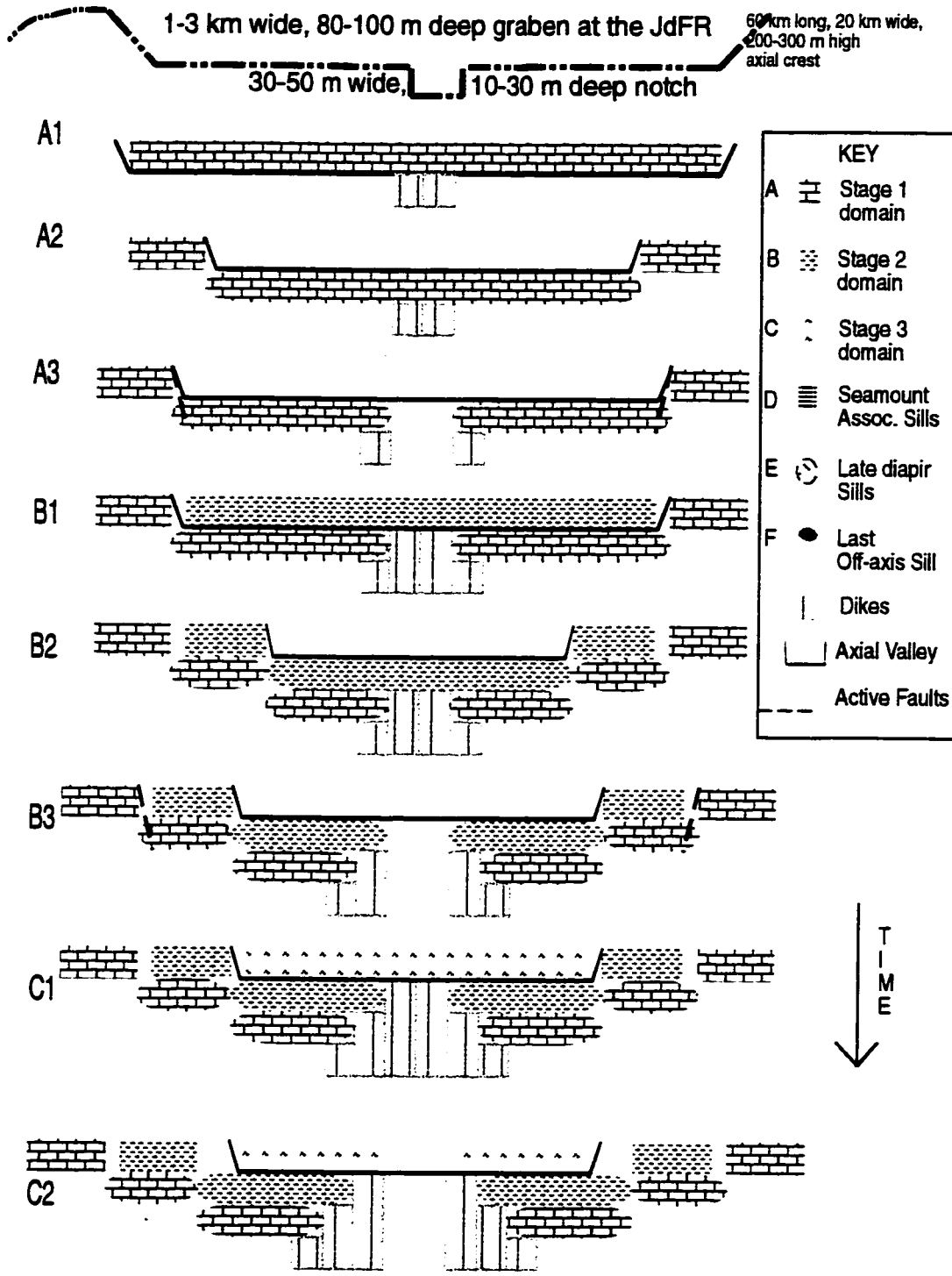
1-3 km wide, 80-100 m deep graben at the JdFR
60 km long, 20 km wide, 200-300 m high axial crest
30-50 m wide,
10-30 m deep notch
A1
A2
A3
B1
B2
B3
C1
C2
KEY
A Stage 1 domain
B Stage 2 domain
C Stage 3 domain
D Seamount Assoc. Sills
E Late diapir Sills
F Last Off-axis Sill
Dikes
Axial Valley
Active Faults
TIME

D

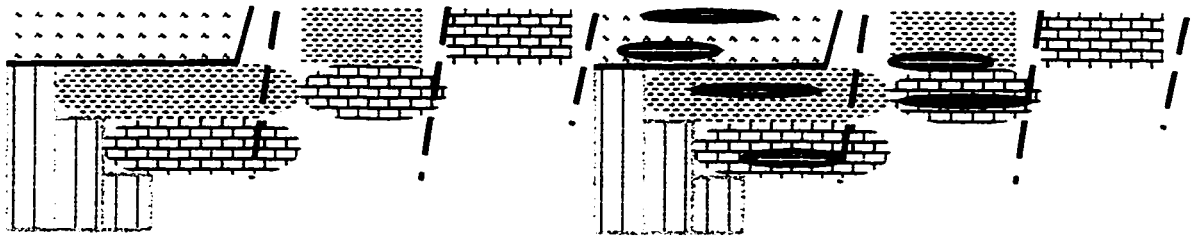

Intrusion of N- and T-type dykes/sills into domains from near-axis seamount

E

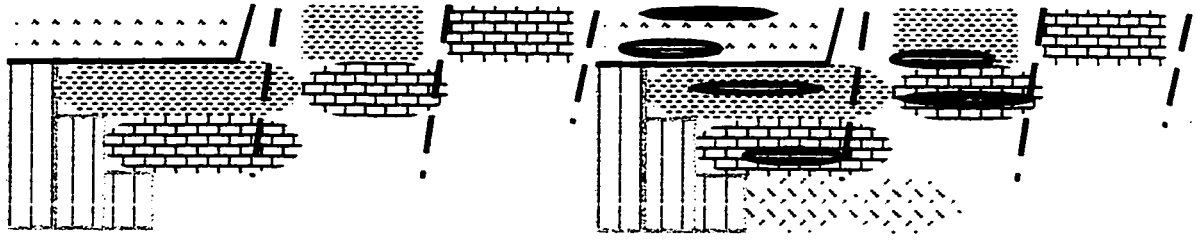

Near-axis intrusion of M-type diabase sills at the base of the domains from late stage of diapir

F

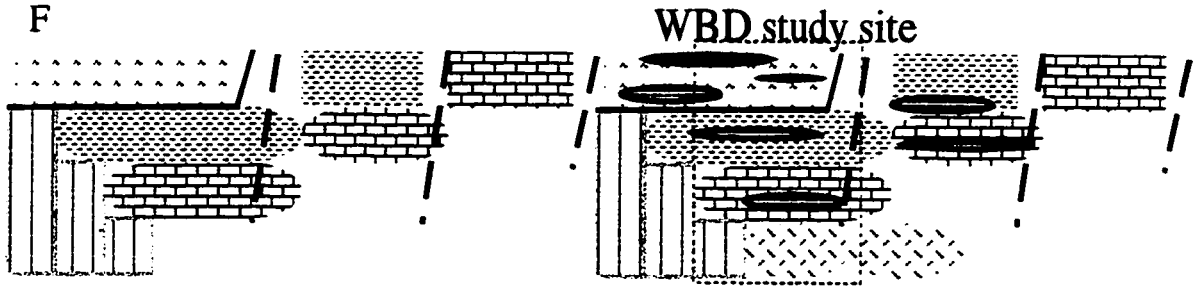

Minor off-axis intrusion of EG-type lava into upper domain from source below Parks Plateau

Figure 9-13:
Accretion model showing a multi-stage process of on-axis construction (A-C) each involving three events:
lava flows infilling the axial valley (1),
subsidence of the valley floor (2), and
spreading by dike intrusion and faulting related extension (3).
Two near-axis (D-E) and one off-axis (F) phase of sill intrusions continue crustal building of the previous magmatic province.

LIST OF REFERENCES

Adamson, A.C., 1985. Basement lithostratigraphy, Deep Sea Drilling Project, Hole 504B. Deep Sea Drilling Project, 83, 121-127.

Alabaster, T., Pearce J.A. and Malpas, J., 1982. The volcanic stratigraphy and petrogenesis of the Oman Ophiolite complex. Contrib. Mineral. Petrol., 81, 168-183.

Allan, J.F., Batiza, R. and Lonsdale, P., 1987. Petrology and chemistry of lavas from seamounts flanking the East Pacific Rise axis, 21°N: implications concerning the mantle source composition for both seamount and adjacent EPR lavas. In: Keating, B.H., Fryer, P., Batiza, R. and Boehlert, G.W. (eds), Seamounts, Islands and Atolls, Am. Geophys. Un. Geophys. Monogr., 43, 255-282.

Allegre, C.J. and Turcotte, D.L., 1986. Implications of a two-component marble-cake mantle. Nature, 323, 123-127.

Alt, J.C., et al., 1993. Site 504. Proc. ODP, Sci. Results, 148: College Station, TX (ODP), 27-45.

Anderson, R.N., Honnorez, J., Becker, K., Adamson, A.C., Alt, J.C., Emmermann, R., Kempton, P.D., Kinoshita, H., Laverne, C., Mottl, M. and Newmark, R.L., 1982. DSDP Hole 504B, the first reference section over 1 km through Layer 2 of the oceanic crust. Nature, 300, 589-594.

ARCYANA, 1975. Transform Fault and Rift Valley from Bathyscaph and Diving Saucer. Science, 190, 108-116.

Atwater, T.M., 1979. Constraints from the FAMOUS area concerning the structure of the oceanic section. In: Talwani, M., Harrison, C.G. and Hayes, D.E. (eds), Deep Drilling Results in the Atlantic Ocean: Ocean Crust. Am. Geophys. Un., Maurice Ewing Ser., 2, 33-42.

Atwater, T. and Macdonald, K.C., 1977. Are spreading centres perpendicular to their transform faults? Nature, 270, 715-719.

Autio, L.K. and Rhodes, J.M., 1983. Costa Rica Rift zone basalts: Geochemical and experimental data from a possible example of multistage melting. Init. Repts., DSDP, 69: Washington (U.S. Govt. Printing Office), 729-745.

Autio, L.K., Sparks, J.W. and Rhodes, J.M., 1989. Geochemistry of Leg 111 basalts: Intrusive feeders for highly depleted pillows and flows. Proc. ODP, Sci. Results, 111, 3-16.

Auzende, J.M., Bideau, D., Bonatti, E., Cannat, M., Honnorez, J., Lagabrielle, Y., Malavielle, J., Mamaloukas-Frangoulis, V. and Mevel, C., 1989. Direct observation of a section through slow-spreading oceanic crust. Nature, 337, 726-729.

Bach, W., Erzinger, J., Alt, J.C. and Teagle, D.A.H., 1996. Chemistry of the lower sheeted dike complex, Hole 504B (Leg 148): influence of magmatic differentiation and hydrothermal alteration. Proc. ODP, Sci. Results, 148, 39-55.

Ballard, R.D. and Moore, J.G., 1977. Photographic Atlas of the Mid-Atlantic Ridge Rift Valley. Springer-Verlag, New York, 114pp.

Ballard, R.D., Holcomb, R.T. and van Andel, T.H., 1979. The Galapagos rift at 86°W: 3. Sheet flows, collapse pits and lava lakes on the rift valley. J. Geophys. Res., 84, 5407-5422.

Ballard, R.D., Francheteau, J., Juteau, T., Rangan, C. and Normark, W., 1981. East Pacific Rise at 21°N: the volcanic, tectonic and hydrothermal processes of the central axis. Earth Planet. Sci. Lett., 55, 1-10.

Barker, S.E., Kudo, A.M. and Keil, K., 1983. Mineral chemistry of basalts from Holes 483 and 483B. Init. Repts. DSDP, 65: Washington (U.S. Govt. Printing Office), 635-642.

Barth, G.A., 1994. Oceanic crust thickens approaching the Clipperton Fracture Zone. Mar. Geophys. Res., 16(1), 51-64.

Barth, G.A., Kastens, K.A. and Klein, E.M., 1994. The origin of bathymetric highs at ridge-transform intersections: a multi-disciplinary case study at the Clipperton Fracture Zone. Mar. Geophys. Res., 16(1), 1-50.

Basaltic Volcanism Study Project (BVSP), 1981. Basaltic Volcanism on the Terrestrial Planets. Pergamon Press, New York, 1286pp.

Batiza, R., 1996. Magmatic segmentation of mid-ocean ridges: a review. In: MacLeod, C.J., Tyler, P.A. and Walker, C.L. (eds.). Tectonic, Magmatic, Hydrothermal and Biological Segmentation of Mid-Ocean Ridges. Geol. Soc. Spec. Publ., 118, 1-15.

Batiza, R. and Vanko, D., 1984. Petrology of young Pacific seamounts. J. Geophys. Res., 89, 11235-11260.

Batiza, R., Smith, T.L. and Niu, Y., 1989. Geological and petrologic evolution of seamounts near the EPR based on submersible and camera study. Mar. Geophys. Res., 11(3), 169-236.

Batiza, R., Niu, Y., Karsten, J.L., Boger, W., Potts, E., Norby, L. and Butler, R., 1996. Steady and non-steady state magma chambers below the East Pacific Rise. Geophys. Res. Lett., 23(3), 221-224.

Becker, K., Sakai, H., Adamson, A.C., Alexandrovich, J., Alt, J.C., Anderson, R.N., Bideau, D., Gable, R. et al., 1989. Drilling deep into young oceanic crust, Hole 504B, Costa Rica Rift. Rev. Geophys., 27, 79-102.

Bender, J.F., Hodges, F.N. and Bence, A.E., 1978. Petrogenesis of basalts from the project FAMOUS area: experimental study from 0 to 15 kbars. Earth Planet. Sci. Lett., 41, 277-302.

Bender, J.F., Langmuir, C.H. and Hanson, G.N., 1984. Petrogenesis of basalt glasses from the Tamayo region, East Pacific Rise. J. Petrol., 25, 213-254.

Blanconaute Shipboard Party, 1991. The Western Blanco Transform: Preliminary Insights into the Oceanic Crustal Architecture and Transform Zone Processes. Eos Trans. Am. Geophys. Un., 72, 519.

Bodvarsson, G. and Walker, G.P.L., 1964. Crustal drift in Iceland. Geophys. J. R. Astr. Soc., 8, 285-930.

Bolt, B.A., Lomnitz, C. and McEvilly, T.V., 1968. Seismological evidence on the tectonics of central and northern California and the Mendocino escarpment. Bull. Seismological Soc. Am., 58, 1725-1767.

Bonatti, E. and Harrison, C.G.A., 1988. Eruption styles of basalt in oceanic spreading ridges and seamounts: effect of magma temperature and viscosity. J. Geophys. Res., 93, 2967-2980.

Bonatti, E., Sartori, R., and Boersma, A., 1983. Vertical crustal movements at the Vema Fracture Zone in the Atlantic: evidence from dredged limestones. Tectonophysics, 91, 213-232.

Bonatti, E, Ottonello, G. and Hamlyn, P.R., 1986. Peridotites from the island of Zabargad (St. John's), Red Sea: petrology and geochemistry. J. Geophys. Res., 21, 599-631.

Brodholt, J.P., Batiza, R., Klein, E.M. and Langmuir, C.H., 1988. Global systematics of unaveraged mid-ocean ridge basalt compositions: comment on 'Global correlations of ocean ridge basalt chemistry with axial depth and crustal thickness. J. Geophys. Res., 94, 4231-4252.

Bryan, W.B., 1983. Systematics of Modal Phenocryst Assemblages in Submarine Basalts: Petrologic Implications. Contrib. Min. Petrol., 83, 62-74.

Bryan, W.B. and Dick, H.J.B., 1982. Contrasted abyssal basalt liquidus trends: evidence for mantle major element heterogeneity. Earth Planet. Sci. Lett., 58(1), 15-26.

Bryan, W.B., Thompson, G., Frey, F.A. and Dickey, J.S., 1976. Inferred Geologic Settings and Differentiation in Basalts from the Deep-Sea Drilling Project. J. Geophys. Res., 81, 4285-4304.

Bryan, W.B., Thompson, G. and Michael, P.J., 1979. Compositional variation in a steady-state zoned magma chamber: mid-Atlantic ridge at 36°50'N. Tectonophysics, 55, 63-85.

Byerly, G.R. and Wright, T.L., 1978. Origin of major element chemical trends in DSDP Leg 37 basalts, Mid-Atlantic Ridge. J. Volc. Geotherm. Res., 3, 229-279.

Calvert, A.J., Hasselgren, E.A. and Clowes, R.M., 1990. Oceanic rift propagation - a cause of crustal underplating and seamount volcanism. Geology, 18(9), 886-889.

Cambon, P., Bougault, H., Joron, J.L. and Treuil, M., 1983. Basalts from the East Pacific Rise: An example of typical oceanic crust depleted in magmaphile elements. Init. Repts. DSDP, 65: Washington (U.S. Govt. Printing Office), 623-634.

Cann, J.R., 1974. A model for oceanic crustal structure developed. Geophys. J. R. Astron. Soc. London, 268, 443-446.

Cannat, M., Mevel, C., Maia, M., Deplus, C., Durant, C., Gente, P., Agrinier, P., Belarouchi, A., Dubuisson, G., Humler, E. and Reynolds, J., 1995. Thin crust, ultramafic exposures, and rugged faulting patterns at the Mid-Atlantic Ridge (22°-24°N). Geology, 23, 49-52.

Carbotte, S.M. and Macdonald, K.C., 1994. The axial topographic high at intermediate and fast spreading ridges. Earth Planet. Sci. Lett., 128/3-4, 85-97.

Carlson, R.L. and Herrick, C.N., 1990. Densities and porosities in the oceanic crust and their variations with depth and age. J. Geophys. Res., 95, 9153-9170.

Chadwick, W.W. Jr. and Embley, R.W., 1994. Lava flows from a mid-1980s submarine eruption on the Cleft Segment, Juan de Fuca Ridge. J. Geophys. Res., 99, 4761-4776.

Chadwick, W.W. Jr., Embley, R.W. and Fox, C.G., 1991. Evidence for volcanic eruption on the southern Juan de Fuca ridge between 1981 and 1987. Nature, 350, 416-418.

Chandra, U., 1974. Seismicity, earthquake mechanisms and tectonics along the western coast of North America, from 42°N to 61°N. Bull. Seismological Soc. Am., 64, 1529-1549.

Chen, Y.J., 1992. Oceanic crustal thickness versus spreading rate. Geophys. Res. Lett, 19, 753-756.

Christeson, G.L., Purdy, G.M. and Fryer, G.J., 1992. Structure of young upper crust at the East Pacific Rise near 93°30' N. Geophys. Res. Lett., 19(10), 1045-1048.

Christeson, G.L., Purdy, G.M. and Rohr, K.M.M., 1993. Structure of the Northern Symmetrical Segment of the Juan de Fuca Ridge. Mar. Geophys. Res., 15, 219-240.

Christie, D.M. and Sinton, J.M., 1981. Evolution of abyssal lavas along propagating segments of the Galapagos spreading center. Earth Planet. Sci. Lett., 56, 321-335.

Collier, J. and Sinha, M., 1990. Seismic images of a magma chamber beneath the Lau Basin back-arc spreading centre. Nature, 346, 646-648.

Cormier, M.-H., Macdonald, K.C. and Wilson, D.S., 1995. A three-dimensional gravity analysis of the East Pacific Rise from 18° to 21°30'S. J. Geophys. Res., 100, 8063-8082.

Cudrak, C.F. and Clowes, R.M., 1993. Crustal structure of Endeavour Ridge Segment, Juan de Fuca Ridge, from a detailed seismic refraction survey. J. Geophys. Res., 98, 6329-6349.

CYAMEX Scientific Team, 1981. First manned submersible dives on the East Pacific Rise at 21°N (Project RITA): General Results. Mar. Geophys. Res., 4, 345-379.

Dauteuil, O., 1995. Fault pattern from SeaBeam processing: The western part of the Blanco Fracture Zone (N.E. Pacific). Mar. Geophys. Res., 17, 399-430

Davis, E.E. and Karsten, J.L., 1986. On the cause of the asymmetric distribution of seamounts about the Juan de Fuca Ridge: Ridge-crest migration over a heterogeneous asthenosphere. Earth Planet. Sci. Lett., 79, 385-396.

Davis, E.E., Lister, C.R.B. and Lewis, B.T.R., 1976. Seismic structure of the Juan de Fuca Ridge: Ocean Bottom Seismometer Results From the Median Valley. J. Geophys. Res., 81, 3541-3555.

deCharon, A.V., 1988. Structure and Tectonics of Cascadia Segment, Central Blanco Transform Fault Zone. MS. Thesis, Oregon State University, Corvallis, Oregon, 73pp.

Dehlinger, P., Couch, R.W., McManus, D.A. and Gemperle, M., 1970. Northeast Pacific Structure. In: Maxwell, A. (ed.). The Sea, vol. 4, John Wiley and Sons, New York, 133-189.

Delaney, J.R., Spiess, F.N., Colony, W.E., Karsten, J.L., Kelley, D.S. and Nehlig, P., 1987. A complete Deep-Tow swath map of south-facing "wall" of the Blanco Trough, Juan de Fuca Region. Eos Trans. Am. Geophy. Un., 68, 1402.

Detrick, R.S., Buhl, P., Vera, E., Mutter, J., Orcutt, J., Madsen, J. and Brocher, T., 1987. Multichannel seismic imaging of a crustal magma chamber along the East Pacific Rise between 9°N and 13°N. Nature, 326, 35-41.

Detrick, R.S., Collins, J., Stephen, R. and Swift, S., 1994. *In situ* evidence for the nature of the seismic layer 2/3 boundary in oceanic crust. Nature, 370, 288-290.

Dick, H.J.B and Johnson, K.T.M., 1995. REE and trace element composition of clinopyroxene megacrysts, xenocrysts, and phenocrysts in two diabase dikes from Leg 140, Hole 504B. Proc. of the ODP, 137/140, 121-130.

Dixon, J.E., Clague, D.A. and Eissen, J.-P., 1986. Gabbroic Xenoliths and Host Ferrobasalt From the Southern Juan de Fuca Ridge. J. Geophys. Res., 91, 3795-3820.

Donnelly, T.W. et al., 1980. Introduction and Explanatory Notes. Initial Reports of the Deep Sea Drilling Project, v. 51, 52, 53: Washington (U.S. Government Printing Office), p. 5-22.

Duncan, R.A. and Green, D.H., 1987. The genesis of refractory melts in the formation of oceanic crust. Contrib. Min. Petrol., 96, 326-342.

Dungan, M.A., Long, P.E. and Rhodes, J.M., 1978. Magma mixing at mid-ocean ridges: Evidence from Legs 45 and 46 DSDP. Geophys. Res. Lett., 5(5), 423-425.

Dziak, R.P., Fox, C.G. and Embley, R.W., 1991. Relationship between the seismicity and geologic structure of the Blanco Transform Fault zone. Mar. Geophys. Res., 13(3), 203-208.

Dziak, R.P., Fox, C.G. and Schreiner, A.E., 1995. The June-July 1993 seismo-acoustic event at CoAxial segment, Juan de Fuca Ridge: Evidence for a lateral dike injection. Geophys. Res. Lett., 22(2), 135-138.

EEZ Scan 84 Scientific Staff, 1986. Atlas of the Exclusive Economic Zone, Western Coterminous United States, U.S. Geological Survey Misc. Investigations.

Eliason, E.M. and McEwen, A.S., 1990. Adaptive box filters for removal of random noise from digital images. Photogrammetric Eng. and Remote Sensing, 56, 453-458.

Elthon, D., 1984. Plagioclase buoyancy in oceanic basalts: Chemical effects. Geochim. Cosmochim. Acta, 48, 753-768.

Elthon, D., 1991. Experimental phase petrology of mid-ocean ridge basalts. In: Floyd, P.A. (ed), Oceanic Basalts. Blackie, London, 94-115pp.

Elthon, D., 1992. Chemical trends in abyssal peridotites: refertilisation of depleted suboceanic mantle. J. Geophys. Res., 97, 9015-9025.

Elthon, D. and Casey, J., 1985. The very depleted nature of certain primary mid-ocean ridge basalts. Geochim. Cosmochim. Acta, 49, 289-298.

Elvers, D., Srivasta, S.P., Potter, K., Morley, J. and Seidel, D., 1973. Asymmetric spreading across the Juan de Fuca and Gorda Ridges as obtained from a detailed magnetic survey. Earth Planet. Sci. Lett., 20, 211-219.

Embley, R.W. and Chadwick, W.W., 1994. Volcanic and hydrothermal processes associated with a recent phase of seafloor spreading at northern Cleft segment: Juan de Fuca Ridge. J. Geophys. Res., 99, 4741-4760.

Embley, R.W. and Wilson, D., 1992. Morphology of the Blanco Transform Fault zone - NE Pacific: Implications for its tectonic evolution. Mar. Geophys. Res., 14, 25-45.

Embley, R.W., Kulm, L.D., Massoth, G., Abbott, D. and Holmes, M., 1987. Morphology, Structure, and Resource Potential of the Blanco Transform Fault Zone. In: Scholl, D.W., Grantz, A. and Vedder, J.G., (eds), Geology and Resource Potential of the Continental Margin of Western North America and Adjacent Ocean Basins - Beaufort Sea to Baja, California. Circum-Pacific Council for Energy and Mineral Resources, Earth Science Series, vol. 6, 549-561.

Embley, R.W., Murphy, K.M. and Fox, C.G., 1990. High-resolution studies of the summit of Axial Volcano. J. Geophys. Res., 95, 12785-12812.

Embley, R.W., Chadwick, W., Perfit, M.R. and Baker, E.T., 1991. Geology of the northern Cleft segment, Juan de Fuca Ridge: Recent lava flows, sea-floor spreading, and the formation of megaplumes. Geology, 19, 771-775.

Embley, R.W., Chadwick, W.W. Jr., Jonasson, I.R., Butterfield, D.A. and Baker, E.T., 1995. Initial results of the rapid response to the 1993 CoAxial event: relationships between hydrothermal and volcanic processes. Geophys. Res. Lett., 22(2), 143-146.

Emmermann, R., 1985. Basement geochemistry, Hole 504B. Init. Repts. DSDP, 83: Washington (U.S. Govt. Printing Office), 183-199.

Emmermann, R., Hubberten, H.-W. and Puchelt, H., 1983. Geochemistry of basalts erupted at the Galapagos spreading center between 85 and 87°W. Init. Repts. DSDP, 70, 409-418.

Engeln, J.F., Stein, S., Werner, J. and Gordon, R.G., 1988. Microplate and shear zone models for oceanic spreading center reorganizations. J. Geophys. Res., 93, 2839-2856.

Fisk, M.R., 1984. Depths and temperatures of mid-ocean ridge magma chambers and the composition of their source magmas. In: Gass, I.G., Lippard, S.J. and Shelton, A.W. (eds), Ophiolites and Oceanic Lithosphere, Geol. Soc. London, Spec. Publ., 13, 17-23.

Fisk, M.R., Schilling, J.-G. and Sigurdsson, H.. 1980. An experimental investigation of Iceland and Reykjanes Ridge tholeiites: I. Phase relations. Contrib. Min. Petrol., 74, 361-374.

Fleutelot, C., Juteau, T. and Tivey, M.A., 1995. The Parks Plateau Unveiled. Eos Trans. Am. Geophys. Un., 76 (46), F420-421.

Flower, M., 1991. Magmatic processes in oceanic ridge and intraplate settings. In: Floyd, P.A. (ed), Oceanic Basalts. Blackie, London, p116-147.

Flower, M.F.J., Pritchard, R.G., Schmincke, H.-U. and Robinson, P.T., 1983. Geochemistry of basalts: Deep Sea Drilling Project Sites 482, 483, and 485 near the Tamayo Fracture Zone, Gulf of California. Init. Repts. DSDP, 65: Washington (U.S. Govt. Printing Office), 559-578.

Fodor, R.V., Berkley, J.L., Keil, K., Hustler, J.W., Ma, M.-S. and Schmitt, R.A., 1980. Petrology of basalt drilled from the Galapagos spreading center, Deep Sea Drilling Project Leg 54. Initial Reports of the Deep Sea Drilling Project, v. 54: Washington (U.S. Government Printing Office), 737-750.

Fornari, D.J. and Embley, R.W., 1995. Tectonic and Volcanic Controls on Hydrothermal Processes at the Mid-Ocean Ridge: An Overview Based on Near-Bottom and Submersible Studies. In: Humphris, S. et al. (eds), Seafloor hydrothermal systems: physical, chemical, biological, and geological interactions. American Geophysical Union Monograph 91, Washington, D.C., 1-46.

Fornari, D.J., Perfit, M.R., Malahoff, A. and Embley, R., 1983. Geochemical studies of abyssal lavas recovered by DSRV Alvin from eastern Galapagos rift, Inca transform, and Ecuador rift. I. Major element variations in natural glasses and spatial distribution of lavas. J. Geophys. Res., 88, 10519-10529.

Fouquet, Y., Ondreas, H., Charlou, J.L., Donval, J.P., Radford-Knoery, J., Costa, I., Lourenco, N. and Tivey, M.K., 1995. Atlantic lava lakes and hot vents. Nature. 377, 201.

Fox, C.G., Radford, W.E., Dziak, R.P., Lau, T.K., Matsumoto, H. and Schreiner, A.E., 1995. Acoustic detection of a seafloor spreading episode on the Juan de Fuca Ridge using military hydrophone arrays. Geophys. Res. Lett., 22(2), 131-134.

Fox, P.J. and Gallo, D.G., 1984. A tectonic model for ridge-transform-ridge plate boundaries: Implications for the structure of oceanic lithosphere. Tectonophysics, 104, 204-242.

Fox, P.J. and Gallo, D.G., 1986. The geology of North Atlantic transform plate boundaries and their aseismic extensions. In: Vogt, P.R. and Tucholke, B.E. (eds), The Geology of North America, Vol. M, The Western North Atlantic Region. Geol. Soc. of Am., 157-168.

Francheteau, J., Choukroune, P., Hekinian, R., Le Pichon, X. and Needham, H.D., 1976. Oceanic fracture zones do not provide deep sections of the crust. Can. J. Earth Sci., 13, 1223-1235.

Francheteau, J., Juteau, T. and Rangin, C., 1979. Basaltic pillows in collapsed lava-pools on the deep ocean-floor. Nature, 281, 209-211.

Francheteau, J., Armijo, R., Cheminee, J.L., Hekinian, R., Lonsdale, P. and Blum, N., 1990. 1 Ma East Pacific Rise oceanic crust and uppermost mantle exposed by rifting in Hess Deep (equatorial Pacific Ocean). Earth Planet. Sci. Lett., 101, 281-295.

Francheteau, J., Armijo, R., Cheminee, J.L., Hekinian, R., Lonsdale, P. and Blum, N., 1992. Dyke complex of the East Pacific Rise exposed in the walls of Hess Deep and the structure of the upper oceanic crust. Earth and Planet. Sci. Lett., 111, 109-121.

Francis, T.J.G., 1981. Serpentinization faults and their role in the tectonics of slow spreading ridges. J. Geophys. Res., 86, 11616-11622.

Frey, F.A., Green, D.H. and Roy, S.D., 1978. Integrated models of Basalt Petrogenesis: A Study of Quartz Tholeiites to Olivine Melilites from South Eastern Australia Utilizing Geochemical and Experimental Petrological Data. J. Petrol., 19, 463-513.

Fujii, T. and Bougault, H., 1983. Melting relations and viscosity of an abyssal tholeiite and the origin of MORBs. Earth Planet. Sci. Lett., 62, 283-295.

Gaetani, G.A., DeLong, S.E. and Wark, D.A., 1995. Petrogenesis of basalts from the Blanco Trough, northeast Pacific: Inferences for off-axis melt generation. J. Geophys. Res., 100, 4197-4214.

Gente, P., Auzende, J.M., Renard, V., Fouquet, Y. and Bideau, D., 1986. Detailed geological mapping by submersible of the East Pacific Rise axial graben near 13°N. Earth Planet. Sci. Lett., 78(2-3), 224-236.

Gente, P., Pockalny, R.A., Durand, C., Deplus, C., Maia, M., Ceuleneer, G., Mevel, C., Cannat, M. and Laverne, C., 1995. Characteristics and evolution of the

segmentation of the Mid-Atlantic Ridge between 20°N and 24°N during the last 10 million years. Earth Planet. Sci. Lett., 129(1-4), 55-71.

Goff, J.A., 1991. A global and regional stochastic analysis of near-ridge abyssal hill morphology. J. Geophys. Res., 96, 21713-21737.

Goff, J.A., Tucholke, B.E., Lin, J., Jaroslow, G.E. and Kleinrock, M.C., 1995. Quantitative analysis of abyssal hills in the Atlantic Ocean: a correlation between inferred crustal thickness and extensional faulting. J. Geophys. Res., 100, 22509-22522.

Goldfarb, M.S., 1986. Petrography of basalts from Deep Sea Drilling Project Leg 92. Init. Repts. DSDP, 92, 459-469.

Goldstein, S.J., Murrell, M.T., Janecky, D.R., Delaney, J.R. and Clague. D.A., 1991. Geochronology and petrogenesis of MORB from the Juan de Fuca and Gorda ridges by /sup 238/U-/sup 230/Th disequilibrium. Earth Planet. Sci. Lett., 107(1), 25-41.

Goud, M. R. and Karson, J.A, 1985. Tectonics of slow-slipping short-offset transform faults in the FAMOUS area, Mid-Atlantic ridge. Mar. Geophys. Res., 7, 489-514.

Gregg, T.K.P. and Fink, J.H., 1995. Quantification of submarine lava-flow morphology through analog experiments. Geology, 23, 73-76.

Gregg, T.K.P., Fornari, D.J., Perfit, M.R., Haymon, R.M. and Fink, J.H., 1996. Rapid emplacement of a mid-ocean ridge lava flow on the East Pacific rise at 9° 46'-51'N. Earth Planet. Sci. Lett., 144, E1-7.

Griffiths, R.W. and Fink, J.H., 1992. Solidification and Morphology of Submarine Lavas: A Dependence on Extrusion Rate. J. Geophys. Res., 97, 19729-19737.

Grove, T.L. and Bryan, W.B., 1983. Fractionation of pyroxene-phyric MORB at low pressure: an experimental study. Contrib. Min. Petrol., 84, 293-309.

Grove, T.L., Kinzler, R.J. and Bryan, W.B., 1992. Fractionation of mid-ocean ridge basalt (MORB). In: Phipps-Morgan, J. et al. (eds), Mantle flow and melt generation at mid-ocean ridges. Am. Geophys. Un. Geophys. Monogr. Ser. 71, 281-310.

Gudmundsson, A., 1988. Formation of collapse calderas. Geology, 16(9), 808-810.

Hall, J.M. and Robinson, P.T., 1979. Deep Crustal Drilling in the North Atlantic Ocean. Science, 204, 573-586.

Hanson, G.N., 1989. An approach to trace element modeling using a simple igneous system as an example. In: Lipin, R. and McKay, G.A. (eds), Geochemistry and Mineralogy of the Rare Earth Elements - Reviews of Mineralogy, v.21, Min. Soc. of Am., Washington D.C.

Harding, A.J., Kent, G.M. and Orcutt, J.A., 1993. A multichannel seismic investigation of upper crustal structure at 9°N on the East Pacific Rise: implications for crustal accretion. J. Geophys. Res., 98, 13925-13944.

Hart, S.R., 1988. Heterogeneous mantle domains: signatures, genesis and mixing chronologies. Earth Planet. Sci. Lett., 90, 273-296.

Harte, B., 1987. Metasomatic events recorded in mantle xenoliths: an overview. In: Nixon, P.H. (ed), Mantle xenoliths, Wiley, Chichester, 625-640.

Hasselgren, E., Clowes, R.M. and Calvert, A.J., 1992. Propagating rift pseudofaults-zones of crustal underplating imaged by multichannel seismic reflection data. Geophys. Res. Lett., 19(5), 485-488.

Hawkesworth, C.J., Rogers, N.W., van Calsteren, P.W.C. and Menzies, M.A., 1984. Mantle enrichment processes. Nature, 311, 331-335.

Hébert, R., Bideau, D. and Hekinian, R., 1983. Ultramafic and mafic rocks from the Garrett Transform Fault near 13°30'S on the East Pacific Rise: igneous petrology. Earth Planet. Sci. Lett., 65, 107-125.

Haymon, R.M., Fornari, D.J., Edwards, M.H., Carbotte, S., Wright, D. and Macdonald, K.C., 1991. Hydrothermal vent distribution along the East Pacific Rise crest (9° 09'-54'N) and its relationship to magmatic and tectonic processes on fast-spreading mid-ocean ridges. Earth Planet. Sci. Lett., 104/2-4, 513-534.

Haymon, R.M., Fornari, D.J., Von Damm, K.L., Lilley, M.D., Perfit, M.R., Edmond, J.M., Shanks, W.C. III, Lutz, R.A., Grebmeier, J.M., Carbotte, S., Wright, D., McLaughlin, E., Smith, M., Beedle, N. and Olson, E., 1993. Volcanic eruption of the mid-ocean ridge along the East Pacific Rise crest at 9° 45'-52'N: direct submersible observations of seafloor phenomena associated with an eruption event in April, 1991. Earth Planet. Sci. Lett., 119(1-2), 85-101.

Haymon, R.M., 1997. The response of ridge-crest hydrothermal systems to segmented episodic magma supply. In: MacLeod, C.J., Tyler, P.A. and Walker, C.L. (eds), Tectonic, Magmatic, Hydrothermal and Biological Segmentation of Mid-Ocean Ridges. Geol. Soc. Spec. Publ., 118, 1-15.

Hekinian, R., 1982. Petrology of the ocean floor. Elsevier Scientific Pub. Co., New York, 393pp.

Hekinian, R. and Morel, J.M., 1980. Basement rocks from the East Pacific Rise near 9°N compared with other ocean-floor volcanic provinces. Init. Repts. DSDP, 54, 819-828.

Hekinian, R., Thompson, G. and Bideau, D., 1989. Axial and off-axial heterogeneity of basaltic rocks from the East Pacific Rise at 12°35'N-12°51'N and 11°26'N-11°30'N. J. Geophys. Res., 94, 17437-17463.

Hekinian, R., Bideau, D., Francheteau, J., Cheminee, J.-L., Armijo, R., Lonsdale, P. and Blum, N., 1993. Petrology of the East Pacific Rise crust and upper mantle exposed in Hess Deep (eastern equatorial Pacific). J. Geophys. Res., 98, 8069-8094.

Herron, T.J., 1982. Lava flow layer-East Pacific Rise. Geophys. Res. Lett., 9(1), 17-20.

Hess, P. C., 1989. Origins of igneous rocks. Harvard University Press, Cambridge, Mass., 336pp.

Hey, R.N. and Wilson, D.S., 1982. Propagating rift explanation for the tectonic evolution of the northeast Pacific - the pseudomovie. Earth and Planet. Sci. Lett., 58, 167-188.

Hey, R.N., Duennebier, F.K. and Morgan, W.J., 1980. Propagating rifts on mid-oceanic ridges. J. Geophys. Res., 85, 3647-3658.

Hey, R.N., Menard, H.W., Atwater, T.M. and Caress, D.W., 1988. Changes in direction of seafloor spreading revisited. J. Geophys. Res., 93, 2803-2811.

Hey, R.N., Sinton, J.M. and Duennebier, F.K., 1989. Propagating rifts and spreading centres. In: Winterer, E.L., Hussong, D.M. and Decker, R.W. (eds), The Eastern Pacific Ocean and Hawaii. Boulder, Colorado, Geological Society of America, v. N, 161-176.

Hey, R.N., Sinton, J.M., Kleinrock, M.C., Yonover, R.N., Macdonald, K.C., Miller, S.P., Searle, R.C., Christie, D.M., Atwater, T.M., Sleep, N.H., Johnson, H.P. and Neal, C.A., 1992. ALVIN Investigation of an Active Propagating Rift System, Galapagos 95.5°W. Mar. Geophys. Res., 14, 207-226.

Hey, R.N., Johnson, P.D., Martinez, F., Korenaga, J., Somers, M.L., Huggett, Q.J., LeBas, T.P., Rusby, R.I. and Naar, D.F., 1995. Plate boundary reorganization at a large-offset, rapidly propagating rift. Nature, 378, 167-170.

Holcomb, R.T., 1980. Kilauea Volcano, Hawaii: Chronology and Morphology of the Surficial Lava Flows. Stanford University, Ph.D. dissertation, 321pp.

Holmes, M.L., Gardner, J.V., Johnson, H., Campbell, J.F., Carlson, P., Edwards, B. and Karl, H., 1984. SeaMARC II studies of the Juan de Fuca and Gorda Ridges. Eos Trans. Am. Geophys. Un., 65, 279.

Hooft, E.E.E., Schouten, H. and Detrick, R.S., 1996. Constraining crustal emplacement processes from the variation in seismic layer 2A thickness at the East Pacific Rise. Earth Planet. Sci. Lett., 142, 289-309.

Hurst, S.D., Karson, J.A. and Verosub, K.L., 1994. Paleomagnetism of tilted dikes in fast spread oceanic crust exposed in the Hess Deep Rift: implications for spreading and rift propagation. Tectonics. 13(4), 789-802.

Hyndman, R.D. and Salisbury, M.H., 1984. The Physical Nature of the Oceanic Crust on the Mid-Atlantic Ridge, DSDP Hole 395A. Init. Repts. DSDP, 78B: Washington (U.S. Govt. Printing Office), 839-848.

Ibach, D.H., 1981. The Structure and Tectonics of the Blanco Fracture Zone. MS. Thesis, Oregon State University, Corvallis, Oregon, 60pp.

Johnson, H.P., Van Patten, D. and Tivey, M.T., 1996. Structure of Upper Oceanic Crust from Seafloor Gravity Measurements Near the Blanco Fracture Zone. Eos Trans. Am. Geophys. Un., 76 (46), F707.

Johnson, K.T.M. and Dick, H.J.B., 1992. Open system melting and temporal and spatial variation of peridotite and basalt at the Atlantis II Fracture Zone. J. Geophys. Res., 97, 9219-9241.

Johnson, K.T.M., Dick, H.J.B. and Shimizu, N., 1990. Melting in the oceanic upper mantle: an ion microprobe study of diopsides in abyssal peridotites. J. Geophys. Res., 95, 2661-2678.

Juteau, T., Eissen, J.P., Francheteau, J., Needham, D., Choukroune, P., Rangin, C., Séguret, M., Ballard, R.D., Fox, P.J., Normark, W.R., Carranza, A., Cordoba, D. and Guerrero, J., 1980. Homogeneous basalts from the East Pacific Rise at 21°N: steady state magma reservoirs at moderately fast spreading centers. Oceanologica Acta, 3(4), 487-503.

Juteau, T, Bideau, D., Dauteuil, O., Manac'h, G., Naidoo, D.D., Nehlig, P., Ondreas, H., Tivey, M. and Whipple, K., 1995. A submersible study in the western Blanco Fracture Zone, N.E. Pacific: Structure and Evolution during the last 1.6 Ma. Mar. Geophys. Res., 17, 399-430.

Kappel, E.S. and Normark, W.R., 1987. Morphometric variability within the Axial Zone of the southern Juan de Fuca Ridge: Interpretation from SeaMARC II, SeaMARC I, and Deep-Sea Photography. J. Geophys. Res., 92, 11291-11302.

Kappel, E.S. and Ryan, W.B.F., 1986. Volcanic Epidosicity and a Non-Steady State Rift Valley along Northeast Spreading Centres: Evidence from Sea MARC I. J. Geophys. Res., 91, 13925-13940.

Karson, J.A., 1986. Lithosphere age, depth and structural complications resulting from migrating transform faults. J. Geol. Soc., 143, 785-788.

Karson, J.A. and Dick, H.J.B., 1984. Deformed and metamorphosed oceanic crust on the Mid-Atlantic Ridge. Ofioliti, 9, 279-302.

Karson, J.A. and Winters, A.T., 1992. Along-Axis Variations in Tectonic Extension and Accommodation Zones in the MARK Area, Mid-Atlantic Ridge 23°N Latitude, In: Parson, L.M., Murton, B.J. and Browning, P. (eds), Ophiolites and Their Modern Oceanic Analogues. Geological Society of London, Special Publication 60, Blackwell Scientific Publishers, 107-116.

Karson, J. A., Thompson, G., Humphris, S.E., Edmond, J.M., Bryan, W.B., Brown, J.R., Winters, A.T., Pockalny, R.A., Casey, J.F., Campbell, A.C., Klinkhammer, G., Palmer, M.R., Kinzler, R.J. and Sulanowska, M.M., 1987. Along-axis variations in seafloor spreading in the MARK area. Nature, 328, 681-685.

Karson, J.A., Hurst, S.D. and Lonsdale, P., 1992. Tectonic Rotations of Dikes in Fast-Spread Oceanic Crust Exposed at Hess Deep. Geology, 20, 685-688.

Karsten, J.L. and Delaney, J.R., 1988. Temporal Variations in the Composition of Ridge Axis Basalts from the Ridge-Transform Intersection of the southern Juan de Fuca Ridge. Eos Trans. Am. Geophy. Un., 69, 1426.

Karsten, J.L. and Delaney, J.R., 1991. Temporal variations in Axial Basalt Composition at the So. Juan de Fuca Ridge-Blanco Transform Intersection: Major and Trace Element Constraints. Eos Trans. Am. Geophy. Un., 69, 519.

Karsten, J.L., Delaney, J.R., Rhodes, J.M. and Liias, R.A., 1990. Spatial and temporal evolution of magmatic systems beneath the Endeavour Segment, Juan de Fuca Ridge: tectonic and petrologic constraints. J. Geophys. Res., 95, 19235-19256.

Kay, P.N., Hubbard, N.J. and Gast, P.W., 1970. Chemical characteristics and origin of oceanic ridge volcanic rocks. J. Geophys. Res., 75, 1585-?.

Kempner, W.C. and Gettrust, J.F., 1982. Ophiolites, synthetic seismograms, and oceanic crustal structure. II. A comparison of synthetic seismograms of the Samail ophiolite, Oman, and the Rose refraction data from the East Pacific Rise. J. Geophys. Res., 87, 8463-8476.

Kempton, P.D., 1985. An interpretation of contrasting nucleation and growth histories from the petrographic analysis of pillow and dike chilled margins, Hole 504B, Deep Sea Drilling Project, Leg 83. Init. Repts. DSDP, 83, 165-181.

Kempton, P.D., Autio, L.K., Rhodes, J.M., Holdaway, M.J., Dungan, M.A. and Johnson, P., 1985. Petrology of basalts for hole 504B, Deep Sea Drilling Project, leg 83. Init. Repts. DSDP, 83: Washington (U.S. Govt. Printing Office), 129-164.

Kent, G.M., Harding, A.J., Orcutt, J.A., Detrick, R.S., Mutter, J.C. and Buhl, P., 1994. Uniform accretion of oceanic crust south of the Garrett transform at 14°15'S on the East Pacific Rise. J. Geophys. Res., 99, 9097-9116.

Kidd, R.G.W., 1977. A model for the process of formation of the upper oceanic crust. Geophys. J. R. Astr. Soc., 50, 149-183.

Kinzler, R.J. and Grove, T.L., 1992. Primary magmas of mid-ocean ridge basalts. 2. Applications. J. Geophys. Res., 97, 6907-6926.

Klein, E.M. and Langmuir, C.H., 1987. Global correlations of ocean ridge basalt chemistry with axial depth and crustal thickness. J. Geophys. Res., 92, 8089-8115.

Klein, E.M. and Langmuir, C.H., 1989. Local versus global variations in ocean ridge basalt composition: a reply. J. Geophys. Res., 94, 4241-4252.

Kleinrock, M.C. and Hey, R.N., 1989a. Detailed Tectonics Near the Tip of the Galapagos 95.5°W Propagator: How the Lithospshere Tears and a Spreading Axis Develops. J. Geophys. Res., 94, 13801-13838.

Kleinrock, M.C. and Hey, R.N., 1989b. Tectonics of the Failing Spreading System Associated With the Galapagos 95.5°W Propagator. J. Geophys. Res., 94, 13839-13857.

Kleinrock, M.C. and Hey, R.N., 1989c. Migrating Transform Zone and Lithospheric Transfer at the Galapagos 95.5°W Propagator. J. Geophys. Res., 94, 13859-13878.

Langmuir, C.H. and Bender, J.F., 1984. The geochemistry of basalts in the vicinity of transform faults: observations and implications. Earth Planet. Sci. Lett., 698, 107-127.

Langmuir, C.H., Bender, J.F., Bence, A.E., Hansen, G.N., and Taylor, S.R., 1977. Petrogenesis of basalts from the FAMOUS area: Mid-Atlantic Ridge. Earth Planet. Sci. Lett., 36, 133-156.

Langmuir, C.H., Vocke, R.D., Hanson, G.N. and Hart, S.R., 1978. A general mixing equation with applications to Icelandic basalts. Earth Planet. Sci. Lett., 37, 380-392.

Langmuir, C.H., Bender, J.F. and Batiza, R., 1986. Petrological and tectonic segmentation of the East Pacific Rise, 5°30'N-14°30'N. Nature, 322, 422-427.

Langmuir, C.H., Klein, E.M. and Plank, T., 1992. Petrological Systematics of Mid-Ocean Ridge Basalts: Constraints on Melt Generation Beneath Ocean Ridges. In: Phipps-Morgan, J. et al. (eds), Mantle flow and melt generation at mid-ocean ridges. Am. Geophys. Un. Geophys. Monogr. Ser. 71, 183-280.

Laverne, C. and Vivier, G., 1983. Petrographical and chemical study of basement basalts from the Galapagos spreading center, Leg 70. Init. Repts. DSDP, 70, 375-386.

le Roex, A.P., Erlank, A.J. and Needham, H.D., 1981. Geochemical and mineralogical evidence for the occurrence of at least three distinct magma types in the 'FAMOUS' region. Contrib. Min. Petrol., 77, 24-37.

le Roex, A.P., Dick, H.J.B., Erlank, A.J., Reid, A.M., Frey, F.A. and Hart, S.R., 1983. Geochemistry, mineralogy and petrogenesis of lavas erupted along the Southwest Indian Ridge between the Bouvet triple junction and 11°E. J. Petrol., 24(3), 267-318.

le Roex, A.P., Dick, H.J.B. and Fisher, R.L., 1989. Petrology and Geochemistry of MORB from 25°,E to 46°E along the Southwest Indian Ridge: Evidence for Contrasting Styles of Mantle Enrichment. J. Petrol., 30(4), 947-986.

le Roex, A.P., Dick, H.J.B. and Watkins, R.T., 1992. Petrogenesis of anomalous K-enriched MORB from the Southwest Indian Ridge: 11°53'E to 14°38'E. Contrib. Min. Petrol., 110, 253-268.

Leg 78 Shipboard Scientific Party, 1984. 7. Site 395: 23°N, Mid-Atlantic Ridge. Init. Repts. DSDP, 78, 131-170.

Leg 111 Shipboard Scientific Party, 1989. 3. Site 504: Costa Rica Rift. Init. Repts. ODP, 111, 35-186.

Leg 140 Shipboard Scientific Party, 1992. 2. Site 504. Init. Repts. ODP, 140, 37-133.

Leg 140 Shipboard Scientific Party, 1992. ODP Drills Deepest Hole in Ocean Crust. Eos Trans. Am. Geophys. Un., 73, 537-540.

Leg 148 Shipboard Scientific Party, 1993. 2. Site 504. Init. Repts. ODP, 148, 27-141.

Lewis, B.T.R. et al., 1983a. Site 482. Init. Repts. DSDP, 65: Washington (U.S. Govt. Printing Office), 21-67.

Lewis, B.T.R. et al., 1983b. Site 483. Init. Repts. DSDP, 65: Washington (U.S. Govt. Printing Office), 137-168.

Lichtman, G.S. and Eissen, J.-P., 1983. Time and space constraints on the evolution of medium-rate spreading centers. Geology, 11, 592-595.

Lichtman, G.S., Normark, W.R., Delaney, J.R., Morton, J.L., Johnson, H.P. and Karsten, J.L., 1983. Photogeology and evolution of the Juan de Fuca Ridge. U.S. Geol. Surv. Open File Rept., 83 64, 16p.

Lupton, J.E., Graham, D.W., Delaney, J.R. and Johnson, H.P., 1993. Helium isotope variations in Juan de Fuca ridge basalts. Geophys. Res. Lett., 20(17), 1851-1854.

Macdonald, K.C., 1982. Mid-Ocean Ridges: fine-scale tectonic, volcanic and hydrothermal processes within the plate boundary zone. Ann. Rev. Earth Planet. Sci., 10, 155-190.

Macdonald, K.C., 1983. Crustal processes at spreading centers. Rev. Geophys., 21, 1441-1454.

Macdonald, K.C. and Fox, P.J., 1988. The axial summit graben and cross-sectional shape of the East Pacific Rise as indicators of axial magma chambers and recent volcanic eruptions. Earth Planet. Sci. Lett., 88/1-2, 119-131.

Macdonald, K.C., Fox, P.J., Perram, L.J., Eisen, M.H., Haymon, R.M., Miller, S.P., Carbotte, S.M., Cormier, M.H. and Shor, A.N., 1988. A new view of the mid-ocean ridge from the behaviour of ridge-axis discontinuities. Nature, 335, 217-225.

Macdonald, K.C., Fox, P.J., Alexander, R.T., Pockalny, R. and Gente, P., 1996. Volcanic growth faults and the origin of Pacific abyssal hills. Nature, 380, 125-129.

MacKenzie, W.S., Donaldson, C.H. and Guilford, C., 1982. Atlas of igneous rocks and their textures. Longman, Essex, 141pp.

Marsh, N.G., Tarney, J. and Hendry, G.L., 1983. Trace element geochemistry of basalts from Hole 504B, Panama Basin, Deep Sea Drilling Project Legs 69 and 70. Init. Repts., DSDP, 69: Washington (U.S. Govt. Printing Office), 729-745.

Mattey, D.P. and Muir, I.D., 1980. Geochemistry and mineralogy of basalts from the Galapagos spreading center, Deep Sea Drilling Project Leg 54. Initial Reports of the Deep Sea Drilling Project, v. 54: Washington (U.S. Government Printing Office), 755-772.

McDonald, M.A., Hildebrand, J.A., Web, S.C. and Fox, C.G., 1994. Seismic structure and anisotropy of the southern Juan de Fuca Ridge. J. Geophys. Res., 99, 4857-4873.

McKenzie, D., 1985. ^{230}Th-^{238}U disequilibrium and the melting process beneath ridge axes. Earth Planet. Sci. Lett., 72, 149-157.

McKenzie, D. and O'Nions, R.K., 1991. Partial melt distributions from inversion of rare earth element concentrations. J. Petrol., 32, 1021-1091.

McKenzie, D. and O'Nions, R.K., 1995. The Source Regions of Ocean Island Basalts. J. Petrol., 36, 133-159.

McKenzie, D.P., 1984. The generation and compaction of partially molten rock. J. Petrol., 25, 713-765.

McManus, D., 1965. Blanco Fracture Zone, Northeast Pacific Ocean. Marine Geology, 3, 429-455.

Melson, W.G., 1969. Preliminary results of a geophysical study of portions of the Juan de Fuca Ridge and Blanco Fracture Zone. ESSA Technical Memorandum C&GSTM, 6, 33pp.

Melson, W.G., Vallier, T.L, Wright, T.L., Byerly, G., and Nelen, J., 1976. Chemical Diversity of Abyssal Volcanic Glass Erupted Along Pacific, Atlantic, and Indian Ocean Sea-Floor Spreading Centers. In: Sitton, G.H., Manghnani, M.H. and Moberly, R. (eds), The Geophysics of the Pacific Ocean Basin and Its Margin. American Geophysical Union, Washington D.C., 351-367.

Melson, W.G., Byerly, G.R., Nelen, J.A., O'Hearn, T., Wright, T.L. and Vallier, T., 1977. A catalog of the major element chemistry of abyssal volcanic glasses. In: Mason, B. (ed), Mineral Sciences Investigations, 1974-1975, Smithsonian Contrib. Earth Sci., no. 19, 31-60.

Melson, W.G., et al., 1979. Site 395: 23°N, Mid-Atlantic Ridge. Initial Reports of the Deep Sea Drilling Project. v. 45: Washington (U.S. Government Printing Office), 131-171.

Michael, P.J., Chase, R.L. and Allan, J.F., 1989. Petrologic and geologic variations along the Southern Explorer Ridge, northeast Pacific Ocean. J. Geophys. Res., 94, 13895-13918.

Moore, J.G., Fleming, H.S. and Phillips, J.D., 1974. Preliminary model for extrusion and rifting at the axis of the Mid-Atlantic Ridge, 36°48'N. Geology, 2, 437-440.

Moores, E.M. and Vine, F.J., 1971. The Troodos Massif, Cyprus and other ophiolites as oceanic crust: evaluation and implications. Phil. Trans. Roy. Soc. Lond. A, 268, 443-446.

Moos, D. and Marion, D., 1994. Morphology of extrusive basalts and its relationship to seismic velocities in the shallow oceanic crust. J. Geophys. Res., 99, 2985-2994.

Morton, J.L., Sleep, N.H., Normark, W.R. and Tompkins, D.H., 1987. Structure of the southern Juan de Fuca Ridge from Seismic Reflection records. J. Geophys. Res., 92, 11315-11326.

Naar, D.F. and Hey, R.N., 1986. Fast rift propagation along the East Pacific Rise near Easter Island. J. Geophys. Res., 91, 3425-3438.

Naidoo, D.D., Delaney, J.R. and Juteau, T., 1994. A 2.7 Ma History of 4D Accretion at the S. Juan de Fuca Ridge (JdFR) From the West Blanco Depression (WBD) North Scarp. Eos Trans. Am. Geophys. Un. (Supplement), 75(44), 314-315.

Natland, J.H., 1980. The effect of axial magma chambers beneath spreading centres on the compositions of basaltic rocks. Init. Repts., DSDP, 69, U.S. Govt. Printing Office, Washington, D.C., 833-850.

Natland, J.H., 1989. Partial melting of a lithologically heterogeneous mantle: inferences from crystallization histories of magnesian abyssal tholeiites from the Siqueiros Fracture Zone. In: Saunders, A.D. and Norry, M.J. (eds). Magmatism in the Ocean Basins. Geol. Soc. Spec. Publ., 42, 41-70.

Natland, J., 1991. Mineralogy and crystallization of oceanic basalts. In: Floyd, P.A. (ed), Oceanic Basalts. Blackie, Glasgow, 63-93.

Natland, J.H. and Rosendahl, B.R., 1980. Drilling difficulties in basement during Deep Sea Drilling Project Leg 54. In: Rosendahl, B.R., Hekinian, R., et al., Init. Repts. DSDP, 54: Washington (U.S. Govt. Printing Office): 593-603.

Natland, J.H., Adamson, A.C., Laverne, C. and O'Hearn, T., 1983. A compositionally nearly steady-state magma chamber at the Costa Rica Rift: Evidence from basalt glass and mineral data, DSDP Sites 501, 504 and 505. Init. Repts., DSDP, 69, U.S. Govt. Printing Office, Washington D.C., 811-858.

Nehlig, P., Juteau, T. and Naidoo, D.D., 1992. The Western Blanco Depression: An example of an asymmetric basin with transform normal extension. Eos Trans. Am. Geophys. Un., 73, 554.

Nicolas, A., 1989. Structures of Ophiolites and Dynamics of Oceanic Lithosphere. Kluwer Academic Publishers, Dordrecht, 367pp.

Niu, Y. and Batiza, R., 1991. An empirical method for calculating melt compositions produced beneath mid-ocean ridges: application for axis and off-axis (seamounts) melting. J. Geophys. Res., 96, 21753-21777.

Niu, Y. and Batiza, R., 1993. Chemical variation trends at fast and slow spreading mid-ocean ridges. J. Geophys. Res., 98, 7887-7902.

Niu, Y. and Hekinian, R., 1997. Spreading-rate dependence of the extent of mantle melting beneath ocean ridges. Nature, 385, 326-329.

Normark, W.R., Lupton, J.E., Murray, J.W., Koski, R.A., Clague, D.A., Morton, J.L., Delaney, J.R. and Johnson, H.P., 1982. Polymetallic sulfide deposits and water-column tracers of active hydrothermal vents on the southern Juan de Fuca Ridge. Mar. Technol. Soc. J., 16(3), 46-53.

Normark, W.R., Morton, J.L., Koski, R.A., Clague, D.A. and Delaney, J.R., 1983. Active hydrothermal vents and sulfide deposits on the southern Juan de Fuca Ridge. Geology, 11, 158-163.

Normark, W.R., Morton, J.L. and Ross, S.L., 1987. Submersible Observations along the southern Juan de Fuca Ridge: 1984 Alvin Program. J. Geophys. Res., 92, 11283-11290.

O'Donnell, T.H. and Presnall, D.C., 1980. Chemical variations of the glass and mineral phases in basalts dredged from 25°-38°N along the mid-Atlantic Ridge. Am. J. Sci., 280, 845-868.

O'Hara, M.J., 1977. Geochemical evolution during fractional crystallisation of a periodically refilled magma chamber. Nature, 266, 503-507.

OTTER, 1984. The Geology of the Oceanographer Transform: The Ridge-Transform Intersection. Mar. Geophys. Res., 6, 109-141.

Palmer, J., Delaney, J.R. and Spiess, F.N., 1987. Recent Deep Tow Observations at the Blanco Fracture Zone - Juan de Fuca Ridge Intersection. Eos Trans. Am. Geophys. Un., 68, 1492.

Pearce, J.A., Rogers, N., Tindle, A.J. and Watson, J.S., 1986. Geochemistry and petrogenesis of basalts from Deep Sea Drilling Project Leg 92, Eastern Pacific. Init. Repts. DSDP, 92, 435-451.

Perfit, M.R., Fornari, D.J., Smith, M.C., Bender, J.F., Langmuir, C.H. and Haymon, R.M., 1994. Small-scale spatial and temporal variations in mid-ocean ridge crest magmatic processes. Geology, 22, 375-379.

Peterson, D.W. and Tilling, R.I., 1980. Transition of basaltic lavas from pahoehoe to aa, Kilauea volcano, Hawaii: Field observations and key factors. J. Volcanol. Geotherm. Res., 7, 271-298.

Pezard, P.A., Anderson, R.N., Ryan, W.B.F., Becker, K., Alt, J.C. and Gente, P., 1992. Accretion, structure and hydrology of intermediate spreading-rate oceanic crust from drillhole experiments and seafloor observations. Mar. Geophys. Res., 14, 93-123.

Pflumio, C., 1991. Evidences for Polyphased Oceanic Alteration of the Extrusive Sequence of the Semail Ophiolite from the Salahi Block (Northern Oman). In: Tj. Peters et al. (eds), Ophiolite Genesis and Evolution of the Oceanic Lithosphere, 313-351.

Pockalny, R.A., Detrick, R.S. and Fox, P.J., 1988. Morphology and tectonics of the Kane Transform from Sea Beam Bathymetry Data. J. Geophys. Res., 93, 3179-3194.

Reynolds, J.R., Langmuir, C.H., Bender, J.F., Kastens, K.A. and Ryan, W.B.F., 1992. Spatial and temporal variability in the geochemistry of basalts from the East Pacific rise. Nature, 359, 493-499.

Rhodes, J.M., Morgan, C. and Liias, R.A., 1990. Geochemistry of Axial Seamount Lavas: Magmatic Relationship Between the Cobb Hotspot and the Juan de Fuca Ridge. J. Geophys. Res., 95, 12713-12733.

Riddihough, R., 1984. Recent movements of the Juan de Fuca Plate System. J. Geophys. Res., 89, 6980-6994.

Ringwood, A.E., 1982. Phase transformations and the differentiation in subducted lithosphere: Implications for mantle dynamics, basalt petrogenesis, and crustal evolution. J. Geol., 90, 611-643.

Robinson, P.T., Mehegan, J., Gibson, I.L. and Schmincke, H.-U., 1982. Lithology and structure of the volcanic sequence in eastern Iceland. J. Geophys. Res., 87, 6429-6436.

Rohr, K.M.M., Milkereit, B. and Yorath, C.J., 1988. Asymmetric deep crustal structure across the Juan de Fuca Ridge. Geology, 16(6), 533-537.

Rosencrantz, E., 1982. Formation of uppermost oceanic crust. Tectonics, 1(6), 471-494.

Rosencrantz, E., 1983. The structure of sheeted dikes and associated rocks in North Arm massif, Bay of Islands ophiolite complex and the intrusive process at oceanic spreading centers. Can. J. Earth Sci., 20, 787-801.

Rubin, K.H., Macdougall, J, D. and Perfit, M.R., 1994. /sup 210/Po-/sup 210/Pb dating of recent volcanic eruptions on the sea floor. Nature, 368, 841-844.

Saemundsson, 1986. Subaerial volcanism in the western North Atlantic. In: Vogt, P.R. and Tucholke, B.E. (eds) The Geology of North America, The Western Atlantic Region, Geological Society of America, Boulder, CO, p. 69-86.

Salisbury, M.H., 1983. Basement logs from the mouth of the Gulf of California, Deep Sea Drilling Project Leg 65. Init. Repts. DSDP, 65: Washington (U.S. Govt. Printing Office), 329-342.

Saunders, A.D., 1983. Geochemistry of basalts recovered from the Gulf of California during Leg 65 of the Deep Sea Drilling Project. Init. Repts. DSDP, 65: Washington (U.S. Govt. Printing Office), 591-622.

Scheirer, D.S. and Macdonald, K.C., 1993. Variation in cross-sectional area of the axial ridge along the East Pacific Rise: evidence for the magmatic budget of a fast spreading center. J. Geophys. Res., 98, 7871-7885.

Schmincke, H.-U. and Bednarz, U., 1990. Pillow, sheet flow and breccia flow volcanoes and volcano-tectonic hydrothermal cycles in the Extrusive Series of the northeastern Troodos ophiolite (Cyprus). p. 185-206. In: Malpas, J., Moores, E.M., Panayiotou, A. and Xenophontos, C. (eds), Ophiolites - Oceanic Crustal Analogues: Proceedings of the Symposium "Troodos 1987". Geological Survey Department, Cyprus, 733pp.

Schmincke, H.-U., Rautenschlein, M., Robinson, P.T. and Mehegan, J.M., 1983. Troodos extrusive series of Cyprus: A comparison with oceanic crust. Geology, 11, 405-409.

Schouten, H., Klitgord, Dick, H.J.B. and Klitgord, K.D., 1987. Migration of mid-ocean ridge volcanic segments. Nature, 326, 835-839.

Scott, D.R. and Stevenson, D.J., 1989. A self-consistent model of melting, magma migration and buoyancy-driven circulation beneath mid-ocean ridges. J. Geophys. Res., 94, 2973-2988.

Searle, R.C., 1989. Location and Segmentation of the Cocos-Nazca Spreading center West of 95°W. Mar. Geophys. Res., 11, 15-26.

Sempéré, J.-C. and Macdonald, K.C., 1987. Marine teconics: Processes at Mid-Ocean Ridges. Rev. Geophys., 25, 1313-1347.

Sempéré, J.-C., West, B.P. and Géli, L., 1996. The Southeast Indian Ridge between 127° and 132°40'E: contrasts in segmentation characteristics and implications for

crustal accretion. In: MacLeod, C.J., Tyler, P.A. and Walker, C.L. (eds), Tectonic, Magmatic, Hydrothermal and Biological Segmentation of Mid-Ocean Ridges. Geol. Soc. Spec. Publ., 118, 1-15.

Shipboard Scientific Party, 1988. Site 504. Proc. Ocean Drill. Prog., Init. Rep., Part A, 111, Ocean Drilling Prog., College Station, TX, 35-186.

Shipboard Scientific Party, 1992. Site 504. In: Dick, H.J.B., Erzinger, J., Stokking, L.B., et al., 1992. Proc. ODP, Init. Repts., 140: College Station, TX (Ocean Drilling Program), 37-200.

Shippert, P., Bradshaw, G. and Willis, S., 1990. Washington Image and Spectral Package (WISP) Preliminary Documentation. Unpubl.

Sinton, J.M. and Detrick, R.S., 1992. Mid-Ocean Ridge Magma Chambers. J. Geophys. Res., 97, 197-224.

Sinton, J.M., Wilson, D.S., Christie, D.M., Hey, R.N. and Delaney, J.R., 1983. Petrologic consequences of rift propagation on oceanic spreading ridges. Earth Planet. Sci. Lett., 62, 193-207.

Sinton, J.M., Smagiik, S.M., Mahoney, J.J. and Macdonald, K.C., 1991. Magmatic processes at superfast spreading mid-ocean ridges: glass compositional variations along the East Pacific Rise 13°-23° S. J. Geophys. Res., 96, 6133-6155.

Sleep, N.H., 1984. Tapping of Magmas from Ubiquitous Mantle Heterogeneities: An Alternative to Mantle Plumes? J. Geophys. Res., 89, 10029-10041.

Smith, M.C., Perfit, M.R. and Jonasson, I.R., 1994. Petrology and geochemistry of basalts from the southern Juan de Fuca Ridge: Controls on the spatial and temporal evolution of MORB. J. Geophys. Res., 99, 4787-4812.

Sparks, J.W., 1995. Geochemistry of the lower sheeted dike complex, Hole 504B, Leg 140. Proc. ODP, Sci. Results, 137/140, 81-97.

Spence, W., 1989. Stress origins and earthquake potentials in Cascadias. J. Geophys. Res., 94, 3076-3088.

Spiegelman, M., 1996. Geochemical consequences of melt transport in 2-D: the sensitivity of trace elements to mantle dynamics. Earth Planet. Sci. Lett., 139, 115-32.

Spiegelman, M. and Kenyon, P., 1992. The requirements for chemical disequilibrium during magma migration. Earth Planet. Sci. Lett., 109, 611-620.

Stakes, D.S., Shervais, J.W. and Hopson, C.A., 1984. The volcanic-tectonic cycle of the FAMOUS and AMAR valleys, Mid-Atlantic ridge (36°47'N): evidence from basalt glass and phenocryst compositional variations for a steady state magma chamber beneath the valley midsections, AMAR 3. J. Geophys. Res., 89, 6995-7028.

Stevenson, J.M., Hildebrand, J.A., Zumberge, M.A. and Fox, C.G., 1994. An ocean-bottom gravity survey of the Southern Juan de Fuca Ridge. J. Geophys. Res., 99, 4875-4888.

Su, W., Mutter, C.Z., Mutter, J.C. and Buck, W.R., 1994. Some theoretical predictions on the relationships among spreading rate, mantle temperature, and crustal thickness. J. Geophys. Res., 99, 3215-3227.

Sun, S.-S. and McDonough, W.F., 1989. Chemical and isotopic systematics of oceanic basalts: implications for mantle compositions and processes. In: Saunders, A.D. and Norry, M.J. (eds), Magmatism in the Ocean Basins. Geol. Soc. Spec. Publ., 42, 313-345.

Sun, S.-S., Nesbitt, R.W. and Sharaskin, A.Y., 1979. Geochemical characteristics of mid-ocean ridge basalts. Earth Planet. Sci. Lett., 44, 119-138.

Tagore, Rabindranath, 1917. Gitanjali (Song Offerings). The MacMillan Company, New York, 101p.

Thompson, G., 1991. Metamorphic and hydrothermal processes: basalt-seawater interactions. In: Floyd, P.A. (ed), Oceanic Basalts. Blackie, Glasgow, 148-173.

Thompson, G., Bryan, W.B., Frey, F.A., Dickey, J.S. and Suen, C.J., 1976. Petrology and geochemistry of basalts from DSDP Leg 34, Nazca Plate. Init. Repts. DSDP, 34, 215-235.

Thompson, G., Bryan, W.B., Ballard, R., Hamuro, K. and Melson, W.G., 1985. Axial processes along a segment of the East Pacific Rise, 10°-12°N. Nature, 318, 429-433.

Thy, P., 1989. Phase equilibrium constraints on the evolution of transitional and mildly alkalic Fe-Ti basalts in the rift zones of Iceland. In: Sinton, J.M. (ed), Evolution of Mid Ocean Ridges. Geophys. Monog. 57, IUGG Vol. 8, 39-51.

Tivey, M.A., 1994. Fine-scale magnetic anomaly field over the southern Juan de Fuca Ridge: Axial magnetization low and implications for crustal structure. J. Geophys. Res., 99, 4833-4855.

Tivey, M.A., 1996. Vertical magnetic structure of ocean crust determined from near-bottom magnetic field measurements. J. Geophys. Res., 101, 20275-20296.

Tobin, D.G. and Sykes, L.R., 1968. Seismicity and Tectonics of the Northeast Pacific Ocean. J. Geophys. Res., 73, 3821-3845.

U. S. Geological Survey Juan de Fuca Study Group, 1986. Submarine fissure eruptions and hydrothermal vents on the southern Juan de Fuca Ridge: Preliminary observations from the submersible Alvin. Geology, 14, 823-827.

Vera, E.E. and Diebold, J.B., 1994. Seismic imaging of oceanic layer 2A between 9°30'N and 10°N on the East Pacific Rise from two-ship wide-aperture profiles. J. Geophys. Res., 99, 3031-3041.

Verosub, K.L. and Moores, E.M., 1981. Tectonic rotations in extensional regimes and their palaeomagnetic consequences for oceanic basalts. J. Geophys. Res., 86, 6335-6350.

Vine, F.J., 1966. Spreading of the ocean floor: New evidence. Science, 154, 1405-1415.

Vine, F.J. and Smith, G.C., 1990. Structure and physical properties of the Troodos crustal section at ICRDG drillholes CY1, 1a and 4. p113-124. In: Malpas, J., Moores, E.M., Panayiotou, A. and Xenophontos, C. (eds), Ophiolites - Oceanic Crustal Analogues: Proceedings of the Symposium "Troodos 1987". Geological Survey Department, Cyprus, 733pp.

Vogt, P.R. and Byerly, G.R., 1976. Magnetic anomalies and basalt composition in the Juan de Fuca - Gorda Ridge area. Earth Planet. Sci. Lett., 33, 185-207.

Walker, G.P.L., 1988. Three Hawaiian calderas: An origin through loading by shallow intrusions? J. Geophys. Res., 93, 14773-14784.

Walker, G.P.L., 1992a. Morphometric study of pillow-size spectrum among pillow lavas. Bull. Volc., 52, 459-474.

Walker, G.P.L., 1992b. "Coherent intrusion complexes" in large basaltic volcanoes - a new structural model. J. Volc. Geotherm. Res., 50, 41-54.

Wang, X. and Cochran, J.R., 1995. Along-axis gravity gradients at mid-ocean ridges: Implications for mantle flow and axial morphology. Geology, 23(1), 29-32.

Whipple, K.X. and Naidoo, D.D., 1991. Mass wasting processes in the transform fault environment. Eos Trans. Am. Geophys. Un., 72, 519.

White, D.J. and Clowes, R.M., 1990. Shallow crustal structure beneath the Juan de Fuca Ridge from 2-D seismic refraction tomography. Geophys. J. Int., 100, 349-367.

White, D.J. and Clowes, R.M., 1994. Seismic attenuation structure beneath the Juan de Fuca Ridge from tomographic inversion of amplitudes. J. Geophys. Res., 99, 3043-3056.

White, R.S. and Williams, C.A., 1986. Oceanic fracture zones. J. Geol. Soc. Lond., 143, 737-741.

Whitehead, J. A., Dick, H.J.B. and Schouten, H., 1984. A mechanism for magmatic accretion under spreading centers. Nature, 312, 146-148.

Wilkinson, J.F.G., 1982. The genesis of Mid-Ocean Ridge Basalt. Earth Sci. Rev., 18, 1-57.

Wilson, D.S., 1988. Tectonic History of the Juan de Fuca Ridge Over the Last 40 Million Years. J. Geophys. Res., 93, 11863-11876.

Wilson, D.S. and Hey, R.N., 1995. History of rift propagation and magnetization intensity for the Cocos-Nazca spreading center. J. Geophys. Res., 100, 10041-10056.

Wilson, D.S., Hey, R.N. and Nishimura, C., 1984. Propagation as a mechanism of reorientation of the Juan de Fuca ridge. J. Geophys. Res., 89, 9215-9225.

Wilson, M.B., 1989. Igneous petrogenesis. Unwin Hyman, London/Boston, 466pp.

APPENDIX A: DATA SETS AND METHODS FOR THEIR INTEGRATION

The geologic map compiled for the study area on the north Blanco scarp is based on twelve data sets that were collected during four separate field programs in the WBD area over a span of about a decade:

a) NOAA survey in 1981-83 under Loran-C navigational control (Embley and Wilson, 1992)

i) Sea Beam data of the Blanco fracture zone (Figure 3-1);

b) CREST operation (Chief scientist: D. Yoerger of the Deep Submergence Laboratory (DSL) at Woods Hole Oceanographic Institute) in June-July 1991 aboard the *RV Laney Chouest* with access to an undistorted version of the Global Position System (GPS)

i) Sea Beam data of the study area on the north wall of the West Blanco Depression (Figure 4-1b) - a comparison to (a)(i) indicates no major changes in cliff topography over the past decade;

c) Blancotrough (BT) cruise (Chief Scientist: J. R. Delaney from the University of Washington (UW) and F. N. Spiess from Scripps Institute of Oceanography (SIO) in July 1987 aboard the *RV Melville* and conducted primarily under Loran-C but also GPS when available (Delaney et al., 1987)

i) slope profiles using the down-looking sounder in conjunction with a precision pressure gauge that was calibrated against the 23 kHz, 25° broad-beam, upward directed sounder sonars on Deep Tow;

ii) seismic profiles using the 4 kHz sonar on Deep Tow;

iii) up- and down-looking, high resolution sonar imagery using 110 kHz transducers on Deep Tow (Figures 4a and 4b);

iv) 2000 black-and-white stereo pairs and 1400 color photographs taken by the three cameras and strobe on Deep Tow; and

v) 8 dredges located by ship's position at roughly five-minute intervals; 85 representative samples were examined petrographically and labelled by rock type (See Plate A-1) and percent volume of each haul.

		D	R	E	D	G	E		#
	Dredge Number	8	7	6	12	5	4	11	3
	Sector (see Chapter VI)	W	C/CW	C	C	CE	CE	E	E
	Zone - upper or lower	upper	upper	upper	lower	upper	upper	lower	upper
	Start of dredge	44° 23.10' 130° 03.58'	44° 22.85' 130° 01.77'	44· 22.17' 129° 59.55'	44° 21.99' 129° 59.42'	44° 21.63' 129° 58.32'	44° 21.53' 129° 56.52'	44° 20.85' 129° 56.35'	44° 20.69' 129° 54.65'
	End of dredge	44° 24.13' 130° 03.84'	44° 23.33 130° 02.38'	44° 22.77' 129° 59.72'	44° 21.89' 130° 00.48'	44° 22.49' 129° 57.95'	44° 22.06' 129° 56.83'	44° 21.09' 129° 57.47'	44° 21.41' 129° 54.50
	Distance from axis (km)	33.5	35.9	39.4	39.0	41.5	43.7	43.4	46.8
	Depth interval (km)	3523-3580	2984-3878	2390-3455	3827-3975	2336-3681	2460-3262	3815-4032	2974-3600
*	Vertical distance by rank	1	6	7	2	8	5	3	4
*	Traverse distance by rank	4	8	3	6	5	2	1	7
*	Rock abundance by rank	7	1	1	5	4	-	1	6
R	Sediment							5	
O	Glassy basalt					30	77	45	99
C	Crystalline basalt	10		20	50		33	45	
K	Veined basalt		99		10	20		2	
T	Diabase			20	6	30			
Y	Veined diabase				20				
P	Volcaniclastic breccia	90			30				1
E(%)	Hyaloclastite products		1	60		20		3	

Table A-1: Summary of Blancotrough dredges within study site

* 1 represents the shortest upslope or lateral distance amongst the eight dredges or the least material recovered in any of the hauls

d) Blanconaute (BN) mission (Chief Scientist: Th. Juteau of the Université de Bretagne Occidentale) in July-August 1991 aboard the *RV Nadir* and conducted under GPS. The fourteen track lines shown in Figure 4-2 were obtained by editing (eliminating points based on velocity jumps as well as comparison to the in-hull Doppler navigation) the acoustic navigation (the ship's fixes on the submersible) collected in Universal Transverse Mercator (UTM) coordinates.

i) slope profiles of each *Nautile* dive track;

ii) scientific observer's reports of each of 14 dives in the study area;

iii) color photographs totaling 3725 in number that were taken from either of the narrow- or wide-angle cameras during the 14 dives;

iv) color video recordings of the 14 dives providing a total of 70.57 hours of on-bottom time (each dive ranging from 3.2 hours to 5.95 hours, and averaging 5.04±0.71 hours); and

v) 143 rocks (5 to 20 samples per dive and averaging 11).

The particular approach of this study relies on about 10 meter scale accuracy. Therefore, it is imperative to check for possible shifts in the coordinate systems of the different data sets and to find methods for translating them into one standard framework. Here, two methods are evaluated. Method I is based on an internal reference in the form of a transponder that is left in place and re-surveyed during subsequent field programs in the area to determine the relative shifts between data sets. Method II works by comparing data sets to a single referential to arrive at a geologically reasonable fit. The referential chosen for both these methods is that of Program (b). The shifts estimated according to the two methods are given in Table A-2.

Method I

Method I is based on the assumptions that a transponder left behind on the seafloor will remain in-place over the time period between cruises and that the position of the transponder can be measured with equal accuracy by various survey teams. If this is the case, then a difference in the values obtained may be attributed to a change in reference frame. The method was not applied until Program (c) however, and so the relation of Program (a) data cannot be determined.

In Program (c), an SIO transponder was surveyed in position at 44° 20.9' N, 129° 59.4' W by the Deep Tow group. This spot is in grid-square c-6 marked in Figure 4-2. In Program (b), its location was reckoned to be 44° 20.6521' N, 129° 59.3243' W and at 4704.7 m depth by the DSL group. This implies that the coordinate system in Program (c) data must be shifted 450 m north and 100 m west.

In Program (d), the SIO transponder could not be interrogated and instead two of the DSL transponders from Program (b) were resurveyed. The one transponder was measured to be 26 m north and 12 m west of its given position while the other transponder was measured to be 46 m south and 37 m east of its given position. This would imply that there is no systematic shift in the coordinate grid of Program (d) data sets, and any difference at all is less than 50 m.

Method II

A comparison of Program (a) with Program (b) Sea Beam data shows no major changes in topography bar minor differences in contouring. However, the major exception is that the latitudinal coordinates of the NOAA map need to be shifted about 200 m south.

For Program (c), the bathymetric data obtained in topographic profiling can be used in conjunction with several distinctive features on the sonar mosaics to assess the relation to the Program (b) Sea Beam data. In the north-south direction, the edge between the seafloor plateau and the steep scarp must match on the sonar mosaics and the Sea Beam map. Also, the base of the cliff is known to be at 4200 m in the west-central part and 4300 m in the east-central part of the study site. In the east-west direction, the bathymetric contours have to follow the protuberances of outcrop in the upper zone of the face e.g.. the distinct convex curvature that was imaged in grid squares f-8 and f-9 or the smaller feature in grid square d-12. Based on the correspondence in expression of such features in the imagery and bathymetry data sets, it can be ascertained that the Program (b) coordinate system needs to be shifted about 100 m south and 480 m east.

Program (d) verifies the depths at which unique features were observed or samples were taken along the dive tracks against the Program (b) Sea Beam data. The north-south shift can again be estimated from the well marked base and top of the outcrop cliff. The former is reached between 4200 m (BN-24-01) to 4230 m (BN-02-01, BN-03-02, BN-23-03) in the west-central part and 4300 m (BN-05-01) in the east-central part. Likewise, the lowermost outcrop in the eastern part was sampled at 3820 m (BN-08-02). The east-west shift is less easily constrained directly against the Sea Beam map. For this reason, it may be preferable to overlay the Program (d) information on the Program (c) sonar imagery before interfacing it with the Program (b) bathymetry. On this basis, the Program (d) coordinate system needs to be shifted about 370 m south and 660 m east.

Evaluating Methods I and II

Methods I and II ought to provide independent but equivalent estimates of the relative shifts between data sets. Method I would certainly be the more preferred of the two since it requires a quantifiable shift that can be routinely measured. One drawback of this method though is that it has to be instituted at the very beginning of a long-term field study. Method II, by contrast, is relatively subjective but still provides geologically convincing motivations. It also has the advantage of being able to mesh all the existing data sets in hindsight.

Table A-2 lists the shifts estimated by the two methods. As can be seen, the shifts differ in both magnitude and sense of direction. One explanation for this might be that the SIO transponder has moved over the four year time period which should not be unexpected given its location on the actively mass wasting debris slope. Therefore in the WBD study, the shifts obtained by Method II have been applied to the data sets.

Shift relative to Program (b) coordinate system of the data from -				
		Program (a)	**Program (c)**	**Program (d)**
Method I				
	Latitude	-	450 m north	0-50 m
	Longitude	-	100 m west	0-50 m
Method II				
	Latitude	200 m south	100 m south	370 m south
	Longitude	0 m	480 m east	660 m east

Table A-2:

Plate A-1: Photomicrographs of representative rock types from the Blancotrough dredges. The field of view in each case is 3.3 mm. (Courtesy of V. Robigou)

(a) Glassy basalt (BT-1-5) with discrete laths of plagioclase, and glomerocrysts of plagioclase, olivine and minor pyroxene minerals

(b) Hypocrystalline basalt (BT-9-4) with plagioclase, pyroxene and minor olivine phenocrysts

(c) Vein of quartz and epidote cross-cutting glassy, porphyritic basalt (BT-12-1) with crystals of plagioclas

(d) Diabase (BT-1-3) with plagioclase, pyroxene and oxides is pervasively altered by chlorite and cross-cut by a quartz vein

(e) Volcanic breccia (BT-12-2) with clasts of plagioclase and amphibole in an altered, very fine-grained matrix

(f) Angular fragments of hyaloclastite in a matrix (BT-2-5) of fine-grained clays

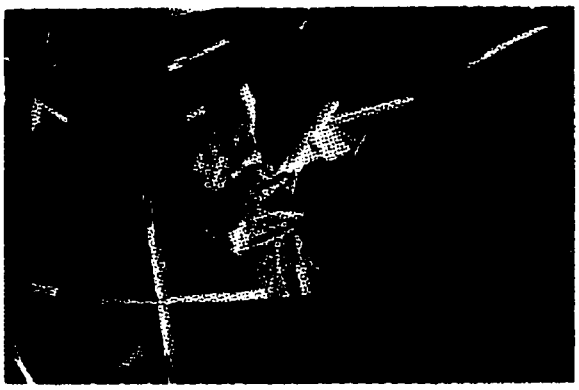

(a)

(b)

(c)

(d)

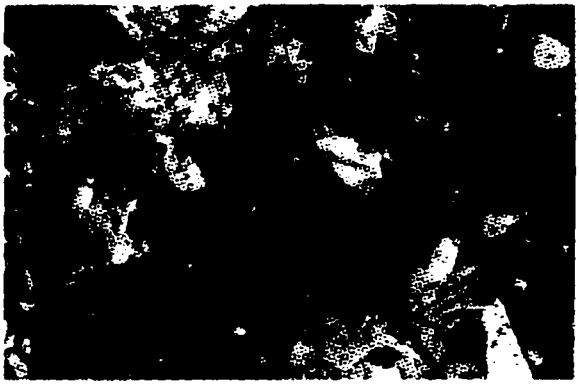

(e)

(f)

Plate A-1

APPENDIX B: CLASSIFICATION SYSTEM FOR COMPILING OBSERVATIONS FROM THE PHOTOGRAPHS AND VIDEOS OF EACH *NAUTILE* DIVE

The nomenclature introduced for compiling observations along each *Nautile* dive is grouped into five major categories. Within each class, the descriptive terms are generally self-explanatory or of common geological usage. Here, a brief summary is provided for each label.

A. Original flow morphologies (Legend a): The 11 types are discussed extensively in the text.

B. Unrecognizable flow morphologies (Legend b)

1. Smoothed outcrop: This outcrop generally occurs on a semi-vertical face which is interpreted to be a fault plane with its smoothed appearance resulting from shear movement.
2. Fractured outcrop: This outcrop shows a series of parallel fractures
3. Diced outcrop: This outcrop has the appearance of roof-tiles and is interpreted to result from intense parallel fracturing of a thin layered unit that could give rise to an intersecting set of cleavages.
4. Tectonized outcrop: This outcrop is brecciated in appearance.
5. Altered outcrop: This outcrop stands out by its white color that is clearly the result of alteration since the rock is friable.
6. Sedimented outcrop: The degree of sediment cover on this outcrop obstructs identification of the underlying flow form

C. Outcrop features (Legend a)

1. Lobate outcrop: Broad lobate front of a flow.
2. Vein: Thin, commonly white or blue in color, and cross-cutting the outcrop. Occurs in a dense net in places
3. Oxidation trace: Orange-yellow staining
4. Gouge: Deep cove within the face which creates an overhang
5. Overhang: Part of the cliff projecting outwards
6. Ledge: May also be referred to as a step or bench in the face. Not of significant width. May have accumulation of mass wasting material.
7. Crest: Extend outwards as narrow, protruding ribs from the face

D. Structurally related features (Legend b)

1. Striation: Occur on semi-vertical faces and highlight these as fault planes. Both horizontal and vertical striations were observed indicating that there had been motion along transverse and normal faults.
2. Fracture: By geological definition.
3. Fault: By geological definition.
4. Slide block: Large block of outcrop on the face which is most likely out of place.

E. Mass wasting forms (Legend b)

1. Flagstone block: Huge slabs of rock at the base of the cliff
2. Talus: Extensive collection of fallen blocks at base of outcrop
3. Rubble: Loose, angular blocks on sediment
4. Sediment: Sediment that occurs on the plateau and scarp differ with the former being layered and indurated.
5. Chute: Marking the presence of narrow debris slides or grain flow deposits

In order to portray these descriptions graphically, each term is represented by a symbol given in the legends (a and b) following. The 13 lithological profiles, Figures B-1 to B-13, are contained in the Pocket.

LEGEND (a)

Original flow morphologies


Bulbous pillow lavas


Pillow basalt lavas

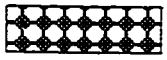
Basalt blocks - disrupted flow


Coarse blocky basalt/jumbled sheet flow


Fine blocky basalt / jumbled sheet flow


Thin-sheeted / thin sheet flow


Thick slabs


Thickly-layered/thick sheet flow or sill

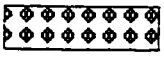
Jointed-massive / diabase intrusive

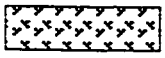
Dike

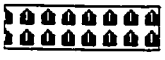
Spire structure / basalt lava pillar

Outcrop characteristics


Lobate outcrop


Vein


Oxidation trace

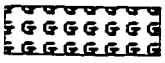
Gouge


Overhang


Ledge

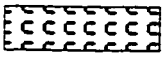
Crest

L E G E N D (b)

Unrecognisable flow morphologies


Smoothed outcrop


Fractured outcrop


Diced outcrop


Tectonized outcrop


Altered outcrop


Sedimented outcrop

Structurally related features


Striation - vertical or horizontal


Fracture


Fault

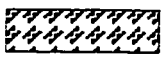
Fissure


Slide block

Mass wasting forms


Huge flagstones


Talus field


Rubble blocks

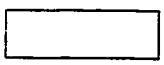
Sediment

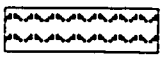
Debris chute

APPENDIX C: Labelled domains defined geologically from dive data.

The dives are indicated by number (BN) and the depth interval (DEPTH INT.) over which the domain was traversed.

The rock samples retrieved are identified by number (RX), depth location (RX. HT.) and given a brief petrographic description recording:

(a) grain size, -

Gl = glassy (45% hypohyaline - 100% hyaline)
V. fg = Very fine-grained (<0.25 mm)
Fg = fine grained (0.25 - 1.5 mm)
Mg = medium grained (1.5-3 mm)
Cg = coarse grained (3-5 mm)

(b) the degree of crystallisation, -

ap = aphyric i.e. 0-1%
sp = sparsely phyric i.e. 1 - 10 %
mp = moderately phyric i.e. 10 - 25 %
hp = highly phyric i.e. >25 %
xeno = xenocryst/megacryst
pheno = phenocryst

(c) the phenocrysts present, -

p = plagioclase
c = clinopyroxene
o = olivine

(d) the rock type -

Brx = breccia
B or MB = basalt or metamorphosed basalt
Sed = sediment
D or MD = diabase or metamorphosed diabase

Descriptions of the exposure are provided both from scientific observers' notes in their dive reports as well as my own observations from the photographs and video. The latter is more detailed but the basic observations are replicated, albeit in slightly differing terminology, in both accounts as shown in the last two columns.

Other abbreviation: oc = outcrop
Plat = plateau

UNIT	BN	DEPTH INT. (m)	RX	RX. HT.	PETRO-GRAPHY	DIVE DESCRIPTION	CAMERA-VIDEO DESCRIPTION
Plat	1	<2295	5	2294	Indurated sediment	Semi-indurated sediment blanket	Indurated sediment on plateau
Plat	1	<2295	6	2336	Flow breccia	Lava mound	Basalt fields on sediment
Plat	4	<2230	14	2289	Fg, hp, pco B	Pillows	Tumuli with rubble on sediment
Plat	6	<2302	14	2627	V. fg, sp, pc B	Pillows	Blocky field with tumulus and pillow
Plat	12	2189-2088	1	2189	Fg, hp, pc B	Pillows	Lava fields with flows of various forms and intervening sediment
			2	2088	Fg, mp, pc B		
Plat	24	<2110	14	2594	Mg, sp, pc B	Pillows	Bulbous blobs amidst rubble on sediment floor -> talus -> tube flows
A6	7	>4610				Sediment with huge blocks	Sediment littered with large blocks -> talus
A6	9	>4560	1	4641	Gl, mp, op B	Sediment with fault scarps	Sediment with steps of diced (#1) or tectonised (#2) oc
			2	4570	Sediment		
A5	7	4580-4610				Secondary slump with talus at foot of brecciated oc	Altered and tectonised oc

UNIT	BN	DEPTH INT. (m)	RX	RX. HT.	PETRO-GRAPHY	DIVE DESCRIPTION	CAMERA-VIDEO DESCRIPTION
A5	9	4310-4560	3	4390	Fg, mp, op B	Fractured pillows and lava flows	Sediment with oc step and littered with rubble -> sediment -> sediment with talus and scattered rubble -> thickly-layered oc
A5/A4	9	4180-4310	4	4210	MB	2 steps separated by bench; 20m relief; cut through intensely brecciated and altered rock	Thin-sheeted oc -> diced oc (#4)
A4	8	4200-4380				Fine sediment with scarce blocks	Sediment with occasional clusters of large blocks and tectonic-related features
A4	9	3945-4180	5	4211	Crystalline B	Sediment with rubble and maybe fractured lava flow rills	Sediment with intervals of scattered rubble and at least 3 oc ledges (#5&6)
			6	4035	Crystalline, phyric B		
B6	3	3660-3760	7	3715	Mg, sp, pc B	Veined and brecciated diabase	Blocky oc (#7) -> thin-sheeted
		3290-3410	11	3300	V. fg, mp, pc mB	Flows with pinnacle	Blocky oc -> spire -> finely-blocky oc -> blocky oc
B5	4	3055-3180	4	3125	Fg B	Dykes -> massive oc -> jointed oc -> pinnacle	Thickly-layered oc with spires -> blocky oc with dykes (#4-6) -> thickly-layered oc with spires (#7)
			5	3118	Fg, sp, p B		
			6	3119	B		
			7	3089	V. fg, mp, pc B		
B4	4	2910-3055	8	2956	B brx	Massive -> talus -> blocky -> altered oc+talus -> massive -> altered oc+talus -> jointed oc	Jointed oc fractured at base -> brief intervals of blocky oc on crests (#8) with intervening sediment and talus
B3	4	2495-2750	9	2745	Cg, hp, pco B	Pillows->lobate+talus->blocky->massive->smooth->finely-blocky->smooth->blocky with pillows	Blocky oc with dykes; also gouges toward base, with crests toward top
			10	2552	Fg, ap B		
B2	4	2310-2495	11	2396	Fg, mp, pco B	Blocky oc with pillows at base	Pillow oc -> 4 alternations of blocky oc (#11) with basalt block parts (includes spires)
B1	4	2230-2310	12	2289	V. fg, hp, pco B	Pillows in blocky oc	Pillows
			13	2288	Fg, hp, pco B		
B1	24	2110-2170				Pillows	Pillows toward top of blocky oc
D5	3	4090-4250	3	4160	MB	Diabase with veins and steps	Finely-jointed oc with altered parts
			4	4152	MB brx		
D4	3	3760-4090	5	3978	Fg, ap D	Veined diabase	Altered & tectonised -> jointed (#5) thickly-layered oc alternating with sediment (#6)
			6	3767	Cg, ap D		

UNIT	BN	DEPTH INT. (m)	RX	RX. HT.	PETRO-GRAPHY	DIVE DESCRIPTION	CAMERA-VIDEO DESCRIPTION
D3	23	4060-4150	3	4144	Fg, sp, p B	Veined and tectonised massive diabase (#3&4) -> dykes -> jointed oc	Thickly-layered oc with dykes -> jointed oc -> thickly-layered oc (#5&6) with dykes and spires
			4	4143	Phyric MB		
			5	4077	Mg, ap D		
			6	4078	Fg MB		
D2-S	23	3925-4060				Jointed oc alternating with talus	Fractured oc -> sediment with rubble -> tectonised and altered oc -> thickly-layered oc on crest -> sediment with rubble -> talus -> blocky oc slide block -> sediment with rubble
D1-S	3	3570-3660	8	3604	MB		Thickly-layered -> thin-sheeted (#8) -> thickly-layered -> blocky -> thin-sheeted
D1-S	4	3650-3740	1	3738	Mg, sp, p B	Dark and massive oc with veins	Tectonised and fractured oc -> thickly-layered oc -> blocky oc -> thickly-layered oc on crest
			2	3726	Cg D		
D1-N	3	3410-3570	9	3506	MB	Altered oc with talus -> pillows	Thickly-layered oc alternating with sediment
			10	3465	Mg, ap D		
D1-N	4	3180-3650	3	3280	Cg B	Pillows->smoothed face->talus->massive with ledges->pillows on crest->jointed->dark oc->pillows->jointed->massive->blocky->massive with pinnacles	Jointed oc with ledges -> pillow oc below fissure -> thickly-layered oc with increasing sediment toward top
E10	5	3100-3500	9	3464	Fg, hp, pc B	Highly fractured lava flows with vertical striations	Brief oc intervals alternating with sediment: blocky (#9) -> thin-sheeted -> plated; lobated bases to thickly-layered (#10) -> blocky -> plated oc
			10	3279	Mg, sp, p B		
E10	6	3160-3470	6	3453	Gl/Fg, hp, pco B	Highly fractured lavas with two intervals of pillows	Basalt block oc (#6) -> sediment with scattered rubble -> 3 intervals of plated oc with lobated bases
E9-S	5	3040-3100	11	3045	Fg, B brx	Lava flows	Basalt block -> blocky -> thickly-layered -> blocky -> thin-sheeted -> thickly-layered
E9-S	6	2975-3160	7	3062	Gl/Fg, hp, pco B	Pillows on series of cliffs	Fractured oc -> alternations of diced (#7) and thickly-layered oc
E9-N	6	2830-2975	8	2972	Fg, sp, p B	Pillow->dyke->pillow->dyke->pillow->pinnacle	Blocky oc (#8) with sediment -> talus -> blocky -> spire (#9&10)
			9	2838	Glassy, phyric, pc B brx		
			10	2839	V. fg, mp, pc B		

UNIT	BN	DEPTH INT. (m)	RX	RX. HT.	PETRO-GRAPHY	DIVE DESCRIPTION	CAMERA-VIDEO DESCRIPTION
E8	6	2645-2830	11	2729	V. fg, sp, pco B	Pillows with two intervals of dykes below pinnacles	Fractured, thickly-layered oc with spires at two intervals -> pillow oc
E7	6	2450-2645	12	2627	Gl/v. fg, hp, pco B	Pillows with a dyke toward base	Blocky oc with spires at top -> pillow oc -> blocky oc with dykes at top -> pillow oc
E5	6	2302-2450	13	2407	Gl/fg, mp, pc B	Pillows	4 successions of blocky oc, sometimes basalt block parts, topped by pillow oc
E4	2	3465-3635	9 10 11	3626 3601 3491	Mg, sp, po B Fg, sp, p B Gl/fg, mp, pc B	Diabase -> fault -> diabase -> fault -> rubble and sediemt -> fault	Diced -> pillows (#9) -> thickly-layered -> dykes (#10) -> diced -> thin-sheeted -> blocky crest -> plated -> thin-sheeted crest -> diced (#11) -> thickly-layered -> thin-sheeted oc -> blocky crest
E3	2	3250-3465	12 13	3409 3277	Fg, ap B Sediment	Basaltic lava -> indurated sediment	Sediment with rubble -> thickly-layered (#12) oc -> plated oc -> sediment with rubble -> smoothed (#13) oc
E3-NW	4	2750-2910				Well-sedimented blocky oc and boulders	Blocky oc ledges in sediment scattered with rubble and large blocks
F5	6	3620-3815	3	3744	Mg, ap D	Talus -> altered diabase -> dykes -> talus/rubble/sediment	Talus -> jointed oc (#3) with dykes -> no obs.
F4	2	3635-3800	8	3760	Mg, ap D	Diabase -> fault	3 successions of thin-sheeted oc with thickly-layered oc (lowermost with dykes #8); ends on bench
F4	23	3660-3740	9	3739	Gl-fg, hp, pc B	Blocky and jointed oc	2 successions of blocky/thin-sheeted -> jointed/thin-sheeted -> thickly-layered oc
F4-E /F3	23	3615-3670				Blocky oc with pillows has spires toward top	Blocky oc, largely tectonised, with crests -> pillow oc
F3	5	3500-3660	7	3644	Fg/mg D	Fractured and altered diabase with crests -> fractured lava flows	Two alternations of thin-sheeted oc with crests -> thickly-layered oc with ledges; thin-sheeted oc with lobated bases at top
F3	6	3470-3620	4 5	3553 3553	Gl, sp, pc B Crystalline B brx	Fractured pillows -> lava flows with altered part	3 oc intervals with crests and ledges: thickly-layered oc -> basalt blocks; tectonised oc (#4&5) -> oc below sediment
G8	5	4095-4310	1 2	4301 4302	V. fg MD Fg, sp, pc D	Diabase with flagstone scars (#1&2) overlain by fractured gabbro (#3&4)	Finely-jointed oc with ledges and brief intervals of thin-sheeted oc
G8	7	4090-4160	4	4126	Fg, sp, p D	Talus below jointed, massive oc	Talus (#4) -> sedimented oc

APPENDIX D: RELATION OF PETROGRAPHY TO LITHOLOGY FOR BLANCONAUTE SAMPLES

Petrographic characteristics are summarised here for the Blanconaute samples which are shown by a bracketed number (#). The abbreviations used are the same as in Appendix C. The petrographic type (see Appendix E) is in the square bracket alongside. The sample characteristics are listed by dive number (BN-) in the columns and by the lithomorphologic unit recovered in the rows. The order of the dives is given from west to east or by sectors: Sector CW = BN-13; Sector C = BN-12, -24, -03, -04, -23, and -02; Sector CE = BN-06, -05, -07, -10, and -01; and Sector E = BN-08 and -09. The tables are laid out according to zone from north to south.

Table D-1: Summary

	Type I - PC basalt	Type II - A diabase	Type III - PCO basalt	Type IV - A basalt	Type V - P basalt	Type VI - OP/PO basalt	Type VII - P diabase	Type VIII - PC diabase	Type IX - basalt breccia
Pillows	5		5			1			
Broken pillows			1						
Blocky	4		4	1	2				
Spires	2		1		1				1
Thin-sheeted	2								1
Diced	2	1	1						
Thickly-layered, massive	2	9		3	4		1		4
Brecciated/ Altered	4	1		3		2			3
Jointed,massive		5						1	
Dykes	2	2	1		1		1		1
Sedimented oc		2			1				
Rubble/Talus	6	3	1	4		1	2	1	7

Table D-2: Plateau

	BN-13	BN-12	BN-24	BN-03	BN-04	BN-23	BN-02
Pillows		Fg, hp, pc B (#1) [I] Fg, mp, pc B (#2) [I]	Mg, sp, pc B (#14) [I]		V.fg, hp, pco B (#14) [III]		

	BN-06	BN-05	BN-07	BN-10	BN-01	BN-08	BN-09
Pillows	Fg, sp, pc B (#14) [I]						
Lava mound					Flow breccia (#6)		
Sediment					Indurated sediment (#5)		

Table D-3: Upper part of basaltic zone

	BN-13	BN-24	BN-03	BN-04	BN-23	BN-02
Pillows				Fg, hp, pco B (#13) [III] V.fg, hp, pco B (#12) [III] V.fg, hp, pco B (#9) [III]		
Blocky			V.fg, mp, pc mB (#11) [I]	Fg, mp, pco B (#11) [III] Fg, ap B (#10) [IV] mB (#6) Fg, sp, p B (#5) [V]		
Sedimented outcrop		Cg, ap D (#12) [II] Fg, sp, p B (#11) [V]				
Brec./Alt.	Gl, mp, pc B (#15) [I]			B brx (#8) [IX]		
Dykes	mB (#14a) B brx (#14b) [IX]	Fg, sp, pc B (#13) [I]				
Spires				V.fg, mp, pc B (#7) [I] Fg B (#4) [V]		

	BN-06	BN-05	7	BN-10	BN-01	BN-08	9
Pillows	Gl/fg, mp, pc B (#13) [I]				Mg, mp, pco B + plag xeno + gl (#4) [III]		
Blocky	Gl/fg, hp, pco B (#12) [III] Fg, sp, p B (#8) [V]	Fg, hp, pc B (#9) [I]		Fg, sp, pco B + gl (#20) [III] Fg, mp, pc B (#15) [I] Fg B (#17) V.fg, sp, pc B + gl (#18) [I]	Mg, hp, pco+plag xeno B (#2) [III]		
Thickly -layered		Fg, B brx (#11) [IX] Mg, sp, p B (#10) [V]		Fg, ap, p xeno D (#19) [II] V. fg D (#16) [II]			
Diced	Gl/fg, hp, pco B (#7) [III]						
Alt./				Fg B (#14)			
Dykes					Mg, mp, pco B (#3) [III]		
Spires	V.fg, sp, pco B (#11) [III] Gl, phyric, pc B brx (#9) [IX] V.fg, mp, pc B (#10) [I]						
Rubble						Fg, mp, pco B (#5) [III]	

Table D-4: Lower part of basaltic zone

	BN-13	BN-24	BN-03	BN-04	BN-23	BN-02
Pillows						Mg, sp, po B (#9) [VI]
Blocky			Mg, sp, pc B (#7) [I]			
Thickly-layered, massive	Fg, sp, p B (#13) [I] Fg, hp, pc B (#11) [I] Mg, ap B (#12) [IV] Fg, pc B brx (#7) [IX]		Mg, ap D (#10) [II]	Cg B (#3) [IV] Cg D (#2) [II] Mg, sp, p B (#1) [V]		Fg, ap B (#12) [IV]
Thin-sheeted		V.fg, sp, pc B (#6) [I]	mB brx (#8) [IX]			
Diced					V.fg, hp, pc B (#8) [I]	Gl, mp, pc B (#11) [I]
Brecciated/ Altered	B (#10) B brx (#9) [IX]		mB (#9)		Gl-fg, hp, pc B (#9) [I]	
Dykes		Fg, sp, p D (#7) [VII]				Fg, sp, p B (#10) [V] Mg, ap D (#8) [II]
Talus	V.fg, ap B (#8) [IV]	Fg, ap B (#10) [IV] V.fg, mp, pc B (#9) [I] V.fg, ap D (#8) [II]				

	BN-06	BN-05	BN-07	BN-10	BN-01	BN-08	-9
Broken basalt	Gl/fg, hp, pco B (#6) [III]						
Blocky				B brx (#3) [IX]		Fg, ap B (#4) [IV]	
Thick-layered		Mg, ap D (#6) [II]		Mg, sp, p B (#13) [V]			
Thin-sheeted	Gl, sp, pc B (#4) [I]						
Brecciated/ Altered			Gl/v.fg, mp, pc B (#7) [I] ap B + gl (#6) [IV]	B (#12) Mg, sp, pc B (#11) [I] mB (#9) mB (#8) Mg, ap D (#7) [II] Mg, sp, po B (#6) [VI] B (#5) Fg, ap mB (#4) [IV]	Phyric B (#1)		
Talus	B brx (#5) [IX]	Fg/mg D (#7 on crest)		Fg, ap B (#10) [IV] Mg, sp/x, p B brx (#2) [IX] Fg, sp, po B (#1) [VI]			

Table D-5: Lower diabasic zone

	BN-13	BN-24	BN-03	-4	BN-23	BN-02
Thickly-layered, massive	Fg, pc, mB brx (#7) [IX]	Fg, sp, p B (#3) [V]	Cg, ap D (#6) [II] Fg, ap D (#5) [II]		Cg, ap D (#7) [II] Mg, ap D (#5) [II] phyric mB (#4) [IX] Fg, sp, p D (#3) [VII]	
Jointed		Cg, ap D (#2) [II]	mD (#2)			Mg, ap D (#3) [II]
Brecciated/ Altered		V.fg, ap, p xeno, B (#4) [IV]	mB brx (#4) [IX] mB (#3)		Fg, mB (#6)	
Dykes		V.fg, hp, pc B (#5) [I]				F/mg, sp, p D (#7) [VII] Cg D (#6)
Talus	B brx (#6) [IX] Fg, mp, pc B (#5) [I] V.fg, mp, pc B (#4) [I] V.fg, sp, pc B (#3) [I] V.fg, ap, p xeno B (#2) [IV] Gl, ap B (#1) [I]	Volcanic brx (#1) [IX]	mB brx (#1) [IX]		Cg, mB brx (#2) [IX] mB brx (#1) [IX]	Fg, ap D (#5) [II] Mg, sp, cp D (#4) [VIII] mB (#2) Mg, ap D (#1) [II]

	BN-06	BN-05	BN-07	10	-1	BN-08	BN-09
Thickly-layered	Mg, ap D (#2) [II]						Crystalline, phyric B (#6) Fg, mp, op B (#3) [VI]
Jointed, massive	Mg, ap D (#1) [II] Mg, ap D (#3) [II]	Cg, ap D (#4) [II] D (#3)					
Thin-sheeted						mB (#3)	
Diced		Mg, ap D (#5) [II]					
Brecciated/ Altered		V. fg, mD (#1)	mB (#3 in L6)			Mg D (#2)	mB (#4) Crystalline B (#5) Gl, mp, op B (#1) [VI]
Sedimented outcrop		Mg, ap D (#4) [II]					Sediment (#2 in A6)
Talus		Fg, sp, pc D (#2) [VII]	Fg, sp, p D (#4) [VII]			Gl, mp, pc B (#1) [I]	

APPENDIX E: THIN SECTION DESCRIPTIONS OF BLANCONAUTE ROCKS

1. Rock samples

143 rocks were retrieved by sampling from the *Nautile* submersible in the WBD study site (Figure 5-1). A hand sample description of each by D. D. Naidoo and G. Manac'h is given in the Blanconaute report (unpubl.). Based on these descriptions, thin sections were made of 100 rocks which excluded 6 samples consisting of fragments (BN 1-01, 4-08, 8-02, 9-05, 10-09, 10-12), 9 samples with insufficient material (BN 2-06, 4-02, 5-07, 9-06, 10-05, 10-16, 10-17, 13-01, and 23-09), 11 breccia samples (BN 1-06, 3-01, 3-03, 3-04, 3-08, 5-11, 10-03, 13-06, 13-09, 13-14, and 23-01), and 17 samples that were extremely altered (BN 2-02, 3-09, 4-03, 4-04, 4-06, 7-01, 7-02, 7-03, 7-05, 7-06, 8-03, 9-04, 10-08, 10-14, 13-10, 23-04, and 23-06).

97 thin sections were studied under a petrographic microscope with the objective of identifying the phases, estimating their proportion in the assemblage, examining their textural relations, assessing the degree of alteration, and classifying the rock type. These descriptions are summarized by dive number in Section E-2 and detailed in Section E-3. Abbreviations include: P or plag = plagioclase, C or cpx = clinopyroxene, O or ol = olivine, chl = chlorite, epi = epidote, and alt = alteration. The definitions of grain size, degree of crystallization, and other abbreviations follow that in Appendix C. The alteration characteristics of these samples are given by Manac'h (dissertation in prep.).

2. Total samples per dive by petrographic characteristic

T-ype	Lithology	Phenonature	Granu-larity	1	2	3	4	5	6	7	8	9	10	12	13	23	24
III	Basalt	hp PCO	gl-mg	1			4		3								
III	Basalt	mp PCO	fg-mg	2			1				1						
III	Basalt	sp PCO	fg-mg						1				1				
I	Basalt	hp PC	gl-mg					1						1	1	2	1
I	Basalt	mp PC	gl-fg		1	1	1		2	1	1		1	1	3		1
I	Basalt	sp PC	gl-mg			1			2				2		2		3
VIb	Basalt	sp-mp OP	gl-mg				1	1				2	1				
VIa	Basalt	sp PO	fg-mg		1		1				1		1				
V	Basalt	sp P	fg-mg		1		1		1				1		1		2
IV	Basalt	ap	v.fg-mg		1								2		2		2
VIII	Diabase	sp PC	fg-mg		1			1									
VII	Diabase	sp P	fg		1					1						1	1
II	Diabase	ap	fg-cg		4	3		3	3				2			2	3
IX	Brx								1				1		1	1	1

3. Petrographic descriptions

BN-01-02 [III]: Basalt - medium grained, highly phyric (plag-cpx-ol), glomeroporphyritic, plag megacryst
Groundmass: 65%
plag - 28%, 0.5 - 1.5 mm, seriate textured, skeletal laths, larger laths have simple and deformed multiple twins. Smaller sized crystals fairly altered
cpx - 25%, <<0.2 mm anhedral grains; smaller crystals indistinct and altered
opaques - 5%, small, black, concentrations with chl patches
chl - 5%, <0.8 mm dark patches
alt - 2%, <1 mm, orange-brown, anhedral, occurs as ol replacement and also rimming vesicles
Glomerocrysts: 20%, <3 mm across
plag - 11%, <2 mm, simple- and multiple-twinned; 2V = 30
cpx - 8%, <0.6 mm, anhedral, encloses plag
ol - 1%, 0.5 mm, anhedral, mostly in glomerocrysts
Megacrysts: plag - 10%, >6 mm length and 5.5 mm width, subhedral, multiple-twinned; 2V = 42-50 => An-rich; encloses roughly rectangular patches (1 mm) of dark material concentrated along centre; IV-shaped fracture bisects central plane
Vesicles: 5%, <1 mm, round, generally unfilled although many rimmed by chl+opaques followed by brown material with empty core

BN-01-03 [III]: Basalt - medium-grained, moderately phyric (plag-cpx-ol), glomeroporphyritic, vesicular
Groundmass: 70%
plag - 30%, <1.6 mm, seriate texture, subhedral laths
cpx - 25%, <0.2 mm, anhedral
epi - 2%, <0.4 mm patches, rimming grains and vesicles
opaques - 5%, <0.2 mm, black
chl - 5%, <0.8 mm patches
Glomerocrysts: 15%, <3 mm across
plag - 10%, <3 mm, subhedral lath, <1 mm tabular grains have oscillatory zoning
cpx - 5%, <0.4 mm, anhedral, intergrowth with plag
Phenocrysts: 5%
plag - 4%, <0.6 mm, euhedral, tabular laths, discontinuous oscillatory and sector zoning
ol - 1%, <0.9 mm, subeuhedral, oscillatory zoning in one
Vesicles: 10%, <1.8 mm, round, rimmed with chl+opaques
Similar to BN-01-02 sample except no plag megacryst, round vesicles larger (<1.5 mm), and tiny equant vesicles

BN-01-04 [III]: Basalt - medium-grained, moderately phyric (plag-cpx-ol), altered, glomeroporphyritic, plag megacryst, microcrystalline
Groundmass: 75%
plag - 20%, <1.6 mm, seriate-textured, subhedral laths
cpx - 35%, <0.2 mm, anhedral
opaques - 15%, tiny, concentrated in chl patches
chl - 5%, feathery patches, alt after cpx
Glomerocrysts: 15%, about 1.5 mm extent
cpx - 6%, <0.6 mm, subhedral
plag - 7%, <2.8 mm, subhedral laths
ol - 2%, <0.6 mm, subanhedral, often rimmed by brown alt, pleochroic
Phenocrysts: 2%
plag - 1%, <2 mm, subeuhedral
ol - 1%, <1.4 mm, one twinned
Megacryst: plag - 5%, <2.8 mm, euhedral laths, generally simple-twinned, discontinuous oscillatory zoning
Vesicles: 3%, <0.75 mm, round to irregular

BN-02-01 [II]: Diabase - medium-grained, aphyric, altered, subophitic
plag - 40%, 1 mm, subhedral, laths and few tabular, with oscillatory zoning, simple and multiple twins, multiple lamellae deformed, highly altered
augite-titanaugite - 35%, 1 mm, anhedral, occasionally twinned
opaque - 5%, 0.3 mm, black, anhedral,
chl - 15%, <1.8 mm patches throughout
Vein: 5%, 1 mm, diffuse boundary, chl

BN-02-03 [II]: Diabase - medium-grained, aphyric, subophitic
plag - 45%, <1.8 mm, laths and tabular, subanhedral; 1.4 mm, tabular, subhedral grain is oscillatory zoned
augite - 40%, <0.5 mm, eu/an-hedral, subophitically enclosing plag
opaque - 5%, 1 mm, black, anhedral, associated with chl
chl - 7%, <1 mm patches and filling vesicles
Vesicles: 2%, <1.2 mm, almost totally filled with chl material
Vug: 1%, <2 mm, irregular, unfilled to completely filled with chl

BN-02-04 [VIII]: Diabase - medium-grained, sparsely phyric (cpx-pl)
Groundmass: 85%
plag - 40%, <1.2 mm, laths and tabular, anhedral, altered
pyx - 30%, cannot assess extent because of ophitic to subophitic intergrowth with plag
chl - 10%, occurs as <2.8 mm pseudomorphs, as thin vein, intergrown with matrix, and associated with opaques
opaques - 5%, <0.4 mm, black, anhedral
Phenocrysts: 10%
cpx - 7%, 2.6 mm, anhedral, one simple-twinned
plag - 3%, <1.6 mm, tabular, subanhedral, some simple-twinned, heavy alt
Vein: 5%, 0.05 mm, albite+chl+brown alt, others more diffusely bounded

BN-02-05 [II]: Diabase - fine-grained, aphyric, altered
plag - 45%, <1.2 mm, laths, subanhedral, altered
pyx - 30%, small anhedral 0.25 mm grains, throughout matrix
opaques - <4%; occurs as 0.25 mm, black, anhedral, throughout matrix; as <2 mm interdigitated concentrations; as <0.5 mm grains in carbonate vein; and filling crack
chl - 5%, occurs throughout matrix and as <1.5 mm, generally round pseudomorphs
Veins: 15%
carbonate - 13%, 4 mm vein and 0.1 mm stringer, sharp-sided; later than quartz
quartz - 2%, in <0.5 mm veins anastomosing in various orientations through sample
Vugs/crack: <1%, <0.2 mm across, empty

BN-02-07 [VII]: Diabase - fine/medium-grained, sparsely phyric (plag), highly altered
Alteration makes it difficult to assess optical continuity of grains and hence size as well as textural relations
plag - 40%, <4 mm, massive tabular grains and smaller laths, simple and multiple twins, sericite covers; 3 mm phenocrysts
cpx - 25%, 1 mm, subanhedral, subophitically encloses plag
opaque - 5%, 0.5 mm, black, anhedral
chl - 20%, <1.8 mm patches but throughout rock
Veins: 10%, <0.5 mm, recrystallized quartz surrounding vugs or groundmass in centre and subparallel, diffuse chl sides

BN-02-08 [II]: Diabase - medium-grained, aphyric, subophitic

plag - 55%, <1.7 mm, laths and tabular; tabular grains occassionally oscillatory zoned, fresh, multiple- and simple-twinned; one with cross-hatch twinning, 2V >50 => An-rich
cpx (augite) - 35%, <1 mm, subhedral, often twinned, subophitically enclosing plag
chl - 5%, as alt product throughout sample, sometimes <3 mm patches
opaque metal - 3%, 0.25 mm, dark grey core with dark rim, anhedral, associated with chl alt
Vein: 2%, 0.3 mm, quartz, anastomosing but does not penetrate sample; later than chl alt

BN-02-09 [VI]: Basalt - medium-grained, sparsely phyric (plag-ol)
Groundmass: 85%
plag - 40%, <<1.4 mm, seriate texture, laths
cpx - 30%, <0.4 mm, anhedral
chl - <10%, 0.25 mm patches throughout giving green colour
opaques - 5%, 0.1 mm, black, anhedral, throughout.
Phenocrysts: <5%
plag - 4%, <3 mm crystals of simple-twinned, altered feldspar, some indications of overgrowth
ol - 1%, 0.5 mm, equant, unaltered crystals
Veins: 10%; of 1.5 mm wide, albite cement; and of 0.1 mm wide carbonate and quartz criss-crossing sample.

BN-02-10 [V]: Basalt - fine-grained, sparsely phyric (plag), glomeroporphyritic
Groundmass: 94%
plag - 50%, <1 mm laths, subhedral
pyx - 30%, cryptocrystalline
opaque - 5%, 0.01 mm, black, equant, dusted throughout the pyx
chl - 4%, pervasive, giving green color
epi/chl - 6%, <0.5 mm grains and patches throughout, subhedral, also lining vesicles
Pheno- and Glomero-crysts: plag - 2%, 0.5-1.5 mm, sub-eu/an-hedral, tabular, simple- and multiple-twinned, discontinuous oscillatory zoning in some
Vesicles: 1%, <0.8 mm, rimmed to almost filled with epi-chl material
Veins: 1%, <0.05 mm, dark material, opaque
Crack: 2%, 0.3 mm, empty

BN-02-11 [I]: Basalt - glassy, moderately phyric (plag-cpx), hypohaline with glomerocrystic nuclei
Groundmass:
glass - 70%, devitrified
plag - 20%, 0.5-1.5 mm subeuhedral laths and 0.25 mm equant grains (simple-twinned)
cpx - 5%, 0.5 mm equant grains scattered but commonly associated with plag clusters
honey-brown alt - 4%, rimming veins, 0.25 mm grains and part of glassy groundmass
Cracks: 1%, <0.25 mm, several in various orientations, sharp boundary but anastomosing
Vugs: <0.6 mm

BN-02-12 [IV]: Basalt - fine-grained, aphyric
Groundmass: 100%
plag - 45%, 0.75 mm laths and 0.5 mm crystallites
cpx - 25%, forms microlites and <0.2 mm
opaques - 10%, <0.2 mm, black, anhedral, scattered through
chl - 15%, brown overprint
honey-brown phase - 5%, <0.5 mm, subhedral, zoning/overgrowth look

BN-03-05 [II]: Diabase - fine-grained, aphyric
plag - 50%, <2mm, highly altered boundaries and difficult to estimate

cpx - 25%, 0.2 mm, subhedral grains, few 0.5 mm grains, some oscillatory zoned
opaque - 10%, <0.3 mm, black, anhedral, equant grains and 1 mm elongate rods
chl - 14%, <0.75 mm patches throughout
Vein: 1%, 0.2 mm, of recrystallized quartz mostly. Syn-formational

BN-03-06 [II]: Diabase - coarse-grained, aphyric, subophitic to ophitic
plag - 50%, range in size from 0.5-3 mm, several of the larger show oscillatory zoning; 2V of 60 => An-rich
cpx - 40%, 1 grain of 7 mm length and twinned, smallest 0.5 mm, span range
opaque - 3%, 0.2 mm, black, anhedral
chl - 5%, large (1 mm scale), irregular patches
Vesicles: 1%, <0.8 mm, subround
Vugs: 1%, <1 mm, subround to irregular, empty

BN-03-07 [I]: Basalt - medium-grained, sparsely phyric (plag-cpx), vesicular
Groundmass: 80%
plag - 40%, 0.5 mm laths, also 0.25 mm equant grains, intrafasciculate with dark core
cpx - 30%, microcrystalline in general and altered to chl
opaque - 5%, 0.1 mm, black, anhedral, scattered through
chl - 5%, feathery, after cpx, occurs throughout
Phenocrysts: 10%
plag - 9%, <3.6 mm, laths and tabular, subeuhedral, laths with butterfly shape and overgrowth rim, others multiple-twinned, fractured and altered
cpx - 1%, 0.7 mm, subhedral, simple-twinned
Vesicles: 8%, <1 mm, 90% infilled with yellow rim and dark green core. Forms train in places. Others partially to infilled but with diffuse yellow alt in surrounding
Vein: 2%, 0.2 mm, unfilled but rimmed with chl. Does not disrupt vesicles and alt

BN-03-10 [II]: Diabase - medium-grained, aphyric, subophitic
plag - 50%, 0.5-3 mm, laths, multiple- and simple-twinned
cpx - 35%, augite to Ti-augite composition, anhedral, <1.5 mm, few have sector zoning
opaque - 5%, black, anhedral, <0.5 mm but enlarged by association with Ti-rich phase
alt - 10%, irregular brown phase associated with opaque; also in <1 mm clots alone; sometimes rimming chl core

BN-03-11 [I]: Metabasalt - very fine-grained, moderately phyric (plag-cpx), altered, tectonized, cryptocrystalline
Groundmass: 75%
plag - 20%, micrograins
cpx - 10%, barely visible few grains
chl - 35%, pervasive
opaques - 7%, 0.25 mm, black, anhedral,
alt - 3%, Fe-Ti rich, orange-brown phase, occurs as 0.75 mm round clots in groundmass => ol replacement
Phenocrysts: 15%
plag - 10%, 0.5-2 mm, laths
cpx - 5%, 0.5 mm, equant grains, most often associated with plag
Veins: 2%, 0.1 mm; with red-brown material and opaques
Cracks: 8%, <0.5 mm, empty but rimmed with red-brown material, perpendicular sets

BN-04-01 [VI]: Basalt - medium-grained, sparsely phyric (plag-ol) in finer matrix
Groundmass: 86%

plag - 45%, laths from 0.5-1.5 mm and 0.2 mm equant grains; intrafasciculate with dark inner core. Larger grains are oscillatory zoned
cpx - 35%, occurs as 0.2-0.5 mm grains and bunches of radiating fibres (zeolite)
opaque - 2%, tiny, generally <<0.1 mm, black, anhedral grains, scattered throughout
chl - 3%; occurs as pseudomorphs of 2.5 mm grains and throughout groundmass giving green colour
alt - 1%, rimming 0.1 and 0.2 mm subparallel veins
Phenocrysts: 11%
plag - 10%, <2.4 mm, subhedral, tabular and laths, some relatively unaltered while others enclose chl patches, simple and compound twins, many with discontinuous oscillatory zoning. Few others show oscillatory zoning
alt ol - 1%, dark honey brown phases; occurs as discrete 0.2 mm replacement of ol grains
Vesicles: <1%, <0.75 mm, round to irregular, partly filled with dark chl groundmass and opaques
Veins: 2%, <0.1 mm, rimmed to filled with dark brown material

BN-04-05 [V]: Basalt - fine-grained, sparsely phyric (plag)
Groundmass: 95%
plag - <50%, from microlites to 1.5 mm laths and <1.2 mm tabular phenocrysts; laths subhedral
cpx - 30%, from microlites to 0.5 mm, larger in proto-glomerocrysts, anhedral grains (except ol)
opaques - 5%, form indistinct, dark, concentrations within brown patches, associated with chl alt
chl - 10%, forming large, irregular, dark green patches in groundmass
Phenocrysts: minor - euhedral to anhedral phenocrysts show oscillatory zoning
Vesicles: 4%, <0.8 mm, round, rimmed to filled with chl and opaques mostly
Vein: <1%, <0.2 mm, two perpendicular, one dominantly chl and other with opaques filling; late-stage

BN-04-07 [I]: Basalt - very fine-grained, moderately phyric (plag-cpx), tectonized, cryptocrystalline with coarser patches and glomerocrysts
Groundmass: 60%, cryptocrystalline
plag - 35%, <0.2 mm laths to tiny grains
opaques - 5%, 0.2 mm, black, anhedral
pyx - 20%, <0.05 mm to tiny indistinct grains
chl - 5%, pervasive green colour
Phenocrysts: 10%
plag - 6%, <1.5 mm, laths, some oscillatory zoned
alt - 3%, 1 mm pseudomorphs, dark brown
pyx - 1%, 0.4 mm, subhedral
Glomerocrysts (3 mm): 15%
plag - 8%, <1.5 mm laths, euhedral, multiple laths
cpx - 7%, <0.6 mm, anhedral, to Ti-augite comp, subophitically enclose plag
Coarse grained concentrations: 14%
plag - 5%, <0.75 mm, laths mostly, unaltered
cpx - 2%, <0.2 mm, anhedral
carbonate - 1%, <1.4 mm patch
alt - 1%, 0.2 mm patches, brown
ol - <1%, 0.1 mm
opaque - 3%, <0.1 mm, black, anhedral
chl - 1%, concentrated inbetween
Veins: 1%; brown phase in diffuse, 0.5 mm wide veins; <0.05 mm wide veins rimmed with late-stage chl

BN-04-09 [III]: Basalt - very fine-grained, highly phyric (plag-cpx-ol), glomeroporphyritic
Groundmass: 55%, skeletal-textured
plag - 25%, microlaths to 1 mm laths and equant grains
pyx - 10%, tiny (0.1 mm) equant grains
opaques - 7%, tiny <0.1 mm, anhedral and variously shaped
chl - 12%, throughout
vugs - 1%, <0.5 mm, irregular, throughout
Glomerocrysts: 44%, <4 mm extent, plag-plag and plag-cpx/ol, some subophitic growth

plag - 24%, <3.4 mm, laths to tabular, euhedral to anhedral, some oscillatory zoned, some fractured
cpx (+ ol) - 20%, <1.5 mm, subeuhedral, sometimes simple-twinned, lack cleavage
Vesicles: 1%, <1 mm, round, rimmed with dark chl+opaques

BN-04-10 [VI]: Basalt - fine-grained, sparsely phyric (ol-plag)
plag - 38%, <0.5 mm laths
pyx - 40%, <0.5 mm, anhedral
opaques - 7%, 0.1 mm, irregular but occasionally elongate to 0.2 mm, scattered throughout but concentrated with chl
epi - 1%, small 0.2 mm patches in one section and rims one vesicle
chl - 8%, in <2 mm patches
Phenocrysts: 4%
ol - 2%, largest 1 mm but generally 0.5 mm, subeuhedral, visible from rimming alt
plag - 2%, <1.5 mm; few tabular. Few with overgrowth rims
Vesicles: 2%, round (0.5 mm) and irregular vugs (<0.5 mm), both unfilled. In places, material around it appears altered with chl

BN-04-11 [III]: Basalt - fine-grained, moderately phyric (plag-cpx-ol)
Groundmass: 77%, skeletal-textured
plag - 35%, laths in groundmass av. 0.5 mm but <2 mm (seriate-texture), anhedral
pyx - 25%, tiny (<1 mm) grains throughout, anhedral; some subhedral 0.75 mm grains. Alt giving green colour
opaques - 8%, <0.1 mm, black, variety of shapes but sharp-sided, scattered throughout but occasionally in clusters associated with chl or rimming vesicle
chl - 8%, pervasive
alt - 1%, 0.1 mm, brown, patches in small part of thin section
Phenocrysts: 22%, proto-glomerocrystic
plag - 14%, <1.4 mm, anhedral laths to 0.6 mm tabular anhedral grains
cpx - 5%, <0.6 mm, euhedral outline but subhedral
ol - 3%, some 0.2 mm grains; few 0.5 mm subhedral grains
Vesicles: 1%, few, small <0.5 mm, round and irregular, unfilled

BN-04-12 [III]: Basalt - very fine-grained, highly phyric (plag-cpx-ol), hypocrystalline with glomerocrysts
Groundmass: 57%
plag - 15%, 0.2 mm microlites. More distinct plag laths <1 mm and simple-twinned.
pyx - 5%, 0.1 mm grains, barely visible
opaques - 10%, tiny, black, throughout
glass alt - 27%, light brown, feathery, chl
Phenocrysts: 10%
plag - 5%, <1.4 mm lath, subhedral
cpx - 3%, <0.3 mm, subhedral
ol - 2%, <0.3 mm, subeuhedral
Glomerocrysts - 25%, <3 mm extent; subophitically intergrown
plag - 13%, 5 <2 mm, laths, subhedral, commonly simple-twinned
pyx - 11%, <0.4 mm, subhedral
ol - 1%, <0.2 mm, anhedral
epi - 1%, in vein and rimming grain boundaries of pyx and vesicles in two sectors extending less than 3 mm from vein
Vesicles: 2%, <0.3 mm round, unfilled to partly or completely filled glass and opaques
Vugs: 3%, <0.75 mm, irregular, unfilled

Vein: 2%, en echelon, rough-sided with varying width (max 0.3 mm), generally unfilled but in one place includes part of groundmass and elsewhere is infilled with epi; distinctly cuts across crystal grains

BN-04-13 [III]: Basalt - fine-grained, highly phyric (plag-cpx-ol), gradational from holo-hypocrystalline groundmass with glomerocrysts
Glassy part: 30% - 9 mm section
groundmass - 15%, glass
phenocrysts - 5%, plag laths av. 0.5 mm but <1.5 mm
glomerocrysts - 10%, <3 mm extent
plag - 5%, 1.5 mm laths cpx - 4%, 0.5 mm, euhedral
vesicles/vugs - 1%, 0.5 mm, mostly round but few irregular, rounded ones are unfilled to partly filled with glass
crack - 0.01 mm
Transition: gradational from compact to feathery glass
Hypocrystalline part: 70%
groundmass: 35%
plag - 12%, <0.6 mm, laths pyx - 8%, <0.2 mm, grains
opaques - 7%, <0.1 mm, black, irregular chl - 7%, feathery alt
epi - 1%, also filling and rimming surrounding vesicles and surrounding some grains in nearby glomerocryst, occupies small part of thin section
phenocrysts: 5%
plag - 4%, <1 mm laths, subhedral; one 2.2 mm euhedral lath oscillatory zoned
ol - 1%, <0.5 mm, eu/an-hedral
glomerocrysts: 25% - <3 mm extent, plag-cpx and plag-ol
plag - 14%, <1.5 mm, laths, subophitically enclosing cpx
pyx - 10%, 0.2-1 mm, euhedral-rounded, the largest is simple-twinned
ol - 1%, <0.3 mm, subhedral
vesicles - 4%, <0.5 mm, round, unfilled to partly or totally filled with dark green chl+opaques
vein - <1%, 0.1 mm partly filled with epi

BN-04-14 [III]: Basalt - very fine-grained, highly phyric (plag-cpx-ol), holo- to hypo-hyaline, glomeroporphyritic
Groundmass: 47%, gradational from 100% glassy to cryptocrystalline
plag - 5%, av. 0.1 mm, tiny laths cpx - 10%, av. 0.02 mm, tiny grains
opaques - 14%, tiny, concentrated in 0.1 mm, black
chl - 17%, pervasive epi - 1%, <0.8 mm irregular patches and rimming ol
Phenocrysts: 15%
plag - 10%, <1 mm laths, simple-twinned; also 2, 1.5-2 mm euhedral grains
cpx - 5%, <0.5 mm euhedral augite, some with circle of inclusions
ol - 1%
Glomerocrysts: 35% - <4 mm but are more concentrated in glassy patches within hypocrystalline part
plag - 20%, subophitic intergrowth, <1.5 mm laths and tabular, mostly simple-twinned; some tabular 0.8 mm plag ophitically enclose several 0.2 mm pyx grains
cpx - 15%, <1 mm, euhedral
Vesicles: 3%, <0.5 mm, round, unfilled in glass section but filled with dark material (glass) in cryptocrystalline section

BN-05-02 [VIII]: Diabase - fine-grained, sparsely phyric (plag-cpx), altered
Groundmass: 90%
plag - 40%, 0.5 mm, laths and tabular cpx - 35%, 0.2 mm subhedral; altering to chl patches
opaque - 5%, <0.5 mm, black, anhedral chl - 10%, <0.8 mm patches in groundmass

Phenocrysts: 7%
plag - 4%, <4 mm, subeuhedral, twinned, highly altered; some subophitically enclose groundmass pyx
pyx - 3%, 2 mm, subhedral, unaltered but associated with altered pyx and chl phenocrysts; others composed of chl and one 3 mm grain ophitically encloses opaque
Vein: 3%; as 0.3 mm wide crack unfilled but appears in one section that groundmass seeps in; as 0.2 mm wide, en echelon, carbonate vein perpendicular to previous

BN-05-04 [II]: Diabase - coarse-grained, aphyric
plag - 55%, <2.5 mm, subhedral, mostly simple-twinned, oscillatory zoning, heavily altered
pyx - 30%, <3 mm, anhedral, ophitic-subophitically enclosing plag, alt
chl - 10%, <1 mm patches, irregular
opaque - 3%, black, <0.5 mm, irregular shape; associated with chl patches
Vein: 1%, subparallel stringers; in <0.05 mm wide cracks with dominantly chl and carbonate-albite on sides
Crack: 2%, 2 mm, unfilled

BN-05-05 [II]: Diabase - medium-grained, aphyric
plag - 50%, <3 mm, subanhedral, very sericite altered
augite - 30%, <1 mm, anhedral, intergrown with plag, no cleavage, to Ti-aug composition
chl - 10%, <1 mm, broad irregular patches
opaque metals - 5%, 1 mm, grey interior with dark rim, irregular
Vein: 2%, <0.3 mm, diffuse, chl rimming carbonate interior with quartz grains
Crack: 3%, 0.6 mm, branching

BN-05-06 [II]: Diabase - medium-grained, aphyric, subophitic
plag - 50%, <2 mm laths; subhedral
cpx - 30%, <0.7 mm, anhedral,
chl - 15%, extensive and irregular; <1.7 mm; associated with opaques
opaques - 5%, black, irregular, <0.5 mm

BN-05-09 [I]: Basalt - fine-grained, highly phyric (plag-cpx), hypocrystalline with skeletal groundmass and glomerocrysts
Groundmass: 55%, skeletal-textured
plag - 25%, seriate-textured laths (<1.2 mm) and 0.2 mm intrafasciculate squares with dark cores
pyx - 10%, microlites with skeletal texture
glass - 10%, dark amorphous often in round 1 mm clots
opaque - 10%, black, cannot distinguish individual grains, concentrated particularly with glass
Glomerocrysts: 40%, <2 mm extent
plag - 25%, <2 mm laths (or tabular grains), subophitically enclosing pyx
pyx - 15%, 0.5 mm, anhedral, to Ti-augite composition
alt - 2%; as brown-green, 0.5 mm, diamond-shaped patches; as honey-brown phase, round, <0.7 mm, associated particularly with glass clots but occasionally found within pyx too
Vesicles: 2%, <0.8 mm, filled with dark chl groundmass or brown alt or former rimming core of latter
Vein: 1%, three, 0.1 mm wide, semi-parallel, winding, one filled entirely with green material, another with black material and the other partially filled with green and black material

BN-05-10 [VI]: Basalt - medium-grained, sparsely phyric (ol-plag)
Groundmass: 92%
plag - 45%, <3 mm laths and rectangular (<2 mm) to square (1 mm) tabular phenocrysts; where lamellae evident, none undeformed
pyx - 30%, <1.2 mm, anhedral, subophitically enclosing plag
opaques - 8%, black, rods, <0.4 mm

chl - 8%, 1 mm scale patches, irregular, dark green
alt - 1%, brown, rimming vesicle, fractures in ol and in 0.2 mm patches
Phenocrysts: 7%
ol - 5%, generally 0.2-1.2 mm, hexagonal to rounded, often distinguished by honey-brown alt along concoidal fractures
plag - 2%, <1.8 mm, euhedral tabular laths and anhedral grains, one sector and oscillatory zoned
Vesicles: 1%, 0.6 mm, round, one rimmed by brown alt and empty, one filled with carbonate

BN-06-01 [II]: Diabase - medium-grained, aphyric, altered
plag - 50%, <4.5 mm, simple and multiple twins, fair amount of sericite alt
cpx - 33%, subophitic intergrowth with plag
chl - 10%, <1.4 mm patches, irregular
opaque metals - 5%, <0.6 mm, irregular, two types - one Sulphide
Vein - 2%, 0.2 mm wide, carbonate, synformational - one grain spans vein

BN-06-02 [II]: Diabase - medium-grained, aphyric, similar to BN-06-01 except more altered
plag - 50%, <3 mm, anhedral, heavily altered, difficult to distinguish individually
cpx - 30%, <1 mm, anhedral, intergrown with plag
opaques - 7%, <0.6 mm, black, irregular, few
chl - 11%, <1.2 mm, in two forms: round clots with sheafs and irregular patches commonly replacing grains
Veins: 1%, as 0.1 mm wide quartz veins and 0.1 mm wide diffuse-bounded vein of dark brown material
Vesicles: 1%, <0.9 mm, filled with chl

BN-06-03 [II]: Diabase - medium-grained, aphyric, altered
plag - 45%, <2 mm laths, quite altered
cpx - 30%, <0.8 mm, anhedral, subophitically enclose plag, to Ti-augite comp
opaques - 5%, av. 0.4 mm, black
chl - 19%, <1.5 mm round clots, and irregular patches <2.5 mm
Vein: <1%, 0.1 mm, quartz, post-chl alt

BN-06-04 [I]: Basalt - glassy, hypohyaline, axiolitic, sparsely phyric (plag-cpx), gradation from area with more to less vugs
Groundmass: glass (fresh); plag - skeletal microlaths
Phenocrysts: plag - 0.1 mm, oscillatory zoned, euhedral; cpx - 0.25 mm, subhedral
Vugs

BN-06-06 [III]: Basalt - glassy/fine-grained, highly phyric (plag-cpx-ol), hypocrystalline with glomerocrysts
Groundmass: 60%
glass - 45%, devitrified brown opaques - 2%, tiny
plag - 11%, seriate laths <1.2 mm; some intrafasciculate with dark inner core, swallow-tail ends
cpx - 1%, from 0.2-0.4 mm euhedral alt - 1%, brown, tiny 0.1 mm clots of material
Phenocrysts: 3%
plag - 2%, <1.2 mm, euhedral tabular, some simple-twinned, oscillatory zoning
ol - 1%, <0.8 mm, euhedral, alt along cracks
Glomerocrysts: 35%
plag - 20%, from 0.2 mm equant to 3 mm laths, fresh
cpx - 15%, <0.8 mm, subeuhedral, ophitic-subophitically enclosing plag such that plag appears arrow-like; some penetrated by brown material; one patch surrounding glomerocryst of microlites
Vein: 1%, <0.1 mm, filled with red-brown material, cross-cuts phase grains

Vesicles: 1%, 0.5 mm, round, empty but rimmed with brown material and completely filled along vein with red-brown material

BN-06-07 [III]: Basalt - glassy/fine-grained, highly phyric (plag-cpx-ol), hypohyaline, more vesicles than BN-06-06
Groundmass: 70%
opaques - 4%, tiny
glass - 55%, gradational from previous to devitrified brown
cpx - 1%, <0.1 mm, euhedral
plag - 10%, seriate laths <1 mm
Phenocrysts: 5%
plag - 3%, <1.3 mm, euhedral, tabular and laths, some simple-twinned, oscillatory zoning
ol - 2%, <0.5 mm, subhedral to anhedral, latter partly filling euhedral outline
Glomerocrysts: 23%
plag - 13%, <2.5 mm laths
cpx - 10%, 0.4 mm subeuhedral, subophitically enclosing plag
Vesicles: 2%, 0.4 mm, round, unfilled; occasionally rimmed with epi

BN-06-08 [V]: Basalt - fine-grained, sparsely phyric (plag)
Groundmass: 90%
plag - 40%, <0.4 mm laths
cpx - 30%, <0.2 mm, anhedral
chl - 10%, 1 mm scale irregular patches
opaques - 10%, <0.3 mm rods of black
Phenocrysts: plag - 1%, few; 0.6 mm, zoned to 1.8 mm laths
Veins: 1%, perpendicular, en echelon 0.1 mm wide of red-brown material
Crack: 7%, 0.3 mm, rimmed with red-brown alt material
Vesicles: 1%; 0.4-0.6 mm, subround; one along vein rimmed by red-brown material

BN-06-09 [IX]: Basalt breccia - possibly magmatic breccia, very altered
Glassy basalt fragments with plag micro-laths and tiny mafics
Cemented by other similar parts that are only more tectonized

BN-06-10 [I]: Basalt - very fine-grained, moderately phyric (plag-cpx), altered, glomeroporphyritic
Groundmass: 70%
plag - 20%, laths <0.5 mm, subhedral
cpx - 10%, microlites
chl - 30%, feathery look
opaque - 10%, tiny, black
Glomerocrysts: 20% - 2 mm scale
plag - 12%, <2 mm laths
cpx - 8%, <0.4 mm subanhedral
Phenocrysts: plag - 1%, 0.5 mm, subhedral, tabular, oscillatory zoned
Vesicles: 2% - <0.5 mm, round, varying from empty to completely filled with altered glassy groundmass
Veins: 7% - roughly subparallel, branching, <0.2 mm, rimmed to filled with yellow-red-brown alt material

BN-06-11 [III]: Basalt - very fine-grained, sparsely phyric (plag-cpx-ol), hypohyaline, glomeroporphyritic, trachytic texture
Groundmass: 94%
plag - 0.1-0.3 mm, subhedral, acicular
diopside - 0.2 mm, green pleochroic, subhedral
glass - devitrified, dark + black rods
alt - brown clots, round to hexagonal, <0.2 mm generally, scattered through
Phenocrysts: 2%
plag - av. 1 mm, laths enclosing dark patches to av. 0.4 mm tabular, euhedral grains
ol - quite pleochroic; 0.4 mm anhedral grains visible by rimming brown alt;
ol - 0.1 mm, clear, pleochroic, euhedral, enclosing dark patches
Glomerocrysts: 1% - subophitic intergrowth

plag - 1-1.8 mm laths
cpx (augite) - <0.4 mm, subeuhedral; parts pleochroic
Vesicles: 2%; between 0.4-0.8 mm diameter; round; unfilled but occasionally rimmed by 0.5 mm dark brown material
Vein: <0.05 mm, green material rims inner vein of recrystallized material; cuts across phases.

BN-06-12 [III]: Basalt - glassy/very fine-grained, highly phyric (plag-cpx-ol), hypocrystalline, glomeroporphyritic
Groundmass:- 50%
glass - alt predominates — plag - 0.2 mm crystallites
alt - <0.2 mm honey brown clots
Phenocrysts: plag - 20%, 0.2-1.8 mm, laths, euhedral, enclosing patches of dark material similar to glass groundmass
Glomerocrysts: 25% - subophitic intergrowth of cpx enclosing plag
Ti-augite - subhedral, hexagonal, highly pleochroic, 0.2-1.2 mm. In some, feathery appearance around edges indicates continuing reaction relationship
ol — plag - laths, 0.2-2.0 mm
Vesicles: 4% - round to subround, most often thinly rimmed with brown material, mostly filled entirely with carbonate or few unfilled
Vein: 1% - 0.05 mm, filled with honey-brown material

BN-06-13 [I]: Basalt - glassy/fine-grained, moderately phyric (plag-cpx), hypohyaline, glomeroporphyritic
Groundmass: 75%
glass - feathery patches with black grains
plag laths - <0.4 mm, subhedral — mafic phase - <0.05 mm
Glomerocrysts: 23% - <2 mm across
Ti-augite - pleochroic some highly green-pink, <0.6 mm, subanhedral, rectangular to hexagonal shape
plag - <1.2 mm, laths
Vesicles: 2% - 0.2-0.7 mm, round to irregular, unfilled

BN-06-14 [I]: Basalt - fine-grained, sparsely phyric (plag-cpx), glomeroporphyritic
Groundmass: 91%
plag - 45%, <1 mm laths but generally <0.4 mm — pyx - 25%, <0.2 mm but generally 0.1 mm
opaques - 10%, black, <0.2 mm rods — chl - 10%, in <1 mm irregular patches
alt - 1%, brown, rimming and filling vesicles and replacing grains
Phenocrysts: plag - 3%, <1.5 mm, euhedral, tabular, simple-twinned plag
Glomerocryst: 2%, <2 mm extent
plag - <0.8 mm sized laths — cpx - 0.2 mm, subhedral, square
Vesicles: <4% - <1 mm, generally round, rimmed with brown material

BN-07-04 [VII]: Diabase - fine-grained, sparsely phyric (plag)
plag - few massive, tabular, highly altered grains one of which is about 2.8 mm across; rest are highly altered laths <2.2 mm
Ti-augite - <1.8 mm, anhedral, sub- to ophitically enclosing plag; many show intense green-red pleochroism
opaques - black, irregular, 0.05-0.45 mm, associated with chl
chl - as irregular patches replacing pyx and <1.4 mm round patches
Vein: <0.05 mm, chl, late-stage

BN-07-07 [I]: Basalt - glassy/very fine-grained, moderately phyric (plag-cpx), hypohyaline
Groundmass: glass with plag microcrystallite

Phenocrysts: cpx - 0.1-1.2 mm, euhedral plag - <0.6 mm, laths
Glomerocrysts: <1.2 mm concentrations
plag - laths, <1 mm cpx - 0.2 mm, subhedral
chl - <0.8 mm round patches; some rimmed by recrystallization
Veins: - quartz (recrystallized) + dark brown material, braided, in two perpendicular sets

BN-08-01 [I]: Basalt - glassy, moderately phyric (plag-cpx), hypohyaline
Groundmass: glass
Phenocrysts:
ti-augite - <0.5 mm, euhedral, hexagonal, but some green-pink pleochroic
plag - <0.5 mm laths, generally skeletal
Vesicles: <0.2 mm round to <0.45 mm irregular, unfilled
Crack: unfilled

BN-08-04 [VI]: Basalt - fine-grained, phyric (plag-ol), hypohyaline
Groundmass:
plag - <1 mm, subhedral laths
cpx - <0.5 mm, subanhedral, some simple-twinned
glass - throughout filling interstices between grains; altered, with black opaques
Phenocrysts:
plag - <1 mm, few tabular
ol - 0.2 mm, anhedral
alt - honey-brown, round to irregular, <0.45 mm grains
Vesicles: <0.5 mm, round, unfilled to partly rimmed/filled with brown material

BN-08-05 [III]: Basalt - fine-grained, moderately phyric (plag-cpx-ol), hypohyaline, seriate texture
Groundmass:
cpx - <<0.6 mm, anhedral
plag - <1.2 mm, subhedral, lamellae deformed
glass - inbetween, altered, with black rod opaques
alt - brown, rimming grains
Phenocrysts:
plag - 6 mm, euhedral lath, encloses dark patches, fractures extend into 1.45 mm lath alongside, zoning in one
cpx - 2.8 mm, subophitic intergrowth with plag, simple-twinned
ol - <0.4 mm, anhedral, occasionally surrounded by brown alt

BN-09-01 [VI]: Basalt - glassy, moderately phyric (ol-plag)
Groundmass:
glass appearance but seems to be formed of <0.05 mm black opaques and incipient plag±pyx
Phenocrysts:
ol - 0.1 mm grains to 3 mm phenocrysts, subanhedral
plag - <1.8 mm, anhedral laths with pronounced swallow-tails, tabular grains enclose groundmass
Vesicles: <0.3 mm round or <0.8 mm irregular, unfilled

BN-09-03 [VI]: Basalt - fine-grained, moderately phyric (ol-plag), altered
Groundmass: 80%
plag - <1.4 mm, laths, subhedral, enclose groundmass patches
cpx - av. 0.05 mm, forms indistinguishable
opaques - black, <<1 mm, anhedral, associated with chl
chl - filling groundmass interstices and associated with cpx

alt - 0.05 mm patches only in small part of thin section, brown-green, occasionally associated with ol
Phenocrysts: 20%
ol - 19%, 0.1-1 mm though one of 1.6 mm, subanhedral
plag - <1%, 1 mm, tabular, anhedral

BN-10-01 [VI]: Basalt - fine-grained, sparsely phyric (plag-ol), crystalline
Groundmass: 90%
plag - laths, <<1.2 mm, subhedral, enclose dark patches
cpx-titanaugite - av. 0.2 mm, anhedral
opaques - <0.2 mm, black, irregular, associated with chl alt
chl - large alt patches throughout sample
alt - <0.3 mm patches, brown-green, occurs in small part of thin section
Phenocrysts: 7%
plag - <2 mm simple-twinned lath and <1 mm tabular, fractured
ol - <0.8 mm, anhedral, rimmed by alt
Vesicles: 3%, generally irregular (<2 mm) to subround (0.4 mm), unfilled

BN-10-02 [IX]: Basalt breccia - medium-grained, sparsely phyric (plag pheno/mega), highy altered
Original groundmass: 50%
plag - <1.8 mm laths and 1 mm altered tabular grain, anhedral
cpx + Ti-augite - <0.4 mm, anhedral
alt - 30%, quite pervasive, chl
opaques - 5%, <0.05 mm, black, anhedral, associated with alt
Pheno/megacrysts: 5% plag - <4 mm tabular and twinned laths, subhedral, fractured
Vesicles: 8%, <3 mm vugs, irregular, empty
Vein: 1%, <0.6 mm (varying width) broadening to 2 mm patch - appears to mark passage of alt fluid - includes quartz grains though pyx fragments still visible
Cracks: 1%, <1 mm but widens to train of irregular 3 mm vugs

BN-10-04 [IV]: Metabasalt - fine-grained, aphyric, very altered
Original groundmass:
plag - 60%, <1 mm, subhedral laths, altered; feathery variety totally altered
cpx - 10%, <0.4 mm, anhedral
opaques - 5%, 0.02 mm, dark, anhedral, associated with alt between feathery altered plag
opaque alt - 6%, <0.6 mm, irregular alt patches, blue colour, rimming grain
alt - 15%, pervasive greenschist
Vein: 3%, <0.2 mm, varying width, brown material, branching, criss-cross thin section
Vesicles: 1%, 0.2-0.8 mm, distinguished by roundness, filled with alt product

BN-10-06 [VI]: Basalt - medium-grained, sparsely phyric (ol-plag)
Groundmass:
plag - 40-45%, <1.6 mm, laths, anhedral due to intergrowth with cpx
cpx - 10%, 0.2 mm, anhedral
opaques - 5%, <<0.4 mm, dark, irregular, associated with alt
alt - 13%, chl, throughout are irregular patches
Phenocrysts:
ol - 15-20%, <0.8 mm, one of 2.4 mm, anhedral, subophitically enclose plag
plag - 10%, <1.4 mm grains, subhedral, alt patches within, occasionally encloses other smaller ones, some oscillatory zoned
Vesicles: 5%, 1 mm and filled with carbonate and quartz, 1 mm with core of quartz and surrounded by 2 layers of chl, <1 mm subround and unfilled, <0.9 mm filled with chl

Vein: <1%, train of 0.02 mm opaques
Crack: <1%, 0.2 mm, unfilled

BN-10-07 [II]: Diabase - medium-grained, aphyric
plag - 45%, <2 mm slightly altered laths and <2 mm unaltered tabular grains
cpx - 35%, <<2 mm, anhedral due to intergrowth, some simple twinned, some subophitic enclosure of plag, includes Ti-augite
opaques - 5%, <0.4 mm, dark blue-black, irregular, associated with alt
alt - 14%, <<1.2 mm brown patches throughout probably replacing pyx
Crack: 1%, 0.2 mm train of empty vugs

BN-10-10 [IV]: Basalt - fine-grained, aphyric
Groundmass:
plag - 50%, <0.8 mm subhedral laths and single 0.8 mm tabular euhedral grain though smaller anhedral ones enclosing pyx
cpx - 30%, grades in size from 2 mm in small part of thin section to where majority is <0.1 mm (with recrystallized look), anhedral
opaques - 9%, 0.2 mm, blue-black, irregular
alt - 10%, chl, with pyx
Vesicles: 1%, <0.6 mm subround to <0.8 mm irregular, unfilled

BN-10-11 [I]: Basalt - medium-grained, sparsely phyric (plag-cpx)
Groundmass:
plag - 40%, <2 mm subhedral laths, one 4.8 mm lath, subophitically enclosed by cpx
cpx - 30%, <0.8 mm, anhedral, to Ti-augite composition
honey-brown phase - 5%, <<0.8 mm, replacement alt
opaques - 5%, <0.2 mm, blue-black, irregular, associated with alt
alt - 15%, <2 mm patches throughout
Phenocrysts:
plag - 4%, <2.6 mm, subeuhedral
cpx - 4%, 2 mm anhedral simple-twinned cpx and Ti-augite, 1.4 mm anhedral grain
Vesicles: 1%, 0.6 mm, round, filled with brown-green alt material
Vein: <1%, <0.05 mm, brown material, en echelon strands

BN-10-13 [V]: Basalt - medium-grained, sparsely phyric (plag)
Groundmass:
plag - 45%, <1.4 mm subhedral laths and <1 mm tabular anhedral grains
cpx - 30%, <0.4 mm, anhedral
opaque - 5%, <0.2 mm, blue-black, irregular
alt - 20%, <1.4 mm patches sometimes clearly replacing or rimming grains, honey-brown
Phenocrysts:
plag - 2%, <2 mm, euhedral, simple-twinned, oscillatory zoning
Vesicle: 2%, 2 mm, round, partly-filled with chl and brown alt material, 0.3 mm round and unfilled
Crack: 1%, <0.7 mm, unfilled

BN-10-15 [I]: Basalt - fine-grained, moderately phyric (plag-cpx), altered, glomeroporphyritic
Groundmass: 70%
plag - 60%, <1 mm laths to 0.3 mm patches with inclusions to altered feathery variety
cpx - 2%, 0.01 mm, anhedral
opaques - 8%, <0.01 mm, black, irregular, filling areas between feathery alt
Phenocrysts: 5%

plag - 3%, <1.4 mm tabular grains and laths, euhedral, hour-glass zoning in some
cpx - 2%, <0.4 mm, anhedral
Glomerocrysts: 10% - 3 mm across
plag - 6%, <0.9 mm though one lath of 2.8 mm, subeuhedral, occasionally includes some groundmass
cpx - 4%, <0.6 mm, anhedral
alt - 3%, <1 mm, honey-brown, replacing grains
Vesicles: 2% - <0.3 mm, round, filled by honey-brown alt phase
Vein: 2% - <0.2 mm, braided, filled with brown phase and a few blue-black opaques, late-stage
Crack: 8% - 0.8 mm, unfilled, sides rimmed in places by brown alt phase

BN-10-18 [I]: Basalt - very fine-grained, sparsely phyric (plag-cpx), glomeroporphyritic
Groundmass: trachytic texture
plag - 70%, crystallites av. 0.2 mm though subeuhedral phenocrysts av. 0.6 mm, crystallites totally altered
cpx - 15%, <0.1 mm
opaques - 8%, black, concentrated, individual grains indistinguishable, interstitial between plag
Glomerocrysts: 5%, <<2 mm across
plag - 3%, <1 mm laths, subeuhedral, subophitically encloses pyx
cpx - 2%, <0.2 mm, subhedral
Vesicles: 1%, <0.7 mm, filled with chl.
Veins: <1%, <0.02 mm, one of light brown material and the other of blue-black

BN-10-19 [III]: Diabase - fine-grained, aphyric, plag megacryst
plag - 50%, <<1.8 mm lath, anhedral
cpx - 30%, <<0.4 mm, subhedral, simple twinning in euhedral larger grain, fair amount of alt
opaques - 7%, <0.4 mm, dark concentrations
alt - 2%, chl, <0.6 mm brown-green concentrations
Megacryst: plag - one 2.2 mm tabular simple-twinned grain with growth/reaction rim
Vein: 1%, <0.1 mm, chl
Vugs: 10%, <1.4 mm, irregular, empty, only in one half of thin section

BN-10-20 [III]: Basalt - fine-grained, sparsely phyric (plag-cpx-ol), vesicular, glomeroporphyritic
Groundmass: 80%
plag - 60%, av. 0.4 mm, subhedral laths cpx - 20%, <0.2 mm, anhedral
opaques - 5%, <0.2 mm, black, rods and irregular, throughout but concentrated with chl patches in interstices
chl - 15%, as broad patches throughout with opaques in interstices; <0.3 mm concentrations in small part of thin section especially close to veins
Glomerocrysts: 5%, 3 mm across
plag - 3%, <1.8 mm, subhedral cpx - 2%, <0.3 mm, anhedral
Phenocrysts: 5%
plag - 4%, <2 mm, subeuhedral; one of 3 mm encloses smaller plag
ol - 1%, <0.5 mm, anhedral
Vesicles: 9%, <1 mm, round to subround, empty or rimmed by Fe-brown alt, and filled with chl or filled with altered groundmass
Veins: 1%, as 0.1 mm wide veins filled with outer rim of yellow material and inner thread of red material; late-stage since cuts and rims vesicles; as 0.05 mm chl vein joining with previous

BN-12-01 [I]: Basalt - fine-grained, highly phyric (plag-cpx), glomeroporphyritic, plag pheno/megacryst
Groundmass : 55%
plag - 25%, generally <0.6 mm, subeuhedral to crystallites and altered feathery forms
cpx - 15%, generally <0.1 mm, small forms indistinguishable

opaques - 5%, forms within <0.3 mm patches with chl in interstices between feathery plag, forms indistinguishable
chl - 10%, throughout but particularly in <0.5 mm alt patches
Glomerocrysts: 35%, <3 mm across
plag - 20%, <2 mm, subhedral laths
cpx - 15%, <0.6 mm, subanhedral, subophitically enclose cpx
Pheno/megacrysts: plag - 2%, <1.8 mm, euhedral, tabular and laths
Vesicles: 7%, <1 mm, round, most unfilled some with edges rimmed by epi or groundmass material
Vein: <1%, <0.1 mm, albite

BN-12-02 [I]: Basalt - fine-grained, moderately phyric (plag-cpx), glomeroporphyritic
Groundmass: 70%
plag - 53%, <1 mm laths to crystallites to altered feathery forms; roughly oriented fabric
cpx - 10%, <<0.2 mm subhedral grains, smaller forms indistinguishable
opaques - 5%, black, tiny grain, form indistinguishable, fill interstices between feathery patches
epi - 1%, 0.1 mm, subhedral to irregular, replacement alt, only in small part of thin section
Fe-rich phase - <1%, <<0.5 mm, round to irregular, in smaller part of thin section with epi
chl - general overprint
Glomerocrysts: 20%, <2.2 mm across
plag - 10%, <<2.2 mm, subeuhedral, occasionally encloses some groundmass material
cpx - 10%, <1 mm, subhedral, ophitically to subophitically encloses plag
Phenocrysts: 3%
plag - 2%, <0.8 mm, euhedral and unaltered laths and tabular grains
cpx - 1%, <0.8 mm euhedral hexagonals filled partly by anhedral cpx
Vesicles: 7%, <0.5 mm, round to irregular, unfilled though occasionally partly rimmed by groundmass material; 1 mm hexagonal empty

BN-13-02 [IV]: Basalt - very fine-grained, plag megacryst
Groundmass: 85%, homogeneous, fine-grained and altered
plag - 40%, <0.1 mm crystallites
brown phase - 30%, cpx altered, pervasive though varying degrees
opaques - 15%, size indistinguishable, black
Megacryst: plag - 1%, 1 grain of 1 mm and others of 0.2 mm
Vesicles: 1%, 0.2 mm, round, empty, rimmed to completely with reddish-brown material
Vugs: 12%, 0.8 mm - >3 mm, irregular, unfilled
Veins: 1%, as <0.05 mm, blue-black and reddish-brown parts to same strand, perpendicular sets; as 0.1 mm, chl; as <0.01 mm, albite strands with 0.1 mm grain nearby

BN-13-03 [I]: Basalt - very fine-grained, sparsely phyric (plag-cpx), glomeroporphyritic, plag megacryst
Groundmass: 90%, fine-grained, recrystallized look
plag - 40%, <0.2 mm crystallites
cpx - 20%, <0.05 mm, not totally altered
brown phase - 10%, alt after cpx
chl - 10%, general overprint
opaques - 10%, black, form indistinguishable, associated with brown phase
Phenocrysts: plag - 2%, <0.6 mm, subeuhedral laths and few grains
Megacryst: plag - 1%, <1 mm, euhedral laths, twinned
Glomerocrysts: 3%, <1 mm across
plag - 2%, <0.6 mm, subhedral
cpx - 1%, <0.4 mm, subhedral
Vesicles: 2%, <0.6 mm, round to irregular, unfilled to partly filled with altered material
Vein: 2%, <0.1 mm, marked by red-brown trail

BN-13-04 [I]: Basalt - very fine-grained, moderately phyric (plag-cpx), glomeroporphyritic

Groundmass: 75%
plag - 35%, <0.2 mm crystallites cpx - 25%, throughout but mostly altered to chl
opaques - 15%, <0.02 mm, black, irregular
Phenocrysts: plag - 5%, <1.8 mm subeuhedral laths and tabular grains
Glomerocryst: 10%, 2 mm across, plag and plag-cpx
plag - 7%, <1.2 mm, subhedral cpx - 2%, <0.4 mm, anhedral
amphibole? - 1%, 0.7 mm, subhedral => cpx alteration
Veins: 10%, <0.2 mm, unfilled to alt filling smaller or rimming larger, late-stage

BN-13-05 [I]: Basalt - fine-grained, moderately phyric (plag-cpx), glomeroporphyritic
Groundmass: 75%
plag - 30%, <0.8 mm, subhedral laths cpx - 20%, 0.1 mm, anhedral
opaques - 10%, <<0.2 mm, irregular, blue-black chl - 15%, after cpx
Phenocrysts: 4%
cpx/ol - 2%, 0.8 mm subhedral grain with growth rim
plag - 2%, 1 mm, subeuhedral lath, altered
Glomerocryst: 11%, <2.6 mm across, plag-cpx
plag - 7%, <1 mm, subhedral lath cpx - 4%, <0.3 mm, anhedral
Vesicles: 1%, <0.4 mm, rimmed with groundmass
Veins: 2%, <0.1 mm, filled with red-brown material and rimmed/filled by chl, opaques along parts
Cracks: 7%, <0.8 mm, perpendicular set, smaller has en-echelon strands with right-angle turns

BN-13-07 [IX]: Basalt Breccia - fine-grained
Groundmass: totally altered except for remnant phenocrysts and glomerocrysts
plag - <0.6 mm, subhedral laths
cpx - <1 mm, subhedral
Matrix cementing:- mix of vugs, altered material, feldspar alt

BN-13-08 [I]: Basalt - very fine-grained, sparse PC proto-glomerocrysts
plag - 40%, <0.4 mm, subhedral laths cpx - 25%, <0.01 mm, anhedral
cpx - 1%, 0.2 mm, subhedral grains, associated with larger plag in proto-glomerocrystic arrangement
opaques - 10%, tiny, black, irregular, associated with chl
chl - 20%, after cpx, throughout though of varying degrees
Vesicles: 2%, <0.4 mm, filled by anhedral deformed quartz grains
Veins: 2%, <0.1 mm, light brown strands; also subparallel <2 mm stringers of quartz

BN-13-11 [I]: Juxtaposition with no obvious boundaries of brecciated altered parts next to fine-grained, highly phyric (plag-cpx) basalt
Dominantly basalt part:
groundmass : brown - 40%, totally altered
Glomerocrysts: 20%, <2 mm across
plag - 10%, <1.8 mm subeuhedral laths
cpx - 10%, <0.4 mm, subhedral
Phenocrysts: 25%
plag - 15%, <1 mm laths, subeuhedral with slight swallow-tail ends
cpx - 5%, <0.2 mm, anhedral
chl - 5%, <0.4 mm, euhedral replacement probably after pyx
veins: 5%, <0.2 mm to very fine; empty or filled; criss-crossing and branching; late-stage
vugs: 10%, <1.8 mm, filled with chl except perhaps for small empty inner core
Midsection basalt part: brecciated look, cemented part with recrystallized look enclosing previous groundmass, highly chl altered

matrix: 0.1 mm grains of subhedral plag laths and cpx grains recognisable; rest chl
veins: <0.1 mm, empty or filled with Fe-rich material
Rest of basalt: intruding matrix contains remnant cpx - 1.8 mm subhedral

BN-13-12 [IV]: Basalt - medium-grained, aphyric
plag - 40%, <2 mm, size range in subhedral laths and grains
cpx - 20%, <0.3 mm, anhedral
opaques - 20%, <0.1 mm, black, irregular
chl - 18%, pervasive, after pyx
Vesicles: 1%, <0.8 mm, occasionally rimmed by groundmass but with core of chl or quartz
Veins: 1%, <0.1 mm, filled by chl and opaques

BN-13-13 [V]: Basalt - fine-grained, sparsely phyric (plag)
plag - <38%, <1.2 mm subhedral laths and anhedral tabular grains
cpx - 25%, 0.2 mm, anhedral
opaques - 15%, <0.2 mm, black, irregular
brown alt phase - 20%, <<0.6 mm patches, concentrated in varying degrees, after mafic phase
Phenocrysts: minor - plag - <1.2 mm subeuhedral tabular grains, some with oscillatory zoning
Vesicles: 2%, <1 mm, rim of brown material and/or groundmass but core of chl

BN-13-15 [I]: Basalt - glassy, moderately phyric (plag-cpx), hypohyaline
Groundmass: glass - 75%, honey-brown with dark blotches to completely dark
Phenocrysts: plag - 10%, <1.2 mm euhedral laths, unaltered
Glomerocrysts: 5%, <2 mm across, plag and plag-cpx
plag - 4%, <1.2 mm, subhedral lath cpx - 1%, <0.2 mm, anhedral
Vesicles: 2%, <1 mm, occasionally rimmed with opaques and/or filled with recrystallized feldspar and brown phase or filled only with chl
Veins: 8%, <0.4 mm, empty or filled; braided and criss-crossing

BN-23-02 [IX]: Basalt breccia - completely altered

BN-23-03 [VII]: Diabase - fine-grained, sparsely phyric (plag)
Groundmass: 85%
plag - 30%, <1.4 mm, subhedral laths, altered
cpx - 25%, <0.8 mm, anhedral, subophitic intergrowth with plag
opaques - 10%, 2 populations of metals, one 0.8 mm and other <0.2 mm, anhedral
chl - 20%, <1.2 mm patches of only l.green chl (blue under cross-nicols)
Phenocrysts: plag - 5%, <3.4 mm, euhedral laths to tabular grains, strange alt, occasionally encloses pyx, also some sector zoning
Veins: 10%, subparallel; as 0.6 mm carbonate veins that includes parts of groundmass; as 0.4 mm recrystallized quartz veins with small inner core of or interspersed with carbonate; as <0.5 mm chl veins

BN-23-05 [II]: Diabase - medium-grained, aphyric, altered, veined
plag - 50%, <1.6 mm, subhedral laths, altered
cpx - 30%, 1 mm, anhedral, ophitic to subophitic intergrowth with plag, actual extent larger
opaques - 5%, 0.6 mm, anhedral, blue-black
chl - 10%, >0.2 mm patches throughout, anhedral, after pyx
Veins: 5%, <1 mm though broad diffuse effects, chl + carbonate destroys original fabric

BN-23-07 [II]: Diabase - coarse-grained, aphyric

plag - 45%, <3 mm, anhedral because of intergrowth, altered though sometimes concentrated in inner core, also appears to be carbonate alt within some
cpx - 35%, <1.8 mm, anhedral, to ti-aug composition, ophitically to subophitically enclosing plag
opaques - 5%, <0.6 mm, anhedral, dark metal
chl - 12%, <<3 mm patches, irregular
Veins: 3%, 0.4 mm, albite alt, late-stage - cuts through and branches around albite grain

BN-23-08 [I]: Basalt - very fine-grained, highly phyric (plag-pyx)
Groundmass: 60%
plag - 20%, mostly feathery and altered, small <0.4 mm, few
cpx - 10%, <0.05 mm, barely visible through alt
opaques - 10%, <0.1 mm, black, anhedral
chl - 10%, general overprint, with <0.2 mm anhedral patches
red-brown alt - 10%, in 5 mm area in part of slide close to vein with opaques, forms small <0.2 mm patches often associated with opaques
Glomerocrysts: 35%, altered
plag - 20%, <1 mm, subhedral lath
cpx - 15%, <0.3 mm, anhedral, one simple-twinned
Phenocryst: cpx - 1%, 1 mm, subhedral, twinned
Vesicles: 2%, <1 mm, 1 empty, others filled entirely with chl, blue-black opaques, blue-black opaque with small chl core
Veins: 2%, subparallel strands; as <2 mm, chl and/or opaques in parts; as <0.05 mm wide recrystallizations

BN-23-09 [I]: Basalt - glassy/fine-grained, highly phyric (plag-cpx), hypocrystalline, glomeroporphyritic
Groundmass: 60%
glass - 40%, feathery, altered totally
opaques - 8%, <0.02 mm, black, irregular
plag - 10%, <0.6 mm, thin laths with swallow-tail ends
cpx - 2%, <0.2 mm, barely visible anhedral patches
Glomerocrysts: 30%
i) plag-cpx - <<3 mm but generally <2 mm across
plag - 15%, <2 mm, subhedral lath
cpx - 10%, <<1 mm, generally <0.2 mm, anhedral
yellow-brown alt - 2%, <0.6 mm
ii) plag - 3%, <3.5 mm across; <1.6 mm subhedral laths with groundmass material within
Phenocrysts: 5%
plag - 4%, <1.8 mm euhedral laths with distinct growth rim in almost all, occasionally occurs in concentrations <3 mm across
yellow-green alt phase - 1%, <<1.8 mm, as replacement infilling hexagonal phase
Vesicles: 5%, <0.9 mm, subround, varying from empty to totally filled

BN-24-01 [IX]: Volcanic breccia of tuffaceous/glassy fragments with carbonate infilling

BN-24-02 [II]: Diabase - coarse-grained, aphyric, altered
plag - 40%, <3.6 mm anhedral lath and tabular grain, fairly altered, simple, multiple and vague trace of cross-hatch twinning
cpx - 20%, <1.2 mm, anhedral due to ophitic intergrowth with plag
opaques - <5%, <1 mm, black, irregular
chl - 30%, <2.7 mm, irregular patch, light green, blue under cross-nicols
Veins: <5%, vein types frequently cross-cut; as <0.2 mm wide recrystallized + chl veins; as <0.1 mm, chl and/or epi centred veins

BN-24-03 [V]: Basalt - fine-grained, sparsely phyric (plag)

Groundmass: 90%
plag - 40%, <1.2 mm, subhedral laths
cpx - 20%, <0.4 mm, subanhedral, close intergrowth with plag
feathery alt - 15%
opaques - 5%, black, irregular, concentrated in brown patches
brown alt patches - 10%, 0.6 mm, irregular
Phenocrysts: 2% plag - <1.4 mm, euhedral, most with distinct rim, simple-twinned
Vesicles: 5%, 0.9 mm, filled with chlorite-altered parts of groundmass and opaques
Cracks: 2%, <0.2 mm, one side has alt material
Vugs: 1%, <1 mm, irregular, empty or filled with yellow-brown material

BN-24-04 [IV]: Basalt - very fine-grained, aphyric, plag megacrysts, chl alt
Groundmass: 80%, shattered, gradation in extent of chloritisation
plag - 35%, <0.3 mm, anhedral laths grading to anhedral grains in more altered part
cpx - 15%, <0.05 mm, barely visible, altered; gone in altered part
opaques - 5%, <0.05 mm, black, subhedral, itself altered
chl - 25%, overall imprint
opaques: 1%, <1.8 mm, black, elongate along vein, size decreases further away from vein
Megacrysts: 13%, plag - <2 mm, subeuhedral laths, odd alt some with carbonate
Vein: 4%, <0.1 mm, probably carbonate
Crack: 2%, 0.1 mm

BN-24-05 [I]: Basalt - very fine-grained, highly phyric (plag-cpx), glomeroporphyritic, plag-cpx megacrysts, chl alt
Groundmass: 55%
plag - 4%, microlites barely visible
cpx - tiny grains
chl - 50%, pervasive
opaques - 1%, <0.05 mm, black, irregular, few, no association, found even within grains in some cases in chlorite-altered interior
Phenocrysts: 25%
plag - 20%, <0.6 mm, subeuhedral laths; define rough subparallel fabric => trachytic texture
cpx - 5%, generally 0.1 mm, anhedral; one 0.6 mm, hexagonal, euhedral grain; other grains <0.6 mm, subeuhedral, diamond-shaped, simple-twinning common to even smaller size
Glomerocrysts: 7%, <2 mm across
plag - 4%, <<1.1 mm, subhedral lath
cpx - 3%, <<0.3 mm, larger subhedral while smaller anhedral
Mega-/pheno-crysts: 10%
plag - 6%, <4.6 mm, euhedral, lath to tabular, occasionally has carbonate alt, some with multiple twins
cpx - 4%, <3 mm, anhedral, ophitically and subophitically enclosing and associated with plag megacrysts
Vein: 1%, 0.2 mm, branching and braided
Crack and vug: 2%, 1-2 mm and >2-3 mm vugs linked by 0.1 mm crack

BN-24-06 [I]: Basalt - very fine-grained, sparsely phyric (plag-cpx), chl alt
Groundmass:75%
plag - 40%, 0.2 mm subhedral microlaths
chl - 30%, pervasive
opaques - 5%, <<0.2 mm, dark brown patch, irregular
Phenocrysts: 3%
plag - 2%, <1.2 mm, subeuhedral, tabular, odd zoning/growth pattern
cpx - 1%, <0.8 mm, euhedral, 4- to 6-sided, some very altered

Glomerocrysts: 6%
plag - 2%, <2 mm laths and <0.6 mm euhedral grains, simple-twinned, one with odd zoning, quite altered
cpx - 4%, <1.8 mm, euhedral to anhedral with only fragments of grain remaining, some simple-twinned
Veins: 15%, subparallel, in order from one side of thin section
- 0.8 mm, dominantly chl with inner 0.1 mm crack
- 0.4 mm, recrystallized quartz (with thin crack between previous)
- <0.1 mm, recrystallizations, IV-shape and separated strands within groundmass
- 0.2 mm, twister of dark brown opaque, chl and light brown alt (connects to following)
- 0.9 mm, strands of recrystallizations, chl and opaque stringers
Cracks and vugs: 1%, irregular <0.3 mm crack connecting <0.6 mm vugs

BN-24-07 [VII]: Diabase - fine-grained, sparsely phyric (plag), vesicular
Groundmass: 80%
cpx - 30%, <1 mm, anhedral due to subophitic enclosure of plag
plag - 35%, <3 mm, anhedral lath
opaques - 5%, <0.2 mm, blue-black, irregular
brown alt - 10%, 0.4 mm scale, patches
Phenocrysts: 10% plag - <2 mm, subhedral, odd zoning in some, odd fracture pattern
Vesicles: 9%, <1.6 mm, round to subround, empty to rimmed or partly filled with very altered green-brown material
Vugs: <1%, <0.4 mm, grouped together

BN-24-08 [II]: Diabase - fine-grained, aphyric, altered
Groundmass: subophitic texture makes size estimation difficult
plag - <0.5 mm, subhedral, very altered with sericite
cpx - 0.2 mm av., anhedral, altered to chl
opaques - dark, associated with alt
Vugs: <0.5 mm, irregular, one with chl

BN-24-09 [I]: Basalt - very fine-grained, moderately phyric (plag-cpx), glomeroporphyritic
Groundmass: 45%
plag - 20%, 0.2 mm microlaths cpx - 10%, <0.05 mm, anhedral form
opaques - 5%, <0.02 mm, black, irregular, scattered throughout
chl - 10%, pervasive, after cpx
Phenocrysts: 10%
plag - 7%, 1.6 mm, subhedral laths to tabular grain cpx - 3%, 0.4 mm, subanhedral
Glomerocrysts: 15%, 1.8 mm across
cpx - 10%, <0.4 mm, euhedral to anhedral, simple-twinned, subophitically encloses plag and smaller pyx
plag - 5%, <1.6 mm, subhedral lath to tabular grains
Vesicles: 2%, <2 mm, av. 0.8 mm, round, rimmed to filled with chl
Veins: 17%, roughly subparallel, broad diffuse bands throughout; as <0.2 mm, chl, braiding ± 0.8 mm opaques; as 5 mm diffuse band of chl but original texture still visible
Vugs: <1%, 0.6 mm, irregular, empty, common along vein zones

BN-24-10 [IV]: Basalt - fine-grained, aphyric
Groundmass:
plag - 35%, <1.2 mm anhedral laths
cpx - 25%, <0.5 mm, anhedral due to subophitic enclosure of plag, some simple twinning
chl - 5%, <0.2 mm, anhedral, clear green patch
opaques - 5%, 0.2 mm, black, irregular, within brown patches
brown patches - <20%, 4 mm, occupying interstices between phenocrysts

Vesicles: <1%, 0.4 mm, round, filled with chl or groundmass of brown alt and opaques
Veins: 7%, <0.6 mm wide braided band enclosing and altering matrix to <0.1 mm veins rimmed to filled with chl; two sets - one parallel to vugs and other perpendicular
Vugs: 2%, subparallel, <5 mm, elongate, found at end of and along veins, rimmed by chl forming veins

BN-24-11 [V]: Basalt - fine-grained, sparsely phyric (plag), in contact with honey-brown alt layer
plag - 35%; 1 mm, anhedral due to alt, relict laths; <0.6 mm subhedral laths
cpx - 15%, <0.3 mm, anhedral whether alone or in association with plag
opaques - 5%, <<0.2 mm, black, irregular, associated with alt
alt - 25%, feathery and dark green to brown chl patches
Phenocrysts: plag - <1%, subeuhedral diamond and rectangular grains
Vesicles: 2%, <1.8 mm, round, filled with chl and/or quartz
Veins: 2%, <0.05 mm red-brown veins trailing off from crack
Cracks: 15%, 0.3 mm widening in places to 1 mm but trailing off elsewhere to 0.01 mm, occasionally rimmed by red-brown material and opaques, two perpendicular sets, late-stage tearing through vesicles.

BN-24-12 [II]: Diabase - coarse-grained, aphyric
plag - 50%, <3.6 mm subhedral laths and < 2mm tabular grains with oscillatory zoning, unaltered
cpx - 35%, <2.4 mm, anhedral, ophitic and subophitic enclosure of plag, some simple-twinned
opaques - 5%, <0.6 mm, black, irregular, most likely present where chl alt
chl - 10%, <1.2 mm of pure alt, larger where alt continuous

BN-24-13 [I]: Basalt - fine-grained, sparsely phyric (plag-cpx), glomeroporphyritic
Groundmass:
plag - 45%, <1.2 mm, anhedral laths; concentrations of <0.7 mm euhedral phenocrysts
cpx including Ti-augite - 30%, <<1 mm, anhedral, subophitically enclose plag
opaques - 18%, <3 mm dark black patches
alt - 1%, 0.6 mm patch rimming grain, vugs, vesicles and filling other vesicles, only in small part
Pheno- and glomero-crysts:
plag - 0.8 mm grains, subeuhedral, in cluster
cpx - 1 mm, anhedral grain, isolated though others in glomerocrystic cluster with plag
Vesicles: 5%, <0.6 mm, round, generally empty except for small part with chl filling
Vugs: <1%, <1 mm, irregular, occasionally rimmed with red-brown and green material but generally empty

BN-24-14 [I]: Basalt - medium-grained, sparsely phyric (plag-cpx), glomeroporphyritic
Groundmass: 80%
plag - 35%, <<1.8 mm, seriate sized, anhedral laths
cpx - 15%, <0.3 mm, anhedral
opaques - 10%, <0.01 mm, black, irregular, forms dark patch within broader alt area
chl - 20%, feathery alt
Phenocrysts: plag - 2%, 2.2 mm lath or smaller 0.6 mm oscillatory zoned grain, euhedral
Glomerocryst: 8%, <2 mm across
plag - 4%, <2 mm, anhedral lath, some oscillatory zoned
cpx - 4%, <1 mm, anhedral, subophitic enclosure of plag
epi and chl - 1%, <0.2 mm patches, rimming and filling vesicle, only occurs in small part of thin section
Vesicles: 6%, <0.8 mm, empty or filled with dark chl and opaques
Vugs: 3%, <2 mm, irregular, empty though one rimmed with chl or brown material, forms trains

APPENDIX F: ACQUISITION OF GEOCHEMICAL DATA

1. Rock samples

Of the 97 samples selected for petrographic study, 10 samples were rejected for geochemical analysis because they were either too veined (2-05, 2-07, 3-11, 4-05), cut through by cracks (2-11, 10-04), of breccia type (13-07), or not enough of the sample was available in the University of Washington (UW) collection (4-12, 7-07, 23-09). They were replaced by 8 other importantly located samples although of small amount (3-02, 10-16, 13-01) or altered to a minor extent (4-06, 5-01, 7-05, 23-04, 24-02). In total, 95 samples were analysed from the WBD study site for major, trace and rare earth elements.

2. Sample powder preparation

At the UW, approximately 1 cm thick slabs of the rocks were cut, the altered edges trimmed and minor veins or cracks sawed through. To remove the marks of the saw blade, the slab faces were ground smooth on a diamond wheel. The slabs were well-wrapped, broken into <1 cm size pieces by hammering and stored in plastic vials. At the Université de Bretagne Occidentale (UBO), the sample was crushed in a Habisch mortar and batches of the pieces were reduced to a talc-size powder by grinding in a ball mill with an agate canister and balls.

3. Preparation of samples for bulk rock chemical analyses

A solution was prepared by weighing 300 mg of the pulverized sample into a teflon (PTFE) flask and adding 3.5 ml of hydrofluoric acid (HF at 40% concentration) plus 0.5 ml of nitric acid (HNO_3 at 65% concentration). The sealed mixture was heated to 80°C for 4 hours to accelerate the attack of the acids. The excess HF was neutralised and the flourine compounds redissolved by adding 96 ml of boric acid (H_3BO_3 at 25 g/l concentration) to obtain a 100 ml solution. Internal (CB -1, -2, -3 and -15) and external (BEN, JB2 and ACE) French and U.S.G.S. (United States Geological Survey) standards (BCR-1, BHVO-1), which were used to check the precision of the results obtained, were prepared according to the same procedure described.

4. Chemical analyses by ICP-ES, AES and AAS

Chemical analyses were performed in the UBO laboratory under the direction of J. Cotten during June/July 1992. The concentrations of the major and trace elements were determined on a ISA.JOBIN.YVON JY70 Plys inductively coupled plasma emission spectrometer (ICP-ES) interfaced with a Laboratory Computer. The equipment consists of a polychromatic spectrometer for analysis of major elements (except Na and K) and Sr, a flat-field spectrometer for Na and K, and a sequential spectrometer for P, Sc, V, Cr, Co, Ni, Ba, Y, Zr, Nb, La, Nd, Eu, Dy, Er, and Yb. During each sample run, all the standards were analysed at the start and three of the internal laboratory standards were re-measured after every ten samples to eventually calculate the drift. The detection limits and error estimates for the Blanconaute samples (J. Cotten, pers. comm.) are listed in Table F-1. Rb was analysed by atomic emission spectrometry (flame) (AES) and K was re-checked by atomic absorption spectrometry (AAS) using a PERKIN-ELMER 5000 emission spectrometer. These measurements were carried out by comparison to the concentration of known standards.

Table F-1: Detection limits and error estimates of ICP analyses

Abbreviations: L.O.D. = limit of detection Rel. std. dev. = relative standard deviation

BN Major Elements: - analysed July 1992

ELEMENTS	SiO_2	TiO_2	Al_2O_3	Fe_2O_3	MnO	MgO	CaO	Na_2O	K_2O	P_2O_5
L.O.D. (%) - 2σ	0.2	0.05	0.05	0.05	0.02	0.05	0.10	0.05	0.02	0.03
Rel. std. dev. %	1	2	2	2	2	2	2	3	3	3

BN Trace elements: - analysed July 1992

ELEMENTS	Rb	Sr	Ba	Sc	V	Cr	Co	Ni	Zr
L.O.D. (ppm) - 2σ	0.5	0.5	3	0.5	3	3	2	3	2
Rel. std. dev. %	5	5	5	5	5	5	5	5	5

ELEMENTS	Nb	Y	La	Nd	Eu	Dy	Er	Yb
L.O.D. (ppm) - 2σ	1	0.5	0.8	2	0.2	0.5	1	0.2
Rel. std. dev. %	5	5	5	5	5	5	10	5

Example: U.B.O. External Standards - analysed January 1991

STANDARDS	Nb	La	Nd	Eu	Dy	Er	Yb
JB2 measured	1.05	2.9	7.1	0.83	3.9	2.3	2.42
JB2 recommend.	0.8	2.4	6.5	0.85	3.85	2.4	2.5

STANDARDS	Nb	La	Nd	Eu	Dy	Er	Yb
BEN measured	99	83	69.5	3.47	6.3	2.4	1.7
BEN recomm.	100	82	70	3.6	6.4	2.5	1.8

STANDARDS	Nb	La	Nd	Eu	Dy	Er	Yb
ACE measured	104	62	95	1.92	29.5	17.4	17.7
ACE recomm.	108	59	92	2.00	29.0	17.7	17.4

U.S.G.S. Standards - analysed July 1992

	BCR-1 - mean measured	BCR-1 - recommended	BHVO-1 - mean measured	BHVO-1 - recommended
SiO_2	54.35	54.06	50.25	49.94
TiO_2	2.21	2.24	2.70	2.71
Al_2O_3	13.60	13.64	13.88	13.80
Fe_2O_3	13.50	13.41	12.34	12.23
MnO	0.19	0.177	0.17	0.168
MgO	3.43	3.48	7.16	7.23
CaO	6.87	6.95	11.28	11.40
Na_2O	3.16	3.27	2.22	2.26
K_2O	1.67	1.69	0.52	0.52
P_2O_5	0.37	0.36	0.29	0.273
LOI		1.59		0.246
Total	99.35	100.867	100.81	100.777
Rb	47.00	47.2	10.20	11
Sr	325.00	330	389.00	403
Ba	686.00	681	135.00	139
Sc	32.00	32.6	31.00	31.8
V	425.00	407	323.00	317
Cr	11.00	16	290.00	289
Co	37.00	37	45.00	45
Ni	10.00	13	116.00	121
Y	37.00	38	27.50	27.6
Zr	178.00	190	168.00	179
Nb	11.70	14	18.00	19
La	26.05	24.9	16.00	15.8
Ce	53.00	53.7	38.00	39
Nd	30.00	28.8	26.00	25.2
Eu	2.00	1.95	2.20	2.06
Dy	6.50	6.34	5.50	5.2
Er	4.00	3.63	2.80	2.4
Yb	3.35	3.38	2.03	2.02

APPENDIX G: MAJOR, TRACE AND RARE EARTH ELEMENT ANALYSES

In addition to the geochemical data for the Blanconaute rocks, Table G-1 includes a brief summary of the petrographic characteristics, some geochemical indices, and a CIPW norm calculation for every sample. An explanation of these abbreviations follows:

1. Sample numbers (*Smp. #*): Twelve of the rocks analysed by other students at the Université de Bretagne Occidentale (UBO) laboratory under the supervision of Jo Cotten are indicated by a symbol attached to the sample number:

^: M. Boulafia (1992 DEA student at UBO)
#: C. Fleutelot (1993 DEA student at UBO)
$: G. Manac'h (Ph.D. candidate at UBO)

2. Rock Type (*Type*): Capital notation indicates that the sample was examined in thin section while small letters indicate a description from the hand sample (unpubl. Blanconaute report). The rock type is prefixed with a grain size descriptor.

B or b: Basalt
MB or mb: Pervasively altered basalt
D or d: Diabase
MD or md: Pervasively altered diabase
Brx or brx: Breccia

gl: glassy
v. fg: very fine-grained i.e. <0.25 mm
fg: fine-grained i.e. 0.25 - 1 mm
mg: medium-grained i.e. 1 - 3 mm
cg: coarse-grained i.e. 3 - 5 mm

3. Minerals and textures (*Xstal.*):

a: aphyric i.e. 0%
s: sparsely phyric i.e. 1-10%
m: moderately phyric i.e. 11-25%
h: highly phyric i.e. >26%
o: subophitic to ophitic texture

P: plagioclase
C: clinopyroxene
O: olivine
p: phenocrysts
g: glomerocrysts

4. Distinctive Features (*Char.*):

x: xenolith
mv: 6-10% vesicles

sv: 1-5% vesicles
hv: 11-15% vesicles

5. Metamorphic Character (*Meta.*):

A: alteration mainly as chlorite replacement
V: veins

s: 1-5% - scarce abundance
m: 6-10% - moderate abundance
h: >10% - high abundance

6. Sample retrieval (*in-pl/talus*):

i: in-place

t: talus

7a-d. Sample location: The sample height (*smp. ht.*) is that obtained from the video of the dive. The distance of the dive from the axis (*dist.-axis*) is calculated according to a 29 mm/yr. half-spreading rate. The location of the sample is also given by *sector* and *domain*.

8. Geochemical indices:

Fe_2O_3*: total iron measured as Fe^{3+}

FeO*: calculated from Fe_2O_3* with total iron as Fe^{2+}

Fe_2O_3 and FeO: calculated from FeO* assuming $Fe_2O_3/FeO = 0.15$ (Brooks, 1976)

$Mg\# = ((Mg^{2+})/(Mg^{2+} + 0.87Fe^{2+}_T))*100$

$Fe_8 = FeO^* + 1.664 (MgO - 8)$ (Klein and Langmuir, 1987)

$Na_8 = Na_2O + 0.373 (MgO - 8)$ (Klein and Langmuir, 1987)

$Si_8 = SiO_2 + 0.31 (MgO - 8)$ (Klein and Langmuir, 1989)

Smp. #	BN-01-02	BN-01-03	BN-01-04	BN-02-01	BN-02-03	BN-02-04	BN-02-08	BN-02-09	BN-02-10	BN-02-12	BN-03-02B	BN-03-05	BN-03-06	BN-03-07	BN-03-10	BN-04-01	BN-04-06	BN-04-07	BN-04-09	BN-04-10	BN-04-11	BN-04-13
MORB Grp.	N	N	N	M	T'	N	M	M	M	T'	M	M	M	M	N	M	N	N	T'	N	N	N
Petro. Grp.	III	III	III	II	II	VIII	II	VI	V	IV		II	II	I	II	V		I	III	VI	III	III
Rock Type	mg-B	mg-B	mg-B	mg-D	mg-D	mg-D	mg-D	mg-B	fg-B	fg-B	md	fg-D	cg-D	mg-B	mg-D	mg-B	b	fg-B	cg-B	v.fg-B	v.fg-B	fg-B
Xstal.	m-PCOg	m-PCg,POp	h-POOg,POp	a-o	a-o	a-CPp	a-o	a-POp	a-Pp,Pg	a		a-o	a-o	a-PCp	a-o	a-Pp		m-PCp,PCg	h-POOg	a-OPp	m-POOp	h-POOg,POp
Char.	Px,av	mv	aP,av		av				av					av	mv		v	POOx	av	av	av	av
Meta.	sA	sA	sA	hA,sV	mA	mA,sV	sA,sV	mA,mV	sA,sV	hA	V	hA,sV	sA	sV	mA	sA,sV	V	sA,sV	hA	mA	mA	mA,sV
in-pl/talus	ip	I	ip	I	I-ip	I	I-ip	ip	ip	ip	I-ip	ip	I	ip	ip	ip	ip	ip	ip	ip	ip	ip
emp. ht.	2753.00	2492.00	2336.00	4355.00	4172.00	4083.00	3760.00	3626.00	3601.00	3409.00	4255.00	3978.00	3767.00	3715.00	3485.00	3738.00	3119.00	3089.00	2745.00	2552.00	2396.00	2288.00
dist-axis	43.78	43.78	43.78	40.43	40.43	40.43	40.43	40.43	40.43	40.43	38.61	38.61	38.61	38.61	38.61	39.24	39.24	39.24	39.24	39.24	39.24	39.24
Sector	E	E	E	CE	CE	CE	C	C	C	C	C	C	C	C	C	C	C	C	C	C	C	C
Domain	K10	K9	K8	Talus	G5	G4	F4	E4	E4	E3	Z3	D4	D4	B6	D1-N	D1-S	B5	B5	B3	B3	B2	B1
SiO2	49.50	50.70	50.00	49.15	50.25	48.65	50.00	48.70	48.90	48.85	50.65	48.80	48.50	48.00	48.65	47.80	48.50	47.70	49.50	50.20	50.20	49.55
TiO2	1.97	2.38	2.07	1.16	1.21	1.71	1.34	1.17	1.08	3.61	1.17	2.88	1.20	1.04	1.77	1.40	1.50	2.12	2.52	1.88	1.70	1.92
Al2O3	14.15	14.60	14.00	15.30	14.65	14.32	14.84	15.34	15.58	11.62	15.70	13.37	17.20	16.40	14.37	15.95	15.10	13.30	13.45	14.25	14.30	13.78
Fe2O3*	12.75	12.73	13.28	9.72	10.20	12.50	10.85	10.22	9.59	19.10	8.90	14.85	9.55	8.20	12.20	10.00	11.25	13.25	14.65	12.60	11.85	13.59
MnO	0.19	0.21	0.22	0.17	0.18	0.22	0.22	0.18	0.18	0.26	0.15	0.24	0.15	0.14	0.21	0.23	0.19	0.20	0.23	0.21	0.21	0.21
MgO	6.30	5.14	6.71	8.21	7.44	8.93	7.50	8.59	8.15	4.27	6.75	5.81	6.48	7.87	6.85	6.81	7.00	6.68	5.58	6.54	6.95	6.73
CaO	11.45	11.49	11.27	11.66	11.45	10.40	11.40	10.95	11.87	7.78	9.80	9.20	12.50	11.90	11.35	12.00	11.48	9.80	10.13	11.86	12.10	11.00
Na2O	2.40	2.69	2.56	2.71	2.75	3.34	2.66	2.76	2.27	3.10	4.45	3.71	2.65	2.71	2.85	2.73	2.55	2.76	2.82	2.56	2.55	2.56
K2O	0.18	0.38	0.27	0.30	0.11	0.08	0.33	0.28	0.13	0.34	0.06	0.04	0.06	0.05	0.10	0.06	0.12	0.14	0.38	0.23	0.20	0.20
P2O5	0.22	0.26	0.24	0.13	0.16	0.18	0.14	0.12	0.12	0.52	0.14	0.30	0.12	0.11	0.17	0.16	0.15	0.21	0.30	0.18	0.18	0.20
LOI	1.11	0.10	-0.12	2.31	1.94	2.08	1.38	2.29	2.38	1.08	2.75	2.73	2.30	3.27	2.03	3.22	2.02	2.77	0.34	-0.17	-0.29	-0.30
Total	100.22	100.68	100.50	100.82	100.34	100.29	100.66	100.62	100.21	100.53	100.52	99.73	100.69	99.69	100.55	100.36	99.86	99.05	99.90	100.24	99.93	99.42
Q	1.14	2.08	0.01						1.60	2.77												
or	1.06	2.25	1.60	1.77	0.65	0.47	1.95	1.65	0.77	2.01	0.35	0.24	0.35	0.30	0.59	0.35	0.71	0.83	2.25	1.36	1.18	1.18
ab	20.31	22.76	21.66	22.93	23.27	28.26	22.51	23.52	19.21	26.23	36.05	31.39	22.42	22.93	24.12	23.10	21.58	23.52	23.86	21.66	21.58	21.66
an	27.31	26.64	25.91	26.70	27.31	23.85	27.58	28.55	31.94	16.79	22.69	19.71	34.86	32.44	26.12	31.09	29.40	23.40	22.92	26.71	26.99	25.47
ne											0.87											
di	23.14	23.76	23.43	22.89	23.21	21.85	22.93	20.30	20.79	15.56	20.37	19.90	21.55	20.94	23.89	22.39	21.77	20.06	21.09	25.48	26.26	22.94
hy	18.46	14.53	19.93	7.14	16.76	5.54	13.96	6.85	14.83	22.86		3.17	7.09	5.84	10.23	6.25	13.90	17.65	19.29	17.76	16.16	20.23
ol				9.86	1.78	11.21	4.56	12.19			12.48	12.79	6.96	9.53	6.52	8.23	4.24	2.73			1.24	0.48
mt	2.17	2.16	2.26	1.65	1.74	2.13	1.84	1.74	13.90	3.25	1.51	2.52	1.62	1.39	2.07	1.70	1.91	2.26	2.49	2.13	2.02	2.32
il	3.74	4.52	3.93	2.20	2.30	3.25	2.54	2.22	2.01	6.86	2.22	5.09	2.28	1.98	3.36	2.66	2.85	4.03	4.79	3.57	3.23	3.65
ap	0.51	0.60	0.56	0.30	0.37	0.42	0.32	0.28	0.28	1.20	0.32	0.70	0.28	0.25	0.39	0.37	0.35	0.48	0.70	0.42	0.37	0.46
Pl comp.-An	57	54	54	58	54	46	55	55	62	39	39	39	61	59	52	57	58	50	49	55	56	54
Sc	44.00	46.00	45.00	40.00	41.00	44.00	42.00	41.00	39.00	40.00	32.00	42.00	37.00	39.00	45.00	39.00	42.00	43.00	44.00	45.00	46.00	45.00
V	415.00	445.00	390.00	257.00	261.00	356.00	292.00	271.00	257.00	410.00	235.00	420.00	258.00	240.00	365.00	285.00	340.00	410.00	450.00	380.00	365.00	406.00
Cr	175.00	105.00	155.00	357.00	330.00	142.00	250.00	396.00	372.00	7.50	290.00	130.00	220.00	360.00	184.00	270.00	182.00	148.00	55.00	148.00	190.00	109.00
Co	46.00	46.00	44.00	43.00	41.00	47.00	44.00	45.00	44.00	46.00	32.00	41.00	39.00	38.00	45.00	42.00	46.00	44.00	47.00	47.00	45.00	46.00
Ni	70.00	49.00	59.00	93.00	72.00	83.00	87.00	112.00	108.00	15.00	75.00	62.00	74.00	116.00	81.00	112.00	72.00	63.00	40.00	72.00	68.00	52.00
Rb	1.90	4.40	3.50	2.80	1.20	1.10	3.80	2.40	2.50	4.70	1.00	0.60	0.40	0.50	0.70	0.50	1.80	1.50	3.10	2.70	2.20	3.20
Ba	15.00	23.00	26.00	35.00	12.00	10.00	35.00	31.00	12.00	38.00	7.00	5.00	7.00	5.00	10.00	8.00	8.00	12.00	30.00	16.00	13.00	15.00
Nb	4.55	5.40	5.55	3.05	3.55	3.70	2.85	1.80	2.55	12.10	3.10	7.15	2.45	1.40	3.60	3.45	2.20	4.30	7.25	3.50	2.75	3.85
La	5.25	6.00	5.95	2.95	5.00	4.50	3.55	3.00	3.25	13.35	3.90	8.15	2.80	2.50	4.40	4.30	3.45	4.95	8.15	4.35	3.65	4.65
Ce	14.00	16.50	16.00	11.50	14.50	14.50	10.50	9.50	9.50	42.00	14.00	24.50	9.00	8.50	13.00	12.00	11.00	14.00	23.00	12.00	12.00	14.00
Sr	100.00	117.00	120.00	145.00	115.00	148.00	115.00	140.00	117.00	115.00	78.00	47.00	124.00	117.00	105.00	135.00	106.00	105.00	131.00	105.00	105.00	106.00
Nd	15.00	18.00	17.00	9.00	14.00	13.50	11.00	9.00	10.00	40.00	9.00	25.50	8.50	8.00	14.00	12.00	11.00	16.00	22.00	15.00	14.00	14.50
Zr	130.00	155.00	142.00	58.00	114.00	109.00	69.00	82.00	84.00	332.00	40.00	145.00	60.00	53.00	106.00	75.00	85.00	123.00	181.00	113.00	100.00	118.00
Eu	1.60	1.95	1.70	0.95	1.25	1.45	1.15	1.00	0.95	3.30	0.95	2.05	1.00	0.90	1.45	1.05	1.20	1.55	1.95	1.50	1.45	1.55
Dy	7.70	8.70	7.60	4.30	5.80	6.60	4.80	4.20	3.90	18.20	4.30	9.50	4.40	3.90	7.00	5.00	5.80	7.60	9.50	7.10	6.70	7.00
Y	47.00	53.00	46.00	25.00	35.00	38.00	28.00	26.50	24.00	100.00	26.00	55.00	26.00	23.00	42.00	30.00	35.00	45.00	57.00	42.00	40.00	44.00
Er	4.90	5.70	4.90	2.80	3.50	4.10	3.10	2.70	2.60	10.70	2.50	6.00	2.60	2.70	4.40	3.00	3.90	4.70	6.10	4.70	4.20	4.70
Yb	4.65	5.18	4.58	2.38	3.38	3.88	2.70	2.60	2.33	9.68	2.25	5.13	2.55	2.23	4.13	2.90	3.48	4.58	5.53	4.28	3.98	4.38
Eu*-man	1.16	0.79	1.09	0.50	1.42	0.73	0.31	0.13	0.47	5.36	0.50	3.06	0.14	0.18	1.20	1.37	0.83	1.69	2.63	1.28	0.98	0.76
FeO*	11.47	11.45	11.95	8.75	9.18	11.25	9.76	9.20	8.63	17.19	8.01	13.36	8.59	7.38	10.98	9.00	10.12	11.92	13.18	11.25	10.66	12.23
Mg#	52.95	47.91	53.51	65.80	62.43	55.61	61.16	65.68	65.94	33.74	63.34	47.12	60.64	68.61	56.12	60.80	58.63	53.45	46.46	54.37	57.19	53.01
CaO/Al2O3	0.81	0.79	0.81	0.76	0.78	0.73	0.77	0.71	0.76	0.67	0.62	0.69	0.73	0.73	0.79	0.75	0.76	0.74	0.75	0.83	0.85	0.80
Al2O3/TiO2	7.18	6.13	6.76	13.19	12.11	8.37	11.07	13.11	14.70	3.22	13.42	4.99	14.33	15.77	8.12	11.39	10.07	6.27	5.34	7.58	8.41	7.17
CaO/Na2O	4.77	4.27	4.40	4.30	4.16	3.11	4.29	3.94	5.23	2.51	2.20	2.48	4.72	4.39	3.98	4.40	4.50	3.56	3.59	4.63	4.75	4.30
Si8	48.97	49.61	49.80	49.22	50.08	48.22	49.85	48.88	48.95	47.69	50.26	48.12	48.02	47.86	48.29	47.43	48.19	47.29	48.75	49.75	49.87	49.19
Na8	1.77	1.62	2.08	2.79	2.54	2.94	2.47	3.00	2.33	1.71	3.98	2.89	2.08	2.66	2.42	2.29	2.18	2.29	1.92	2.02	2.16	2.09
Fe8	8.64	8.70	9.80	9.10	8.25	9.47	8.93	10.18	8.88	10.98	8.93	9.72	8.03	7.16	9.06	7.02	8.46	9.73	9.16	8.82	8.92	10.12
Zr/Nb	28.57	28.70	25.59	18.36	32.11	29.46	24.21	34.44	25.10	27.44	12.90	20.28	24.49	37.86	29.44	21.74	38.64	28.80	24.97	32.29	38.36	30.65
Zr/Y	2.77	2.92	3.09	2.24	3.26	2.87	2.46	2.34	2.67	3.32	1.54	2.64	2.31	2.30	2.52	2.50	2.43	2.73	3.18	2.69	2.50	2.68
Ti/Zr	90.85	92.05	87.39	124.18	63.63	94.05	116.43	113.13	99.29	65.19	175.36	110.81	119.90	117.64	100.11	111.91	105.80	103.33	83.47	99.74	101.92	97.55
(La/Yb)n	0.81	0.83	0.93	0.89	1.06	0.88	0.94	0.83	1.00	0.99	1.24	1.14	0.82	0.81	0.77	1.06	0.71	0.78	1.06	0.73	0.66	0.76

Smp. #	BN-04-14	BN-05-01§	BN-05-02	BN-05-04	BN-05-05	BN-05-06	BN-05-09	BN-05-10	BN-06-01^	BN-06-02	BN-06-03	BN-06-04§	BN-06-05§	BN-06-06	BN-06-07	BN-06-08	BN-06-09^	BN-06-10§	BN-06-11	BN-06-12	BN-06-13	BN-06-14§
MORB Grp.	N	M	N	M	M	M	N	N	M	M	N	Altered	M	N	N	N	N	N	N	N	N	N
Petro. Grp.	III		VII	II	II	II	I	VI	II	II	II	I	IX	III	III	V	IX	I	III	III	I	I
Type	v.fg-B	ud	fg-D	cg-D	mg-D	mg-D	fg-B	mg-B	mg-D	mg-D	mg-MD	gl-B	b-brs	gVfg-B	gVfg-B	fg-B	B-Bm	v.fg-B	v.fg-B	gVfg-B	gVfg-B	fg-B
Xstal.	h-PCg,PCOp		s-PCp	a-o	a	a-o	h-PCg	s-OPp	a-o	a	a-o	s-PCp		h-PCg,POp	h-PCg,POp	s-Pp	PCp	m-Pp,PCg	s-CPg,POp	h-PCOg,Pp	m-PCg	s-PCg,Pp
Char.	sv						sv	sv		sv				sv	sv	sv		sv	sv	sv	sv	sv
Meta.	hA	V	mA,sV	mA,sV	mA,sV	hA	sA,sV	sA	mA,sV	hA,sV	hA,sV			sA,sV		mA,mV		hA,mV	sV	sV		mA
in-pl/talus	lp	lp	l	lp	lp	lp	lp	lp	lp	l	lp	lp	l	l	l	lp	lp	lp	lp	lp	lp	lp
emp. ht.	2218.00	4301.00	4302.00	3994.00	3906.00	3780.00	3484.00	3279.00	4081.00	3896.00	3744.00	3553.00	3553.00	3453.00	3062.00	2972.00	2838.00	2839.00	2729.00	2627.00	2407.00	2301.00
dist-axis	39.24	40.82	40.82	40.82	40.82	40.82	40.82	40.82	40.53	40.53	40.53	40.53	40.53	40.53	40.53	40.53	40.53	40.53	40.53	40.53	40.53	40.53
Sector	C	CE	CE	CE	CE	CE	CE	CE	CE	CE	CE	CE	CE	CE	CE	CE	CE	CE	CE	CE	CE	CE
Domain	Plateau	G8	G8	G7-C	G7-C	G6	E-10	E10	G4	G4	F5	F3	F3	E10	EP-S	EP-N	EP-N	EP-N	E8	E7	E5	Plateau
SiO2	50.40	51.20	48.70	48.25	49.60	49.60	49.50	49.20	50.60	49.80	49.00	47.60	48.30	49.40	48.60	49.50	49.40	49.10	48.70	49.55	49.55	50.20
TiO2	1.92	1.65	1.39	0.85	1.81	1.52	2.35	1.99	1.43	1.67	2.21	1.00	1.15	2.00	1.66	2.14	2.02	2.17	2.24	2.04	2.20	1.65
Al2O3	14.08	12.60	14.92	19.40	14.20	14.45	13.47	13.95	14.65	14.01	13.54	15.30	16.40	13.82	14.30	13.55	13.44	13.30	13.40	13.94	13.50	14.54
Fe2O3*	12.99	11.30	10.94	7.90	12.85	11.58	13.40	12.95	11.20	12.25	14.20	9.00	8.46	13.15	12.30	13.65	13.73	14.00	14.15	13.13	13.80	11.80
MnO	0.22	0.18	0.19	0.18	0.25	0.20	0.21	0.20	0.25	0.25	0.21	0.14	0.14	0.20	0.20	0.22	0.22	0.21	0.21	0.20	0.21	0.20
MgO	6.47	6.95	7.46	7.12	6.88	7.59	6.01	6.47	6.93	7.06	6.75	8.30	7.80	6.65	7.20	6.02	6.50	6.40	6.93	6.45	6.35	7.32
CaO	11.15	8.80	10.75	11.35	9.55	10.45	10.34	11.28	9.92	9.40	10.55	9.65	11.55	11.20	11.73	10.65	11.00	10.70	10.53	11.52	10.75	11.85
Na2O	2.61	3.40	3.18	2.72	3.62	2.78	2.58	2.50	3.18	3.28	2.52	3.10	2.78	2.51	2.51	2.50	2.57	2.70	2.50	2.56	2.65	2.56
K2O	0.23	0.62	0.12	0.37	0.40	0.24	0.27	0.23	0.44	0.54	0.29	0.61	0.08	0.19	0.15	0.35	0.36	0.19	0.30	0.18	0.23	0.21
P2O5	0.19	0.17	0.15	0.10	0.20	0.17	0.26	0.12	0.17	0.18	0.23	0.13	0.12	0.20	0.17	0.24	0.24	0.24	0.22	0.24	0.24	0.17
L.O.I.	-0.36	3.00	1.92	2.40	1.46	1.48	1.25	0.88	1.94	1.42	1.02	5.41	3.20	0.48	-0.35	0.96	1.55	0.40	1.07	0.47	0.39	-0.25
Total	99.87	99.85	99.62	100.62	100.70	100.04	99.64	99.77	100.71	99.89	100.52	100.14	99.97	99.80	99.87	99.76	101.03	99.40	99.97	100.26	99.87	100.25
Q	0.74						1.94							0.16								
or	1.36	3.66	0.71	2.19	2.38	1.42	1.60	1.36	2.60	3.19	1.71	3.60	0.47	1.12	0.89	1.33				0.06	0.42	
ab	22.09	28.77	26.91	23.02	29.79	23.52	21.93	21.15	26.91	27.75	21.32	26.23	23.52	21.24	21.24	2.07	2.13	1.12	1.77	1.06	1.36	1.24
an	26.03	17.29	25.81	38.64	21.77	26.24	24.38	26.16	24.40	21.91	24.78	26.03	32.04	25.88	27.31	21.15	21.75	22.85	21.15	21.66	22.42	21.66
ne																24.72	24.07	23.61	24.46	26.02	24.26	27.56
Di	23.13	20.69	21.69	13.00	20.01	20.04	20.84	23.92	19.43	19.34	21.52	16.61	19.82	23.39	24.44	21.98	23.90	23.07	21.65	24.50	22.73	24.67
Hy	19.29	19.80	5.70	4.51	9.99	16.85	19.11	18.72	15.09	11.54	20.66	2.67	7.36	19.72	17.20	19.27	18.89	19.37	20.60	18.56	19.82	16.08
Ol		0.05	10.94	11.89	10.94	4.09		0.02	4.20	7.79	0.94	14.94	8.80		2.07		0.85	0.53	0.62			2.57
mt	2.20	1.93	1.86	1.35	2.19	1.97	2.28	2.20	1.90	2.09	2.42	1.54	1.44	2.23	2.09	2.32	2.33	2.28	2.41	2.23	2.35	2.00
il	3.65	3.13	2.64	1.61	3.44	2.89	4.46	3.78	2.72	3.17	4.20	1.90	2.18	3.80	3.15	4.08	3.84	4.12	4.25	3.87	4.18	3.13
ap	0.44	0.39	0.35	0.23	0.46	0.39	0.60	0.28	0.39	0.42	0.53	0.30	0.28	0.46	0.39	0.56	0.56	0.56	0.56	0.51	0.56	0.39
Pl comp.-An	54	38	49	63	42	53	53	55	48	44	54	50	56	55	56	54	53	51	54	55	52	56
Sc	46.00	39.00	41.00	31.00	41.00	43.00	45.00	43.00	41.00	42.00	42.00	36.00	37.00	42.00	44.00	43.00	43.00	44.00	43.00	44.00	45.00	44.00
V	405.00	330.00	293.00	192.00	345.00	310.00	445.00	386.00	293.00	330.00	417.00	244.00	244.00	384.00	356.00	405.00	400.00	405.00	425.00	393.00	431.00	345.00
Cr	118.00	66.00	220.00	268.00	99.00	212.00	104.00	175.00	180.00	175.00	85.00	350.00	275.00	188.00	208.00	109.00	137.00	80.00	87.00	183.00	77.00	200.00
Co	49.00	41.00	42.00	36.00	45.00	42.00	48.00	43.00	42.00	44.00	44.00	43.00	38.00	43.00	43.00	44.00	44.00	45.00	45.00	46.00	47.00	43.00
Ni	57.00	55.00	70.00	77.00	47.00	61.00	57.00	61.00	59.00	56.00	47.00	112.00	101.00	59.00	69.00	52.00	49.00	51.00	49.00	66.00	50.00	71.00
Pb	2.80	2.50	0.90	3.30	3.60	2.70	3.10	3.90	6.50	6.60	2.70	-	-	2.20	1.70	4.60	5.10	-	2.00	2.40	2.20	2.00
Ba	18.00	10.00	16.00	42.00	29.00	21.00	16.00	15.00	60.00	73.00	17.00	20.00	7.00	18.00	12.00	25.00	21.00	18.00	16.00	18.00	18.00	13.00
Nb	3.80	3.80	3.10	1.20	4.50	3.90	5.25	4.80	4.30	4.60	4.95	3.00	2.40	5.05	3.25	5.50	4.55	5.60	5.15	4.80	6.05	2.80
La	4.65	5.00	3.65	2.30	5.40	4.40	6.70	5.20	5.65	4.70	5.70	3.00	3.10	5.35	3.70	6.15	5.75	6.00	6.00	5.30	6.30	4.20
Ce	14.50	16.00	12.50	8.50	16.00	14.00	20.00	16.00	18.00	13.50	17.00	-	-	16.00	12.50	19.00	17.00	-	18.00	17.00	18.00	12.00
Sr	107.00	100.00	145.00	168.00	126.00	114.00	112.00	115.00	113.00	116.00	110.00	108.00	127.00	114.00	101.00	113.00	116.00	115.00	110.00	118.00	117.00	104.00
Nd	14.00	13.00	10.50	8.50	14.00	13.00	18.00	16.00	16.00	12.00	17.00	-	-	16.00	12.00	18.00	18.00	-	17.00	16.00	17.50	11.50
Zr	119.00	73.00	86.00	40.00	98.00	81.00	161.00	131.00	101.00	97.00	145.00	60.00	82.00	131.00	99.00	149.00	136.00	147.00	150.00	135.00	150.00	100.00
Eu	1.65	1.45	1.20	0.85	1.50	1.30	1.90	1.60	1.25	1.30	1.80	-	-	1.60	1.35	1.85	1.50	-	1.75	1.55	1.70	1.25
Dy	7.20	6.10	5.10	2.90	6.20	5.50	9.20	7.40	5.60	6.40	9.10	-	-	7.20	6.10	8.30	7.60	-	8.40	7.60	8.00	6.30
Y	45.00	38.00	30.00	17.00	39.00	34.00	56.00	46.00	52.00	33.00	51.00	23.00	24.50	45.00	38.00	50.00	48.00	47.00	50.00	45.00	50.00	38.00
Er	4.70	3.20	3.20	1.70	3.80	3.70	5.80	5.00	3.50	3.50	5.20	-	-	4.90	4.10	5.00	4.80	-	5.20	4.80	5.20	3.90
Yb	4.35	3.40	3.10	1.55	3.33	3.05	5.40	4.35	3.50	3.20	4.75	2.20	2.35	4.40	3.68	4.78	4.52	4.70	4.80	4.35	4.83	3.65
Eu*-man	0.77	0.18	0.11	-0.78	0.25	0.58	1.50	1.23	1.85	1.02	0.90			1.08	0.48	2.25	2.58		1.44	1.69	1.58	1.09
FeO*	11.68	10.17	9.84	7.11	11.56	10.40	12.08	11.65	10.08	11.02	12.78	8.10	7.61	11.83	11.07	12.28	12.35	12.60	12.73	11.81	12.42	10.62
Mg#	53.21	58.35	60.83	67.24	54.67	59.93	50.53	53.23	58.50	56.76	51.99	67.74	67.75	53.53	57.14	50.11	51.89	51.01	51.63	52.81	51.18	58.56
CaO/Al2O3	0.79	0.70	0.73	0.59	0.67	0.72	0.77	0.81	0.68	0.67	0.78	0.62	0.70	0.81	0.82	0.78	0.82	0.80	0.79	0.83	0.80	0.81
Al2O3/TiO2	7.33	7.64	10.66	22.82	7.85	9.51	5.73	7.01	10.24	8.39	6.13	15.30	14.26	6.91	8.61	6.33	6.05	6.13	5.98	6.83	6.14	8.81
CaO/Na2O	4.27	2.59	3.38	4.17	2.71	3.76	4.01	4.51	3.12	2.87	4.19	3.09	4.15	4.46	4.67	4.26	4.28	3.96	4.21	4.50	4.06	4.63
Si8	49.93	50.87	48.53	47.98	49.25	49.47	48.88	48.73	50.27	49.51	48.61	47.69	48.24	48.98	49.55	48.88	48.94	48.60	48.28	49.07	49.04	49.99
Na8	2.04	3.01	2.98	2.39	3.09	2.63	1.84	1.93	2.78	2.93	2.05	3.21	2.71	2.01	2.21	1.76	2.01	2.10	1.99	1.98	2.03	2.31
Fe8	9.12	8.42	8.95	5.64	9.67	9.72	8.75	9.11	8.30	9.46	10.70	8.60	7.28	9.59	9.74	8.99	9.88	9.94	10.45	9.24	9.87	9.49
Zr/Nb	31.32	19.21	27.74	33.33	22.00	20.77	30.67	27.29	23.49	11.88	29.29	20.00	25.83	25.94	30.46	27.09	29.69	26.25	29.13	28.13	24.79	35.71
Zr/Y	2.64	1.92	2.87	2.35	2.54	2.38	2.88	2.85	1.94	1.73	2.84	2.61	2.53	2.91	2.61	2.98	2.83	3.13	3.00	3.00	3.00	2.63
Ti/Zr	96.73	135.51	96.90	127.40	109.61	112.50	87.51	91.07	84.88	175.65	91.37	99.92	111.20	91.53	100.52	86.10	89.04	86.60	89.53	90.59	87.93	98.92
(La/Yb)n	0.77	1.06	0.84	1.06	1.17	1.04	0.89	0.86	1.16	1.05	0.86	0.88	0.95	0.87	0.72	0.92	0.91	0.92	0.88	0.87	0.94	0.83

Smp. #	BN-07-04	BN-07-05	BN-08-01	BN-08-04	BN-08-05	BN-09-01	BN-09-03	BN-10-01	BN-10-02B	BN-10-06	BN-10-07	BN-10-10	BN-10-11	BN-10-13	BN-10-15	BN-10-16	BN-10-18	BN-10-19	BN-10-20	BN-12-01	BN-12-02	BN-13-01
MORB Grp.	N	Altered	N	N	N	M	N	N	N	N	N	N	N	N'	N	N	M	N	N	N	N	Altered
Petro. Grp.	VII	I	I	VI	III	VI	VI	VI	IX	VI	II	IV	I	V	I		I	II	III	I	I	IV
Type	fg-D	GV/fg-B	gl-B	fg-B	fg-B	gl-B	fg-B	fg-B	mg-B-Bra	mg-B	mg-D	fg-B	mg B	mg-B	fg-B	ud	v.fg-B	fg-D	fg-B	fg-B	fg-B	b
Xstal.	s-Pp	m-PCs,PCp	m-PCp	PCp	m-PCOp	m-OPp	m-OPp	s-POp	s-Pp	s-OPp	s-o	a	s-PCp	s-Pp	s-PCg,PCp		s-PCg	a	s-PCg,POp	h-PCg,Pp	m-PCg,PCp	a
Char.			v	v		v		sv	Px,mv	sv		sv	sv	sv			sv	Px	mv	Px,mv	mv	sv
Meta.	A	V	V	A			A	A	hA,sV	hA,sV	hA	mA	hA,sV	hA	sA,sV		sV	sA,sV	hA,sV	mA,sV		V
In-pl/satus	I	Ip	Ip	Ip	I	Ip	Ip	I	Ip	Ip	Ip	Ip	Ip	Ip	Ip	Ip	Ip	Ip	Ip	Ip	Ip	I
emp. ht.	4126.00	4048.00	4530.00	3543.00	3199.00	4641.00	4380.00	3709.00	3630.00	3581.00	3577.00	3510.00	3481.00	3456.00	3057.00	2992.00	2937.00	2937.00	2841.00	2189.00	2089.00	4402.00
diel-axis	42.26	42.26	44.00	44.00	44.00	44.13	44.13	42.74	42.74	42.74	42.74	42.74	42.74	42.74	42.74	42.74	42.74	42.74	42.74	37.56	37.56	35.09
Sector	Œ	Œ	E	E	E	E	E	Œ	Œ	Œ	Œ	Œ	Œ	Œ	Œ	Œ	Œ	Œ	Œ	C	C	OW
Domain	G8	G7-E	L7-E	Q6	Q3	A6	A5	L2-W	K3	L2-E	L2-E	L1	L1	L1	P1	K7	P1	K7	K4	Plateau	Plateau	V4
SiO2	48.80	50.00	49.70	49.20	49.20	48.20	49.00	49.20	48.40	49.40	49.10	48.80	48.60	47.60	49.00	48.90	49.40	49.10	49.55	50.30	50.70	45.90
TiO2	1.11	1.20	2.28	2.34	2.10	1.03	2.15	2.70	2.15	1.78	1.56	2.44	1.54	2.34	1.64	1.54	1.99	2.02	2.26	1.91	1.97	3.37
Al2O3	15.77	14.35	14.35	13.40	13.57	16.10	13.80	13.30	13.40	14.90	14.80	13.20	14.45	13.54	14.25	14.65	13.32	13.80	13.95	14.26	14.38	12.39
Fe2O3*	9.53	8.98	13.30	14.30	13.61	10.60	13.70	14.90	13.27	10.62	10.63	14.90	11.75	14.10	12.00	11.22	14.57	13.15	13.27	12.69	12.36	16.08
MnO	0.17	0.16	0.20	0.22	0.21	0.18	0.21	0.22	0.22	0.19	0.21	0.21	0.19	0.21	0.20	0.20	0.21	0.20	0.20	0.21	0.22	0.20
MgO	8.57	7.67	7.00	6.25	6.20	10.10	7.83	5.42	6.80	7.07	7.55	6.25	7.15	6.25	7.30	7.50	6.69	7.07	6.57	6.57	6.45	5.76
CaO	10.67	9.45	10.65	10.65	10.63	10.90	10.30	10.50	9.40	10.75	11.70	9.60	11.92	10.00	12.00	11.75	9.77	10.29	11.20	11.18	11.35	9.04
Na2O	2.85	4.18	2.63	2.50	2.34	2.41	2.48	2.56	2.90	3.03	2.72	2.75	2.39	2.87	2.30	2.70	2.58	2.70	2.57	2.63	2.63	3.20
K2O	0.36	0.80	0.33	0.28	0.28	0.17	0.25	0.40	0.08	0.17	0.10	0.12	0.07	0.10	0.11	0.10	0.16	0.18	0.38	0.24	0.23	0.26
P2O5	0.12	0.13	0.27	0.26	0.24	0.13	0.25	0.31	0.22	0.19	0.16	0.27	0.17	0.29	0.18	0.16	0.22	0.24	0.24	0.19	0.21	0.40
L.O.I.	2.60	2.97	0.37	0.93	0.99	-0.23	0.36	0.74	3.31	2.55	2.09	1.14	1.70	2.60	1.34	1.77	0.94	1.37	1.07	0.25	-0.23	0.96
Total	100.55	99.89	101.05	100.33	99.57	99.79	100.43	100.25	100.15	100.83	100.62	99.68	99.93	99.89	100.32	100.49	99.83	100.12	100.25	100.43	100.27	99.56
Q				0.78	1.56			1.54				0.65					0.93		1.12	0.39	1.02	1.39
or	2.13	4.73	1.95	1.65	1.65	1.00	1.48	2.36	0.47	1.00	0.59	0.71	0.41	0.59	0.65	0.59	0.95	1.08	2.25	1.42	1.36	1.54
ab	24.12	30.33	22.25	21.15	19.80	20.39	20.99	21.68	24.54	25.64	23.02	23.27	20.22	25.13	19.46	22.85	21.66	22.85	21.75	22.25	22.25	27.08
an	29.18	18.03	26.38	24.52	25.70	32.61	26.06	23.62	23.31	26.56	27.88	23.32	28.50	23.32	28.24	27.56	24.38	25.01	25.41	26.40	26.75	18.68
ne		2.73																				
Di	18.63	22.73	20.31	22.03	21.88	18.71	19.21	22.01	18.02	20.86	23.75	18.66	24.22	20.23	24.70	24.27	18.74	20.13	23.68	22.92	23.20	3.09
Hy	6.73		19.60	20.35	19.76	8.21	20.47	19.45	21.29	12.54	11.23	22.62	15.43	14.32	17.42	10.26	24.00	20.12	16.55	19.30	19.35	29.16
Ol	12.21	13.38	1.70			15.91	3.51		1.02	4.97	5.86		2.95	4.88	1.74	6.87		1.64				
mt	1.82	1.52	2.28	2.44	2.32	1.84	2.33	2.54	2.26	1.84	1.81	2.54	2.00	2.39	2.04	1.81	2.48	2.23	2.26	2.16	2.10	2.74
il	2.11	2.28	4.27	4.44	3.99	1.96	4.08	5.13	4.08	3.34	2.96	4.63	2.92	4.44	3.11	2.92	3.78	3.84	4.27	3.63	3.74	6.40
ap	0.28	0.30	0.63	0.60	0.58	0.30	0.58	0.72	0.51	0.44	0.37	0.63	0.39	0.65	0.42	0.37	0.51	0.58	0.56	0.44	0.49	0.93
Pl comp.-An	55	37	54	54	56	62	55	52	49	51	55	50	56	48	59	55	53	52	54	54	55	41
Sc	39.00	44.00	42.00	44.00	44.00	38.00	40.00	42.00	44.00	45.00	44.00	44.00	44.00	45.00	45.00	45.00	44.00	44.00	44.00	47.00	46.00	44.00
V	254.00	272.00	410.00	430.00	400.00	222.00	395.00	470.00	413.00	370.00	336.00	460.00	340.00	418.00	350.00	328.00	420.00	380.00	420.00	395.00	400.00	550.00
Cr	350.00	383.00	250.00	98.00	130.00	386.00	270.00	134.00	95.00	200.00	307.00	67.00	285.00	122.00	296.00	308.00	81.00	151.00	98.00	117.00	97.00	17.00
Co	43.00	41.00	46.00	47.00	47.00	56.00	47.00	48.00	47.00	51.00	45.00	47.00	43.00	44.00	45.00	44.00	47.00	45.00	53.00	46.00	47.00	50.00
Ni	118.00	68.00	110.00	56.00	64.00	255.00	135.00	58.00	48.00	77.00	81.00	44.00	77.00	48.00	74.00	62.00	45.00	53.00	67.00	59.00	55.00	20.00
Pb	2.70	7.60	5.20	4.90	6.50	2.10	3.50	6.20	1.00	1.80	1.40	1.40	1.00	1.10	1.30	1.10	1.60	1.80	6.10	2.80	2.20	3.80
Ba	48.00	95.00	27.00	14.00	17.00	16.00	19.00	28.00	8.00	12.00	8.00	18.00	8.00	11.00	11.00	8.00	11.00	22.00	17.00	20.00	19.00	25.00
Nb	2.05	2.60	7.00	4.40	4.55	3.35	5.60	7.10	4.00	3.80	2.95	5.35	2.95	5.55	4.00	3.25	3.25	5.55	5.05	3.40	3.85	8.60
La	2.35	2.85	6.85	5.90	5.35	2.95	6.00	7.75	5.75	4.35	3.60	6.10	3.85	6.90	4.60	3.50	4.75	6.00	5.75	4.15	4.90	8.80
Ce	9.00	11.00	20.00	19.00	18.00	10.00	18.50	26.00	19.00	15.00	12.00	18.50	11.00	21.00	14.50	12.00	14.00	18.50	19.00	14.50	16.50	31.00
Sr	156.00	142.00	125.00	106.00	115.00	116.00	114.00	115.00	97.00	110.00	104.00	109.00	104.00	108.00	116.00	106.00	93.00	117.00	117.00	110.00	111.00	118.00
Nd	8.00	10.00	18.00	18.50	17.50	8.50	17.50	23.00	16.00	13.00	13.00	20.00	12.50	22.00	13.00	10.50	16.00	17.50	18.00	14.00	16.00	26.00
Zr	83.00	74.00	162.00	160.00	140.00	64.00	150.00	185.00	140.00	110.00	94.00	162.00	96.00	190.00	105.00	94.00	104.00	140.00	144.00	115.00	126.00	234.00
Eu	0.90	1.00	1.75	1.80	1.70	0.85	1.75	2.20	1.65	1.50	1.35	1.95	1.30	2.05	1.40	1.35	1.60	1.75	1.80	1.55	1.65	2.50
Dy	4.40	4.50	8.70	8.80	7.80	4.20	8.30	10.00	8.00	6.80	6.20	9.30	6.10	9.90	6.30	5.90	7.80	7.80	8.70	7.50	8.10	12.20
Y	24.00	27.50	54.00	55.00	47.00	26.00	51.00	61.00	49.00	40.00	35.00	56.00	37.00	62.00	37.00	37.00	47.00	47.00	50.00	46.00	49.00	72.00
Er	2.50	2.80	5.40	5.70	5.10	2.80	5.50	6.50	4.50	4.40	4.00	5.80	4.10	6.30	4.10	3.80	5.00	5.20	5.50	4.90	5.20	7.80
Yb	2.28	2.55	5.15	5.30	4.65	2.55	4.88	5.80	4.75	3.93	3.63	5.43	3.56	6.10	3.75	3.60	4.35	4.55	4.95	4.40	4.68	6.85
Eu'-man	0.59	0.67	1.98	1.92	1.40	0.87	1.51	1.84	1.42	0.45	0.85	1.87	0.92	2.36	0.84	-0.13	1.55	1.10	1.69	1.02	1.50	2.73
FeO*	8.58	8.08	11.97	12.87	12.25	9.72	12.33	13.41	11.94	9.74	9.56	13.41	10.57	12.69	10.80	10.10	13.11	11.93	11.94	11.42	11.12	14.47
Mg#	67.20	66.05	54.52	49.89	50.92	68.05	56.56	45.31	53.86	59.81	61.80	49.86	58.09	50.24	59.08	60.36	51.12	55.05	48.86	54.11	54.31	44.93
CaO/Al2O3	0.68	0.66	0.74	0.79	0.80	0.68	0.74	0.79	0.70	0.72	0.79	0.73	0.82	0.74	0.84	0.80	0.73	0.75	0.80	0.78	0.79	0.41
Al2O3/TiO2	14.21	11.96	6.30	5.73	6.46	15.63	6.47	4.93	6.23	8.47	9.49	5.41	9.36	5.79	8.69	9.51	6.69	6.83	6.20	7.47	7.30	3.68
CaO/Na2O	3.74	2.26	4.05	4.26	4.63	4.52	4.15	4.10	3.24	3.55	4.30	3.49	4.99	3.37	5.22	4.35	3.82	3.81	4.36	4.25	4.32	1.58
Si8	46.88	49.90	49.39	48.66	48.64	48.65	48.95	48.40	48.03	49.11	48.86	48.26	48.34	47.06	48.78	48.75	48.99	48.81	48.80	49.66	50.22	45.21
Na8	3.06	4.06	2.26	1.85	1.87	3.19	2.42	1.80	2.45	2.68	2.55	2.10	2.07	2.32	2.04	2.51	2.07	2.35	1.66	2.10	2.05	2.36
Fe8	9.52	7.53	10.30	9.98	9.25	13.21	12.04	9.11	9.94	8.19	8.82	10.50	9.16	9.78	9.63	9.26	10.93	10.28	7.90	9.04	8.54	10.74
Zr/Nb	30.73	28.46	23.14	36.36	30.77	19.10	26.79	26.06	35.00	28.21	31.86	30.28	32.54	34.23	26.25	28.92	32.00	25.23	28.51	33.82	32.73	27.21
Zr/Y	3.63	2.69	3.00	2.91	2.98	2.46	2.94	3.03	2.86	2.75	2.69	2.89	2.59	3.06	2.84	2.54	2.21	2.98	2.88	2.50	2.57	3.25
TiV/Zr	105.63	97.22	83.27	87.68	89.95	96.48	85.93	87.50	92.07	95.02	99.49	90.30	96.17	73.83	93.64	98.22	114.71	86.50	93.67	99.57	93.73	86.34
(La/Yb)n	0.74	0.80	0.95	0.80	0.83	0.83	0.86	0.96	0.87	0.80	0.71	0.81	0.77	0.81	0.88	0.70	0.78	0.95	0.83	0.88	0.75	0.92

Smp. #	BN-13-02	BN-13-03	BN-13-04	BN-13-05	BN-13-08	BN-13-11	BN-13-12	BN-13-13	BN-13-15	BN-23-02	BN-23-03	BN-23-04§	BN-23-05	BN-23-07	BN-23-08§	BN-24-01§	BN-24-02	BN-24-03	BN-24-04	BN-24-05^	BN-24-06§	BN-24-07
MORB Grp.	N	T	N	Altered	N	N	N	N	N	Altered	M	M	N	M	T	Altered	M	N	M	M	Altered	M
Petro. Grp.	IV	I	I	I	I	I	IV	V	I	IX	VII	IX	I	I	I	IX	I	V	IV	I	I	VII
Type	v.fg-B	v.fg-B	v.fg-B	fg-B	v.fg-MB	fg-B	mg-MB	fg-B	gt-B	MB-Bm	fg-D	mb	mg-Q	cg-D	v.fg-B	Bm	cg-MD	fg-B	v.fg-B	v.fg-B	v.fg-B	fg-D
Ketel.	e	e-PCg,Pp	m-PCg,Pp	PCg,PC/Op	e-PCg	h-PCg,PCg	e	e-Pp	m-PCg,Pp		e-Pa,e		e-e	e-e	h-PCg,Cp		e-e	e-Pp	e	h-PCg,PCg	e-PCg,PCp	e-Pp,e
Char.	Px,ev	Px,ev	ev	ev	ev	ev	ev	ev	ev						ev			ev	Pa	PCa		mv
Meta.	eV	mA,eV	mV	hA,eV	hA,eV	eA,eV	hA,eV		mV		hA,mV	V	mA,eV	hA,eV	mA,eV		hA,eV	A,eV	hA,eV	hA,eV	hA,hV	
in-pl/talus	I	I	I	I	I	I	I	Ip	Ip	I	I	Ip	Ip	Ip	Ip	I	Ip	Ip	Ip	Ip	Ip	Ip
emp. ht.	4400.00	4298.00	4277.00	4209.00	3788.00	3531.00	3532.00	3479.00	3330.00	4227.00	4144.00	4143.00	4077.00	3836.00	3684.00	4229.00	4197.00	4051.00	3984.00	3976.00	3792.00	3706.00
dist-axis	35.09	35.09	35.09	35.09	35.09	35.09	35.09	35.09	35.09	39.18	39.18	39.18	39.18	39.67	39.67	37.99	37.99	37.99	37.99	37.99	37.99	37.99
Sector	OW	OW	OW	OW	OW	OW	OW	OW	OW	C	C	C	C	C	C	C	C	C	C	C	C	C
Domain	V4	V3	V3	V3	U3	U2	U2	U2	U1	Talus	D3	D3	D3	G2	G1-N	Z3	Z3	Z2	Z2	Z2	Y2	Y2
SiO2	46.00	49.25	47.25	50.30	52.20	50.50	47.30	49.00	49.40	47.70	49.80	50.00	48.10	47.45	50.00	55.80	51.40	48.80	49.00	49.10	47.60	48.40
TiO2	3.05	2.85	2.61	2.20	2.28	1.80	3.67	1.84	2.92	0.99	1.92	1.30	2.13	1.03	1.69	1.13	1.34	1.51	1.62	1.77	1.00	1.23
Al2O3	11.90	12.32	13.10	13.08	13.03	13.10	12.08	13.85	12.30	16.64	14.55	15.05	13.45	16.51	14.20	12.30	13.85	14.94	14.20	14.10	15.20	15.41
Fe2O3*	17.65	15.79	15.00	13.09	12.97	12.64	18.00	13.25	15.12	8.80	11.35	10.80	13.65	9.65	12.40	8.88	10.88	10.88	12.36	12.48	8.10	10.29
MnO	0.30	0.24	0.25	0.21	0.23	0.19	0.26	0.21	0.28	0.13	0.25	0.20	0.23	0.20	0.21	0.17	0.17	0.20	0.21	0.23	0.13	0.17
MgO	9.13	4.48	6.30	5.90	5.69	6.20	5.27	6.48	5.25	7.17	6.85	7.30	6.81	7.73	6.40	5.32	7.33	6.77	7.20	6.88	8.40	7.98
CaO	8.85	9.11	9.33	8.56	8.63	8.24	7.45	10.95	9.05	8.33	9.85	7.60	7.77	11.55	10.10	8.50	7.16	11.70	9.90	9.71	9.58	11.50
Na2O	2.60	3.39	2.85	4.22	3.45	4.77	3.95	2.68	2.81	5.18	3.60	4.47	4.33	2.70	3.40	1.65	4.62	2.78	2.75	2.93	3.15	2.63
K2O	0.20	0.44	0.18	0.75	0.17	0.18	0.10	0.11	0.74	0.13	0.06	0.07	0.06	0.21	0.55	0.05	0.04	0.06	0.10	0.18	0.51	0.09
P2O5	0.35	0.34	0.18	0.23	0.26	0.21	0.45	0.22	0.35	0.10	0.20	0.14	0.23	0.12	0.18	0.12	0.15	0.15	0.17	0.17	0.12	0.13
L.O.I.	2.68	1.73	2.75	1.47	0.69	1.89	2.41	1.92	1.02	5.15	1.67	3.23	2.66	2.58	1.02	5.39	2.59	2.55	2.24	2.79	5.49	2.72
Total	100.09	99.94	99.81	100.01	100.50	99.70	100.84	100.61	99.24	100.12	99.80	100.16	99.62	99.73	100.22	99.28	99.71	100.12	99.75	100.32	99.26	100.64
Q		0.02		2.63					1.87							17.60						
or	1.18	2.60	1.12	4.43	1.00	0.95	0.59	0.65	4.37	0.77	0.35	0.41	0.35	1.24	3.25	0.30	0.24	0.35	0.59	1.09	3.01	0.53
ab	22.68	28.69	24.12	35.71	28.19	40.28	33.42	22.68	23.78	30.51	30.46	37.92	38.64	22.85	28.77	13.96	40.78	23.52	23.27	24.78	26.65	22.25
an	19.85	17.10	22.39	14.63	19.67	13.86	14.94	25.44	18.76	21.77	23.37	20.60	17.09	32.31	21.86	26.01	16.04	28.11	26.11	24.79	25.83	29.99
ne						0.04				7.22												
Di	18.57	23.57	18.82	21.85	21.62	21.17	15.98	22.65	19.87	15.36	19.84	13.08	16.46	19.71	22.26	12.72	15.13	23.72	17.99	18.32	16.81	21.35
Hy	18.76	16.20	17.18	1.48	17.56		12.13	19.42	19.13		9.82	4.58	9.80	2.72	7.16	19.96	7.19	10.41	21.06	19.10	3.66	9.63
Ol	4.95		4.01	12.28		14.19	8.66	1.08		14.91	7.98	14.62	17.19	13.49	8.88		11.02	5.31	1.69	2.34	13.44	8.65
m1	3.03	2.68	2.55	2.23	2.20	2.15	3.06	2.26	2.57	1.46	1.93	1.84	2.36	1.64	2.12	1.84	1.84	1.84	2.10	2.12	1.38	1.76
il	5.79	5.41	4.86	4.18	4.33	3.42	6.78	3.68	5.55	1.88	3.68	2.47	4.05	1.96	3.21	2.15	2.94	2.87	3.08	3.36	1.90	2.34
ap	0.81		0.42	0.53	0.60	0.49	1.04	0.51	0.81	0.23	0.46	0.33	0.53	0.28	0.44	0.28	0.35	0.35	0.39	0.39	0.28	0.30
Pl comp.-An	47	37	48	29	40	26	31	53	44	42	43	35	32	59	43	65	28	54	53	50	49	57
Sc	43.00	42.00	44.00	43.00	44.00	42.00	44.00	48.00	43.00	38.00	41.00	35.00	45.00	38.00	42.00	31.00	38.00	43.00	45.00	43.00	36.00	42.00
V	510.00	480.00	472.00	433.00	454.00	387.00	600.00	408.00	535.00	241.00	300.00	280.00	400.00	250.00	330.00	230.00	280.00	317.00	353.00	347.00	240.00	285.00
Cr	18.00	12.00	58.00	91.00	62.00	136.00	28.00	138.00	103.00	314.00	214.00	225.00	88.00	259.00	122.00	166.00	198.00	220.00	120.00	132.00	345.00	353.00
Co	45.00	46.00	43.00	48.00	53.00	45.00	46.00	46.00	42.00	44.00	46.00	39.00	46.00	42.00	41.00	29.00	41.00	41.00	45.00	50.00	43.00	43.00
Ni	21.00	20.00	38.00	55.00	60.00	49.00	34.00	53.00	47.00	87.00	99.00	96.00	54.00	73.00	43.00	51.00	92.00	72.00	55.00	62.00	109.00	88.00
Pb	2.60	4.60	3.00	7.30	2.00	1.20	1.20	1.50	7.30	4.00	0.90	0.50	1.00	2.80	9.00	-	1.00	0.90	1.00	2.30	-	0.90
Sn	12.00	30.00	13.00	47.00	18.00	26.00	14.00	13.00	78.00	9.00	12.00	10.00	10.00	40.00	18.00	8.00	4.00	8.00	15.00	28.00	17.00	7.00
Nb	7.80	8.65	7.25	4.80	4.85	3.90	8.75	4.30	8.85	1.85	4.40	3.70	5.05	1.80	4.30	2.70	3.85	3.05	3.60	5.10	3.10	2.60
La	8.55	9.25	7.23	5.35	5.85	5.05	10.60	5.60	8.20	2.80	6.15	4.60	5.30	2.58	6.00	3.20	3.80	3.45	3.60	4.30	3.10	3.00
Ce	30.00	28.00	24.00	18.00	20.00	17.00	31.00	16.50	25.00	8.50	19.00	13.00	16.00	9.00	19.00	-	13.00	12.00	12.00	14.00	-	10.50
Sr	110.00	109.00	120.00	98.00	90.00	103.00	79.00	108.00	80.00	84.00	133.00	93.00	132.00	151.00	130.00	18.00	51.00	125.00	99.00	102.00	106.00	115.00
Nd	27.00	25.00	22.00	17.00	18.00	14.60	30.00	14.00	23.00	8.00	18.00	11.00	17.00	8.00	14.00	-	12.00	11.50	11.50	14.00	-	8.00
Zr	210.00	210.00	178.00	148.00	151.00	118.00	270.00	126.00	205.00	58.00	88.00	63.00	127.00	42.00	132.00	45.00	47.00	89.00	74.00	78.00	60.00	68.00
Eu	2.60	2.35	2.20	1.80	1.85	1.45	2.80	1.45	2.30	0.90	1.50	1.25	1.60	0.80	1.55	-	0.95	1.35	1.35	1.95	-	1.05
Dy	12.30	11.40	9.50	8.20	8.50	7.00	14.50	7.40	11.30	3.80	7.30	5.00	8.00	3.80	8.80	-	5.10	5.20	6.20	6.60	-	4.80
Y	74.00	66.00	59.00	52.00	57.00	43.00	91.00	46.00	71.00	23.00	43.00	30.00	48.00	21.00	42.00	24.00	29.00	33.00	36.00	38.00	23.00	28.00
Er	7.80	7.00	6.40	5.20	5.70	4.30	8.60	4.50	7.20	2.40	4.20	3.20	4.70	2.30	4.20	-	3.20	3.60	3.80	4.10	-	2.80
Yb	6.85	6.38	5.70	5.00	5.50	4.05	8.58	4.43	6.85	2.18	4.28	2.73	4.48	2.00	4.05	2.30	2.80	3.20	3.38	3.60	2.25	2.65
Eu*-man	3.11	2.88	1.14	0.98	1.23	1.35	4.00	1.53	2.30	0.10	1.74	-0.12	2.01	-0.08	0.53		2.04	-0.40	0.41	-1.50		0.10
FeO*	16.06	14.21	13.50	11.79	11.67	11.37	16.20	11.92	13.61	7.74	10.21	9.72	12.46	8.68	11.21	7.97	9.77	9.77	11.12	11.23	7.29	9.25
Mg#	43.89	39.26	48.89	50.68	49.98	52.77	40.01	52.70	44.16	65.51	57.89	60.02	52.83	64.90	53.92	57.77	60.59	58.68	57.02	56.90	70.25	63.88
CaO/Al2O3	0.75	0.74	0.71	0.65	0.73	0.63	0.62	0.79	0.74	0.50	0.66	0.50	0.58	0.70	0.71	0.69	0.52	0.78	0.70	0.69	0.63	0.75
Al2O3/TiO2	3.90	4.32	5.02	5.95	5.71	7.28	3.38	7.14	4.21	16.81	8.88	11.58	6.31	16.03	8.40	10.88	10.34	9.89	8.77	7.97	15.20	12.53
CaO/Na2O	3.34	2.69	3.27	2.03	2.76	1.73	1.89	4.09	3.22	1.61	2.74	1.70	1.79	4.28	2.97	5.15	1.49	4.21	3.60	3.31	3.03	4.37
Si8	45.42	48.16	46.72	49.65	51.48	49.94	46.45	48.53	48.55	47.44	49.44	49.78	47.73	47.37	49.50	54.97	51.19	48.22	48.76	48.75	47.72	49.39
Na8	1.99	2.08	2.22	3.44	2.58	4.10	2.93	2.11	1.78	4.97	3.17	4.21	3.89	2.00	2.80	0.85	4.67	2.32	2.45	2.50	3.30	2.92
Fe8	12.95	9.35	10.67	8.28	7.83	8.39	11.65	9.39	9.03	6.36	8.30	8.55	10.48	8.23	8.55	3.51	8.66	7.73	8.79	9.33	7.96	9.22
Zr/Nb	26.92	24.28	24.55	32.17	31.13	30.26	30.86	29.30	29.50	31.35	20.00	17.03	25.15	23.33	30.70	18.67	12.21	29.18	20.56	24.52	19.35	29.15
Zr/Y	2.84	3.18	3.02	2.85	2.65	2.74	2.97	2.74	2.89	2.52	2.05	2.10	2.65	2.00	3.14	1.88	1.62	2.70	2.06	2.05	2.61	2.43
Ti/Zr	87.07	81.36	87.91	88.12	90.62	91.45	78.27	92.31	85.39	102.33	110.38	123.71	100.65	147.02	76.76	150.64	170.82	101.71	131.24	139.62	99.92	108.44
(La/Yb)n	0.90	1.04	0.91	0.77	0.78	0.89	0.89	0.91	0.85	0.86	1.04	1.21	0.85	0.81	1.06	1.00	0.97	0.77	0.77	0.86	0.99	0.81

Smp. #	BN-24-08S	BN-24-09S	BN-24-10^	BN-24-11S	BN-24-12	BN-24-13	BN-24-14^	BN-14-04S	BN-14-07S	BN-14-09S	BN-14-11S	BN-15-02S	BN-15-03S	BN-15-04S	BN-15-06S	BN-15-08S	BN-15-09S	BN-16-01S	BN-16-03S	BN-16-05S	BN-16-08S
MORB Grp.	N*	Altered	N	EI	N	N	N	EI	EI	EI	EI	EI	EI	EI	EI	N*	EI	EI	EI	EI	EI
Petro. Grp.	II	I	IV	V	II	I	I														
Type	v.fg-D	v.fg-B	fg-B	fg-MB	cg-D	fg-B	mg-B														
Xstal.	a-o	m-PCg,PCp	a,o	a-Pp	a-o	a-Cp,PCg,o	a-PCg,Pp														
Char.		sv	sv	sv		sv	mv														
Meta.		mA,hV	sA,mV	hA,eV	mA		hA														
in-pl/talus	I	I	ip	ip	ip	ip	ip														
emp. ht.	3497.00	3468.00	3448.00	2898.00	2594.00	2213.00	2113.00	3652.00	3561.00	3190.00	3093.00	2703.00	2495.00	2391.00	2193.00	2188.00	2129.00	3197.00	2785.00	2553.00	2528.00
dist-axis	37.99	37.99	37.99	37.99	37.99	37.99	37.99	38.43	38.43	38.43	38.43	42.23	42.23	42.23	42.23	42.23	42.23	39.62	39.62	39.62	39.62
Sector	C	C	C	C	C	C	C														
Domain	X4	X4	X4	X2-N	X1	X1	Plateau														
SiO2	48.20	45.80	48.30	47.75	49.40	50.20	50.20	49.00	47.90	49.20	47.50	50.30	50.10	50.50	50.60	50.50	49.75	49.10	50.00	50.50	50.35
TiO2	1.84	1.09	2.26	1.74	1.87	1.71	1.99	2.15	1.54	1.51	1.70	1.80	1.84	1.90	1.54	1.55	2.38	1.60	2.10	1.88	2.07
Al2O3	13.32	17.90	13.60	15.00	14.50	14.37	14.30	14.45	15.20	15.45	14.65	15.72	15.41	15.18	15.60	15.60	14.00	16.35	14.72	15.60	15.05
Fe2O3*	13.10	7.58	13.68	10.20	12.25	11.98	12.52	12.66	10.40	10.44	10.80	10.70	10.96	10.92	9.50	10.27	14.00	10.87	11.90	10.32	11.20
MnO	0.33	0.14	0.21	0.20	0.19	0.19	0.21	0.19	0.16	0.16	0.20	0.19	0.20	0.19	0.17	0.18	0.22	0.17	0.20	0.18	0.20
MgO	6.89	5.45	6.27	6.78	6.78	6.84	6.34	7.20	10.20	6.73	7.60	6.20	6.55	6.54	6.80	6.80	7.00	6.88	4.72	5.70	5.30
CaO	9.25	10.80	10.80	12.50	11.14	12.27	11.85	10.50	10.80	11.95	11.55	12.05	11.85	11.75	12.60	12.55	9.90	12.05	10.64	11.69	11.75
Na2O	3.67	4.52	3.78	2.86	2.63	2.08	2.63	2.85	2.65	2.80	2.77	2.93	2.81	2.85	2.72	2.67	2.80	2.59	3.10	3.02	3.06
K2O	0.26	0.65	0.11	0.21	0.12	0.20	0.25	0.38	0.26	0.35	0.22	0.37	0.33	0.32	0.29	0.31	0.32	0.46	0.89	0.53	0.42
P2O5	0.18	0.12	0.25	0.22	0.22	0.20	0.20	0.25	0.17	0.17	0.21	0.21	0.22	0.22	0.17	0.18	0.32	0.19	0.32	0.27	0.24
L.O.I.	2.48	6.12	1.70	3.11	1.18	0.33	-0.22	0.73	0.80	1.60	2.34	0.18	-0.20	-0.13	-0.08	-0.13	-0.72	0.88	1.12	0.37	0.42
Total	99.53	100.13	100.96	100.57	100.28	100.45	100.27	100.36	100.08	100.35	99.84	100.55	100.06	100.24	99.90	100.46	99.97	100.14	99.91	100.23	100.06
Q						1.83	0.04														
or	1.54	3.84	0.65	1.24	0.71	1.18	1.48	2.30	1.54	2.07	1.30	2.18	1.95	1.89	1.65	1.83	1.89	2.72	5.26	3.13	2.48
ab	31.05	18.65	29.45	24.20	22.25	17.60	22.25	24.12	22.42	23.69	23.44	23.95	23.78	24.12	23.02	22.59	23.69	21.92	25.23	25.55	25.89
an	19.10	26.64	19.82	27.47	27.41	29.28	26.48	25.48	26.81	26.56	26.89	29.10	28.48	27.68	29.53	29.67	24.69	31.63	23.62	27.45	26.09
ne		10.61	1.37																		
Di	21.05	21.33	26.55	27.03	21.71	24.66	25.55	20.48	19.11	24.23	23.68	24.03	23.67	23.89	25.96	25.78	18.40	22.13	23.29	24.40	25.27
Hy	2.82			0.46	19.01	18.63	17.08	12.43	4.04	7.20	4.12	11.44	11.99	13.90	11.66	11.31	21.25	10.23	10.76	9.87	11.58
Ol	14.01	8.57	12.85	10.49	0.64			6.73	17.23	6.94	11.14	2.87	3.46	1.93	2.28	3.32	1.74	4.21	1.66	2.52	0.82
mt	2.23	1.29	2.93	1.74	2.09	2.03	2.13	2.16	1.77	1.77	1.84	1.83	1.87	1.88	1.62	1.75	2.38	1.86	2.03	1.75	1.80
il	3.49	2.05	4.29	3.30	3.55	3.25	3.78	4.08	2.92	2.87	3.23	3.42	3.49	3.61	2.92	2.94	4.52	3.04	3.99	3.53	3.93
ap	0.44	0.28	0.58	0.51	0.51	0.46	0.46	0.58	0.39	0.39	0.49	0.48	0.51	0.51	0.39	0.37	0.74	0.44	0.74	0.63	0.59
Pl comp.-An	38	59	40	53	55	62	54	51	58	55	53	55	54	53	56	57	51	59	47	52	50
Sc	40.00	29.50	45.00	37.00	44.00	44.00	46.00	39.00	36.00	43.00	37.00	43.00	42.00	42.00	42.00	42.00	37.00	36.00	40.00	41.00	44.00
V	365.00	220.00	422.00	285.00	383.00	396.00	402.00	350.00	270.00	285.00	280.00	350.00	340.00	345.00	310.00	305.00	350.00	300.00	380.00	340.00	370.00
Cr	175.00	205.00	85.00	300.00	200.00	320.00	130.00	225.00	450.00	235.00	280.00	146.00	200.00	190.00	286.00	280.00	227.00	220.00	70.00	116.00	74.00
Co	44.00	29.00	45.00	43.00	45.00	45.00	47.00	48.00	58.00	48.00	44.00	57.00	43.00	48.00	48.00	43.00	47.00	40.00	48.00	43.00	53.00
Ni	72.00	58.00	51.00	135.00	71.00	94.00	63.00	125.00	330.00	88.00	125.00	85.00	58.00	57.00	72.00	60.00	110.00	55.00	48.00	53.00	41.00
Rb	-	-	1.90	2.20	2.00	3.20	2.80	4.70	2.70	4.10	2.50	3.30	4.00	4.00	3.30	3.40	4.40	8.20	17.20	7.30	3.50
Ba	18.00	13.00	10.00	35.00	18.00	13.00	17.00	35.00	18.00	25.00	34.00	27	28	35	34	40.00	44.00	32.00	98.00	63.00	33.00
Nb	4.30	2.60	4.90	6.85	5.05	3.79	3.80	6.70	4.30	5.10	6.55	6.10	6.45	6.90	4.70	5.00	9.80	5.20	13.00	11.50	6.80
La	4.30	2.90	6.35	6.60	5.30	4.50	4.85	7.30	4.70	5.30	6.20	6.10	6.40	6.45	4.80	4.85	9.25	5.50	10.80	9.40	7.00
Ce	-	-	19.50	17.00	16.50	13.50	14.00	20.00	13.00	12.50	15.50	14.00	16.00	17.00	13.00	15.00	26.00	16.00	27.00	21.00	17.00
Sr	97.00	170.00	104.00	202.00	118.00	88.00	107.00	158.00	189.00	181.00	175.00	169.00	154.00	153.00	153.00	152.00	138.00	155.00	175.00	172.00	177.00
Nd	-	-	19.50	13.50	15.00	13.00	16.00	16.00	11.50	11.00	13.50	14.00	14.00	15.00	11.00	11.00	21.00	12.00	19.00	17.00	15.00
Zr	122.00	88.00	136.00	125.00	130.00	109.00	126.00	150.00	108.00	105.00	120.00	130.00	125.00	135.00	100.00	103.00	200.00	110.00	180.00	150.00	145.00
Eu	-	-	1.85	1.45	1.70	1.35	1.55	1.80	1.35	1.40	1.40	1.50	1.55	1.65	1.25	1.30	2.05	1.30	1.80	1.65	1.75
Dy	-	-	9.20	5.80	6.90	6.80	7.50	7.40	5.00	5.10	5.60	6.50	6.50	6.50	5.40	5.50	8.80	5.70	7.40	6.80	7.40
Y	40.00	24.00	54.00	36.00	41.00	43.00	46.00	47.00	32.00	32.00	35.00	41.00	42.00	42.00	34.00	34.00	56.00	36.00	46.00	42.00	46.00
Er	-	-	6.00	3.60	4.50	4.40	5.40	4.60	3.00	3.20	3.30	4.20	4.20	4.40	3.30	3.50	5.80	3.50	4.30	4.00	4.70
Yb	4.00	2.40	5.55	3.20	3.95	4.13	4.65	4.20	2.85	2.80	3.20	3.80	3.85	3.15	3.15	5.05	3.30	3.30	4.25	3.85	4.30
Eu*-man			2.24	0.08	-0.07	1.34	1.31	0.04	-0.57	-0.93	0.21	0.50	0.20	-0.10	0.21	-0.01	1.17	0.45	0.92	0.57	0.04
FeO*	11.79	6.80	12.31	9.18	11.02	10.78	11.27	11.39	9.36	9.39	9.72	9.63	9.86	9.83	8.55	9.24	12.60	9.78	10.71	9.29	10.08
Mg#	54.50	62.16	51.06	60.22	55.77	56.93	53.56	60.29	68.46	58.32	61.31	59.78	59.23	51.55	58.76	58.55	60.70	54.45	46.99	50.83	48.77
CaO/Al2O3	0.69	0.60	0.79	0.83	0.77	0.85	0.83	0.73	0.71	0.77	0.79	0.77	0.77	0.77	0.81	0.80	0.71	0.74	0.74	0.75	0.78
Al2O3/TiO2	7.24	16.57	6.02	8.62	7.75	8.40	7.19	6.72	9.87	10.23	8.62	8.73	8.38	7.99	10.13	10.06	5.88	10.22	7.01	8.30	7.27
CaO/Na2O	2.52	2.39	2.86	4.37	4.24	5.90	4.51	3.68	4.08	4.27	4.17	4.26	4.22	4.12	4.63	4.70	3.54	4.65	3.50	3.93	3.84
Si8	47.86	45.01	47.76	47.37	49.02	49.87	49.69	48.75	49.59	48.61	47.38	49.74	49.65	50.05	50.23	50.13	49.44	48.44	48.98	49.79	49.51
Na8	3.26	3.57	3.13	2.40	2.17	1.68	2.01	2.55	3.47	2.33	2.62	2.16	2.27	2.31	2.27	2.22	2.43	1.80	1.88	2.16	2.05
Fe8	9.84	2.56	9.43	7.15	8.99	9.00	8.50	10.06	13.02	7.28	9.05	6.63	7.45	7.40	6.55	7.24	10.94	8.25	5.26	5.46	5.58
Zr/Nb	28.37	26.15	27.76	18.25	25.74	29.07	35.00	17.24	25.12	20.59	18.32	21.31	19.36	19.57	21.28	20.60	20.41	21.15	13.85	13.04	21.32
Zr/Y	3.05	2.83	2.52	3.47	3.17	2.53	2.74	3.19	3.38	3.28	3.43	3.17	2.98	3.21	2.94	3.03	3.57	3.06	3.91	3.57	3.15
Ti/Zr	90.42	95.22	99.62	83.45	86.24	94.05	94.66	85.93	85.49	86.22	84.93	83.01	88.25	84.38	92.32	90.22	71.34	87.20	69.94	74.34	85.58
(La/Yb)n	0.77	0.87	0.82	1.48	0.96	0.78	0.75	1.25	1.18	1.36	1.39	1.15	1.19	1.47	1.09	0.89	2.01	1.20	1.82	1.75	1.17

APPENDIX H: CRYSTALLIZATION AND MELTING MODELS

Table H-1:

Partition coefficients for olivine (OL), plagioclase (PLAG), clinopyroxene (CPX), spinel (SP), orthopyroxene (OPX) and garnet (GT) from the literature. These references include Reiners (1996), Smith et al. (1994), Elthon (1992), Johnson and Dick (1992), McKenzie and O'Nions (1991), Johnson et al. (1990), Le Roex et al. (1981) and Frey et al. (1978) and citations therein. The values of Reiners (1996) are averages primarily of McKenzie and O'Nions (1991) and Frey et al. (1978). For the calculations here, the value from the most recent compilation is used. In the case where none other is available, that of Reiners (1996) is included. These choices are reflected by the bold type.

Figures H-1 to H-5:

This series of figures displays the trace element modelling of equilibrium and fractional crystallization for the N- (Figure H-1), M- (Figure H-2), EG- (Figure H-3) and T- (Figure H-4) type chemical groups using the most primitive sample of each as the parent. For the T-MORBs, two additional parents are modelled (Figure H-5): a more primitive T-type parent on the north WBD scarp to the east, and the primitive N-type source within the site.

The phenocryst assemblage and the ratio of these crystallizing phases used to calculate bulk D for each group was obtained by iteration. Initially, the phases and modes were obtained from thin section observations (Appendix E). As a next step, modelling of major elements could have better constrained the fractionating assemblage. Instead, the approach here relied on petro-logic to find the best model fit to the data trend. The distribution coefficients of certain elements for these minerals (Table H) gives an idea of the vectors for each pair of elements plotted. These served as a guide in estimating the modal proportions of a phase assemblage that would be required to explain what is driving trace element change in the residual melt. The solution in each case was found by trying multiple permutations.

A summary of the results is given in Table 8-2.

Min.	OL	OL	OL	OL	OL	OL	OL	Min.	AMPH	Min.	PLAG	PLAG	PLAG	PLAG
Ref.	Reiners	Smith et al	Elthon	McK&ONions	Johnson&Dick	Le Roex et al	Frey et al	Ref.	McK&ONions	Ref.	Smith et al	McK&ONions	Le Roex et al	Hanson
Yr.	96	94	92	91	92	81	78	Yr.	91	Yr.	94	91	81	80
La	0.00045			0.0004			0.0005	La	0.17	La		0.27		
Ce	0.00065		0.001	0.0005	0.0010		0.0008	Ce	0.26	Ce		0.2		0.200
Pr				0.0008				Pr	0.35	Pr		0.17		
Nd	0.00115			0.0010	0.0008		0.0013	Nd	0.44	Nd		0.14		0.140
Sm	0.0016			0.0013	0.0010		0.0019	Sm	0.76	Sm		0.11		0.110
Eu	0.00175			0.0016	0.0030		0.0019	Eu	0.88	Eu		0.73		0.730
Gd				0.0015				Gd	0.86	Gd		0.066		0.067
Tb	0.0017			0.0015			0.0019	Tb	0.83	Tb		0.06		
Dy				0.0017	0.0120			Dy	0.78	Dy		0.055		0.055
Ho	0.0018			0.0016			0.0020	Ho	0.73	Ho		0.048		
Er				0.0015	0.0250			Er	0.68	Er		0.041		0.041
Tm				0.0015				Tm	0.64	Tm		0.036		
Yb	0.00275		0.03	0.0015	0.0050		0.0040	Yb	0.59	Yb		0.031		0.031
Lu	0.00315			0.0015			0.0048	Lu	0.51	Lu		0.025		
Zr	0.001	0.0070	0.0100		0.003	0.010		Zr		Zr	0.0050		0.010	
Nb	0.000			0.01		0.010		Nb	0.8	Nb		0.0100	0.010	
Y		0.0036				0.050	0.002	Y		Y	0.0200		0.180	
Rb	0.010			0.00018		0.010	0.01	Rb	-	Rb		0.1000	0.010	
Ba	0.000					0.010		Ba		Ba			0.010	
V		0.0500					0.09	V		V	0.0000			
Sr	0.002			0.00019		0.010	0.016	Sr	0.12	Sr		2.0000	1.800	
Sc	0.250	0.2650				0.150	0.25	Sc		Sc	0.0170		0.010	
Ga						0.010		Ga		Ga			0.900	
Ni	10.000	10.0000					~19.4	Ni	2.9	Ni	0.0400		0.010	
Co							~3.9	Co		Co			0.010	
Cr	0.300	0.6300						Cr		Cr	0.0000			
P	0.001							P		P				
P2O5						0.010		P2O5		P2O5				
K2O						0.010		K2O		K2O				
TiO2						0.010		TiO2		TiO2				
Ti			0.01	0.006	0.007			Ti	0.69	Ti		0.04		
Na			0.005					Na		Na				
								PHASE	amphi perid	PHASE	plag perid			
								Ref.	McK&ONions	Rel.	McK&ONions			
								Yr.	91	Yr.	91			
								ol	0.599	ol	0.636			
								opx	0.247	opx	0.263			
								cpx	0.038	cpx	0.012			
								amphi	0.116	plag	0.089			

Min.	CPX	CPX	CPX	CPX	CPX	CPX	CPX
Ref.	Reiners	Smith et al	Elthon	McK&ONions	Johnson&Dick	Le Roex et al	Frey et al
Yr.	96	94	92	91	92	81	78
La	0.00125			0.054			0.020
Ce	0.00195		0.12	0.098	0.100		0.040
Pr				0.150			
Nd	0.00435			0.210	0.220		0.090
Sm	0.0064			0.260	0.370		0.140
Eu	0.0083			0.310	0.420		0.160
Gd				0.300			
Tb	0.01245			0.310			0.190
Dy				0.330	0.500		
Ho	0.01745			0.310			0.195
Er				0.300	0.510		
Tm				0.290			
Yb	0.0388		0.45	0.280	0.490		0.200
Lu	0.049			0.280			0.190
Zr	0.200	0.0500	0.1500		0.15	0.200	
Nb	0.010			0.05		0.030	
Y		0.4200				0.500	0.2
Rb	0.050			0.011		0.010	0.05
Ba	0.001					0.010	
V		0.8000					1.5
Sr	0.100			0.067		0.100	0.165
Sc	3.100	1.7000				2.000	3.1
Ga						0.300	
Ni	2.000	3.0000				1.500	3
Co						1.000	1.2
Cr	4.000	8.0000					
P	0.020						
P2O5						0.010	
K2O						0.010	
TiO2						0.200	
Ti			0.4	0.1	0.35		
Na			0.15				
PHASE							
Ref.							
Yr.							

Min.	SP	SP	SP	SP
Ref.	Reiners	Elthon	McK&ONions	Johnson&Dick
Yr.	96	92	91	92
La	0.01		0.010	
Ce	0.01	0.001	0.010	0.0005
Pr			0.010	
Nd	0.01		0.010	0.0008
Sm	0.01		0.010	0.0008
Eu	0.01		0.010	0.0009
Gd			0.010	
Tb	0.01		0.010	
Dy			0.010	0.0015
Ho	0.01		0.010	
Er			0.010	0.0030
Tm			0.010	
Yb	0.01	0.03	0.010	0.0008
Lu	0.01		0.010	
Zr	0.001	0.100		0.0400
Nb	0.100			
Y				
Rb	0.001			
Ba	0.000			
V				
Sr	0.001			
Sc	0.001			
Ga				
Ni	1.300			
Co				
Cr	1.000			
P	0.001			
P2O5				
K2O				
TiO2				
Ti		0.15	0.048	0.0700
Na		0.005		
PHASE	melt mode	sp src mode	sp src mode	sp perid	sp lhz (%)
Ref.	Johnson et al	Johnson et al	Spiegelman	McK&ONions	Wilson
Yr.	90	90	96	91	89
ol	0.1	0.55	0.577	0.578	0.66
opx	0.2	0.25	0.29	0.27	0.24
cpx	0.68	0.18	0.1	0.119	0.08
sp	0.02	0.02	0.033	0.033	0.02

Min.	OPX	OPX	OPX	OPX	OPX	OPX	Min.	GT	GT	GT	GT	GT	
Ref.	Reiners	Elthon	McK&ONions	Johnson&Dick	Le Roex et al	Frey et al	Ref.	Reiners	McK&ONions	Johnson et al	Le Roex et al	Frey et al	
Yr.	96	92	91	92	81	78	Yr.	96	91	90	81	78	
La	0.037		0.0020			0.0005	La	0.007	0.010			0.0010	
Ce	0.069	0.001	0.0030	0.0050		0.0009	Ce	0.021	0.021	0.008		0.0033	
Pr			0.0048				Pr		0.054				
Nd	0.15		0.0068	0.0250		0.0019	Nd	0.087	0.087	0.057		0.0184	
Sm	0.2		0.0100	0.0400		0.0028	Sm	0.217	0.217	0.217		0.0823	
Eu	0.235		0.0130	0.0300		0.0036	Eu	0.32	0.320	0.450		0.1333	
Gd			0.0160				Gd		0.498				
Tb	0.25		0.0190			0.0059	Tb	0.725	0.750			0.2568	
Dy			0.0220	0.0450			Dy		1.060	2.000			
Ho	0.2525		0.0260			0.0089	Ho	1.465	1.530			1.0830	
Er			0.0300	0.0600			Er		2.000	3.500			
Tm			0.0400				Tm		3.000				
Yb	0.24	0.05	0.0490	0.0800		0.0286	Yb	4.03	4.030	7.000		4.0000	
Lu	0.235		0.0600			0.0360	Lu	5.6	5.500			7.0000	
Zr	0.010	0.040		0.02	0.010		Zr	0.300		0.5	1.200		
Nb	0.001				0.010		Nb	0.050			0.030		
Y					0.100	0.009	Y				3.000	1.4	
Rb	0.020		0.0006		0.010	0.020	Rb	0.020	0.0007		0.015	0.02	
Ba	0.000				0.010		Ba	0.000			0.020		
V						0.300	V					0.27	
Sr	0.016		0.007		0.010	0.016	Sr	0.008	0.0011		0.010	0.014	
Sc	1.100				0.400	1.100	Sc	6.500			10.000	6.5	
Ga					0.010		Ga				0.010		
Ni	1.000				3.000	4.000	Ni	0.800			0.100		
Co						2.000	Co					2	
Cr	1.000						Cr	4.000					
P	0.010						P	0.100					
P2O5					0.010		P2O5				0.015		
K2O					0.010		K2O				0.100		
TiO2					0.020		TiO2				0.200		
Ti		0.1	0.024	0.08			Ti		0.1	0.6			
Na		0.02					Na						
							PHASE	hi p - melt mode	lo p - melt mode	gt src mode	gt src mode	gt perid	gt thz (%)
							Ref.	Johnson et al	Johnson et al	Johnson et al	Spiegelman	McK&ONions	Wilson
							Yr.	90	90	90	96	91	89
							ol	0.03	0.13	0.55	0.5690	0.598	0.63
							opx	0.03	0.12	0.2	0.2200	0.211	0.3
							cpx	0.44	0.25	0.15	0.0660	0.076	0.02
							gt	0.5	0.5	0.1	0.1450	0.115	0.05

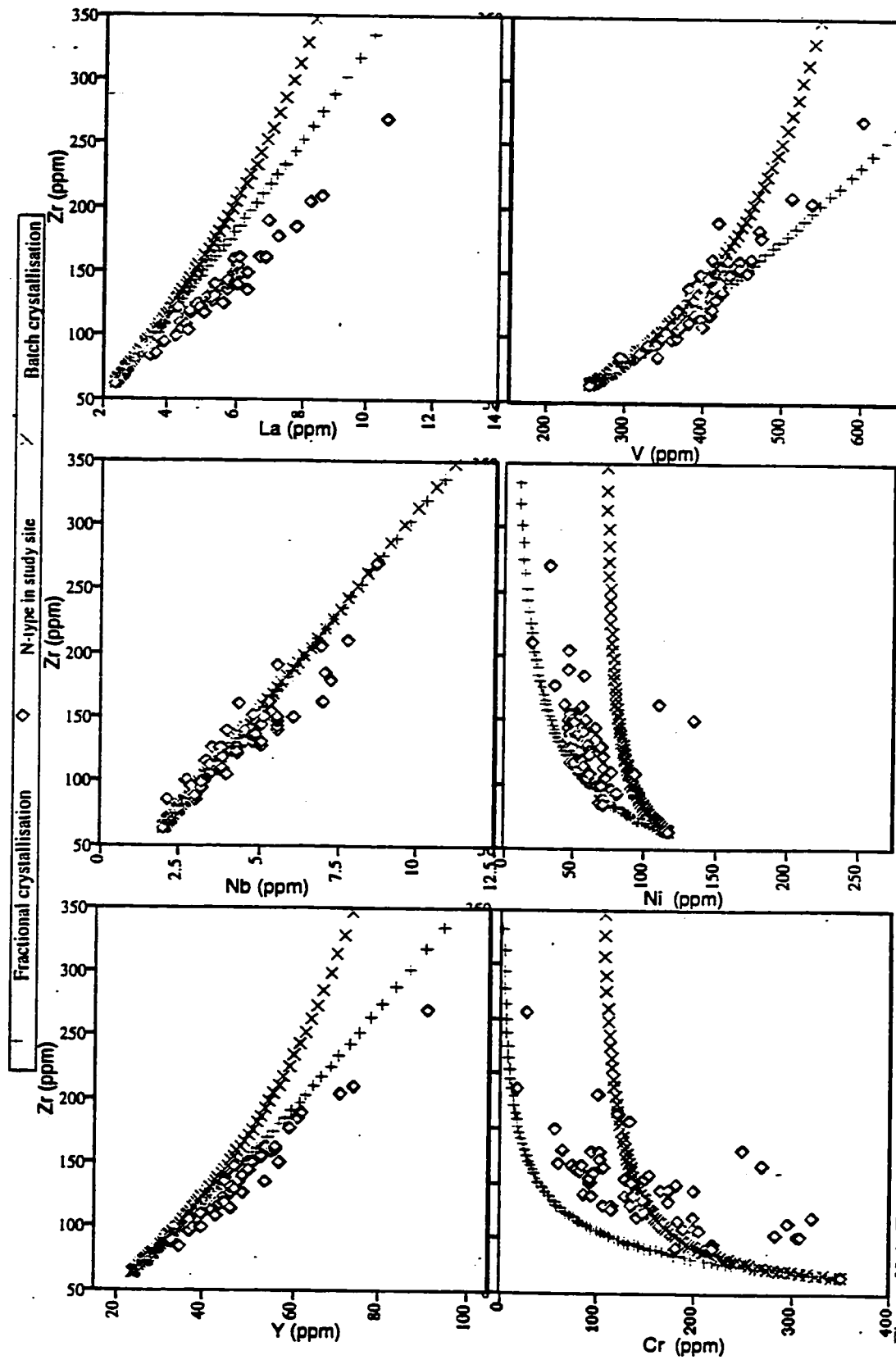

Figure H-1: Trace element crystallization model for the N-type MORB. Each cross represents 0.1 steps in F (fraction of liquid remaining). Fractional rather than equilibrium crystallization produces a better fit to the data. The phenocryst assemblage crystallizing is plag:cpx:ol = 0.45 : 0.45 : 0.1. The percentage of crystallization averages 74% with a range of 60-83%.

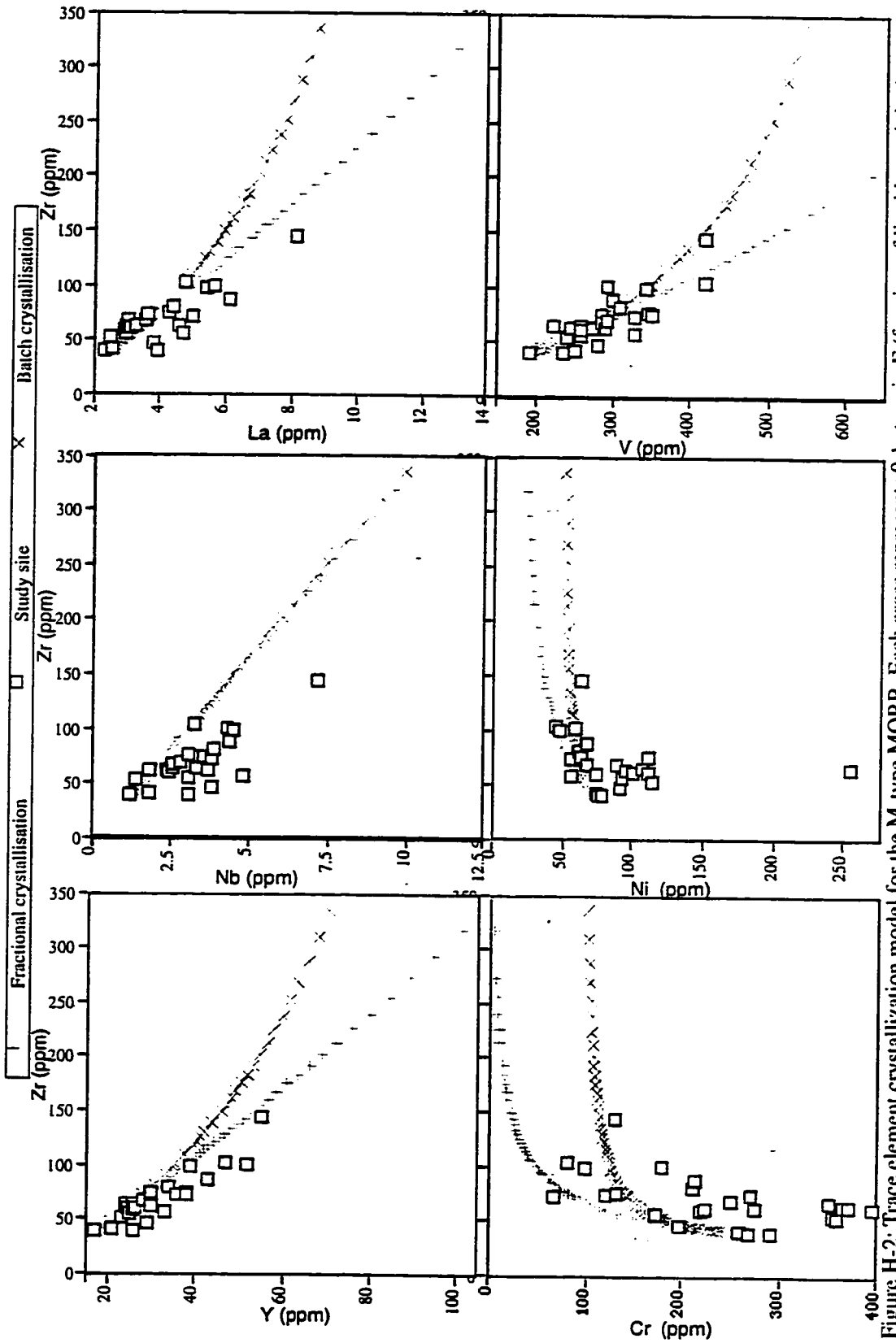

Figure H-2: Trace element crystallization model for the M-type MORB. Each cross represents 0.1 steps in F (fraction of liquid remaining). Fractional rather than equilibrium crystallization produces a better fit to the data. The phenocryst assemblage crystallizing is plag:cpx:ol = 60 : 35 : 5. The percentage of crystallization averages 68% with a range of 33-84%.

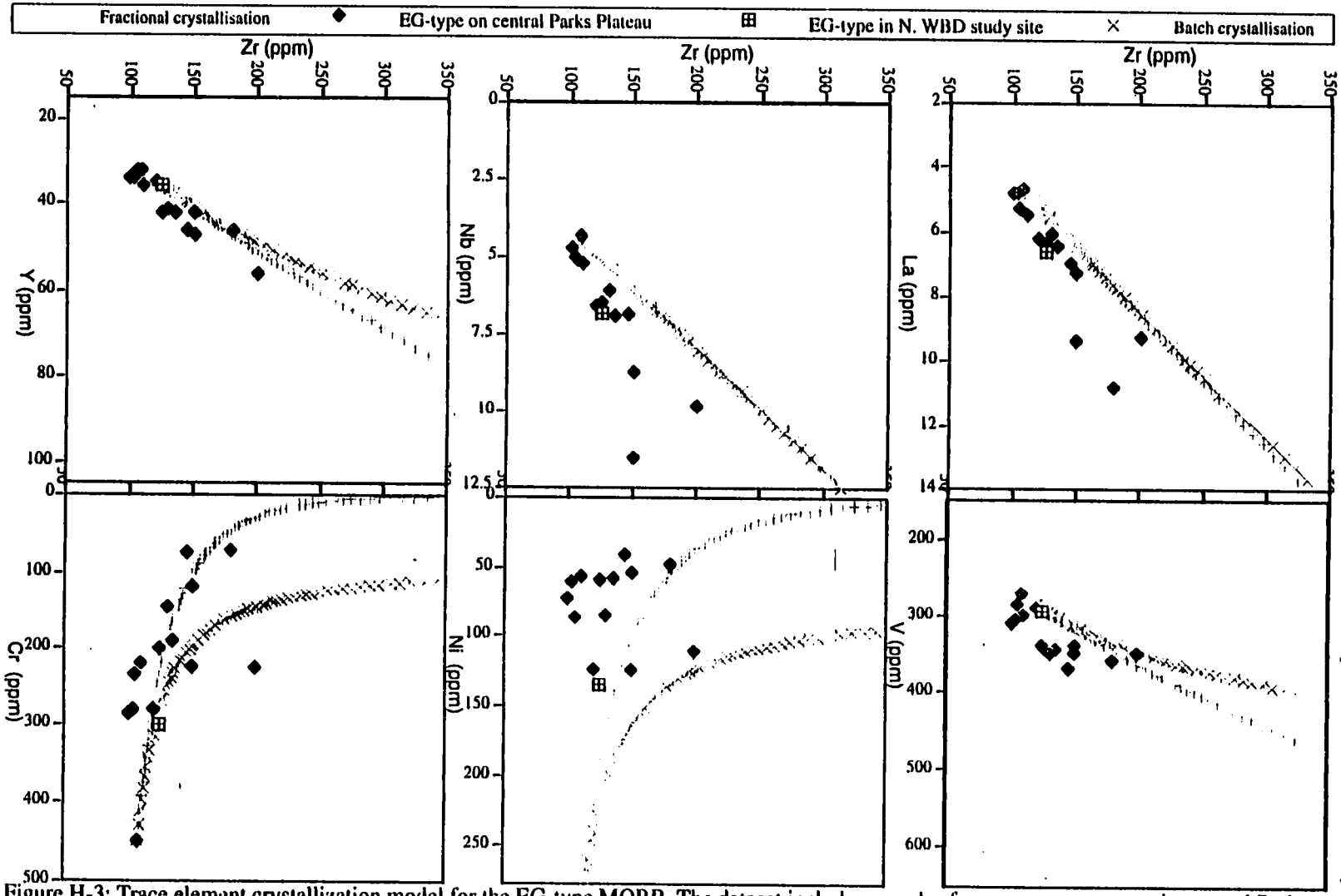

Figure H-3: Trace element crystallization model for the EG-type MORB. The dataset includes samples from a transect across the central Parks Plateau to the south of the study site (Juteau et al., 1995). Each cross represents 0.1 steps in F (fraction of liquid remaining). Fractional rather than equilibrium crystallization produces a better fit to the data. The assemblage is plag:cpx:ol = 10 : 65 : 25. The percentage of crystallization averages 21% with a range of 9-38%.

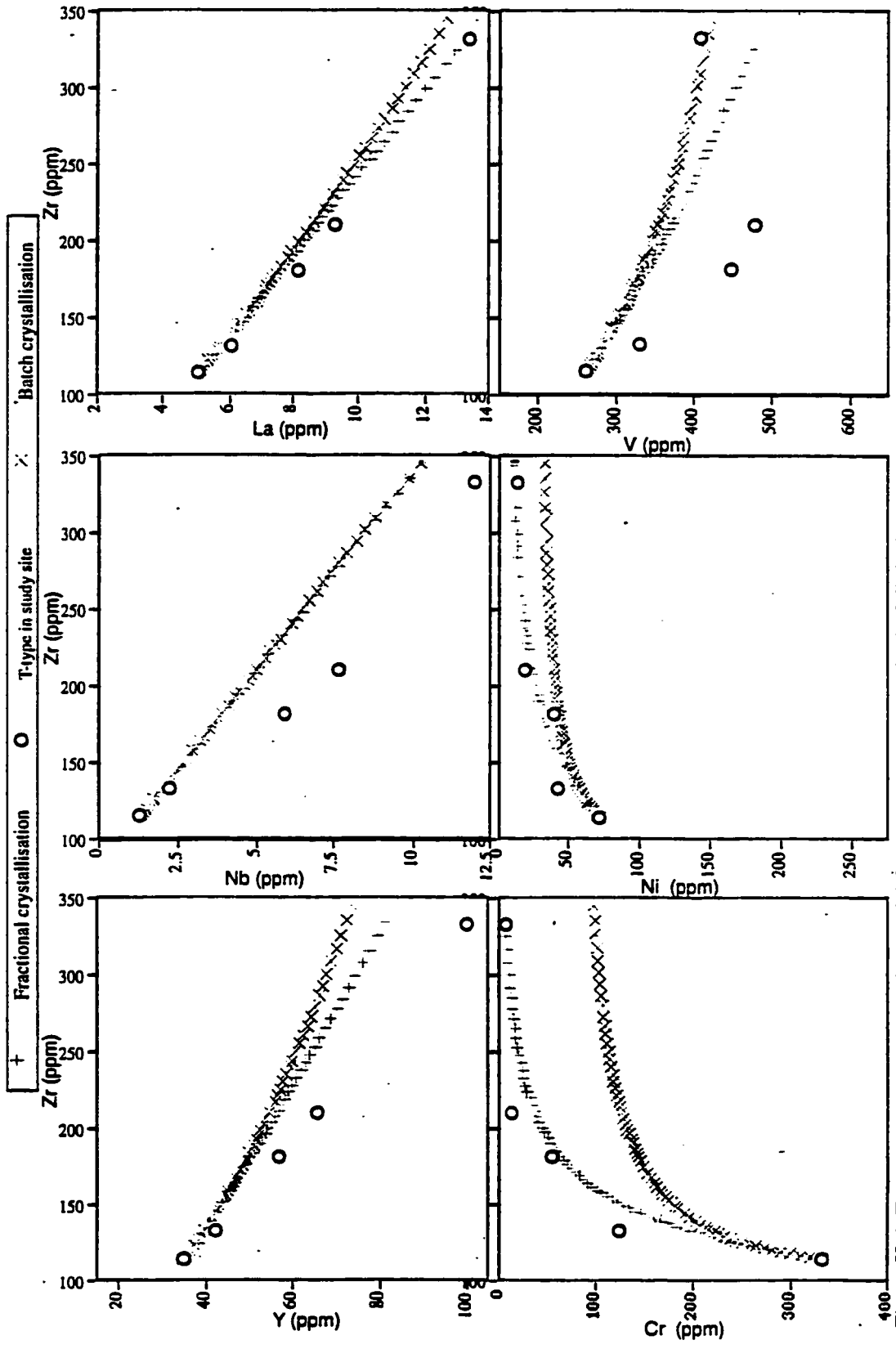

Figure H-4: Trace element crystallization model for the T-type MORBs in the WBD site. Each cross represents 0.1 steps in F (fraction of liquid remaining). Fractional rather than equilibrium crystallisation produces a better fit to the data. The phenocryst assemblage crystallizing is plag:cpx:ol = 35 : 55 : 10. The percentage of crystallization averages 66% with a range of 56-75%.

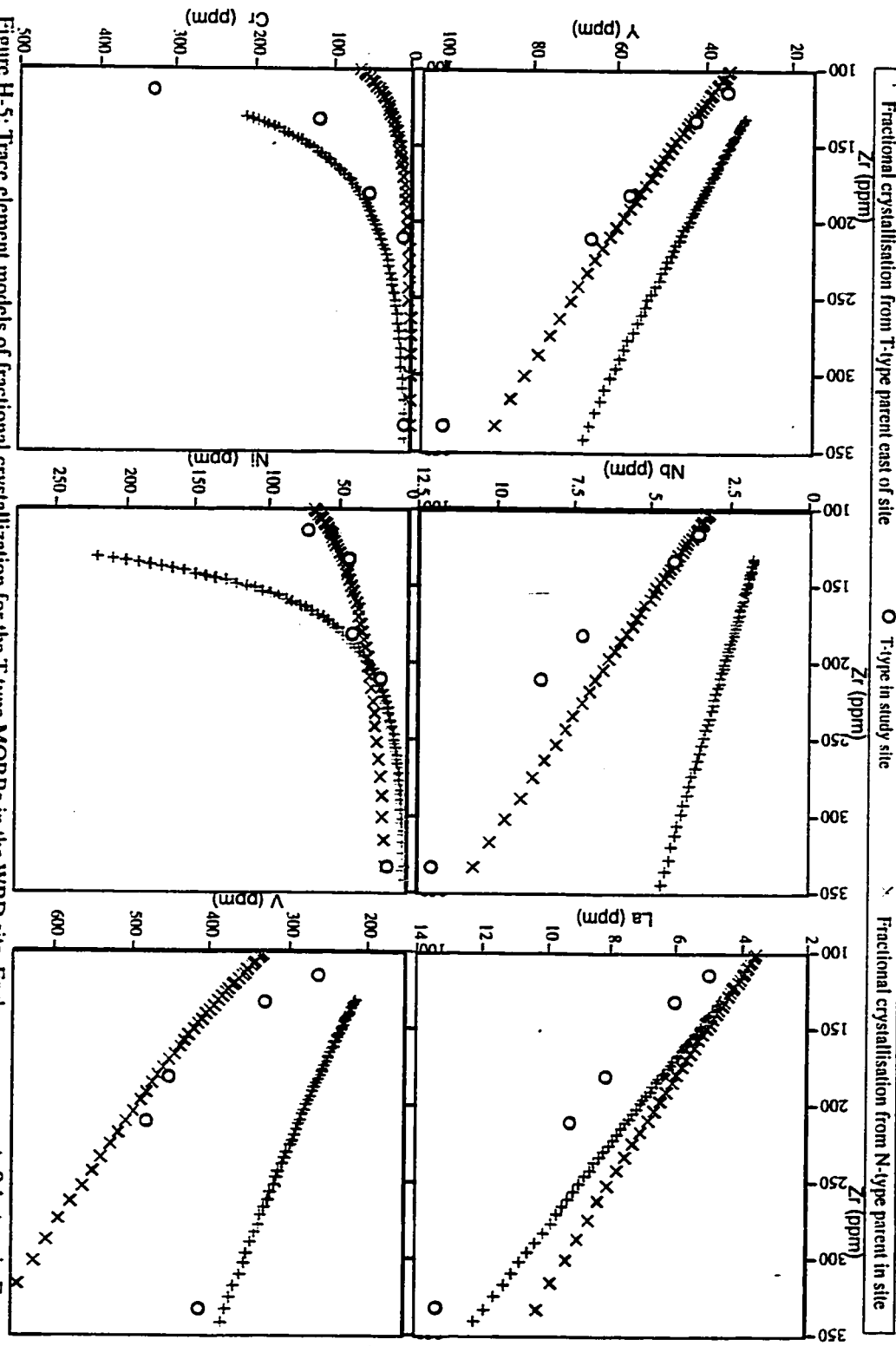

Figure H-5: Trace element models of fractional crystallization for the T-type MORBs in the WBD site. Each cross represents 0.1 steps in F (fraction of liquid remaining). The models reflect two alternative parental compositions: a more primitive parent (BN-22-12 - Juteau et al., 1995) from the north WBD scarp to the east, and the N-type parent within the study site. At best fit, they respectively require crystallizing phenocryst assemblages of cpx:ol:spinel = 40 : 50 : 10 and plag:cpx:ol = 40 : 55 : 5, and percentages of crystallization which average 70% and 81%. Nonetheless, the scarp T-parent does not produce a fit to the data (except for Cr) while the N-parent produces a better fit for Ni and Y, a reasonable fit for Nb and V, and a poorer fit for Cr and La.

CURRICULUM VITAE

DEVAMONIE D. NAIDOO

University of Washington, School of Oceanography,
Box 357940, Seattle, WA 98195-7940
Tel: (206) 543-5098 Fax: (206) 543-0275 monie@u.washington.edu

EDUCATION

Ph.D. candidate,	Oceanography, University of Washington, U.S.A.	*1997*
Thesis:	Crustal accretion of the upper oceanic crust	
Advisor:	J. R. Delaney / R. W. Sternberg	
M.S.,	Geology, Duke University, U.S.A.	*1988*
Thesis:	A petrographic and geochemical study of the metavolcanic rocks from the Proterozoic Bou Azzer ophiolite complex, Morocco	
Advisor:	Sherman H. Bloomer	
B.Sc. Honours,	Geology and Geochemistry, University of Cape Town, S.A.	*1985*
Thesis:	The multiphase intrusion of a granitic dyke into calcite wall-rock at Marble Delta near Port Shepstone, Natal	
Advisor:	Peter J. Betton [deceased] and David J. Waters	
B.Sc.,	Geology and Geochemistry, University of Cape Town, S.A.	*1984*

RESEARCH AND TEACHING EXPERIENCE

Graduate Research Assistant
Northwest Center for Research on Women *1996*
School of Oceanography *1989 - 1995*

Researcher
Geochronology Division of the Council for Scientific and Industrial Research
Summer: *1982 - 1984*; January *1986* - July *1986*

Teaching assistant, University of Washington
Oceanography 460 *1993*
Oceanography 201 *1993*
Oceanography 101 *1990 - 1991*

Laboratory instructor, Chemistry, University of Cape Town *1983*

OCEANOGRAPHIC FIELD EXPERIENCE

BLANCOVIN cruise, M. A. Tivey (Chief Scientist), R.V. Atlantis II *1995*
R. Sternberg (OC201) & M. Holmes (OC460) (Chief Scientists), R.V. Thompson *1993*
Tow-the-MARK cr., F. N. Spiess & J. R. Delaney (co-Chief Scientists), R.V. Knorr *1992*
CREST operation, D. Yoerger (Chief Scientist), R.V. Laney Chouest *1991*
CREST operation, J. R. Delaney (Chief Scientist), R.V. Atlantis II *1991*
BLANCONAUTE cruise, T. Juteau (Chief Scientist), R.V. Nadir *1991*
CREVEX cruise, H. P. Johnson (Chief Scientist), R.V. Atlantis II *1990*
J. Karsten (Chief Scientist), R.V. Wecoma *1989*

PRESENTATIONS

Invited Talk

"The Challenge of Difference", Women of Colour and Scholarship in Academia
Northwest Center for Research on Women - 15th Anniversary Celebration

Presented Abstracts

Naidoo, D.D., Delaney, J.R. and Juteau, T., 1994. A 2.7 Ma history of 4D Accretion at the S. Juan de Fuca Ridge (JdFR) From the West Blanco Depression (WBD) North Scarp. EOS, Trans. Am. Geophys. Un., vol. 75, no. 44, pg. 314.

Naidoo, D.D., Delaney, J.R. and Juteau, T., 1994. Profiles of the lives and accretionary times of the S. Juan de Fuca Ridge (JdFR) between 1.2-1.6 Ma. EOS, Trans. Am. Geophys. Un., vol. 75, no. 25, pg. 81.

Naidoo, D.D., Delaney, J.R. and Juteau, T., 1992. A scarp-map profile of upper oceanic crust at the West Blanco Transform (WBT): Insights into magmatic accretion. EOS, Trans. Am. Geophys. Un., 73, 502.

Blanconaute Shipboard Party, 1991. The Western Blanco Transform: Preliminary insights into the oceanic crustal architecture and transform zone processes. EOS, Trans. Am. Geophys. Un., 72, 519.

PUBLICATIONS

Papers

Juteau, T., Bideau, D., Dauteuil, O., Manac'h, G., Naidoo, D.D., Nehlig, P., Ondreas, H., Tivey, M.A., Whipple, K.X. and Delaney, J.R., 1995. A submersible study in the western Blanco Fracture Zone, N.E. Pacific: Structure and Evolution during the last 1.6 Ma. Mar. Geophys. Res., 17, 399-430.

Naidoo, D.D., Bloomer, S.H., Saquaque, A. and Hefferan, K., 1993. Reply to Leblanc's Comment. Precambrian Research, 62, 369-371.

Naidoo, D.D., Bloomer, S.H., Saquaque, A. and Hefferan, K., 1991. Geochemistry and significance of metavolcanic rocks from the Bou Azzer-El Graara Ophiolite (Morocco). Precambrian Research, 53, 79-97.

Naidoo, D.D., Eglington, B.M. and Harmer, R.E., 1989. A Rb-Sr study of a young granitic sheet at Marble Delta, southern Natal. South African Journal of Geology, 92, 389-392.

Additional abstracts

Tivey, M.A., Fleutelot, C., Hussenoeder, S., Johnson, H.P., Lawrence, R.M., Naidoo, D.D., van Patten, D., Waters, C. and Wooding, F.B., 1995. BLANCOVIN: A Submersible Study of Oceanic Crust at a Magnetic Polarity Reversal Boundary. EOS, Trans. Am. Geophys. Un., 76/46, p. F421.

Juteau, T., Bideau, D., Dauteuil, O., Manac'h, G., Naidoo, D.D., Nehlig, P., Ondreas, H., Tivey, M. and Whipple, K., 1993. The Western Blanco Trough: Lithology, tectonics and magnetic structure of a young oceanic crust. Terra Nova, vol. 5, C4, A13, pg. 194.

Manac'h, G., Bideau, D., Juteau, T. and Naidoo, D.D., 1993. The Western Blanco Trough: Petrology of the northern wall between 0 Ma and 1.5 Ma. Terra Nova, v. 5, C4, A13, p. 196.

Tivey, M.A., Juteau, T. and the Blanconaute Scientific Team, 1993. The vertical magnetic structure of ocean crust determined by submersible. EUG, A8, C21, E14, p81.

Nehlig, P., Juteau, T. and Naidoo, D.D., 1992. The Western Blanco Depression: An example of an asymmetric basin with transform-normal extension. EOS, Trans. Am. Geophys. Un., 73, 554.

Karson, J.A., Delaney, J.R., Spiess, F.N., Hurst, S., Lawhead, B., Bigger, S., Naidoo, D.D. and Gente, P., 1992. Deep-Tow operations at the eastern intersection of the Mid-Atlantic Ridge and the Kane Fracture Zone. EOS, Trans. Am. Geophys. Un., 73, 552.

Whipple, K.X. and Naidoo, D.D., 1991. Mass wasting processes in the transform fault environment. EOS, Trans. Am. Geophys. Un., 72, 519.

CREVEX-1 Shipboard Party, 1990. Studies of crustal evolution, 0 to 1 My: The Endeavour Segment of the Juan de Fuca Ridge. EOS, Trans. Am. Geophys. Un., 71, 1675.

Karsten, J.L., Batiza, R., Vanko, D., Niu, Y., Robigou-Nelson, V., Naidoo, D., Hacksel, P., Little, D., Lopas, J., McCallum, D., Mueller, T., Suen, J. and Underwood, G., 1990. Petrology of Heck, Heckle, and Springfield seamounts. EOS, Trans. Am. Geophys. Un., 71, 259.

PERSONAL

Academic Awards:

South African Education Program Scholarship, Duke University, 1986 - 1988
Harry Crossley Scholarship, University of Cape Town, 1985
A.P. Bender Entrance Scholarship, University of Cape Town, 1982 - 1984
Dux Medal, Durban Girls Secondary School, 1981

POCKET MATERIAL:

Figure B-1: BN-01 STRATIGRAPHIC SECTION

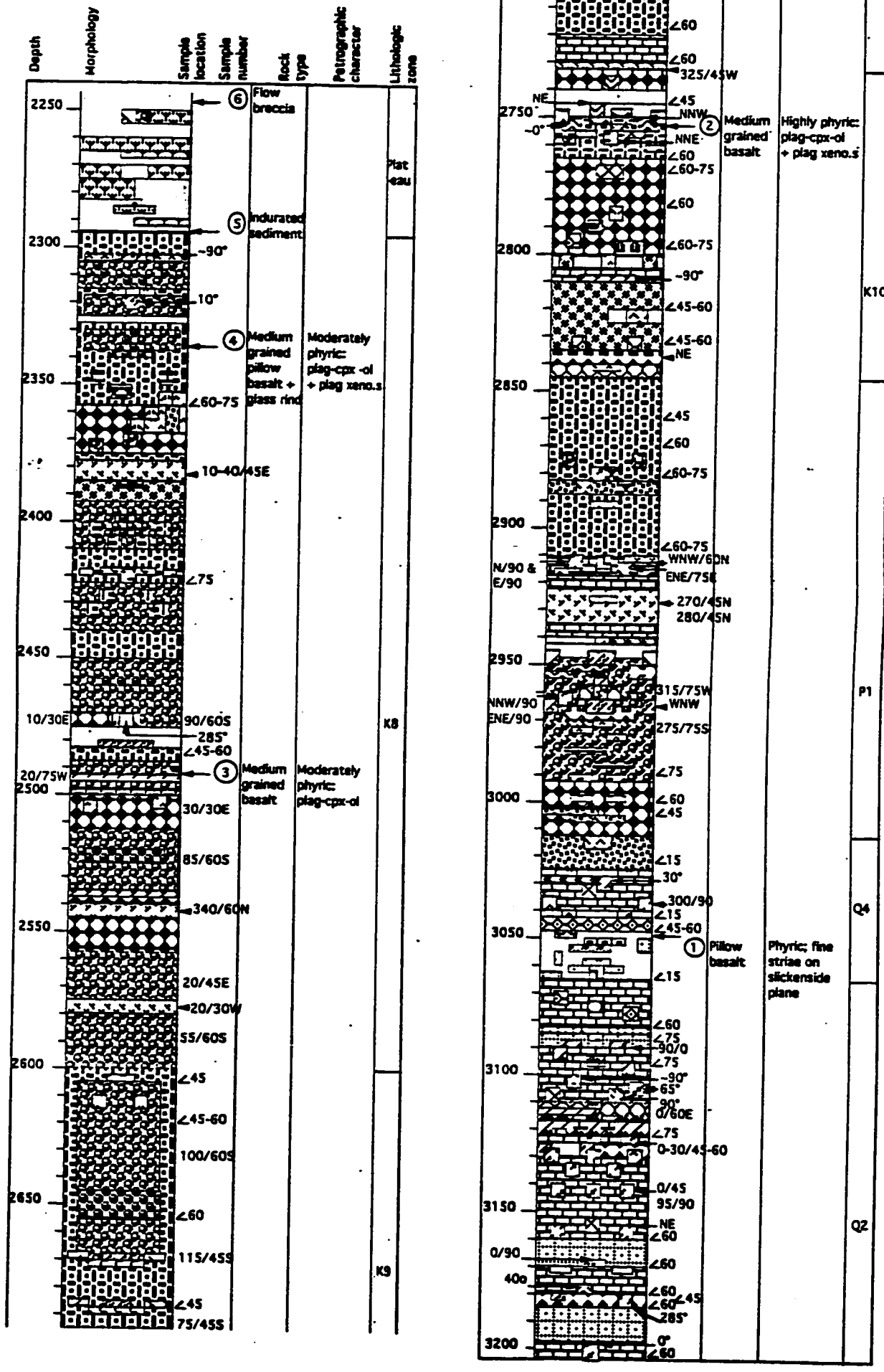

Figure B-2: BN-02 STRATIGRAPHIC SECTION

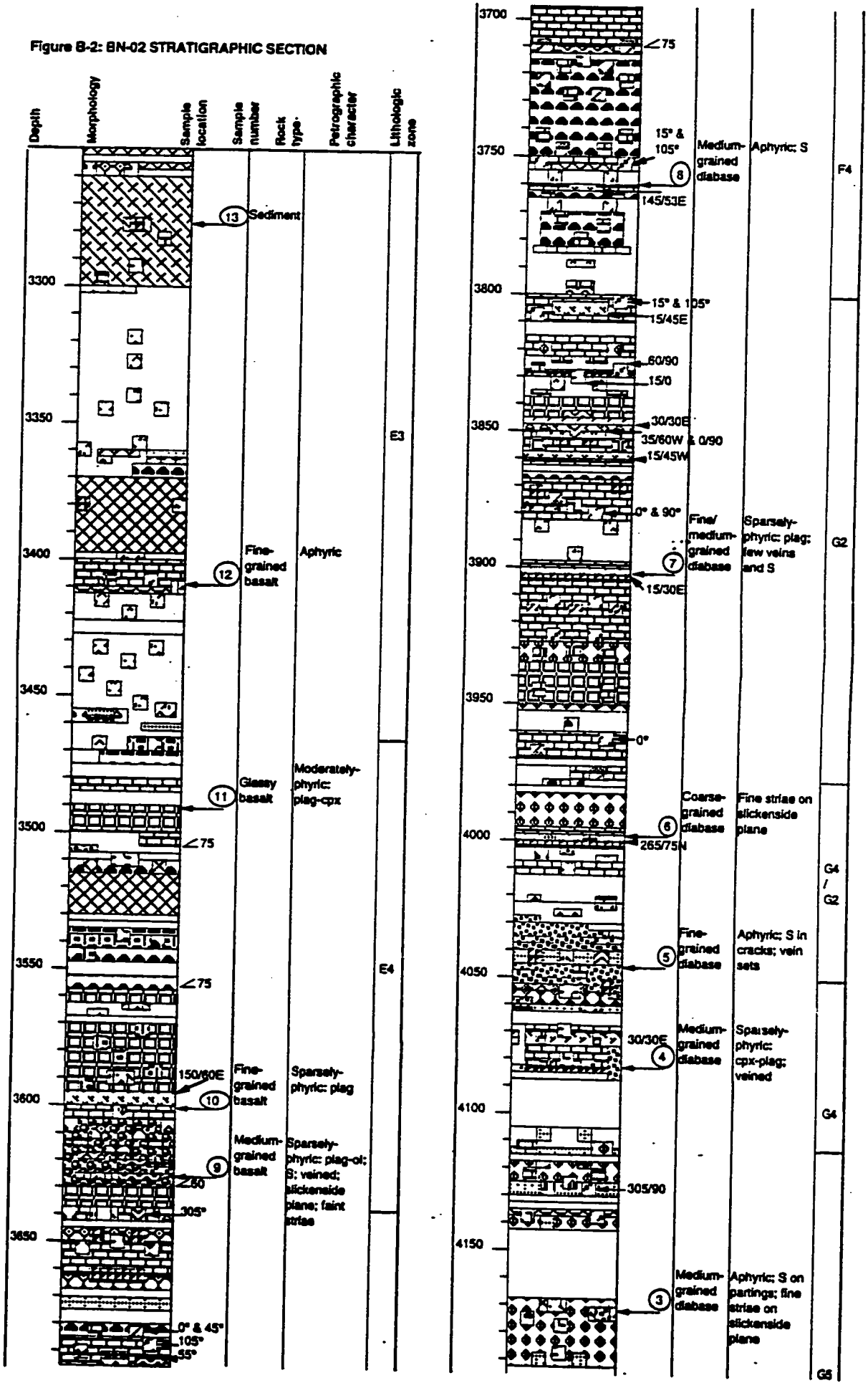

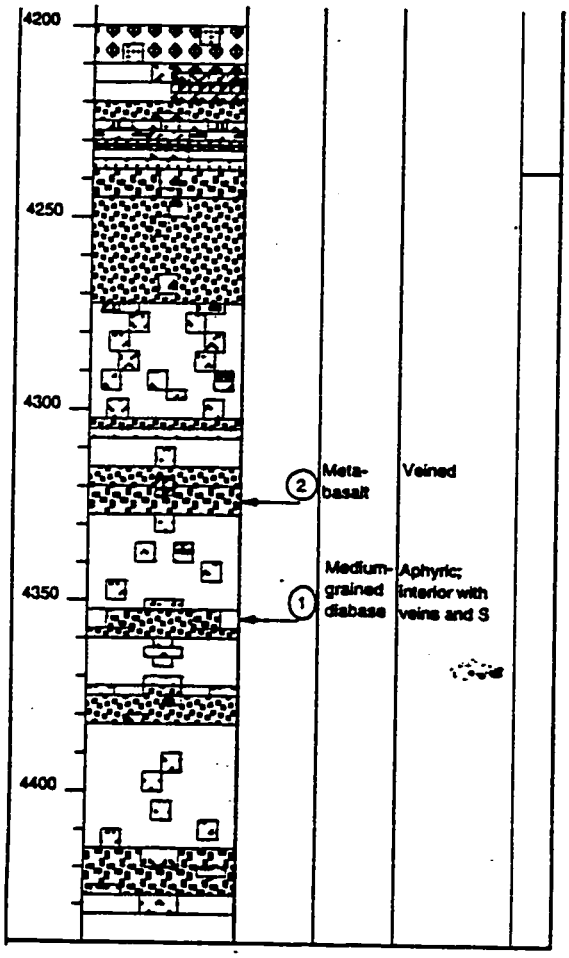
4200
4250
4300
4350
4400
2
Meta-
basalt
Veined
1
Medium-
grained
diabase
Aphyric;
interior with
veins and S

Figure B-3: BN-03 STRATIGRAPHIC SECTION

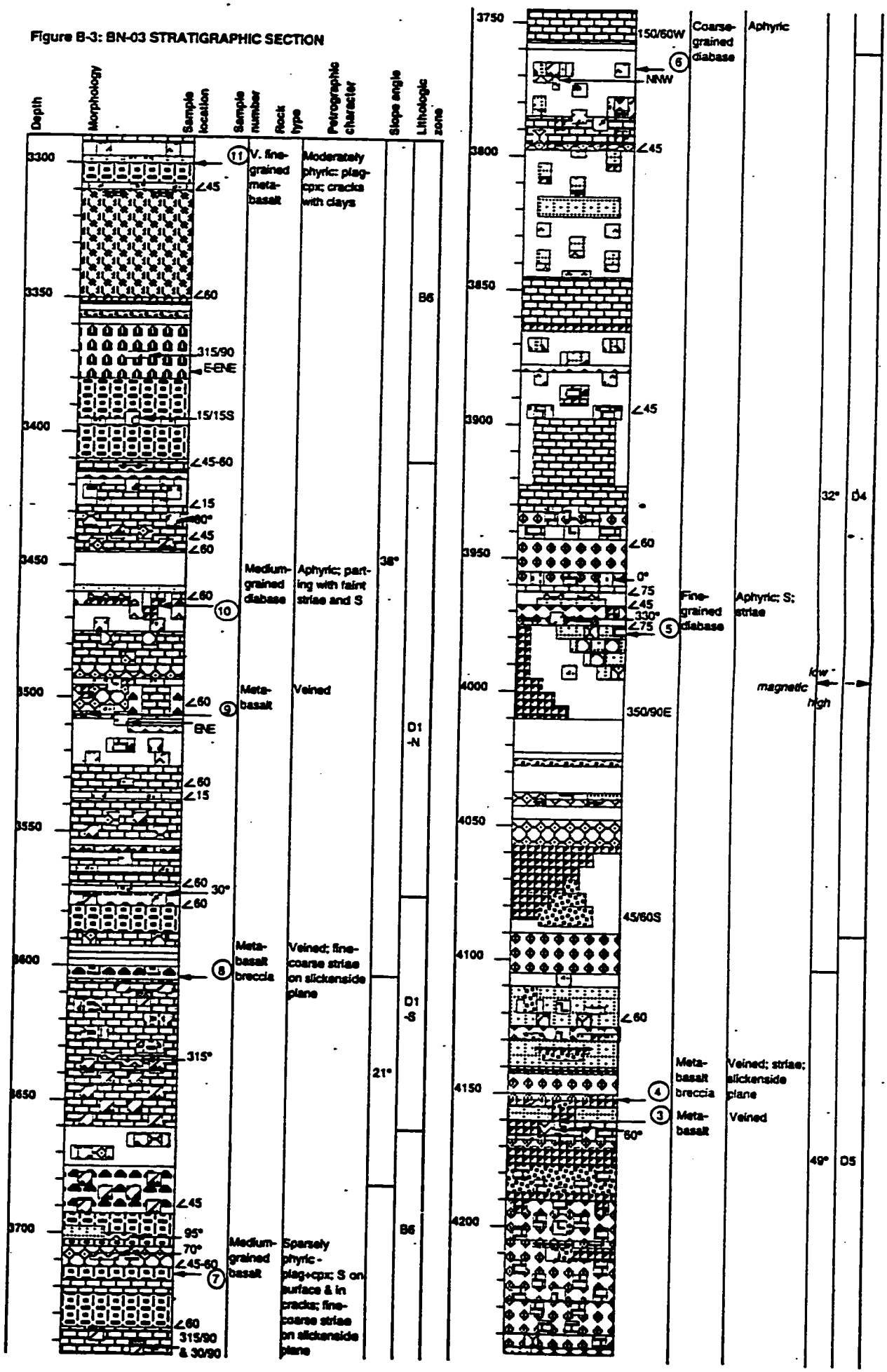

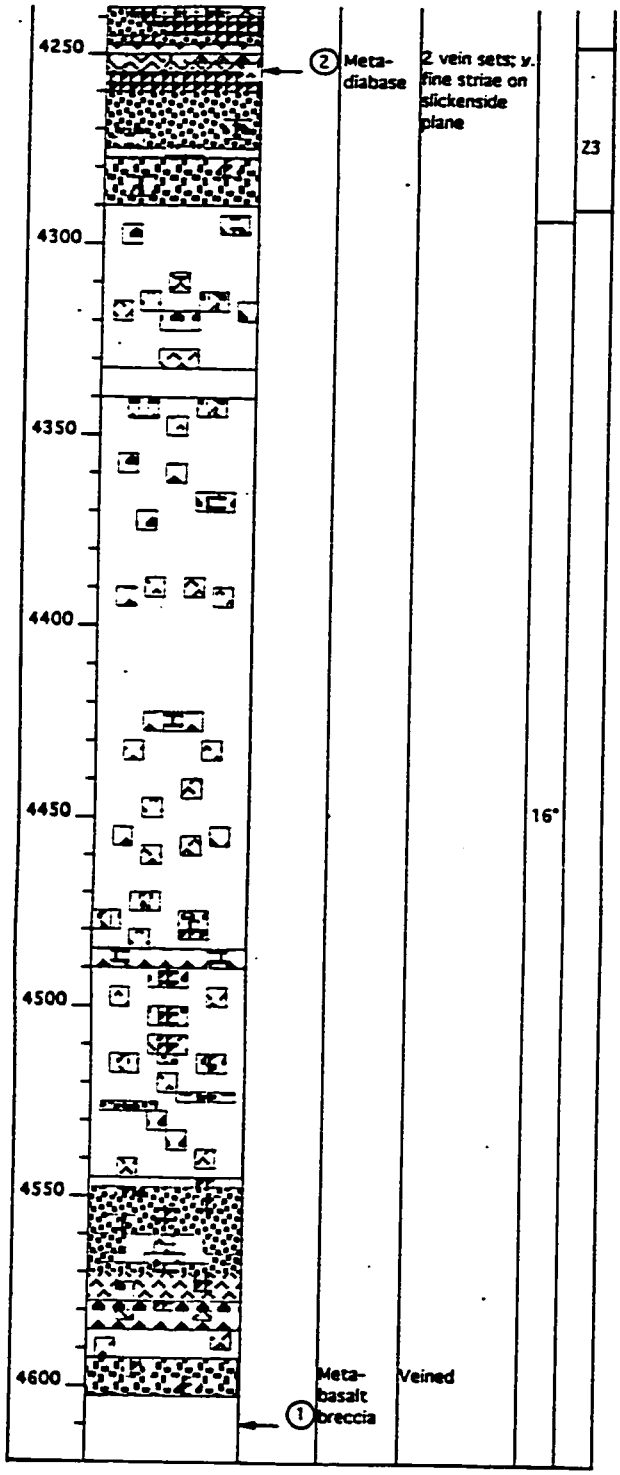
4250
4300
4350
4400
4450
4500
4550
4600
② Meta-diabase
2 vein sets; v. fine striae on slickenside plane
Z3
16°
Meta-basalt breccia
Veined
①

Figure B-4: BN-04 STRATIGRAPHIC SECTION

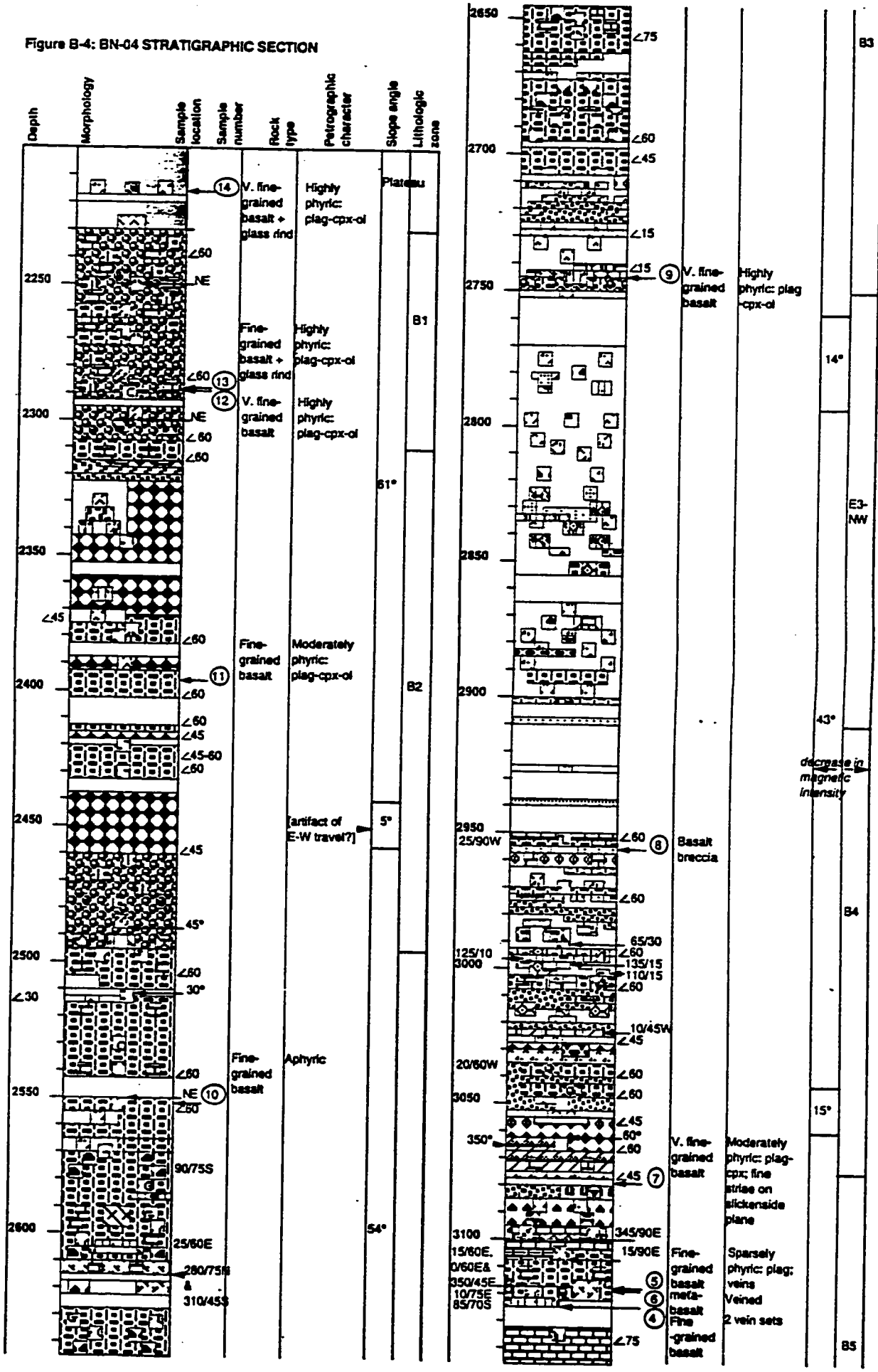

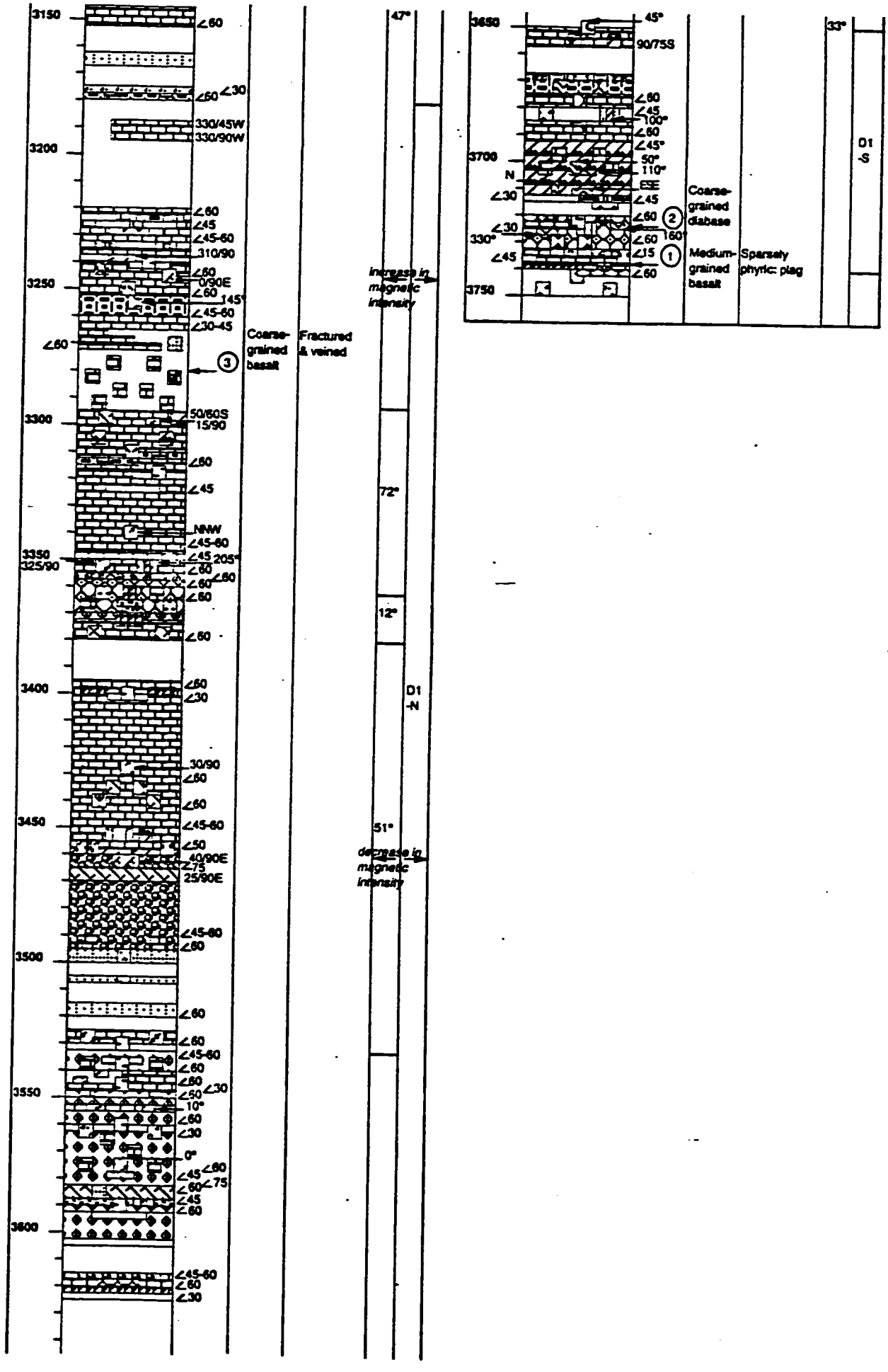
3150
3200
3250
3300
3350
3400
3450
3500
3550
3600
3650
3700
3750
∠60
∠60 ∠30
330/45W
330/90W
∠60
∠45
∠45-60
310/90
∠60
0/90E
∠60
145°
∠45-60
∠30-45
∠60
3
Coarse-grained basalt
Fractured & veined
50/60S
15/90
∠60
∠45
NNW
∠45-60
∠45
205°
325/90
∠60
∠60
∠60
∠60
∠60
∠30
30/90
∠60
∠60
∠45-60
∠50
40/90E
∠75
25/90E
∠45-60
∠60
∠60
∠60
∠45-60
∠60
∠60
∠30
∠60
10°
∠60
∠30
0°
∠60
∠45
∠60
∠75
∠45
∠60
∠45-60
∠60
∠30
47°
Increase in magnetic intensity
72°
12°
D1 -N
51°
decrease in magnetic intensity
45°
90/75S
∠60
∠45
100°
∠60
∠45°
50°
110°
N
ESE
∠30
∠45
Coarse-grained diabase
∠60
2
∠30
∠60
160°
330°
∠45
∠15
1
Medium-grained basalt
Sparsely phyric: plag
∠60
33°
D1 -S

Figure 8-5: BN-05 STRATIGRAPHIC SECTION

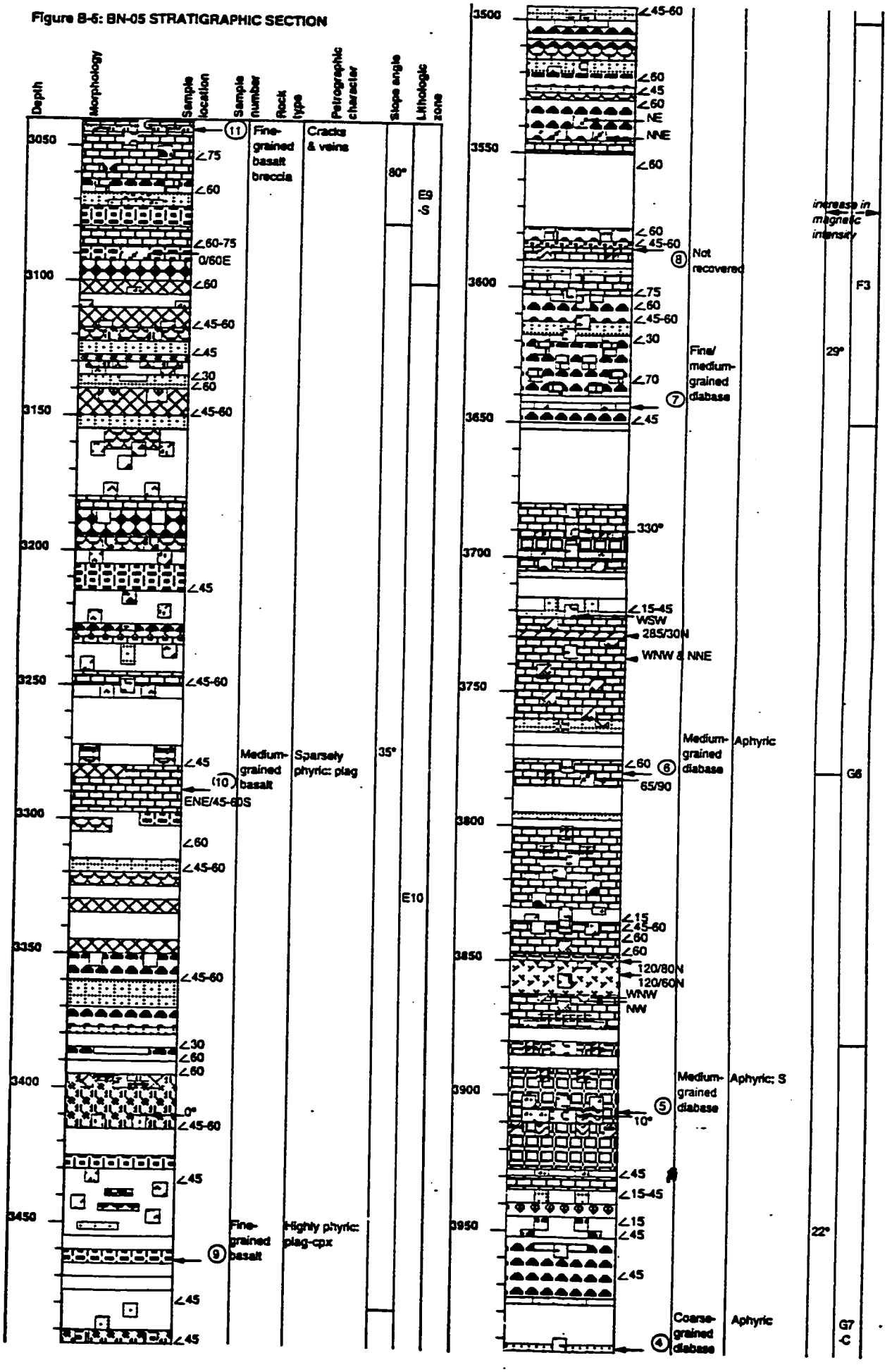

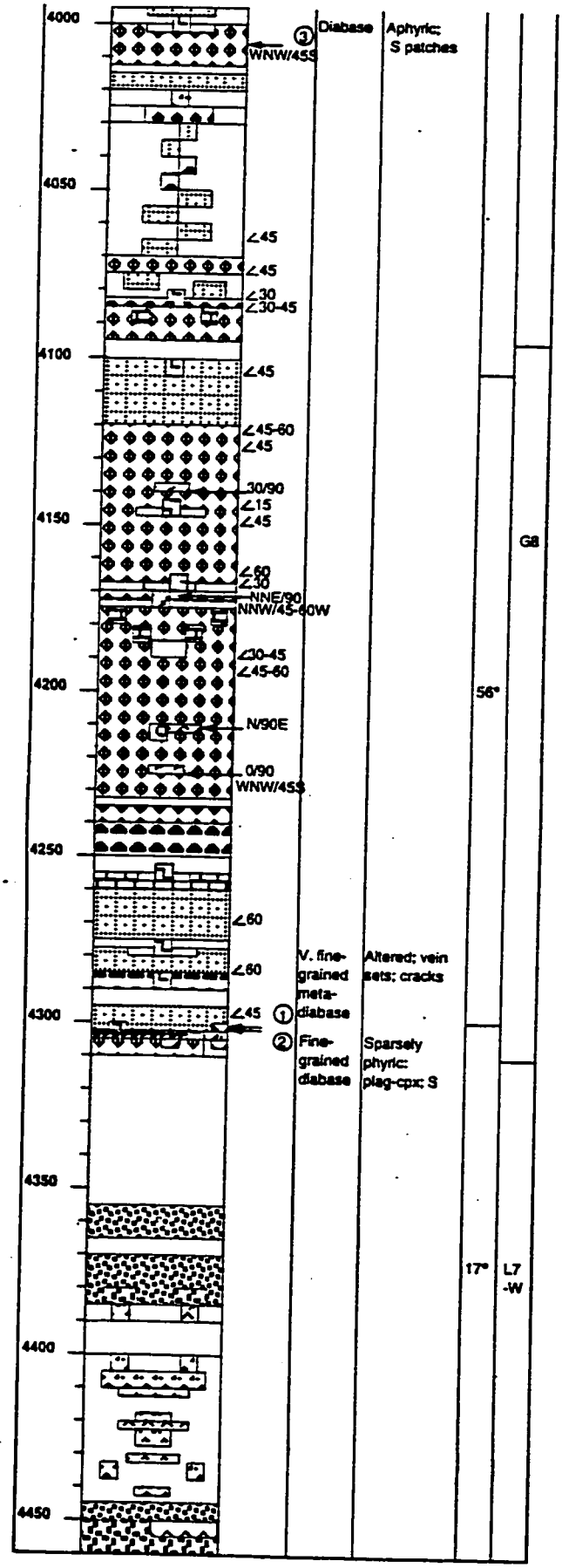
4000
4050
4100
4150
4200
4250
4300
4350
4400
4450
③ Diabase
Aphyric: S patches
WNW/45S
∠45
∠45
∠30
∠30-45
∠45
∠45-60
∠45
30/90
∠15
∠45
∠60
∠30
NNE/90
NNW/45-60W
∠30-45
∠45-60
N/90E
0/90
WNW/45S
∠60
∠60
∠45
V. fine-grained meta-diabase
① diabase
② Fine-grained diabase
Altered; vein sets; cracks
Sparsely phyric: plag-cpx; S
G8
56°
17°
L7 -W

Figure B-6: BN-06 STRATIGRAPHIC SECTION

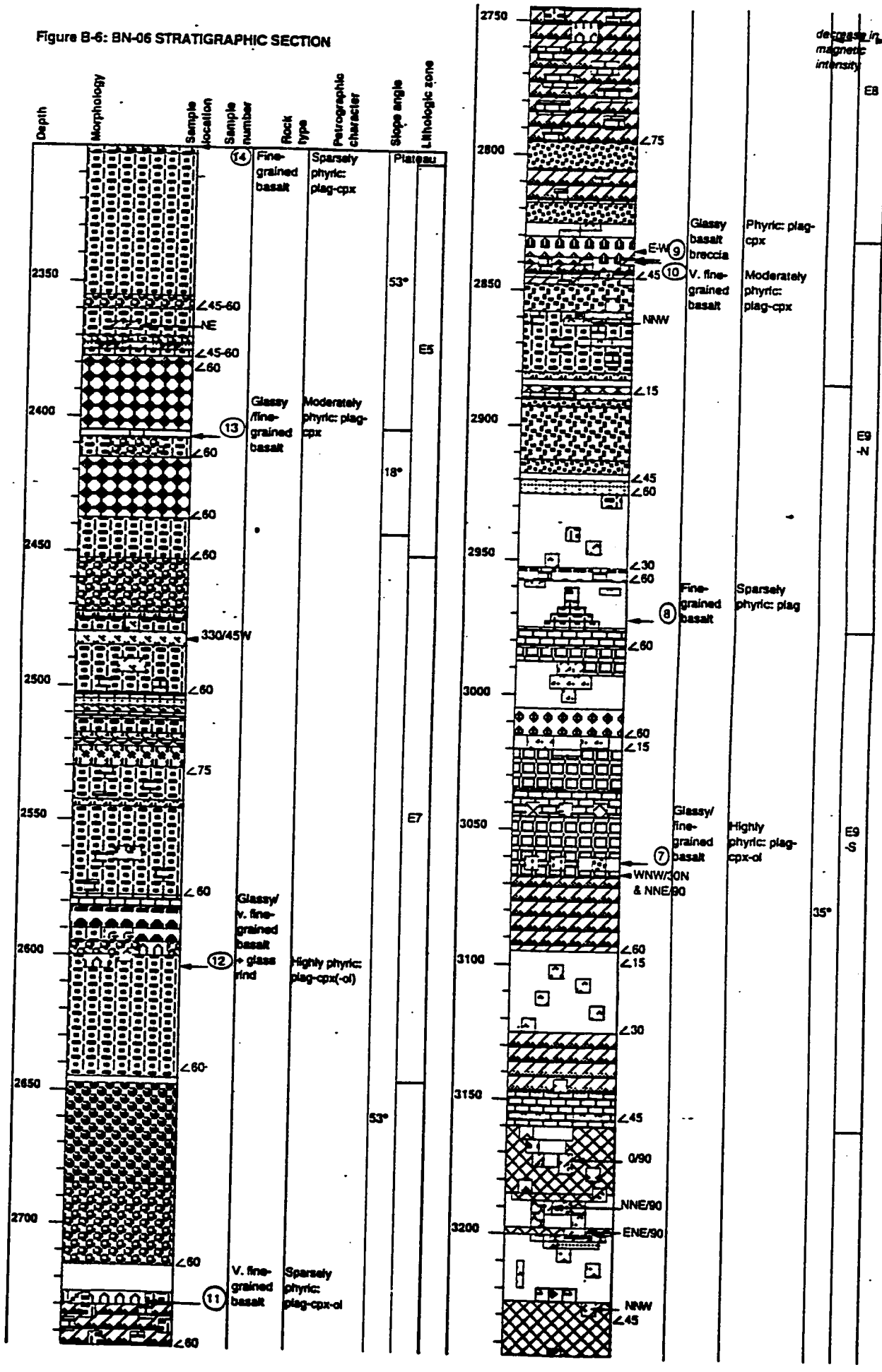

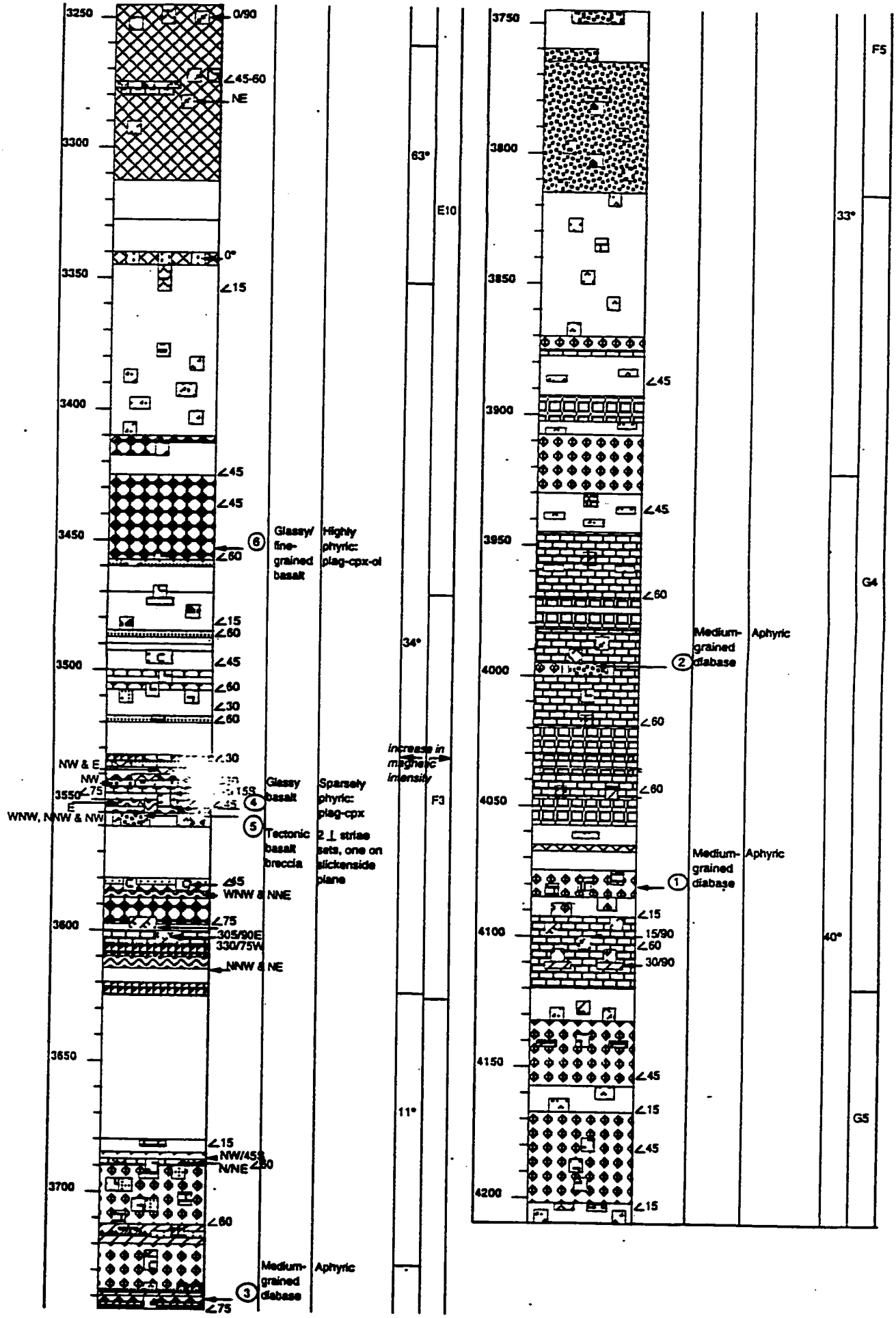
3250
3300
3350
3400
3450
3500
3550
3600
3650
3700
3750
3800
3850
3900
3950
4000
4050
4100
4150
4200
0/90
∠45-60
NE
0°
∠15
∠45
∠45
∠60
∠15
∠60
∠45
∠60
∠30
∠60
∠30
NW & E
NW
∠75
E
WNW, NNW & NW
∠45
∠45
WNW & NNE
∠75
305/90E
330/75W
NNW & NE
∠15
NW/45S
N/NE
∠60
∠75
∠45
∠15
∠60
∠45
∠60
∠15
15/90
∠60
30/90
∠45
∠15
∠45
∠15
6
Glassy/ fine-grained basalt
Highly phyric: plag-cpx-ol
4
Glassy basalt
Sparsely phyric: plag-cpx
5
Tectonic basalt breccia
2 ⊥ striae sets, one on slickenside plane
3
Medium-grained diabase
Aphyric
2
Medium-grained diabase
Aphyric
1
Medium-grained diabase
Aphyric
63°
E10
34°
Increase in magnetic intensity
F3
11°
33°
F5
G4
40°
G5

Figure B-7: BN-07 STRATIGRAPHIC SECTION

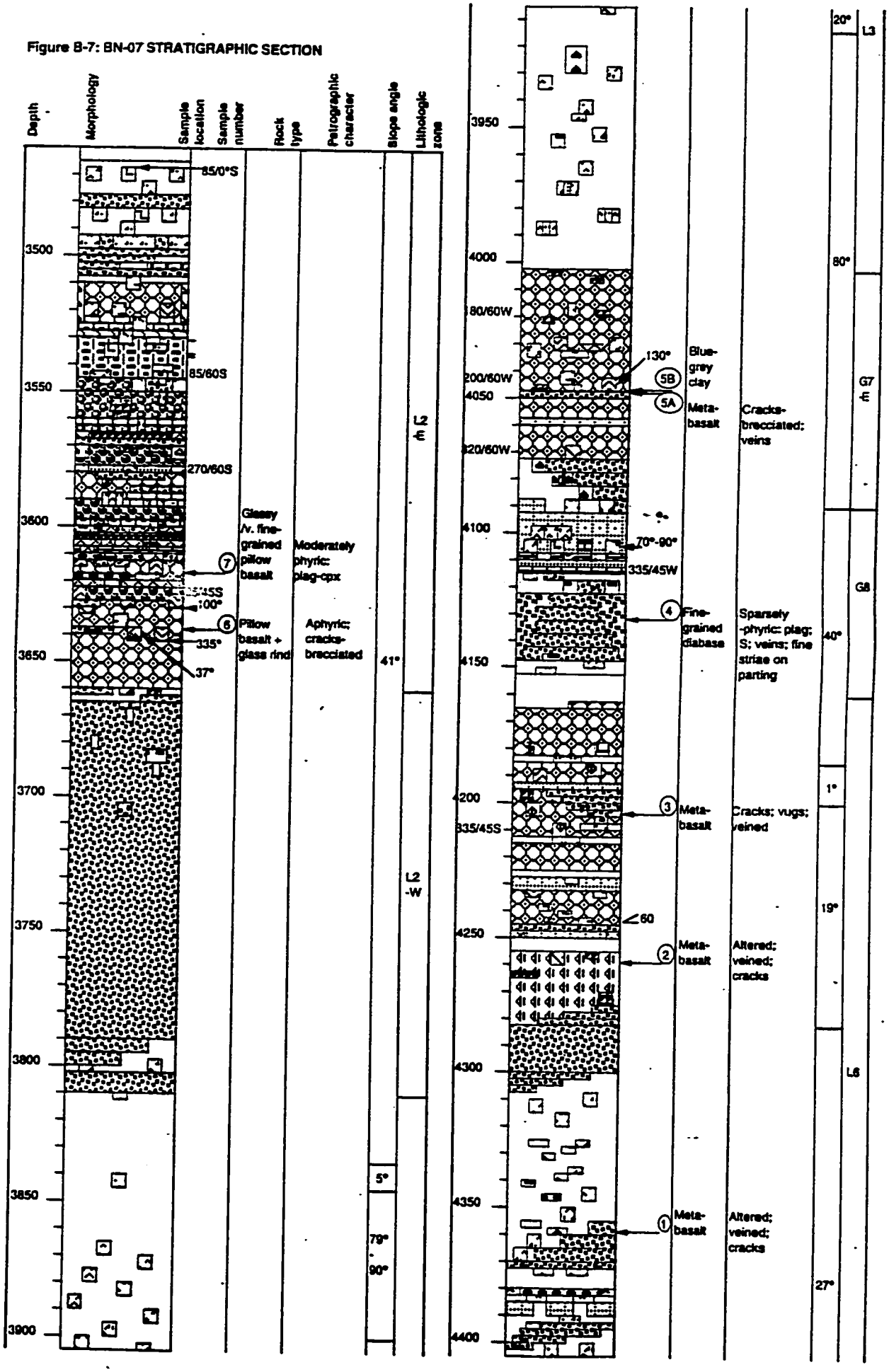

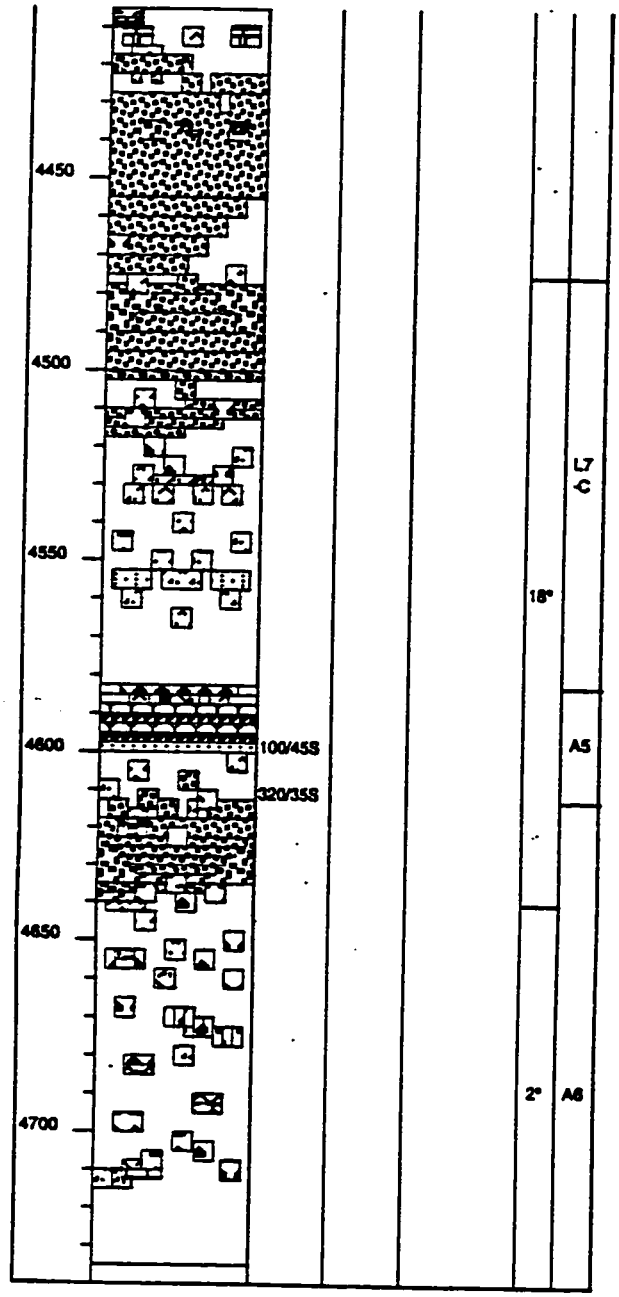
4450
4500
4550
4600
4650
4700
100/45S
320/35S
18°
2°
L7
C
A5
A6

Figure B-8: BN-08 STRATIGRAPHIC SECTION

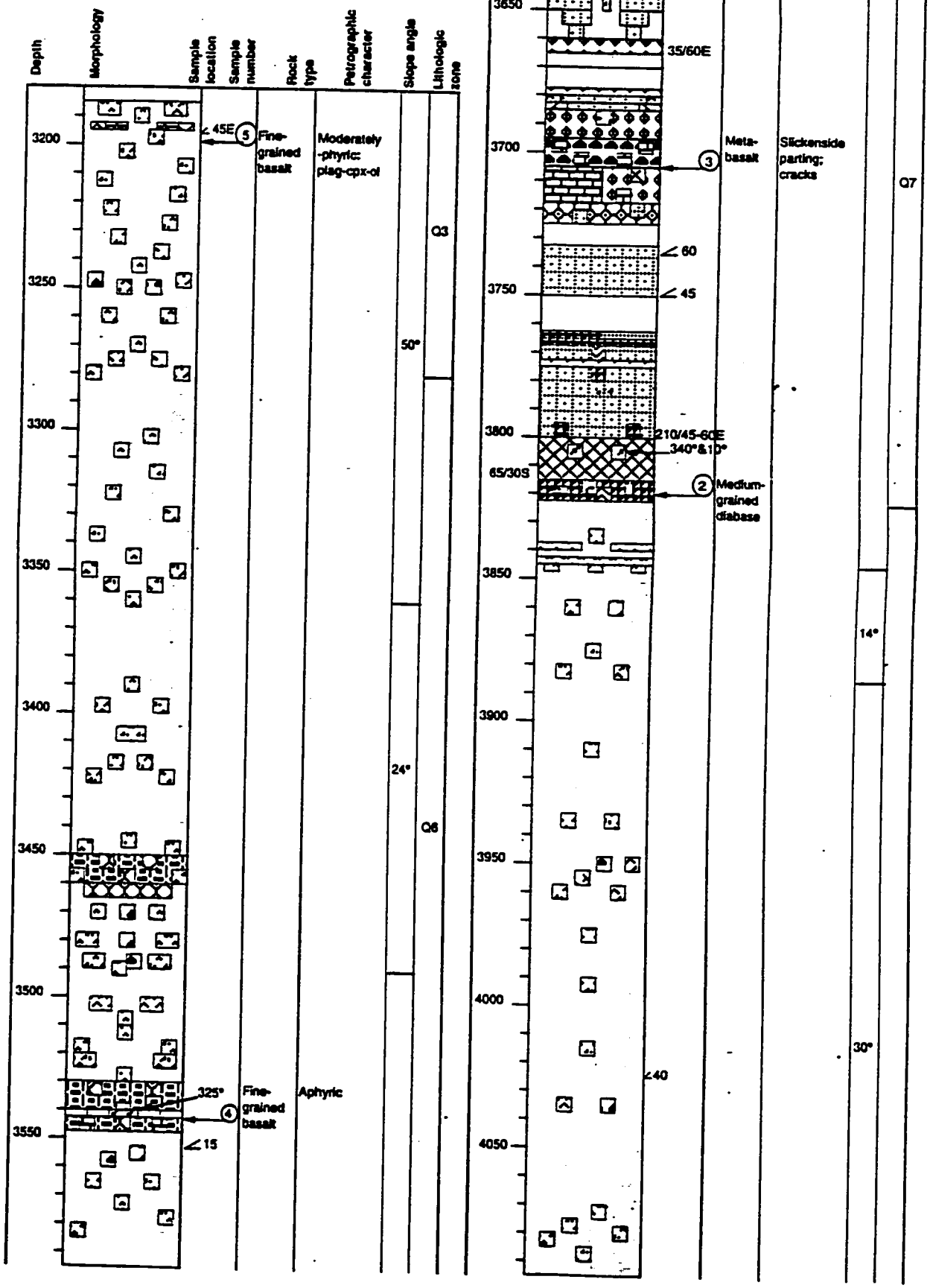

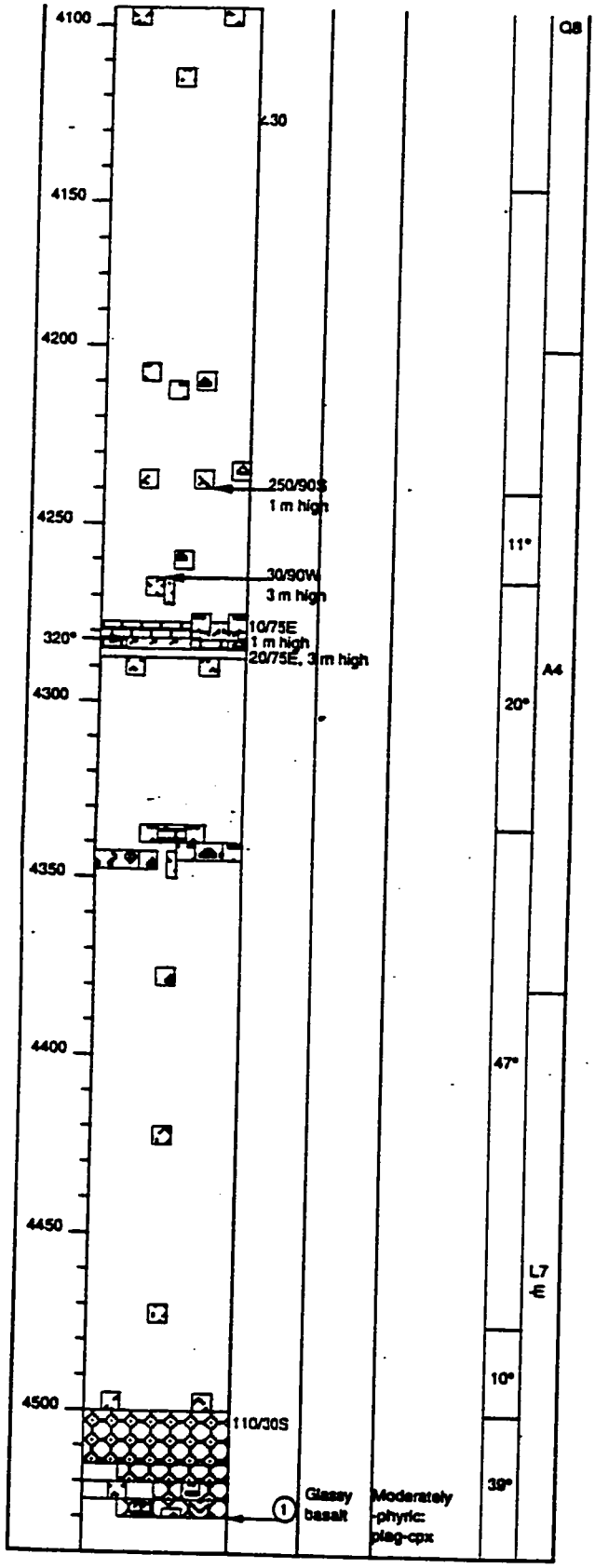
4100
4150
4200
4250
4300
4350
4400
4450
4500
230
250/90S
1 m high
30/90W
3 m high
320°
10/75E
1 m high
20/75E, 3 m high
110/30S
1
Glassy basalt
Moderately -phyric: plag-cpx
Q8
11°
A4
20°
47°
L7
10°
39°

Figure B-9: BN-09 STRATIGRAPHIC SECTION

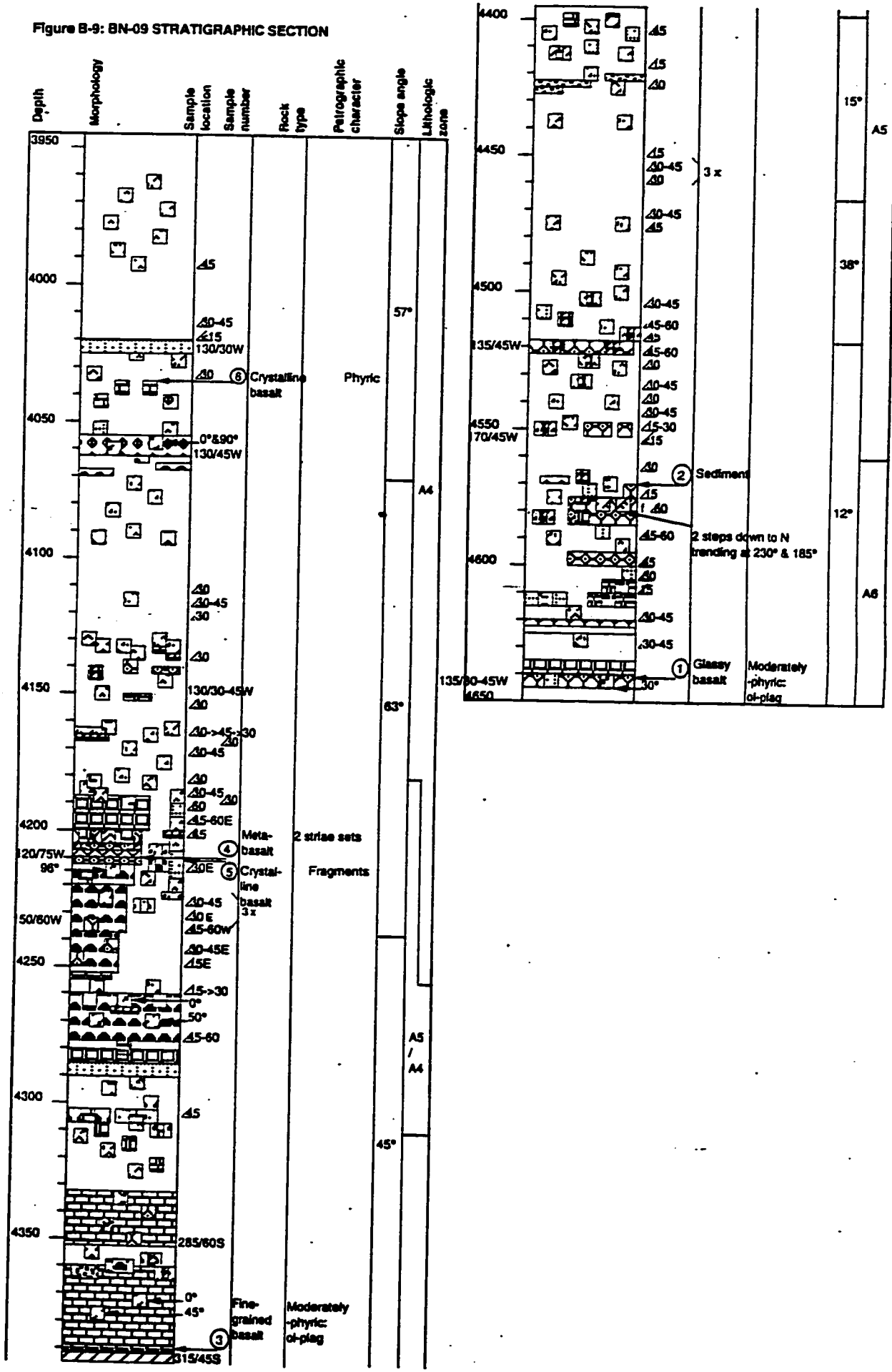

Figure B-10: BN-10 STRATIGRAPHIC SECTION

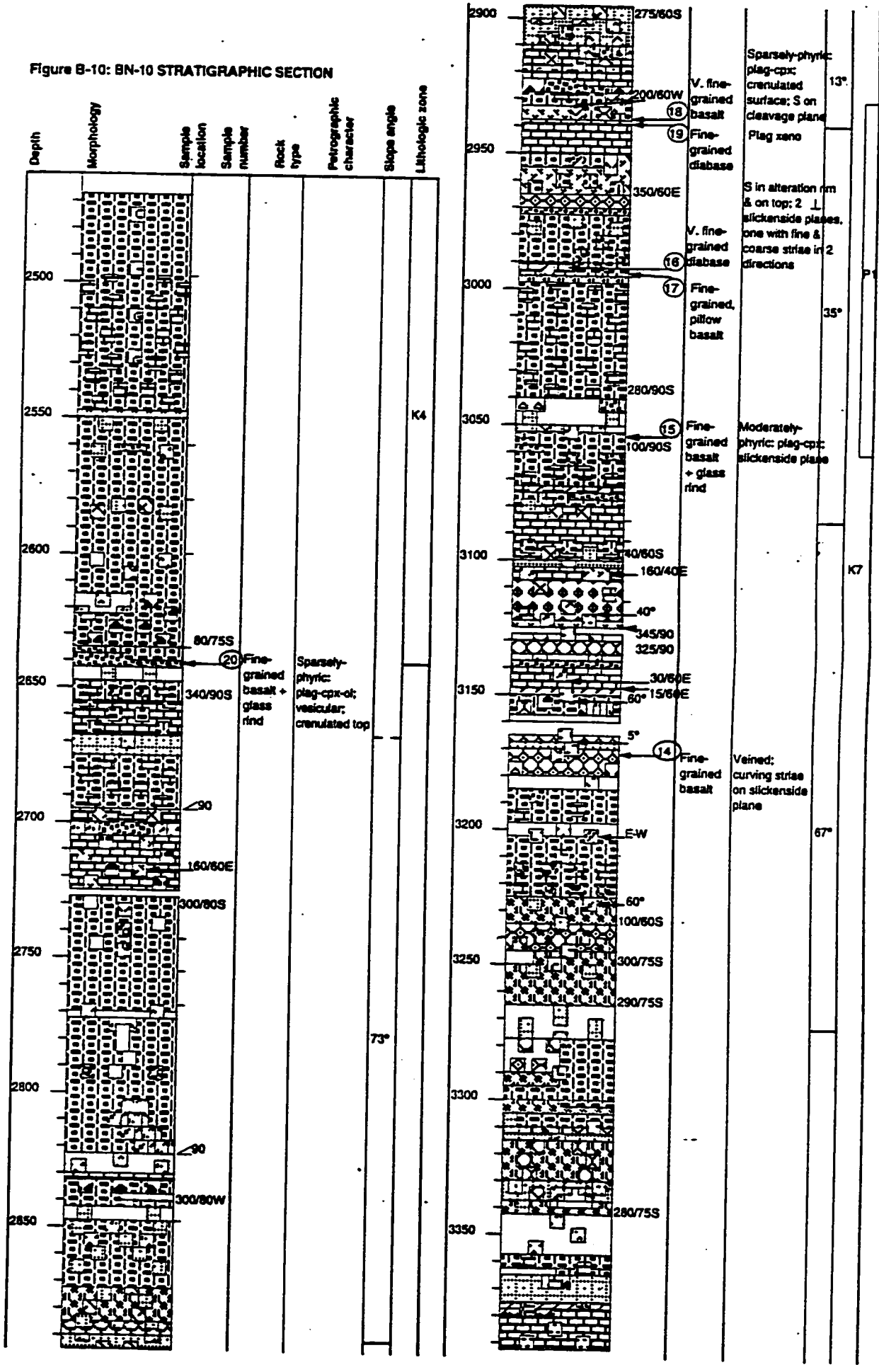

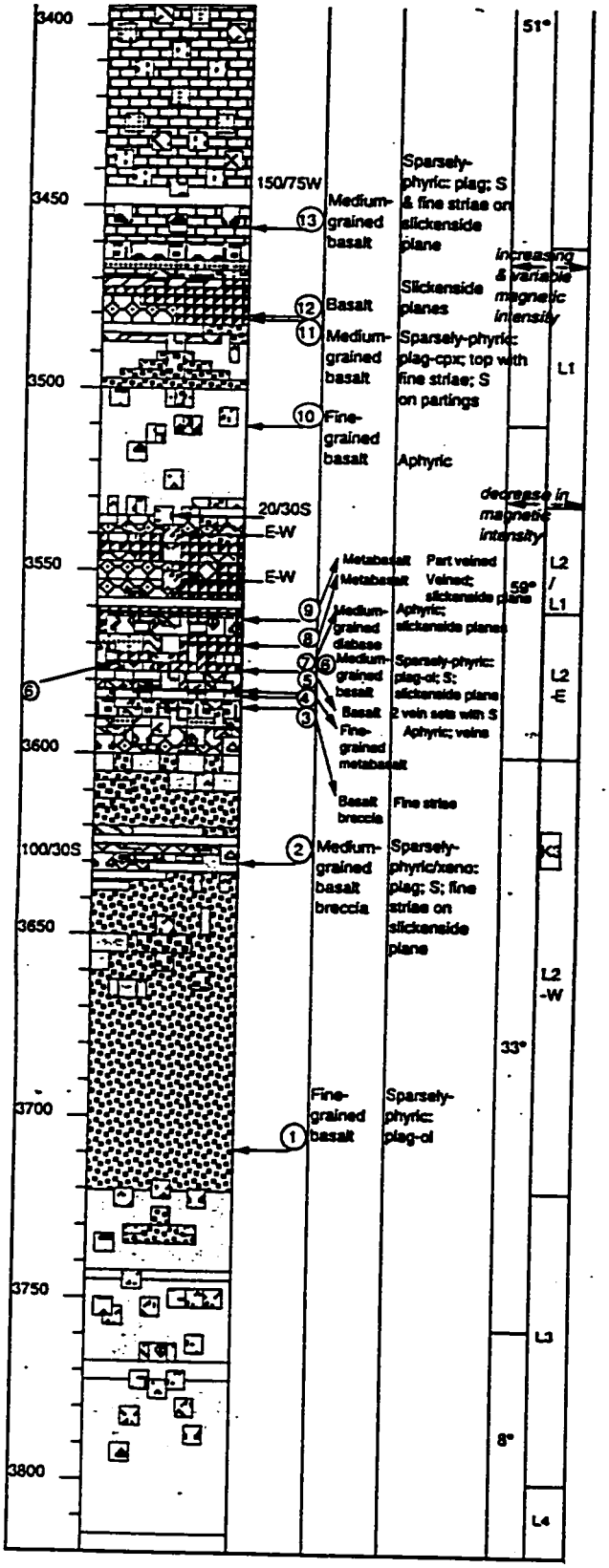
3400
3450
3500
3550
3600
3650
3700
3750
3800
150/75W
20/30S
E-W
E-W
100/30S
13
12
11
10
9
8
7
6
5
4
3
2
1
6
Medium-grained basalt
Basalt
Medium-grained basalt
Fine-grained basalt
Metabasalt
Metabasalt
Medium-grained dabase
Medium-grained basalt
Basalt
Fine-grained metabasalt
Basalt breccia
Medium-grained basalt breccia
Fine-grained basalt
Sparsely-phyric: plag; S & fine striae on slickenside plane
Slickenside planes
Sparsely-phyric: plag-cpx; top with fine striae; S on partings
Aphyric
Part veined
Veined; slickenside plane
Aphyric; slickenside planes
Sparsely-phyric: plag-ol; S; slickenside plane
2 vein sets with S
Aphyric; veins
Fine striae
Sparsely-phyric/xeno: plag; S; fine striae on slickenside plane
Sparsely-phyric: plag-ol
51°
increasing & variable magnetic intensity
L1
decrease in magnetic intensity
59°
L2 / L1
L2 -E
L2 -W
33°
L3
8°
L4

Figure 8-11: BN-13 STRATIGRAPHIC SECTION

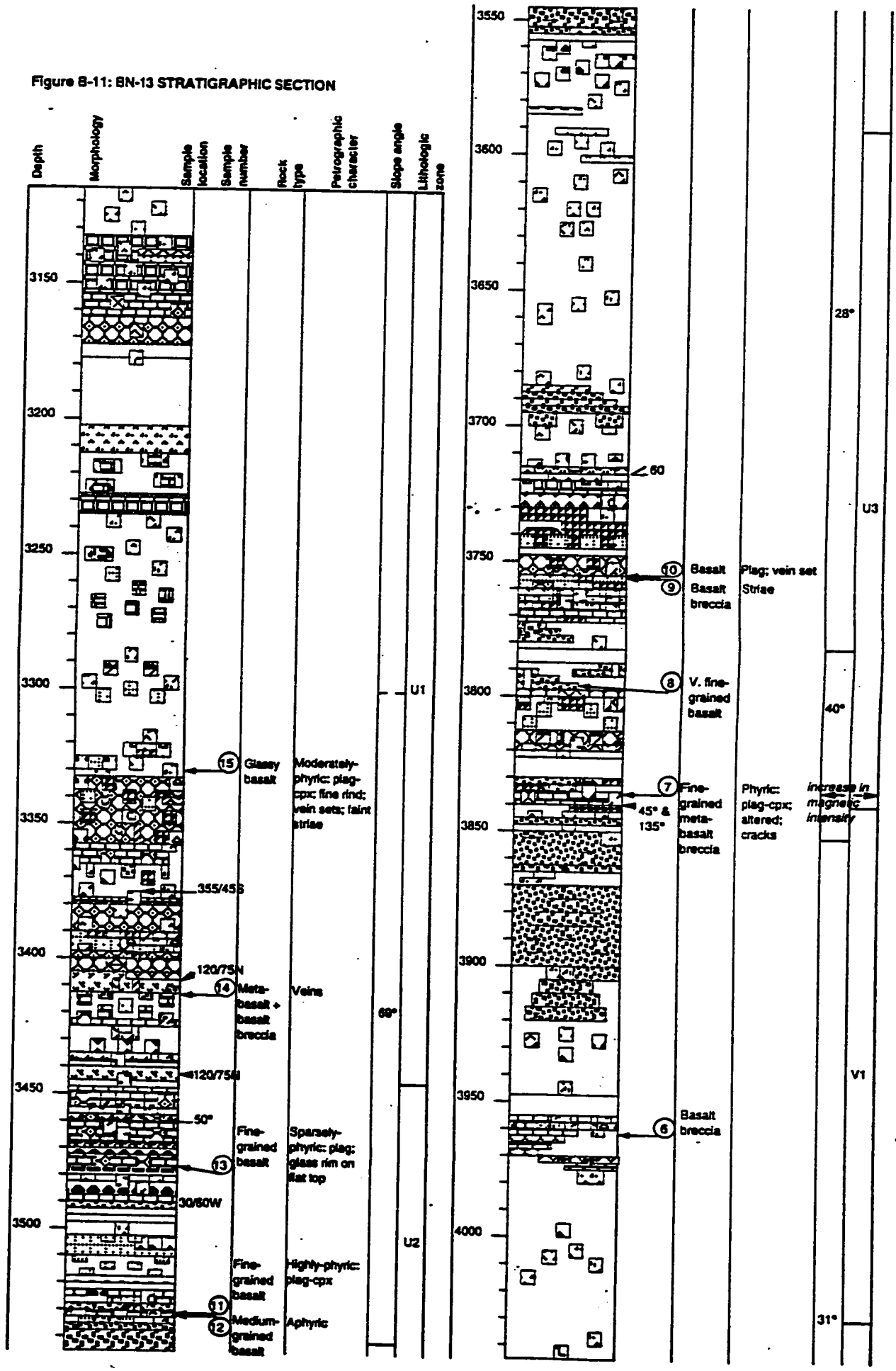

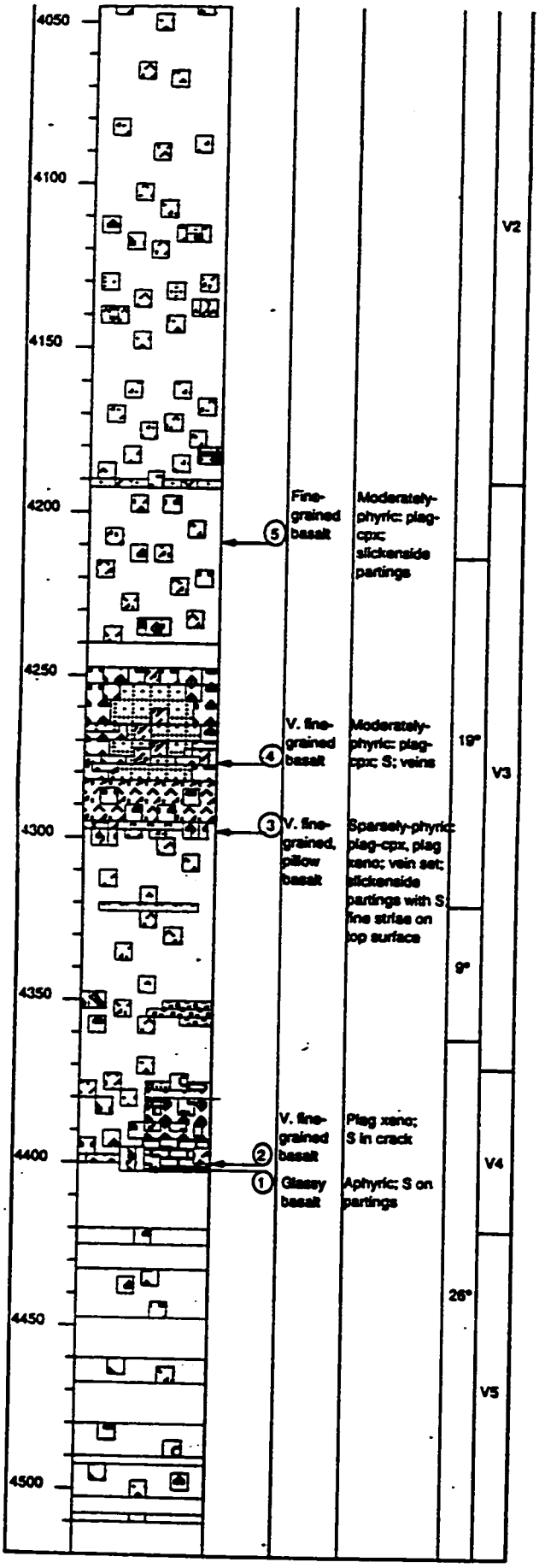
4050
4100
4150
4200
4250
4300
4350
4400
4450
4500
Fine-grained basalt
Moderately-phyric: plag-cpx; slickenside partings
V. fine-grained basalt
Moderately-phyric: plag-cpx; S; veins
V. fine-grained, pillow basalt
Sparsely-phyric: plag-cpx, plag xeno; vein set; slickenside partings with S; fine striae on top surface
V. fine-grained basalt
Plag xeno; S in crack
Glassy basalt
Aphyric; S on partings
19°
9°
26°
V2
V3
V4
V5

Figure B-12: BN-23 STRATIGRAPHIC SECTION

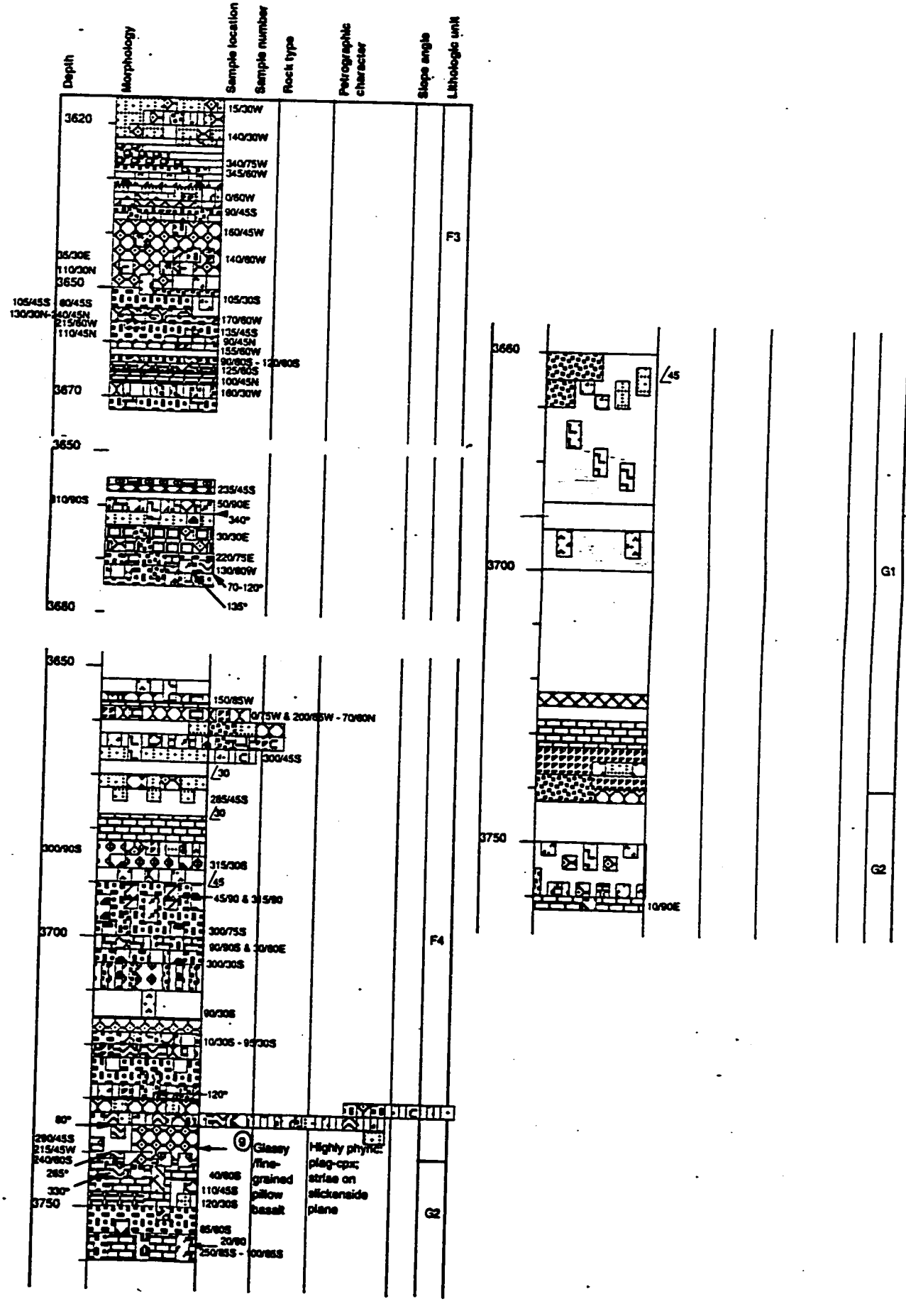

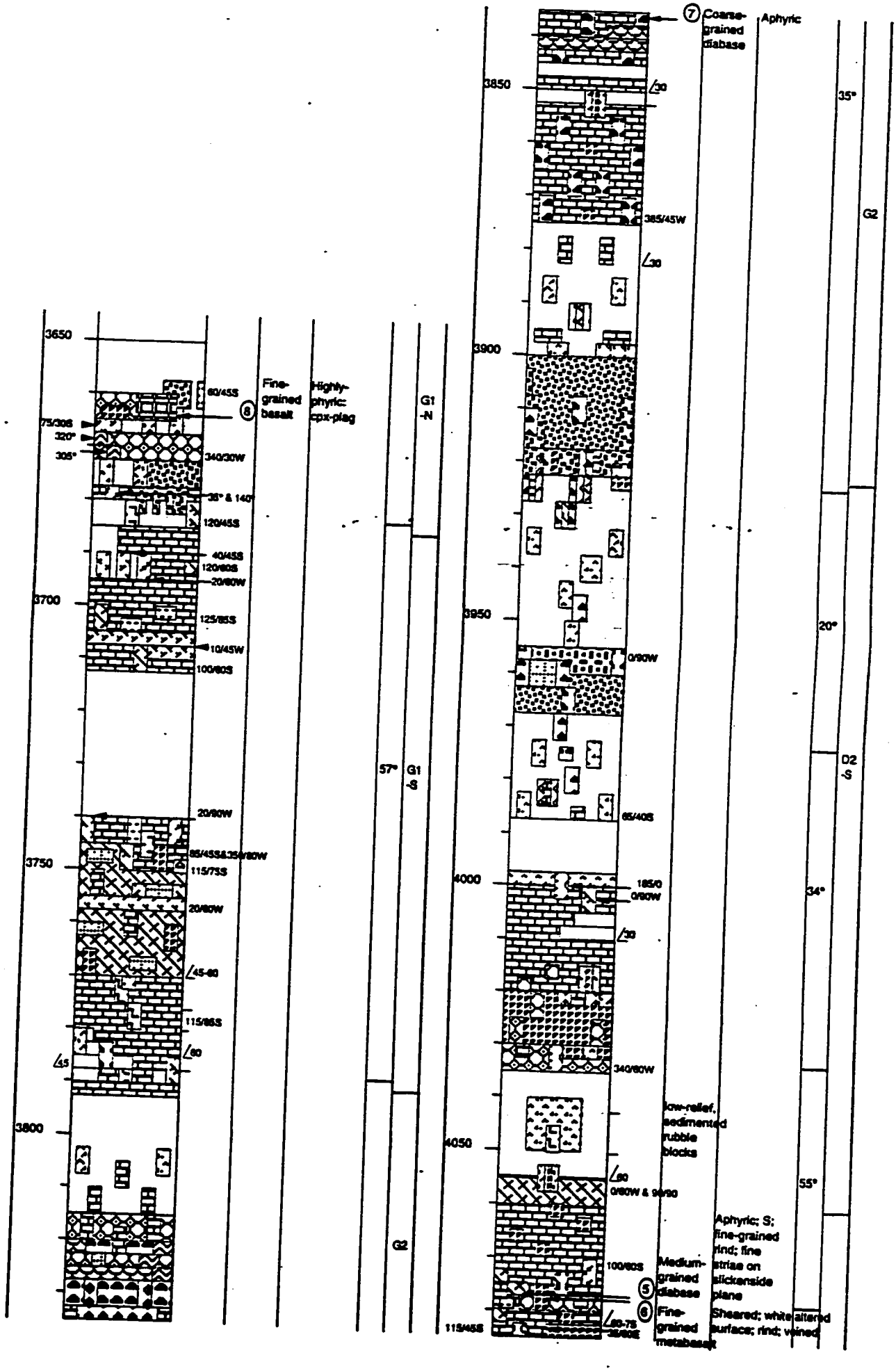
3650
3700
3750
3800
3850
3900
3950
4000
4050
60/45S
75/30S
320°
305°
340/30W
38° & 140°
120/45S
40/45S
120/60S
20/60W
125/85S
10/45W
100/60S
20/80W
85/45S&35/80W
115/75S
20/80W
45-60
115/65S
80
45
Fine-grained basalt
8
Highly-phyric: cpx-plag
G1 -N
57°
G1 -S
G2
7
Coarse-grained diabase
Aphyric
30
385/45W
30
0/90W
65/40S
185/0
0/80W
30
340/80W
low-relief, sedimented rubble blocks
80
0/80W & 90/90
100/60S
5
Medium-grained diabase
6
Fine-grained metabasalt
115/45S
80-75
35/60S
35°
G2
20°
D2 -S
34°
55°
Aphyric; S; fine-grained rind; fine striae on slickenside plane
Sheared; white altered surface; rind; veined

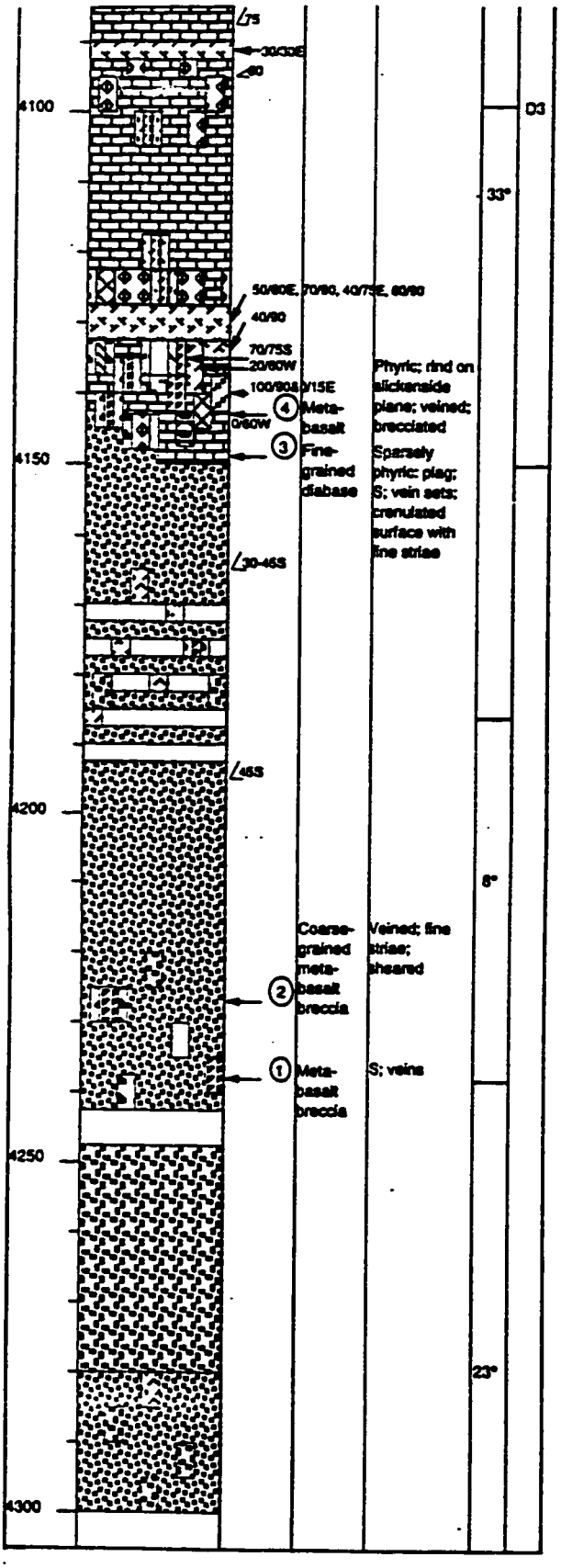
75
30/30E
80
4100
50/60E, 70/80, 40/75E, 60/80
40/80
70/75S
20/60W
100/90S
0/15E
4
Meta-basalt
0/60W
3
Fine-grained diabase
Phyric; rind on slickenside plane; veined; brecciated
Sparsely phyric: plag; S; vein sets; crenulated surface with fine striae
4150
30-45S
45S
4200
Coarse-grained meta-basalt breccia
Veined; fine striae; sheared
2
1
Meta-basalt breccia
S; veins
4250
4300
D3
33°
8°
23°

Figure B-13: BN-24 STRATIGRAPHIC SECTION

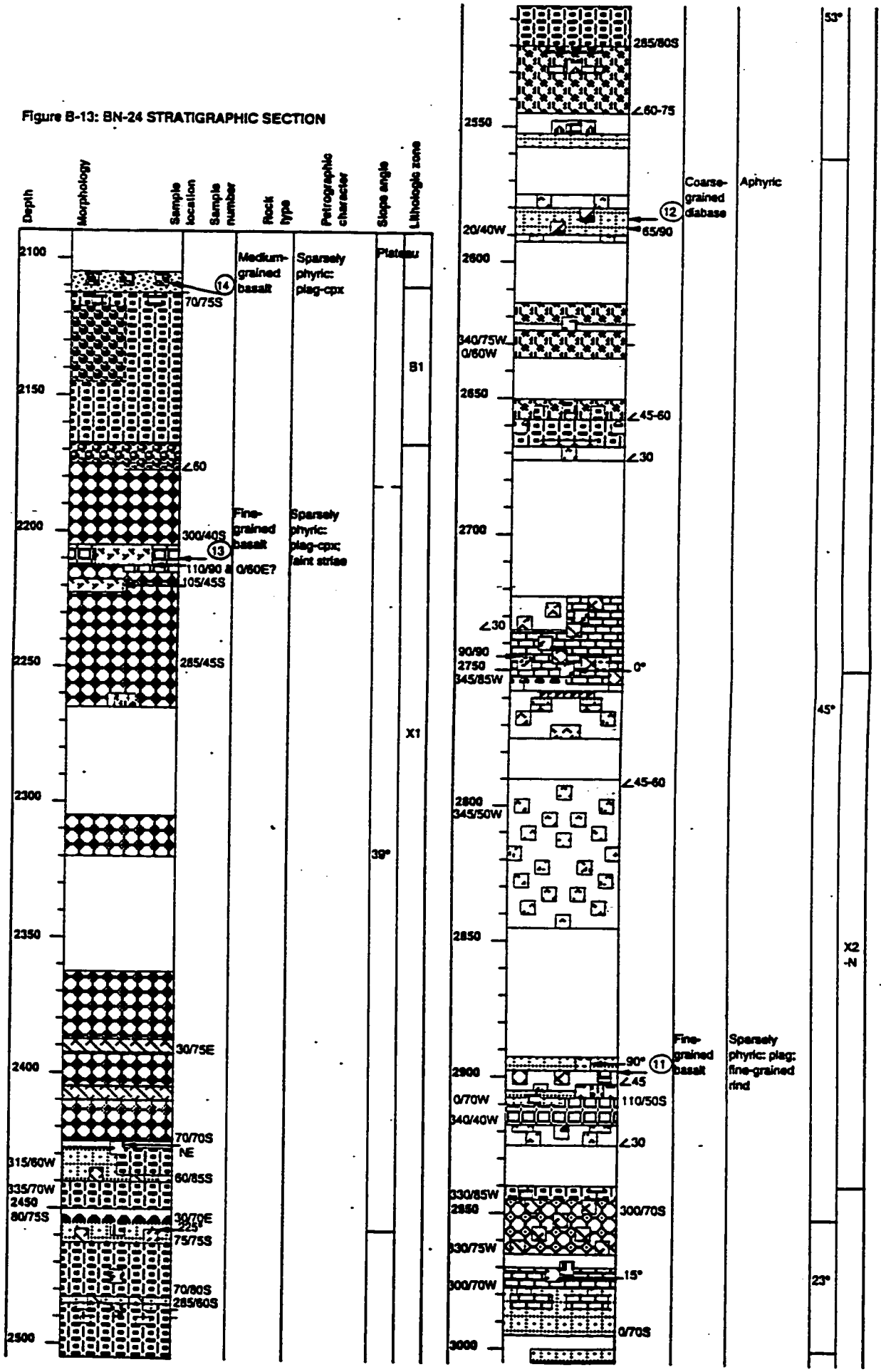

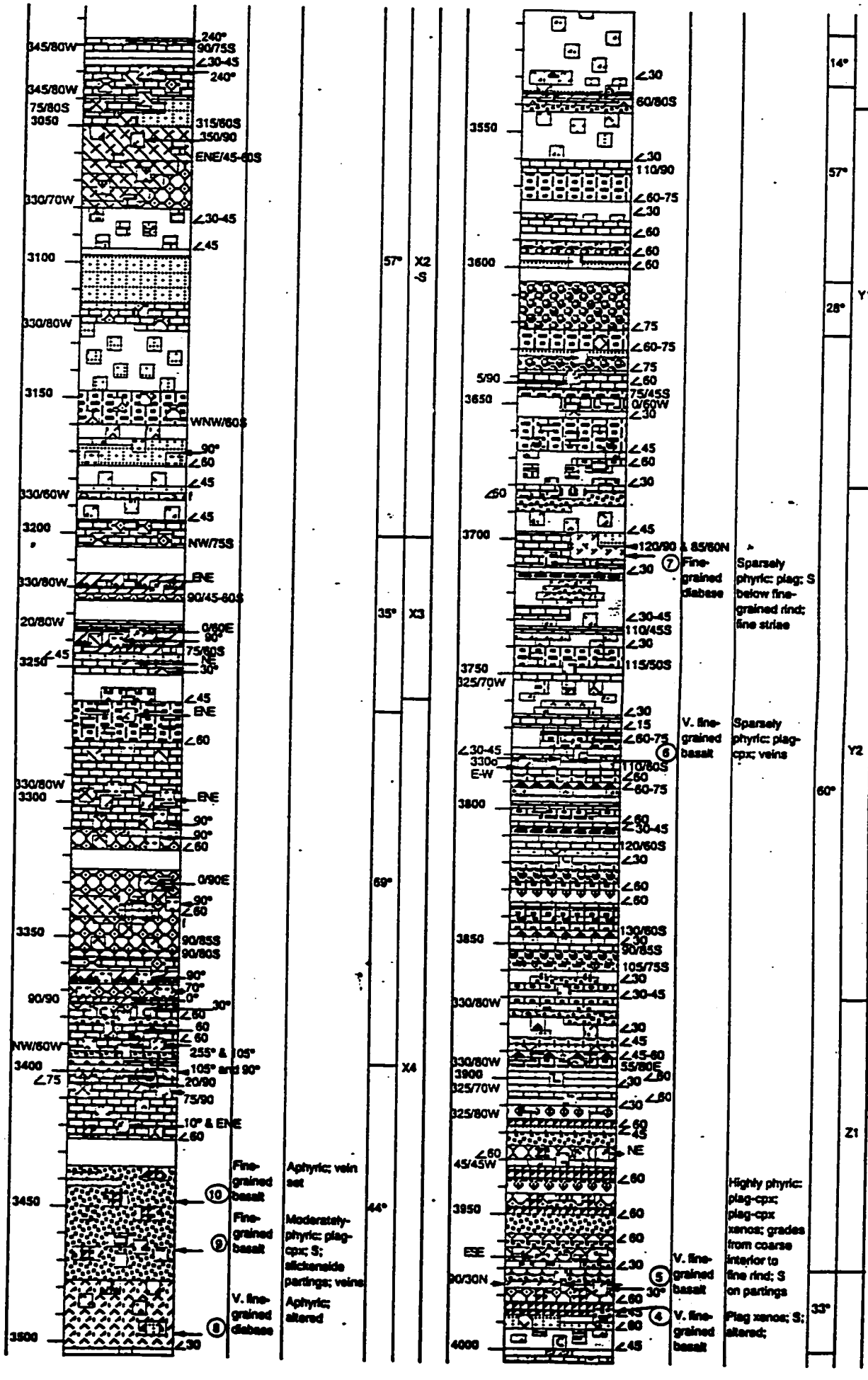
345/80W
240°
90/75S
∠30-45
240°
345/80W
75/80S
3050
315/80S
350/90
ENE/45-60S
330/70W
∠30-45
∠45
3100
330/80W
3150
WNW/60S
90°
∠60
∠45
330/60W
∠45
3200
NW/75S
330/80W
ENE
90/45-60S
20/80W
0/80E
90°
75/80S
3250
∠45
NE
30°
∠45
ENE
∠60
330/80W
3300
ENE
90°
90°
∠60
0/90E
90°
∠60
3350
90/85S
90/80S
90°
70°
90/90
0°
30°
∠60
60
∠60
NW/60W
255° & 105°
3400
105° and 90°
∠75
20/90
75/90
10° & ENE
∠60
Fine-grained diabase
10
3450
Fine-grained basalt
9
V. fine-grained diabase
8
3500
∠30
Aphyric; vein set
Moderately-phyric; plag-cpx; S; slickenside partings; veins
Aphyric; altered
57°
X2
S
35°
X3
69°
X4
44°
∠30
60/80S
3550
∠30
110/90
∠60-75
∠30
∠60
∠60
3600
∠60
∠75
∠60-75
∠75
5/90
∠60
75/45S
3650
0/60W
∠30
∠45
∠60
∠30
∠60
∠45
3700
120/90 & 85/60N
7
Fine-grained diabase
∠30
∠30-45
110/45S
∠30
115/50S
3750
325/70W
∠30
∠15
V. fine-grained basalt
∠60-75
6
∠30-45
330°
E-W
110/80S
∠60
∠60-75
3800
∠60
∠30-45
120/60S
∠30
∠60
∠60
130/80S
∠30
3850
90/85S
105/75S
∠30
330/80W
∠30-45
∠30
∠45
∠45-60
330/80W
55/80E
3900
∠30
∠80
325/70W
∠30
∠80
325/80W
∠60
45
NE
∠60
45/45W
∠60
3950
∠60
∠60
ESE
∠30
V. fine-grained basalt
5
90/30N
30°
∠60
∠45
4
V. fine-grained basalt
∠60
4000
∠45
Sparsely phyric: plag; S below fine-grained rind; fine striae
Sparsely phyric: plag-cpx; veins
Highly phyric: plag-cpx; plag-cpx xenos; grades from coarse interior to fine rind; S on partings
Plag xenos; S; altered;
14°
57°
28°
Y1
Y2
60°
Z1
33°

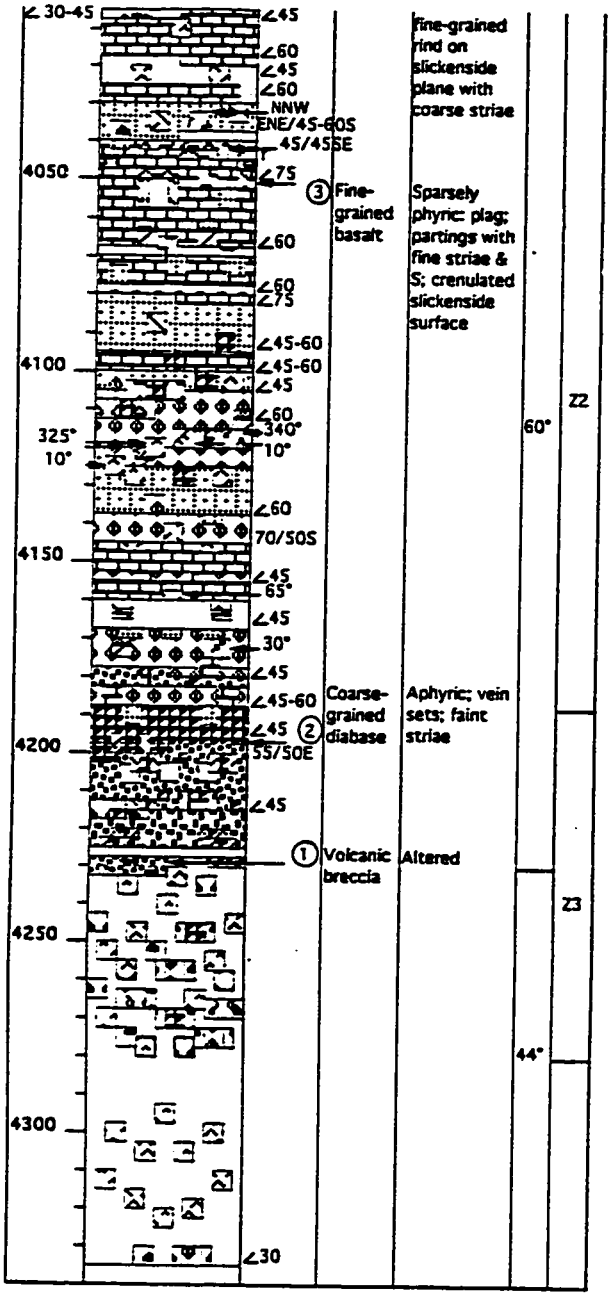
∠30-45
∠45
∠60
∠45
∠60
NNW
ENE/45-60S
45/45SE
4050
∠75
③ Fine-grained basalt
Sparsely phyric: plag; partings with fine striae & S; crenulated slickenside surface
∠60
∠60
∠75
∠45-60
4100
∠45-60
∠45
∠60
325°
10°
340°
10°
∠60
70/50S
4150
∠45
65°
∠45
30°
∠45
∠45-60
Coarse-grained diabase
Aphyric; vein sets; faint striae
∠45
② diabase
4200
55/50E
∠45
① Volcanic breccia
Altered
4250
4300
∠30
fine-grained rind on slickenside plane with coarse striae
60°
44°
Z2
Z3

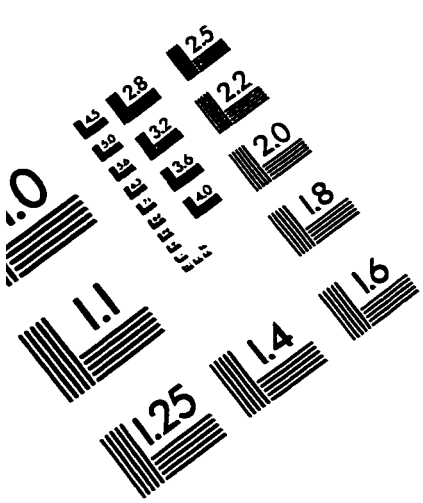

IMAGE EVALUATION
TEST TARGET (QA-3)

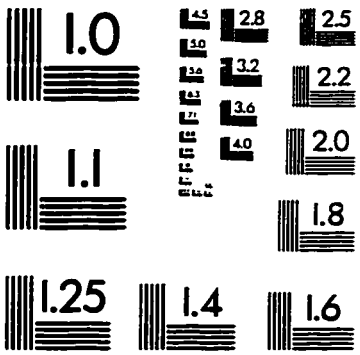

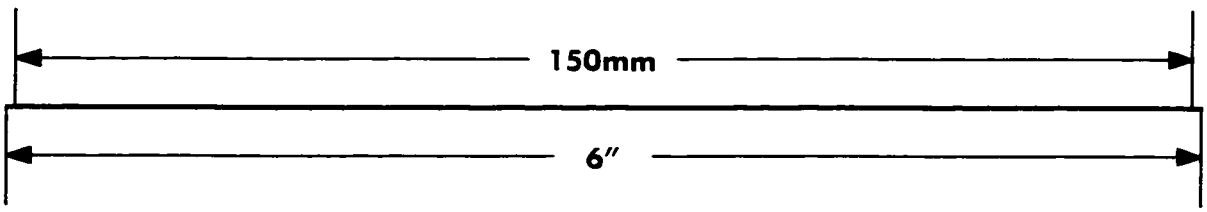

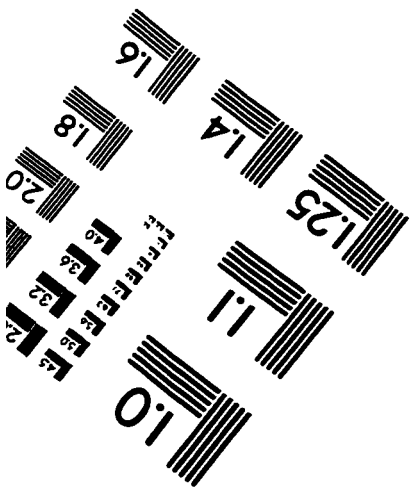

APPLIED IMAGE, Inc
1653 East Main Street
Rochester, NY 14609 USA
Phone: 716/482-0300
Fax: 716/288-5989